DOE/CE/41000-3

MELT INFILTRATED CERAMIC COMPOSITES (HIPERCOMP®) FOR GAS TURBINE ENGINE APPLICATIONS

Continuous Fiber Ceramic Composites Program
Phase II Final Report
for the Period May 1994 - September 2005

By
Gregory S. Corman and Krishan L. Luthra
GE Global Research

Principle Investigator: Krishan L. Luthra

Contract Monitors: Joseph Mavec, Paul Bakke and Donald Geiling

January, 2006

Work Performed Under Contract DE-FC26-92CE41000

For
U.S. Department of Energy
Office of Energy Efficiency and Renewable Energy
Washington, D.C. 20585

Submitted By
GE Global Reasearch
High Temperature Ceramics Laboratory
Niskayuna, NY 12309

DISCLAIMER

DOE/CE/41000-2

MELT INFILTRATED CERAMIC COMPOSITES (HIPERCOMP™) FOR GAS TURBINE ENGINE APPLICATIONS: PHASE II FINAL REPORT

Continuous Fiber Ceramic Composites Program
Phase II Final Report
for the Period May 1994 – September 2005

By
Gregory S. Corman and Krishan L. Luthra
GE Global Research

Principle Investigator: Krishan L. Luthra
DOE Contract Monitors: Joseph Mavec, Paul. Bakke, and Donald Geiling

January, 2006

Work Performed Under Contract DE-FC26-92CE-41000

Prepared for
U.S. Department of Energy
Office of Energy Efficiency and Renewable Energy
Washington, D.C. 20585

Prepared by
GE Global Research
High Temperature and Structural Ceramics Laboratory
Niskayuna, NY 12309

ABSTRACT

This report covers work performed under the Continuous Fiber Ceramic Composites (CFCC) program by GE Global Research and its partners from 1994 through 2005. The processing of prepreg-derived, melt infiltrated (MI) composite systems based on monofilament and multifilament tow SiC fibers is described. Extensive mechanical and environmental exposure characterizations were performed on these systems, as well as on competing Ceramic Matrix Composite (CMC) systems. Although current monofilament SiC fibers have inherent oxidative stability limitations due to their carbon surface coatings, the MI CMC system based on multifilament tow (Hi-Nicalon™) proved to have excellent mechanical, thermal and time-dependent properties. The materials database generated from the material testing was used to design turbine hot gas path components, namely the shroud and combustor liner, utilizing the CMC materials. The feasibility of using such MI CMC materials in gas turbine engines was demonstrated via combustion rig testing of turbine shrouds and combustor liners, and through field engine tests of shrouds in a 2MW engine for >1000 hours. A unique combustion test facility was also developed that allowed coupons of the CMC materials to be exposed to high-pressure, high-velocity combustion gas environments for times up to ~4000 hours.

TABLE OF CONTENTS

1 EXECUTIVE SUMMARY

Ceramic Matrix Composites (CMCs) are a revolutionary new class of materials that potentially represent a game changing technology in the power generation industry. CMC's offer substantially higher material operating temperatures than are possible with metallic alloys. GE has invented silicon carbide fiber reinforced SiC-Si matrix composites, commonly referred to as Melt Infiltrated (MI) composites, which are particularly attractive for hot stage components of industrial and aircraft gas turbines. These materials offer the potential to improve the efficiency of gas turbines, lower the cost of electricity, and reduce harmful NOx and CO_2 emissions. DOE sponsorship of the development of this composite system is partly responsible for its now being commercially available from GE Ceramic Composite Products under the HiPerComp® trade name.

GE has been working with the Department of Energy on the development of Melt Infiltrated composites under the Continuous Fiber Ceramic Composites (CFCC) program since 1992. The development of MI-CMC's started with material and process development, first under Phase 1 starting in 1992 and then under Phase 2 starting in 1994. Results from the Phase 1 program have been summarized in previous reports (references 3 and 4). Since then the program has been focused on reducing the risk of CMC product introduction by providing for the collection of material database information, long-term material testing experience, and the opportunities to perform rig and engine testing of turbine components, although material development work continued throughout the entire program. The accomplishments realized under the CFCC program led to further development and demonstration of CMC turbine components under the DOE-sponsored Advanced Materials for Advanced Industrial Gas Turbines (AMAIGT) program, DOE project number DE-FC26-00CH11047.

The particular components of interest for the CFCC program were the turbine shroud and combustor liner, but the technology developed could also be applied to other stationary hot stage components. GE's installed base of over 1000 advanced gas turbine engines provides a ready market for introduction of such CMC turbine components. The use of CMCs in stationary hot stage components such as shrouds, combustor liners, and nozzles could provide an improvement of up to 1.1 percentage points in simple cycle efficiency beyond the current efficiency of ~34%. Furthermore, the use of CMCs in all of these types of components could increase the output by up to 3%, thereby further reducing the cost of electricity. Assuming a growth rate of 6% per year and a market penetration of 20% by 2020, the use of CMCs in gas turbines offers the potential to save annually ~290 trillion BTU of energy, which is equivalent to ~0.29 trillion cubic feet of natural gas at a cost of ~$960 million. The use of CMCs also offers the potential to save ~4.3 million metric tons carbon equivalent (MTCE) of CO_2 emissions and ~51,000 metric tons (MT) of NOx emissions per year.

The MI composite developed partly under the CFCC program is made by melt infiltration (MI) of liquid silicon into carbonaceous preforms containing coated silicon carbide

fibers. The composite is fully dense, and the process has a near-net complex shape capability. The material offers good oxidation resistance, high thermal conductivity (comparable to cast iron), low thermal expansion (one-third that of metal), and excellent thermal shock resistance. These properties make it very attractive for a variety of high temperature structural applications.

The development process of a new class of potentially revolutionary materials, such as CMCs, for large industrial gas turbines is complex. It involves development of materials in the laboratory, rig tests that simulate the engine conditions, small engine testing (to reduce the risk), and finally field tests in a commercially operating engine. GE and DOE have been working on all aspects of this development. The various major activities and overall development path are summarized in Figure 1-1.

Initially, processes were developed for the fabrication of MI CMCs. Laboratory testing of these materials was performed, which was followed by combustion rig testing of shrouds and combustor liners that simulated the conditions in a large industrial turbine. The rig testing was very successful with CMC components surviving the extreme gas temperatures of up to 1540°C and material temperatures up to 1200°C. Metal components used for comparison failed in a very short time. Rig testing was followed by successful engine testing of first and second stage shroud components in a 2MW machine for over 1000 hours at a GE facility in Italy. Concurrent material development activities were focused on long-term environmental exposure testing of MI CMCs under engine-like conditions in a high pressure combustion rig, and the establishment of a material property database for use in component design.

Unfortunately the current high cost of MI CMC materials limits their use to applications, such as the hot stage components of gas turbine engines, where the payoff in terms of improved turbine performance exceeds the added material cost. The technology developed here could also be applicable to commercial and military aircraft engines and other military applications requiring high temperature structural materials. Once the gas turbine uses have matured, the cost of these materials will come down because of the increased production volume. This will provide opportunities in other high temperature and more cost sensitive applications, such as various types of heat exchangers and recuperators.

The technology development path described above was a risk-reducing, step-wise approach to CMC material development aimed at demonstrating the feasibility of CMC use in Power Generation equipment. This approach minimizes the burden of risk of the high payoff CMC technology for the power generation industry, and will enable them to continue to provide the reliable, low cost electricity supply that the US public consumers demand.

During the performance of Phase 2 of this contract many important milestones were successfully completed. Some of the more important achievements are listed below:

- The MI CMC system and process developed in Phase 1, based on SiC monofilament reinforcing fibers, was further optimized. New fiber coating systems and matrix compositions were demonstrated and characterized.
- Detailed interface oxidation studies of monofilament-reinforced MI CMCs clearly demonstrated the negative consequences that carbon surface layers on the fibers have on composite oxidation life. Since a short-term solution for eliminating such carbon layers on existing SiC monofilament fibers was not available further development of the monofilament system was halted.
- A second MI CMC material and process, referred to as prepreg MI CMCs or HiPerComp®, using small diameter fibers in the forms of multifilament tow (such as Hi-Nicalon™ fiber) was developed and optimized. (The term prepreg is borrowed from organic composite terminology, and refers to sheets or tapes of fiber that are "pre-impregnated" with matrix constituents prior to lay-up into the shaped parts. In this report "prepreg" will also be used to designate a type of MI CMC where formation and lay-up of prepreg tapes is part of the overall fabrication process.) This CMC system had the advantage of not requiring carbon interface layers on the fibers, and also allowed for greater shape capability compared to the monofilament reinforced system. This composite system provides the highest mechanical properties for a given level of reinforcing fiber, as well as the highest overall thermal conductivity and interlaminar strength properties, of any CMC system of which we are aware.
- A primary need for the development of the fine fiber reinforced CMC system was the establishment of a source for fiber coatings on tow-based fibers. The coating of fine diameter, tow-based fibers using chemical vapor deposition (CVD) was investigated with four separate coating vendors: Advanced Ceramics Corp., 3M, Synterials, Inc., and General Atomics. Fiber coatings from Synterials, 3M and Advanced Ceramics Corp. were all shown to be capable of producing strong, tough MI composites. The performance of coatings from ACC were the most consistent, and consequently were developed and optimized to a greater degree than fiber coatings from the other vendors. Unfortunately, ACC made a decision to leave the tow coating business, requiring GE to develop a tow coating system in-house.
- A continuous tow coating process was developed at GEGR to handle multiple tows in a compact reactor. This CVD reactor was used to further optimize the fiber coating configuration and composition. A larger scale tow coater was subsequently designed and built at GEGR, having 5X the capacity of the small coater and 2X the capacity of ACC's production reactor. The fiber coating process in this reactor was developed to the point where it was giving comparable quality composites as the smaller tow coater.
- The mechanical and thermal properties of the prepreg MI composite system were extensively characterized, including measurements of the fast fracture properties, thermal stability, fatigue, creep, thermal cycling resistance, thermal conductivity and thermal expansion. This effort provided a valuable material property database for component designers.
- Methodology for testing CMC materials under high water vapor (i.e. steam) atmospheres was developed. Such cyclic steam furnace exposure testing proved to

be highly valuable in screening CMC material candidates for use in gas turbine environments, for validating SiO_2 volatilization rate models, and for identifying CMC degradation mechanisms related to steam exposure.

- A methodology for evaluating the "foreign object damage" susceptibility of the CMC materials, based on ballistic impact testing, was developed and utilized to evaluate the damage initiation and damage propagation properties of CMC materials.
- A preliminary shroud design was developed that had reduced stresses and improved manufacturability over the conceptual design developed in Phase 1. CMC inner shroud components were fabricated by GE and by subcontractors to the preliminary design using seven CMC systems. Overall 33 CMC inner shroud components were fabricated for this program.
- A combustion test rig, capable of operating at similar pressures and higher temperatures than those seen in a GE 7FA class engine, was designed and fabricated at GEGR. The rig was capable of testing four CMC shrouds, a CMC combustor liner, and up to 24 CMC test coupons to high temperature, high pressure and high gas velocity conditions simultaneously. The shroud test rig was operated for over 300 hours of hot component testing, with 27 CMC and 2 metal shrouds being tested. Post rig test nondestructive and destructive characterization was done on most of the rig-tested shrouds, and the changes in shroud mechanical properties and microstructures were evaluated.
- The design process for a third generation CMC shroud was started under the CFCC program, but was then transitioned to the DOE-sponsored Advanced Materials for Advanced Industrial Gas Turbines program.
- A conceptual design for a CMC combustor system for a GE Frame 5 (35 MW) engine was developed. A rig test combustor liner configuration was developed, based on the combustor conceptual design, that was capable of testing two sections of CMC liner simultaneously. A prepreg MI combustor liner was fabricated at GEGR, and a slurry cast MI liner was fabricated by GE Ceramic Composite Products (then known as Allied Signal Composites). The CMC combustor liners were successfully rig tested for 150 hours of hot exposure, both under cooled and uncooled conditions.
- Designs for both stage 2 and stage 1 shroud rings for a GE Oil and Gas GE-2 engine (then known as Nuovo Pignone PGT-2) were developed and analyzed. First and second stage shroud rings were fabricated at GEGR using the GE prepreg MI composite system. Engine testing of the shroud rings was carried out for >1000 hours of engine running time. Both shrouds experienced blade tip rub events during the preliminary testing without any damage being caused to the CMC shroud rings. The survival of the shroud rings through such an event dramatically demonstrated the durability and damage resistance of the CMC material.
- A unique, long-term test facility for exposing coupon samples to a high pressure, high velocity, combustion gas environment was designed and constructed at GEGR. This facility is highly automated and capable of safe, extended operation without operator intervention. The durability of the rig was maximized through

the utilization of an all-CMC hot section. Eight sets of combustion rig tests were performed, totaling roughly 6500 hours of test rig fired hours. Several individual test samples were exposed for up to 3922 hours. Post-exposure characterization of the coupons from the long-term exposure rig provided valuable information about the thermal and oxidative stability of bare and EBC-coated CMC samples.

Overall GE considers its participation in the CFCC program to have been a resounding technical success. The successes of the shroud and combustor component rig tests, and of the GE-2 shroud ring engine tests, dispelled much of the skepticism within the turbine design community at GE toward ceramic materials. The acceptance of CMC technology at GE Energy was demonstrated by the willingness of that organization to participate in the AMAIGT program and eventually push the CMC shroud to a field engine test in an F-class (160MW) engine, which was the first ever test of a ceramic component in a GE industrial turbine.

The program has also been highly successful in disseminating information about the fabrication and use of CMC materials. Patents, presentations and publications related to the work performed on the CFCC Phase 2 program are listed in the Appendix.

Development Path for Introducing CMCs into Gas Turbine Engines

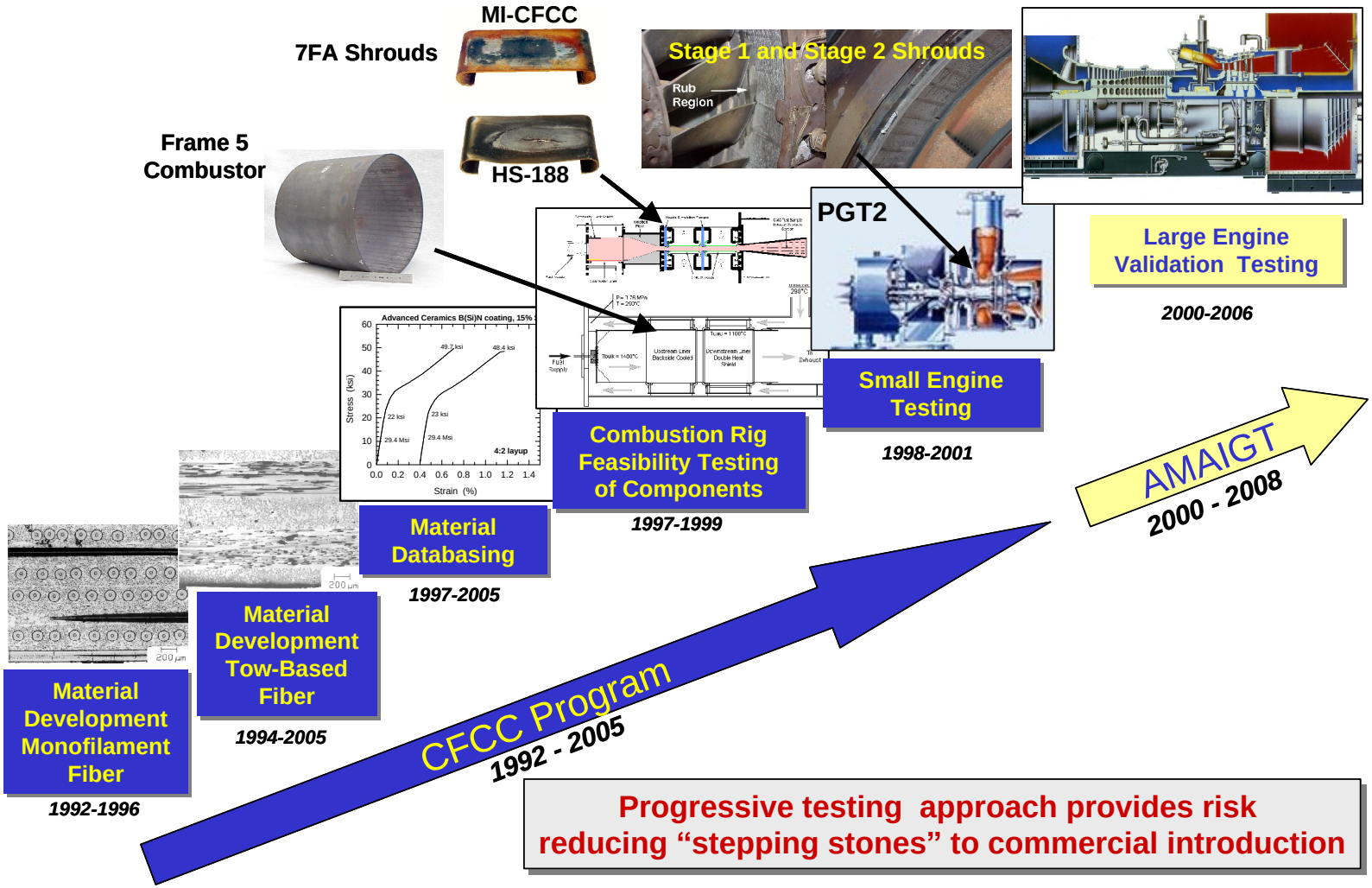

Figure 1-1. Schematic representation of the material and component development path and major activities performed by GE during the CFCC program and leading into the AMAIGT program.

2 INTRODUCTION AND BACKGROUND

Improvements in gas turbine engine performance have historically followed developments in materials and cooling technologies that have allowed engines to operate at higher and higher firing temperatures. It is commonly recognized that superalloy components are currently operating at their temperature limits and that a new materials and/or cooling technology will be needed for further improvements in engine performance. Ceramic materials have long been considered the next step in turbine materials technology. Ceramics, in the form of zirconia-based thermal barrier coatings (TBCs), are currently in use in many gas turbine engines; however, utilization of ceramics as structural components has not been commercially adopted.

The major barrier to utilization of ceramic components has been the risks associated with catastrophic failure, which is typical of monolithic ceramics. In order to alleviate these risks there has been substantial research on the development of continuous fiber reinforced Ceramic Matrix Composites (CMCs) over the last 25 years. CMCs are a relatively new class of materials that combine the refractoriness and environmental stability of ceramics with the toughness and damage tolerance of composites. The increased toughness and damage tolerance of the CMCs are expected to result in increased reliability of these materials compared to typically brittle monolithic ceramics, thereby making them suitable for a variety of gas turbine engine applications.

There are a variety of turbine hot-gas path components for which CMC materials are attractive candidates. A cross section of a generic GE industrial gas turbine engine is shown in Figure 2-1, which indicates several components for which CMC materials would offer a substantial performance benefit. By allowing for higher firing temperatures and having reduced cooling air requirements, CMC components offer performance benefits can be realized in terms of higher turbine efficiency, greater power output, lowered pollutant emissions, and improved component reliability. By DOE estimates[1], a new gas turbine completely redesigned to utilize CMCs for the components indicated in Figure 2-1 could reduce overall turbine fuel consumption by 13% and reduce NOx, CO and unburned hydrocarbon (UHC) emissions by over 75%.

The selection of components for implementation under the Continuous Fiber Ceramic Composite (CFCC) program was done by considering the potential benefit of each component compared to the level of risk. Although first stage turbine buckets have the greatest potential benefit to the overall engine cycle they also represent the greatest challenge in that substantial centrifugal and aerodynamic stresses are present in addition to thermal stresses. The two components selected were the first stage shroud and the combustor liner. The introduction of ceramic composites for these components was judged to entail relatively low risk while producing very substantial efficiency and emission benefits. The engine platform selected as a reference for evaluation of the CMC components is the MS7001FA, a 160MW industrial gas turbine used primarily for generation of electricity[2].

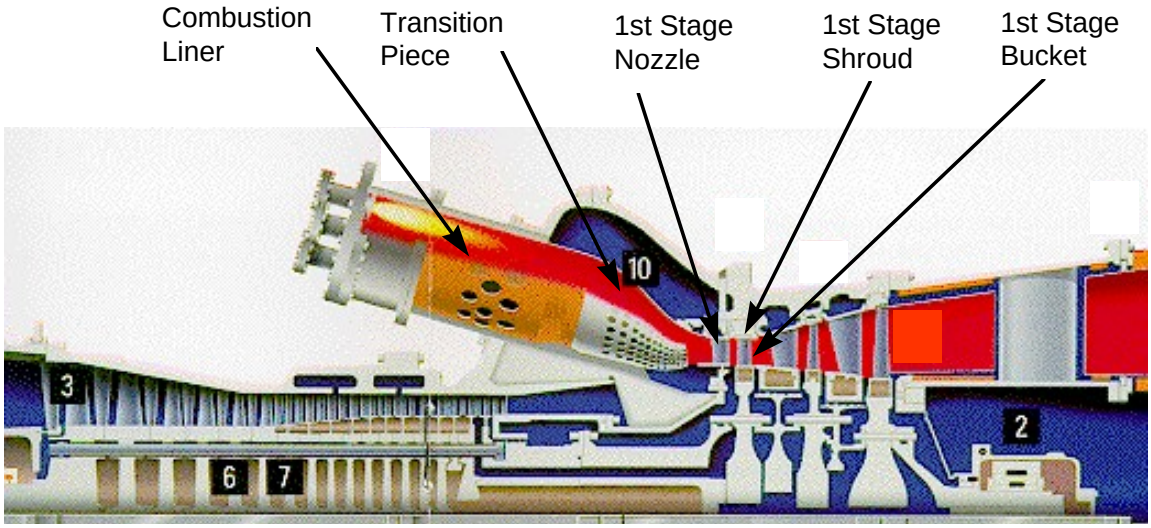

Figure 2-1. Cut-away view of one half of a typical industrial gas turbine engine showing the positions of several components for which CMC materials would be beneficial.

The prime material of interest for these applications is GE's silicon melt infiltrated, SiC-SiC/Si composite system, which is currently named HiPerComp® although the older versions based on monofilament fibers were generally referred to as "Toughened Silcomp" in the past. The specific fabrication approach developed at GE Global Research (GEGR) under the CFCC program is based on wet drum winding of coated monofilament fibers or fiber tows to form unidirectional prepreg tapes, lamination of the tapes to form a composite preform, and silicon infiltration of the preform to yield a near-net-shape CMC component. This process was initially developed using monofilament SiC fiber (Textron's SCS-6 and SCS-9) in Phase I of this program, and then modified in Phase II to utilize multifilament tow fibers, such as Hi-Nicalon™. In this report this fabrication process will be referred to as the "prepreg MI" process. Major advantages of the silicon melt infiltrated (MI) composites are high matrix density, which gives the composite high matrix cracking strength, high interlaminar strengths and high thermal conductivity, relatively short processing times, and near-net-shape fabrication capability.

A related process for making MI composite preforms is the slurry casting process developed under the High Speed Civil Transport - Enabling Propulsion Materials program. Although the specific fabrication steps of this process differ from those of the GE prepreg MI process, the resulting composites are nearly identical in composition and have very similar mechanical and thermal properties. This later process developed under the HSCT program will be referred to as the "slurry cast MI" process, and materials made via this process are also commercially available under the HiPerComp® name from GE Energy Ceramic Composite Products (CCP). Differences between the two fabrication processes are shown schematically in Figure 2-2.

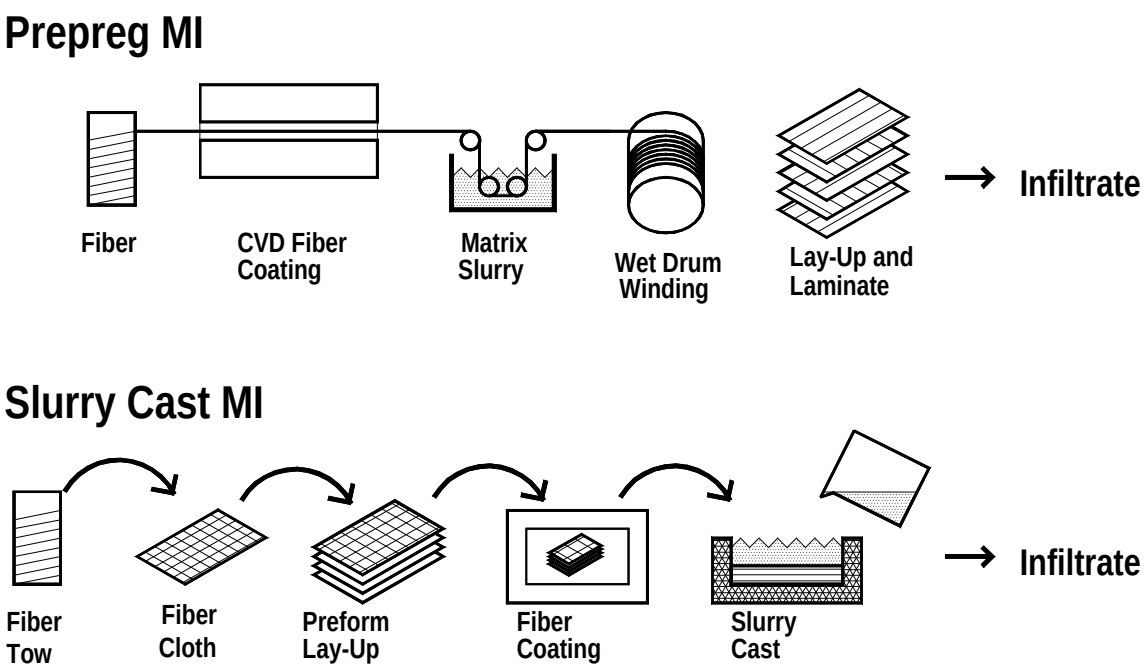

Figure 2-2. Schematic representations of the prepreg MI and slurry cast MI composite preform fabrication processes.

GEGR has been actively developing MI ceramic composites for gas turbine applications since 1992 under the U.S. Department of Energy CFCC program. This report describes the progress made during Phase II of this program from May 1994 through September 2005.

2.1 Application Requirements

The requirements on the materials used for first stage shrouds and combustor liners in a MS7001FA engine are quite severe. Life requirement, in particular, are very demanding. Turbine components for base-load machines must be able to withstand the turbine combustion gases at pressures of up to ~14 atmospheres and gas temperatures of up to 1500ºC for a minimum of 24,000 hours (combustor) to 48,000 hours (shroud). The actual component temperatures are well below the hot gas temperatures because of the backside convective and impingement cooling and film cooling techniques used. Nevertheless, with reduced cooling of CMC components the material surface temperatures are expected to reach as high as 1200ºC. Because of the long life requirements for these components a detailed understanding of composite environmental stability is necessary for acceptance of these materials.

Other requirements include the ability to withstand up to 500 thermal cycles (both normal start-stop cycles and emergency shut-downs, or trips), and possible operation at partial

load. More details regarding the operational requirements of CMC components can be found in references [3] and [4].

2.2 Status at the End of Phase I

The status of our CFCC program was described in detail in the Phase I final report[3], so that only a summary will be given here. Highlights of the progress made during Phase 1 are as follows:

- Operational benefits for using CMC combustor liners and first stage shrouds in an MS7001FA class turbine include up to a $830k reduction in fuel costs per year per machine along with significant reductions in NOx, CO and UHC emissions.
- Preliminary conceptual designs for both the shroud and combustor liner were generated and analyzed using standard FEM techniques.
- Of the material systems evaluated, which included DuPont-Lanxide Composites' (Allied Signal Composites') DIMOX Al_2O_3-SiC and CVI Enhanced SiC-SiC, Amercom's CVI SiC-SiC, Babcox and Wilcox (McDermott Technologies') Oxide-Oxide and GE's Toughened Silcomp SiC-SiC/Si (prepreg MI), only the prepreg MI material met all of the short-term material property requirements for these applications.
- Textron Specialty Materials was established as a continuous fiber coatings vendor for SCS-6, SCS-9 and SCS-0 monofilament SiC fibers.
- Composite fabrication using wet drum winding of continuous lengths of SCS-6 and SCS-9 fiber was demonstrated. This process replaced a laborious process of batch coating of short fiber lengths followed by hand alignment of the fibers and tape casting of the matrix.
- Drum wound 0º-90º crossply composites made using the standard BN-based fiber coating on SCS-6 fiber showed a 20% increase in matrix cracking stress and a 2X increase in ultimate strength compared to pre-CFCC materials due to process improvements and the introduction of a continuous fiber coating process.
- A new fiber coating based on Si_3N_4 was demonstrated for SCS-6 fiber, and was shown to give a 50% improvement in matrix cracking stress and 75% increase in ultimate strength compared to pre-CFCC material.
- Drum wound cylinders were demonstrated and found to have properties comparable to those of flat panel composite specimens.
- Variations in the level of residual silicon in the composite matrix, from 15% to 30%, were found to have little impact on composite properties. This result indicated that tight control of preform carbon content was not necessary and that the process has a relatively wide processing window.

2.3 Needs for Phase II

The long design lives of the selected components require that the steady-state operation of the components be below the first matrix cracking strain/stress. Even though composites will be designed for operation below the first matrix cracking strain/stress, matrix cracking will result from accidental loading beyond the first matrix cracking strain. Under these

conditions, the load will relax after such an event, and subsequent exposure will occur at strains below the first matrix cracking strain. Although the crack opening displacement will reduce with a reduction in load, we believe the cracks will still stay open. Therefore, prevention of oxidation of the fiber and fiber-matrix interface is still of paramount importance to meet component life goals.

Three main approaches were envisioned to deal with the interface stability issue. First, elimination of carbon at the fiber-matrix interface would be necessary. Carbon, in the form of a multi-layer fiber coating, is a constituent of the SCS-6 and SCS-9 fibers used in Phase I. Because carbon is rapidly oxidized and forms only gaseous oxidation products it is considered to be impractical for long-term, high temperature applications. Carbon interface layers would be eliminated by using other fibers, either monofilaments such as SCS-0 or fiber tows such as Hi-Nicalon, which do not have such carbon surface layers.

Secondly, an oxygen getter and crack sealant can be added to the composite matrix. By gettering the oxygen that may penetrate a matrix crack, and rapidly oxidizing to seal the matrix crack, such an additive would minimize the amount of exposure of the fiber-matrix interface to the environment, and thereby minimize mechanical degradation of the composite caused by this exposure.

Thirdly, improving the inherent oxidation resistance of the coating is desirable. Initial fiber coatings in Phase I were based on BN. Boron nitride is much more stable than carbon to oxidizing environments, but its oxidation products can still be highly volatile, especially in the presence of water vapor as is common in combustion gases. Thus fiber coatings that are more oxidation resistant than BN, such as silicon nitride or other materials, would be desirable to minimize the oxidative degradation of the interface before the matrix getters could seal any accidental cracks.

Another need from Phase I was the need for additional component design effort. The designs that emerged from the Phase I evolved from the use of metallic systems and were generic, i.e., they were not optimized to take advantage of the unique properties of CMCs. The designs also incorporated some features that were anticipated to be difficult to fabricate in a CMC. It was therefore desirable in Phase II to first fabricate the components as designed in Phase I to learn the shape limitations of the fibers and process, and to provide guidance to the development of new designs that would have lower material strength requirements and would be easier to fabricate. However, the rigorous design of an optimized CMC component would require a large amount of composite property data that was not available in Phase I. Generation of a property database for the improved material of Phase II would be required to proceed to more detailed design and engine testing of components in the future.

Another important issue that arose during the course of Phase II has to do with stability of silicon-based ceramics in high-pressure combustion atmospheres. The main constituent of many CMC materials, such as prepreg MI composites, is SiC, which relies on the formation of a protective oxide layer of SiO_2 to limit high temperature oxidation. However, it has now been well established [5,6] that silica forms volatile silicon hydroxide

species in the presence of water vapor at high temperatures. Typical ceramic hardware for turbine applications are expected to operate with surface temperatures in the range of 1000° to 1200°C, and the combustion gas atmosphere in a turbine typically contains water vapor at a partial pressure of 0.5 to 1 bar. Under these conditions the volatilization rate of the protective silica layer occurs at a sufficient rate that paralinear oxidation of the base SiC or Si_3N_4 is observed. In other words, the self-limiting, parabolic oxidation process is replaced by a constant rate oxidation/recession process. The rate of the recession process depends on the turbine operating conditions, including gas velocity, water vapor content of the combustion gases and material temperature. In extreme conditions recession can be as high as 0.5mm per 1000 hours of exposure. The desired life of the CMC components in a large industrial turbine is of the order of 24,000 to 48,000 hours. Since the desired wall thickness of these components is only a few millimeters such a material loss rate would be unacceptable. Consequently it became necessary to better understand and to mitigate this potential life-limiting mechanism.

The overriding need for Phase II was to demonstrate the use of CMC components in gas turbine engines. When a new metallic alloy is introduced into a turbine application the development path often goes directly from initial coupon tests on the alloy to limited insertion of the material into a small or large turbine engine. This approach is possible because the development of new alloys is generally evolutionary in nature, i.e. the new alloys are similar to existing alloys in many aspects, accepted design methodologies for alloy components already exist, and the uncertainty associated with the behavior of the material is often small. However, introduction of a CMC component is more revolutionary in nature because new design approaches need to be implemented, there is often very limited material property data available, and there is no existing experience base on which to build. Consequently the immediate insertion of a CMC component directly into a large turbine engine was judged to be too risky of an approach, especially considering the very high costs associated with machine downtime and repair.

Because of the uncertainties associated with the new CMC materials a more conservative path to introduction was required, which included initial component testing in high temperature, high pressure combustion test rigs. This introduction path is shown schematically in Figure 2-3. Such test rigs have been used extensively within GE for the evaluation of the thermodynamic and aerodynamic performance of new combustion and turbine hardware for both GE Energy and GE Aviation. These rigs can simulate many of the conditions of the actual turbine engines, including combustion gas composition, temperature, pressure and flow rate. Adaptation of such combustion rigs for the exposure of CMC shrouds and combustors to turbine-like conditions was therefore the next step in the development of these materials. With these tests the response of the CMC materials to the turbine environment would be evaluated. Also, these tests allowed for the verification and validation of the design methodologies and thermal and mechanical analysis tools used.

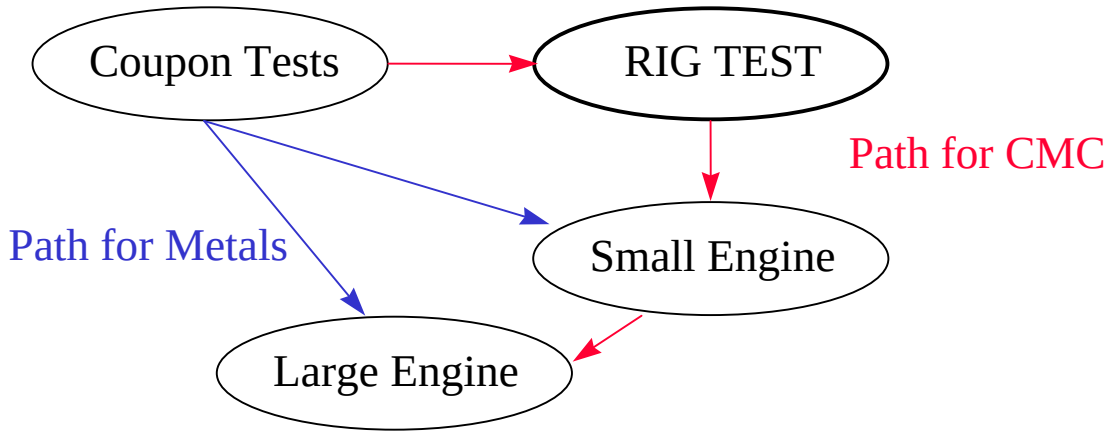

Figure 2-3. Schematic of the development paths for introduction of new materials into a large turbine engine.

2.4 Overall Program Structure

GE's Phase II CFCC program was initially based on the results from Phase 1 and the resulting technical needs, as discussed above. The exact task structure changed considerably over the course of the program to adjust to the changing status of the technology and to the changing priorities of GE Energy. The original Phase II contract was awarded in 1994, and then was amended in 1998 (Phase II Add-On), 1999 (Phase II+) and in 2001.

The overall structure of the program was divided into Tasks as laid out in the original DOE request for proposal. A listing of the individual tasks, when they were added to the program, their status at the end of the program, and the report sections where the work under those tasks are discussed is given in Table 2-1.

Table 2-1. Summary of the Program Task Structure for GE's CFCC Phase II Program

Task Number and Title	When Added to the Program	Status at End of Program	Report Section
1. Application Assessment	Add-On	completed	3.1
3. Materials & Process Development			
3.1. Process Feasibility			
3.1.a. Oxidation Resistant Monofilament System	Phase II	completed	3.2.1
3.1.b. Small Diameter Fiber System	Phase II	completed	3.2.2
3.1.c. Shape Demonstration	Phase II	completed	3.2.1.7, 3.2.2.7
3.2. Process Engineering			
3.2.a. Process/Material Optimization	Phase II	completed	3.2.1, 3.2.2
3.2.a.5. Fiber Coating Cost Reduction and Vendor Qualification	II+	completed	3.2.2.6.2, 3.2.2.2
3.2.a.6. Composite Coating (EBC) Development	II+	completed	3.5
3.2.b. Composite Property Measurement	Phase II, Add-On	completed	3.4
3.2.c. Process Modeling	Phase II	completed	3.6
3.2.d. Process Economics	Phase II	completed	3.7
3.3. Component Fabrication and Testing			
3.3.a. Shroud Feasibility Testing	Phase II	completed	3.8.1
3.3.b. Frame 5 Combustor Liner	Add-On	completed	3.8.2
3.3.c. Testing of Baseline Metallic Frame 5 Combustor	Add-On	completed	3.8.2.1
3.3.d. Long-Term Rig Testing	II+	completed	3.8.4
3.3.e. 2MW Turbine Stage 2 Shroud	II+	completed	3.8.3.1
3.3.f. 2MW Turbine Stage 1 Shroud	II+	completed	3.8.3.2
3.3.g. 5MW Turbine Shroud	II+	dropped	-
3.3.h. 5MW Turbine Combustor	II+	dropped	-
3.3.i. Large Turbine Component (Next Generation7FA Shroud)	II+	completed	3.8.1.10
3.4. Component Evaluation	Phase II	completed	3.8.1.6, 3.8.2.6, 3.8.3.1.4, 3.8.3.2.4
3.5. Composite Joining	Phase II	completed	3.3
5. Report Writing and Program Management	Phase II	completed	-

2.5 Mechanical Testing Definitions

Throughout the material development, testing and characterization efforts of this program the in-plane tensile fracture properties of the CMC material were utilized extensively as indications of the quality of the material and as evidence for material degradation. A description of the fracture behavior of ceramic composites, and of melt infiltrated CMCs in particular, is therefore warranted so that the reader will be familiar with procedures and terminology used throughout this report.

The in-plane tensile fracture response of CMC materials is typically characterized by a stress-strain curve as shown in Figure 2-4. In general, the curve can be divided into four sections (shown by the dotted lines in Figure 2-4), with the first section representing the simple linear elastic loading of the composite. As the stress increases multiple matrix cracks are generated in the composite and the fibers bridging the cracks are shear debonded from the matrix (Section II). It is this matrix cracking and fiber-matrix debonding that are primarily responsible for the "pseudoplastic" behavior and high toughness of these types of CMCs. Eventually the crack density saturates and the bridging fibers become completely debonded in the regions between the matrix cracks, such that continued loading (Section III) represents the elastic response of the bridging fibers. At still higher loads fiber fracture begins to occur (section IV), which often leads to a slight leveling of the stress-strain curve just before ultimate failure.

Some of the important fracture parameters that are determined from the stress-strain curves are also illustrated in Figure 2-4, and include the initial modulus, proportional limit stress, ultimate strength and strain to failure. It is often very difficult to determine unambiguously the stress at which the first matrix crack occurs, so the proportional limit stress, i.e. the stress at which the strain deviates by 0.005% from linear loading, is more commonly used to characterize this important stress level. All of the in-plane fracture data reported here was measured at initial strain rates (prior to matrix cracking) between $3x10^{-5}$ and 10^{-4} s^{-1} unless otherwise noted.

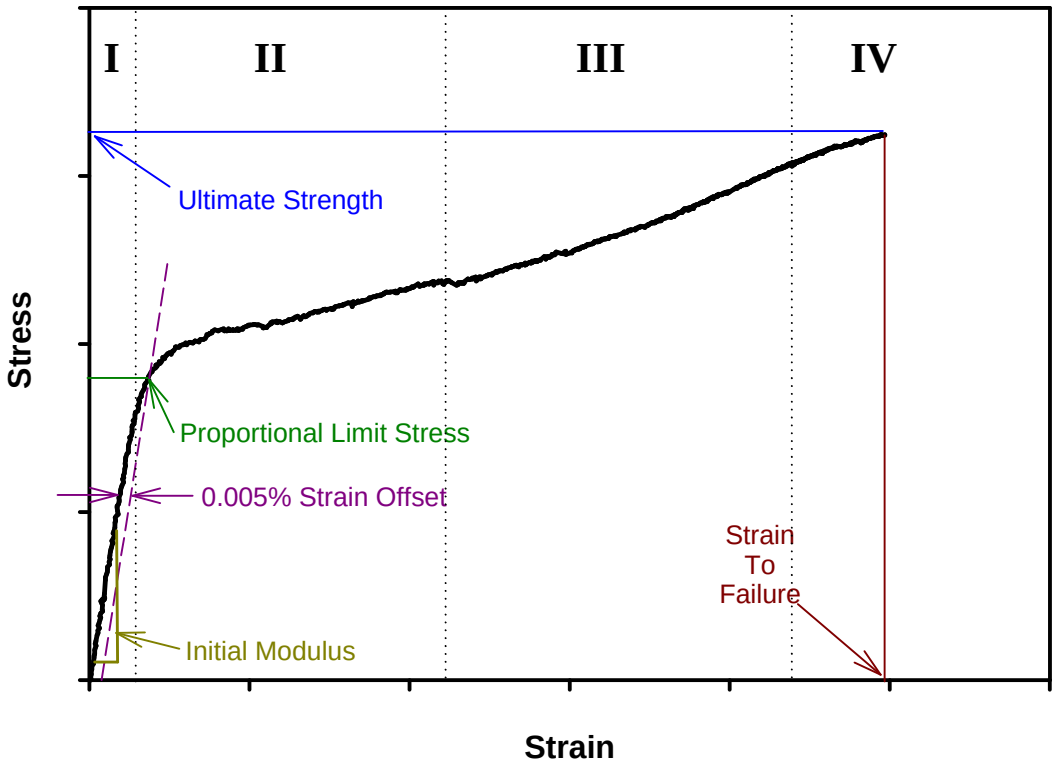

Figure 2-4. Typical in-plane tensile stress-strain behavior for a continuous fiber reinforced ceramic composite.

3 TECHNICAL APPROACH AND RESULTS

Where appropriate, the discussion of the technical results of the program is arranged by program task number. The purpose of each task will be reviewed followed by the experimental results of that task.

3.1 Task 1. Application Assessment

The purposes of this task were to 1) define and quantify the potential benefits that would be realized by the utilization of CMC materials for the targeted components, 2) to define the technical requirements of the targeted components and the resultant material property requirements, and 3) to perform preliminary design studies to evaluate the fitness of the CMC systems for the applications. Most of this work for the shroud and combustor liner components for a MS7001FA gas turbine was done in Phase I of the program and has been reported previously[4].

During Phase II the development effort for the combustor liner was redirected to addressing a liner concept for the smaller MS5002C (Frame 5) engine. As discussed above in Section 2, the large risks involved with component tests in large engines made it obvious that small engine applications would be the first opportunities for CMC field testing and possible commercial introduction. Although Phase I identified substantial performance benefits for CMC components in a large 7F class engine, it was unclear how much benefit could be gained in smaller engines. Additional Task 1 effort was then carried out under Phase II to evaluate these benefits to help better direct the selection of small turbine components for development and testing.

System need considerations for this task were done as part of the Phase II extension and Phase II+ proposals where the Frame 5 combustors, GE-2 (aka PGT-2) shrouds and GE-5 (aka PGT-5) combustors and shrouds were chosen as the target components. In addition, considerable work was done with regard to benefit assessments for the "large turbine component" in Task 3.3.i. This effort studied the use of CMC shroud components in 6FA, 7FA, 9FA, 7H and 9H gas turbines. Revised estimates for the potential engine cycle benefits for all of these components were derived and are summarized in Table 3.1. The benefits calculated for the 7FA engine are based on more detailed cooling flow modeling and cycle deck calculations than were done in Phase 1, and thus the benefit estimates differ somewhat from previous estimates. Cycle benefits for the GE-2 and GE-5B engines are based on simple cycle operation while those for the Frame 7 and Frame 9 engines are based on combined cycle operation.

It should be noted that the benefits calculations were performed relatively early in the program and include various assumptions as to the realizable reductions in cooling air for the different components. Thus the results presented in Table 3-1 are only estimates. More precise determination of the benefits for each component would require a detailed design and analysis of each CMC component, which was beyond the scope of this task.

Overall the benefits, particularly with regard to increased power output, tend to be higher for the larger sized engines. This is because the large F-class engines operate at higher firing temperatures and thus require larger amounts of compressor discharge for component cooling purposes. Use of minimally cooled CMC shrouds for these engines would thus allow for a larger relative reduction in overall chargeable cooling air flow than in the smaller engines. Benefits for the GE-2 are relatively small because these shrouds are not actively cooled, and thus all benefits are obtained from a projected reduction in the blade tip to shroud clearance that the lower thermal expansion of the ceramic shroud should make possible. Benefits for the 9H engine are relatively small compared to those for the 7H because the 9H uses steam cooling for the 1st stage shroud whereas the 7H uses air cooling. Nevertheless, the substitution of a CMC shroud with minimal air cooling for the steam-cooled metal shroud still results in an overall cycle benefit. In the advanced H-class machines there is also substantial cooling air used in the 2nd stage shrouds, such that substitution of CMC's in both stages would give even greater cycle benefits.

These benefit analysis results indicate that the advanced technology (F and H class) machines would benefit most from the introduction of ceramic components. However, to introduce CMC materials into these engines first would be too risky considering the excessively high liability associated with component failure. That is why we have been pursuing the development and testing of components for small engines first, where the costs and risks are much lower. Such testing is necessary to evaluate both material and design performance under real engine operation conditions before introduction in a large engine can be justified. Nevertheless, the larger benefits to be gained with CMC's in the larger engines makes it likely that the first commercial introduction of the technology at GE will be for these larger, advanced technology (F and H class) engines.

Table 3-1. Estimated Engine Cycle Benefits for CMC Component Substitution

Engine	Component	Nature of Benefit	Efficiency	Output
GE-2	2nd stage shroud	Reduced blade-shroud clearance		
GE-2	1st stage shroud	Reduced blade-shroud clearance		
GE-5B	1st stage shroud	Reduced chargeable cooling air		
GE-5B	Combustor liner	Reduced combustor pressure drop		
6FA	1st stage shroud	Reduced chargeable cooling air		
7FA / 9FA	1st stage shroud	Reduced chargeable cooling air		
7H / 9H	1st stage shroud	Reduced chargeable cooling air		

Increasing

Increasing

* estimated from efficiency increase only

3.2 Material and Process Development

The purpose of this effort was to continue the material development efforts started in Phase I. In particular, efforts on the monofilament-reinforced system were to be concentrated on development of a continuous fiber coating process for Si_3N_4 in cooperation with Textron Specialty Materials (TSM) (continuous BN fiber coatings had already been demonstrated in Phase I), and on the elimination of the carbon surface layer on the monofilament fibers through the utilization of SCS-0 or other suitable monofilament fiber. During Phase II all coatings used on monofilament fibers were deposited by TSM.

A second objective was to develop a prepreg MI composite system using a multifilament tow fiber. At the start of Phase II the only such small diameter fiber that had sufficient high temperature mechanical properties and thermal stability to meet the application requirements was Hi-Nicalon™ from Nippon Carbon. All process development on the multifilament tow reinforced system was therefore done with the Hi-Nicalon™ or Hi-Nicalon Type-S™ fiber.

A third objective of this work was to periodically characterize the status of the material development effort by generating material property databases. Such databases were generated whenever there was a significant change in the composite constituents or fabrication process. Each "generation" of CMC went through a substantial "optimization" effort prior to database characterization so that databases were representative of a fixed, standardized material and process that were capable of yielding reproducible results.

The work described in this section fell under program Task 3.1 Process Feasibility, Task 3.2.a Process/Material Optimization, and Task 3.2.b Property Measurement.

3.2.1 Monofilament System

Various material improvement measures were tried with the monofilament-reinforced composite system, all of which were intended to increase expected composite life by improving the resistance of the system to fiber-matrix interface oxidation effects. These improvement measures included evaluations of alternate fibers (SCS-0 and SCS-Ultra first pass), alternate oxidation resistant fiber coatings (Si_3N_4 and Si-doped BN), and alternate matrix compositions. Many of these process/material variations were evaluated using short term mechanical testing and oxidation exposure testing on both uncracked and cracked composite samples. Although many of the experiments conducted included effects of multiple variables, for the sake of clarity the composite modifications are discussed separately in sections 3.2.1.1 through 3.2.1.4. The oxidation testing results on the different composite variations are then discussed in sections 3.2.1.5 through 3.2.1.6, and the monofilament system summarized in section 3.2.1.7.

3.2.1.1 Utilization of SCS-0 Fiber

There were three major concerns with utilization of the SCS-0 fiber. First, Textron had relatively little experience in making this fiber since it is not a commercial item, and what

experience they did have indicated that the fiber strengths were typically low and poorly reproducible. Moreover, there was no high temperature strength data available for SCS-0 fiber. The second concern was that the carbon surface layers on the SCS-6 and SCS-9 fibers used in Phase I were providing a protective barrier to chemical degradation of the fiber during the coating process, and that since SCS-0 did not have this layer it could be degraded substantially by the fiber coating process. The third concern was that the carbon surface layers on SCS-6 and SCS-9 may in fact be necessary to attain high fiber strength and promote fiber debonding and pullout. Whether an appropriate fiber coating could be found for SCS-0 fibers that would perform as well as the carbon surface layers was not known.

The second concern was addressed early in the program by comparing tensile strengths of uncoated and BN-coated SCS-0 fiber from the same production spool. Forty to fifty fibers were tested for each condition and the tensile strengths are shown in the Weibull plot in Figure 3-1. Within the range of scatter of the data the two strength distributions are indistinguishable, indicating that the BN coating process at TSM was not degrading the SCS-0 fiber strengths.

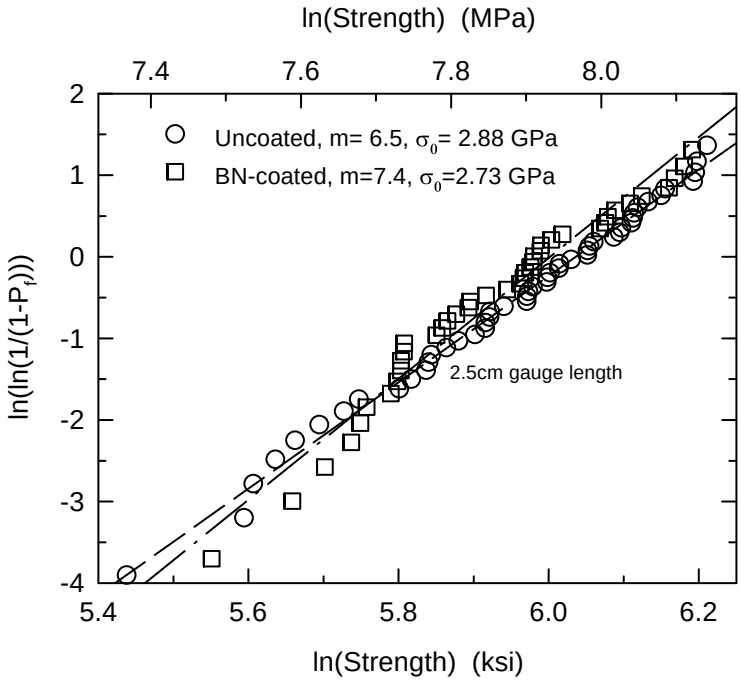

Figure 3-1. Weibull plot of the fiber tensile strength distributions for uncoated and BN-coated SCS-0 from the same fiber spool.

The lack of high temperature strength data for SCS-0 fiber was alleviated by measuring the tensile strength of this fiber in air. Figure 3-2 shows the strength data obtained. As expected the room temperature strengths were much lower for the SCS-0 fiber than for SCS-6 fiber measured under comparable conditions. However, at high temperature the strength of the SCS-0 fiber dropped much less than did the strength of SCS-6 fiber. At first the cause of the loss of strength of the SCS-6 fiber at high temperature was thought to

be oxidation of the carbon fiber surface coatings; however, a similar trend is seen in the data of Tressler and DiCarlo[7] where the measurements were done under an inert atmosphere. These results indicated that although the low temperature strengths of the SCS-0 composites would be lower than for SCS-6 reinforced composites, at the intended use temperature of 1100°-1200°C the composite strengths should actually be comparable for the two fiber types.

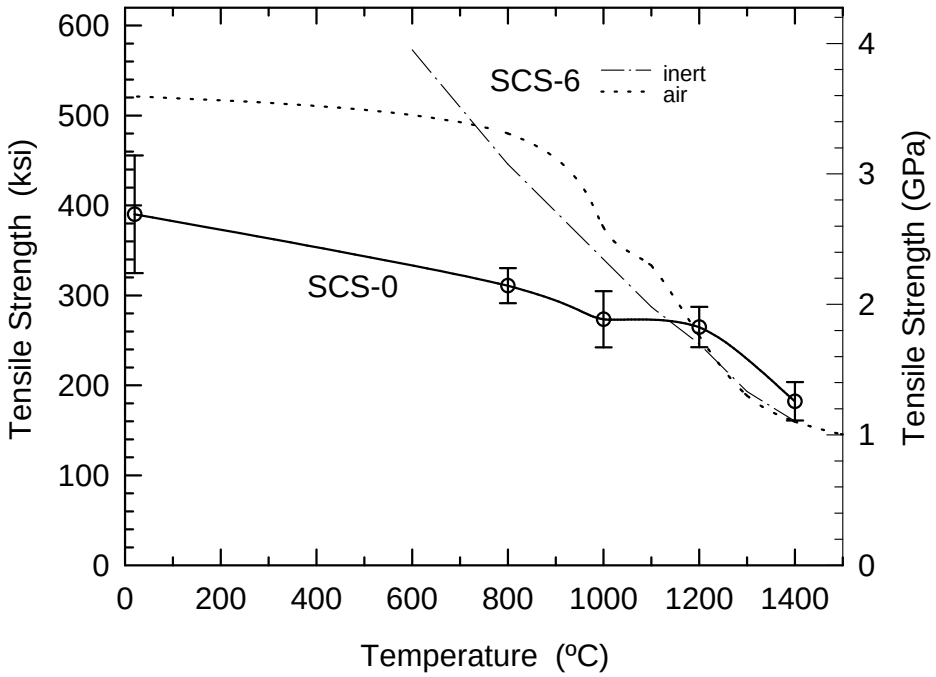

Figure 3-2. High temperature tensile strength behavior of uncoated SCS-0 fiber measured in air (strain rate approximately $2x10^{-4}$/s). The trend line shown for SCS-6 fiber in air is from previously unpublished measurements done at GE Aircraft Engines. Both data sets used a 2.5cm gage length for testing. The line for SCS-6 in inert atmosphere is from Tressler and DiCarlo[7].

The remaining concern about the utilization of the SCS-0 fiber was whether an effective fiber coating system could be developed that gave fiber-matrix debonding and fiber pullout behavior similar to that observed for SCS-6 fibers. A large variety of fiber coating thicknesses and configurations were tried with SCS-0 fibers with varying degrees of success. Initial trials were with BN-C-BN fiber coatings applied by TSM, which had been shown to work very well with SCS-6 and SCS-9 fibers in Phase I. The optimum coating thickness for use with SCS-6 fiber had been determined in Phase I to be 4.5µm, and so coatings near this thickness were tried with SCS-0 fibers also. Results of these initial coating evaluations are listed in Table 3-2. (Unless otherwise stated, all strength data reported for monofilament-reinforced composites is for 9-ply, 0°-90° crossply composites with nominally 18-20 vol% fiber.)

Although the TSM BN-based fiber coatings gave composites with non-brittle failure, the ultimate strength and strain to failure values of the composites were all less than half those of comparable SCS-6 reinforced composites. This is a larger loss of strength relative to SCS-6 than would be expected based only on the differences in starting fiber strengths. Because of the limited success with BN-based coatings we also evaluated several BN-Si_3N_4 layered coatings with SCS-0. Such layered coatings had been shown in Phase I to work with SCS-6 fibers and it was hoped that they would work well with SCS-0 monofilament fibers also.

Table 3-2. Initial BN-Based Fiber Coatings Evaluated with SCS-0 Fiber and Resulting Composite Tensile Strength Properties

Source	Coating Configuration*	Proportional Limit (MPa)	Ultimate Strength (MPa)	Strain to Failure (%)
TSM	3.5µm BN-C-BN	99.3	150	0.31
TSM	4.5µm BN-C-BN	95.2	182	0.33
TSM	5.5µm BN-C-BN	102	132	0.16

* The multiple BN layers are nominally of equal thickness and the carbon layers are nominally 0.05µm.

The initial layered coating on SCS-0 obtained from TSM, consisting of 2µm BN + 2µm Si_3N_4, was not successful. Only a very limited amount of fiber was coated because of fiber failures within the coater. Preliminary examination at GEGR indicated that the Si_3N_4 coating layer was highly cracked and that the entire coating, including the BN layer, had actually spalled from the fiber over about 50% of the fiber surface area. This was an unexpected result since layered BN-Si_3N_4 coatings had been deposited on SCS-6 fibers at GEGR during Phase I using a batch coating process.

In order to better understand the coating spallation problem fiber coatings of 3µm Si_3N_4 and of 2µm BN + 2µm Si_3N_4 were deposited onto SCS-0 fibers at GEGR in a batch reactor. Visual examination of the coatings showed the Si_3N_4 coating to be cracked and spalling, similar to the TSM layered coating. The 2µm BN + 2µm Si_3N_4 coating had much less coating spallation, but the Si_3N_4 layer was still highly cracked. Tensile strength measurements were made on the coated fiber and compared to the strength of the uncoated fiber from the same spool. Results of these tests are shown in Figure 3-3. The straight Si_3N_4 coating caused a substantial drop in the fiber strength, as would be expected from the highly cracked nature of the coating. Apparently cracks starting in the coating are free to propagate into the SCS-0 fiber, thus acting as strength limiting flaws. The presence of a BN layer was not sufficient to alleviate the effects of the cracks in the Si_3N_4 layer, as the BN - Si_3N_4 coating still caused very substantial strength degradation to the fiber.

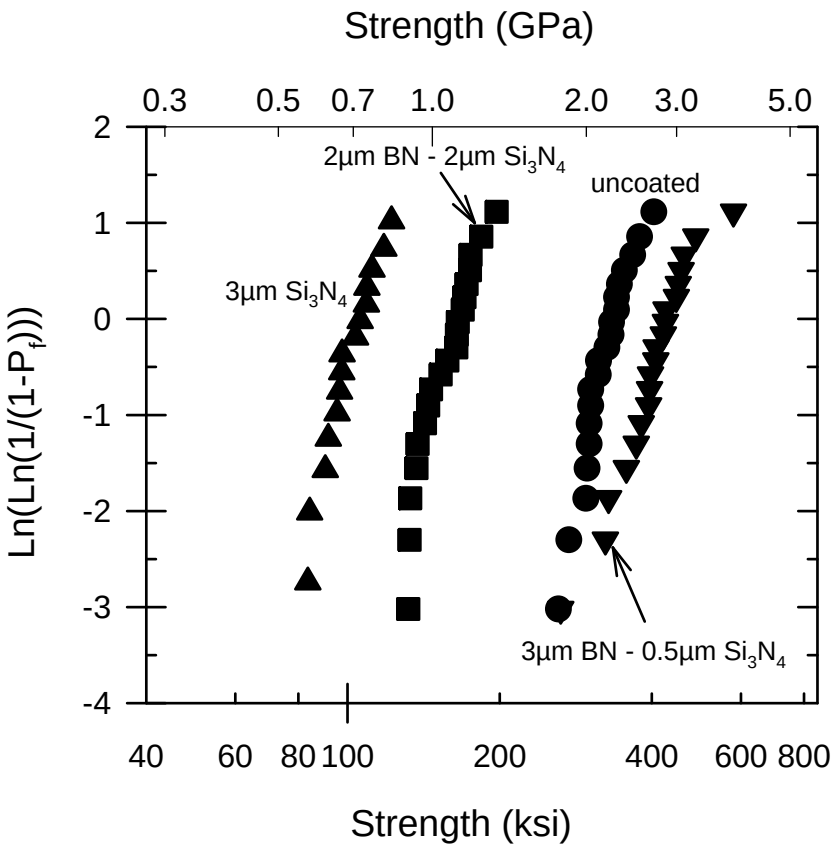

Figure 3-3. Weibull strength distribution plots for SCS-0 fiber coated with Si3N4 - containing coatings at GEGR. (2.5cm gage length)

The cause of the cracking and spalling of the Si_3N_4 coatings appeared to be the thermal expansion mismatch of the Si_3N_4 coating and the SiC-based SCS-0 fibers. During cooling from the coating deposition temperature the Si_3N_4 fiber coating would be put into compression, causing coating buckling and cracking. Stress calculations using a concentric cylinders model[8] indicated that the axial and hoop compressive stresses in the Si_3N_4 coating could approach 300MPa when deposited onto SCS-0 at 1400°C and then cooled to room temperature. On SCS-6 fiber, with the presence of the highly compliant carbon surface layers, the axial stress drops by only about 10%, but the hoop stress drops by over 40%. The calculated stress profiles through the fiber and coatings are shown in Figure 3-4. This large difference in hoop stress may explain why the Si_3N_4 coatings tended to adhere better to SCS-6 than to SCS-0 fibers.

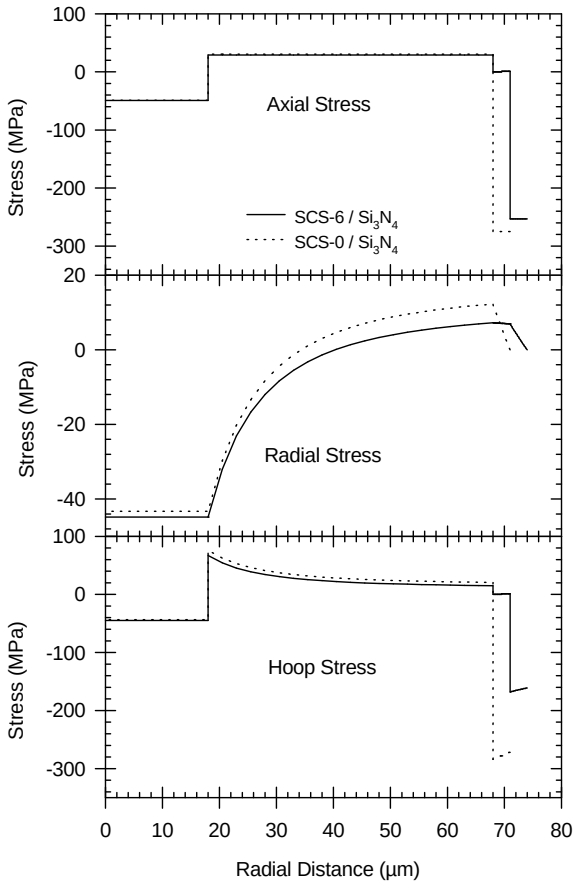

Figure 3-4. Calculated stress distributions in SCS-0 and SCS-6 fibers coated with 3μm of Si3N4 at 1400°C and then cooled to room temperature.

Typically the adherence of stressed coatings is found to improve as the thickness of the coating is decreased. Also, as demonstrated by the stress calculations, increasing the compliance of the material under the stressed coating should also improve its adherence. These two approaches were utilized in the next fiber coating processed at GEGR, where the thickness of the BN layer was increased to 3μm and the Si_3N_4 layer was decreased to 0.5μm. Two variations of this fiber coating were prepared, one with an intermediate 0.03μm carbon layer between the BN and Si_3N_4 layers and one without this carbon layer. Both fiber coatings appeared to remain adherent to the fiber as hoped, and the strength of the coated fiber was actually slightly higher than for the uncoated fiber, as shown in Figure 3-3. Unfortunately composites made from this coated fiber showed poor strengths and near brittle fracture behavior. The coating with the intermediate carbon layer produced a composite that was only marginally better than the one without the intermediate carbon layer. Metallographic examination of the composites showed that the BN and Si_3N_4 layers were still largely intact, but that the coating had lifted partially away from the fiber surface at the fiber-BN interface. The small gaps between the fiber and coating were filled with silicon during composite infiltration, indicating that some coating cracks still persisted. Experience has shown that any time the silicon infiltrant comes into contact with the reinforcing fibers fiber-matrix bonding occurs, resulting in weak, brittle composites.

At this point all attempts at developing Si_3N_4 or BN-Si_3N_4 layered coatings for use with SCS-0 fiber had been unsuccessful. It would therefore be necessary to perform all of the mechanical properties and oxidation resistance evaluations of SCS-0 composites using BN-base fiber coatings. Additional coated fiber was processed by TSM for this purpose, but the resulting composite properties were very poor (under 140MPa ultimate strength with near-brittle behavior), much worse than the earlier composites listed in Table 3-2. The reasons for the poor composite properties were not entirely clear, but a contributing factor may have been the fiber selection process being done at TSM. Because SCS-0 was not a standard production item it was necessary for TSM to specially produce about 2 kg of SCS-0 fiber for use in this program. During the coating trials described above TSM personnel would select the highest strength fiber available from this production run. As this fiber was being used the strength of the fiber being used in the program was continually decreasing with time. Strength tests on fiber from the last coating batch gave an as-coated fiber strength of 2.43GPa whereas all previous BN-coated fiber batches had strengths ranging from 3.46 to 2.56GPa. This result indicates that the strength of the new coated fiber was lower than for previous batches, which would have contributed to the relatively poor properties of the new composite; however, it was not so low as to completely explain the low strengths.

The overall result of these evaluations was that the poor reproducibility of the SCS-0 fiber itself, and the poor reproducibility of coatings on this fiber, made it a very unlikely that a reliable composite system could ever be developed. Nevertheless there was sufficient academic interest in this fiber because of its unique lack of a carbon surface layer to warrant further characterization on a limited basis. Specimens for oxidation exposure testing, to be described in Section 3.2.1.5, were fabricated from what little coated fiber remained from the batches of fiber used for the samples in Table 2-1. Further development of composites with SCS-0 fibers and mechanical characterization of such composites were not pursued.

3.2.1.2 Use of SCS-Ultra Fiber

Because of the poor strength and poor reproducibility of the SCS-0 fiber it was necessary to consider alternate fibers with reduced surface carbon. The most promising alternate monofilament was a fiber being developed by TSM at that time and referred to as SCS-Ultra. SCS-Ultra differed from SCS-6 fiber primarily in that the stoichiometry of the SiC in the fiber was better controlled and the fibers had improved strengths, occasionally reaching over 1 Msi. Unfortunately the normal SCS-Ultra fiber had a 3µm, carbon-rich surface layer very similar to that on SCS-6 so that little oxidation benefit would be anticipated. However, SCS-Ultra was being fabricated in a two-pass deposition process and the intermediate fiber product, called SCS-Ultra first pass (SCS-UFP), had only a 0.5µm surface carbon layer. The high strength of the SCS-UFP fiber (actually slightly higher that the finished SCS-Ultra) and the relatively thin carbon surface layer made it an attractive fiber for evaluating in the prepreg MI composite.

The first task was to verify the high fiber strengths being reported by TSM. Tensile strength testing of SCS-UFP fiber was done at GEGR. A Weibull distribution plot of the measured fiber strengths is shown in Figure 3-5. There appears to be at least two flaw populations in the tested fibers, one at high strengths which has a regression line fitted to it in the figure, and a lower strength population. TSM claimed that during fabrication the fiber was put through a 3.45GPa proof test so that strengths below this value should not have been possible. This indicates that the low strength flaw population was probably introduced when the fiber was run through a fiber cutter at GE in order to prepare the tensile samples. This fiber cutter had been used extensively for cutting SCS-6, SCS-9 and SCS-0 fiber for strength testing and for composite fabrication. There had been no evidence that the fiber cutter degraded the strength of any of these fibers since the strengths of fiber run through the cutter agreed with those cut by hand. Nevertheless it is possible that the thin carbon surface layer on the SCS-Ultra first pass fiber would be less protective than the thicker layers on SCS-6 and SCS-9, and because of the very high starting strength of the SCS-Ultra first pass fiber even very minor damage would have a significant effect on strength whereas such damage could go unnoticed in a lower strength fiber like SCS-0. This result suggests that increased care in handling of the SCS-UFP fiber would be necessary in order to take advantage of its full strength potential. Regardless of the cause of the low-strength tail in the strength distribution, even this "damaged" SCS-UFP fiber still had a very high average strength, about 700MPa above the strength of a typical SCS-6 fiber.

Production schedule conflicts and budgetary constraints made it impossible to obtain a large quantity of the SCS-UFP fiber for composite evaluations. The only fiber available was left-over from earlier production runs and existed only in relatively short lengths. This situation made it impractical to attempt continuous fiber coating at TSM with this fiber. Consequently the SCS-UFP fiber was coated with the standard 4.5μm BN-C-BN coating developed for SCS-6 at GEGR using a batch process. This batch coating process required cutting the fiber to handleable lengths in the fiber cutter, and thus the fiber used for composite fabrication probably had a strength distribution similar to that shown in Figure 3-5 rather than the very high strength distribution that may have been obtained with continuous coating.

Since only batch coatings could be applied to the SCS-UFP fiber it was necessary to fabricate composite samples using an older hand alignment of fibers and tape casting process. This procedure overall does not yield as uniform a fiber coating or composite microstructure as the continuous coating and drum winding approach. When practiced with SCS-6 fibers this process would typically yield composites with ultimate strengths in the 200-240MPa range. Unfortunately an error during the processing of these SCS-UFP samples occurred which resulted in the composites having a fiber volume fraction of only 13%, as compared to the nominal 20% for other monofilament composites.

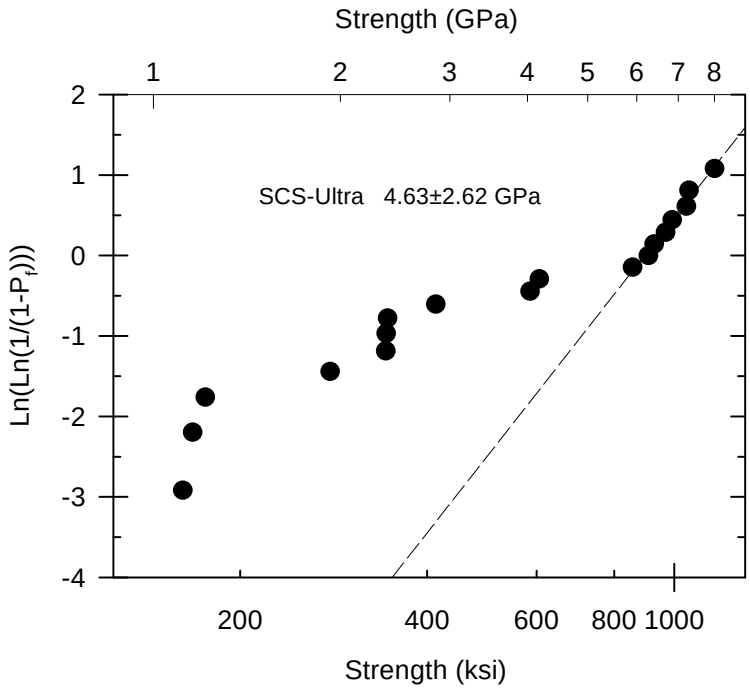

Figure 3-5. Weibull strength distribution plot for SCS-Ultra first pass fiber after passing through GEGR's fiber cutter. (25mm gage length) The trend line for the high strength portion of the distribution shows the expected strength distribution for "undamaged" fiber.

Room and elevated temperature tensile strength data for the SCS-UFP bars is shown in Figure 3-6. The apparently low ultimate strengths of these composites are caused by the low fiber volume fraction. When normalized to 20 vol% fiber the ultimate strengths are around 275MPa, which is slightly higher than SCS-6 reinforced composites fabricated by the same process. If composites could be fabricated by the continuous coating and drum winding process, where no fiber damage from a fiber cutter would occur, ultimate strengths could be expected to exceed 345MPa. Also note that the composite strength does not decrease at elevated temperatures. This result differs markedly to that for SCS-6 composites, which show about a 40% reduction in ultimate strength going from room temperature to 1316°C (2400°F).

These testing results indicated that the SCS-UFP would be a viable fiber from a composite mechanical properties standpoint; however, issues regarding oxidation stability still needed to be addressed. Results on the oxidation evaluations are given in Sections 3.2.1.5 and 3.2.1.6.

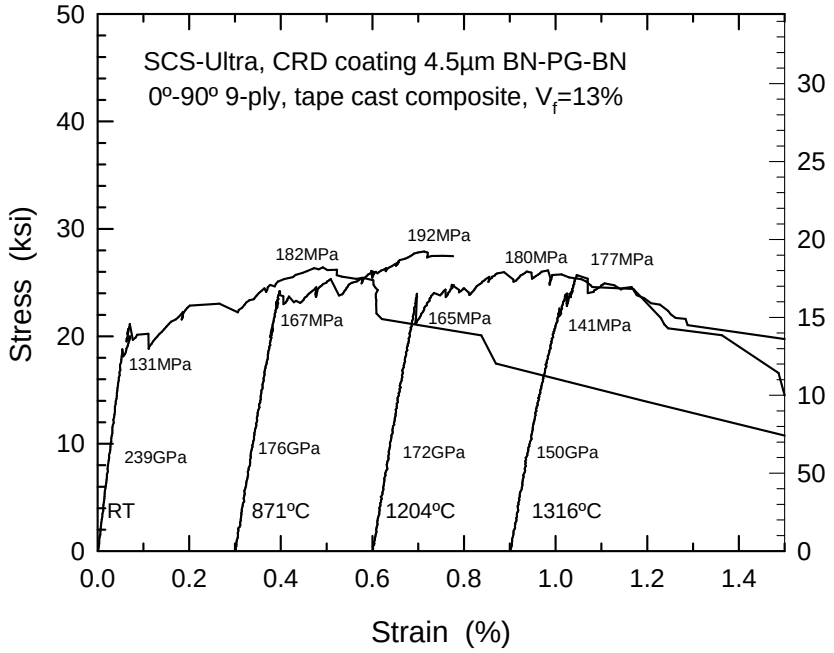

Figure 3-6. Tensile stress-strain behavior of SCS-UFP fiber composites made using the batch coating and tape casting process. Numbers next to the curves give the composite initial modulus, proportional limit stress and ultimate strength values. Curves are offset for clarity.

3.2.1.3 Use of Continuous Si_3N_4 Fiber Coatings

Silicon nitride fiber coatings on SCS-6 and SCS-9 fibers had been demonstrated using batch coatings in Phase I (described as the "alternate" fiber coating in the Phase I final report[3]). The advantages of Si_3N_4 coatings compared to the standard BN coatings are that Si_3N_4 is both more oxidation resistant and more resistant to molten silicon metal than is BN. It was thus hoped that composites with Si_3N_4 fiber coatings would have better mechanical properties and be more reproducible than composites with BN fiber coatings because coating damage during infiltration would be minimized. Also, as long as fiber-matrix debonding occurred between the Si_3N_4 coating and the matrix, the oxidation resistance of the composite in the presence of matrix cracks would be improved.

A continuous process for depositing Si_3N_4 fiber coatings was developed at TSM. Results in Phase I using batch Si_3N_4 coatings on SCS-6 fiber indicated that a 4.5 - 5µm thick coating was needed for optimum composite performance. The optimum thickness for the continuous Si_3N_4 fiber coatings was determined by preparing coatings of 3, 4 and 5µm thickness on SCS-6 and then evaluating the strength behavior of composites made with these fibers. The results of these tests are given in Table 3-3. (Table 3-3 lists composite results for two types of composite matrices, which will be described in Section 3.2.1.4.)

Table 3-3. Tensile Strength Data for Prepreg MI Composites Made with Si_3N_4-Coated SCS-6 Fiber and Having ~20Vol% Fiber in a 0°-90° Architecture.

Coating Thickness	Matrix Used*	Fiber Volume Fraction (%)	Proportional Limit Stress (MPa)	Initial Modulus (GPa)	Proportional Limit Strain (%)	Ultimate Strength (MPa)	Strain to Failure (%)
3µm(a)	Phase I		124			140	0.08
3µm(b)	Phase I	21.3	174	212	0.082	387	0.87
	HGS	27.4	177	334	0.053	407	0.64
4µm	Phase I	21.5	138	177	0.078	365	0.90
	HGS	25.6	117	321	0.036	421	0.72
5µm	Phase I	23.0	132	190	0.070	343	0.80
	HGS	26.9	169	329	0.051	404	0.77

(a) Initial 3µm coating with different carrier gas composition during CVD.
(b) Coating processed with same carrier gas composition as the 4 and 5µm coatings
* Matrices were the standard Phase I matrix composition and the "high green strength" (HGS) composition. Differences in the matrices are discussed in Section 3.2.1.4.

The 3µm Si_3N_4 coating originally supplied by TSM, coating (a) in Table 3-3, was found to perform very poorly, giving composites with only a 140MPa ultimate strength and strain to failure below 0.1%. This contrasted sharply with the composites made from the 4µm and 5µm coatings which gave ultimate strengths above 345MPa and strain to failure values over 0.7%. It was then discovered that TSM had changed the carrier gas used in the CVD deposition of the 3 µm coating from that used in the 4 and 5 µm coatings. A second 3µm Si_3N_4 coating, coating (b) in Table 3-2, was then prepared using the same carrier gas as the other coatings and was found to give much improved composite properties, comparable to the 4 and 5 µm coatings. This result indicated that there is a very wide process window for acceptable thickness of the Si_3N_4 fiber coating on SCS-6 fiber. A 4µm coating thickness was chosen as the "standard" thickness since variations by as much as 1µm from this value would still give good composites.

The high temperature tensile fracture behavior of SCS-6 reinforced composites with Si_3N_4 fiber coatings was found to be very similar to that for similar composites with BN-based fiber coatings as measured in Phase I. The elevated temperature stress-strain curves for composites with Si_3N_4 fiber coatings are shown in Figure 3-7. There is little change in the fracture behavior from room temperature up to about 900°C, but beyond this temperature the ultimate strength and strain to failure values drop. This is consistent with the high temperature strength behavior of SCS-6 fiber.

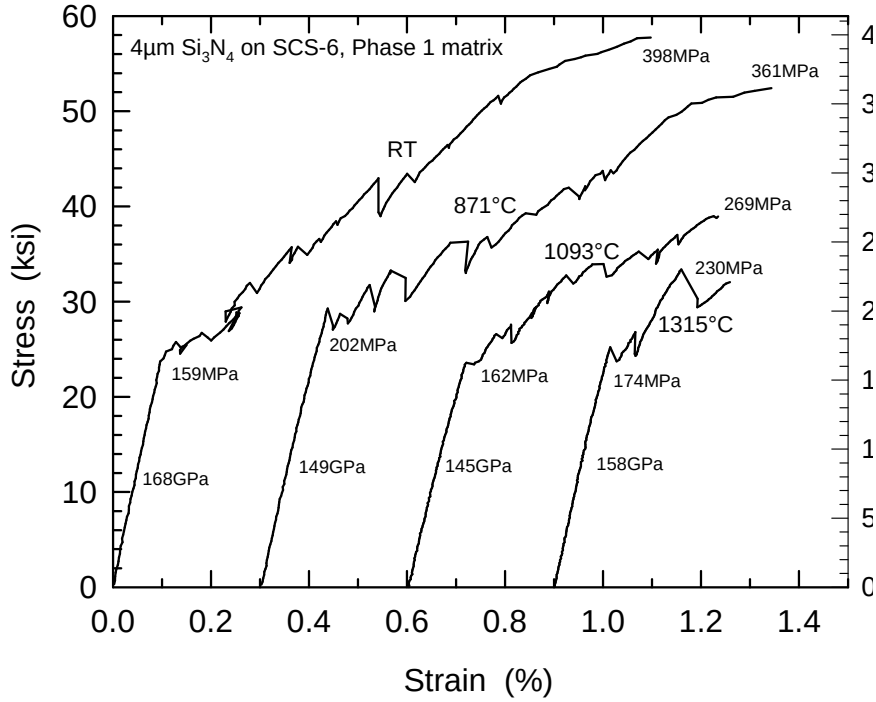

Figure 3-7. Temperature dependence of the tensile fracture behavior of Prepreg MI composites reinforced with Si3N4 coated SCS-6 fibers. The curves are offset for clarity.

3.2.1.4 Matrix Composition Modifications

Two different matrix compositions were evaluated with monofilament fibers. The original matrix composition used in Phase I was made from crushed carbon fiber felt and an epoxy-based binder system. This composition gives composites with a rather coarse matrix microstructure consisting of elongated, polycrystalline SiC particles intermixed with residual Si metal. Because of the short infiltration times used in order to protect the fibers and coating from thermal and chemical degradation, there is typically 10% to 20% by volume of residual carbon in the matrix from the un-reacted cores of the carbon fiber fragments. This matrix composition, hereon referred to as the "Phase I matrix", is the matrix used for all of the composite samples mentioned in the preceding sections. A micrograph of an SCS-6 composite fabricated with this matrix is shown in Figure 3-8.

The second matrix composition that was used in the evaluation of monofilament-reinforced composites was borrowed from the CMC system reinforced with fiber tow. In order to completely infiltrate the tow bundles during prepregging, the particulate constituents of this matrix system (SiC and carbon) are submicron in size. The binders and solvents used are also different. Due to the small size of the carbon phases in the preforms, whether from the carbon particulate in the slurry or from pyrolysis of the binder system, all carbon is fully reacted to SiC during infiltration, yielding a final matrix consisting of SiC and Si

only. This matrix system also had a much higher strength in the green state (i.e. before binder burn-out) than did the standard Phase 1 matrix, largely due to the fine particle size and different binders used. Consequently this matrix system is referred to as the "high green strength" (HGS) system throughout this report, and is discussed in more detail in section 3.2.1.4.2.

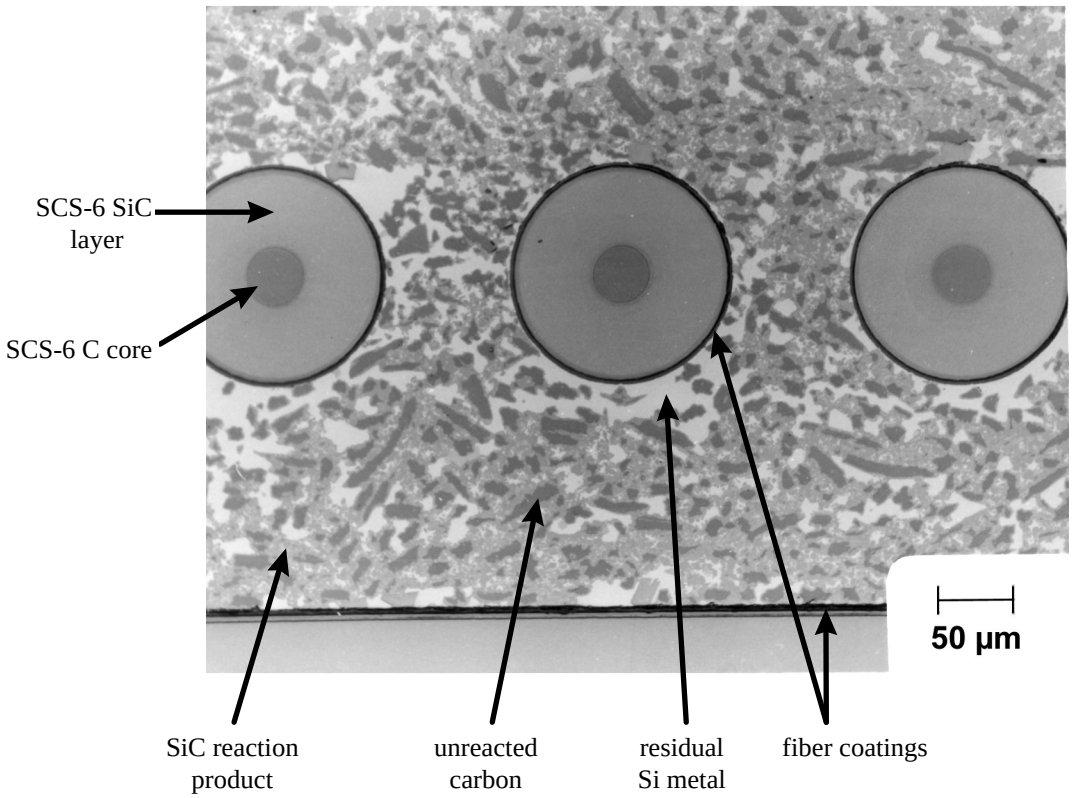

Figure 3-8. Optical micrograph of a typical Prepreg MI composite fabricated from the Phase I matrix composition and reinforced with BN-coated SCS-6 fiber.

3.2.1.4.1 Boron Additions

The first matrix modification was to add boron-containing phases to the composite matrix. This was done in anticipation of improving the oxidation resistance of the composite in the event of matrix cracking. A crack in the composite matrix will allow environmental exposure of the fiber-matrix interface. Since this interface typically contains carbon or BN, both of which are oxidized at high temperatures, the composite becomes susceptible to oxidative embrittlement. In order to lessen the oxidative attack of the interface it would be advantageous for the crack to heal itself via an oxidation reaction, thereby limiting the amount of oxidizing species that can reach the fiber-matrix interface. This process is shown schematically in Figure 3-9. In this diagram, if the oxidation of the crack faces and/or composite surface is sufficiently fast to close off the crack opening at "A" before the fiber coatings are completely oxidized through then the composite should still show fiber-matrix debonding and tough behavior. By adding boron to the matrix its rate of

oxidation is increased so that crack closure by oxidation should occur faster, particularly at moderately high (600-1000°C) temperatures.

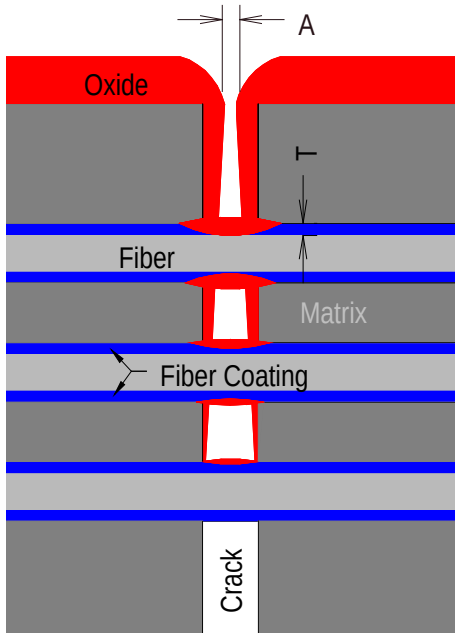

Figure 3-9. Schematic representation of the oxidation of a composite within a matrix crack. Oxidation of the matrix causes the growth of an oxide layer on the inside of the crack that eventually closes the crack opening at the surface, while oxidation of the fiber coatings occurs simultaneously. In order to minimize oxidation damage the crack opening "A" should close from oxidation of the matrix before the fiber coating is completely oxidized through its thickness "T".

The desired composition for adding boron to the composite matrix was determined under the HSCT/EPM program. Samples of MI matrix were prepared with varying levels of B doping by substituting B_4C powder for the SiC and C particulates in the "high green strength" (HGS) matrix. Indentation cracks were then introduced into these matrix specimens and they were then oxidized in air at temperatures from 800° to 1200°C. The time required for the surface oxidation products to "seal" the indentation cracks was then determined. From these experiments a boron doping level at 0.2 atomic ratio of B to Si in the matrix was found to be optimum. This ratio was used for evaluating composite specimens made with the Phase I matrix and SCS-6 fibers (composites made with Hi-Nicalon fiber and the HGS matrix will be discussed in a later section).

It should be noted that in all "standard" composites a silicon-boron alloy with 3-5wt% B has been consistently used for silicon infiltration. The boron is added to the silicon to help depress the dissolution of BN fiber coatings into the silicon during infiltration. Assuming that all of the boron in the alloy would infiltrate into the preform along with the silicon

would give a relative B:Si atom ratio in the infiltrated matrix of roughly 0.09. However, Si-B mixtures used for infiltration of these composites were pre-melted to form an "alloy" prior to the composite infiltration step. During this pre-melting treatment the B and Si form insoluble SiB_3 precipitates which do not readily re-melt and participate in the infiltration. Consequently the actual amount of boron that gets into the matrices gives a B:Si ratio of 0.01 to 0.03. This is the background boron level in the "standard" composite samples. For the boron-doped matrix samples B_4C powder was added to the matrix constituents sufficient to give a B:Si ratio of 0.2 without considering the B from the infiltrant alloy. Thus in the boron-doped matrices the actual B:Si ratio was actually slightly higher than this value.

The effects on short term mechanical properties of adding boron to the Phase I matrix composition were rather minor. Table 3-4 lists the tensile fracture properties for composites made with Si_3N_4-coated SCS-6 fiber using the Phase I matrix both with and without extra boron doping. The only consistent difference between the samples with boron and without is the lower initial elastic modulus for the samples with extra boron, which is consistent with there being less SiC and more residual Si and C in the matrix, as will be discussed below. The proportional limit stresses, ultimate strengths and strain to failure values also tend to be somewhat lower in the boron-doped matrix samples, but the difference is within the normal panel-to-panel scatter observed in such data. The real intent of the boron addition was to improve composite oxidation resistance, and this aspect is discussed in section 3.2.1.5.

Table 3-4. Effects of Added Boron on the Tensile Fracture Properties of Prepreg MI Composites Made with the Phase I Matrix and ~20vol% of Si_3N_4-Coated SCS-6 Fibers in a 0-90° Configuration.

Extra B added?	Test Temperature (°C)	Initial Modulus (GPa)	Proportional Limit (MPa)	Ultimate Strength (MPa)	Strain to Failure (%)
Yes	RT	133	137	366	0.96
	871	127	140	296	0.83
	1093	117	162	253	0.59
	1315	95	140	148	0.24
No	RT	168	159	398	1.10
	871	168	202	361	1.04
	1093	145	162	269	0.63
	1315	158	174	230	0.35

One microstructural difference in the composites with and without boron doping was the amount of residual carbon left in the matrices. This was an unexpected observation which lead to additional experiments to better quantify this effect. (These experiments were done under Task 3.2.c, Process Understanding, but are discussed here for continuity.) Monolithic matrix specimens were prepared from the Phase I composition and were infiltrated with mixtures of B and Si that had not been pre-melted. The non-pre-melted

mixtures were used in an attempt to limit the amount of SiB_3 precipitates formed during the pre-melting and solidification process. Infiltrant mixture compositions ranged from 0 to 10wt% B. The infiltration time-temperature schedule used for these samples was the same as that used for infiltrating monofilament reinforced composites.

For B contents of 0, 0.1 and 0.5 wt% in the infiltrant mix the coarse carbon particles in the matrix were largely converted to SiC with little residual silicon left in the bodies. A micrograph of the sample infiltrated with the 0.5wt% B mixture is shown in Figure 3-10A. Samples infiltrated with 3wt% B to 10wt% B mixtures showed much less reaction of the carbon and silicon to form silicon carbide, resulting in much higher levels of residual carbon and silicon metal. A micrograph of a sample made with the 5wt% B infiltrant is shown in Figure 3-10B. At 1wt% B the infiltrated sample displayed regions with microstructure similar to Figure 3-10A and other regions with a microstructure similar to that in Figure 3-10B. This result would suggest that 1wt% B in the alloy is close to the threshold needed to inhibit the Si-C reaction and that local variations in the B content caused the different microstructural regions.

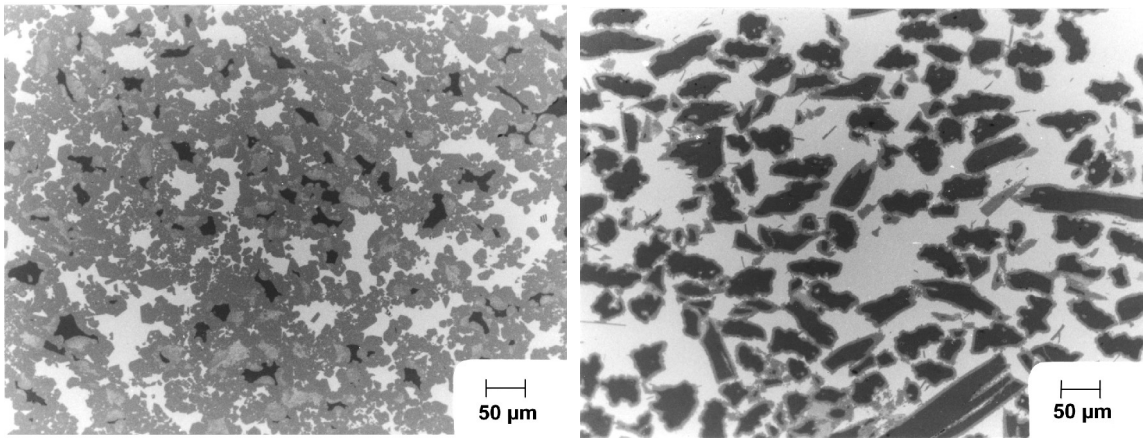

A **B**

Figure 3-10. Figure 3-10. Optical micrographs of Phase 1 matrix samples infiltrated with Si-B mixtures containing (A) 0.5 wt% B and (B) 5 wt% B. The darkest phase is residual carbon, the lightest phase residual Si metal and the gray phase is the reaction formed SiC.

To our knowledge this was the first conclusive observation that B actively inhibits the Si-C reaction. However, during Phase I we had seen variations in the amount of residual C in the composite matrices that we had believed resulted from variations in the time-temperature profile during infiltration. Increasing the reaction temperature did appear to compensate for this poisoning effect of the boron, but since the boron levels in those composites were near the "threshold" range those results may have been confounded by the boron effect.

3.2.1.4.2 Fine Grained, High Green Strength Matrix

The second matrix modification evaluated was to utilize a matrix composition with the monofilament-reinforced composites that was originally developed for use with small diameter fibers. In order to improve the impregnation of the fine fiber tows with matrix slurry during the wet drum winding procedure a matrix composition based on fine SiC and carbon powders with polyvinylbutyral and polyfurfuryl alcohol resins for binders was developed. This set of matrix constituents gives a very fine grained mixture of SiC and Si after silicon infiltration. Because of the fine particle sizes and different binder system used, this matrix composition displayed a higher green strength (both before and after binder burn-out) than did the Phase I matrix composition. The higher green strength gives composites added dimensional stability through the green machining and the silicon infiltration processes. The very fine particle size of the carbon particulate also gave complete conversion of the matrix carbon to SiC during melt infiltration. Because of the higher green strength this composition was better suited for the fabrication of complex shaped parts than was the Phase I matrix composition. The complete reaction of the carbon phase was anticipated to give this matrix improved oxidation resistance of the Phase I matrix also. For these reasons this newer matrix composition, hereon referred to as the "high green strength" or HGS matrix, was evaluated as a matrix for monofilament reinforced composites. A micrograph of a typical monofilament composite made with the HGS matrix is shown in Figure 3-11.

Composite specimens were prepared using both the Phase 1 and HGS matrices with both BN-coated and Si_3N_4-coated SCS-6 fiber. Room and elevated temperature tensile fracture properties of these composites are given in Table 3-5. The early Si_3N_4 fiber coatings were also tested with both Phase I and HGS matrices, and those results were presented in Table 3-3.

In both sets of data presented in Tables 3-5 and in the data in Table 3-3 the differences between the Phase I and HGS matrix compositions are consistent. The HGS matrix gives considerably higher initial modulus values, but comparable proportional limit stresses as the Phase I matrix. Consequently the cracking strain of the HGS matrix is substantially lower. The ultimate strength values for the two types of matrix are similar, which would be expected since ultimate strength is a fiber-dominated property. However, the strain at failure tends to run somewhat lower in the HGS matrix composites, suggesting different fiber-matrix interfacial shear strengths for the two matrices.

From this data it was concluded that either matrix composition, Phase I or HGS, would be acceptable for use with monofilament reinforced composites. The Phase I matrix would be preferred based on mechanical considerations because of its higher proportional limit strain; however, the HGS matrix would be preferred for component fabrication based on its better machinability and ease of producing complex shaped parts.

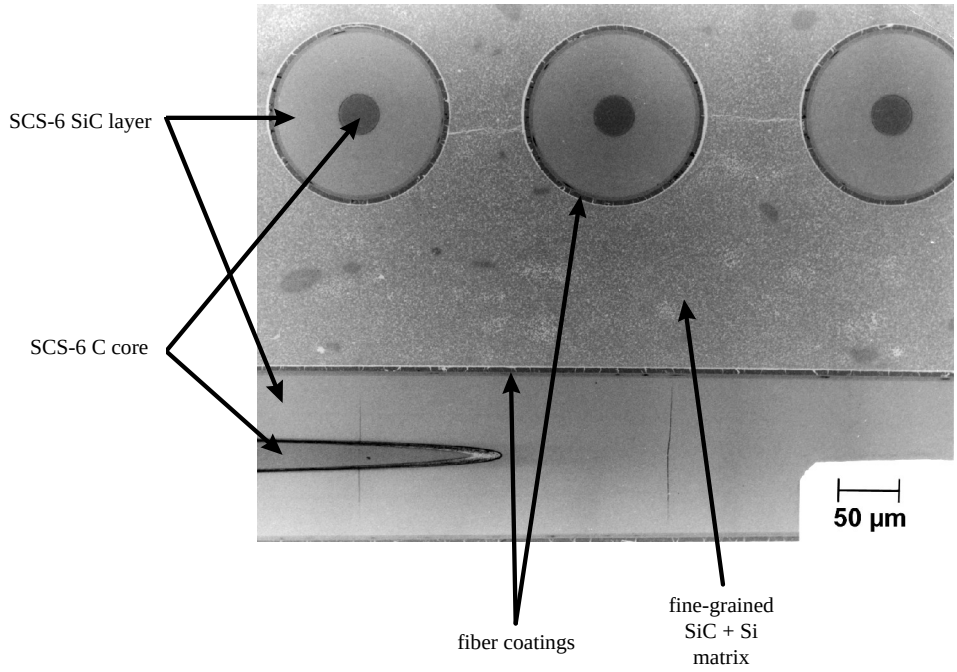

Figure 3-11. Optical micrograph of a Prepreg MI composites fabricated with the HGS matrix composition and Si3N4 coated SCS-6 fiber.

Table 3-5. Tensile Fracture Properties of Prepreg MI Composites Made with the Phase I and HGS Matrices and with BN- and Si_3N_4-Coated SCS-6 Fibers.

Fiber Coating	Matrix	Test Temp. (°C)	Initial Modulus (GPa)	Proportional Limit Stress (MPa)	Proportional Limit Strain (%)	Ultimate Strength (MPa)	Strain at Failure (%)
BN	Phase I	RT	190	117	0.062	264	0.52
		871	328	142	0.114	305	0.70
		1093	136	138	0.102	217	0.46
		1315	126	137	0.109	163	0.22
	HGS	RT	217	132	0.061	336	0.61
		871	245	117	0.048	344	0.89
		1093	247	128	0.052	228	0.41
		1315	252	121	0.048	177	0.13
Si_3N_4	Phase I	RT	168	159	0.095	398	1.10
		871	168	202	0.121	361	1.04
		1093	141	162	0.112	269	0.63
		1315	158	174	0.110	230	0.35
	HGS	RT	294	162	0.055	396	0.73
		871		176		371	0.52
		1093	323	179	0.056	232	0.40
		1315	248	193	0.078	256	0.21

3.2.1.5 End-On Interface Oxidation Testing

The oxidation resistance of the fiber-matrix interface was evaluated using an "ends-on" oxidation test. In this test a unidirectional composite is cut after processing to expose fiber ends and fiber-matrix interfaces along one edge. The cut sample is then exposed at high temperature in air to allow for oxidation of the fiber-matrix interface from the exposed edge. Following oxidation treatment the samples are cut and polished in a plane parallel to the fibers so that the penetration of oxidation damage into the composite along the fiber-matrix interfaces can be measured.

Figure 3-12 shows a schematic of an ends-on oxidation sample following exposure. During the oxidation exposure the carbon surface layers, if present, are being consumed from the surface inward by oxidation to CO_2. However, oxidation of the BN fiber coatings to B_2O_3 is also occurring with the accompanying 74% volume increase. This is a sufficient volume expansion that the nominally 4.5µm BN coatings should oxidize and fill in the 3µm gap left by the oxidation of the carbon surface layers with B_2O_3. Once sufficient B_2O_3 is formed the fiber-matrix gap becomes sealed and little further oxidation of the interface occurs. (Oxidation of the fiber, matrix and Si_3N_4 fiber coatings also occurs to form SiO_2, but this reaction is at a much slower rate and has very little effect on the sealing of the fiber-matrix interface over the time and temperature ranges used for testing. Likewise oxygen transport through the B_2O_3 can still occur after the gap is "sealed", but the rate is again so low compared to the oxidation rate of the open interface that its effects can be neglected.)

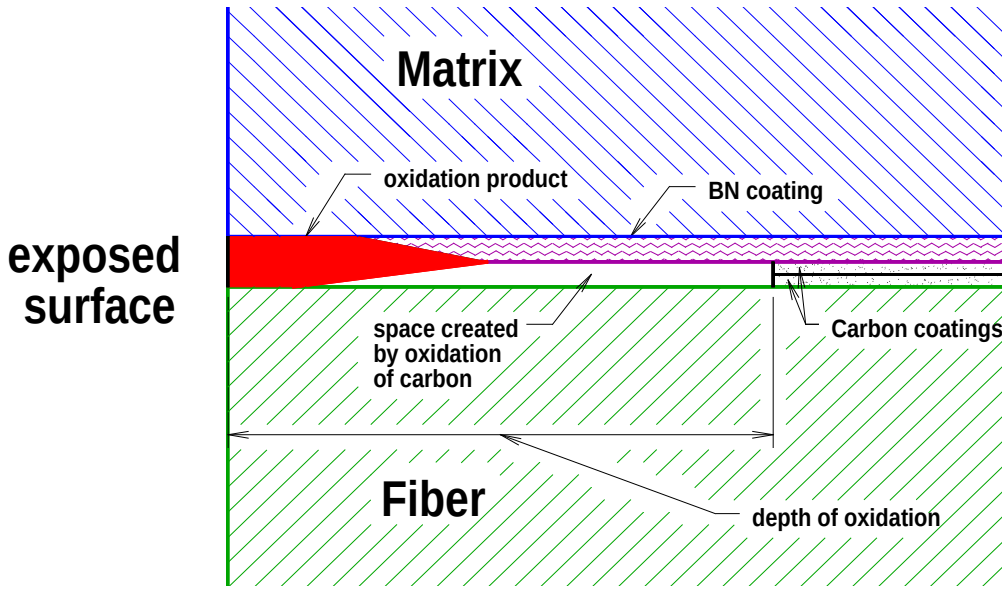

Figure 3-12. Schematic of the fiber-matrix interface for an SCS-6 reinforced composite during ends-on oxidation testing.

Determining the depth of interface damage depends on the interface being studied. For composites reinforced with SCS-6 or SCS-UFP fiber the depth of oxidation was taken as

the depth to which the carbon interface layer has receded, which was rather easily determined optically. For SCS-0 composites, which have no carbon surface layers on the fiber, the depth of oxidation was taken as the depth of the transition between B_2O_3 and BN. Determining the depth of this transition was somewhat more difficult because the transition was often gradual rather than sharp and because it is difficult to discern BN from B_2O_3 optically.

Specimens for ends-on oxidation tests were fabricated using four different fiber/coating combinations (SCS-6 fiber with BN coatings, SCS-6 fiber with Si_3N_4 coatings, SCS-0 fiber with BN coatings and SCS-UFP fiber with BN coatings) and four different matrix compositions (Phase 1 matrix, Phase 1 matrix with B_4C doping, HGS matrix and HGS matrix with B_4C doping). Composite samples were exposed for times of 1, 10 and 100 hours at 1204°C (2200°F) in air, and the interface oxidation depth results for these tests are shown in Figures 3-13 and 3-14. Exposure tests were also done for 100 hours at 704°C (1300°F), for which the results are shown in Figure 3-15.

Although Si_3N_4 was chosen as a fiber coating to improve the interface oxidation behavior, in the ends-on oxidation tests these fiber coatings performed very poorly. This is because there was no BN coating to rapidly oxidize and seal the gap left by the oxidizing carbon layers. Thus the carbon layer was completely oxidized from the entire length of the specimens (10 to 12mm) in about 10 hours or less.

At the other extreme, the composites with SCS-0 fibers, and therefore no interface carbon layers, showed the least amount of oxidation penetration. With no carbon layers there would be no interface gap formed, and thus any oxidation would be simple surface oxidation of the BN. Even after 100 hours at 1204°C the samples showed on average only 0.2mm of oxidation penetration.

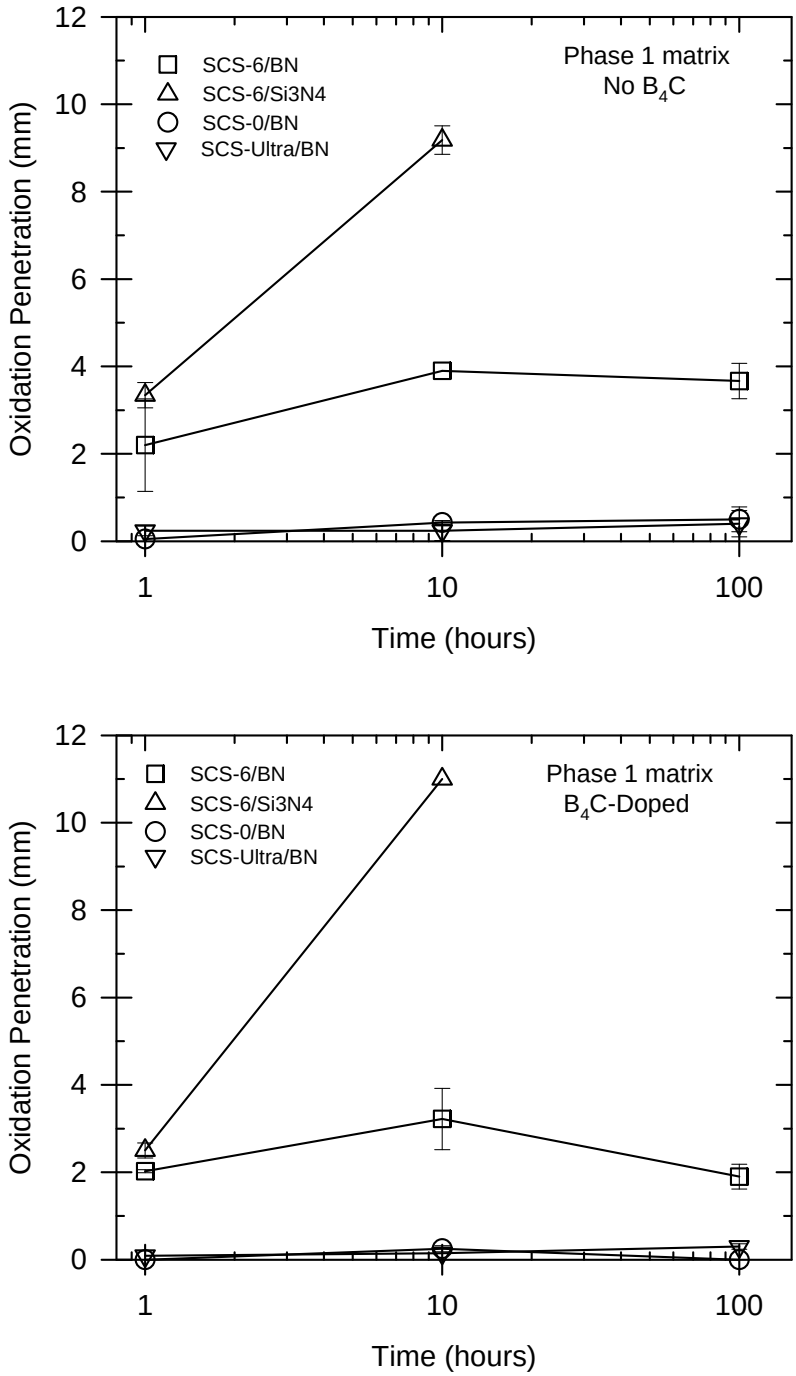

Figure 3-13. Ends-on oxidation results for monofilament reinforced composites made from undoped Phase 1 matrix (top) and with boron-doped Phase 1 matrix (bottom).

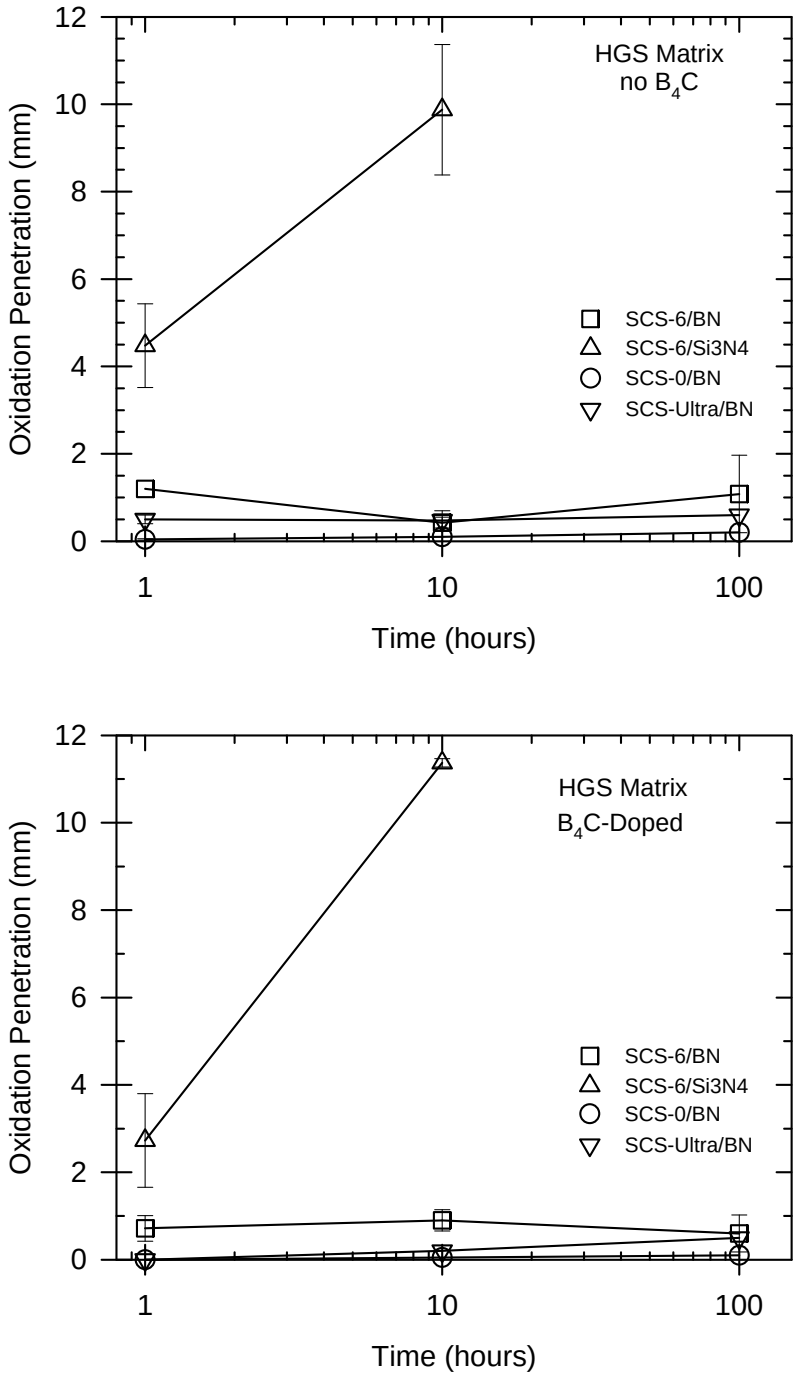

Figure 3-14. Ends-on oxidation results for monofilament reinforced composites made from undoped HGS matrix (top) and with boron-doped HGS matrix (bottom).

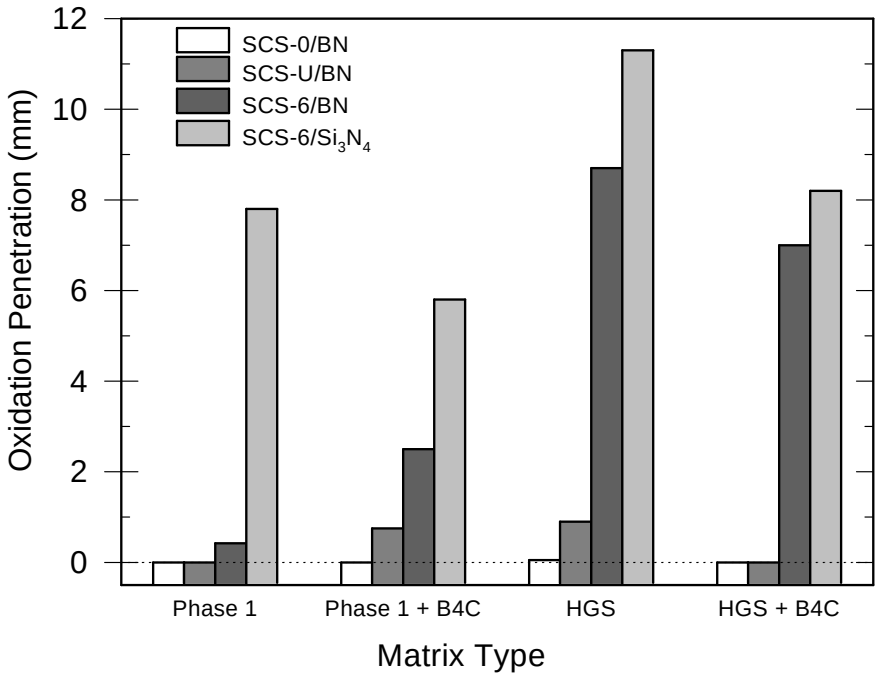

Figure 3-15. Oxidation penetration depth results for ends-on oxidation tests at 704°C for 100 hours. (Bars start below the zero line so that the fill patterns will be observable on the smaller bars.)

The ends-on oxidation results for the BN-coated SCS-6 and SCS-UFP fibers were intermediate to those for the Si_3N_4-coated SCS-6 and BN-coated SCS-0. In the phase 1 matrix the SCS-6/BN composites showed a rapid oxidation penetration of about 2mm after only one hour with only a small increase in oxidation depth for longer times. In the HGS matrix the initial oxidation depth was lower, averaging just under 1mm, and was essentially constant with additional exposure time. This result indicates that the interface gap caused by the oxidation of the carbon layers is sealed by BN oxidation within the first hour of exposure and that little additional oxidation occurs beyond this. The smaller oxidation penetration for the HGS matrix (averaging 0.7mm for all times tested) compared to the phase 1 matrix is probably related to the residual C in the phase 1 matrix. Oxidation of the residual matrix carbon near the BN coating would interfere with sealing of the interface gap by the formation of additional gap volume that would need to be filled. Consequently the time to seal off the gap, and thus the oxidation penetration, would be increased compared to samples with the HGS matrix.

For the BN-coated SCS-UFP fiber the average oxidation penetration distance for all times and matrices was only 0.3mm. This is consistent with the fact that there is a much thinner fiber carbon surface coating compared to SCS-6 fiber (0.5µm vs. 3µm) so that the gap formed by carbon oxidation is smaller and is sealed much more quickly by BN coating oxidation.

At 1200° C oxidation of the BN fiber coating is sufficiently fast to seal the gaps caused by the oxidation of the carbon coatings. However, at lower temperatures around 700°C where carbon oxidation is still occurring but BN oxidation is considerably slower, the oxidation of the BN layer may not be fast enough to seal the coating gaps. Behavior in this temperature range is an important consideration since component cooling air (compressor discharge air) is typically in the range of 350-400ºC and so regions of the CMC components, especially near the attachments, would be expected to operate at 700°C or lower. For these reasons the oxidation penetration behavior of the composites was also measured at 704°C (1300°F), but only at the 100 hour exposure time. The results of these measurements are given in Figure 3-15.

As was the case at 1200°C, oxidation penetration at 704°C was worst for the SCS-6/Si_3N_4 composite with penetration depths from 6 to 11mm after 100 hours. Penetration depths were lower for the SCS-6/BN composites, but the values were very close for the HGS matrices. This would suggest that the BN oxidation rate was insufficient to fully seal the gap left by the oxidation of the carbon layers. The oxidation penetration for this fiber-coating combination was less in the Phase I matrix than in the HGS matrix, which may be a result of a gettering effect of the residual matrix carbon in the Phase I matrix.

Oxidation penetration at 704°C was much lower for the SCS-0/BN and SCS-UFP/BN systems. For the SCS-0/BN composites no discernible oxidation penetration was noted beyond simple surface oxidation. For the SCS-UFP/BN composites measurable oxidation penetration was noted on only two of the four samples tested.

Overall the ends-on oxidation results indicated that composites with SCS-6 fibers would be extremely susceptible to interface degradation via oxidation, as was expected. The SCS-0 fiber composites, because of their complete lack of an interface carbon layer, were the most resistant to interface oxidation effects. The SCS-UFP fiber composites were closer in behavior to the SCS-0 composites than to the SCS-6 composites.

The above end-on oxidation experiments conducted in air suggest that both the SCS-0 and SCS-UFP fiber composites have fiber-coating interfaces that are fairly resistant to oxidation in air. This oxidation resistance is a result of sealing of the interface gap by the B_2O_3 oxidation product from BN fiber coating oxidation. However, the real application environment for these composites is not air but in a gas turbine combustion atmosphere. Such environments typically contain a water vapor partial pressure of 0.2 to 1 atmosphere, and it is well known that water enhances the volatilization of B_2O_3. Thus the oxidation resistance of the fiber-matrix interface could very well be degraded in water-containing environments. End-on oxidation experiments were therefore performed on HGS matrix composites, both with and without added matrix B, containing BN-coated SCS-0, SCS-UFP and SCS-6 fiber, and Si_3N_4-coated SCS-6 fiber. The atmosphere for these tests was 90% H_2O and 10% O_2, and the tests were performed at 1200°C and 700°C for 24 hours. Results of the tests are given in Figure 3-16, which shows the oxidation penetration depth for the various composites and testing conditions. (Results for SCS-6/Si_3N_4 are not shown since the penetration depths were much larger, averaging 4.4mm at 700°C and 5.2mm at 1200°C, than the values for the other fiber/coating combinations). In these experiments

there is considerable difficulty in determining the precise depth of oxidation damage and large scatter in the penetration depths measure on different fibers. Both of these factors contribute to the relatively large error bars (representing 95% confidence intervals for the average values). The solid symbols in Figure 3-16 represent the depth of oxidation that would be expected under dry oxidation conditions based on our previous experiments.

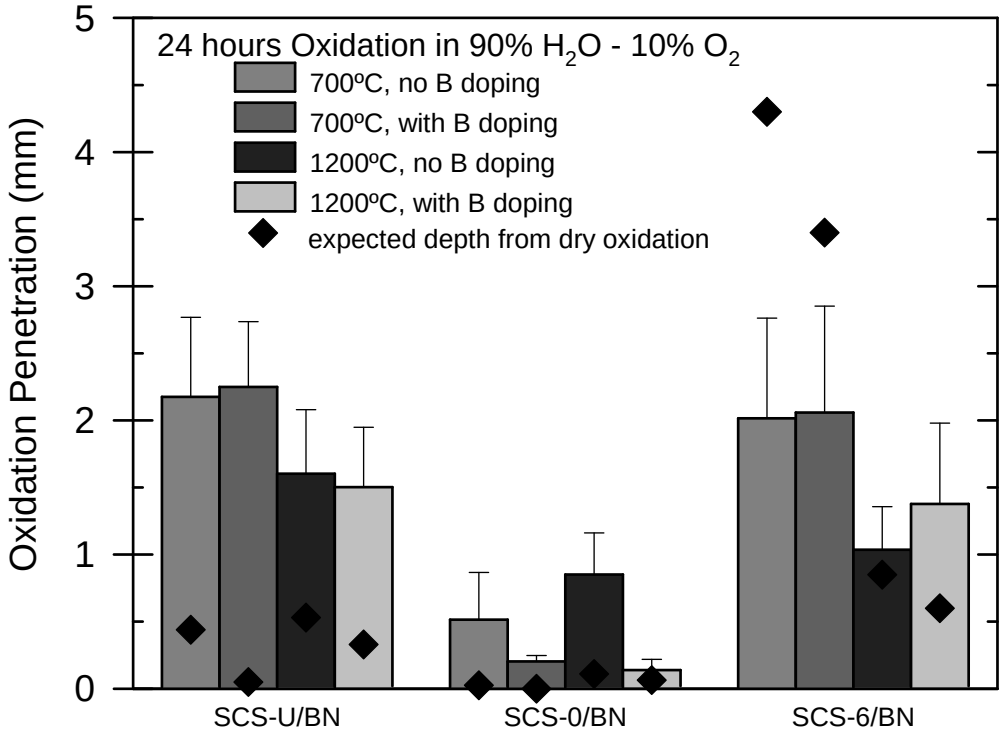

Figure 3-16. Oxidation penetration from end-on oxidation testing of BN-coated monofilament fibers in the HGS matrix. All exposures were done in 90% H2O - 10% O2 for 24 hours. The error bars indicate 95% confidence intervals for the average penetration depth (5 to 10 measurements per condition). The solid diamonds show the oxidation penetration depths predicted from previous end-on oxidation experiments done in dry air. The BN fiber coatings were nominally 4.5µm of BN-PG-BN for the SCS-U and SCS-6 fibers, and 4µm of BN-PG-BN for the SCS-0 fiber.

The uncertainty in the data makes it difficult to offer detailed mechanistic explanations for the observed differences in oxidation penetration. For both the SCS-Ultra and SCS-0 fibers the oxidation penetration was significantly enhanced by the presence of water, as would be expected from the increased volatility of the B_2O_3 oxidation product. For the BN-coated SCS-6 fiber oxidation was enhanced at 1200ºC, but significantly reduced at 700ºC with the use of the wet atmosphere. The reasons for this are not fully understood, but may be related to the complex role that water would play in the oxidation process. Regardless of the exact mechanisms responsible for the observed behavior, the overall

conclusion is that under wet oxidation conditions the SCS-Ultra/BN combination displayed oxidation penetrations quite similar to those for the SCS-6/BN combination.

3.2.1.6 Oxidation Exposure and Mechanical Testing

Three other oxidation tests were performed that were designed to measure interface oxidation effects on the mechanical properties of the composites. The first of these tests was a simple oxidation exposure test where as-fabricated tensile bar specimens were exposed in air for 100 hours at 1200°C. Following exposure the bars were tensile tested to failure at room temperature. Comparison of the post-exposure strength properties to those for unexposed bars gives a relative measure of the degradation caused by the exposure. Because the fiber-matrix interface is not exposed to the environment during this test it is useful mainly for measuring only the thermal stability of the interface.

The second test was a "pre-cracked oxidation" test where tensile bar specimens were first loaded in tension to 0.3% strain (well above the matrix cracking strain) to form typical matrix cracks as might be expected to occur in service. The specimens were then also oxidized unstressed for 100 hours in air at 1200°C and then tensile tested at room temperature following exposure. The presence of the matrix cracks in these specimens means the fiber-matrix interfaces are exposed to the environment during this test; however, the crack opening displacement with no applied stress is rather small (1-3μm) and thus ingress of oxygen to the interface would be greatly limited. Should the oxidation rate of the matrix material itself be appreciable then oxidative sealing of the crack could occur before significant oxidation of the fiber-matrix interface would occur, as illustrated in Figure 3-9.

In real applications some, but not all, of the thermal stresses in a component would be relieved by localize matrix cracking such that the cracked component would still be under stress and the matrix cracks would not be allowed to close. Thus a more realistic testing condition would be to perform the oxidation exposures of the pre-cracked samples while maintaining an applied stress. Such a "stressed oxidation" test was used as the third type of oxidation test. Here the tensile specimens were pre-cracked to 0.2% strain at the test temperature of 1093ºC (2000°F) or 704°C (1300°F) and then the applied stress was lowered to 103MPa (15ksi) and the specimens were held at this stress and test temperature in the testing machine for up to 100 hours. If the sample did not fail within the 100 hours it was then fast-fracture tensile tested at the test temperature of 1093°C.

The stress level for the stressed-oxidation tests, 103MPa, was chosen since it is representative of the average stresses predicted for shroud and combustor liner components in the Phase I, Task 1 design calculations[4]. However, because the component stresses are primarily induced by thermal strains, the presence of matrix cracks would increase the compliance of the composites and thereby lower the effective thermal stresses. As such, the actual stress in a cracked component would be substantially lower than the 103MPa predicted from simple elastic analysis. Consequently stressed oxidation testing at 103MPa represents worse than real-life testing conditions whereas the precracked oxidation testing with no stress represents better than real-life conditions.

Each of these tests involved mechanical testing in conjunction with the oxidation exposures. Because the SCS-0 fiber composites were not giving reproducible composite properties it was decided that this type of fiber would not be used for this testing. Also, because the supply of coated fibers was limited, especially for the SCS-UFP fiber, not all tests were done with all variations of fiber/coating/matrix composition. Also, in nearly all cases only one specimen was tested for each exposure condition.

Results from the uncracked and pre-cracked oxidation tests on an SCS-6/Si_3N_4/Phase 1 matrix composite are shown in Figure 3-17. The other composite systems evaluated (SCS-6/Si_3N_4/Phase 1 matrix, SCS-6/Si_3N_4/Phase 1 + B_4C matrix, SCS-6/BN/Phase 1 matrix and SCS-6/BN/HGS matrix) showed similar behavior to that in Figure 3-17 in that the oxidation exposure in air for 100 to 160 hours caused no discernible degradation. These results indicated that for a range of fiber coating and matrix combinations the fiber-matrix interface is stable to purely thermal exposure at 1200°C.

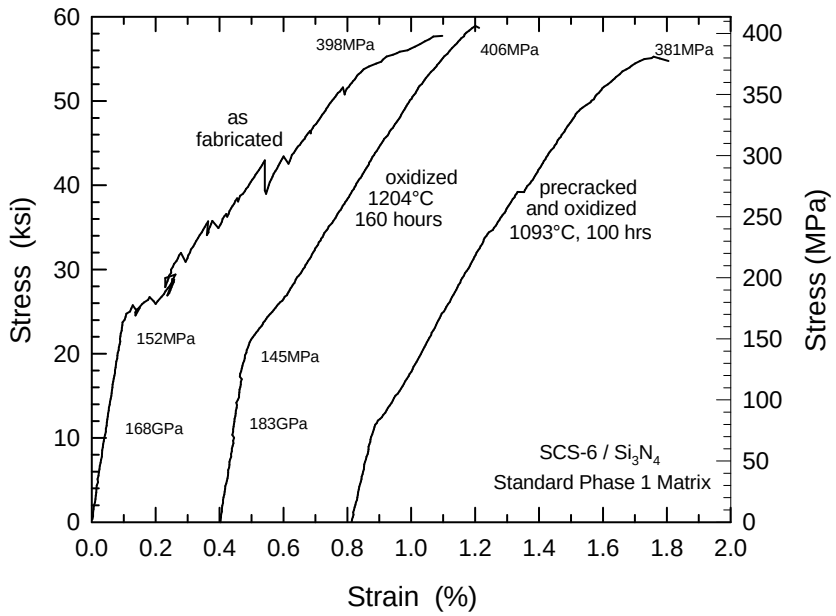

Figure 3-17. Room temperature tensile stress-strain behavior of a prepreg MI composite with SCS-6 fiber and Si3N4 fiber coatings in standard Phase 1 matrix before and after oxidation exposure testing.

The precracked oxidation results for the SCS-6/Si_3N_4/Phase 1 matrix composite in Figure 3-17 also show no discernible degradation. However, this was not the case for most of the other composite systems. Table 3-6 lists the percentages of strength and strain to failure retained after precracked oxidation exposure (relative to an unexposed bar from the same composite panel) for the various fiber/coating/matrix combinations tested. The data in Table 3-6 indicate that samples with the Phase 1 matrix retained most of their as-fabricated

strength, but that HGS matrix specimens showed a dramatic decrease in both ultimate strength and strain to failure following precracked oxidation exposure.

Table 3-6. Summary of Pre-Cracked Oxidation Results with Monofilament Fibers

Fiber	Fiber Coating	Matrix Composition	% Retained Ultimate Strength	% Retained Strain to Failure
SCS-6	Si_3N_4	Phase 1	96	87
SCS-6	Si_3N_4	Phase 1 + B_4C	97	83
SCS-6	Si_3N_4	HGS	14	5
SCS-6	BN	HGS	24	10
SCS-UFP	BN	Phase 1	82	71

Microstructural examination was performed on the precracked and oxidized samples to try to determine the reasons for the different behavior of the Phase 1 and HGS matrix composites. Specimens were sectioned longitudinally so that the matrix cracks could be observed edge-on. Optical micrographs of a SCS-6/Si_3N_4/Phase 1 matrix composite after precracked oxidation are shown in Figure 3-18, and those of an SCS-6/Si_3N_4/HGS matrix composite are shown in Figure 3-19.

In the Phase 1 matrix there was some removal of the carbon fiber coatings at the fiber-matrix interface near the matrix cracks; however, the carbon layers were never observed to be fully oxidized from the interface. In the HGS matrix composites the oxidation of the fiber matrix interface was much more extensive, with complete removal of the carbon layer up to 1mm away from the crack.

Two other distinct differences between the two matrices can be observed. First, the crack opening of the HGS matrix is visibly larger than that for the Phase 1 matrix. Thus oxygen diffusion into the crack would be easier for the HGS matrix than for the Phase 1 matrix. Secondly, in the Phase 1 matrix oxidation of the residual carbon phase along the crack faces is very prominent, particularly near the surface of the composite. Because there is no residual carbon in the HGS matrix no such preferential oxidation of a matrix phase has occurred. It is likely that the residual carbon in the Phase 1 matrix is acting like a “getter” for the oxygen diffusing into the crack, and thereby protecting the carbon layers at the fiber-matrix interfaces. No such protective mechanism is present in the HGS matrix composites so that interface oxidation, and consequent composite strength degradation, occurs more quickly.

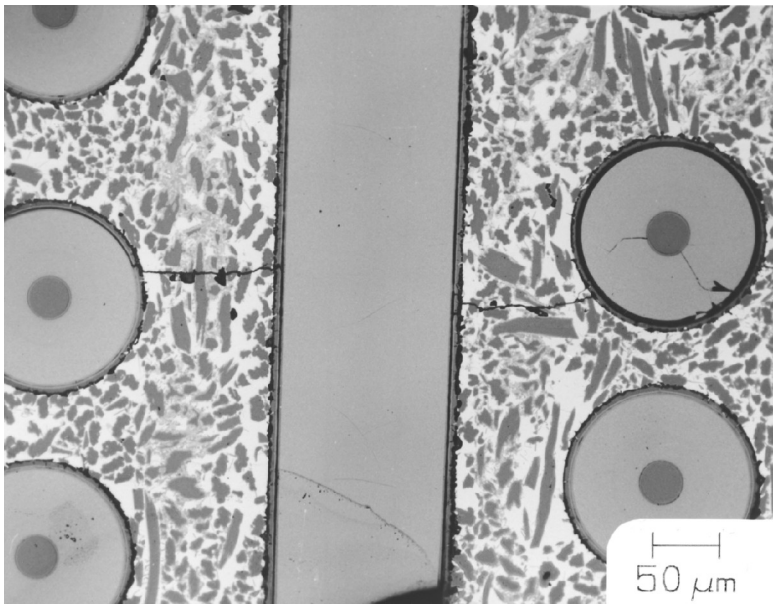

(A)

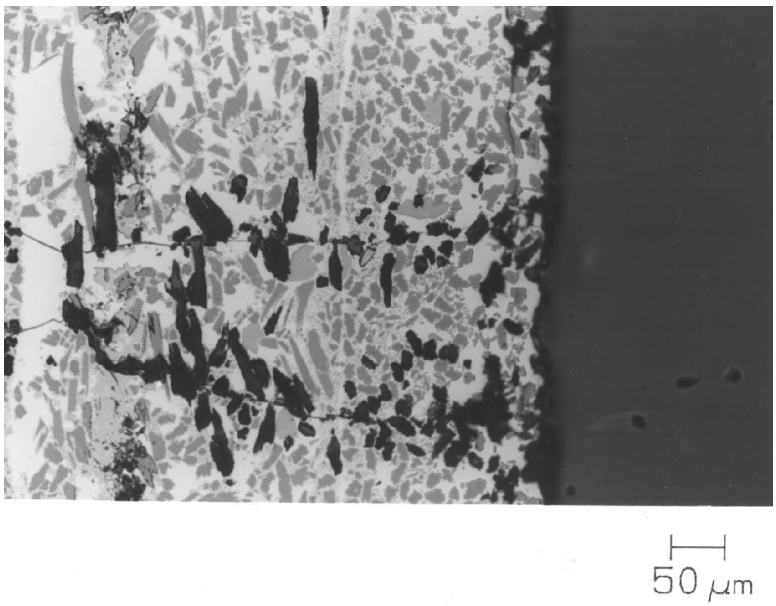

(B)

Figure 3-18. Optical micrographs of a prepreg MI composite made with Si3N4 coated SCS-6 fiber and the Phase 1 matrix composition following precracked oxidation exposure testing: (A) matrix crack region in the interior of the composite; (B) matrix crack near the surface.

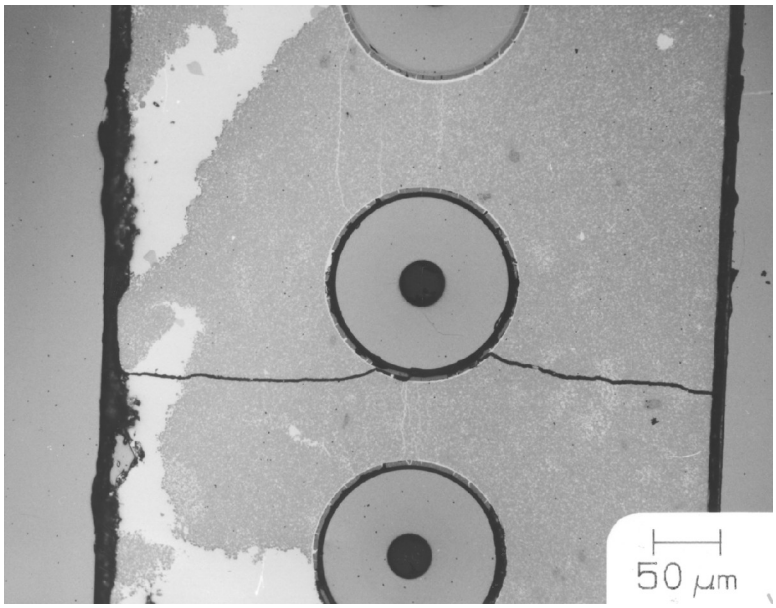

(A)

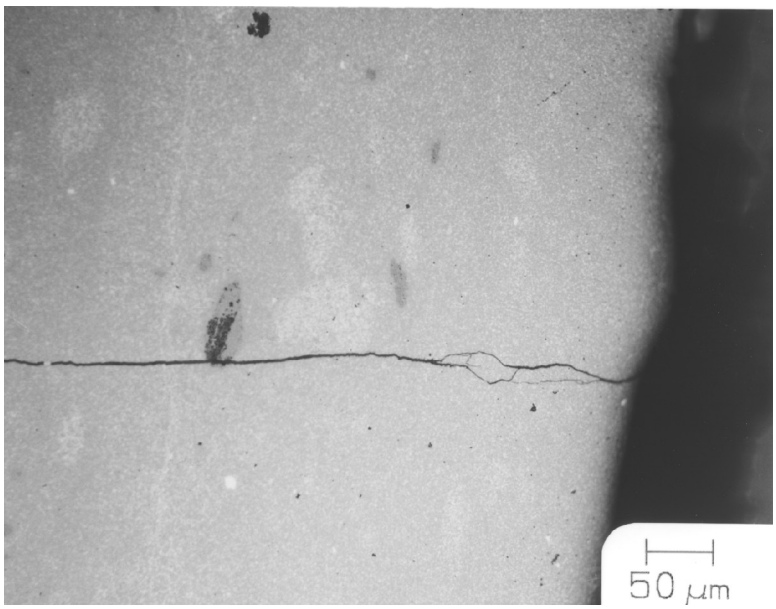

(B)

Figure 3-19. Figure 3-19. Optical micrographs of a prepreg MI composite made with Si3N4 coated SCS-6 fiber and the HGS matrix composition following precracked oxidation exposure testing: (A) matrix crack region in the interior of the composite; (B) matrix crack n near the surface.

Although the smaller crack opening displacement and residual carbon of the Phase 1 matrix appear to be protecting the fiber-matrix interface in the short term, both effects are only delaying the inevitable oxidative degradation of the composite. Eventually the matrix carbon exposed by the crack would be consumed and the interface carbon would be subject to extensive oxidation as is observed in the HGS matrix composites. Whether the delay in

interface attack would be sufficient to allow for crack sealing by oxidation is unclear; however, the added pore volume caused by the matrix carbon oxidation would also act to delay such sealing. Based on these microstructural observations we would expect the degradation in the Phase 1 matrix composites to eventually match that observed in the HGS matrix composites.

Oxidative degradation of the fiber-matrix interfaces in composites with BN fiber coatings was not as distinct as those shown in Figures 3-18 and 3-19 for the Si_3N_4 fiber coatings. Nevertheless a substantial impact on mechanical properties was observed for the SCS-6/BN/HGS composite indicating that crack and/or interface sealing by oxidation of the BN fiber coatings is not particularly effective in preventing composite degradation.

Degradation of the SCS-UFP/BN/Phase 1 matrix composite was similar to that for the SCS-6 fiber composites with the same coating/matrix combination. Again this is likely due to the protective effects of the Phase 1 matrix and not to any inherent stability of the fiber matrix interface. Unfortunately there was not a sufficient quantity of coated SCS-UFP fiber available to allow for fabrication of HGS matrix composites, which would have been a better test of the interface stability.

Results of the stressed oxidation tests performed at 1093°C (2000°F) are listed in Table 3-7. None of the samples tested at 1093°C lasted the full 100 hours. Looking only at composites with SCS-6 fibers, Phase 1 matrix composites survived longer than did the HGS matrix composites, which is consistent with the precracked oxidation test results. Microstructural examination of the samples after testing showed the same features as found for the precracked oxidation specimens shown in Figures 3-18 and 3-19. Oxidation of residual matrix carbon in the Phase 1 matrix was protecting the fiber surface carbon layers by gettering oxygen that was penetrating the cracks whereas no such protective mechanism was present in the HGS matrix.

A somewhat surprising result was that the composite sample with the SCS-UFP fiber, BN fiber coating and Phase 1 matrix failed earlier than any of the SCS-6 samples with Phase 1 matrices. At first this was believed to be caused by the relatively low volume fraction fiber in the SCS-UFP sample. (The quantity of coated SCS-UFP fiber available was limited so the composite samples with this fiber were fabricated using an older tape casting technique rather than the drum winding procedure. A processing error during the tape casting step caused the SCS-UFP samples to have a lower fiber volume fraction, roughly 13 vol%, compared to the SCS-6 fiber composites, which had typically 20 vol% fiber.) Subsequently an SCS-UFP composite sample was tested at a lower stress of 69MPa, which would have given roughly equivalent stress on the fiber bridging the matrix cracks as was experienced in the SCS-6 fiber composites at 103MPa. However the SCS-UFP composite specimen showed even a shorter life at this reduced stress level. Post-test microstructural examination of the test samples did not give any conclusive evidence as to why the SCS-UFP composites had a shorter life than the SCS-6 composites with the same matrix.

Table 3-7. Results of Stressed Oxidation Tests on Monofilament Fiber MI Composites Tested at 1093°C

Fiber	Fiber Coating	Matrix Composition	Stress Level (MPa)	Life (hrs)
SCS-6	Si_3N_4	Phase 1	103	78
		Phase 1 + B_4C	103	31
		HGS	103	0.28
	BN	Phase 1	103	3.2
		HGS	103	0.37
SCS-UFP	BN	Phase 1	103	1.2
			69	0.08

A limited number of stressed oxidation tests were also run at 704°C (1300°F) using only SCS-6 reinforced composite samples. Unlike the tests at 1093°C, all of the specimens survived the 100 hours of stressed oxidation exposure at 704°C and were subsequently tested to failure at 704°C. Results for these tests are listed in Table 3-8. The % retained ultimate strength and strain to failure values in Table 3-8 are relative to the values observed in fast fracture testing of as-fabricated composites tested at 871°C (1600°F).

Quite significant degradation was observed in 3 of the 4 samples tested at 704°C, with a greater than 40% reduction in strength or strain to failure after stressed oxidation exposure. At this temperature there was not the large difference between the Phase 1 and HGS matrices that were seen at 1093°C, indicating that the gettering effect of the matrix carbon in the Phase 1 matrix is not as effective at this lower temperature.

In neither the precracked oxidation nor stressed oxidation testing at both 1093°C and 704° was there any demonstrated benefit from having the B_4C doping the Phase 1 matrix. The anticipated crack sealing benefit of added boron to the Phase 1 matrix may be outweighed by the increase in residual matrix carbon caused by the extra boron, as discussed in section 3.2.1.4. Oxidation of the carbon along the crack faces counteracts the crack sealing benefit of the boron by creating additional volume that must be filled to seal the crack.

Table 3-8. Results of 100 Hour Stressed Oxidation Tests on SCS-6 Fiber Reinforced MI Composites Tested at 704°C

Fiber Coating	Matrix Composition	% Retained Ultimate Strength	% Retained Strain to Failure
Si_3N_4	Phase 1	60	35
Si_3N_4	Phase 1 + B_4C	20	7
BN	Phase 1	91	124
BN	HGS	79	56

3.2.1.7 Shape Demonstration with Monofilament Fiber

The work described here falls under program task 3.1.c Shape Demonstration. The purpose of this effort was to demonstrate the feasibility of fabricating the shroud design developed under Phase 1 of the program. A rendition of that design, affectionately referred to as the "soap dish" design, is shown schematically in Figure 3-20. All fabrication trials with the monofilament-reinforced system were done with uncoated SCS-6 fiber since the main goal was to demonstrate the shape and no mechanical testing of the demonstration parts was planned.

The key challenges to fabricating this design are the sharp right angles where the side walls, end walls and bottom face intersect. It was clear that SCS-type monofilament fibers did not possess the necessary flexibility to bend around these corners. During initial fabrication trials with the standard matrix composition it was determined that the slight bend going from the hot gas path face to the inclined aft section, representing an 11° angle, could not be fabricated from a single piece. Although the fiber could be bent to the necessary shape during compression molding, spring-back of the fiber during release from the mold caused delaminations in this bend region. Also, fiber could not be bent around the front curved section between the front wall and the hot gas path surface, making it necessary to fabricate this section of the shroud with uniaxial reinforcement only in the transverse direction. Consequently, the final shroud configuration that was fabricated was formed from seven separate pieces and then joined in the green state. The ability to engineer such joints and realize tough failure behavior was later demonstrated under Task 3.5 Joining, to be described later.

The seven pieces needed to fabricate the shroud shape are indicated in Figure 3-20, and include the 1) main hot gas path face, 2) aft inclined section of the hot gas path face, 3) front radius section, 4) front wall, 5) rear wall, and 6) and 7) two side walls. Each of the pieces was processed through the lamination and cure step, most as simple flat panels, and then machined to size. The joints between all parts, except those involving the front bend (piece number 3), were fabricated as "fingered" or "tongue-in-groove" joints. Precise cutting of the fingers into part 3 was not possible due to the curvature of the piece and the fact that it was only uniaxially reinforced. Once all the necessary parts were machined the shroud pieces were assembled using additional matrix slurry as the "glue" in the joints. The assembled parts were then held in place between female and male mold pieces and heated in drying oven to dry and cure the matrix slurry glue. The cured shroud preforms were then put through the standard burnout-infiltration cycle.

Successful cutting of the tongue-and-groove features into pieces made with the standard matrix composition was difficult due to the low green strength of this matrix. Delaminations typically formed either during cutting or during the binder burn-out step. Two attempts were made using the standard matrix composite, but both had only marginal success. Machining of the HGS matrix composite material, however, was much easier. This composition was much more resistant to delamination through the machining, curing and burn-out processes. Consequently fabrication of the shroud was much more successful. Photographs of the shroud made with the HGS matrix composition are shown in Figure 3-21.

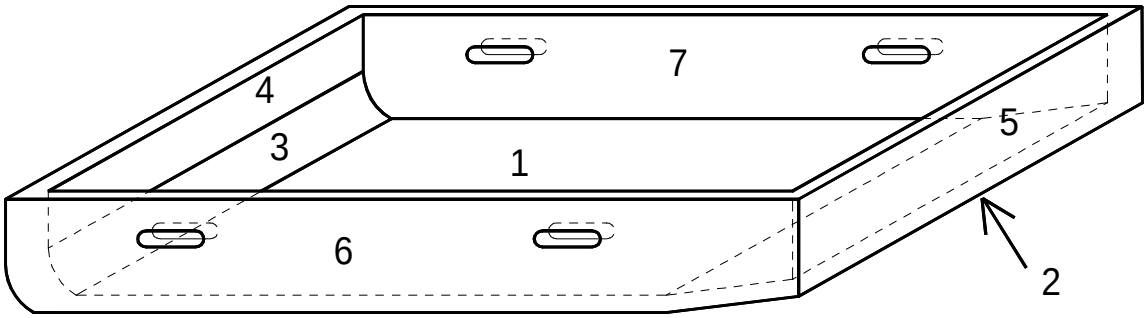

Figure 3-20. Schematic drawing of the "soap dish" shroud design developed in Phase 1 of the CFCC program.

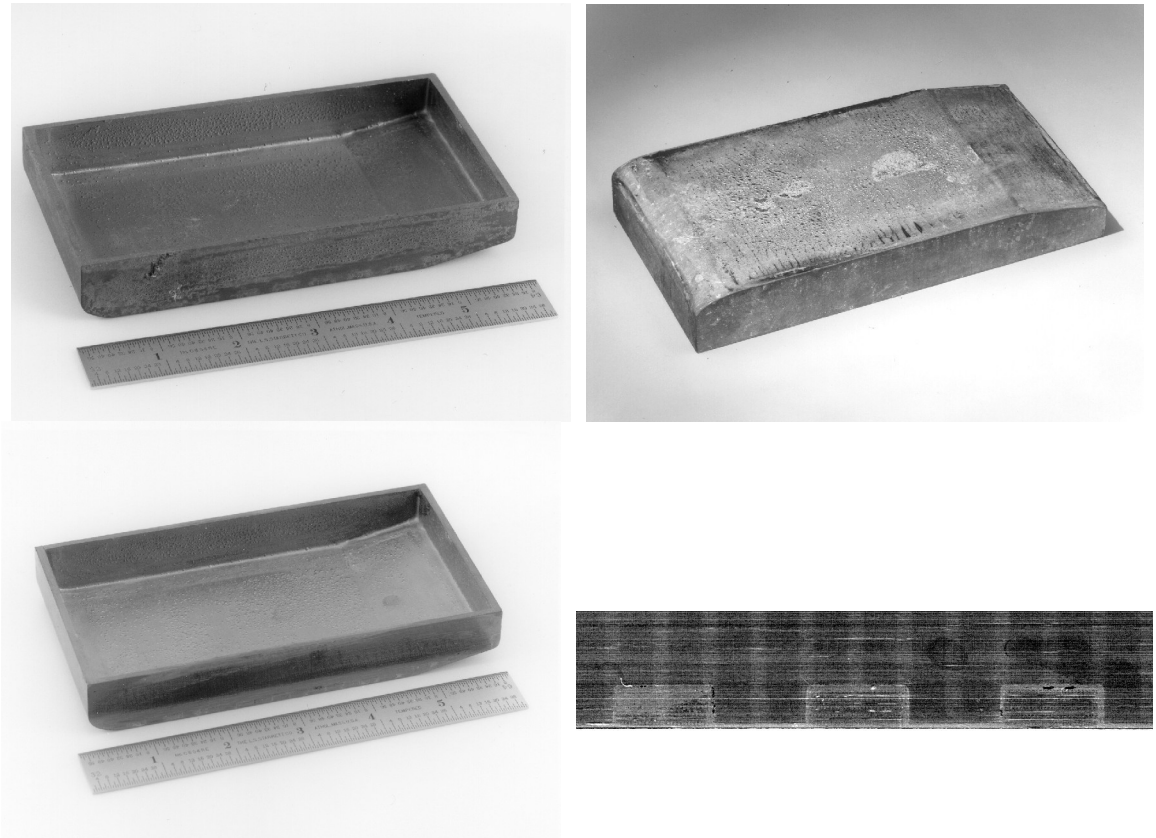

Figure 3-21. Photographs of the demonstration "soap dish" shroud design made from SCS-6 fiber in the HGS matrix:
Top – Photographs in the as-infiltrated condition
Bottom Left – After grinding the surfaces to remove excess Si
Bottom Right – Close up photo showing structure of the fingered joint on the machined shroud edge.

3.2.1.8 Monofilament System Summary

The above results paint a rather bleak picture as to the potential for Textron monofilament-reinforced MI composites to meet the long life requirements of the turbine shroud or combustor liner applications. Combined mechanical/oxidative testing of SCS-6 reinforced composites has clearly shown them to have unacceptable degradation following matrix cracking, largely caused by fiber/matrix interface oxidation dominated by the 3μm thick carbon surface layer on the fibers. The SCS-0 fiber, which has no carbon surface coating and much lower interface oxidation rates, cannot be reproducibly fabricated with acceptable mechanical strength. Our final option was the SCS-Ultra first pass fiber which is fabricated with a very high strength and has only 0.5μm of carbon on its surface. It was our hope that this carbon layer was sufficiently thin that the oxidation resistance of the interface would not be compromised. This was indeed true under dry oxidation conditions, where interface oxidation of BN-coated SCS-Ultra fiber was comparable to that of BN-coated SCS-0 fiber. However, the above results for wet oxidation indicate that BN-coated SCS-Ultra fiber has similar oxidation resistance to BN-coated SCS-6. We already know that composites with BN-coated SCS-6 have unacceptable oxidation behavior, which by comparison implies that the oxidation behavior of composites with BN-coated SCS-Ultra will also be unacceptable, particularly under wet oxidation conditions.

Considering the above results, we decided to drop the Textron monofilament-reinforced composite systems from the program. This action was based on the following considerations: 1) it was always recognized that the monofilament system would have shape-forming limitations relative to the fine-diameter fiber system which can be only partially overcome by composite joining, 2) Textron was unable to reproducibly fabricate SCS-0 fiber with acceptable strengths, 3) the oxidation resistance of SCS-6 and SCS-Ultra first pass fiber are not acceptable for the considered application, and 4) scale-up of the continuous fiber coating process in Task 3.2 yielded coatings which gave low strength, low toughness composites. In the short term it appeared that Textron would be unable to address these limitations of their fibers and coatings. Monofilament-reinforced MI composites may still prove to be useful materials, particularly in applications requiring the highest values of thermal conductivity and interlaminar strength, if a high-strength fiber can be produced with no surface carbon coatings, and if the desired component has a suitable shape. Work at Amercom under the IHPTET consortium was aimed at just such a goal, but development of a commercial fiber in time for evaluation in Phase II was not possible.

3.2.2 Small Diameter Fiber System

Development of a strong, tough MI composite system based on small diameter SiC fibers (such as Hi-Nicalon™) was started under the NASA-sponsored High Speed Civil Transport (HSCT) program. The particular process developed at GEGR was to pre-coat the fibers using a batch CVD reactor and then form pre-impregnated tapes (pre-preg) by a wet drum winding procedure. The pre-preg tapes were then stacked and laminated to form a composite preform, and then silicon melt infiltrated to give a finished composite. (Figure 2-2 shows a schematic representation of the prepreg MI process.) The properties of this

composite system were quite good; however, the batch CVD fiber coating step was limited in scale, and was thus expensive and limited the overall throughput of the process. It therefore became necessary to develop, in conjunction with a commercial fiber coatings vendor, a more scalable process for fiber coating. Based on our work with TSM, a continuous coating process, where the fiber tow is pulled continuously through a CVD reactor vessel, appeared to be the most promising in terms of scalability and fiber coating quality. However, a larger-scale batch coating process was also considered viable. The overall goal of this task was therefore to develop, in cooperation with a coatings vendor, a larger-scale fiber tow coating process for use in MI composites. This effort would also include making any necessary composite processing changes needed to utilize this new fiber coating. Success for this task was to be the demonstration of mechanical properties of composites using the new coatings that were at least as good as, if not better than, properties using the batch CVD coatings.

The pre-CFCC coating configuration that was optimized using GEGR's batch deposition system served as the baseline for all subsequent vendor fiber coating evaluations. The GEGR batch coating contained five layers, consisting of (moving from the fiber surface outward) a thin coating of carbon, BN, a second thin carbon coating, Si_3N_4, and a final thin coating of carbon. Each of these layers was put down using low pressure (<1 Torr), intermediate temperature (700-900°C) chemical vapor deposition (CVD).

The purpose of the initial flash carbon was to protect the fiber from chemical attack by reaction byproducts during BN deposition. The BN layer was deposited by reacting BCl_3 with NH_3, which produces HCl as a byproduct. Due to the slow BN deposition kinetics at these relatively low temperatures, the Hi-Nicalon fiber was exposed to HCl gas for an appreciable period before a continuous BN layer would form, and this exposure to HCl was found to degrade the Hi-Nicalon fiber strength. The thin layer of carbon, deposited via thermal cracking of acetylene, protected the fiber from HCl attack and degradation.

The BN layer is the main fiber-matrix debond layer in the composite, allowing the composites to exhibit high toughness and graceful failure. Unfortunately we knew from prior work on the monofilament system that BN was only marginally stable in contact with molten silicon as occurs during final composite infiltration/densification. This problem could be overcome with the large (~160μm) SiC monofilament fibers by using a relatively thick (>3μm) layer of the BN. However such a thick coating would not be feasible on the much smaller (~13.5μm) Hi-Nicalon fibers. It was therefore necessary to provide a protective coating over top of the BN layer, both to mechanically protect the soft BN coatings from physical damage during subsequent composite processing, and to chemically protect the BN from silicon during melt infiltration.

Silicon nitride was chosen over silicon carbide for the protective layer primarily based on convenience of deposition. Silicon nitride could be easily deposited using mixtures of di-chlorosilane (SiH_2Cl_2) and ammonia using conditions similar to those used for the BN deposition. The reaction byproducts are also very similar for the two reactions. Deposition of SiC coatings would have required different precursor chemistries and would have produced different byproducts, imposing additional waste handling and disposal

considerations. Despite these drawbacks, several attempts were made to deposit SiC-based coatings in the batch CVD reactor, but none of the experiments showed much success. Limited evaluations of vendor coatings using SiC in place of Si_3N_4 were also performed as part of the work described below, but they uniformly gave poorer performance than coatings from the same vendors with Si_3N_4 layers.

The second carbon layer, between the BN and Si_3N_4, served two purposes. First, it was difficult to produce continuous, smooth Si_3N_4 coatings directly on top of the BN layer, which was thought to be caused by poor nucleation of the Si_3N_4 on the BN. Providing a thin intermediate carbon layer greatly improved the continuity and uniformity of Si_3N_4 layer. Secondly, it is extremely difficult to get fully defect-free fiber coatings. Pinholes, cracks or other defects in the protective Si_3N_4 layer would expose the underlying BN to attack from silicon during infiltration. The thin intermediate carbon coating effectively acts as a getter layer, reacting with silicon that penetrates the outer Si_3N_4, forming SiC, and thereby "plugging" the Si_3N_4 coating defects and more effectively protecting the BN layer.

The final carbon layer is largely an aid for further composite processing. Complete wet-out of the fiber tows during the wet drum winding process step was significantly enhanced by the presence of the outer carbon coating due to improved wetting of the fiber by the matrix slurry. The carbon layer also helped with silicon infiltration as the carbon surface was much more readily wet by the molten silicon infiltrant than a Si_3N_4 coating surface.

3.2.2.1 Fiber Coating Vendor Evaluations

Early in the program several potential sources of fiber coatings were identified. These sources included Advanced Ceramics Corp. of Cleveland, OH, 3M of St. Paul, MN, Synterials, Inc. of Herndon, VA and General Atomics of San Diego, CA. During the course of fiber coating development and evaluation, coatings were obtained from each of these vendors. (ACC is now part of GE, and is known as GE Advanced Ceramics. However, at the time that work was performed with their fiber coatings, from 1995-1999, the company was not part of GE. Consequently the name ACC will still be used in this report.)

In most cases the coatings development activity was iterative in nature. Initial coatings to be produced by each vendor were specified to be similar to the "standard" batch fiber coating configuration developed at GEGR. The initial carbon layer of the GEGR batch fiber coating was eliminated from most of the evaluations as each of the coating vendors claimed the ability to deposit BN directly onto Hi-Nicalon without any fiber degradation. Elimination of this layer, resulting in a 4-layer rather than a 5-layer coating, also provided some cost reduction for the coating process. This 4-layer fiber coating with an initial BN layer is referred to as "configuration A" throughout the remainder of this report.

Upon delivery of the coated fibers to GEGR they were processed into test composites for both mechanical and microstructural examination. Characterization of the coated fiber alone, without first processing it into composite samples, proved to be too difficult to do on a routine basis. Such examinations required use of electron microscopy, with which it

was often difficult to obtain reliable measurements of the individual coating layers. Moreover, because of coating thickness variations it was necessary to evaluate many individual fibers in order to obtain "average" coating thicknesses, which were always subject to sampling error. By optical examination of sectioned composite samples one could see the entire fiber tow cross section, making it easier to evaluate overall coating thickness uniformity. Examination of composite samples also gave information about how well the coatings were surviving the fabrication process and melt infiltration procedures, both very important criteria for assessing overall coating performance.

Following composite characterization, recommendations were made for changes in the fiber coating composition and/or thickness for the next round of evaluations. The new coating configuration would then be specified to the coatings vendor and the entire process repeated. Because of the times required for waiting in the vendors' job queue, for processing the fiber coatings, and for carrying out the composite fabrication and characterization steps, the overall coating development process was slower than desired. Unfortunately such an approach was necessary because of the high costs associated with application of the fiber coatings. The large number of coatings variables that needed to be considered would have required an excessive number of coating trials had a "shotgun" or a statistical design of experiments approach been used.

3.2.2.1.1 Fiber Coatings From General Atomics

Of the four prospective fiber coatings vendors, General Atomics (GA) was eliminated from consideration early in the process. The initial fiber coatings order placed with GA took roughly 9 months to complete, fully 3X longer than promised. Moreover, the coated fibers yielded weak, brittle composites. Microstructural examination of the composites showed that the majority of fibers had very little, if any, coating. Given this result, and the fact that GA had the highest coating prices of any of the vendors, no further evaluations were made of GA fiber coatings.

3.2.2.1.2 Fiber Coatings From 3M

The other three vendors all managed to provide coated fiber tow that resulted in tough MI composites. Composite tensile stress-strain plots for samples made from configuration A tow coatings from the three vendors and from a standard GE fiber coating are shown in Figure 3-22.

The fiber coatings obtained from 3M were deposited using a continuous, atmospheric pressure Metallo-Organic Chemical Vapor Deposition (MOCVD) process. This process held a potential cost advantage over the other processes because no vacuum equipment was required. However, 3M was still practicing this process on a laboratory scale with substantial manual control. Also, atmospheric pressure deposition required relatively low deposition temperatures and high reactant dilution in order to obtain uniform thickness coatings throughout the fiber tow. This meant that the overall deposition rates and process throughput were no better than with the vacuum CVD processes. Overall, the small lab scale of the process and the slow throughput combined to make the 3M coatings the next highest cost behind GA of all the vendor coatings being evaluated.

The coated fiber tows from 3M also had significantly more physical damage from the coating process, with many broken fibers within the tows. This fiber damage was presumably caused by the specific designs of the fiber guides and winder used with the coater, and thus could have been remedied. Nevertheless, the presence of the broken fiber made fabrication of uniform prepreg tapes more difficult.

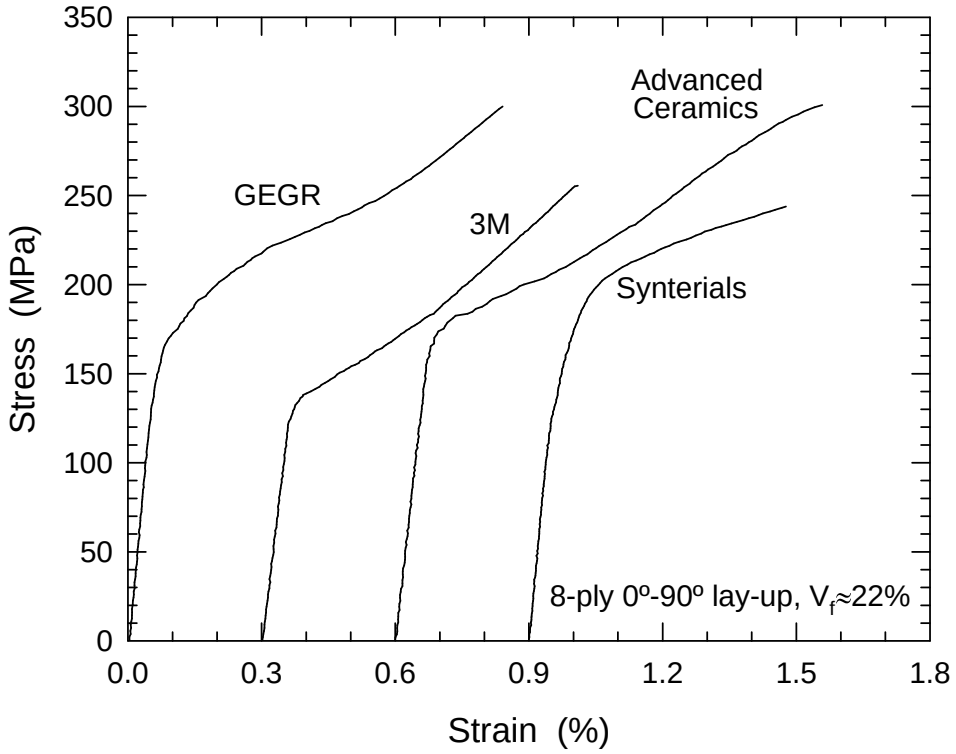

Figure 3-22. Room temperature tensile stress-strain behavior of prepreg MI composite samples made with configuration A fiber coatings from the four sources indicated. (Curves are offset for clarity.)

Despite the slow throughput and low deposition temperatures, coating thickness uniformity was still worse for the 3M coatings than for the other vendors being evaluated. Figure 3-23 shows the typical variation seen between thickest and thinnest fiber coating within a single tow cross section. The low-temperature, low-pressure batch CVD processes used by GEGR and Synterials gave the most uniform fiber coating thicknesses, as would be expected. Advanced Ceramics Corp. (ACC) coatings, which were deposited at low pressure but at high temperatures, were less uniform with a greater spread between thickest and thinnest coatings. The 3M coatings deposited at atmospheric pressure showed the largest spread between thickest and thinnest coatings. The reasons for this behavior was that the reactant dilution, and thus coating deposition rate, was dependent on position within the reactors. As the fiber deviated from the center line of the reactors the deposition rates increased dramatically. The large number of broken fiber within the 3M tows meant that some of the fibers extended well out from the nominal tow position, and thus received

a large excess of coating. An optical micrograph of a composite made with 3M fiber coatings is shown in Figure 3-24, which illustrates the extreme coating thickness variation and roughness of the thicker coatings. Although the number of fibers that exhibited such an extreme coating thickness was small, the strong dependence of deposition rate with position in the reactor would make overall coating thickness reproducibility fairly difficult. Presumably this problem was related to reactor design and could be remedied with reactor modification and scale-up; however, 3M expressed no intentions of upgrading their facilities since there was no long-term business commitment to continuing their CVD fiber coating endeavor.

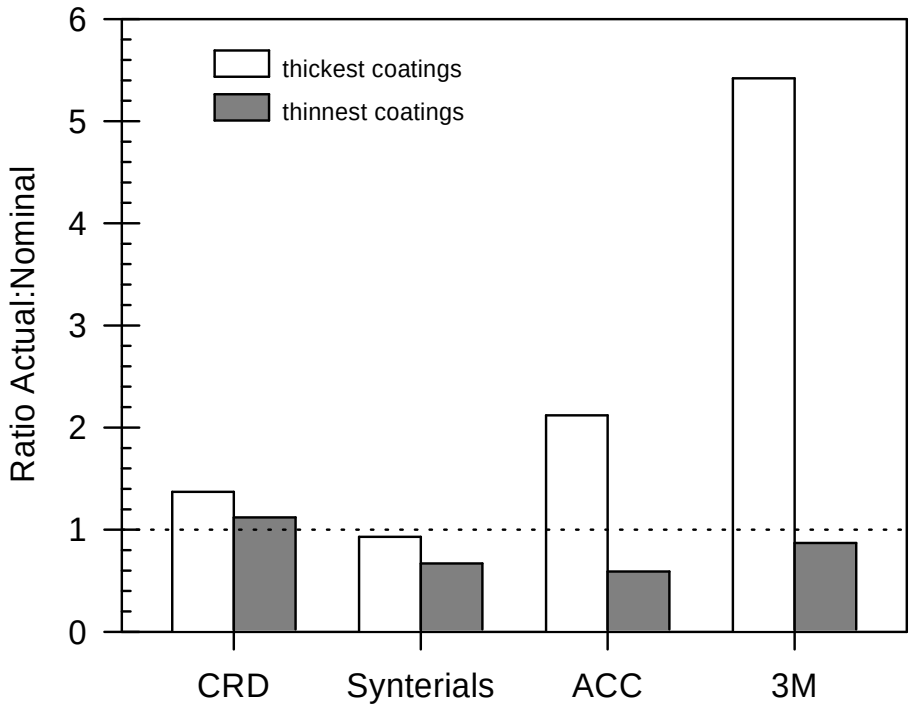

Figure 3-23. Relative coating thickness (actual/target) for the thickest and thinnest fiber coatings observed within a single tow cross section for four fiber coating sources.

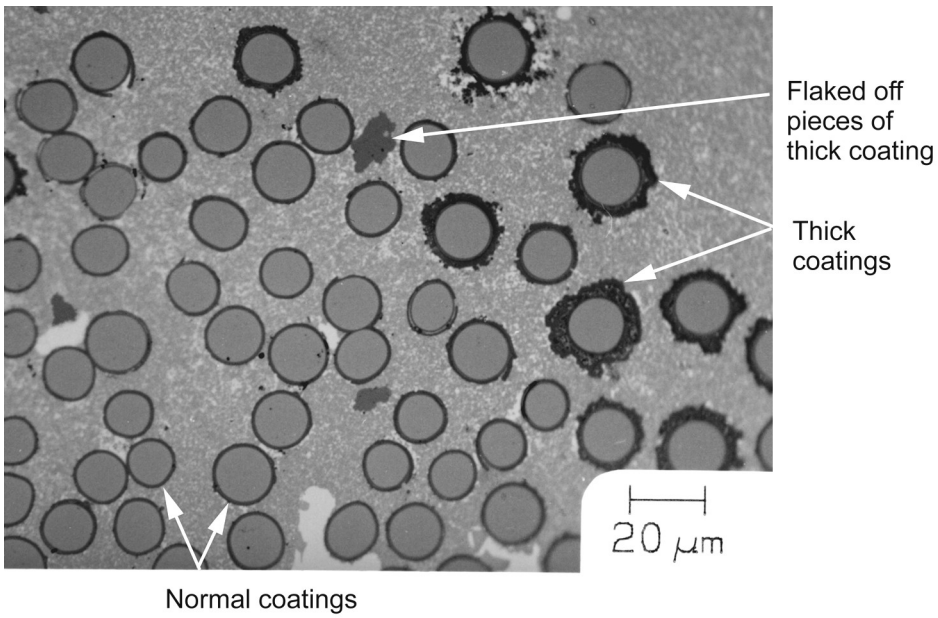

Figure 3-24. Optical photomicrograph of a prepreg MI composite fabricated using fiber coated by 3M.

Only 3 coating iterations, including 5 different coating variations in total, were performed with 3M. The tensile data in Figure 3-20 shows the best performance observed with 3M coatings in the prepreg MI composite. Despite this promising performance in the composite, 3M was also eliminated as a potential fiber coatings source because of cost, poor coating uniformity and lack of business commitment to the fiber coating efforts.

Shortly after they were eliminated from consideration as a fiber coatings source for this program 3M made a business decision to cease its CVD fiber coating efforts. At that time 3M was utilizing the coating facility only intermittently and could not justify the cost of maintaining the facility for the small production levels that it was experiencing or could anticipate from its small number of customers. This decision by 3M confirmed our earlier assessment as to their lack of long-term commitment to the fiber coating business.

3.2.2.1.3 Fiber Coatings From Synterials, Inc.

Synterials, Inc. utilized a batch-mode low pressure, low temperature CVD process that tended to result in very uniform coating thickness across a given tow cross section, as shown by the data in Figure 3-23. However, coating thickness reproducibility batch to batch was not as good. Individual fiber coating batches ranged in thickness from 50% below the desired thickness to 30% over the desired thickness. Even the coating thickness within a single coating run was found to vary along the length of the fiber by as much as 40%.

Because Synterials could wind a large amount of fiber on their coater mandrel, the reactor could coat 2-3 fiber spools simultaneously. This allowed Synterials to offer the lowest cost fiber coatings of any of the vendors; however, when coating large amounts the coating uniformity and performance was found to suffer. The best composite obtained with fiber coated by Synterials, for which the stress-strain plot appears in Figure 3-22, was actually coated as a single wound layer on the coater mandrel and was thus less than ½ of a single fiber spool.

Over ten different coating configurations were evaluated from Synterials with generally poor results. Optical micrographs of composites made from two of the coating variations are shown in Figure 3-25. Due to the fibers being wound on a mandrel the individual fibers within a tow are pressed together by the tension in the tow during the coating process. This situation leads to an increase in the prevalence of fibers being bonded together by the coatings, as shown by the fiber clumps in Figure 3-25. Moreover the Synterials coatings often appeared to be more susceptible to either physical damage or silicon attack. It was not uncommon to find fiber coatings that were broken and partially or fully spalled from the fiber. In the thicker coating iterations evaluated many of the coatings showed spontaneous cracks, presumably caused by residual stresses in the thick coatings.

Poor composite performance from damaged fiber coatings as shown in Figure 3-25 is to be expected; however, there were several coating iterations obtained from Synterials that had very few detectable physical defects. Despite that lack of observable defects, the Synterials coatings almost always resulted in composite strengths below 170MPa with strain to failure values below 0.3%. (The data presented in Figure 3-22 reports the best sample ever obtained from Synterials fiber.) Scanning Auger electron spectroscopy analysis of the fiber coatings indicated that the stoichiometry of the BN and Si_3N_4 coating layers are similar to those of bulk BN and Si_3N_4 standards, but with somewhat higher levels of O and C impurities. The reasons for the relatively poor performance of Synterials fiber coating were never fully understood, and evaluation of the Synterials was halted when an alternate coating source, described below, showed better performance.

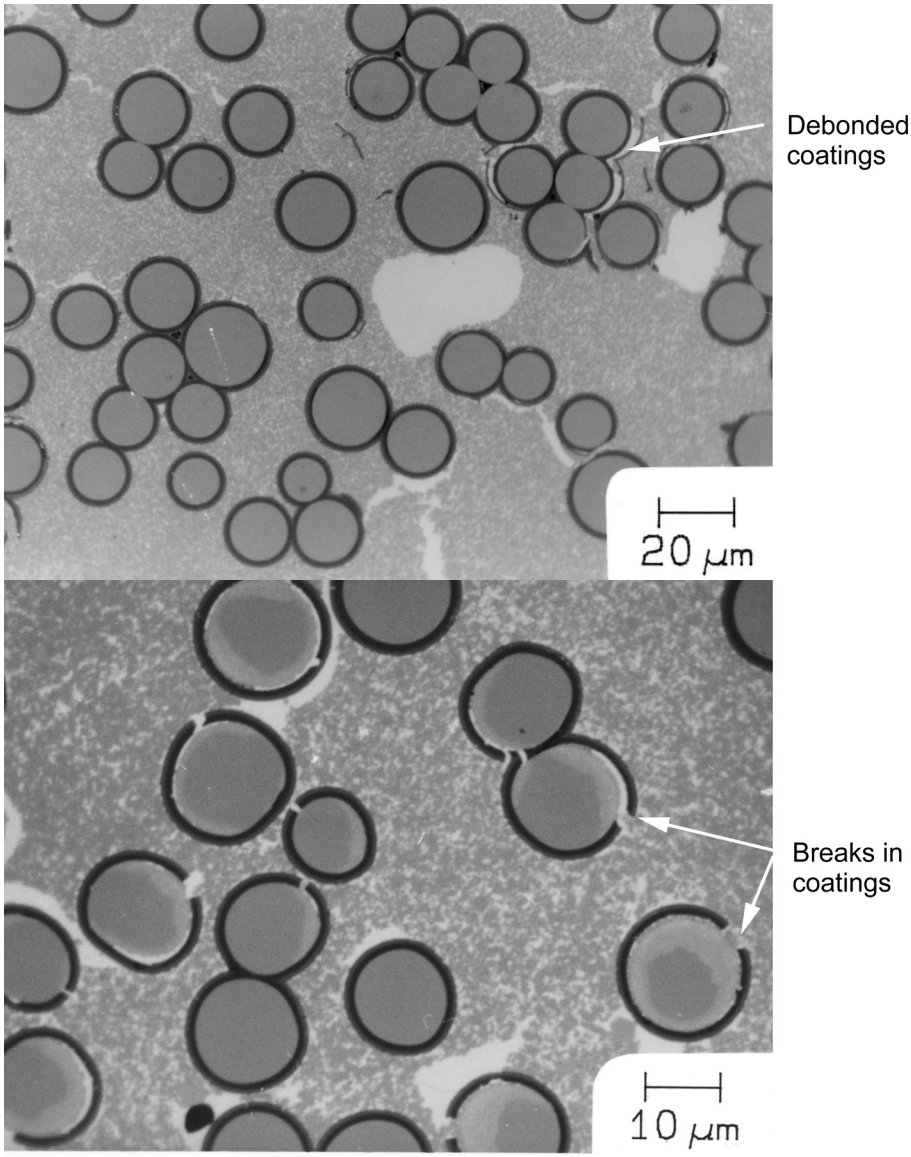

Figure 3-25. Optical photomicrographs of prepreg MI composites made with fiber coated by Synterials, showing the tendency for fiber bonding by the coatings and typical fiber coating spalling and cracking defects.

3.2.2.1.4 Fiber Coatings From Advanced Ceramics Corp.

The greatest success with vendor fiber coatings was with those produced by Advanced Ceramics Corp. (ACC). ACC used a low pressure, high temperature CVD process that is partially based on their bulk CVD BN production practice[9]. Initially all coating fabrication was done in their "experimental" reactor, which was configured for processing 3 fiber tows simultaneously. Also, the fiber handling and transport mechanisms were designed such that each fiber passed through the reactor 3 times, effectively tripling the coater residence time compared to typical once-through coater designs. This allowed ACC to have the lowest coating costs for the continuous fiber coatings vendors.

ACC also had a unique coating microstructure compared to the other vendors thanks to its use of high deposition temperatures. The BN layers in ACC coatings were crystalline (graphitic) in nature, whereas coatings from the other vendors tended to be only partly crystalline with grain sizes on the order of 10's of nanometers. This was considered an advantage since highly crystalline BN coatings deposited at high temperatures are known to have improved resistance to oxidation and hydration compared to low deposition temperature, highly amorphous BN [10,11].

One of the problems encountered during the development of the ACC coatings was again related to coating thickness uniformity. The qualitative thickness distributions for batch (GEGR and Synterials), 3M and ACC fiber coatings are shown schematically in Figure 3-26. The batch CVD coatings from GEGR and Synterials generally showed little fiber-to-fiber thickness variation within a tow, and thus are shown by the relatively narrow distribution in Figure 3-26. The 3M coatings had a fraction of excessively thick coatings, as described previously, such that the distribution could be considered bi-modal. Nevertheless, the thickness of the majority of coatings was similar to that of the batch coatings. The ACC coatings, on the other hand, typically had a broader thickness distribution. Whereas there were not as many of the excessively thick coatings as seen with the 3M coatings, the ACC coatings did show a greater proportion of very thin coatings compared to the other vendors.

The wider distribution of fiber coating thickness was a result of the high deposition temperatures used by ACC. At these high temperatures the chemical reaction rate is so high that the overall CVD process is gas transport rate limited rather than reaction rate limited. Under these conditions the precursor gases tend to react preferentially on the outer fibers of the tows with much less coating deposition on the fibers at the interior of the fiber tows. In fact, the fiber coating thickness was often seen to vary quite considerably across the thickness of a single fiber. A photomicrograph of a composite made from ACC coated fiber having somewhat exaggerated fiber coating thickness variation is shown in Figure 3-27.

Conceptually one can envision that there is an acceptable range for fiber coating thickness below which there is insufficient fiber debonding and potential chemical attack of the fibers during processing and above which there is too little load transfer across the coating from the matrix to the fibers. The range between these high and low limits represents the "desirable range" for the fiber coating operation. With the continuous fiber coating approaches the initial coating thickness distributions were qualitatively perceived to produce substantial fractions of coated fiber outside the desirable range. Therefore much of the efforts with ACC in developing the fiber coatings was either to narrow the distribution in coating thickness or to modify the coating constituents and configurations in order to widen the desirable range.

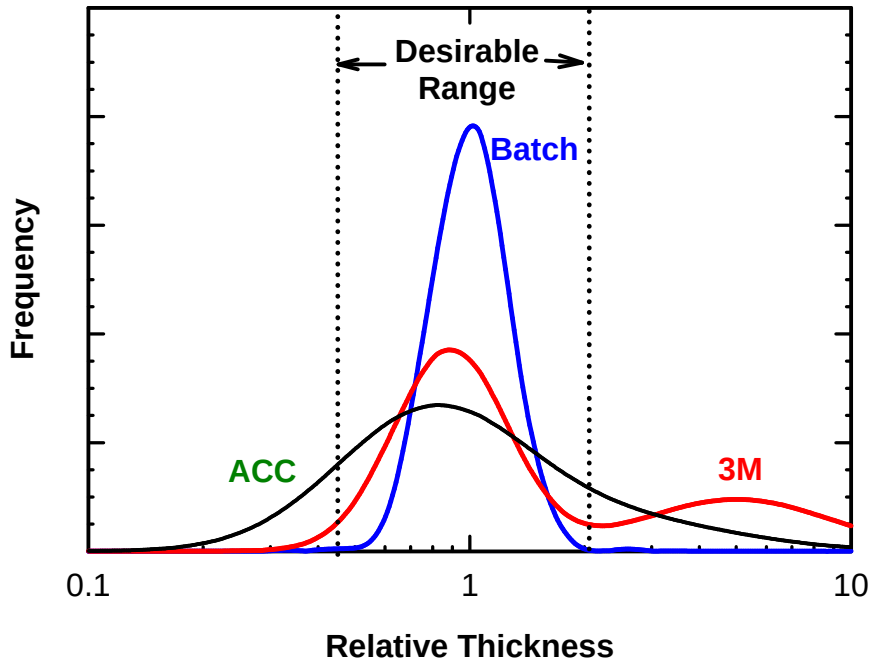

Figure 3-26. Qualitative representation of the coating thickness distributions obtained from different fiber coatings vendors. "Batch" applies to either GEGR or Synterials coatings.

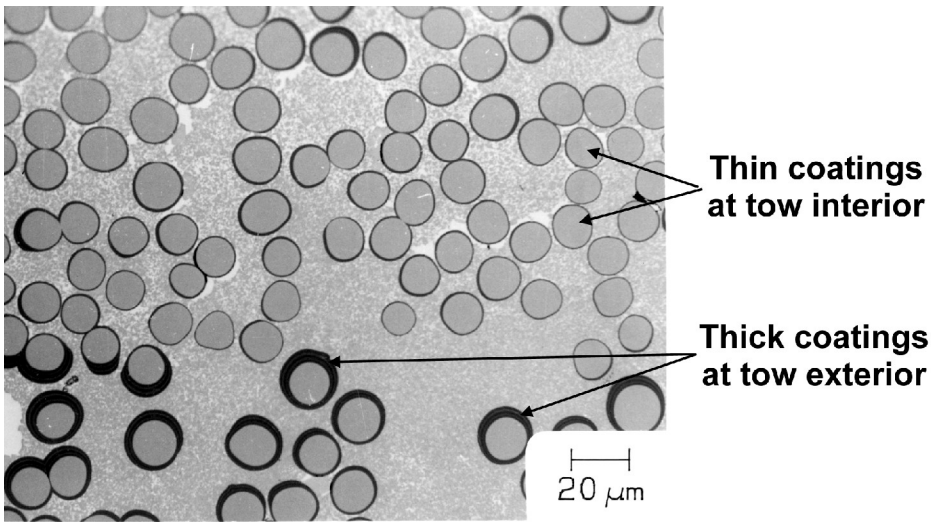

Figure 3-27. Optical photomicrograph of a prepreg MI composite made from fiber coatings obtained from ACC showing an exaggerated case of fiber coating thickness variation.

3.2.2.2 Vendor Fiber Coating Optimization

The work described in this section was performed under program task 3.2.a Process/Material Optimization, and includes work done on the initial coating composition developed at GEGR using the batch deposition approach, and work on coatings incorporating silicon-doped BN for improved oxidation resistance.

Over a 2½ year period roughly fifteen coating deposition iterations were performed in the ACC research reactor with configuration A coatings (i.e. made of BN, C and Si_3N_4 layers), encompassing over 25 coating process variations. From these coatings over 200 individual composite specimens were fabricated and tested. The goal of these experiments was to determine the lowest complexity, and therefore lowest cost, sequence of coating layers necessary to reproducibly yield good composite mechanical properties, and to optimize the thickness of each of the layers. Through theses numerous evaluations, optimum fiber coating layer thicknesses for standard configuration A fiber coatings from ACC were determined.

Fairly early in the coating optimization effort it became obvious that routine direct measurement of coating thickness was impractical due to the tediousness of the measurement and to the relatively wide coating thickness distribution making it necessary to survey a large number of fibers to come to an "average" coating thickness. Consequently fiber coating thickness was tracked by measuring the mass gain of the fiber tow through the coating process. By knowing the density of the deposited coating layers, which were measured from thick flakes of coating that built up on the reactor walls, and the nominal fiber diameter (taken to be 13.5μm for Hi-Nicalon) the nominal or average thickness of the coating layers could be calculated.

Throughout the fiber coating development process GE received considerable assistance from Oak Ridge National Laboratory, and particularly from Dr. Karren More, with characterization of the fiber coatings. Detailed SEM and TEM investigations of coated fiber, both after coating and after processing into composites, were performed to help verify the crystallinity and stoichiometry of the fiber coating layers and to investigate the interactions between the fiber, coatings and composite matrix. An example of such TEM work is shown in Figures 3-28 and 3-29.

Figure 3-28 shows a high resolution TEM micrograph illustrating the graphitic nature of the BN deposit in the center of one of the coating layers in an ACC deposited fiber coating. However, as shown in Figure 3-29, the BN that is deposited during the transitions into and out of the furnace hot section has a much finer crystallite size, bordering on being amorphous. The BN interlayers also have a higher concentration of oxygen, as determined by the EELS analysis that is shown in Figure 3-30. The Si_3N_4 layer, despite also having passed through the reactor three times during deposition, did not display the layered structure as did the BN. This lack of stratification could be related to the lower deposition kinetics at lower temperature for Si_3N_4 compared to BN, thus greatly limiting the amount of deposition that takes place in the cooler regions of the reactor.

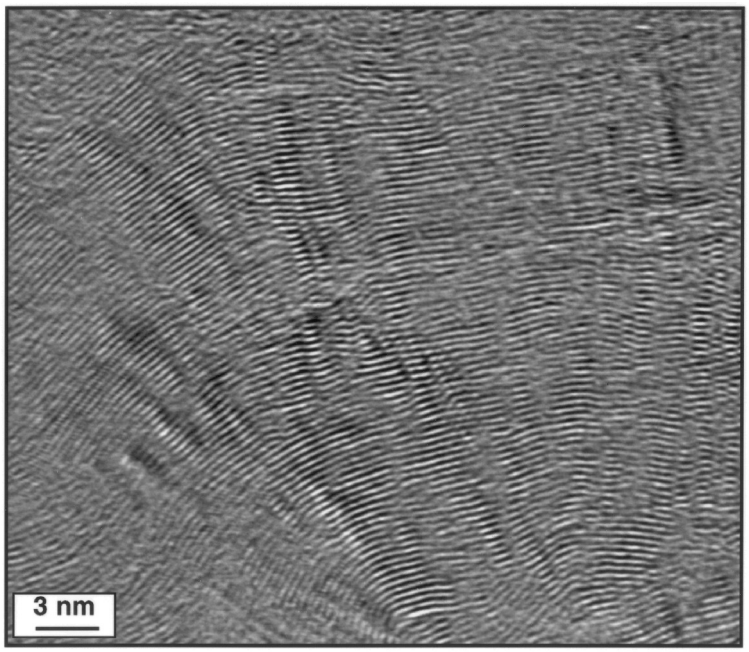

Figure 3-28. TEM micrograph of the center of a BN layer from an ACC fiber coating where relatively well-aligned, graphitic crystallites of BN were found.

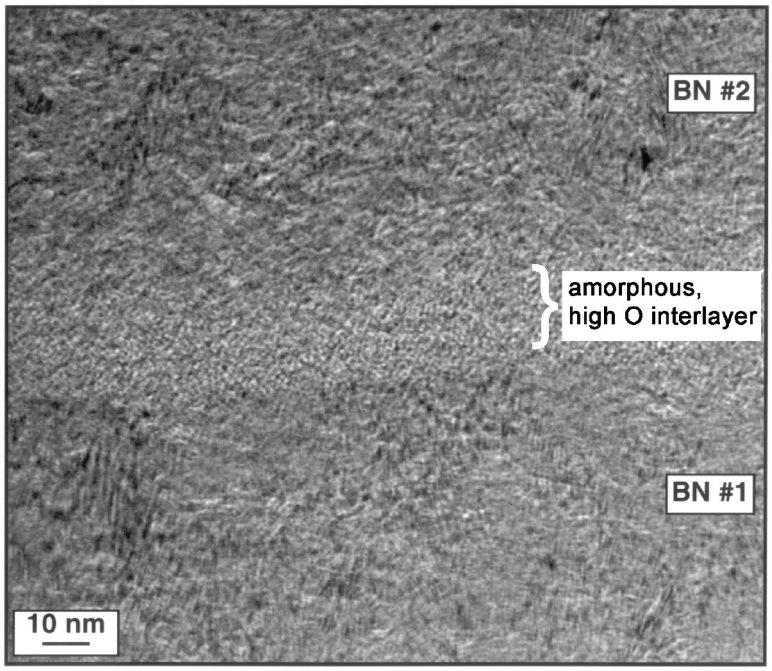

Figure 3-29. TEM micrograph of the interlayer region between two BN layers in an ACC fiber coating, indicating the size of the amorphous, high oxygen interlayer.

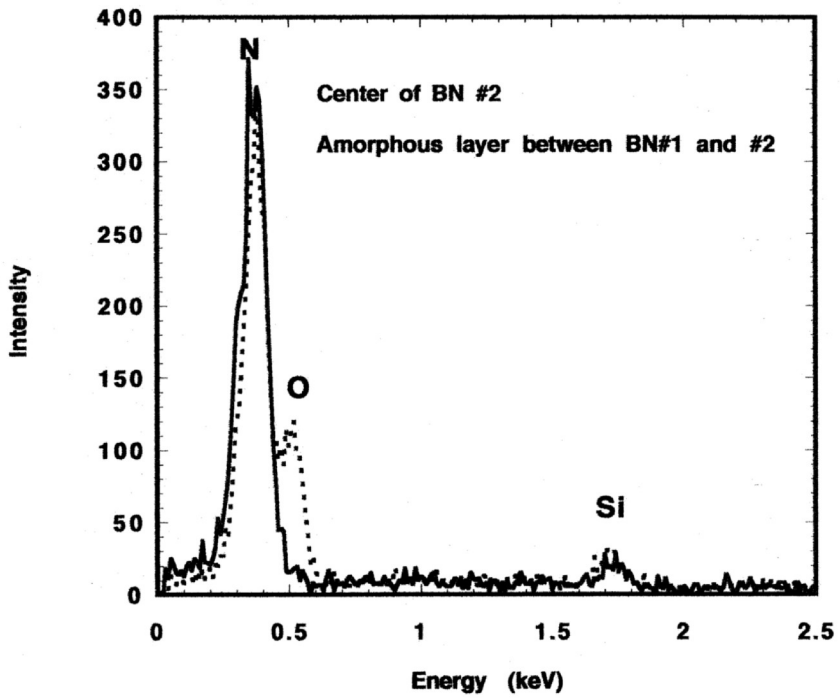

Figure 3-30. EELS analysis results from the BN layer of a standard ACC coating deposited in the experimental coater. The solid line represents the spectrum from the middle of one of the BN layers and the dashed line represents the spectrum from one of the amorphous interlayers. Qualitative analysis indicates 5-6 atomic% oxygen in the interlayer regions.

3.2.2.3 Oxidation Resistant Fiber Coating Development

One of the advantages of the ACC fiber coatings was that the coating layers, particularly the BN layer, were deposited at relatively high temperatures, in the neighborhood of 1400°C-1500°C, as opposed to the 800°C to 1050°C typically used in other CVD fiber coating processes. It had been recognized that the resistance of BN to attack by ambient moisture was improved as the deposition temperature was increased, due to the increased crystallinity and purity of the BN[10]. Similar improvements in the high temperature oxidation resistance in dry air with increased crystalline perfection of BN coatings on C/C had also been demonstrated[11]. It was therefore anticipated, and later proved[12], that the high-temperature deposition of BN, with the improved purity (lower oxygen impurities) and higher crystallinity that the higher temperature process produces, improved fiber coating oxidation resistance as well. Nevertheless, the BN layer of the fiber coatings continued to be the most oxidation prone phase in the CMC, and oxidation of the BN layer also causes severe degradation of the composite mechanical properties due to bonding of the fiber to the matrix from the oxidation products. Hence there was still a strong incentive to develop interface coatings with even greater oxidation resistance.

In late 1995, during the development of the standard ACC fiber coatings, additional work ongoing at ACC regarding using silicon-doped BN (B(Si)N) came to light. The B(Si)N coating had been originally developed as a potential oxidation-resistant coating for carbon[13], and was being considered as a potential fiber-matrix interface coating for SiC-based CMCs [14,15]. Silicon doping of BN at level of 26 to 42 wt% Si had resulted in approximately three orders of magnitude reduction in the oxidation rates in oxygen at 1200°C or in air at 1510°C [15]. However, the response of the B(Si)N materials to high temperature "wet" oxidation was not known. As noted previously, the combustion atmosphere in a gas turbine engine contains on the order or 1 atmosphere of water vapor, and the presence of water was known to greatly influence the oxidation/volatilization rate of BN. Whether Si-doping of the BN would improve the oxidation behavior in wet atmospheres still needed to be determined. Also, strong, tough composites using B(Si)N coatings on small diameter SiC fibers had not yet been demonstrated.

As originally envisioned, the B(Si)N coating would be used as a substitute for the BN layer in the standard fiber coatings. However, if B(Si)N was effective as both a debond layer and was also resistant to Si attack during melt infiltration, then one could consider replacing the BN, 1st carbon and Si_3N_4 layers by a single B(Si)N layer. Alternatively one could also use a graded coating, starting with pure BN at the fiber surface for debonding purposes and then increasing the Si content radially in the coating to a high enough level, even to the point of going to pure Si_3N_4, as to be an effective silicon barrier. However, realization of the graded coating concept would involve major modifications to the ACC fiber coaters, and so this approach was not pursued actively.

The desirability and viability of using B(Si)N fiber coatings in MI composites was therefore dependent on four important factors: 1) did B(Si)N show improved oxidation resistance over BN under wet oxidation, 2) were B(Si)N coatings chemically and physically compatible with the MI composite process, 3) could B(Si)N provide for effective fiber-matrix debonding, and 4) if the answers to questions 1, 2 and 3 were "yes" then what was the optimum silicon doping level to be used.

In order to answer the first question GE obtained several samples of CVD BN from ACC having various levels of Si doping. The pure pyrolytic BN sample had been deposited at 1800°C whereas the B(Si)N samples were deposited in the 1400°-1450°C range. The samples were analyzed at GE using X-ray Photo-electron Spectroscopy (XPS) to determine the actual levels of Si doping. The results of the analyses are shown in Table 3-9. The nominal compositions were estimated by ACC based on the deposit having the same B:Si ratio as the mixture of gas reactants (BCl_3 and $SiHCl_3$) used during deposition. The ACC compositions also assumed that the only other element in the coatings was N at the level needed to mass balance the B and Si (i.e. the deposits were assumed to be essentially atomic mixtures of BN and Si_3N_4). However, the XPS analyses also detected levels of O and C in the coatings. In general, the XPS analyses agreed reasonably well with the nominal compositions supplied by ACC except for the highest doping level. Nevertheless, the nominal compositions supplied by ACC will be used to in all further discussions of these samples.

Table 3-9. Composition Analysis of B(Si)N Deposits Obtained From ACC

ACC Nominal wt% Si	XPS Analysis Results					Equivalent wt% Si from XPS
	Atom% Si	Atom% B	Atom% N	Atom% C	Atom% O	
0	0	47.5	40.5	2.4	9.7	0
3	2.5	47.8	46.0	2.3	1.4	5.5
10	4.6	43.3	43.3	1.5	7.3	9.8
18	10.0	39.8	47.3	1.6	1.3	19.8
35	12.8	37.5	46.1	2.2	1.4	24.6

Wet oxidation exposures were done on each composition for 24 hours using a 90% H_2O / 10% O_2 atmosphere at 700°, 900° and 1200°C. "Dry" oxidation in ambient air was also done at 700°C for comparison, but the mass gains under these conditions were all negligible within experimental error. The % mass loss after the 24 hour exposure under wet oxidation conditions is shown in Figure 3-31 for each of the three temperatures. The reason there is a mass loss on oxidation is due to volatilization of the B_2O_3 oxidation product. The simple oxidation reactions of BN and B(Si)N to produce glassy B_2O_3 and SiO_2 would normally be expected to yield a net mass increase; however, volatilization of the B_2O_3 oxidation product, either by direct evaporation or by the formation of various highly-volatile hydrated species of the general formula $H_xB_yO_z$, leads to an overall mass loss. High water concentrations in the atmosphere promote formation of the hydrated species and lead to accelerated mass loss.

All of the samples showed a substantial mass loss following wet oxidation, except the 18 and 35wt% Si samples at 700°C, which showed slight mass gains. The data trends and interpretation are confounded by two important factors. First, the crystallinity of the B(Si)N samples was strongly affected by the deposition temperature and composition. The pure BN sample, which was deposited at 1800°C, had a highly crystalline, turbostratic structure with highly aligned grains. The Si-doped samples, all of which were deposited at 1400°C, were largely amorphous. The sudden change in crystallinity with composition is shown in the XRD patterns for the pure BN and 3wt% Si samples shown in Figure 3-32. Normally pure BN deposited at 1400°C would also be crystalline, but not to the degree and perfection of the sample deposited at 1800°C. The degree of crystallinity is known to strongly influence the oxidation behavior of BN [12], and thus this sudden change in microstructure going from 0 to 3wt% Si is believed to be the major factor that caused the oxidation resistance of the 3% Si sample to be actually worse than that of the pure BN sample at 900° and 700°C.

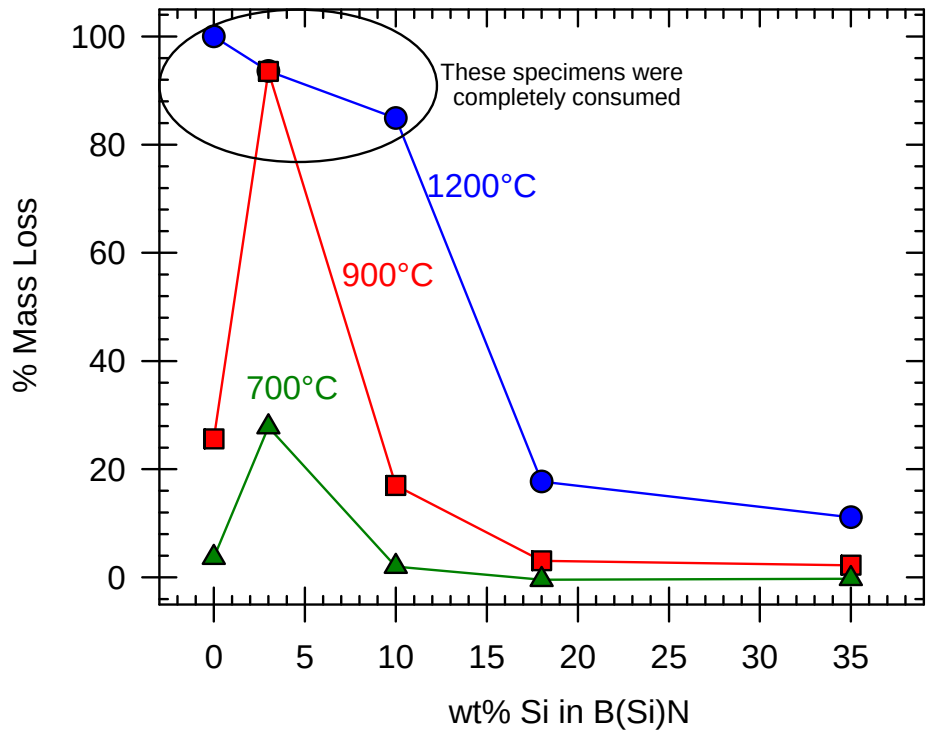

Figure 3-31. Results of wet oxidation exposure on the mass loss of BN as a function of Si-doping level. All exposures were done for 24 hours in a 90% H2O – 10% O2 atmosphere.

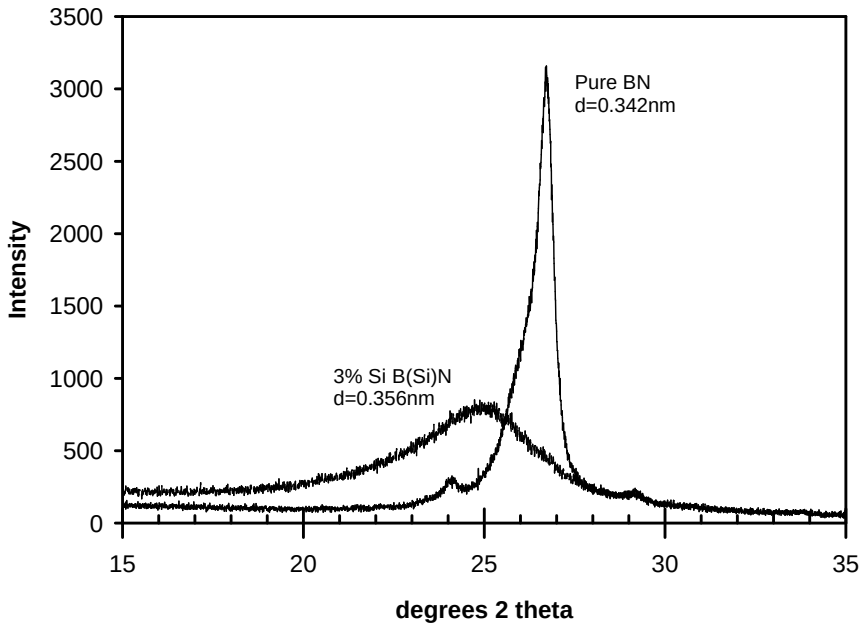

Figure 3-32. Comparison of the powder X-ray diffraction patterns for the pure BN and the 3 wt% Si sample used for the wet oxidation testing.

The second complication is that several of the samples were completely consumed by the oxidation treatment. The samples and conditions where complete oxidation occurred were the pure BN at 1200°C, the 3 wt% Si sample at 1200°C and 900°C, and the 10 wt% Si sample at 1200°C. The final mass losses for these samples are consistent with them having been completely converted to oxide and all of the B_2O_3 having been volatilized, leaving only the SiO_2 oxidation product behind. Obviously estimating any type of oxidation/volatilization rates from these data points would be very misleading. Despite the problems with interpreting the wet oxidation data, it is clear from Figure 3-31 that Si-doping of BN in the range of 18wt% Si or higher dramatically improved its oxidation resistance, particularly at 900° and 1200°C.

The remaining three questions regarding the viability of B(Si)N fiber coatings were all answered in the next experiment. GE obtained coated Hi-Nicalon fiber from ACC having B(Si)N coatings ranging in Si content from 15 to 42 wt% Si that were fabricated into 6-ply (four tensile plies and 2 crossplies) MI composite bars and tensile tested at room temperature. Figure 3-33 shows the trends in ultimate strength and strain to failure as a function of the silicon content in the B(Si)N fiber coating. The sample with 0% Si (i.e. pure BN) coating showed significant degradation in the coating from Si infiltration. This degradation of BN by silicon was well known from earlier observations on GE fiber coatings. Consequently data from a standard BN/C/Si_3N_4/C fiber coating, deposited at the same time frame with the same fiber lot, is used for comparison to the B(Si)N coatings.

The first thing to note about Figure 3-33 is that the properties of the 15%Si B(Si)N coating are very similar to the standard coating, and much better than the BN-only coating, indicating that silicon doping is very effective at improving the resistance of the coating to Si attack during infiltration. However, beyond 15% Si both the strength and, in particular, the strain to failure drop off substantially with increasing Si content. Apparently beyond 20% Si the ability of the coating to act as a debonding layer is greatly reduced. Based on this result a 15% Si doping level would be optimum since at that composition it still acts as an effective fiber-matrix debond layer, and yet still has significantly improved oxidation resistance compared to pure BN.

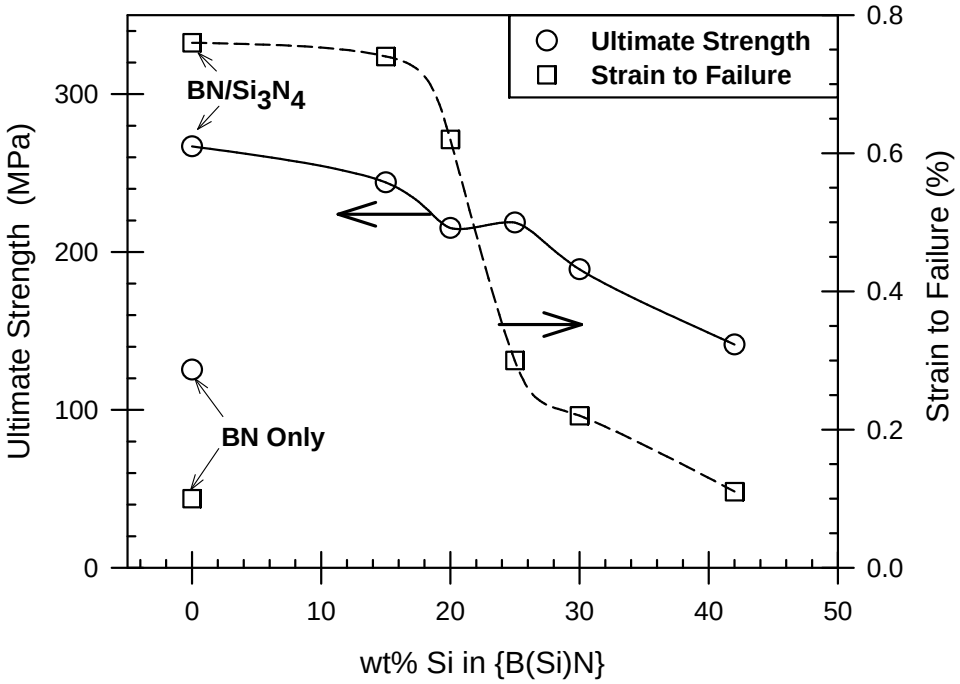

Figure 3-33. Variation of composite ultimate strength and strain to failure as a function of Si content in the B(Si)N fiber coating.

Despite the relatively promising results shown in Figure 3-33, repeated attempts to obtain strong, tough composites from fiber coated with B(Si)N alone proved to be very problematic. Precise control of the weight gain (i.e. thickness) of the coating was more difficult than with pure BN, and the thickness uniformity from the interior to the exterior of the fiber tows qualitatively appeared worse. The different deposition rates for the B and Si precursors potentially meant that coating composition could also be varying from the exterior to the interior of the tows, although this was never determined via analysis. These issues with uniformity of thickness and composition led to speculation that the B(Si)N coatings alone were not robust at resisting Si attack during composite infiltration. There fore the B(Si)N coatings were also tried as a substitute for the BN layer in the standard configuration A coatings where the Si_3N_4 over-coat would provide the needed resistance to Si. However, we again achieved only marginal success. In general the ACC fiber coatings utilizing B(Si)N, either alone or with Si_3N_4 over-coats, resulted in composites with comparable proportional limit and initial modulus values to those made with pure BN initial layers, which would be expected since proportional limit and modulus are matrix-dominated properties. However, the ultimate strength and strain to failure values of the B(Si)N-based fiber coatings were significantly below those made with the BN-based coatings on a statistical basis. This trend is shown in the property distributions in Figure 3-34. This issue with the relatively poor performance of ACC B(Si)N-based fiber coatings was not resolved by the time ACC decided to withdraw from the fiber coating business.

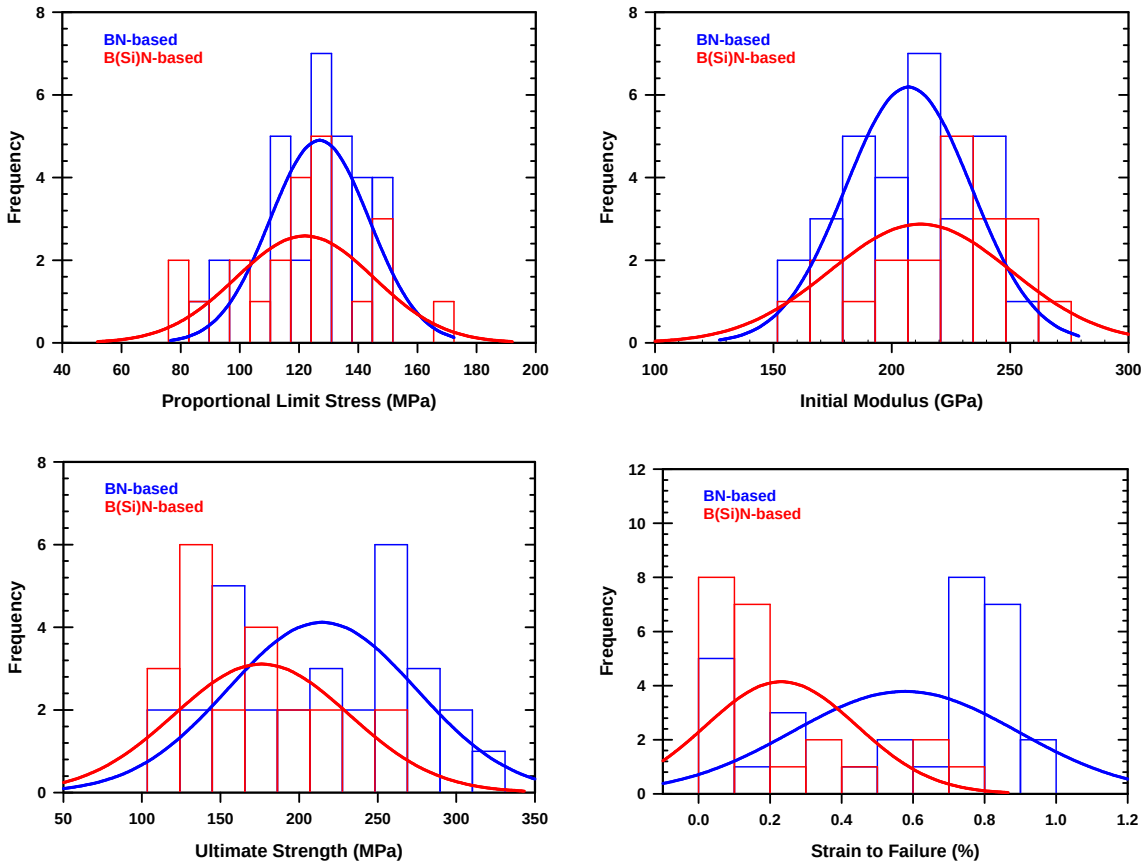

Figure 3-34. Tensile property distributions for composites made using ACC fiber coatings with an initial coating layer made of pure BN or B(Si)N. The data sets represent 20 different coating deposition runs and over 50 separate specimens made from late 1995 through mid 1997

3.2.2.4 Vendor Coating Scale-Up

In the mid 1997 time frame there were substantial concerns regarding the production rate and cost of coated fiber produced in ACC's experimental coater. These concerns were increasingly important given the increasing need for coated fiber to support fabrication of various test components, such as shrouds and combustor liners, to be described later. In addition to being limited to 3 tows, the feed and take-up spools in the experimental reactor were of different designs, requiring the fiber to be manually re-spooled between each coating layer. It was believed that the extra handling of these re-spooling operations was contributing to fiber damage and contributing to difficult composite fabrication in the later stages of the process. In order to address all these problems ACC decided to modify one of there larger production CVD reactors to accommodate fiber coating. The newly designed large reactor had sufficient space to accommodate 12 tow lines simultaneously in a single pass-through configuration. It was also designed to use identical spools for both the feed and take-up operations, thus negating the need for re-spooling between coating layers. By having four times the capacity, and by eliminating the re-spooling operation,

the larger “12-line” coater was expected to result in greater than 4X reduction in coated fiber cost while improving coated tow quality.

Several preliminary coating runs were performed to validate the operation of the reactor and to insure that there was adequate control of the individual CVD coating layers to be able to produce fiber coatings with the intended composition mentioned above. In these early evaluations there were no noticeable differences in coating composition or thickness distribution between the larger 12-line coater and the experimental 3-line coater. However, the 12-line coater produced a BN coating without the layered structure shown in Figure 3-28 due to the fiber passing only once through the furnace deposition zone during coating.

Initially coatings from the 12-line coater gave slightly inferior composite properties to those obtained from the 3-line coater. However, after several coating iterations the composite properties obtained from coated fiber from either reactor were fairly comparable. Figure 3-35 shows the distributions of composite tensile properties measured on samples made from 12-line and 3-line fiber coatings using the same Lot of Hi-Nicalon fiber. The distributions of proportional limit, initial modulus and ultimate strength are statistically indistinguishable; however, the distributions for strain to failure do show a significant difference in the means from the two coaters, with the 3-line coater producing a slightly higher strain to failure. Although not entirely up to the 3-line coater standard, fiber coatings from the 12-line coater were used in several of the components described later in Section 3.7 since the production rate of the 3-line coater was insufficient for all of the coated fiber needs.

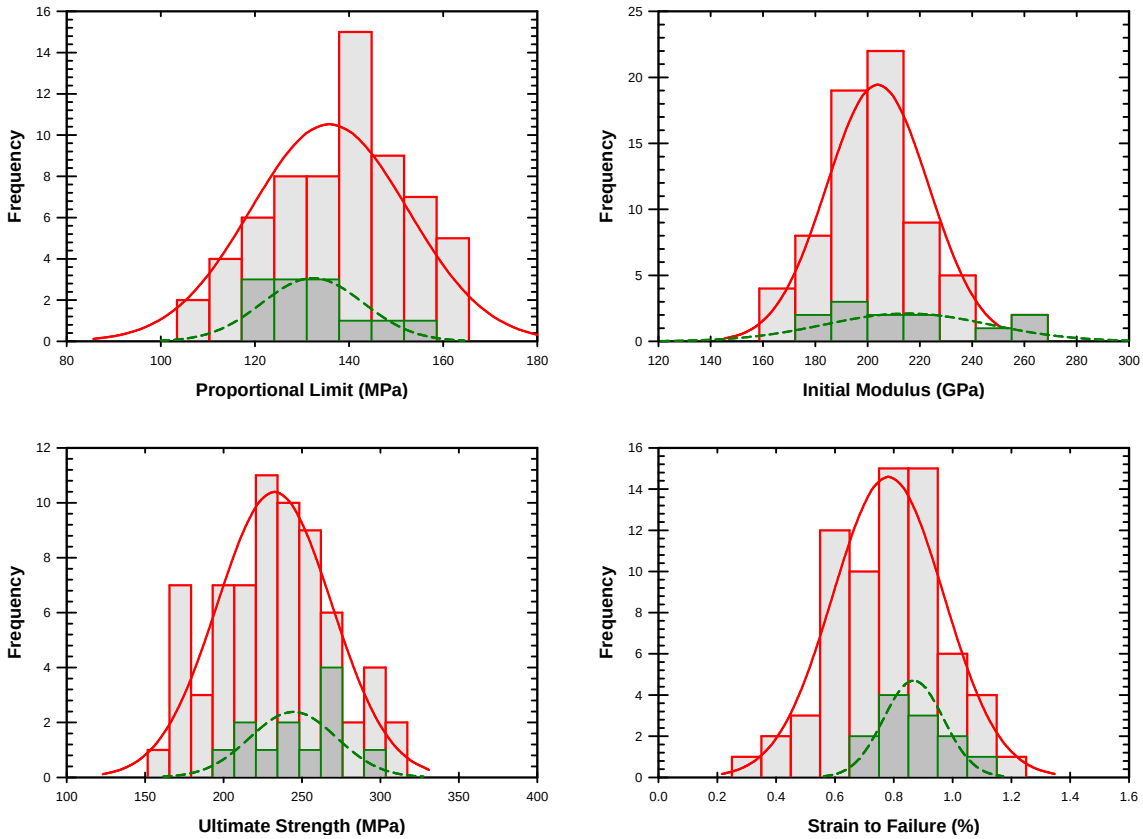

Figure 3-35. Tensile strength property distributions for samples made from fiber coated in ACC's 12-line coater, shown by the red lines and light gray fills, and ACC's 3-line coater, shown by the green lines and dark gray fills. All of the property distributions are statistically equivalent except strain to failure where the distribution for the 3-line coater had a significantly higher mean than did the 12-line coater.

3.2.2.5 Matrix Modifications

Two matrix composition modifications were investigated as methods of improving or tailoring the properties of the CMCs. The first of these modifications was the addition of boron to the matrix to act as a "crack sealant." The main concept was that the glassy borosilicate oxide formed from oxidation of the matrix would effectively seal any matrix cracks that would form, thereby limiting the amount of oxygen penetrating to the fiber coatings and fibers, as described in section 3.2.1.4 and Figure 3-9. Boron doping of the Phase 1 matrix had been investigated with monofilament fibers, but yielded the unintentional result of increased un-reacted carbon in the matrix. During oxidation the additional volume of porosity caused by oxidation of the un-reacted carbon more than compensated for any potential positive effect of the boron doping itself. However, the carbon phase in the high green strength (HGS) matrix used for the fine diameter fiber

systems is sufficiently fine, being sub-micrometer in size, that it is fully reacted during melt infiltration regardless of the boron content.

A technique for controlling the boron content in HGS-type matrices had previously been developed under the HSCT/EPM program. This technique involved the substitution of a submicron B_4C powder for part of the SiC powder in the normal HGS matrix. The B_4C would react with Si during infiltration to form SiB_6 and SiC. The thermal expansion and thermal conductivity behavior of boron-doped matrices had also been characterized under the HSCT/EPM program, and that data is reproduced here in Figure 3-36 for completeness. Overall boron doping to quite high levels had a negligible effect on the thermal expansion behavior of the matrix, and caused only a minor reduction in thermal conductivity. Other prior work done internally at GE had indicated that a doping level resulting in a B:Si atomic ratio of 0.15 was sufficient to promote oxidative sealing of surface cracks caused by indentation. Consequently the B:Si ratio chosen for composite matrix evaluations was also 0.15. The mechanical characterization of composites made with this B-doped matrix will be described in Section 3.4.2.

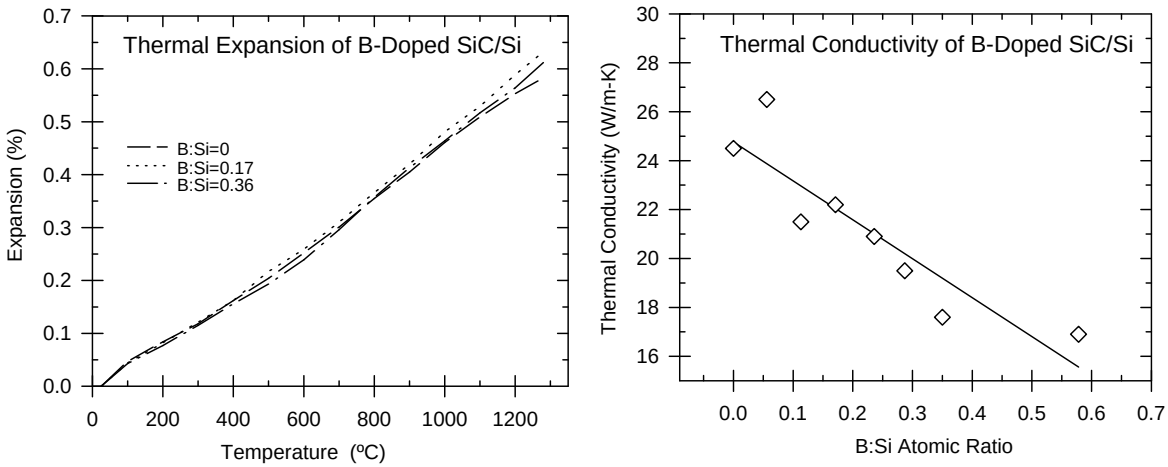

Figure 3-36. Thermal expansion and conductivity behavior of un-reinforced, B-doped SiC/Si HGS matrices as a function of boron content. (Data originally from the HSCT/EPM program.)

The second matrix modification evaluated was that of reducing the matrix elastic modulus in the hope of increasing the proportional limit strain of the composites. The majority of stresses in many of the stationary turbine components investigated, as will be discussed later, are a result of differential thermal strains. Since it is these strains that are largely driving any mechanical failure of the parts, having a larger matrix cracking, or proportional limit, strain is the most important criterion for maximizing the durability of the parts. The hope was that the modulus of the matrix could be reduced without impacting the matrix strength, thus giving a higher matrix cracking strain.

The technique used to reduce the modulus of the HGS matrix was to eliminate the carbon particulate in the slurry composition by substituting an equal volume of SiC particulate. Thus the only reaction-formed SiC in the infiltrated body would come from silicon reacting with the carbon char left behind by the binder system. This substitution had the effect of increasing the Si content of the matrix by 2.5X, from nominally 13 vol% to 33 vol%. Since Si has a lower modulus than SiC the modulus of the mixed Si/SiC matrix would be expected to decrease with increasing Si content. The thermal conductivity and thermal expansivity of SiC and Si are close enough that no major changes in the thermophysical behavior of the matrix was expected. Again, the mechanical characterization of composites made with this low-modulus matrix will be described in Section 3.4.2.

3.2.2.6 Development of Continuous Tow Coatings at GE

Significant progress had been made in the development of continuous coatings of tow-based fibers, as described above. However, the decision by ACC to abandon the tow-coating business represented a significant set-back to the commercialization of the prepreg MI CMC, especially given the relatively poor and erratic performance of the fiber coatings from Synterials, Inc. GE still required a source of substantial quantities of coated tow in order to continue with the turbine component development efforts to be discussed below; however, the quantities needed were still too small to act as a suitable enticement for other potential coating or CMC vendors to build a viable business plan around. Therefore, in mid-1998 we decided to implement a tow-coating operation in-house at GEGR. The intent of this work was both to supply coated tow to the other program activities, and to serve as a method to learn and optimize the continuous tow coating CVD technology so that we could then transition the process to a commercial vendor when the demand for fiber grew sufficiently to warrant such an action. GEGR also had substantial experience with batch CVD coating of fiber tows that could be drawn upon to guide the set-up and operation of a continuous tow coater.

3.2.2.6.1 Design of GE's Small Tow Coater

Fortunately some parts for a suitable tow coating CVD reactor already existed within GE. A small reactor had been set up at GE Aircraft Engines in the late 1980's with the capability to deposit continuous coatings on monofilament fibers. This reactor had subsequently been de-activated and moth-balled due to cost cutting efforts at GEAE. This reactor was then refurbished and put back into operation at GEGR. The refurbishment process was quite extensive as the only parts of the original reactor that were salvageable were the reactor shell and deposition furnace hot section. All of the fiber handling mechanisms had to be re-designed and manufactured. A new furnace power supply, gas flow control system and vacuum system also had to be designed and assembled. This refurbishment process took roughly 9 months and was paid for entirely with GE internal funding. By early 1999 refurbishment of the tow coater was completed and ready for coating trials. Development of the proper coater operating parameters, and of the tow coating process in general, was then done as part of the CFCC program, having been added to the program in Phase 2+.

During the initial coating trials with the GE reactor the fiber tows were not de-sized before coating deposition. Rather we relied on the heating of the tows upon entering the reactor tube to burn off the sizing before the fiber reached a high enough temperature for significant deposition to begin. However, during the sizing removal the tows tend to relax, or stretch, slightly (i.e. there was some waviness to the tow that was being held in place by the sizing), and the amount of stretching varied significantly from tow to tow. The result was that as the coating run progressed the tows that stretched more became relatively loose whereas those tows that stretched less were forced to carry the majority of the tensile load. The loose tows would wander on the alignment pulleys and readily become entangled with neighboring tows or the fiber guide hardware. Those tows that stretched less and carried most of the tension were more prone to breakage during the run. It was therefore necessary to remove the sizing prior to the fiber being introduced into the coating furnace.

One mechanism that limits the length of fiber that can be coated during a single run is the build-up of broken fiber on the inside of the deposition chamber. All Hi-Nicalon tow contains a finite number of broken fibers. During transport through the deposition furnace the loose ends from the broken fibers tend to contact features within the deposition tube and become "glued" to them by the coating. At first, only very loose fiber ends that stick far enough out from the tow are affected; however, as time goes by more of the broken ends become entangled with the fiber already glued to the deposition chamber, and the amount of fiber stuck to the interior of the deposition tube grows geometrically. This stuck fiber acts to block gas flow within the deposition tube, causing a gradual increase in reactor pressure with run time, which causes an increase in the coating deposition rate with time. The change in deposition rate caused by reactor pressure can be compensated for by throttling the vacuum system and/or gradually increasing the fiber transport rate during a run, but eventually the amount of fiber blocking the deposition tube, and therefore the rise in reactor pressure, get outside the process limits that have been established. In such a case the deposition run has to be terminated early, thereby limiting overall reactor throughput.

The vacuum pumping system consists of a 2000m^3/hr (1400 cfm) blower, which is backed by a smaller blower and an oil-filled mechanical pump. There is a set of particulate traps installed between the small blower and the mechanical pump to further protect the mechanical pump. Mechanical pump oil is continuously filtered through a particulate filter and an activated alumina filter element. The exhaust end of the mechanical pump is continuously purged with nitrogen. The purpose of nitrogen flush is to prevent any contact of the minute amount of HCl that may be present in gas from contacting moisture from air while in the pump. Dry HCl does not corrode metals rapidly, but it becomes very corrosive if combined with moisture.

A throttling valve installed in front of the large blower controls reactor pressure. The throttling valve uses a vacuum gauge near the exit end of reactor as a reference.

3.2.2.6.2 Fiber Coating Optimization in GE's Small Tow Coater

Four different coatings layers were deposited in the small tow coater: boron nitride (BN), silicon nitride (Si_3N_4), silicon-doped boron nitride (B(Si)N) and carbon (C). When

multiple coatings are applied to the fiber, each coating is deposited in a separate run since only one type of chemistry can be maintained in the deposition tube at one time. Processes for their deposition of the individual layers will be discussed in the order listed in first sentence. There are many commonalities among the first three coatings, which will be discussed in detail under BN deposition conditions.

Actual fiber coatings contain multiple layers as no single layer was found that could perform all of the important functions required. Although some experimental work was done on a variety of configurations, the experiments quickly converged to three configurations: configuration A, which was a reproduction of the configuration used with the batch CVD coater earlier in the program, configuration B, which included layer(s) of B(Si)N, and configuration C. All of the configurations had a final thin layer of carbon deposited on the outside to enhance wetting of the fibers by the CMC matrix slurry during tape prepregging, and by the silicon alloy during the melt infiltration step. Optimization of these coating systems was done primarily by fabricating composite test samples using the coated fiber and evaluating the tensile strength properties and microstructures. Discussions of the optimization of these coating systems will follow the descriptions of the individual layer processes. Finally, some general observations regarding the operation of a continuous tow coating system will be presented near the end of this section.

3.2.2.6.2.1 Coating Thickness Measurements

The small coating thicknesses used made it impossible for them to be measured accurately by optical microscopy. Coating thickness for BN, B(Si)N and Si_3N_4 layers could be measured directly by SEM. Carbon layers were very thin and could not be imaged well by SEM. Carbon coatings could be imaged by TEM, but the difficulties of sample preparation made that technique impractical as a quality control tool.

Fibers were prepared for SEM examination by two different techniques. Hi-Nicalon fibers are themselves somewhat conductive; however, the coatings are not. It was therefore necessary to add conductive coatings to the fibers to be examined by SEM. The simplest preparation technique involved cutting the fiber tow and coating it with platinum. That technique did not produce good contrast between different coating layers. Coating the tow with platinum first and then cutting it produced much better contrast, but cutting of the tow always causes some flaking of coatings, so not all fibers in the tow were available for examination. Embedding the tow in epoxy and fracturing it at liquid nitrogen temperature produced cleanest breaks and images. Ion etching further enhanced both the delineation between coating layers and also the structure of the individual layers.

Coating thickness on fibers within a tow varies from inside to outside, with fibers on the tow periphery receiving thicker coatings. Reasons for the existence of this variation of coating thickness within the tow are discussed elsewhere in this report. The distribution of coating thickness in the tow meant that taking simple averages would require very large numbers of fibers to be examined in order to come with a representative number. Due to rate of data acquisition on SEM, that would not be a practical solution. Instead, 4-6 fibers from the interior of the tow and an equal number of fibers on the tow periphery were

typically examined, which allowed us to measure the degree of coating thickness gradient from the center to periphery of the tow.

The SEM measurement of fiber thickness was very labor intensive and took too long to be useful for day-to-day monitoring of fiber thickness from the coating process. The technique eventually adopted for measuring average coating thickness was to measure the weight gained by the fiber through the coating process. Weight gain of the fiber is a direct measurement of an average coating thickness. Its main advantage over direct microstructural observations is that it averages over all fibers in the tow so it is not subject to same types of sampling errors as the microscopical methods. At the same time, however, it is not capable of providing information about the coating thickness variability within a fiber tow.

Fiber weight gain can be measured on individual tows or on the multiple tows. Measurements were made on 0.5 to 1 meter long samples. A gage reproducibility study was conducted to determine the accuracy of the overall method, and it indicated that it is not possible to measure weight gain of single fiber tows with the desired accuracy. The main source of error in the weighing of the single fiber tows is not the cutting or weighing processes, but rather the transfer of loose or broken filaments between tows in the coater. As the tows pass through the CVD reactor they spread by the action of passing gases. Spreading of the tows is useful for coating process because it improves coating uniformity through the tow. However, the close spacing of the tows allows fibers on the periphery of one tow to entangle with fibers from the neighboring tows. During separation back into individual tows after coating some of the loose fibers from one tow may remain permanently attached to a neighboring tow. Such fiber transfer between tows will cause errors in tow weight and a significant error in calculated weight gain. Weight gains on the entire set of multiple tows that were coated in a given run were much more reliable as judged by the gage reproducibility study. Although there were errors in the weight gains of individual tows, the sum of the weight gains for all of the individual tows closely matched those measured on all of the tows as a group, as would be expected.

3.2.2.6.2.2 BN Coating Layer Process

The precursors used for BN are ammonia and boron trichloride, which form BN by the following reaction:

$$BCl_3 + NH_3 \rightarrow BN + 3HCl \qquad (1)$$

Typically we use excess ammonia in the reactor in order to ensure that only BN is deposited. If the gases were run in 1:1 ratio and mixing of gases was poor, there could be portions of reactor that have excess BCl_3 which could deposit elemental boron instead of boron nitride. Thus we have used a ratio of ammonia to boron trichloride of greater than1:1 in all work in this reactor. The excess ammonia reacts further with the HCl byproduct to form ammonium chloride as an additional byproduct. The overall chemical reaction then becomes:

$$BCl_3 + 3NH_3 \rightarrow BN + 2NH_4Cl + HCl \qquad (2)$$

Ammonium chloride is a solid at room temperature that sublimes at about 200°C. It represents an engineering challenge in reactor operation. Despite it's being formed at high temperature during the CVD reaction, it will deposit as a solid on any cold surface that it encounters, such as in the coater end boxes or vacuum lines.

The BN deposition rate in a reactor is dependent on number of factors. Previous work [16] had shown that in the presence of excess NH_3 the rate of BN deposition is linearly dependent on the partial pressure of BCl_3. The most important variables that determine coating thickness on the fiber in a continuous process reactor are temperature, partial pressure of BCl_3 and fiber residence time in the reactor.

The partial pressure of BCl_3 in the vicinity of fiber is dependent on the total reactor pressure and the ratio of the BCl_3 flow rate to that of all other gases:

$$P_{BCl3} = P_{total} * [F_{BCl3} / (F_{BCl3}+F_{NH3}+F_{N2})] \quad (3)$$

where P stands for pressures and F for the flow rates of respective gases. The goal of deposition process is to coat all fibers within the tow uniformly, and reactor pressure will have significant impact on the uniformity of coating. The mean free path of gas molecules increases as pressure is lowered, so it becomes more likely for gas molecules to diffuse within the tow before they react. The net result is more uniform coating thickness within the tow at reduced pressure. The local partial pressure of reactant will also depend on the degree of gas mixing in the reactor.

There is a definite upper limit of pressure at which the coating process can be run. The partial pressure of BCl_3 needs to be kept below the value at which spontaneous nucleation can take place. If spontaneous nucleation occurs, BN particles can form in gas phase in addition to the coatings on fibers, a process commonly referred to as "sooting". Clearly that is not a desired deposition mechanism because particulates attach themselves to fiber coatings making them very rough. The partial pressure of BCl_3 is therefore kept at level where a contact with some surface is necessary to make BN nucleation possible. It was found that sooting in our reactor takes place at reactor pressures above 6 Torr.

The coating thickness on the fiber is directly proportional to residence time of the fiber in the reactor, which is inversely proportional to the fiber speed through the reactor. In day-to-day operation of the reactor fiber speed is used to control coating thickness because that allows deposition conditions in reactor to remain constant. Changing gas flow rate, for example, will change partial pressure of the reactant, hence the deposition rate, but will at the same time change gas velocity which may affect temperature and degree of gas mixing in the reactor. Changes in fiber speeds have no direct effect on the other coating process parameters.

Uniformity of deposition through the length of reactor was examined by coating a stationary length of fiber for 30 minutes. This is a rather long time compared to typical residence time of about 30 seconds in a normal coating run, so there was significant

buildup of coating on the fiber. The fiber was then cut into 2.5cm long sections and weighed to determine weight gain as function of position in reactor. The results of this experiment are shown in Figure 3-37. The measured weight gain was zero until about 18cm below the center of reactor. The weight gain remained remarkably steady through the central part of the reactor, and then decreased very slowly until it approached the upper fiber guide about 25cm above the center of the furnace. The negative weight gains near the ends of the tows are caused by loose and broken fiber being "blown-off" of the fiber tow by the gas flow.

There are two competing processes that determine the weight gain (deposition rate): heating of the reactant gases and depletion of the reactants. Gas enters the reactor cold and it takes finite length of residence time for it to heat up, mostly through contact with the hot wall. Thus near the bottom of the reactor the gas temperatures are relatively low, but the concentration of reactants is highest and concentration of reaction byproducts is a minimum. As gas proceeds through the reactor its temperature increases, which tends to increase the deposition rate, while the concentration of reactants drops due to depletion, which would decrease the deposition rate. Apparently the two compensate each other well, producing a remarkably constant deposition rate through the length of reactor.

Deposited BN coatings were analyzed by electron microprobe and auger electron spectroscopy (AES). The coating stoichiometry was found to be correct, with a B:N ratio of 1. Oxygen content of the BN was typically about 0.5%. For comparison, oxygen content of BN coatings from the low temperature CVI process was about 5%.

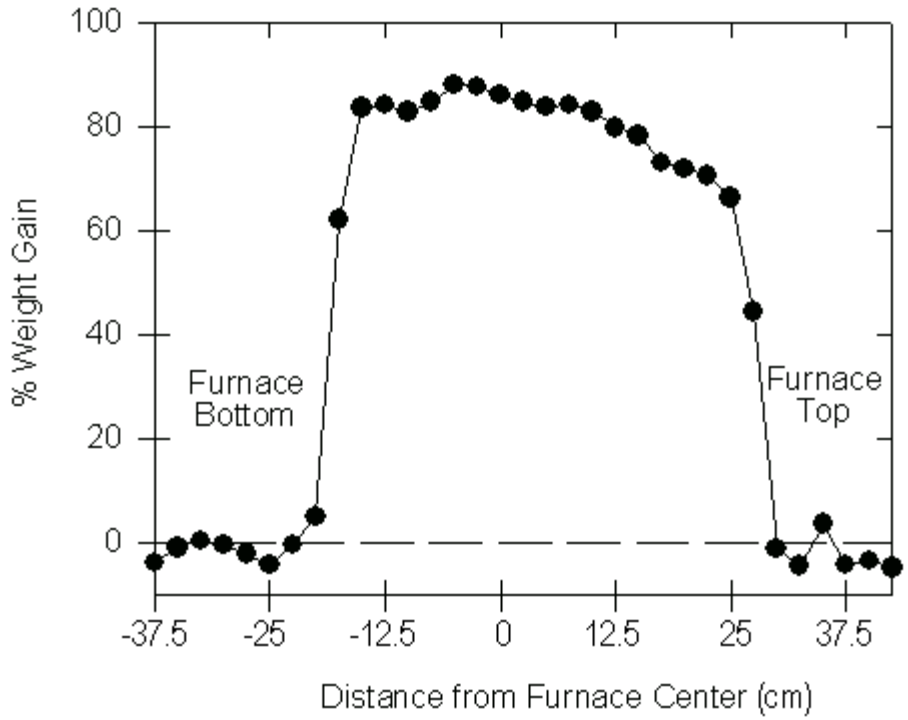

Figure 3-37. Weight gain (or coating deposition rate) for a section of fiber tows held stationary in the reactor for 30 minutes of BN deposition. The zero position on the x-axis corresponds to the center of the deposition furnace with the bottom of the furnace on the left.

3.2.2.6.2.3 Si_3N_4 Coating Layer Process

The first coating system that was used, configuration A, included a Si_3N_4 layer, so conditions for silicon nitride deposition were optimized for that system. It was found later that deposition rate of Si_3N_4 onto B(Si)N was very comparable to the rate obtained when depositing on BN or BN/C coatings. The deposition rate when depositing directly onto Hi-Nicalon fiber, however, was considerably lower. While this phenomenon was not studied in detail, the difference is most likely due to difficulties in nucleating Si_3N_4 on the fiber surface, which is mostly SiC.

Precursors used for deposition of silicon nitride are trichlorosilane and ammonia. The gases are mixed using the same ammonia excess as used for BN, being 3X the amount necessary to fully react the trichlorosilane. The overall deposition reaction therefore becomes:

$$3\ SiHCl_3 + 9\ NH_3 \rightarrow Si_3N_4 + 5\ NH_4Cl + 4\ HCl + 3\ H_2 \qquad (4)$$

The chemistry of Si_3N_4 deposition is very similar to BN deposition, with formation of ammonium chloride and HCl as byproducts. The main difference in the two is the formation of hydrogen during Si_3N_4 deposition.

Initial experimental attempts to deposit Si_3N_4 at 1450°C resulted in deposition of a mixture of Si_3N_4 and Si, with very irreproducible coating thickness. Thermodynamic calculations were performed to better understand this behavior, the results of which are shown in Figure 3-38. The calculations shown in Figure 3-38, when combined with the presence of an axial thermal gradient through the deposition furnace, explained these results.

The local deposition rate of Si_3N_4 through the length of reactor was measured on stationary fiber in the same manner as was done for BN. The results are shown in Figure 3-39. The measured weight gain, and thus deposition rate, increased slowly through the bottom half of the reactor. The highest deposition rates were seen in the upper section of reactor, well past the center of the furnace where the peak in the axial temperature gradient occurs. The pattern of deposition rate is strikingly different than in case of BN deposition, which was relatively uniform through the length of the reactor.

3.2.2.6.2.4 Si-doped Boron Nitride Coating Layer Process

Silicon doped boron nitride, or B(Si)N, was chosen as a possible replacement for pure boron nitride/silicon nitride system because of its enhanced oxidation stability, as described previously in section 3.2.2.3. Prior work with fiber coatings from Advanced Ceramics had shown that mechanical properties of the composites (ultimate strength and strain-to-failure) started decreasing at doping levels of 20% Si and higher. The coating was deposited by reacting a mixture of BCl_3 and $SiHCl_3$ with NH_3. The molar ratio of BCl_3 to $SiHCl_3$ in the reactant gases was the same as that desired in the coating and both gases were introduced through the same gas injector. The stability issue of Si_3N_4 under CVD deposition conditions, as discussed above, required that deposition of B(Si)N also be done at conditions where Si_3N_4 was stable.

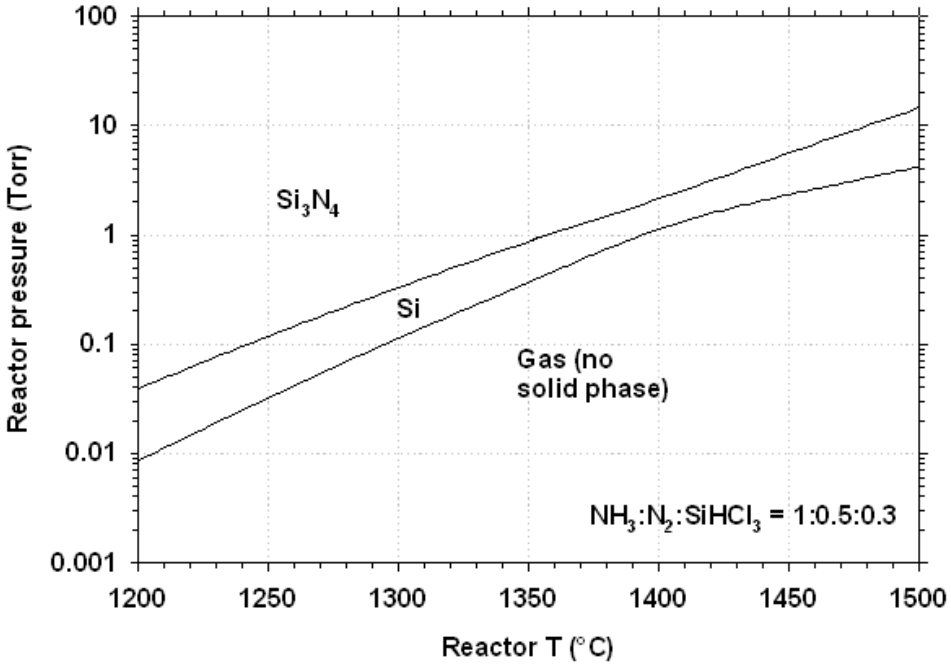

Figure 3-38. Predicted CVD deposit as a function of reactor total pressure and temperature. The different regions show which solid phase should be stable.

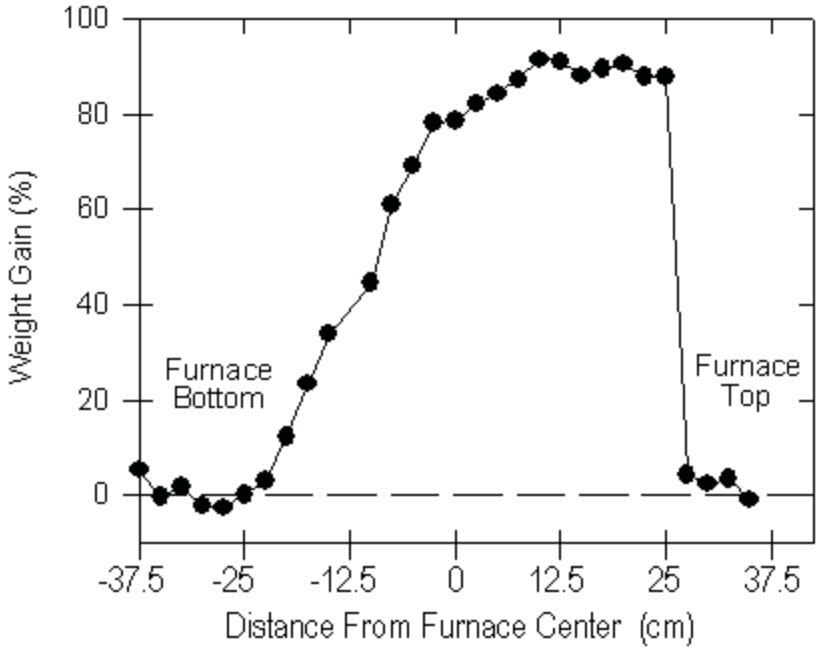

Figure 3-39. Weight gain of Si_3N_4 fiber coating for tow held stationary in the CVD reactor for 30 minutes as a function of position in deposition furnace. The zero position is the center of the deposition furnace.

As was done with BN and Si_3N_4 depositions, the deposition profile axially through the reactor tube was measured by depositing coating onto a piece of stationary tow. The result of these measurements is shown in Figure 3-40. The BN deposition profile is included for comparison. It is apparent that the profile of B(Si)N is very similar to the deposition profile of pure BN, except for the initial part where weight gain lags those of pure BN. Since B(Si)N is mostly BN, it would be expected that the two curves would be similar in appearance. The initial lag of weight gain of B(Si)N is caused by $SiHCl_3$ taking longer time to start reacting, just like in the case of pure Si_3N_4 deposition.

One effect of the slower decomposition of $SiHCl_3$ at the lower temperatures near the entrance to the CVD furnace is a gradient of Si concentration in the B(Si)N layer. TEM observations consistently indicated that the concentration of Si in B(Si)N layer increased from the inside to the outside of the layer. Looking at the deposition profiles in Figure 3-40 it is apparent that the part of the coating that is deposited first as fiber enters the reactor would have lower concentration of Si. As the gas warms up further in the reactor the two precursors will decompose at the same rate and coating will have the desired composition.

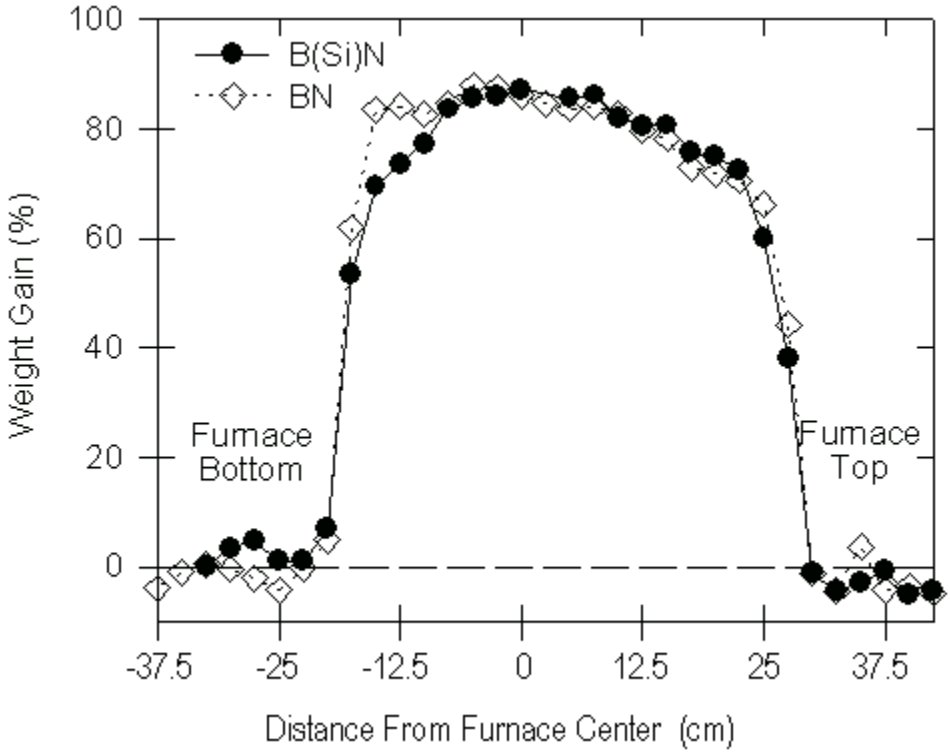

Figure 3-40. Weight gain of B(Si)N fiber coating for tow held stationary in the CVD reactor for 30 minutes as a function of axial position in deposition furnace. The zero position is the center of the deposition furnace. The profile for BN deposition is shown for comparison.

The silicon to boron ratio in the coating was also checked by Auger electron spectroscopy, the results of which are shown in Figure 3-41. The figure shows plots of concentration of different elements as function of sputtering time. Analysis is done by taking a spectrum, sputtering with an Argon ion beam for a period of time and then taking the next spectrum. Sputtering depth is proportional to sputtering time; however, the actual depth cannot be calculated exactly from sputtering time because different materials have different sputtering rates. This particular coating run had a carbon overcoat on the B(Si)N layer, which clearly shows up in the analyses, to help prevent specimen charging. The dashed horizontal lines show the nominal atomic concentrations one would expect for B(Si)N of the particular composition used in this experiment.

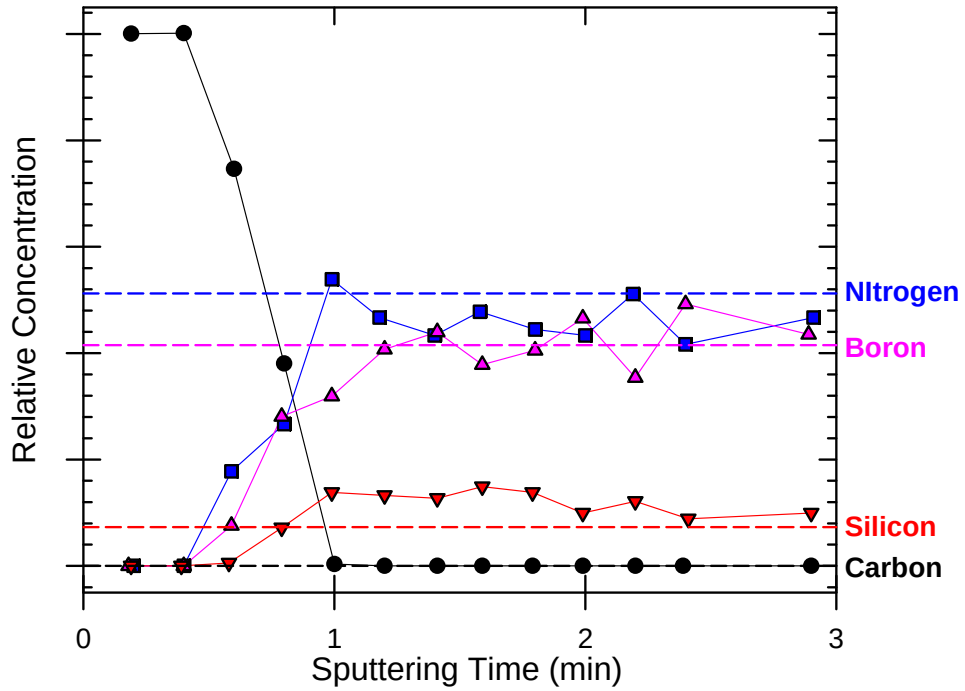

Figure 3-41. Results of Auger electron spectroscopic analysis of a B(Si)N/C fiber coating, showing the concentrations of C, N, B and Si as a function of depth (sputtering time) into the coating. The dashed lines give the nominal concentrations for the intended B(Si)N layer composition. Throughout the analysis oxygen was below the detectability limit.

The carbon concentration starts out at 100% in the outer carbon layer, as expected, and then decreases rapidly to below the detection limit once sputtering reaches the B(Si)N layer. The concentrations of B, Si and N at the same time rise from zero in the carbon layer to their expected values once within the B(Si)N layer. The Auger analysis confirms that the concentration of silicon in the B(Si)N is the same as was in the gas phase used during deposition. This close correspondence between reactant gas composition and deposit composition is an important advantage of the high temperature CVD process. Similar experiments at lower deposition temperatures (~900°C) showed that the

concentration of Si was lower in the deposited material than in the reactant gases, which made it difficult to reproduce the Si dopant level in the coating. Another benefit of the high temperature CVD process is low oxygen content in the coating, as the oxygen levels were always below the detectability limit of the analysis.

3.2.2.6.2.5 Carbon Coating Layer Process

Carbon is deposited by the decomposition of hydrocarbons. The two precursors that were used were methane and acetylene and their respective overall deposition reactions are:

$$CH_4 \rightarrow C + 2\ H_2 \qquad (5)$$

and

$$C_2H_2 \rightarrow 2\ C + H_2 \qquad (6)$$

Both precursors yielded good quality carbon coatings, but CH_4 was selected as the preferred precursor because of safety concerns. Un-reacted acetylene can condense in the cold traps of the reactor vacuum system. Special precautions needed to be taken when the traps were warmed up after a coating run to ensure that the acetylene would go through the gas exhaust and scrubbing system and did not vent back into the reactor. With methane such concerns do not exist because it does not condense in the cold traps.

The carbon coating deposition process is relatively slow compared to the nitride coatings. It was therefore conducted at maximum temperature that fibers were expected to survive without degradation and at the maximum allowable pressure. At partial pressures of methane above about 5 Torr sooting, or gas phase nucleation of solid carbon, was observed in the reactor.

Carbon was typically used as either an intermediate coating layer or as the final outer coating, so it was never deposited on the bare fiber surface. We found that carbon nucleated well on pure BN and Si_3N_4 coatings, but not when deposited on top of B(Si)N layers. TEM observations showed that the carbon coatings deposited on B(Si)N were often non-continuous.

Typically the carbon coatings used were too thin to be reliably measured either directly or by using coating weight gain. Electrical resistance of the tow, as measured with a standard ohmmeter using silver paste contacts, was found to be a more reliable measurement of carbon coating thickness and continuity. The inner BN and Si_3N_4 coating layers acted as insulation, isolating the carbon coating from the conductive SiC fiber.

Initially all carbon coatings were done in the low-pressure CVD reactor. However, the slow deposition kinetics for carbon required more reactor residence time for the carbon coating than for any of the nitride coatings. Consequently an atmospheric pressure carbon coating process was developed, which allowed the final carbon coating to be done without tying up the low pressure reactor, and thereby improving overall productivity in the CVD coatings operation.

The atmospheric pressure carbon coater consists of a spool-to-spool winder that transports multiple tows through a tube furnace and onto another spool at controlled tension and speed. The equipment utilizes identical spools as used in the low pressure reactor. The tows are carried over several pulleys through a narrow slot in a solid graphite end-cap, through the furnace and out an identical end-cap, around several pulleys and onto a spool. Tension can be varied from 0-500 grams and is measured by a transducer that signals a pneumatic brake mounted on the fiber supply shaft. Fiber speed is measured by encoders mounted on fiber transport pulleys, the signal from which is used to control the fiber take-up spool drive motor. A methane/nitrogen gas mixture is used to deposit carbon inside the reactor furnace. The mixed gases are injected through a 6.4mm graphite tube inserted about 10cm into the furnace through the carbon end-cap.

The critical goals of the atmospheric carbon coating process were (1) a uniform and dense coating, (2) similar thickness to that obtained in the low pressure process, (3) similar coating rates to those obtained at low pressures, and (4) no change in mechanical properties of the resulting composites. A 2-factor 2-level factorial experiment was conducted with the process variables of methane partial pressure and residence time of the fiber. Statistical regression of the results showed that coating resistance varied linearly with residence time and that a residence time of 1.2 minutes produced a tow resistance equivalent to the thickest carbon coating deposited in the low pressure carbon process. The partial pressure of methane, over the range investigated, did not significantly affect the coating resistance.

In order to prove functional equivalence between the low pressure and atmospheric pressure carbon deposition processes a total of 30 CMC test samples, cut from 14 individual panels, were produced from three different fiber coating runs and using three different Hi-Nicalon™ fiber lots. These coating runs were processed through the Si_3N_4 deposition and then split, with half of the fiber having the final carbon layer deposited by the low pressure CVD process and the other half using the atmospheric process. In each case, the mechanical properties, including ultimate strength, proportional limit, modulus, and strain to failure, as listed in Table 3-10, were statistically equivalent between the two processes.

In addition to removing the carbon process from tying up the low pressure CVD reactor, the atmospheric carbon process also had additional important advantages. The optimized fiber residence time of 1.2 minutes translates into a tow speed of 20cm per minute, which was a 30% increase in speed from the low pressure process. Also, unlike the low pressure process, the atmospheric pressure coater could be run unattended, reducing labor costs associated with the C coating.

Table 3-10. Comparison of the Mechanical Properties of CMC Samples Made with Low Pressure and Atmospheric Pressure Carbon Final Coatings

CVD Run#	Fiber Lot	Carbon Process Type	# of Samples	Ultimate Strength (MPa)	Proportional Limit Stress (MPa)	Initial Modulus (GPa)	Strain to Failure (%)
217	319	Atmospheric	6	284±57	154±25	223±17	0.95±0.08
219	319	Low pressure	4	265±37	128±26	185±340	0.94±0.13
156	307	Atmospheric	4	276±9	168±9	245±23	0.94±0.02
153	307	Low Pressure	6	284±39	179±23	240±33	0.86±0.11
176A	303	Atmospheric	4	286±18	163±17	239±6	0.88±0.05
176	303	Low Pressure	6	298±48	147±8	265±28	0.85±0.11

± values represent one standard deviation

3.2.2.6.2.6 Optimization of the Configuration A Coating System

This coating system was originally developed under the HSCT/EPM program using a low temperature, batch CVD reactor. Development of this coating system with continuous fiber coaters was pursued with the various coating vendors, including Advanced Ceramics Corp. The work with ACC eventually led to optimized coating weight gain targets, and these weight gain targets were adopted without modification for the GE coater. There were relatively few runs (eight) made with this coating system and they were largely used to become "comfortable" running the reactor.

3.2.2.6.2.7 Optimization of the Configuration B Coating System

As described earlier in Section 3.2.2.3, utilization of silicon-doped BN, or B(Si)N, in place of pure BN in the fiber coatings was seen as a promising technique for improving the environmental resistance of the fiber coatings, and therefore of the overall CMC as well. The initial configuration studied, configuration B-1, was evaluated in the hope that a single B(Si)N layer would act as both a debond coating, replacing the BN layer, and as a Si barrier during infiltration, replacing the inner C and Si_3N_4 layers of the standard 4-layer coating. Such a configuration would also greatly improve the productivity of the coating operation, as the 4-layer coating would be reduced to only 2 layers. However, as had been observed in the fiber coatings from ACC, direct deposition of B(Si)N on the fiber surface resulted in poor reproducibility and generally low ultimate strength and strain to failure properties in the composites. Distributions for the ultimate strength and strain to failure values of composites made with configuration B-1 coatings deposited at GEGR are shown in Figure 3-42, where they are compared to distributions from other fiber coating configurations to be discussed below.

Two other coating configurations based on B(Si)N were also investigated, referred to as configurations B-2 and B-3. These coating configurations did result in improved ultimate strength and strain to failure properties of the composites compared to the B-1 coatings, as shown in Figure 3-42, but still did not reach the levels obtained with the standard configuration A coatings.

3.2.2.6.2.8 Optimization of the Configuration C System

In addition to the poor mechanical properties, the densities of composites made with configuration B coatings were also found to be highly variable and relatively low. Often

the matrix slurry did not fully wet the tows during the tape winding process. Adjusting the coating configuration, including changing the composition of the outer coating layer, improved the density and tensile properties of the composites. This improved configuration is designated as configuration C. Distributions of ultimate strength and strain to failure for the experimental configuration C coating specimens are shown in Figure 3-42. The distributions obtained from the "optimized" configuration A coatings from ACC are also shown for comparison. As shown by the distributions we were able to obtain ultimate strength and strain to failure values from the configuration C system that were comparable to, or better than, those from the configuration A system. The property distributions for the configuration C system are wider than for the configuration A system in Figure 3-42, which is a result of including a variety of coating experiments in the configuration C data set, whereas the configuration A system data set is primarily from samples made after coating optimization had been completed. Samples made with optimized configuration C fiber coatings, as will be described later in the property database section, had even better properties, with narrower distributions, than are shown in Figure 3-42.

Most of the coating experiments reflected in the data in the bottom graphs of Figure 3-42 involved investigating the effects of changing the thickness, or weight gain, of the individual coating layers. Through a series of roughly 20 experiments we converged onto an optimum set of coating weight gain targets. These same coating targets were maintained throughout the remainder of the program, although significant run-to-run variations in the coating layer weight gains were known to occur in practice.

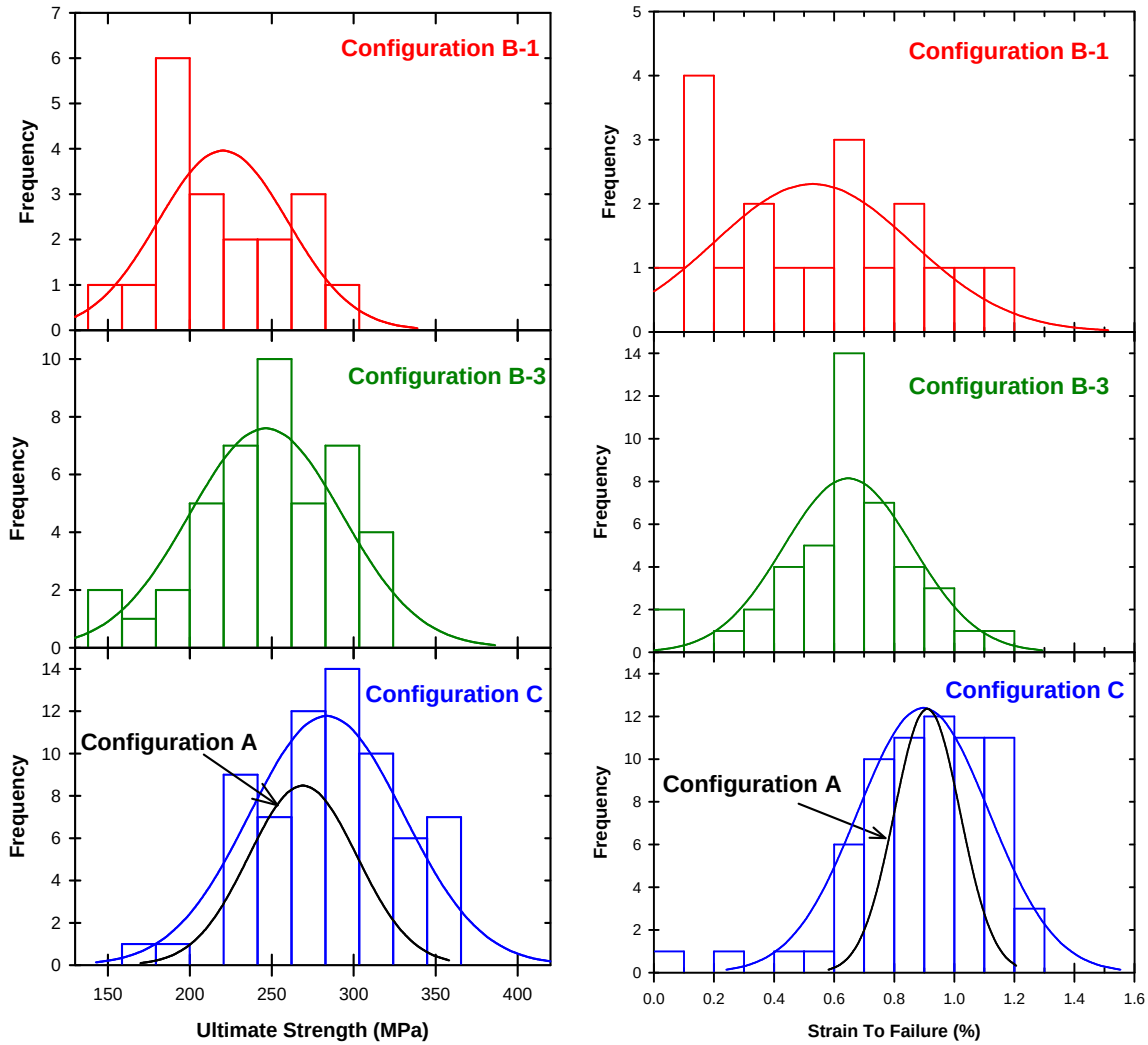

Figure 3-42. Distributions for ultimate strength (left) and strain to failure (right) for composites made with GEGR developmental fiber coatings. The data on the configuration A coating specimens is from ACC coated fiber following coating process optimization.

3.2.2.6.3 Design of GE's Large Tow Coater

The establishment of GE large tow coater fell under program Task 3.2.a.5 Fiber Coating Cost Reduction and Vendor Evaluation. The design, fabrication and assembly of the new coater were done using internal GE funding. However, efforts directed at learning how to operate the coater, such as coating trials and coating process optimization, were done with DOE funding.

The large reactor design philosophy leveraged coating experience from the small coater system in such a way as to minimize cost and the technical risks associated with scaling-up production while still significantly increasing throughput. Design on the furnace began in late 2001. In order to have the coater operational in time to support the shroud and

combustor development programs many features from the smaller reactor were adopted with little or no modification. However, other features necessary to improve productivity were completely redesigned. Full disclosure of the advanced features of the large coater is, unfortunately, not possible due to the fact that the design and operation of the tow coaters is proprietary information.

The overall CVD coater, as shown schematically in Figure 3-43, can be divided into four primary functional groups; a delivery system for the reactant gases (shown in blue), a system for transporting the tow through the reactor furnace (shown in green), the CVD furnace chamber (shown in red, furnace power supply is not shown), and the exhaust gas handling and vacuum system (shown in purple).

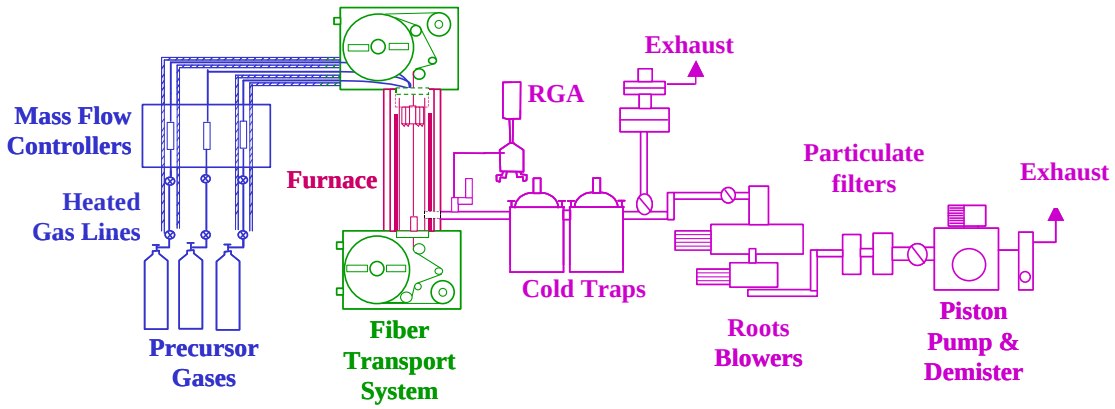

Figure 3-43. Schematic diagram of the large CVD tow coater system designed and built at GEGR.

Temperature of the deposition furnace is controlled by a two wavelength optical pyrometer aimed at the midline of the heating element through a quartz sight port. The sight port is continually fed nitrogen to prevent deposition on the transparent window. A second vacuum port is fitted with a Type S thermocouple to verify furnace temperature. The heating element is connected to a power supply by two water-cooled copper electrodes that are threaded into the top support pieces. This threaded connection also serves as the sole support for the graphite heating element. The stainless steel furnace shell is cooled by an internal water jacket. The furnace shell is also insulated from the heating element with a 6 ply rigid insulating structure made of alternating layers of carbon felt and Grafoil™. Immediately inside of the heating element is a removable graphite deposition chamber. Two water-cooled stainless steel plates are used to seal the furnace and deposition chamber ends to the upper and lower fiber transport boxes. Both plates have cut-outs to allow for graphite inserts that act as fiber guides. The top plate also has brackets welded to the bottom to align and attach the graphite gas injectors.

All of the significant design changes that were incorporated into the large coater design were intended to address known deficiencies in the small coater. However, details of the

design and operation of the CVD tow coating systems is proprietary information of the General Electric Company, and cannot be discussed in this report.

3.2.2.6.4 Optimization of GE's Large Tow Coater

The design, fabrication and operation of the large tow coater followed the optimization of the small coater and standardization around the configuration C coating system. Consequently coating process development and optimization work with the large coater was focused on this coating system.

The precursor gases and deposition reactions utilized in the large coater were identical to those described previously for the small reactor. The maximum deposition temperatures, reactant gas partial pressures and deposition furnace total pressure were all similar between the two systems. However, the reactant gas flow rates differed from the small reactor primarily due to the change in scale and geometry of the reactor tube. The fiber coating rates, i.e. the rates at which the fiber tows were transported through the CVD furnace, were adjusted based on the observed deposition rates to give the desired coating layer weight gains. Many of the early experimental coating runs included an outer carbon layer that was deposited in the large coater; however, the atmospheric pressure carbon coater, described in Section 3.2.2.6.2.5, came on-line during this same time period and was utilized for the majority of the coatings processed in the large reactor. Approximately 30 experimental coating runs were performed, investigating various changes in pressure, gas flow rates and fiber translation rates for all four of the fiber coating layers, before an overall "standardized" coating procedure was defined. However, relatively minor changes to various operating parameters were still made even through the production coating runs in an attempt to further optimize the coating performance.

Using the above coating process parameters identified in the experiments described above, the coating weight gains for the individual layers, and for the entire coating overall, matched those obtained from the small coater fairly well. Figure 3-44 shows histograms of the coating thickness measured on typical coating runs from the small and large fiber coaters. Tow samples from the coating runs were mounted in epoxy and polished to expose the fiber cross sections. The coating thickness measurements were made using digital, quantitative metallography, which measured the equivalent circular diameter of the fiber and of the fiber plus coating, and then subtracted the two values to yield a number equal to twice the average coating thickness on each fiber. Each of the histograms in Figure 3-44 represent measurements on over 1000 individual fibers. Although the distributions show a slight difference in shape, the measured means and standard deviations are practically identical.

The chemical characteristics of the coatings from the two reactors were compared using AES and TEM analyses. TEM of some of the early coatings from the large reactor indicated elevated oxygen levels in individual coating layers, but the layer affected varied from run to run. The oxygen contamination was traced to an intermittent problem with sealing the reactor box doors between coating runs. A procedure was then put into place whereby the quality of the vacuum would be tested using a residual gas analyzer before every coating run, which could detect door seal or other reactor leakage problems. Once

the oxygen contamination issue was resolved the chemical compositions of the individual coating layers were found to be indistinguishable between the two coaters, within the measurement limitations of the techniques used.

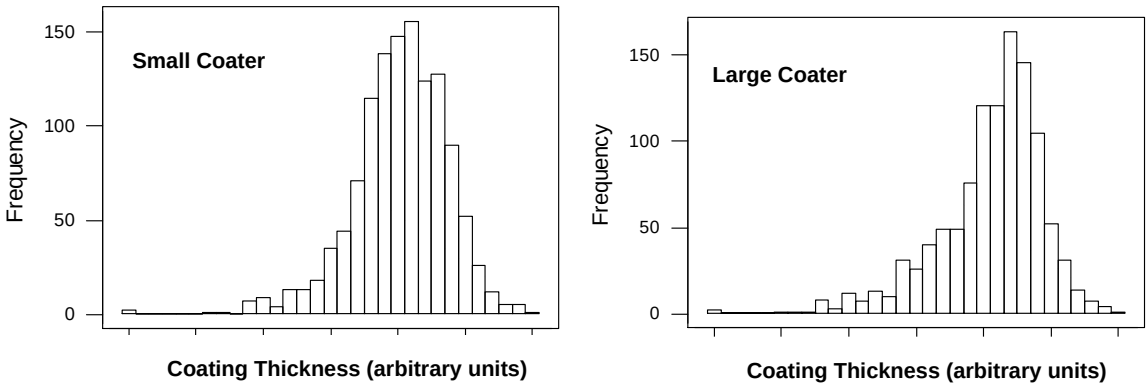

Figure 3-44. Distributions of fiber coating thickness from the small and large fiber coaters.

Despite the similarities in coating thickness and chemistry, the mechanical properties of the CMCs produced with coated fiber from large reactor were typically lower than those of samples with fiber coatings from the small reactor. Figure 3-45 shows the distributions for ultimate strength and strain to failure for composite test samples made over a period of time from fiber coated in the large and small reactors. Each distribution represents results from over 30 coating runs in each reactor. The proportional limit stress and initial modulus of the composites from the two coaters showed a smaller difference, as would be expected since these are matrix-dominated properties as opposed to ultimate strength and strain to failure, which are more influenced by the fiber and fiber coating properties.

Another difference between the coatings from the two reactors was a qualitative difference in the "fuzziness" of the tows produced. The larger coater tended to result in tows with a greater number of broken fibers, many of which were misaligned or entangled with the normal tow filaments, giving the tow a fuzzy and fatter appearance. This greater disruption of the tows in the larger reactor was believed to be caused primarily by the increased gas flow rates and velocities compared to the small coater and to a greater tendency for fiber to stick to the pulleys in the fiber transport system of the large coater. The greater irregularity of the tow presented a challenge during the tape winding process as the broken and misaligned fibers tended to build up and plug the slurry metering orifice, leading to poor matrix slurry pick up or even tow breakage. The orifice diameter used during winding was increased slightly to try to accommodate this increase in tow fuzziness.

The end result of this increased difficulty of tape production was that composites made with coated tow from the large coater tended to have higher porosity on average than composite made from tow coated in the small reactor, as judged by metallographic examinations. This increase in porosity would be expected to negatively affect the

composite mechanical properties, and is no doubt a contributor to the differences in average properties documented in Figure 3-45.

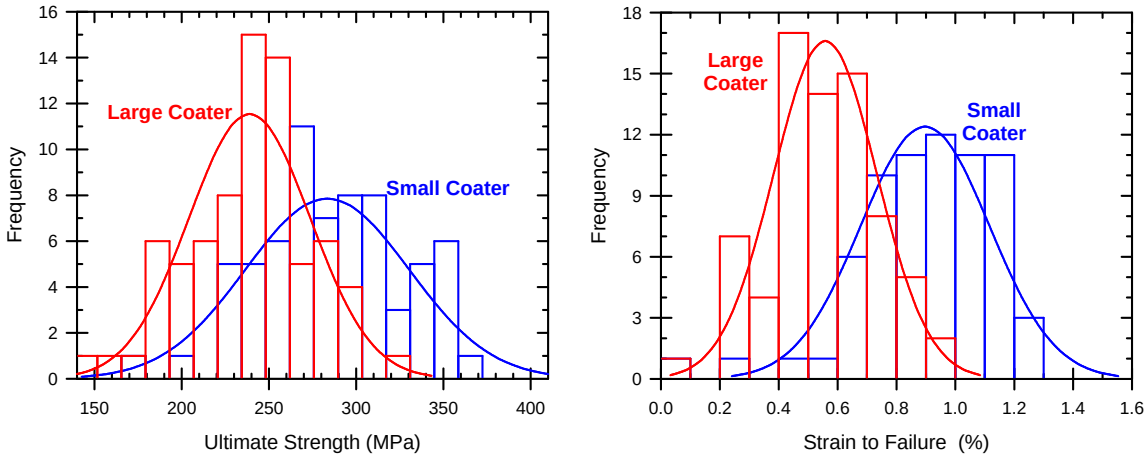

Figure 3-45. Distributions for ultimate strength, left, and strain to failure, right, of CMC test samples made from fiber coated with configuration C coatings in the small CVD coater (shown in blue) and the large coater (shown in red).

During the optimization of the tow coatings in the larger coater at GEGR parallel work was being done under GE funding to design, fabricate and install a next-generation tow coater at GE CCP. The design of this new coater was based on the GEGR large coater, but incorporated several improvements in instrumentation, control automation and fiber transport hardware. In mid-2003 the optimization of the large GEGR coater was stopped in anticipation of having the new coater at CCP available to supply coated Hi-Nicalon fiber for any future GE needs. The small coater at GEGR was kept operational in order to supply reference fiber for process transition work, and to be able to support ongoing work on the coating optimization for other advanced fibers, such as Hi-Nicalon Type S™ and Tyranno SA™.

3.2.2.7 Shape Demonstration with Small Diameter Fibers

The work described in this section was done under program Task 3.1.c Shape Demonstration from the original Phase II program plan. Work under this task with the monofilament reinforced system was previously described in Section 3.2.1.7.

The purpose of this task was to demonstrate the ability to fabricate shroud components to the shape defined by the first 7FA shroud design, as shown in Figure 3-20. The main challenge in fabricating this shroud is forming the sharp corners between the hot gas path surface, i.e. the major bottom surface, and the four sides. Fabricating this shape from the monofilament reinforced system required the joining of several flat plate sections to form the shroud, resulting in no continuous fibers from the shroud major face to the sides. The added flexibility of the small diameter Hi-Nicalon fiber allowed for the possibility of

wrapping fiber around the corners, thereby have continuous reinforcing fiber connecting all of the shroud surfaces.

The initial trial was done by simply joining several individual panels using butt splices at the corners. Extra matrix slurry was used to "glue" the green panel parts together inside the female tooling. Burn-out of the part was done using the standard time-temperature profiles, and infiltration was done by placing the shroud upside down (concave side down) on a carbon cloth wick. The finished dimensional fidelity of the shroud was very good, but cracks formed along most of the monolithic corner joints. This result simply underscored the need for continuous fiber to wrap around the corners.

Clearly, wrapping any fiber around a sharp 90° bend, as suggested by the original shroud design in Figure 3-20, would be impossible. The compromise that was pursued was to put splices in the outer plies so that they would meet in the corners but not be continuous around the corners, which would be backed by inner plies that would wrap fully around the ID of the corners. This concept is illustrated in Figure 3-46.

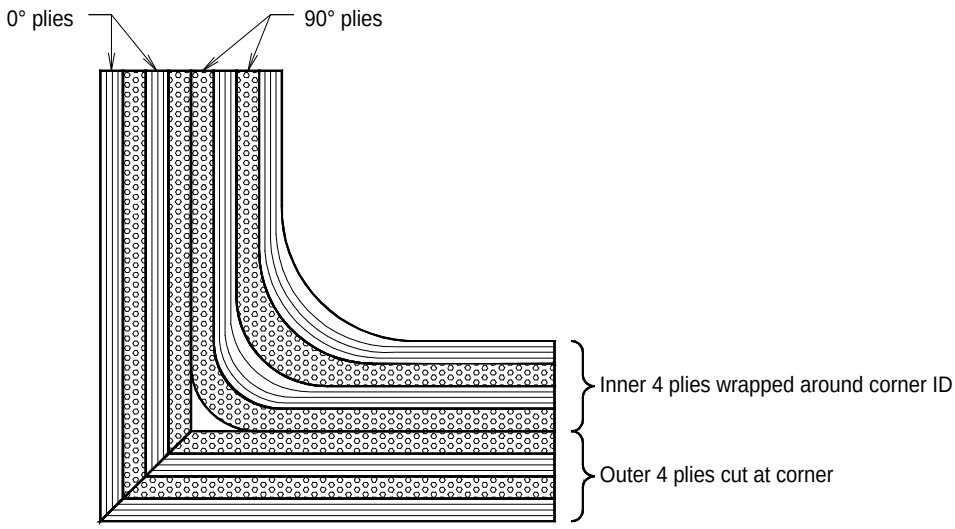

Figure 3-46. Schematic diagram of the ply lay-up pattern for the sharp corners of the first 7FA shroud design. The four outer plies are cut and form a 90° butt joint in the corner whereas the inner four plies bend continuously around the inner radius of the corner.

Two additional shape trials were processed using this corner wrapping scheme with the "soap dish" shroud design. The first attempt used only the as-wound tapes for lay-up with no additional matrix material added to fill in the corners. The tapes were laid into the female tool and laminated outward into the tool using a vacuum bag and autoclave. Again the dimensional control of the outer surface was very good; however, the ID of the inner corners was considerably rounded, as would be expected from the lay-up. The lack of additional matrix in the corners led to gaps forming between the ends of the cut surface plies. When viewing the external surface these gaps appeared as cracks running along the

corners, primarily near the 3-surface corners. None of these defects went fully through the thickness.

A third trial part was then made using the same tape lay-up scheme as the second part; however, additional matrix slurry was added in the corners during lay-up in order to fill in any gaps between the plies. This part was completed through infiltration with no observed corner gaps or cracks. Photographs of this shroud part are shown in Figure 3-47. The rough surface texture, particularly of the inner surfaces, is due to the rather coarse texture of the peal ply used during vacuum bagging and autoclaving. Though not perfect, this shroud part was considered an adequate demonstration of the ability to fabricate this shroud shape, or of a complex shape in general. Additional optimization of the fabrication procedure was not done at this time as the design of the shroud component was evolving away from the first generation soap dish design. Rather than utilize resources optimizing fabrication of this design, we chose to wait until the actual design to be used for rig testing was finalized.

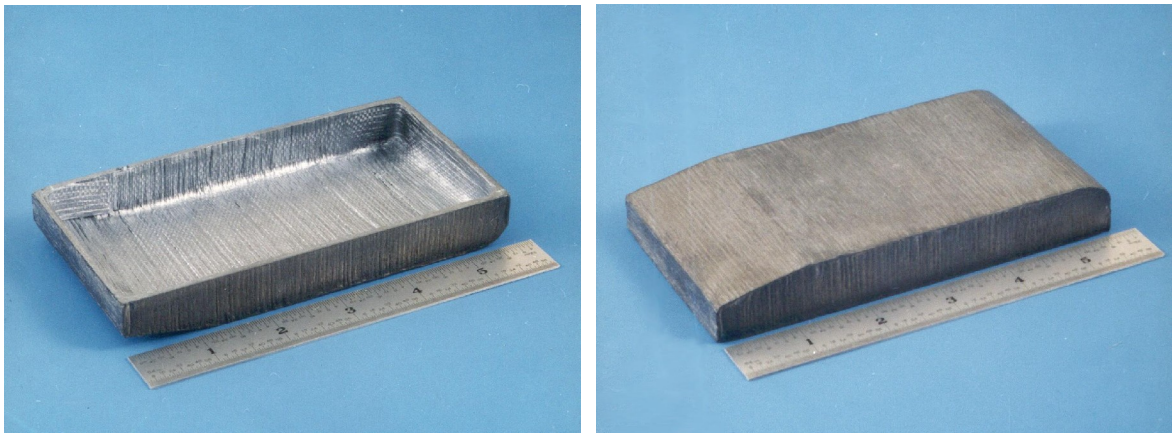

Figure 3-47. Photographs of the third "soap dish" shroud shape demonstration part made with Hi-Nicalon™ fiber.

3.3 Composite Joining

Early in the CFCC program it was well recognized that the ability to join CMC to CMC, or CMC to metal, would be critical for the success of various proposed applications. Due to the wide temperature swings and cyclic nature of turbine operation, and to the large mismatch in coefficient of thermal expansion between MI CMCs and high temperature structural alloys, direct CMC to metal joining was never really considered feasible for turbine components. Rather, thermal mismatch strains between the CMC components and metallic support structures have been accommodated by engineering the attachments to allow for relative motion of the components. The design of such attachments is an integral part of the overall component design, and is very specific to the actual parts. Consequently the attachment, rather than joining, of CMC to metallic components is described in the later sections related to component design and testing.

Nevertheless, there are still instances where joining of CMC to CMC could be beneficial to the development of turbine hardware. One obvious instance would be where the shape complexity of the CMC component would be too difficult, or even impossible, to lay-up as a single part. One could then envision making several simpler sub-component pieces that could then be joined to form the overall CMC component. A second potential need for joining would be for components, such as combustor liners or transition pieces, that are very large and therefore difficult to fabricate as single pieces. Limitations in the size of available forming, lamination or infiltration equipment could also come into play. Again, making several smaller sub-component pieces that could then be joined for form the one large component could prove very advantageous. Work on development of composite joints was performed under program Task 3.5 Joining.

3.3.1 Previous Work On Joint Design

A critical concern with any joined CMC component is the consequences of the joint on the mechanical response of the component. Clearly significant time and expense has gone into the development of CMC systems primarily to take advantage of their tough, non-catastrophic failure behavior. Composite joints are by definition interfaces of primarily monolithic ceramic within the CMC structure, and therefore represent a region where brittle, catastrophic failure can occur, thereby potentially invalidating one of the prime advantages of CMCs over conventional monolithic ceramics. Clearly CMC to CMC joints that retain the tough failure behavior inherent in the composites would be highly desirable.

GE actually began development of CMC joints prior to beginning the work in Task 3.5. Tough CMC to CMC joints were demonstrated using an early version of the SiC monofilament reinforced MI CMC system[18]. Work done under the CFCC program was mostly to refine the results from the earlier study. Nevertheless, the results of the early work are summarized here for continuity.

Joint fabrication could be done in two ways, either by joining already infiltrated composite pieces and then re-infiltrating to densify the joint region, or by joining sections of composite performs in the green state and then infiltrating as a whole. In each case the sections to be joined were diamond abrasive machined to the proper geometry and then "glued" together using matrix slurry. Normally one would try to minimize the clearances between the two parts being joined in order have the minimum volume of CMC affected by the joint, but in practice it proved difficult to consistently get the matrix slurry uniformly distributed in the joint region with very tight clearances, particularly on the fingered joints. The joints were therefore fabricated with a nominal gap of 0.05mm between mating surfaces.

The development of tough composite joints was largely based on simple geometric factors. In order to maintain tough behavior it is necessary to ensure tensile failure of the CMC in regions where there are continuous fibers to bridge the matrix cracks. By definition the reinforcing fiber are not continuous across the joint interface. A simple butt joint, as illustrated in Figure 3-48-A, would not yield a tough joint since a matrix crack at the joint plane would not be bridged by fiber. One could argue that making the joint material much

stronger than the bulk of the CMC parts would prevent failure in the plane of the joint. This is very difficult to do in practice, however, due to the difficulty in getting defect-free microstructures in the joint plane. Also some degree of stress concentration at the joint plane tends to occur from the elastic discontinuities caused by the bonding of the exposed fiber ends along the joint plane. The consequence of these effects is that all butt joints tested in composites showed lower strength than the composite material itself and failed in a brittle fashion.

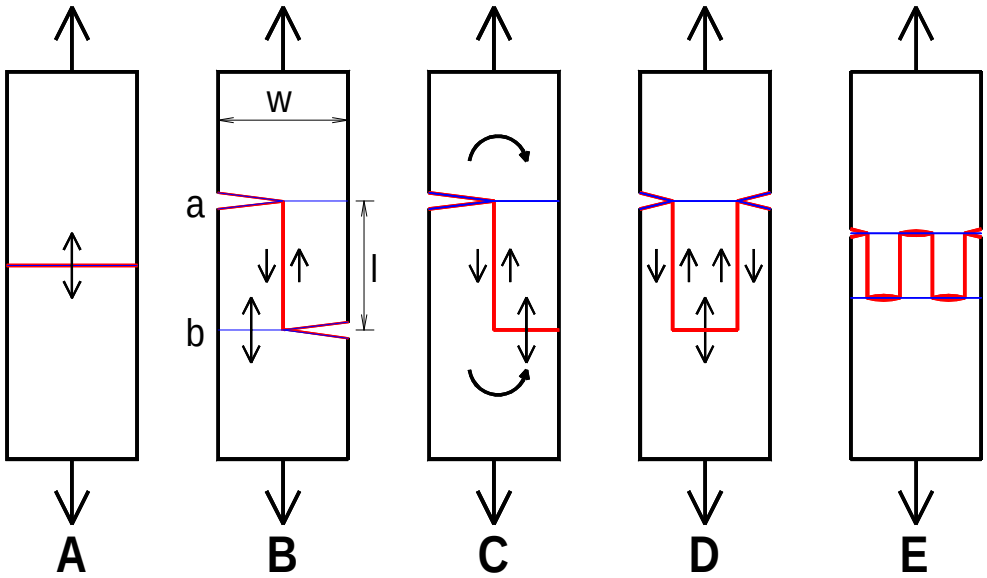

Figure 3-48. Various configurations of tensile joints tested in CMC composites. The red lines show the joint interface and the blue lines show positions of likely matrix cracks during tensile testing. Diagrams B-G show the joints during the initial stages of failure where the joint interfaces loaded in tension have already cracked starting from the edges. A – simple butt joint; B – simple overlap joint, C – simple overlap joint during non-symmetric failure; D – single finger, or tongue-in-groove, joint; E – multiple finger joint during early stages of failure.

The simplest way to get tough joint behavior is to use a lap joint, as in Figure 3-48-B. Due to the stress concentrations and bond line defects mentioned above, during tensile testing of such lap joints it is generally observed that the initial matrix cracks form at the planes a and b, corresponding to the horizontal joint planes. In order to get the remaining CMC ligaments with bridging fibers to fail in a tensile manner, and thus preserve toughness for the overall joint, sufficient load must be carried in shear across the vertical joint plane to load one of the remaining ligaments, or roughly ½ of the total CMC cross section, to tensile failure. In other words,

$$l\,\tau \geq \sigma_u\, w/2 \qquad (7)$$

where l is the length of the lap joint, τ is the in-plane shear strength of the joint, w is the width of the joint finger and σ_u is the ultimate strength of the CMC. For multiple lap, or finger, joints, such as in Figure 3-48-E, the area available for shear load increases as the number of vertical joint interfaces increases, but the total tensile load that needs to be supported remains at roughly ½ the ultimate strength of the composite. Introducing the factor n to represent the number of vertical joint planes, and with rearrangement, equation (7) becomes:

$$l \geq (\sigma_u w) / (2 n \tau) \qquad (8)$$

which defines the minimum length of the lap or finger joint based on the mechanical properties of the CMC and number of fingers. For the SCS-6 monofilament reinforced MI CMC used here the in-plane shear strength was estimated to be about 60MPa at room temperature, and the ultimate strength is roughly 400MPa, and thus a single lap joint on a typical 12mm wide test bar would need to be at least 40mm long to ensure tensile failure of the joint. Of course, the joint length can be substantially reduced by using additional fingers in the joint. For instance, the joint shown in Figure 3-48-E, which has n=4, would only need to be 10mm long in this material system.

Another important aspect governing the strength of the joints is the fiber slip length during fracture. Each composite system has a characteristic slip length, the distance over which debonding between the matrix and the fiber takes place around a bridged matrix crack. In the debonded region the matrix carries only a partial load, the load being transferred through friction at the fiber/matrix interface. If the embedded fiber length in the joint is not at least equal to the slip length of the composite then the fibers will be able to pull out from the joint with relatively low force, and the strength and toughness of the joint will be compromised. The composite matrix crack spacing at saturation represents an upper bound on the fiber slip length, and can thus be used as a limit for the minimum joint length. For the SCS-6 monofilament reinforced system used here the matrix crack spacing is on the order of 2mm.

There are other practical considerations related to the design of CMC joints. Simple lap joints, as shown in Figure 3-48-B, do not work well in practice due to the non-symmetry of the joint. During tensile loading it is invariably observed that one of the first matrix cracks is initiated at one of the joint planes. This situation is illustrated in Figure 3-48-C where all of the tensile load is now being carried on only ½ of the sample. This nonsymmetric loading tends to cause rotation of the two test bar end, thereby inducing additional tensile stresses at the vertical joint plane. The observed result is that such a joint tends to "unzip" by propagating a mixed-mode tensile/shear crack entirely along the joint interfaces, ultimately leading to brittle joint failure. The tongue-in-groove or multiple finger geometries, as shown in Figure 3-48-D and E, give a more symmetric loading of the sample even after the initial matrix crack has occurred. Thus these joint geometries tend to be much more stable and more likely to fail in a tough manner.

One is most often attempting to minimize the overall size of a joint due to various component geometry concerns. Such a constraint would normally drive one to utilize a

joint with multiple small fingers, such as joint E in Figure 3-48. However, such a joint is inherently limited to having only half the strength of the normal CMC since at either joint plane one half of all of the fibers in the tensile direction have been cut. Machining multiple small fingers is also difficult due to the fragile nature of the small fingers. If the constraint on joint length is removed then different geometries are possible that spread the joint out over a longer length and have a smaller fraction of discontinuous fiber on any given plane.

The best joint geometry developed was the "stepped taper" joint shown in Figure 3-49. This joint can be thought of as analogous to a small fingered joint but with the fingers distributed over a larger length of the composite. Both of the joints in Figure 3-49 have the same amount of vertical joint interface for transferring the shear loads through the joint fingers, but for any given matrix crack plane the stepped tapered joint has a larger area fraction of bridging, continuous fiber (a minimum of 79% for the geometry shown) than does the fingered joint (only 50% for cracks along either joint plane). Thus the stepped tapered joint has the potential to have a higher strength than any of the lap or finger joints shown in Figure 3-48. Indeed, the experimental observations were that this joint did have a higher strength and strain to failure of any of the joint geometries tested [17].

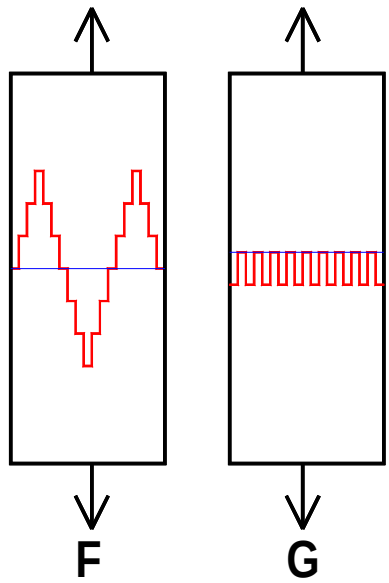

Figure 3-49. Comparison of the stepped tapered joint (F) with an analogous finger joint (G). The joint interfaces are shown by the red lines and the likely location of a matrix crack by the blue lines. Both joints have the same vertical joint interface for transferring shear loads, but the stepped tapered joint has a much smaller fraction of any given cross section affected by the joint.

3.3.2 Joint Development Under the CFCC Program

GE's primary need for CMC joints under the CFCC program was to facilitate the fabrication of shroud components using the monofilament-reinforced system. At the time this work was done the prime shroud design was the first generation "soap dish" design, shown in Figure 3-20. Clearly 90° joints were needed between the bottom and four side surfaces and between the four sides themselves in order to fabricate this shape with the monofilament fiber system. Unfortunately, testing and interpretation of test results from angle joints is complicated, so initial evaluations were conducted on straight joints in coupons; however, limited fabrication and testing of angled joints was also performed.

3.3.2.1 Development of Straight Joints

Again, the purpose of this work was to build upon, and refine, the earlier joint development work described above. The fingered joints evaluated in the previous work were limited to a 12.5mm joint length. However, the angled joints to be used in the shroud components would be limited to a "length" equivalent to the wall thickness, or 2.5 to 3mm. Fingered joints of these lengths were therefore included in this study with the finger width being adjusted to meet the requirements set forth in Equation 8.

The earlier work also primarily utilized uniaxially reinforced composites with BN coatings on the SCS-6 fibers. The very low fiber-matrix interfacial shear strength of the BN system, measured at ~8MPa using fiber push-out tests, gave composites with excessive fiber pull-out, and therefore relatively low joint strengths. The newer Si_3N_4 fiber coatings available in this program yield a much higher interfacial shear strength, on the order of 35MPa. Also, any real application of a joined component would likely require multiaxial (i.e. 0°-90°) fiber architectures. A stepped tapered joint was therefore included in the CFCC work to evaluate any effects the change in fiber architecture (0°-90° vs. uniaxial) and fiber coating (Si_3N_4 vs. BN) would have on the best joint configuration.

Finally, a major factor in defining the geometry of tough fingered joints is the ratio of the joint shear strength to tensile strength of the CMC material. If one can increase the shear strength relative to the tensile strength then simpler joints, with fewer and shorter fingers, could be utilized. One way to artificially increase the joint shear strength is to use a dovetail geometry for the fingers, which converts much of the shear load on the sides of the joint fingers into compressive stresses across these joint interfaces.

The four different straight joint geometries fabricated and tested in this work are shown in Figure 3-50. All samples were fabricated using Si_3N_4-coated SCS-6 monofilament fiber and the Phase 1 matrix slurry using the drum winding tape manufacturing process. Eight ply 0-90 preform panels were laminated from the unidirectional tapes. The two ends of the test specimens, including the joint interface features, were machined from the green perform panels. The sample ends to be joined were painted with a thin layer of matrix slurry and then the two halves pushed together. The sample with the dovetail joint required that the two halves be assembled dry and then matrix slurry was injected into the joint region using a syringe. The samples were then heated to 120°C for 2 hours to dry and

cure the slurry in the joints. Burn-out and infiltration was then done using standard practices. Following fabrication the samples were tensile tested to failure at room temperature.

Tensile stress-strain curves for the 4 joined samples are shown in Figure 3-51 along with that from a bar cut from the same perform panel but without any joint. As can be seen, there is a substantial effect of the joint geometry on the ultimate strength and strain to failure properties of the composite samples, but a relatively minor effect on the proportional limit. These observations are to be expected since ultimate strength and strain to failure are controlled by the fiber bridging the matrix cracks, many of which are no longer continuous due to the presence of the joints. On the other hand, the proportional limit is controlled mostly by matrix properties, which are not strongly affected by the presence of the joint as long as the joint interfaces are well densified.

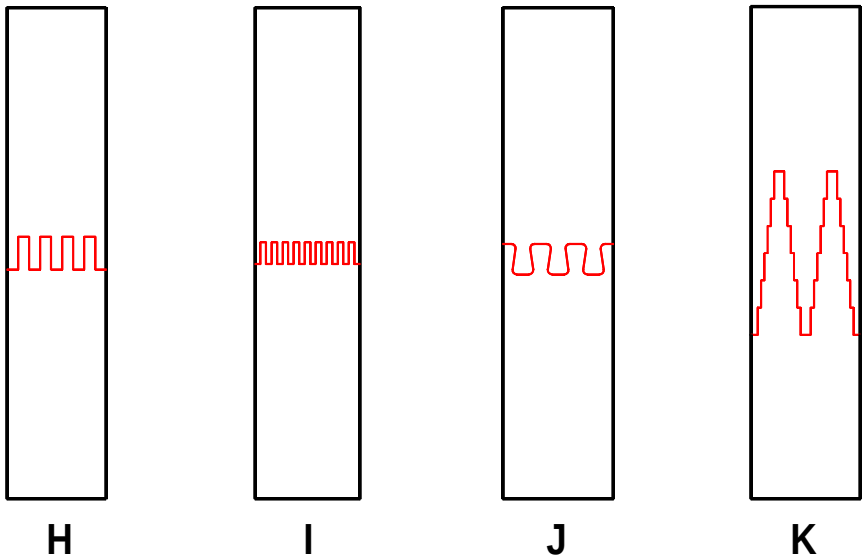

Figure 3-50. Configurations of straight joints evaluated with monofilament fiber reinforced MI-CMC under the CFCC program: H – fingered joint with 1.27mm wide x 3.56mm long fingers; I – fingered joint with 0.64mm wide x 2.54mm long fingers; J – dovetail joint with 2.39mm max width x 1.68mm minimum width x 3.43mm long fingers; K – stepped tapered joint with 0.38mm wide x 3.18mm long steps (total joint length of 19.05mm)

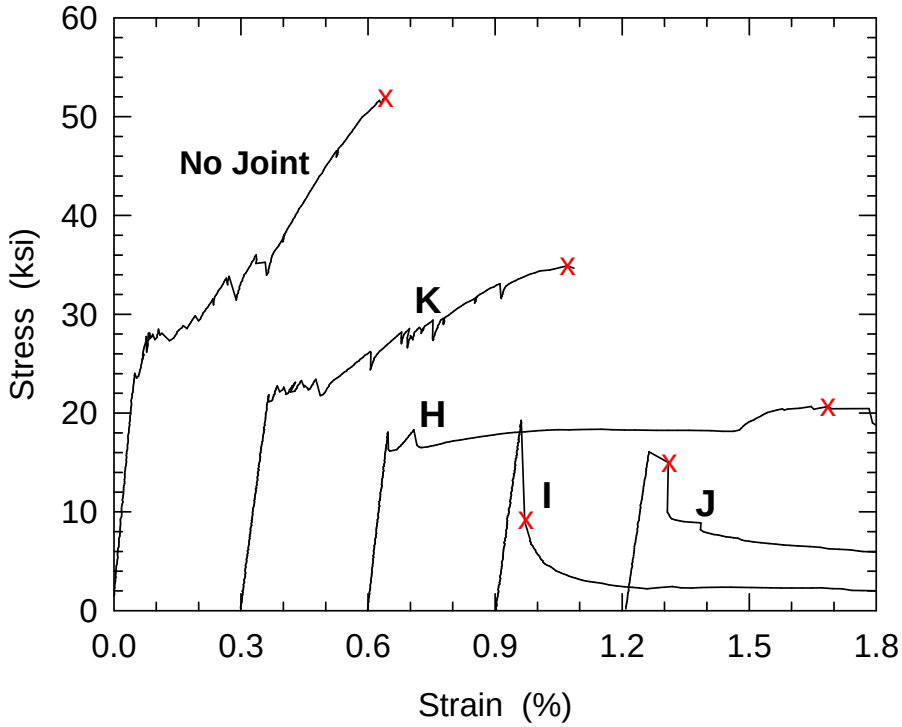

Figure 3-51. Tensile stress-strain response of monofilament-reinforced MI CMC samples with various joint geometries. The letters by the curves refer to the joint configurations shown in Figure 3-50.

As noted above, the ultimate strength of the joined composites should be proportional to the minimum number of intact fiber across the joined region, assuming the joints were long enough to allow for complete fiber loading. Since the first matrix crack was universally observed to occur at one of the major joint planes, the maximum load that the sample would carry following this first matrix crack is a measure of the number of intact fiber across the joint region. Table 3-11 lists the maximum stress across the joint following the first matrix crack, as taken as the highest point on the stress-strain curve following the initial discontinuity (marked by red "x"s in Figure 3-51). The ratio of this stress value to the ultimate strength of the sample with no joint is, to a first approximation, a measure of the fraction of intact fiber still able to sustain load across the joint.

If one assumes the joints are fabricated perfectly, meaning there is no clearance between the joint interfaces of the two pieces and that there is no damage to the performs caused by machining, then the minimum fraction of intact composite is easily calculated from the joint geometry. These values are listed in the fifth column of Table 3-11. The fraction of intact composite calculated from these assumptions of perfection clearly over-predict the observed fraction of intact composite, as measured by the ratio in column 4 of Table 3-11. However, we know that the joints were made with a nominal clearance of 0.05mm between surfaces for assembly purposes. Also, during machining of the joint features any fibers within one fiber diameter of a cut would have had its integrity compromised by the machining procedure. Thus there would be a zone 148μm in width, equivalent to the

coated fiber diameter, along each cut where the fiber would no longer be able to carry load after a matrix crack. Adding the effects of the joint clearance and the fiber damage zone into the calculation of intact fiber following matrix cracking gives the values listed in column 6 of Table 3-11. In general, the agreement between this column and the ratio of strengths is fairly good, indicating that the effects of the joints can be easily estimated from the joint geometry once the clearance and damage factors are taken into account.

Table 3-11. Retained Strength Behavior of Joined Composites Following Matrix Cracking

Joint Configuration	Joint Designation in Figures 3-60 and 3-61	Max Stress Following Matrix Cracking (MPa)	Ratio of Max Stress to Ultimate Strength of CMC without joint	Fraction of intact fiber with no clearance or damage zone	Fraction of intact fiber with 51μm clearance and 148μm damage zone
No Joint	No Joint	359	100	-	-
Wide Finger	H	143	0.40	0.44	0.32
Narrow Finger	I	62	0.17	0.47	0.22
Dovetail	J	103	0.29	0.40	0.29
Stepped Taper	K	241	0.67	0.79	0.73

All of the finger and dovetail joints showed only modest strength retention, all less than 1/3 of a composite without joints. These modest strengths are primary due to the joint being concentrated in a narrow band along the length of the composite, and thus the effects of the cut fiber and machining damage are localized and cumulative. The stepped tapered joint, on the other hand, spreads the material affected by the joint over a much greater length of the sample, and thus any individual matrix crack sees the influence of only a fraction of the joint with most of the material along the crack being normal CMC. As a result the stepped tapered joint displayed very good retention of ultimate strength and strain to failure, reaching 2/3 that of an unjoined composite.

The relatively poor performance of the dovetail joint was initially somewhat surprising, but in retrospect is easily understood by the geometry. Figure 3-52 shows a close-up schematic of a dovetail joint and a straight finger joint having the same average finger spacing. The thin black lines represent the joint interface and the red areas represent the region of composite affected by joint clearance or machining damage, as described above. In the straight finger joint the only material compromised by the joint is that directly adjacent to the joint interface. In the dovetail joint all of the fibers that intersect the angled side cuts, shown by the gray regions, have fiber that are no longer continuous with the parent piece of CMC, and thus do not provide any effective crack bridging for cracks running through the joint. The overall effect is that there is less intact fiber remaining to provide strength and toughness to the joint in the dovetail configuration compared to the straight finger configuration for similar finger lengths and widths. However, the dovetail configuration is still expected to have performance advantages over straight fingers in cases where there is insufficient shear strength of the joint interface, such as when the shear strength of the composite is very low or where the joint length must be kept very short.

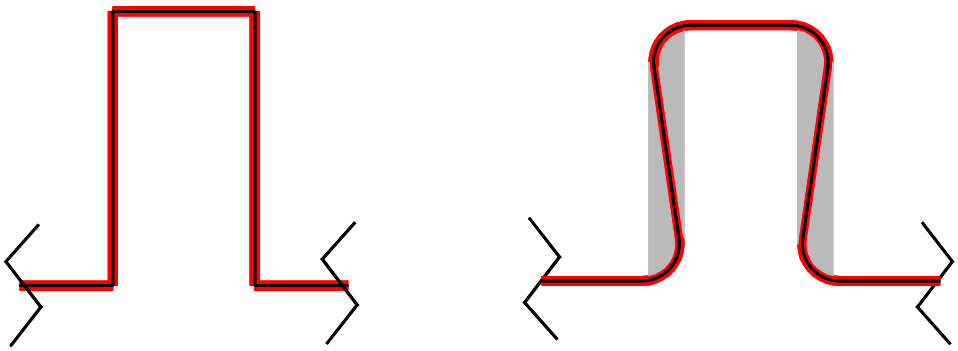

Figure 3-52. Schematic comparing the amount of affected CMC, shown in red and gray, in a dovetail joint (right) compared to a straight finger joint (left).

3.3.2.2 Development of Angled Joints

The primary potential application of CMC joints in the GE program was to be for the fabrication of the soap-dish shroud design, shown schematically in Figure 3-20. The joints in this component would be for joining the side and end walls together and to the major hot gas path face, and consequently would join surfaces at 90° angles. It was therefore desirable to have a measure of the engineering effectiveness of such angled joints, and to determine if the same geometric factors affecting the performance of straight tensile joints were also controlling the behavior of angled joints. Unfortunately, standardized testing techniques for investigating angled joints in composites did not exist so that a test sample geometry and testing method had to be developed.

The first consideration was how to simulate the loading in the shroud. The attachment concept for the soap-dish shroud was to hang the CMC inner shrouds from metallic rods extending through the slots in the side walls. Pressure and/or mechanical damping load would be applied to the inner surface of the shroud pushing it downward toward the turbine hot gas path. This loading situation simulated in a test coupon is shown schematically in Figure 3-53A. In practice the vertical leg of the L would be gripped in the upper grip of the testing machine, and the horizontal leg of the L would be clamped onto a fixture held in the lower grip. However, such loading tends to create a rotational stress trying to open up the angle due to the loads not being applied along the same axis, which in turn applies both tensile sliding and rotational shear loads on the joint interfaces. Such loading would complicate the failure mode and add uncertainty to the data interpretation. Consequently a “T”-shaped sample, as shown in Figure 3-53B, was selected as it would tend to minimize any rotational loading of the joint.

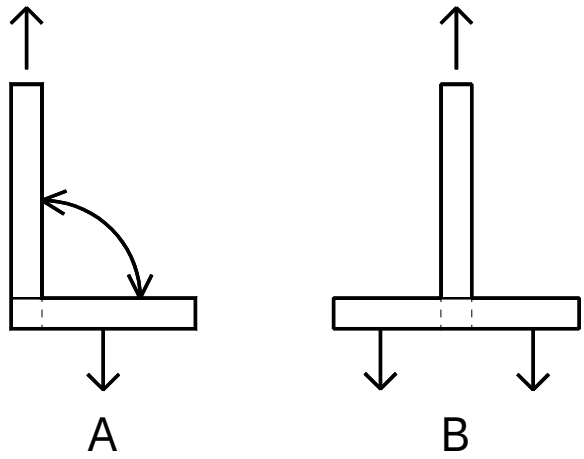

Figure 3-53. Different test sample geometries considered for the angled joint evaluations. A – "L" joint; B – "T" joint.

The joint configurations selected for testing were analogues to the finger and dovetail joints tested in the straight joint evaluations. The best analogue to the straight finger joint would be a through mortise and tenon joint with the horizontal bar of the "T" being the mortise (part with holes) and the vertical bar of the "T" being the tenon (part with the tongue). However, we did not have the ready capability to produce rectangular holes in MI-CMCs and did not wish the joint evaluation to be diverted to a study and development of new machining techniques. Consequently a configuration consisting of mortise slots was devised that would be manufacturable on our existing grinding equipment. The dovetail joint was done similarly to the mortise and tenon joint, but with angled walls on the tongues and grooves to interlock the parts. Schematic representations of the pieces used to construct these joints are shown in Figure 3-54.

The test samples were fabricated using the same process as for the straight joint samples. Laminated and cured panels were cut and ground using diamond abrasive machining. They were then "glued" together using matrix slurry and placed into fixtures for holding the pieces in the proper orientation while the matrix slurry was dried and cured. Specimens then went through normal binder burn-out and infiltration cycles. The straight mortise and tenon joint had 1.52mm wide fingers spaced 1.52mm apart. The dovetail joint had fingers spaced 4.22mm apart with a 30° undercut angle.

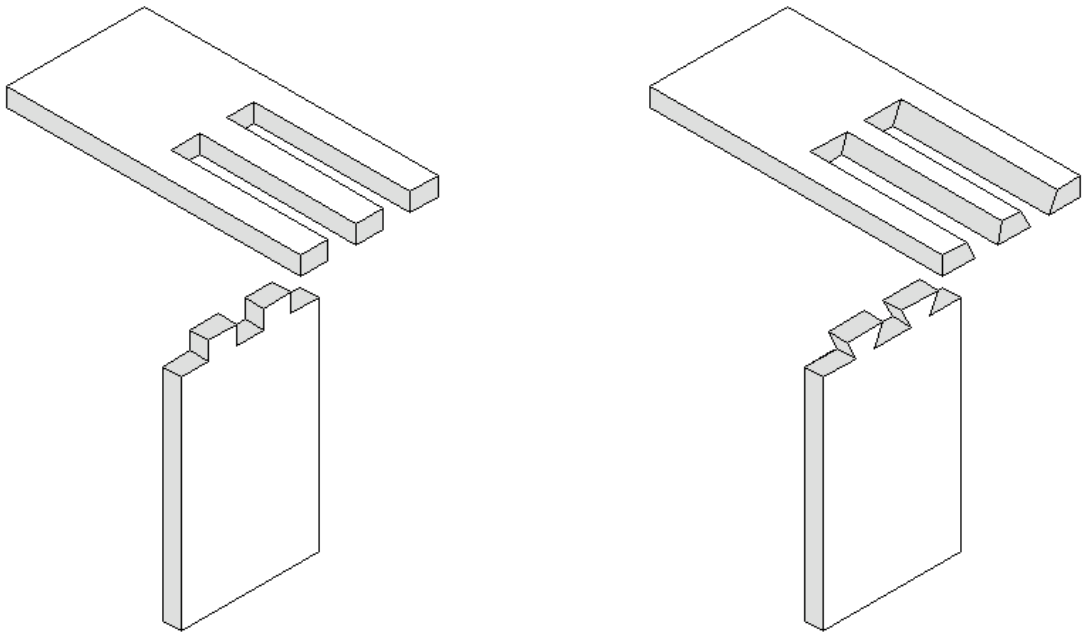

Figure 3-54. Configurations of "slotted" mortise and tenon and dovetail joints developed for ease of fabrication from MI-CMC. The actual samples had more fingers and slots than indicated in these diagrams.

Two different test fixtures were used for testing the "T" joints, both of which are shown schematically in Figure 3-55. The first fixture used consisted of a simple "C"-shaped cavity that surrounded and engaged the ends of the horizontal member of the "T" sample. During testing the horizontal member of the "T" specimens was effectively loaded in 3-point bending, and were found to fail by interlaminar shear stresses caused by the bending loads. The solution was to load the horizontal beam nearer to the joint and to restrain any bending strains by clamping the horizontal member within the fixture. Implementation of these solutions lead to the development of the clamped fixture. Samples tested with the clamped fixture displayed consistent tensile failure of the joints.

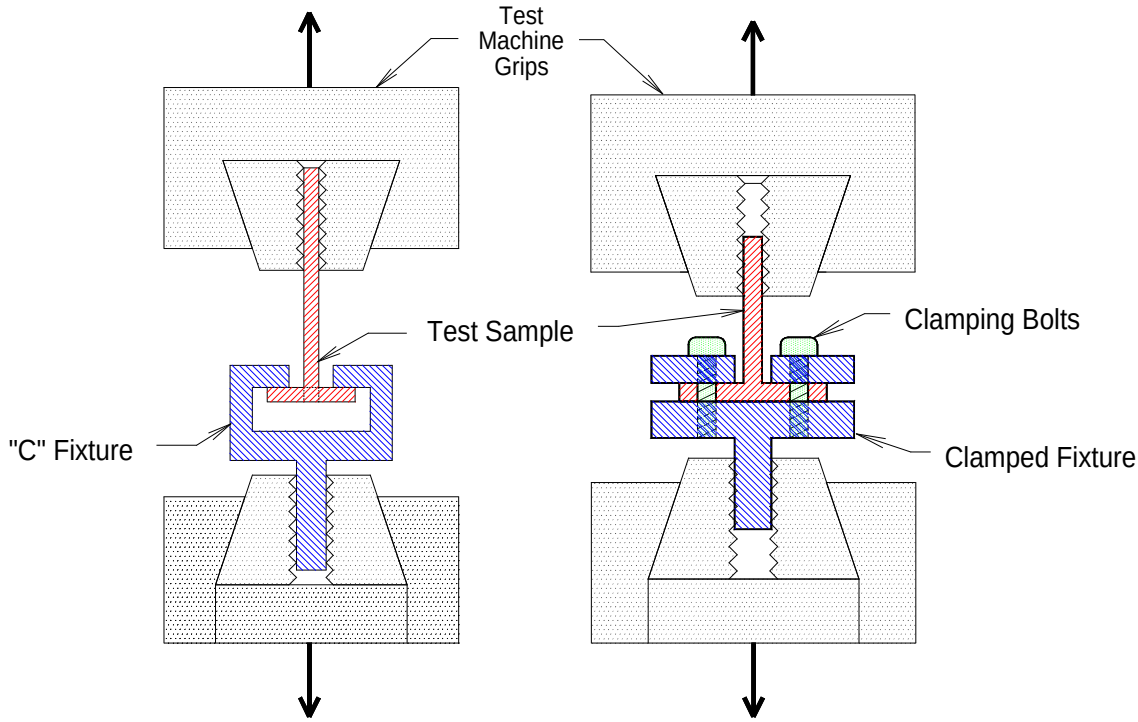

Figure 3-55. Diagrams of test fixtures used for evaluating the "T" joint specimens. The diagram on the left is for the initial "C" fixture and the diagram on the right is for the improved clamped fixture.

Stress-displacement curves for the two types of T joints tested are shown in Figure 3-56. The geometry of the test fixture prevented our using an extensometer during these tests, and compliance within the test fixture and geometry of the specimens made it impractical to estimate the actual strains in the joint. For these reasons Figure 3-56 shows equivalent tensile stress (calculated using the cross sectional area of the middle leg of the T joint) versus the machine crosshead displacement.

The compliance of the test fixture adds some non-linearity to the loading curves in Figure 3-56 so that the first cracking stress is difficult to determine from these plots alone. By listening for the first acoustic emission we estimated the cracking stress to be near 43MPa for the straight fingered joint and roughly 64MPa for the dovetail joint. In both cases there was significant load carrying capacity above and beyond the first cracking stress. It should be noted that the strengths of these joints, which failed in a tensile manner, are about twice those of previous T joints tested with the "C" fixture that failed by shear of the T cross bar. Also, the dovetail geometry displayed higher strengths than did the mortise and tenon (i.e. finger) joint with 1.5mm fingers, which is opposite of the behavior found in the straight tensile joints. These results demonstrated that strong, tough joints can be formed in MI-CMCs for both straight and 90º geometries. There is a decrease in composite strength in joined regions that is geometry dependent, but by proper consideration of joint geometry requirements it should be possible to utilize joined structures as structural components.

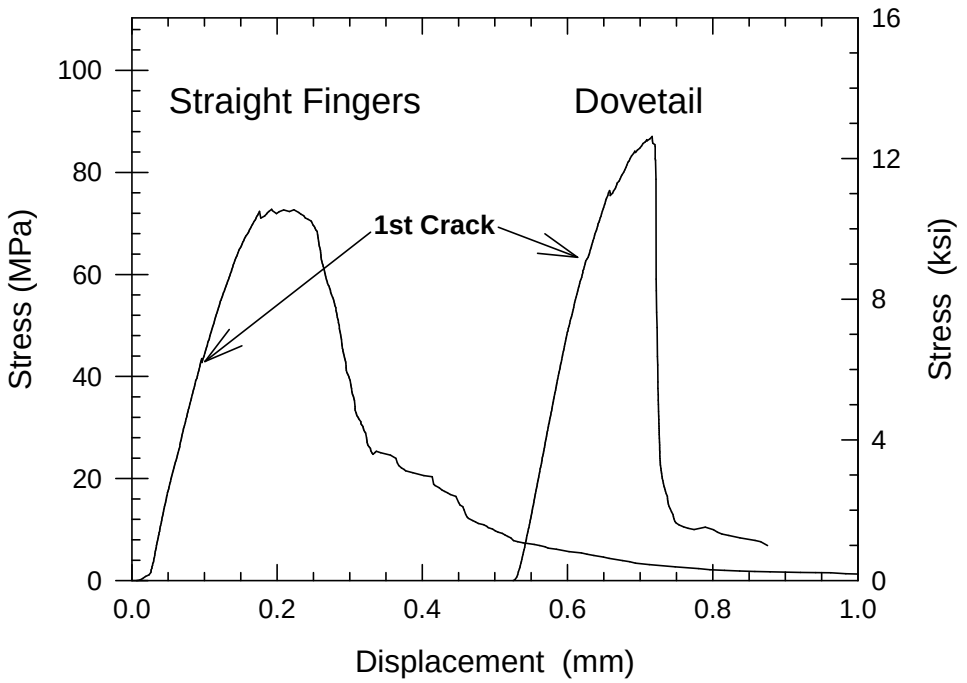

Figure 3-56. Stress-displacement curves measured on "T"-shaped joints using the clamped fixture. Both joints show significant displacement, or strain, following the initial matrix crack event, indicating tough failure behavior. The occurrences of the 1st matrix cracks were estimated from acoustic observations, and correspond to minor discontinuities in the stress-displacement curves.

3.3.2.3 Evaluation of Joints in the Hi-Nicalon Fiber System

All of the above work was conducted using MI CMC reinforced with SCS-6 monofilament fibers, which was the system most in need of joining technology due to the limited shape capability of the monofilament fibers. Nevertheless, joining of parts made from the system reinforced with fine diameter fibers, such as Hi-Nicalon™, could also be needed in the future. A preliminary investigation was therefore performed to evaluate the performance of joints in the Hi-Nicalon CMC system relative to the performance in the monofilament system.

The importance of the various geometric factors discussed previously were expected to also hold for the small fiber systems. Namely, effective composite joint geometry would be governed by factors such as the fiber pull-out length, composite tensile strength and joint interface shear strength. Typically fiber pull-out lengths for well-densified MI-CMC composites with small diameter fibers is on the order of 10's to 100's of microns, so joint length restrictions based on fiber debond length are much less important. The design of the joint would therefore be mostly dependent on the composite tensile strength and the shear strength of the joint interface region. Unfortunately the interface shear strength was not known for the Hi-Nicalon fiber system so that an optimum joint configuration could not be determined beforehand. Consequently the joint configurations tested were similar

to those described above for the monofilament fiber system. In particular, the joint configurations tested were the wide straight finger joint and the stepped taper joint, as shown in Figure 3-50 H and K, respectively.

Joint fabrication in the Hi-Nicalon fiber system was similar to that used for the monofilament fiber system. Crossplied panels were processed through the lamination/cure stage and then the joint features machined in the green state. The joints were then "glued" together using standard matrix slurry and the bars then infiltrated as single pieces. Tensile fracture behavior of the joined bars and of an un-joined sample from the same panel are shown in Figure 3-57.

The specimen with no joint showed very good tensile properties with a cracking stress of about 165MPa and an ultimate strength and strain to failure of 352MPa and 1%, respectively. The fingered joint and tapered joint showed initial cracking at roughly 90MPa and 125MPa, respectively, and ultimate strengths below 170MPa. These strengths are lower than we would have expected based on the results with the monofilament fiber composites. One reason for the difference is that with the monofilament composites the major fracture interfaces were planar, and cut across a substantial fraction of the fibers spanning the joints. In the Hi-Nicalon composites there was a greater tendency for the fracture to follow the joint path, effectively "unzipping" the joint. In the finger joint two of the four fingers unzipped so that fiber in only 2 of the fingers, representing only 1/4 of the composite cross section, were intact and could carry load at failure. In the tapered joint the fracture path followed the joint line almost exclusively, leaving only a small fraction of bridging fibers at the failure surface. Given the small fraction of fibers left intact to span the failure surface, the overall strengths of the joints are surprisingly high. Given this "joint unzipping" mode of failure, a dovetail joint may prove to be a better performer in this composite system.

During the joint fabrication process it was noted that precise machining of the Hi-Nicalon system in the green was somewhat more problematic than with the monofilament system. The difficulties were largely caused by the higher binder content of the small diameter system. During cutting localized heating of the preform caused the binders to soften and “smear” rather than cut cleanly. This smearing could be almost totally eliminated by using copious amounts of coolant during cutting, but this made it difficult to observe the machining process. Since machining was done on a manual controlled surface grinder adjusting the feed rate by observations of the cutting process was often critical. It was thus determined that a more automated technique for perform machining would be desirable, both for possible future need of joining technology or as a technique for green machining of component performs to rough dimensions.

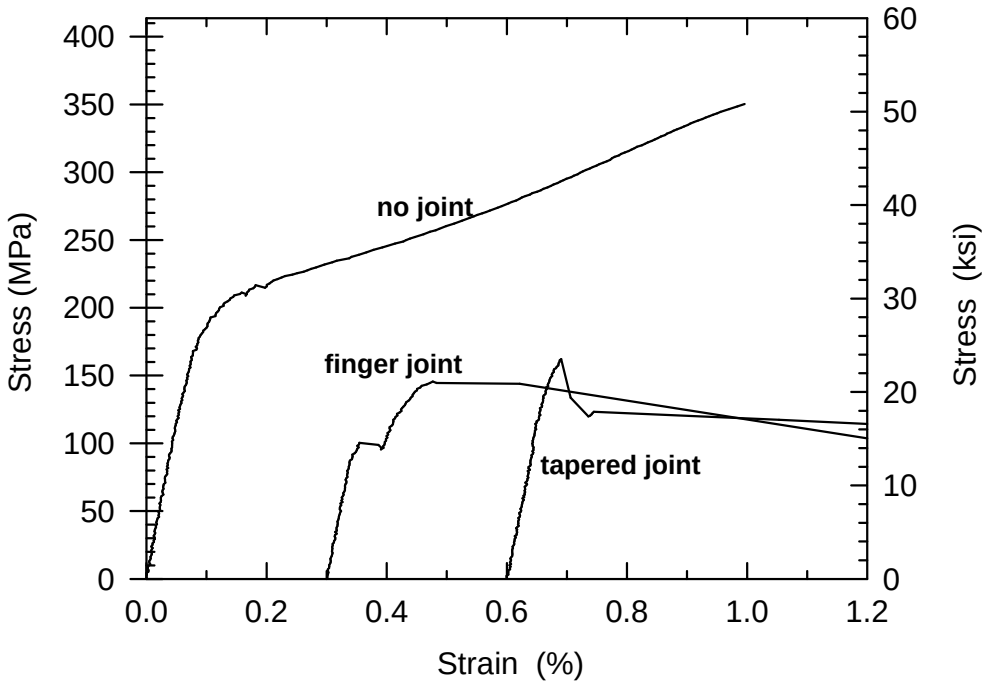

Figure 3-57. Stress-strain response of Hi-Nicalon™ reinforced MI CMC composites with and without composite joints as described in the text.

After reviewing various machining technologies and their suitability for machining of composite structures, water jet cutting was identified as potentially being an effective technique for machining of the green preforms. Small composite panels were prepared using un-coated fiber, and processed as far as the green state (after lamination and cure but prior to binder burn-out) and the burned-out state (just after binder burn-out but prior to silicon infiltration). These panels were then cut in-house at GEGR using an abrasive water jet cutting system, and examined visually for signs of preform damage. Photographs of the cuts made on the two panels are shown in Figure 3-58.

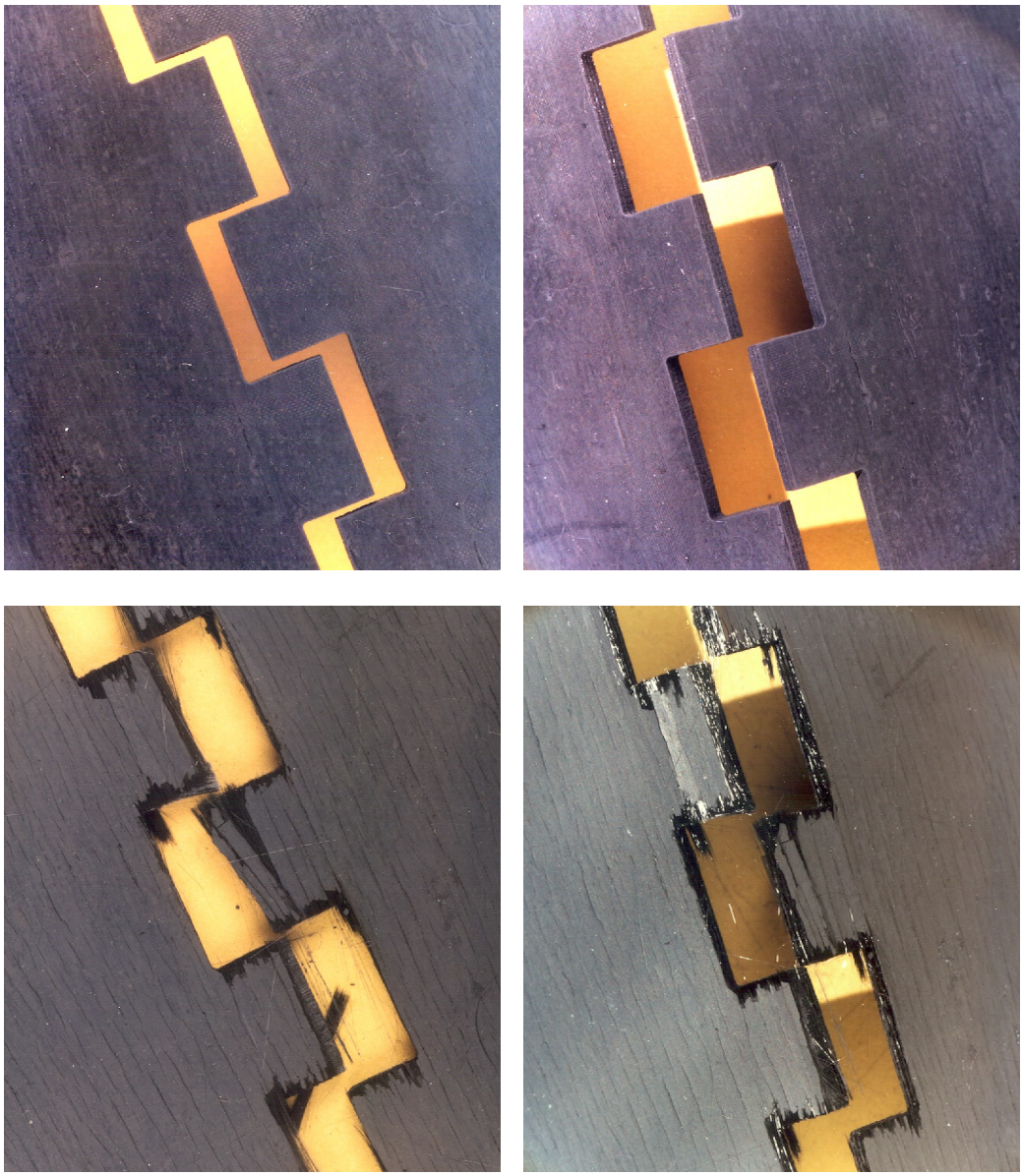

Figure 3-58. Photographs of the water jet cut regions of Hi-Nicalon™ reinforced MI CMC preforms. Top – preform panel cut in the green state; Bottom – preform panel cut after binder burn-out.

The photo on the top in Figure 3-58 shows the cut made in the green preform. The width of the steps in the cut are roughly 12mm. The cut edges are very smooth and straight with little deviation through the preform thickness. Kerf of the cut is very uniform, and should therefore be easily accounted for during machining of actual components. There were also no signs of ply delamination or of fibers or matrix being preferentially removed from the preform. The bottom photo shows the results for the burned-out preform. In this case the cuts show high surface roughness and extensive disruption and removal of fibers and matrix 1-2mm away from the actual cut surfaces. Clearly in the burned-out stage the matrix has become too fragile and is washed away by the water jet. In the green state,

however, the matrix binders preserve the composite integrity during cutting. These results indicate that water jet cutting of green preforms would be a viable machining technique when needed.

At the time in the program when this work was being done the "soap-dish" shroud design had been abandoned in favor of the "toboggan" design, which will be discussed in Section 3.7.1. In the newer design there were no sharp angles that would require joints of the Hi-Nicalon fiber system. Also, work on the monofilament system had been abandoned due to persistent concerns about fiber coating oxidation life. As CMC joints were no longer needed for the shroud component work on joint development was halted. Nevertheless, the main goal of the task had clearly been obtained in that tough, strong CMC joints had been demonstrated for both the monofilament and small diameter fiber systems. Moreover, the general guidelines for the design of effective CMC joints had been established.

3.4 Composite Property Measurement

Material performance characterization is a critical part of the development of any new material system. Such data is useful for a variety of reasons, including as a gage of the effectiveness of process improvements, as a measure of the fundamental material degradation and life-limiting mechanisms, and for providing designers the information necessary to refine the component designs and better predict their behavior. Property evaluations can take the form of laboratory mechanical and physical property tests, low and high velocity impact testing, long-term thermal and environmental exposures, and ultimately exposure in high temperature, high pressure combustion environments that are representative of the actual material use conditions. All of these approaches were utilized in the CFCC Phase II program.

Most of the work discussed in this section was performed under program Task 3.2.b Composite Property Measurement. Exposure testing of coupons in the long-term combustion rig was performed under program Task 3.3.d Long Term Rig Testing of Coupons, but the results are included here for easier comparison of results with the other coupon tests.

Early in Phase II several CMC systems were being considered for eventual turbine applications, including SiC-SiC composites made by CVI from Goodrich Aerospace and DuPont-Lanxide Composites (now GE CCP), SiC-Al_2O_3 composites made by directed metal oxidation (DIMOX™) from DuPont-Lanxide Composites, and SiC-SiC/Si slurry cast MI composites made by Goodrich Aerospace and DuPont-Lanxide Composites, in addition to the GEGR developed prepreg MI composites. For the most part GE assumed responsibility for property characterization of the prepreg MI composites and relied on the other material vendors to supply the material properties for their systems as required by GE Energy Engineering. However, following the initial shroud rig tests, to be described in Section 3.7.1, the material selection was narrowed down to only slurry cast and prepreg MI type CMCs. Unfortunately sufficient material property data did not exist at that time for

slurry cast MI composites made with Hi-Nicalon™ fiber to allow for more detailed shroud design efforts.

Earlier in the program we had allowed for database generation of both monofilament and Hi-Nicalon™ reinforced prepreg MI composites. The monofilament system was dropped from the program, however, due to persistent oxidation resistance problems, as discussed in Section 3.2.1. The resources allotted for database measurements on the monofilament system under program Task 3.2.b were therefore re-directed to making similar composite property measurements on the slurry cast MI system as supplied by Goodrich Aerospace and DuPont-Lanxide Composites. There were insufficient resources to test material from both vendors, so material from Goodrich Aerospace was chosen for characterization because there was less available material property data available from that vendor than from DuPont-Lanxide.

3.4.1 Mechanical Characterization of Goodrich Slurry Cast CMC

Testing of the Goodrich Hi-Nicalon / slurry cast MI composite was overseen by the Materials and Process Engineering (M&PE) division of GE Energy. The CMC material itself consisted of Hi-Nicalon fiber in the form of a balanced 5 harness satin weave 2-D fabric, a BN interface coating, and a SiC/Si matrix formed by chemical vapor infiltration of SiC followed by slurry casting of particulate SiC into remaining pores and final melt infiltration with silicon. The test samples were machined by Goodrich and then a 5μm seal coat of CVD SiC was applied, effectively sealing over any exposed fibers or fiber coatings. The total fiber volume fraction was between 30 and 40%, and the testing direction for all tests was parallel to one of the fiber directions in the cloth. The actual tensile, creep rupture and fatigue measurements were done by Composite Testing and Analysis, LLC in Ann Arbor, MI. The high thermal gradient testing ("jet engine thermal shock", or JETS test) was performed at Materials Characterization Laboratory in Scotia, NY.

3.4.1.1 Fast Fracture Tests

Monotonic tensile tests were conducted in air at RT, 871°C (1600°F), 982°C (1800°F), 1093°C (2000°F), and 1204°C (2200°F), with two samples tested at each temperature. Face-loaded specimens were used with an overall length of 152mm, overall width of 12.7mm, nominal thickness of 3.5mm, gage section length of 38.1mm and gage section width of 7.6mm. Tensile testing was performed on an MTS Model 810 servo-hydraulic load frame using a 10kN load cell and mechanical face-loading "cold" grips. Strain in the gage section was measured using a water-cooled contact extensometer with a 30mm gage length. Specimens were heated in a two-zone, four element furnace with a hot zone height of 80mm. The temperature gradient within the 30mm specimen gage length ranged from 12°C at 871°C to 8°C at 1204°C. During testing the specimens were loaded into the test frame and then heated to the desired test temperature within 30 minutes, followed by a 15 minute equilibration prior to testing. A loading rate of 20MPa/s was used, which gave failure times between 10s and 20s depending on the specimen strength. An 18-bit, 50 Hz data acquisition system was used to gather the load cell and extensometer data.

A summary of the tensile test results is provided in Table 3-12. Individual stress-strain curves are shown in Figure 3-59. The initial elastic modulus in Table 3-12 was calculated from the slope of the stress-strain curves between stresses of 5 and 50MPa. The trends of the properties listed in Table 3-12 with test temperature are shown more clearly in Figure 3-60. Overall the fast fracture tensile properties were found to be relatively insensitive to test temperature up to 1204°C.

Table 3-12. Summary of Tensile Test Results on Goodrich Slurry Cast MI Composites with Hi-Nicalon™ Fiber

Specimen ID	Test Temperature (°C)	Initial Modulus (GPa)	Proportional Limit Stress (MPa)	Ultimate Strength (MPa)	Strain to Failure (%)
T6	RT	238	118	273	0.66
T7	RT	231	113	290	0.67
T8	871	205	152	341	0.97
T9	871	196	117	321	0.68
T10	982	228	132	378	1.22
T11	982	213	112	220	0.44
T12	1093	181	136	265	0.68
T13	1093	202	125	280	0.80
T14	1204	203	105	271	0.81
T15	1204	183	94	276	0.72

3.4.1.2 Fatigue Testing

The low cycle fatigue (LCF) and high cycle fatigue (HCF) behavior of the Goodrich slurry cast MI CMC was determined in air at temperatures of 1093°C (2000°F) and 1204°C (2200°F). The LCF tests were performed at a loading frequency of 0.33Hz and the HCF tests at a 30Hz frequency, both at a stress ratio, or R ratio, of 0.01. Testing was done using an edge-loaded configuration using Inconel 718 hot grips. The test specimens were nominally 112mm long and 3.5mm thick. The sample gage sections were nominally 33mm in length and 6.3mm wide, with 8° angles on the side edges that were loaded by the grips.

A water-cooled extensometer was used to measure the gage section strain in the LCF tests; however, strain could not be measured during HCF testing due to vibration of the extensometer. All testing was done in an MTS Model 810 servo-hydraulic load frame using a 10kN load cell. The test specimens were heated using a two-zone furnace with a 50mm long hot zone, giving a maximum gradient in the specimen gage section of 15°C. Specimens under test were heated to the desired test temperature within 30 minutes and then held at temperature for 15 minutes prior to starting the test. Fatigue run-out was defined as >111,111 cycles (92.6 hours) for LCF testing and as $>10^7$ cycles (92.6 hours) for HCF.

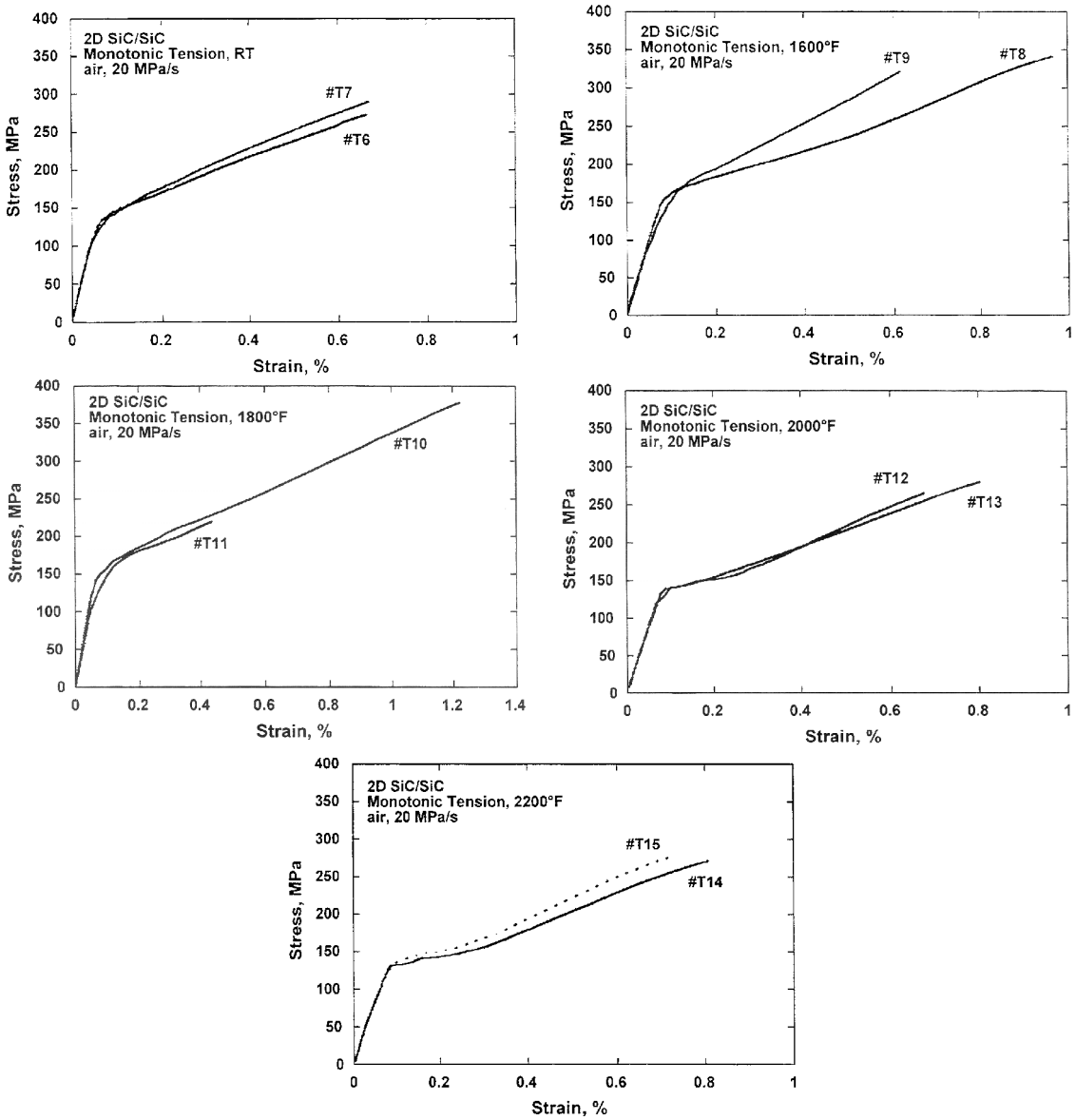

Figure 3-59. Tensile stress-strain plots for Goodrich slurry cast MI composite database samples as measured by GE Energy.

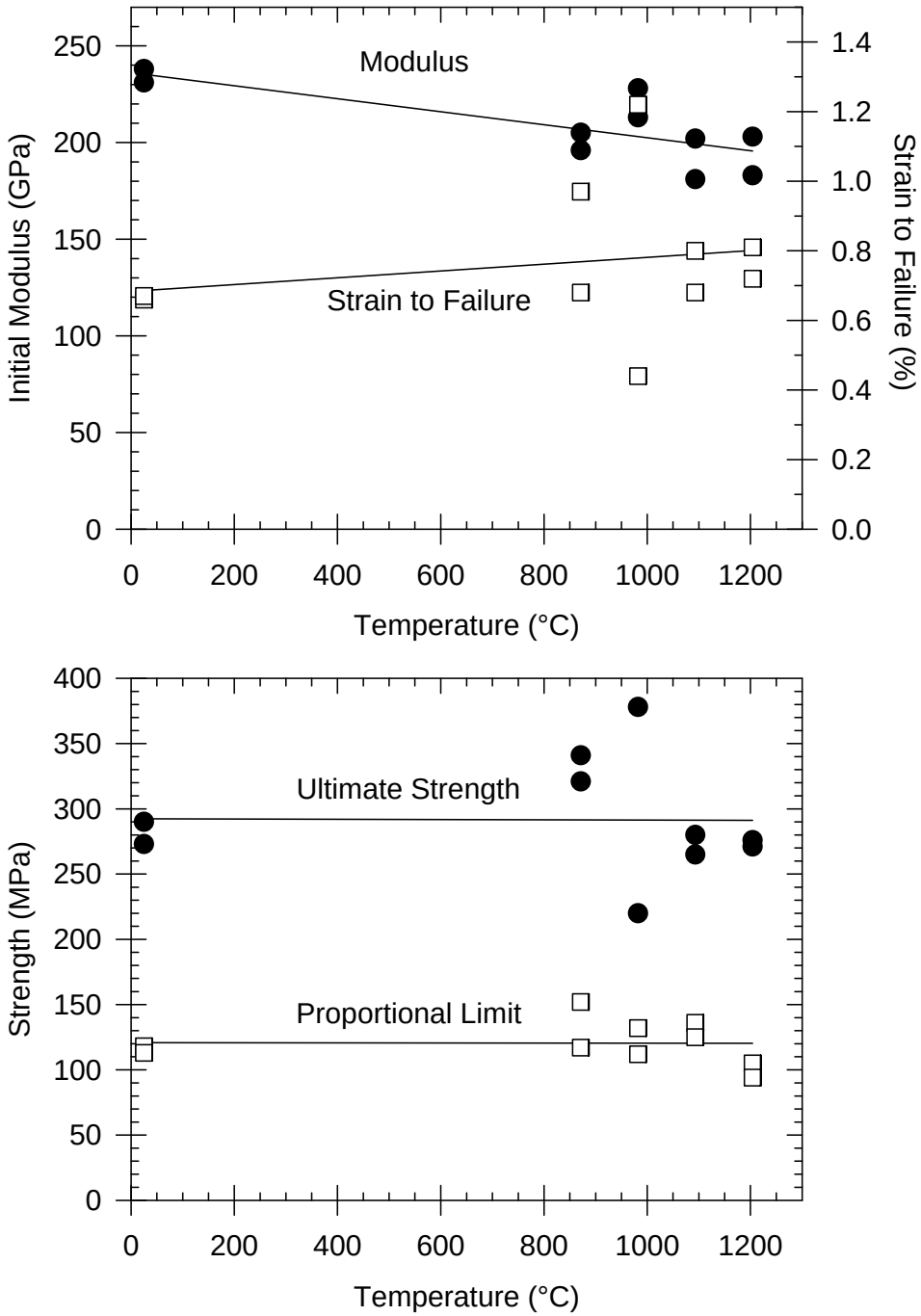

Figure 3-60. Temperature dependence of the fast fracture tensile properties of Goodrich slurry cast MI composite as measured by GE Energy.

The LCF test results are listed in Table 3-13, and those for the HCF tests in Table 3-14. Stress-cycle (S-N) curves for the LCF and HCF results, relating the fatigue to maximum stress, are shown in Figures 3-61 and 3-62, respectively.

Table 3-13. Low Cycle Fatigue Testing Results for Goodrich Slurry Cast MI Composite Samples Tested in Air, 0.33Hz, R=0.01.

Sample ID	Test Temperature (°C)	Maximum Stress (MPa)	Cycles to Failure	Time to Failure (h)
LCF-7	1093	100	>111,111	>92.6
LCF-14	1093	110	18,948	15.95
LCF-8	1093	120	4351	3.66
LCF-10	1093	130	628	0.53
LCF-9	1093	140	751	0.63
LCF-1	1093	165	252	0.21
LCF-15	1093	175	14	0.012
LCF-2	1204	100	>111,111	>92.6
LCF-13	1204	110	10,933	9.20
LCF-3	1204	120	4,402	3.71
LCF-12	1204	130	5,520	4.65
LCF-4	1204	140	905	0.76
LCF-11	1204	160	471	0.40
LCF-16	1204	175	98	0.08

Table 3-14. High Cycle Fatigue Testing Results for Goodrich Slurry Cast MI Composite Samples Tested in Air, 30Hz, R=0.01.

Sample ID	Test Temperature (°C)	Maximum Stress (MPa)	Cycles to Failure	Time to Failure (h)
HCF-17	1093	70	$>10^7$	>92.6
HCF-5	1093	70	922,828	8.54
HCF-9	1093	80	$>10^7$	>92.6
HCF-4	1093	100	408,694	3.78
HCF-3	1093	110	129,212	1.20
HCF-2	1093	120	51,155	0.47
HCF-1	1093	140	33,337	0.31
HCF-7	1204	70	$>10^7$	>92.6
HCF-8	1204	70	$>10^7$	>92.6
HCF-19	1204	80	$>10^7$	>92.6
HCF-15	1204	100	2,100,815	19.45
HCF-16	1204	110	95,474	0.88
HCF-10	1204	120	48,942	0.45
HCF-18	1204	140	15,550	0.14

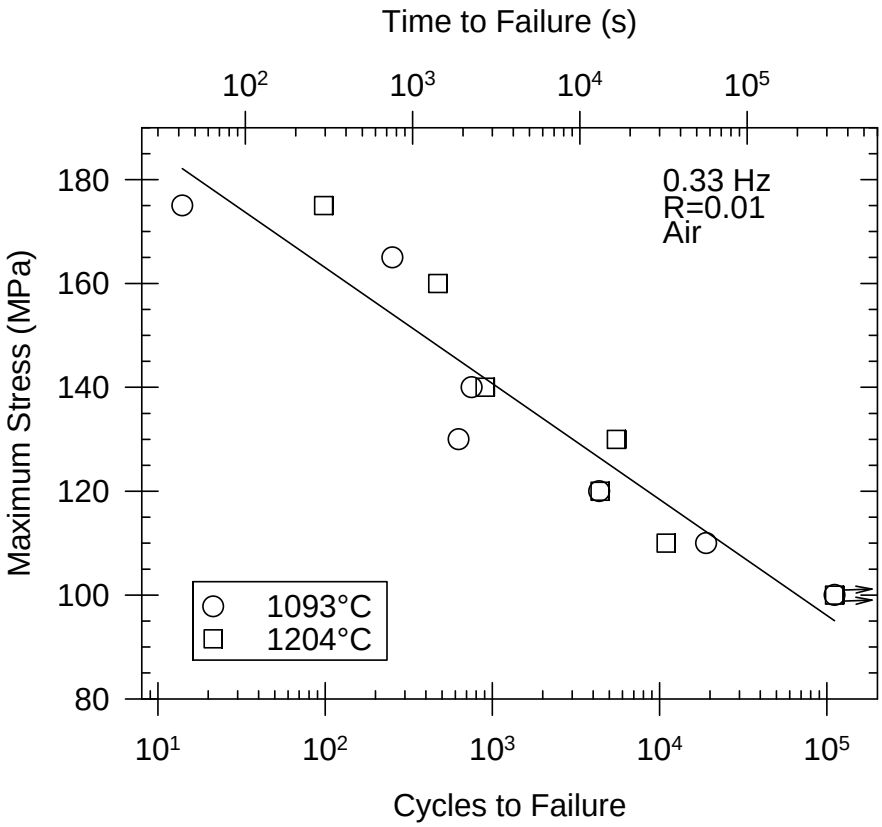

Figure 3-61. Low cycle fatigue response for Goodrich slurry cast MI composites with Hi-Nicalon fiber.

Examination of the fatigue data shows no clear sign of a fatigue limit stress below which fatigue failure would not occur. Within the temperature range tested there was no discernible effect of test temperature on fatigue life. Comparing the failure times for HCF and LCF at the same stress level shows that the higher loading frequency used for the HCF tests was detrimental to fatigue life. For example, at a maximum fatigue stress of 120MPa the time-to-failure under LCF, as calculated from the regression line, was 7.1 hours whereas for HCF the time-to-failure was only 0.60 hours.

Another important observation can be made by comparing the maximum cyclic fatigue stress to the proportional limit stress obtained in the monotonic tensile tests. At 1093°C the proportional limit averaged 130MPa; however, both LCF and HCF failures were noted at 1093°C at stresses below this value. Consequently the proportional limit stress cannot be used as an indicator of a fatigue limit stress for this material.

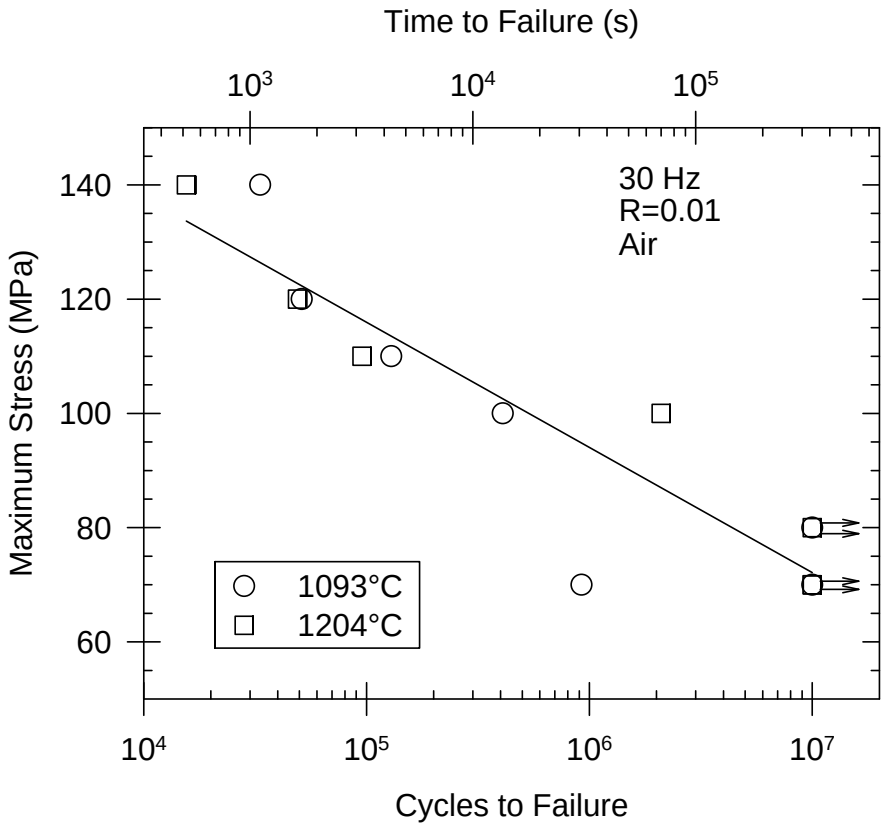

Figure 3-62. High cycle fatigue response for Goodrich slurry cast MI composites with Hi-Nicalon fiber.

3.4.1.3 Creep Testing

The in-plane tensile creep behavior of the seal-coated Goodrich slurry cast MI composite with Hi-Nicalon™ fiber was evaluated in air at 1093° and 1204°C. Face-loaded specimens with an overall length of 190mm, nominal thickness of 3.5mm, and gage section of 40mm length and 8mm width were utilized. The creep tests were performed on a CTA Model 2000 creep frame, which was equipped with mechanical face-loaded grips and a 9kN load cell. A water cooled extensometer with a gage length of 35mm was used to determine the gage section strain. Specimen heating was done using a two-zone furnace with a hot-zone length of 65mm, and the maximum temperature gradient within the 35mm gage length was 11°C. Specimens were mounted in the load frame and then heated under nominal load to the desired test temperature within 30 minutes. The samples were then held at temperature for 30 minutes prior to the start of a test. The dead-loads used for the creep tests were applied in about 10s time using a pneumatically controlled weight table. The specimens were then held under load until failure, or for a maximum duration of 250 or 1000h.

A summary of the creep test results is given in Table 3-15. The creep strain versus time behavior showed a continuously decreasing creep rate with time for all conditions measured, and consequently the creep rates listed are applicable only for the creep times

listed. The total strains at rupture were all lower than the fast fracture strain to failure at the same temperature.

A plot of creep stress versus rupture time is shown in Figure 3-63. Creep rupture times were relatively insensitive to test temperature. The data do not suggest the existence of a creep rupture stress limit for the range of stresses and creep times investigated.

Table 3-15. Summary of Creep Test Results on Goodrich Slurry Cast MI Composites Made With Hi-Nicalon™ Fiber.

Specimen ID	Test Temperature (°C)	Stress (MPa)	Time to Failure (h)	Strain at Failure* (%)	Measured Creep Rate (s^{-1})
68-HN-11-10	1093	110	>1000	>0.17	$5.6x10^{-11}$ @ 1000h
68-HN-11-14	1093	110	>250		$6.9x10^{-11}$ @ 250h
68-HN-11-7	1093	125	91.1	0.21	
68-HN-11-9	1093	125	140.6	0.20	$5.0x10^{-11}$ @ 100h
68-HN-11-6	1093	150	0.021	0.24	
68-HN-11-5	1093	165	0.040	0.44	
68-HN-11-13	1204	110	>1000	>0.59	$5.5x10^{-10}$ @ 1000h
68-HN-11-11	1204	110	>250	>0.39	$1.8x10^{-9}$ @ 250h
68-HN-11-8	1204	120	183.1	0.51	$3.9x10^{-9}$ @ 100h
68-HN-11-3	1204	125	113.8	0.46	$3.6x10^{-9}$ @ 100h
68-HN-11-12	1204	140	0.74	0.53	
68-HN-11-4	1204	140	1.21	0.21	
68-HN-11-2	1204	150	0.0006	0.16	

* includes both elastic and creep strain

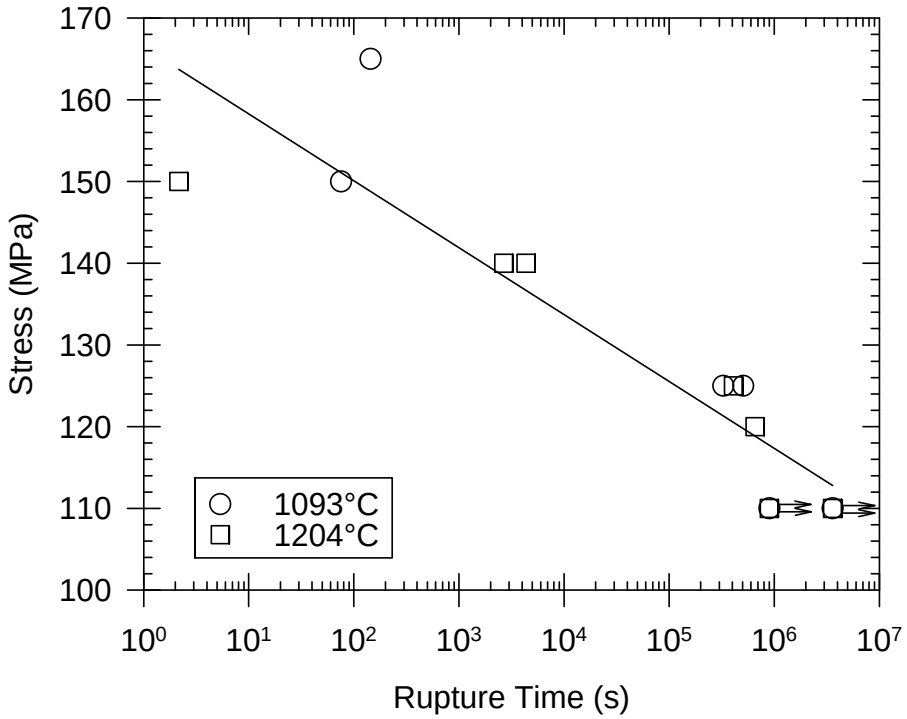

Figure 3-63. Creep rupture response of Goodrich slurry cast MI composites with Hi-Nicalon fiber, measured in air.

3.4.1.4 JETS Testing

JETS testing consisted of a series of thermal gradient (TG) and thermal fatigue (TF) tests. The purpose of this test program was to expose the CMC to an aggressive, high temperature environment on a cyclic time basis. Test specimens were cut from supplied CMC plates into 25mm x 50mm coupons, and therefore did not have CVD SiC seal coatings. Specimen testing was done at the Material Characterization Lab using unique, GE-designed test equipment. The samples were first fitted into metallic sample holders, which were mounted onto a specimen carousel. The carousel holds up to eight samples, and rotates in steps by 45 degrees to move the samples from station to station. The stations can be independently equipped to either heat the sample with a natural gas flame torch, rapidly cool the sample with a forced air jet, or as idle stations where the samples can cool at ambient conditions. At the heating station cool air can also be directed at the back of the specimens to induce through-thickness gradients if desired. The front side sample temperatures in the heating stations were monitored with IR cameras and the flame intensity adjusted to give a maximum sample temperature in the heating stage of roughly 1200°C. Sample back side temperatures in the heating stage were monitored using a two-color pyrometer.

In the thermal gradient test eight samples were mounted in the test machine with a rotation cycle every 120 seconds. At the first station the sample was heated to a nominal front face

temperature of 1200°C. A cool air jet on the back face of the samples kept the backside temperature to about 1025°C at the end of the 120 second heating stage. Stages 2, 3 and 4 were idle stations with only ambient cooling. Stations 5 through 8 repeated the sequence, giving two 8-minute heating/cooling cycles per complete rotation of the carousel. Samples were exposed in the tester for a total of 2000 thermal cycles with inspections at every 500 cycle interval. At each inspection 2 samples were pulled from the test. Post-test characterization was limited to visual examination for the presence of cracks or other damage.

The results of the thermal gradient test are given in Table 3-16. Overall the thermal gradient test showed cracking in all of the Goodrich slurry cast MI composite samples. Cracking at 500 cycles was just as severe as the cracking observed with additional cycles, suggesting that crack growth had ceased before the 500 cycle point. None of the specimens failed completely into multiple pieces.

Thermal fatigue testing was also done in the JETS tester, but with somewhat different exposure conditions. In this test samples were only held at each station for 20 seconds. The first station was again a heating station with a natural gas torch flame that reached a maximum front face temperature of about 1200°C. No back side cooling was applied at this station and the back face temperature climbed to a maximum of about 1080°C during the 20 second exposure. Station two was a 20 second forced air cooling, and stations 3 and 4 were idle stations with cooling at ambient conditions. Stations 5 through 8 repeated this cycle. All samples were run through a total of 2000 thermal cycles.

Table 3-16. Summary of the Thermal Gradient JETS Testing results on Goodrich Slurry Cast MI Composites with Hi-Nicalon Fiber.

Specimen ID	Sample Position	Cycles Completed	General Observations
9	1	1500	10mm crack at center top of specimen
10	2	1000	7mm crack at center bottom
11	3	1000	7mm crack at center bottom
12	4	2000	6mm crack at center bottom and top
13	5	1500	11mm crack at center bottom
14	6	500	7mm crack at center bottom
15	7	500	multiple 11mm cracks in center
16	8	2000	5mm to 12mm crack at center bottom

Damage in the thermal fatigue test was less than that found in the thermal gradient test. All of the samples had a similar appearance after exposure with some slight damage, or crack initiation, on the edges of the front faces.

3.4.2 Database of GE Composite with ACC Fiber Coating

At various stages of the program it became necessary to generate a CMC property database for the prepreg system. Such a material property database was needed to support ongoing component design efforts related to the shroud and combustor liner components. Accurate thermo-physical properties are needed as inputs to the finite element modeling (FEM) codes, and strength data were needed to define the allowable stress limits for components. Any time a major material or process change was made to the CMC system it became necessary to re-establish the property database. Also, as the component design process was maturing additional needs for property measurements beyond the existing databases were identified, both in terms of new measurements and in terms of more numerous measurements in order to assess statistical variation of the properties. Consequently the prepreg MI composite material database was established three times during the course of the program. The work required to generate such databases, including specimen fabrication and testing, fell under program Tasks 3.2.a Process/Material Optimization, and 3.2.b Composite Property Measurement.

It should be noted that since the various database measurement efforts (summarized in Sections 3.4.2 and 3.4.3) fell over an extended period of time that there were inherent differences in the composite samples used for the different sets of measurements. Some of these differences were caused by incremental improvements in the fiber coating and composite fabrication processes with time; however, a major contributor to composite property changes with time was the changes in fiber production lots. Composite ultimate strengths would undoubtedly be affected by changes in fiber strength properties, but the "processability" of the fibers were also observed to change from lot to lot, which would indirectly influence the properties of the composites by affecting the amount of processing defects present. All testing described in report Section 3.4.2 was performed on samples fabricated in early 1997.

3.4.2.1 Mechanical Fracture Measurements

The first GEGR prepreg MI composite database, completed in the Summer and Fall of 1997, included mechanical and thermophysical characterization of composite test samples made with Hi-Nicalon fiber with the standard configuration A fiber coating system from ACC. Samples were fabricated using three matrix compositions: the standard (HGS) matrix, a B-doped composition, and a "low modulus" composition (accomplished by having a lower SiC and higher Si content in the matrix). All test samples were fabricated as 8-ply, [0-90-90-0]s balanced lay-ups, with a nominal panel thickness of 2.3mm and nominal fiber volume fraction of 0.23. The measurements that were performed included in-plane tensile fast fracture behavior of the as-fabricated composites, tensile fracture of samples after air oxidation exposures for times up to 2000 hours, tensile fracture of pre-cracked and oxidized samples, tensile fracture of samples oxidized under stress, interlaminar tensile (ILT) strength, interlaminar shear (ILS) strength, and through-thickness thermal diffusivity.

All in-plane tensile testing for this database was done at GEGR using an Instron 1362 servo-mechanical load frame with upgraded model 8500 electronic controls. The tensile

bars were face-load gripped using MTS model 647.02 hydraulic grips. Sample strain was monitored using an Instron model A735.128 capacitive extensometer with 25mm gage length. The test samples were nominally 152mm in length and 12.7mm in width with a 38mm long by 7.6mm wide gage section. Elevated temperature tensile tests were done in air using a home-built single zone induction furnace with a 38mm hot zone and Type S thermocouple for temperature monitoring and control. The procedure for high temperature testing was to grip the sample in the testing machine, apply a nominal load of 9-13N, and then heat the furnace and test sample to the desired temperature within 10 minutes while under load control. The sample was allowed to equilibrate for 10 minutes at the test temperature, at which time the tester was switched to displacement control and the tensile test performed. All tensile tests were conducted at a machine displacement rate of 0.38mm/min, corresponding to an initial strain rate of roughly $4x10^{-5}s^{-1}$.

The pre-cracked oxidation tests were similar to those described previously in Section 3.2.1.6. The test bars are first strained at room temperature to nominally 0.2%, which is well above the matrix cracking strain of 0.05-0.07%, thus introducing multiple matrix cracks in the bars. The samples were then exposed in air for 100 hours at 1204°C without any mechanical load. Following oxidation the samples were then tensile tested to failure at room temperature. The goal of this test is to determine the susceptibility of the fiber-matrix interfaces to oxidative embrittlement in the presence of matrix cracks.

The stressed oxidation tests were similar to the pre-cracked oxidation test, except that the test samples were held under a tensile stress during oxidation. Samples were first loaded into the test machine and heated up to 1204°C. They were then pre-cracked to 0.2% strain, at which point the load was reduced to the desired stress level and the samples held under constant stress for 100 hours. At the conclusion of the 100 hour oxidation exposure the constant load was reduced to zero and the samples were tensile tested to failure at 1204°C.

The interlaminar tension and interlaminar shear tests were performed at Cincinnati Testing Laboratory (CTL). Epoxy-bonded button samples 25mm in diameter were used for the interlaminar tension tests, and were limited to room temperature due to the epoxy adhesive. Interlaminar shear tests used a double-notched compression specimen (ASTM C1292-00), and were performed both at room temperature and at 1093°C.

Results of the various mechanical tests are summarized in Table 3-17. Examples of RT and elevated temperature stress-strain curves for each of the three matrix compositions are shown in Figures 3-64 through 3-66. The trends in the tensile fracture parameters with test temperature are shown more clearly in Figure 3-67.

Table 3-17. Summary of Mechanical Properties From the First 1997 Prepreg MI Composite Database Measured on Hi-Nicalon Reinforced, GEGR Prepreg MI Composites Made with Configuration A Fiber Coatings from Advanced Ceramics Corp.

Matrix	Test	Number of Samples	Initial Modulus (GPa)	Proportional Limit (MPa)	Ultimate Strength (MPa)	Ultimate Strain (%)
Standard	RT tensile	5	247	154	272	0.95
	871ºC tensile	1	229	170	291	0.82
	1093ºC tensile	2	218	164	220	0.70
	1204ºC tensile	1	191	183	241	0.55
	RT tensile after 100hrs at 1204ºC	1	(313)*	137	248	0.90
	RT tensile after 500hrs at 1204ºC	1	234	(87)*	247	1.05
	RT tensile after 2000hrs at 1204ºC	1	233	134	228	0.99
	Precracked oxidation§	2	207	109	232	1.11
	Stressed oxidation‡	1	185	92	122	0.08
	RT Interlaminar Tension	2			17.7	
	RT Interlaminar Shear	2			45.2	
	1093ºC Interlaminar Shear	2			55.9	
B-Doped	RT tensile	2	238	148	294	0.97
	871ºC tensile	1	219	159	286	0.89
	1093ºC tensile	2	232	179	261	0.72
	1204ºC tensile	1	197	161	209	0.52
	RT tensile after 100hrs at 1204ºC	1	216	121	259	1.00
	RT tensile after 500hrs at 1204ºC	1	226	135	254	0.92
	RT tensile after 2000hrs at 1204ºC	1	264	148	265	0.98
	Precracked oxidation§	1	221	80.7	241	1.00
	Stressed oxidation‡	1	181	150	195	0.19
	RT Interlaminar Tension	2			5.1†	
	RT Interlaminar Shear	2			55.4	
	1093ºC Interlaminar Shear	2			77.9	
Low Modulus	RT tensile	1	152	111	235	0.90
	871ºC tensile	1	155	125	254	0.86
	1093ºC tensile	1	134	143	219	0.50
	1204ºC tensile	1	134	107	223	0.64

* Values in parenthesis may be incorrect because of extensometer errors.

§ Precracked oxidation test is a room temperature tensile strength measurements following pre-cracking the specimens to 0.2% strain and then oxidizing them in air for 100 hours at 1204ºC in a lab furnace without mechanical load. The initial modulus and proportional limit stress values are low because the specimens have been previously loaded to above matrix cracking.

‡ Stressed oxidation involved heating the specimen to 1093°C, loading it to 0.2% strain, reducing the load to achieve 103MPa (15ksi) applied stress, holding at this condition for 100 hours in air, unloading the test sample and then performing a tensile fracture test while still at 1093°C. The initial modulus and proportional limit stresses measured are low because the specimens have been previously loaded to above matrix cracking.

† Interlaminar tensile specimens from the B-doped matrix material had noticeable interlaminar voids after machining which were responsible for the unexpectedly low values. Similar voids were not found in other areas of this panel, as demonstrated by the very high interlaminar shear values.

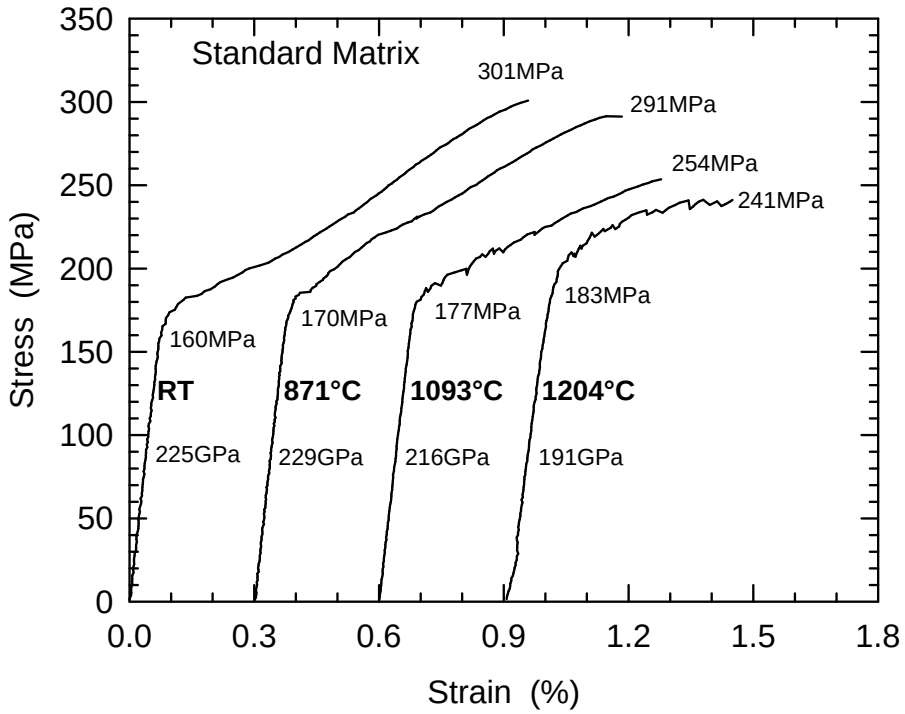

Figure 3-64. Tensile stress-strain curves for prepreg MI composites made in 1997 with standard ACC fiber coatings and the "standard" matrix composition. Numbers next to the curves list the initial modulus, proportional limit stress and ultimate strength values. Curves are offset for clarity.

The strength properties of the samples made with standard matrix or B-doped matrix compositions were essentially identical, with the exception of the ILT strengths. Inspection of the ILT test samples after testing showed the specimens with B-doped matrix had pre-existing interlaminar voids that were responsible for the low strengths observed. Other regions of this particular panel, as well as the other panels made from this composition, did not have similar defects. It is likely that the true ILT strength for the B-doped matrix samples would actually exceed the ILT strength of the standard matrix samples in the same manner as the ILS strengths. Overall ILT and ILS strengths measured were the highest we had ever witnessed at that time for any 2-D ceramic composite material.

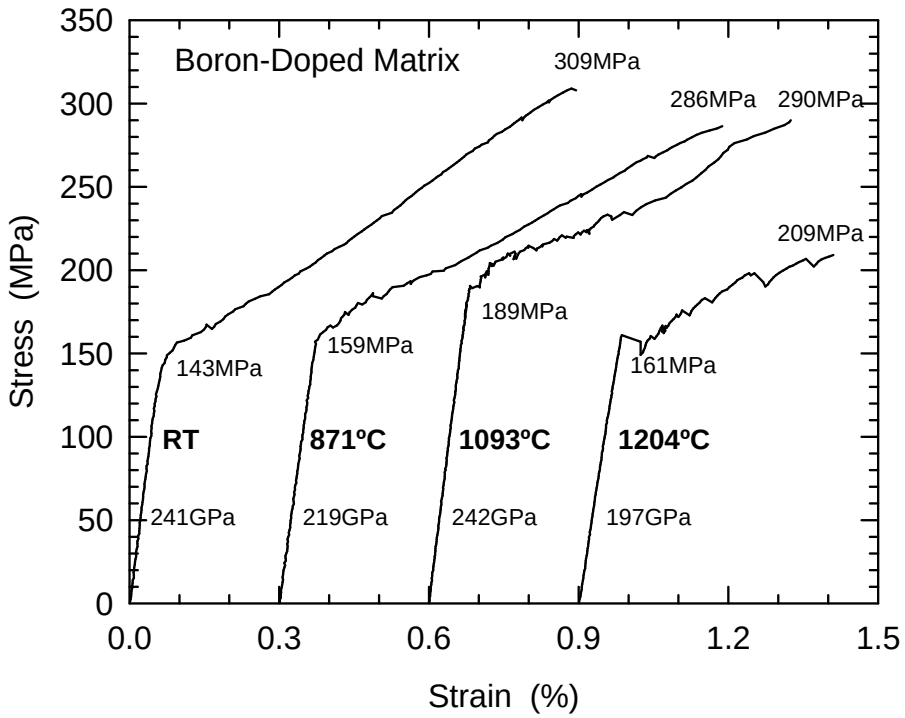

Figure 3-65. Tensile stress-strain curves for Prepreg MI composites made in 1997 with standard ACC fiber coatings and the boron-doped matrix composition. Numbers next to the curves list the initial moduli, proportional limit stresses (matrix cracking stresses) and the ultimate strengths. Curves are offset for clarity.

The intent of the "low-modulus" matrix system was to decrease the modulus of the composite while maintaining the same proportional limit stress, thereby increasing the proportional limit strain. As the majority of stress in the intended shroud and combustor applications arises from thermal gradient strains, having an increase proportional limit strain would provide an increase in the design allowables for the CMC. The matrix formulation modification used was effective in reducing the composite modulus, as shown by the data in Table 3-17; however, the proportional limit stress was also reduced for this composition. The result was that the proportional limit strain of the low-modulus matrix system was practically identical to that for the standard and B-doped matrix systems, as shown in Figure 3-67. Although it was not tested, the higher Si content of the low-modulus matrix was expected to result in reduced creep performance, and since it offered no benefit to proportional limit strain the low modulus matrix was not pursued further in the program.

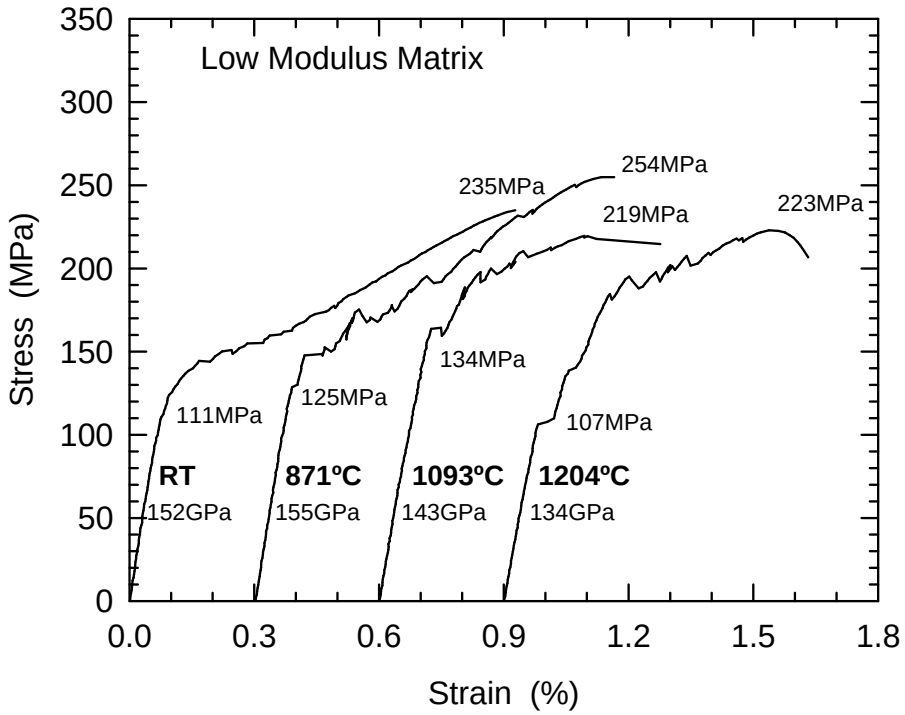

Figure 3-66. Tensile stress-strain curves for Prepreg MI composites made in 1997 with standard ACC fiber coatings and the low-modulus matrix composition. Numbers next to the curves list the initial moduli, proportional limit stresses (matrix cracking stresses) and the ultimate strengths. Curves are offset for clarity.

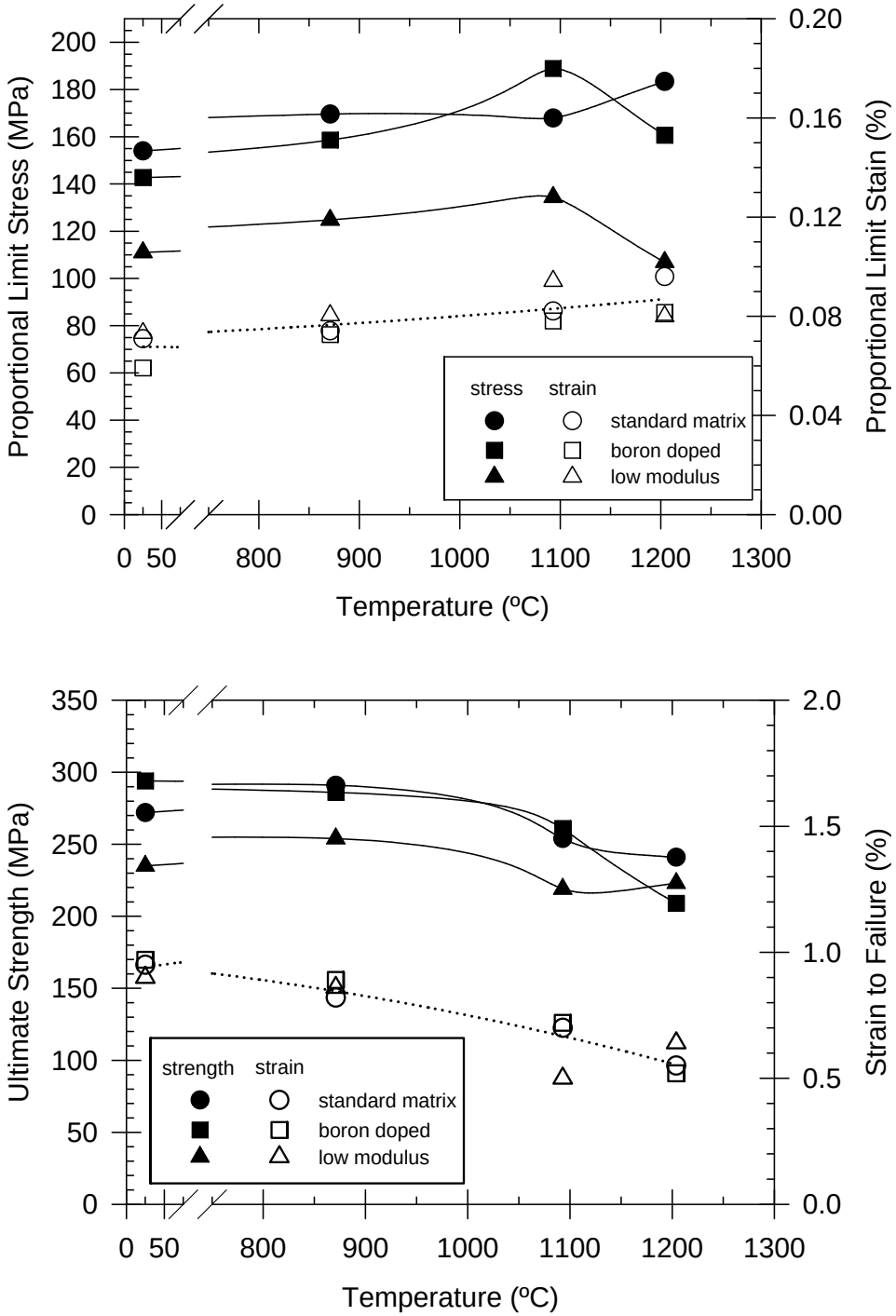

Figure 3-67. Behavior of proportional limit strength and strain (Top), and ultimate strength and strain to failure (Bottom) as a function of test temperature for the three matrix variations.

3.4.2.2 Thermal and Oxidative Stability Measurements

The thermal stability of the composites was determined by measuring the room temperature tensile fracture behavior of samples following high temperature exposure in air at 1204°C for times of 100, 500 and 2000 hours. The results of these tests are given in Figure 3-68. (This testing was not done on the low-modulus composite system.) Overall both the standard and B-doped matrix systems, when used with standard configuration A fiber coatings from ACC, gave stable composite properties for up to 2000 hours. Data for both matrix systems suggest that there may be a minor initial decrease in proportional limit strength with oxidation treatment, but this was almost entirely recovered by the 2000 hour exposure. There also appear to be an initial ~15% decrease in ultimate strength which persists after 2000 hours. All of the specimens, even after 2000 hours of oxidation, had consistently high strain to failure values, indicating that there is no tendency for the composite to become embrittled. These data very strongly suggest that the fiber, fiber coating, matrix, and interfaces between these constituents are all thermally stable at 1204°C.

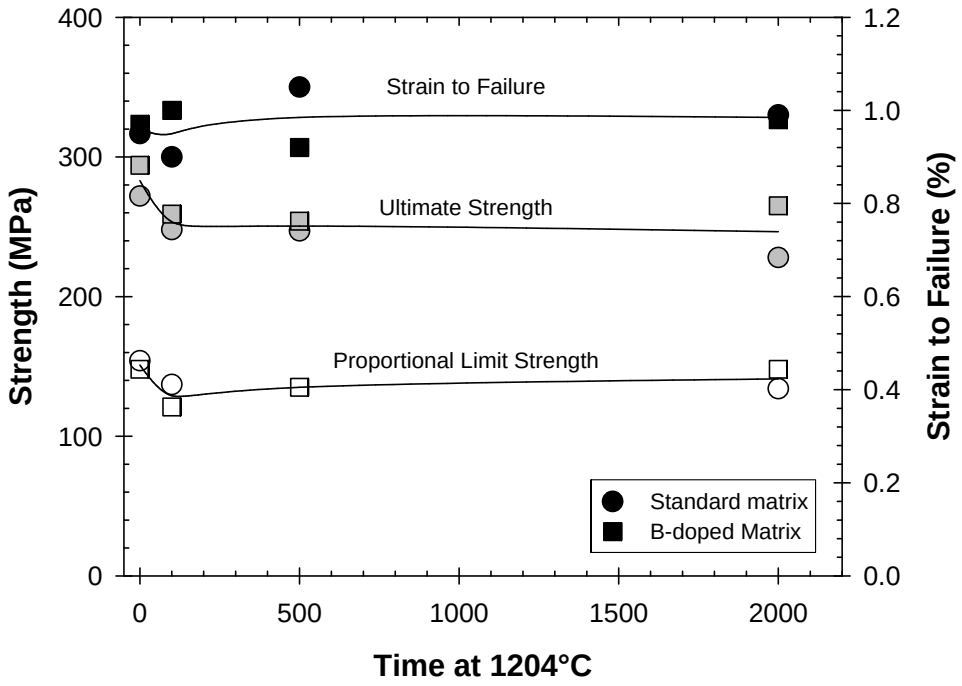

Figure 3-68. Change in tensile fracture parameters of un-cracked GEGR Prepreg MI composites made in 1997 with standard ACC fiber coatings as a function of exposure time for oxidation in air at 1204°C.

Exposure of the uncracked composites demonstrated the thermal stability of the system, but it did not test the overall oxidation resistance of the system, particularly of the fiber-matrix interface. Pre-cracked oxidation and stressed oxidation testing were performed to evaluate the oxidative stability of this interface. Surprisingly the tensile strength of the

composites were minimally affected by pre-cracking and exposing them to air at 1204°C without stress. The initial moduli and proportional limit strengths of the composites were somewhat reduced, as would be expected since the matrices had already been cracked, but ultimate strengths and strain to failure values were similar to those for samples exposed for 100 hours without matrix cracks, as shown in Figures 3-69 and 3-70. Microstructural examination after testing indicated that oxidation of the matrix along the crack surfaces had acted to effectively seal the cracks, thereby limiting any oxidative degradation of the fibers and fiber coatings.

Stressed oxidation, on the other hand, caused a very substantial degradation in composite tensile properties, as shown in the data in Table 3-17. Specimens of both the standard and B-doped matrix compositions lasted through the 100 hour thermal exposure with 103MPa applied stress. This behavior contrasts sharply with our previous results with Textron SCS-6 monofilament reinforced composites using this same matrix, as those samples typically failed in less than 30 minutes, as shown in Figure 3-71. The shorter life of the SCS-6 composites is primarily caused by oxidation of the thick carbon surface layer on the SCS-6 fibers.

After the 100 hours of exposure at 1093°C and 103MPa stress both Hi-Nicalon stressed oxidation specimens were tensile tested to failure at 1093ºC. The stress-strain curves for these composites are shown in Figure 3-72. Both composites showed significant reductions in ultimate strength and strain compared to unexposed composites, showing almost brittle behavior following the stressed oxidation exposure. Microstructural examination after testing indicated that the fiber-matrix interfaces were oxidized during exposure. The additional crack opening displacement caused by the applied stress was sufficient to prevent sealing of the matrix cracks by oxidation product, as had occurred in the pre-cracked oxidation tests. The boron-doped matrix specimen did retain slightly more strength and strain following exposure, which would normally suggest that the boron had a beneficial effect in sealing the matrix cracks via oxidation; however, since there was only one measurement for each composition a definitive conclusion can not be made.

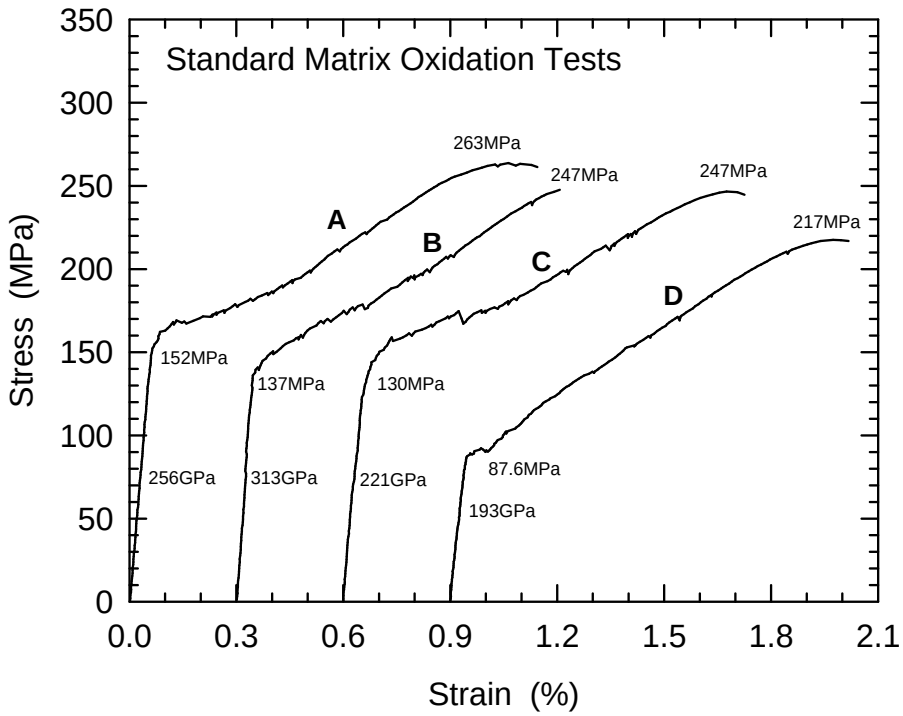

Figure 3-69. Room temperature stress-strain behavior of composite samples made in 1997 with the standard matrix composition and configuration A, ACC fiber coatings following various oxidation treatments in air at 1204ºC:
A : as fabricated (no oxidation)
B : oxidized 100 hours without pre-cracking
C : oxidized 100 hours after precracking to 0.17% strain
D : oxidized 100 hours after precracking to 0.21% strain

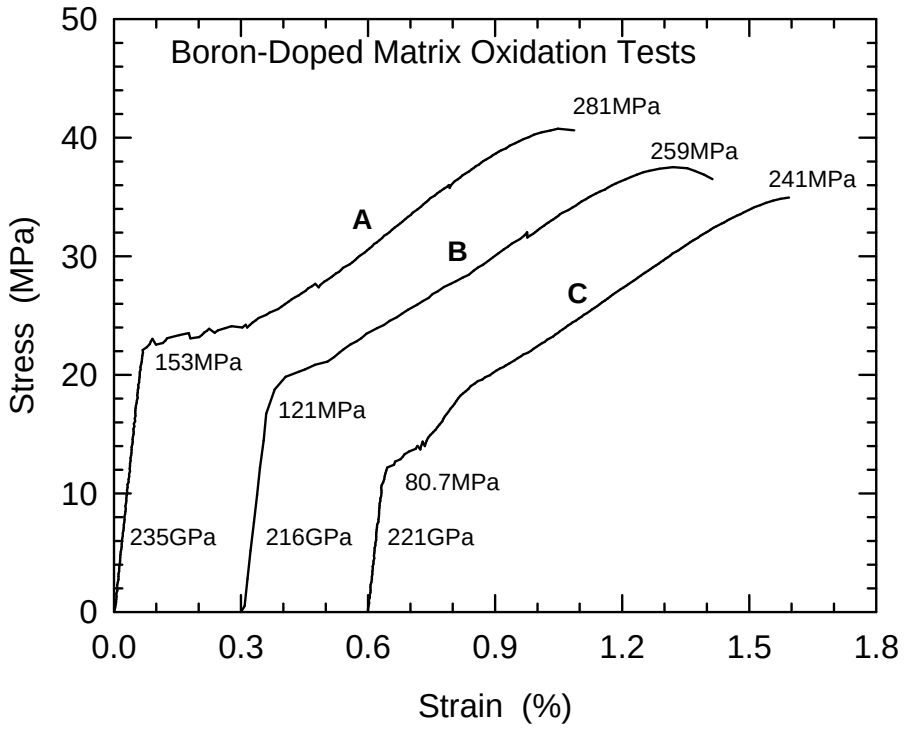

Figure 3-70. Room temperature stress-strain behavior of composite samples made in 1997 with configuration A, ACC coated fiber and with the boron-doped matrix composition following various oxidation treatments in air at 1204ºC:
A : as fabricated (no oxidation)
B : oxidized 100 hours without pre-cracking
C : oxidized 100 hours after precracking to 0.205% strain

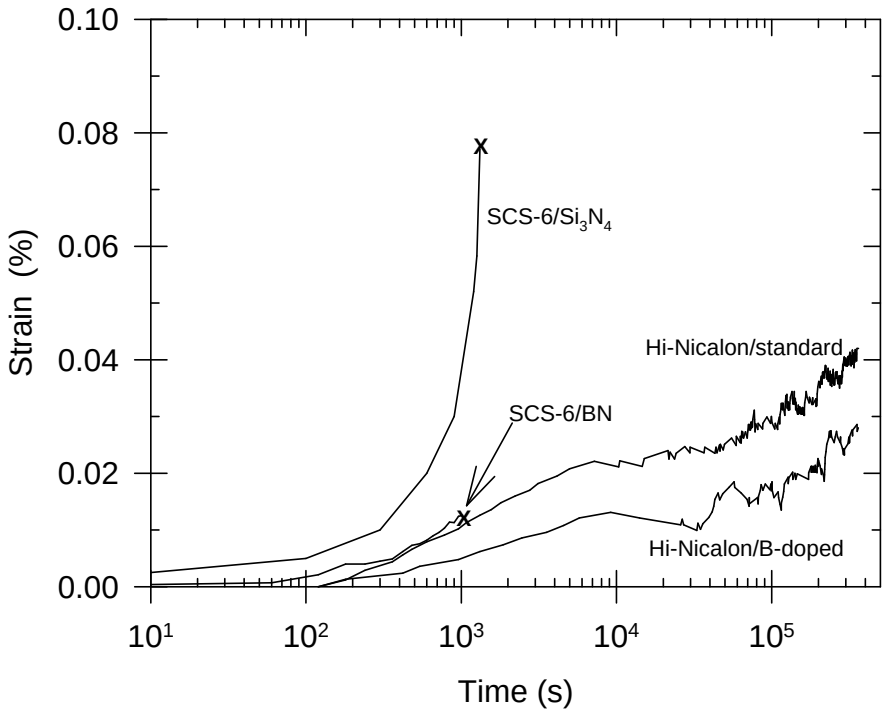

Figure 3-71. Plastic strain behavior during stressed oxidation testing for Hi-Nicalon and SCS-6 reinforced prepreg MI composites. Specimens were held at 1093ºC at 103MPa applied stress following a pre-cracking treatment to 0.2% strain. Data for SCS-6 monofilament reinforced composites is from earlier work on this program. The SCS-6 composites had either BN-based or Si_3N_4-based fiber coatings and a matrix composition identical to the "standard" composition used with the Hi-Nicalon composites. The "X" symbols mark failure of the specimens. Both Hi-Nicalon reinforced composite compositions showed run-out (survived for >100 hr.) in this test.

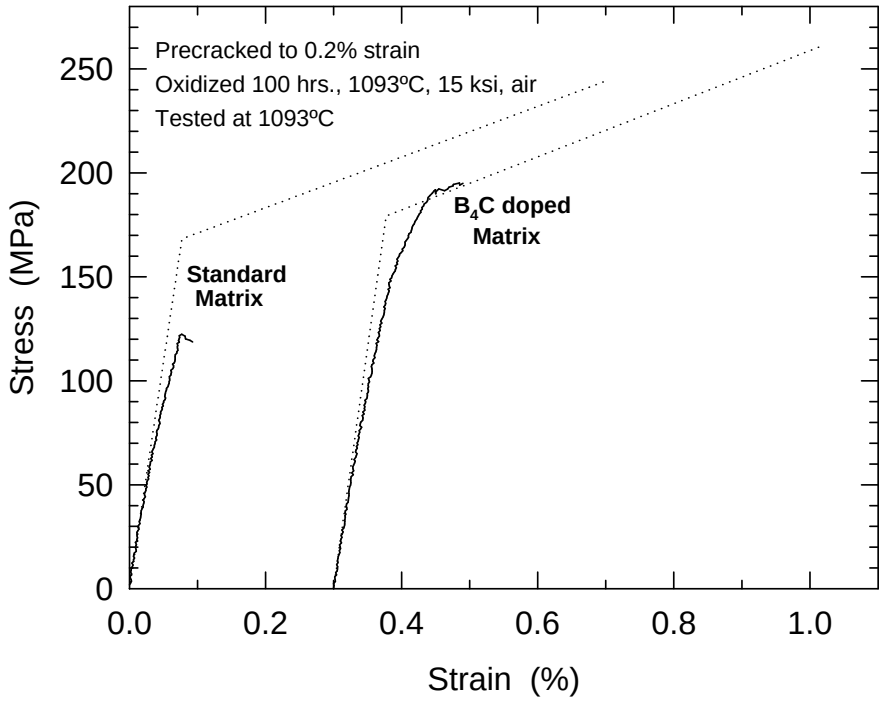

Figure 3-72. Fast fracture behavior of stressed oxidation specimens fabricated in 1997 following the 100 hour exposure at 2000ºF and 103MPa applied stress. The dotted lines show approximately the average stress-strain behavior for unexposed composites tested at the same temperature. (Curves are offset for clarity.)

3.4.2.3 Thermal Property Measurements

Through-thickness thermal diffusivity measurements were made on all three matrix composition panels by Dr. R. Dinwiddie at ORNL. Two specimens of each composition were measured and the average diffusivity values are listed in Table 3-18. Heat capacity values were calculated from standard thermodynamic references and the phase composition of the composites, and the average values for the three compositions are also listed in Table 3-19. Using the measure diffusivity, calculated heat capacity and measured density values, the corresponding thermal conductivity values were calculated. These thermal conductivity values are plotted in Figure 3-73 as a function temperature for the three matrix compositions. At 1093ºC (2000°F) the thermal conductivities of the standard and B-doped matrix compositions are above 15 W/m-K (9 Btu/hr-ft-ºF), which are among the highest values of conductivity for any CMC. The low-modulus composition composite showed appreciably lower thermal conductivity, consistent with the higher porosity content of that particular specimen.

Table 3-18. Through-Thickness Thermal Diffusivity and Calculated Heat Capacity Values for Hi-Nicalon Reinforced Prepreg MI Composites Made in 1997 With ACC Configuration A Fiber Coatings Measured by Dr. Dinwiddie at ORNL.

	Average Calculated	Thermal Diffusivity Values (cm^2/s)		
Temperature	Heat Capacity	Standard	B-doped	Low-Modulus
(ºC)	(J/K-g)	Matrix	Matrix	Matrix
25	0.74	0.144	0.146	0.109
110	0.82	0.116	0.118	0.093
210	0.91	0.099	0.101	0.076
310	0.99	0.082	0.085	0.065
410	1.05	0.074	0.075	0.060
510	1.12	0.065	0.066	0.054
700	1.20	0.055	0.057	0.044
900	1.27	0.048	0.049	0.038
1100	1.29	0.042	0.043	0.034
1200	1.29	0.038	0.039	0.030
1300	1.28	0.035	0.037	0.029

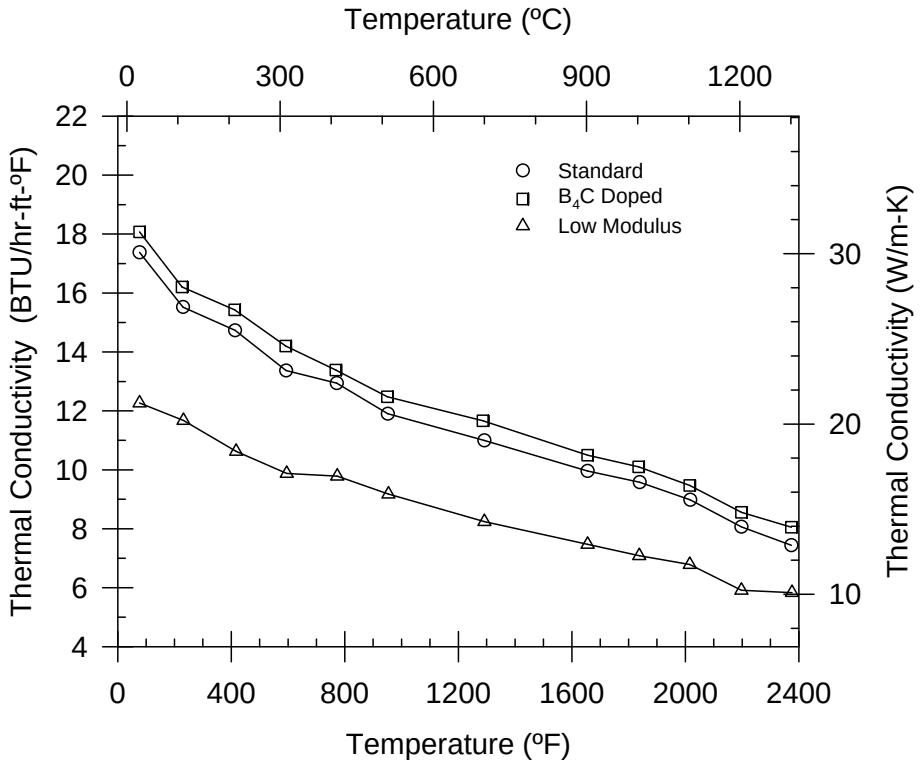

Figure 3-73. Through-thickness thermal conductivity of Hi-Nicalon reinforced GE Prepreg MI composites made in 1997 with configuration A fiber coatings and three matrix variations. Low thermal conductivity of the low-modulus composition was caused by residual porosity in this particular sample.

3.4.3 Database of GE Composite with GE-Coated Fiber

Additional characterization of GE prepreg MI composites made with ACC coated Hi-Nicalon fiber had been planned, including environmental exposures and fatigue measurements in air and steam-rich environments and testing of composites with an "enhanced oxidation resistant", i.e. containing silicon-doped BN, fiber coating. However, ACC made a business decision to discontinue their tow coating operations before the silicon-doped BN fiber coating system could be optimized. Consequently GE began tow coating operations in-house at GEGR. As the fiber coatings have a major impact on the mechanical and thermal performance of the CMC, a change in source of the fiber coatings made it necessary to re-evaluate the prepreg property database. Samples for this investigation were fabricated during the 1999-2001 time frame, all using the optimized configuration C fiber coating described in Section 3.2.2.6.2.8. Unless otherwise noted, all fiber coatings for these specimens were done in the small GEGR tow coater.

3.4.3.1 Mechanical Fracture Measurements

Sample fabrication for all of the testing described in this section occurred over a one year period and included 33 panels fabricated from 12 separate fiber coating runs. All of the panels produced for database use were screened by tensile testing a witness bar from each panel at GEGR before releasing the panels for machining and database testing. At that time, these witness samples represented the largest set of test samples for which processing was carefully controlled at nominally identical conditions and yet still included an extended period of time and number of coating runs. The witness bar tensile data thereby represented our earliest and best opportunity for determining a long-term process capability for the prepreg MI process. The tensile fracture data, including measurements made both at GEGR and at Cincinnati Test Labs (CTL), from this population of samples is given in Table 3-19.

Table 3-19. RT Tensile Fracture Data Measured on the Full Population of Panels Made for Database Testing Using GEGR Optimized Configuration C Fiber Coatings on Hi-Nicalon Fiber

	Proportional Limit Stress (MPa)	Initial Modulus (GPa)	Ultimate Strength (MPa)	Strain to Failure (%)
Mean	159.5	250.8	302.6	0.984
Standard Deviation	22.1	30.1	40.2	0.159
# of Samples	33	33	33	33

More detailed, fast fracture mechanical testing was performed at CTL, including in-plane tensile, interlaminar tensile (ILT) and interlaminar shear (ILS). The testing equipment and procedures were similar to those outlined in Section 3.4.1. The data obtained from this testing is listed in Table 3-20.

Some sample-to-sample and panel-to-panel variation of the tensile properties was noted in the testing, but the scatter was still small enough to reliably measure the effects of testing temperature or thermal exposures. Figure 3-74 shows the individual tensile stress-strain plots for the samples measured at CTL, and they clearly indicate a decreasing trend in ultimate strength and strain to failure with increasing temperature. These trends are seen more clearly in the plots of Figure 3-75. Proportional limit strength was practically unaffected by test temperature, whereas ultimate strength and initial modulus values dropped by roughly 33% and 15%, respectively, when going from room temperature to 1204°C. However, strain to failure showed the largest decrease with test temperature, falling by about 65% from RT to 1204°C.

Table 3-20. Fast Fracture Behavior for Prepreg MI Composites Made in April – June, 2001, With GEGR Coated Hi-Nicalon™ Fiber and Tested at CTL

Test	Number of Samples	Initial Modulus (GPa)	Proportional Limit (MPa)	Ultimate Strength (MPa)	Ultimate Strain (%)
RT tensile	4	285 ± 10	177 ± 15	333 ± 52	0.89 ± 0.17
816ºC tensile	4	268 ± 7	153 ± 20	276 ± 12	0.85 ± 0.09
1093ºC tensile	4	252 ± 27	167 ± 10	251 ± 11	0.60 ± 0.19
1204ºC tensile	5	243 ± 27	165 ± 18	224 ± 24	0.31 ± 0.15
1316°C tensile	4	217 ± 14	146 ± 7	226 ±17	0.31 ± 0.10
RT tensile after 200hrs at 1204ºC	2	292 ± 12	152 ± 55	343 ± 96	1.01 ± 0.26
RT tensile after 1000hrs at 1204ºC	6	252 ± 26	140 ± 23	304 ± 28	1.11 ± 0.11
RT tensile after 4000hrs at 1204ºC	4	217 ± 11	144 ± 23	265 ± 6	1.13 ± 0.15
RT in-plane compression	2			1233 ± 231	
816°C compression	2			1083 ± 276	
1204°C compression	2			> 700	
1316°C compression	2			> 693	
RT compression after 200hrs at 1204°C				1225 ± 32	
RT compression after 1000hrs at 1204°C				1225 ± 26	
RT ILT	4			39.5 ± 6.6	
RT ILS	2			135 ± 22	
815ºC ILS	2			188 ± 58	
1204°C ILS	2			124 ± 6	
1315°C ILS	2			84 ± 7	
RT ILS after 200hrs at 1204°C	2			103 ± 30	
RT ILS after 1000hrs at 1204°C	2			128 ± 43	

Values as listed represent the mean ± one standard deviation.

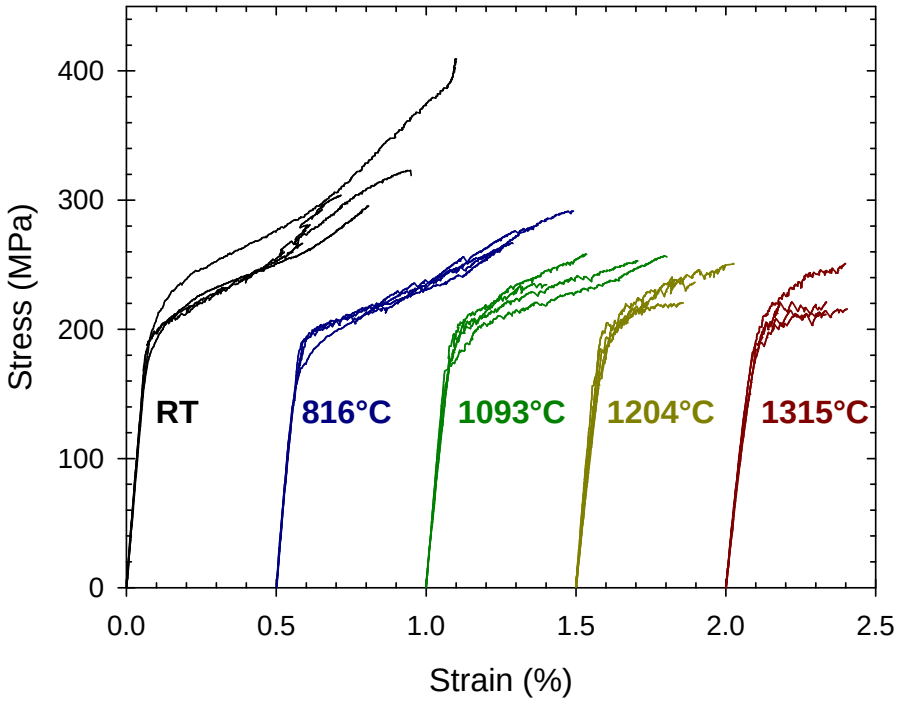

Figure 3-74. Tensile stress-strain curves for GE Prepreg MI composites made in May – June, 2001 with optimized GEGR configuration C fiber coatings and tested at CTL. Curves for the different testing temperatures are offset for clarity.

Considering the statistical scatter of both data sets, the in-plane strength values in Table 3-20 are mostly indistinguishable from those from the 1997 preliminary database with ACC coated fiber as summarized in Table 3-18. The earlier data suggested that proportional limit strength (matrix cracking stress) may increase slightly with increasing test temperature. In the new database the average room temperature proportional limit stress is slightly higher, so that the overall variation with temperature is reduced. Only the strain to failure values differ substantially between the new and old database samples. Both sets of samples have similar strain to failure at room temperature, but at high temperature (2200°F) the new samples with GEGR coated fiber show on average a 0.2% lower strain to failure than did the 1997 data, measured on samples with ACC coated fiber from their smaller reactor. Subsequent testing at GEGR found that the ultimate strength and, particularly, the strain to failure measured in high temperature tensile tests is highly dependent on strain rate. However, this effect can not explain the drop in strain to failure between the two databases as the strain rate for the tensile tests done at CTL for the 2001 database (nominally 0.0002 to 0.0003 s^{-1}) were actually higher than the strain rates used at GEGR for the 1997 database (nominally 0.00005 to 0.0001 s^{-1}), and thus should have produced higher strain to failure values for the same material.

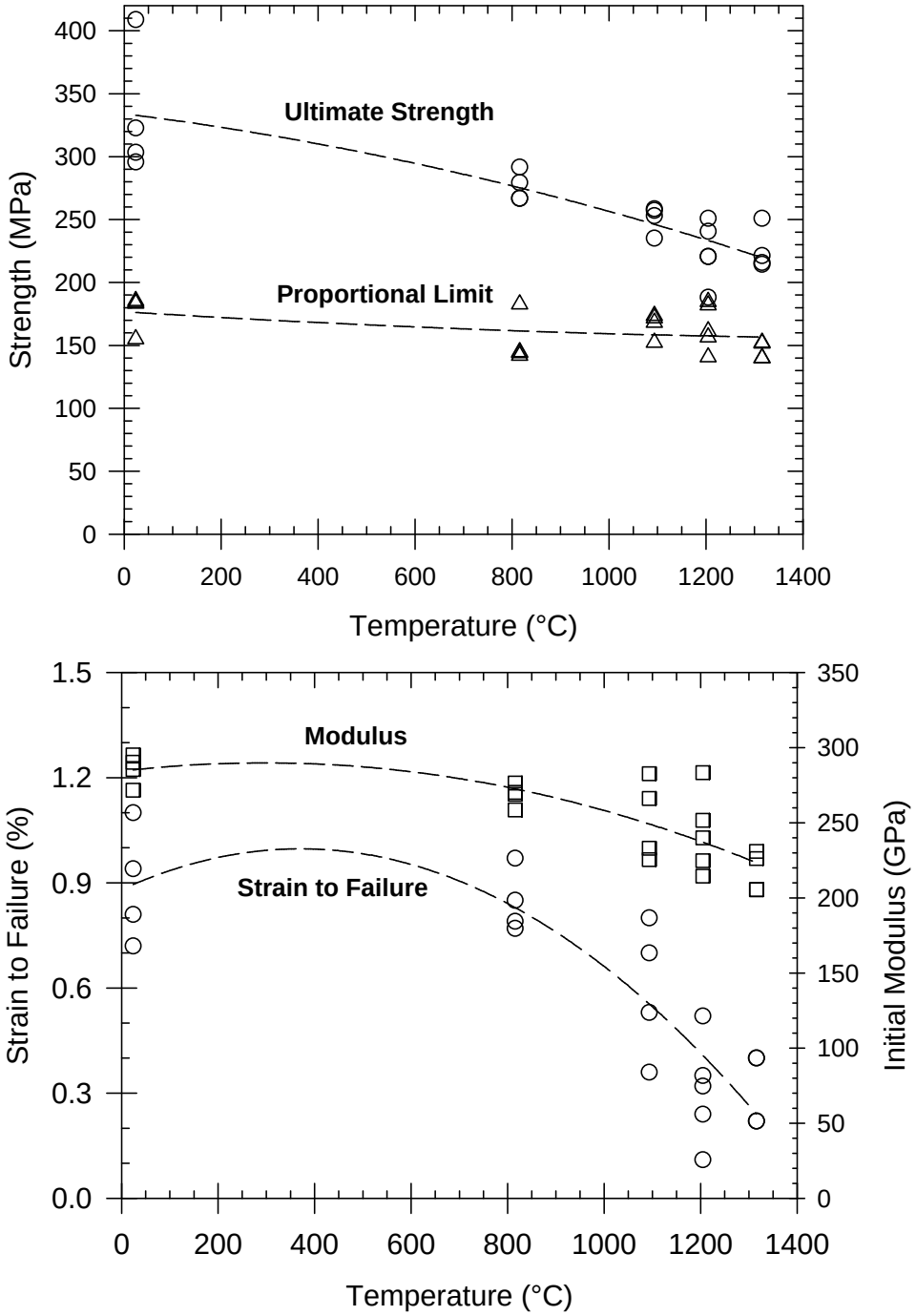

Figure 3-75. Trends of the tensile strength parameters vs. testing temperature for GE Prepreg MI composites made in May – June, 2001 with optimized GEGR configuration C fiber coatings.

In-plane compressive strengths, which were not included in prior database effort, were also measured at CTL using a sample geometry and test method consistent with ASTM D695. The new measurements indicate an average compressive strength of 1186MPa at room

temperature. Initial testing of compressive strength at 1204° and 1316°C was plagued by failures of the alumina loading fixtures before inducing failure in the CMC. The maximum load applied to the CMC specimens was therefore limited at these temperatures to levels where loading fixtures would not fail. Subsequently the true compressive fracture strength at 1204° and 1315°C was not measured, but only a lower bound for the compressive strength was determined. Room temperature compression strength measurements following thermal exposure in air for up to 1000 hours indicated no change.

While the in-plane strength data was similar to the older database, the interlaminar strengths had increased dramatically. Both interlaminar tensile and shear strengths were measured at CTL, which is the same vendor used for the 1997 database tests, and using the same test techniques. The interlaminar tensile (ILT) strength, measured on 4 samples from 2 different panels, had an average value of 39.5MPa with a standard deviation of 6.6MPa. This is more than twice the previously measured value of ILT strength from the 1997 database, and far exceeds published data for other types of CMCs, including slurry cast MI, as shown in Figure 3-76. The interlaminar shear (ILS) strength data shows a similar 2X increase over the older database samples. ILS strength as a function of temperature is shown in Figure 3-77, which shows good property retention at elevated temperatures. Even at 1315°C (2400°F) the ILS strength exceeded 80MPa.

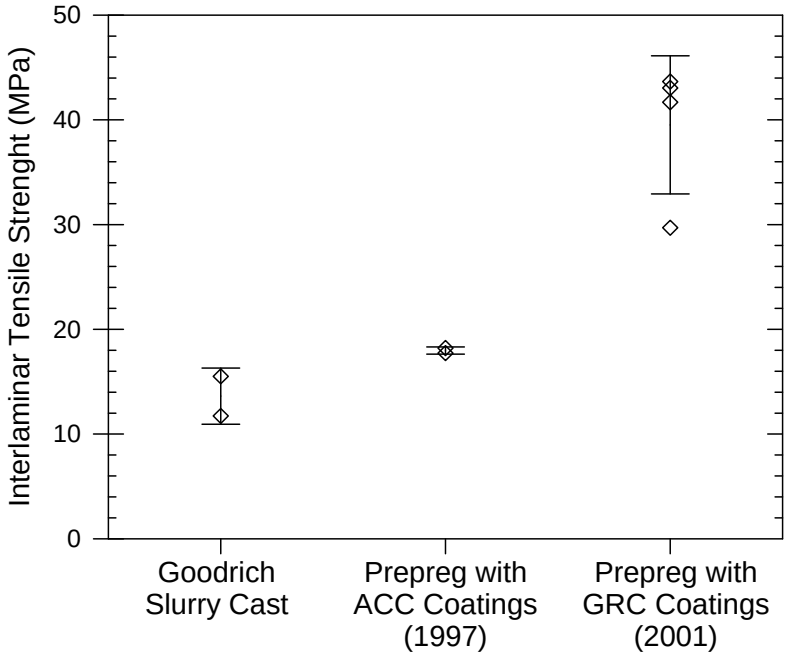

Figure 3-76. Room temperature interlaminar tensile strength for Goodrich-produced slurry cast MI composites, and for GE-produced prepreg MI composite using ACC coated fiber in 1997 and GEGR-coated fiber in 2001.

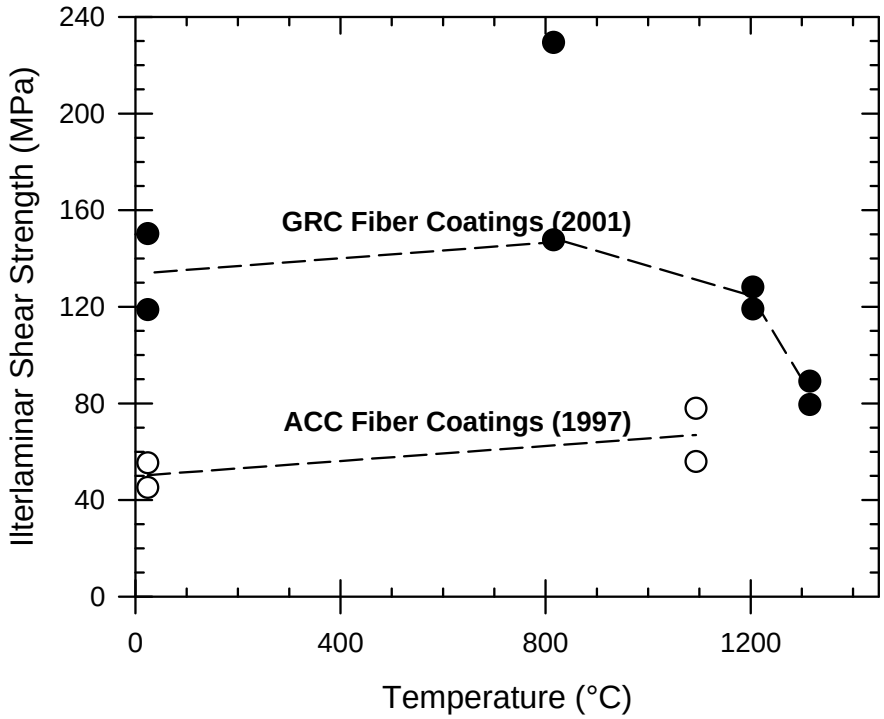

Figure 3-77. Temperature dependence of the ILS strength of prepreg MI composites made from Hi-Nicalon fiber with standard ACC configuration A fiber coatings (from 1997) and with optimized GEGR configuration C fiber coatings (from 2001).

3.4.3.2 Thermal Stability Measurements

The thermal stability of the composite system was characterized as before, by exposing test samples at 1204°C in air for extended times and then measuring the retained RT tensile strength properties. Initially the thermal exposures were done for 200 and 1000 hours and the specimens tested at CTL. The scatter in this initial data made interpretation difficult, but the data did suggest a significant decrease in proportional limit strength with exposure time. In order to determine if this was a real effect additional test samples were exposed for times up to 4000 hours and then tensile tested at GEGR. The thermal exposure data listed in Table 3-20 include both sets of specimens, and the trends in proportional limit and ultimate strengths with exposure time are also shown in Figure 3-78. The overall tends observed were a modest decrease in ultimate strength with exposure time, but practically no effect on proportional limit.

The thermal stability tests used for tensile properties were also expanded to include interlaminar and compression properties. The data in Table 3-20 indicate that ILS and compressive strengths were unaffected by exposure in air at 1204°C for times up to 1000 hours.

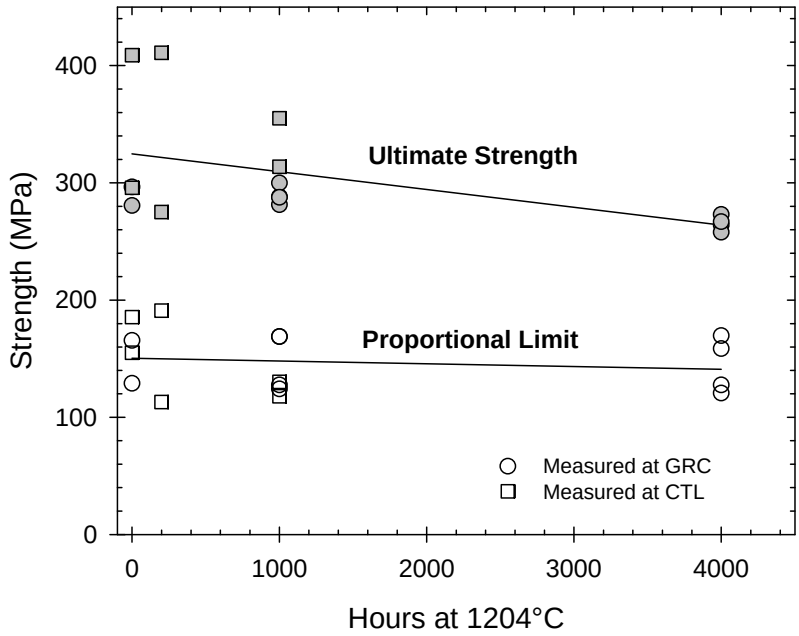

Figure 3-78. Effect of thermal exposure in air at 1204°C on the RT tensile strength of GE Prepreg MI composites made in June-July, 2001 with GEGR optimized configuration C fiber coatings on Hi-Nicalon fiber.

3.4.3.3 Low Cycle and High Cycle Fatigue Measurements

Creep, fatigue and JETS testing were not included in the 1997 database, but were performed for the 2001 database. The testing location, specimen configurations and test techniques used were identical to the creep and fatigue testing of the Goodrich slurry cast material in Sections 3.4.1.2 through 3.4.1.4.

Results from the LCF testing is given in Table 3-21, and are shown graphically in Figure 3-79. Comparing Figure 3-79 to Figure 3-61 indicates that the GE prepreg MI composite has a one to two order of magnitude increase in LCF life over the Goodrich slurry cast composite at 1204°C, with even larger differences at the lower temperatures. However, there was a significant temperature dependence of the LCF life for the prepreg MI samples, whereas the slurry cast MI samples showed no discernible difference in LCF response between 1093°C and 1204°C.

Post-test tensile strengths were measured on all of the run-out samples, and these results are summarized in Table 3-22. The first sample in each set in Table 3-22 gives the properties for a witness bar cut from the same panel in the "as-fabricated" condition. Property values given for the LCF bars show the actual measured values and the % change of the measurement relative to the same property for the as-fabricated bar from the same panel. For instance, the proportional limit for bar 734-4 is given as "186 / +21%", which means the measured value was 186MPa and that this was 21% higher than the proportional limit measured on the witness bar (154MPa). Some of the residual strength measurements were done at the LCF testing vendor, CTA, and were done at the same temperatures as the

LCF tests. Since we do not have witness coupon data at these elevated temperatures for comparison, no "% change" values are listed in Table 3-22 for these tests.

Overall the residual strengths of the LCF run-outs were quite good. The proportional limit stress either remained constant or increased for all of the test conditions examined. The ultimate strengths were relatively constant or showed some minor degradation, but even in the worst case the loss of ultimate strength was less than 20%. Strain to failure, on the other hand, did show substantial degradation for a number of samples. It should also be noted that the strain to failure of the samples re-tested at elevated temperatures were somewhat lower than expected based on previous high temperature strength data from as-fabricated specimens. It thus appears that strain to failure is the strength parameter that is most sensitive to degradation by LCF. Nevertheless, the proportional limit stress is the most critical parameter used for design purposes, and this value was not appreciably affected by LCF exposure.

Table 3-21. Summary of the LCF Testing Results on GE Prepreg MI Composites made in September, 2000 with Optimized GEGR Configuration C Fiber Coatings. All Testing Was Performed in Air at 20 cycles/minute and a Stress Ratio of 0.01.

Specimen	Temp. (°C)	Stress (MPa)	Cycles to failure*	Time to Failure* (h)
735-6	816	150	>600,000	>500
739-3	816	150	>111,000	>92.5
735-7	816	160	>600,000	>500
734-4	816	160	>600,000	>500
739-2	816	160	45,603	38.0
739-5	816	160	35,018	29.2
735-8	816	170	1,124	0.94
734-1	1093	140	>111,000	>92.5
735-3	1093	140	>111,000	>92.5
734-5	1093	140	>600,000	>500
739-1	1093	150	70,992	59.2
734-3	1093	150	38,903	32.4
735-2	1093	160	1,174	0.98
734-6	1204	120	>111,000	>92.5
735-4	1204	130	>111,000	>92.5
735-5	1204	130	>600,000	>500
739-4	1204	130	54,018	45
735-1	1204	140	8,405	7.0
734-2	1204	140	5,539	4.6

* Values listed with a > symbol indicate test run-out and sample survival at the indicated cycles and time.

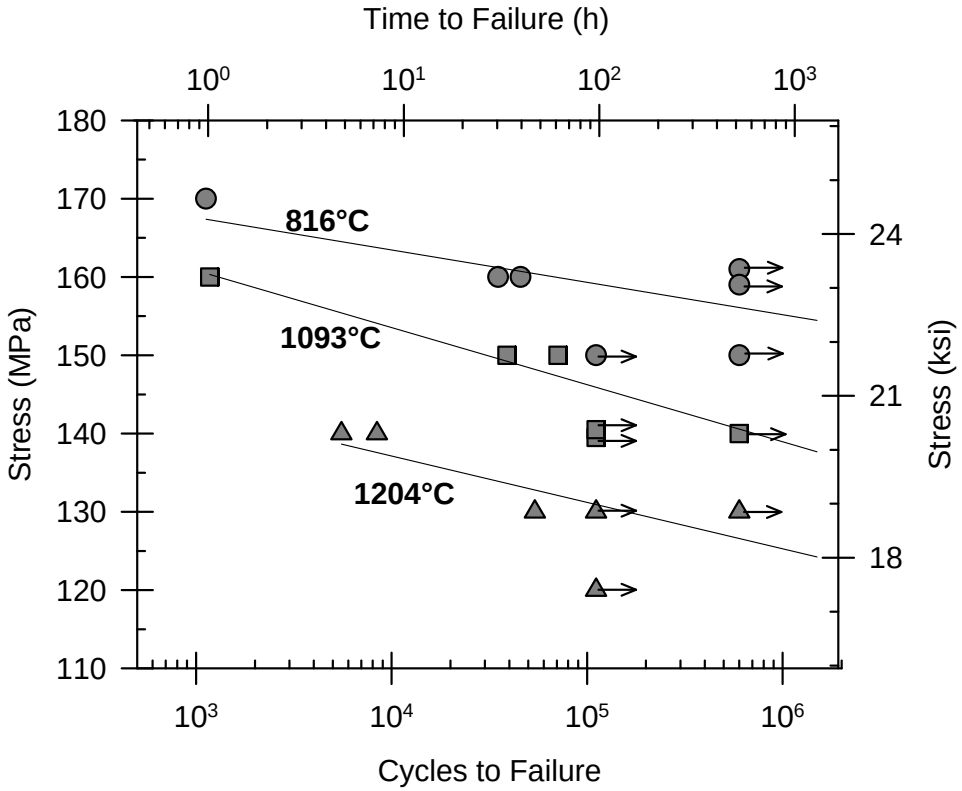

Figure 3-79. Results of LCF testing on GE Prepreg MI composites made in September 2000 from Hi-Nicalon™ fiber with optimized GEGR configuration C fiber coatings. The arrows indicate test run-outs.

Table 3-22. Summary of Residual Tensile Strength Measurements on Run-out Samples from the LCF Tests.

Sample	LCF Test Condition	Tensile Test Temp* (°C)	Proportional Limit (MPa / change)	Ultimate Strength (MPa / change)	Strain to Failure (% / change)
734 AsFab	-	RT	154	258	0.98
734-4	160MPa, 816°C, 500h	RT	186 / +21%	276 / +7%	0.91 / -7%
734-1	140MPa, 1093°C, 92.5h	RT	163 / +6%	269 / +4%	0.83 / -15%
734-5	140MPa, 1093°C, 500h	RT	190 / +24%	234 / -10%	0.50 / -49%
734-6	120MPa, 1204°C, 92.5h	RT	160 / +4%	262 / +2%	0.87 / -11%
735 AsFab	-	RT	160	265	0.97
735-7	160MPa, 816°C, 500h	RT	223 / +40%	273 / +3%	0.49 / -50%
735-5	130MPa, 1204°C, 500h	RT	154 / -3%	218 / -18%	0.65 / -33%
735-6	150MPa, 816°C, 500h	816	192	246	0.38
735-3	140MPa, 1093°C, 92.5h	1093	204	221	0.29
735-4	130MPa, 1204°C, 92.5h	1204	29.2	31.9	0.42
739 AsFab	-	RT	149	252	0.80
739-3	150MPa., 816°C, 92.4h	RT	203 / +36%	230 / -9%	0.23 / -71%

* Tests at RT were done at GE CRD, those at elevated temperatures were performed at Composite Testing and Analysis.

High cycle fatigue (HCF) testing was also conducted using the same sample configuration and procedures as described in Section 3.4.1.2. The majority of these tests were performed in a manner similar to the LCF tests, i.e. at a stress ratio (R-value) of 0.01, but at higher frequencies. Two measurements were also done at an R-value of 0.9 to look for an influence of the minimum stress value. Likewise, most of the tests were done at 30 Hz, but three samples were tested at 150 Hz to look for frequency dependent behavior. Neither the different R-value nor the different frequency had any noticeable effect on the HCF life for the conditions tested. The testing temperature was also extended up to 1316°C, but only for two samples. A summary of the HCF data is given in Table 3-23, and shown graphically in Figure 3-89 (not including the data points at 150Hz or at 1316°C). The trends in the data are similar to those observed for the LCF measurements, i.e. that the GE Prepreg MI samples showed a 2 to 3 orders of magnitude increase in life compared to Goodrich slurry cast MI samples tested at the same stress and temperature.

Table 3-23. Summary of Tensile High Cycle Fatigue Tests Performed on GE Prepreg MI Composites Made in April-May, 2001. All Testing Was Performed in Air.

Specimen	Test Temp. (°C)	Frequency (Hz)	R ratio	Stress (MPa)	Cycles to Failure*	Total Time* (h)
1019-2	816	30	0.01	130	>54,000,000	>500
1030-4	816	30	0.01	140	4,671,210	43.25
1030-7	816	30	0.01	140	2,498,576	23.13
1030-3	816	30	0.01	150	500,454	4.63
1018-4	816	30	0.01	160	19,685	0.18
1018-7	1093	150	0.01	120	>270,000,000	>500
1018-6	1093	30	0.01	120	>54,000,000	>500
1019-6	1093	30	0.01	120	>10,000,000	>92.6
1019-4	1093	30	0.9	120	>54,000,000	>500
1019-3	1093	30	0.01	130	1,108,993	10.27
1030-6	1093	30	0.01	130	509,508	4.72
1019-9	1093	30	0.01	140	647,508	6.00
1018-3	1093	30	0.01	150	12,238	0.11
1018-8	1204	150	0.01	110	>270,000,000	>500
1019-7	1204	30	0.01	110	>54,000,000	>500
1030-5	1204	30	0.9	110	>54,000,000	>500
1030-2	1204	30	0.01	120	4,021,158	37.23
1019-8	1204	30	0.01	130	159,550	1.48
1018-2	1204	30	0.01	140	176,312	1.63
1018-5	1204	30	0.01	150	664	0.006
1030-8	1316	150	0.01	100	>270,000,000	>500
1030-9	1316	30	0.01	110	>54,000,000	>500

* Values listed with a > symbol indicate test run-out and sample survival at the indicated cycles and times.

In general the allowable stresses for a given time to failure were lower under HCF conditions than under LCF conditions for both prepreg and slurry cast MI composites. However, when you consider cycles to failure the data from the two tests are more

comparable. Figure 3-81 shows a plot of maximum stress versus cycles to failure for prepreg MI samples combining the LCF and the HCF data at 0.33Hz, 30Hz and 150Hz. Despite the large data scatter and uncertainties introduced by the run-out samples, there does appear to be consistent trend lines describing the overall cyclic failure of the samples at the three test temperatures studied. This is not unreasonable given that the waveform (sine wave) and stress ranges (R-value of 0.01) were the same for both tests. This apparent dependence on number of cycles rather than on the elapsed time would suggest that there are additional degradation mechanisms active under cyclic loading beyond what may be encountered in a simple thermal exposure test.

Post-test tensile strengths were measured on all of the run-out samples from the HCF tests, and these results are summarized in Table 3-24. The first sample in each set in the table gives the properties for a witness bar cut from the same panel in the "as-fabricated" condition. The subsequent entries give the results from run-out samples, which were tensile tested at room temperature following the indicated HCF exposure.

As noted with the LCF run-out samples, the strain to failure was the most sensitive parameter as it was seen to degrade more following HCF exposure than either the matrix cracking stress or ultimate strength. This was true for the samples showing significant degradation (>20% loss of a property) at 816°C, 1093°C and 1204°C; however, when HCF tested at 1316°C both the cracking stress and ultimate strength showed more degradation than the strain to failure. This may be due to a change in the degradation mechanism at 1316°C compared to the lower temperatures. The loss of strain to failure (i.e. embrittlement) at the lower temperatures would suggest that the degradation mechanism is related to bonding at the fiber-matrix interface whereas at 1316°C the mechanism may be more related to changes in the matrix or residual stress effects.

Despite the good strength retention, the degradation in strain to failure for the tests at 1204°C, even at the lower stresses tested, suggest that we have not yet reached the "fatigue limit" (e.g. the stress below which no degradation is seen following an infinite number of cycles). The determination of a fatigue limit stress would be very useful for component design purposes, particularly for long-life components such as those for gas turbine applications. Therefore, further LCF testing is needed at reduced stress levels in order to determine whether a fatigue limit exists for this material.

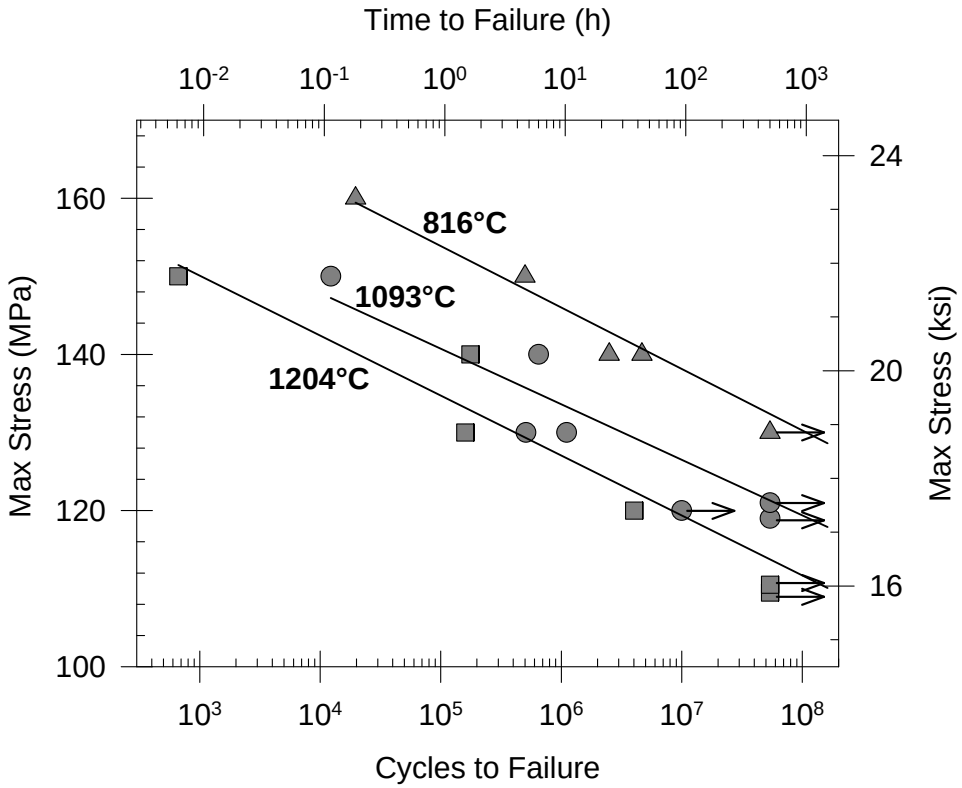

Figure 3-80. Results of the HCF testing on GE Prepreg MI composites made in April, 2001 from Hi-Nicalon™ fiber with optimized GEGR configuration C fiber coatings. The arrows indicate test run-outs.

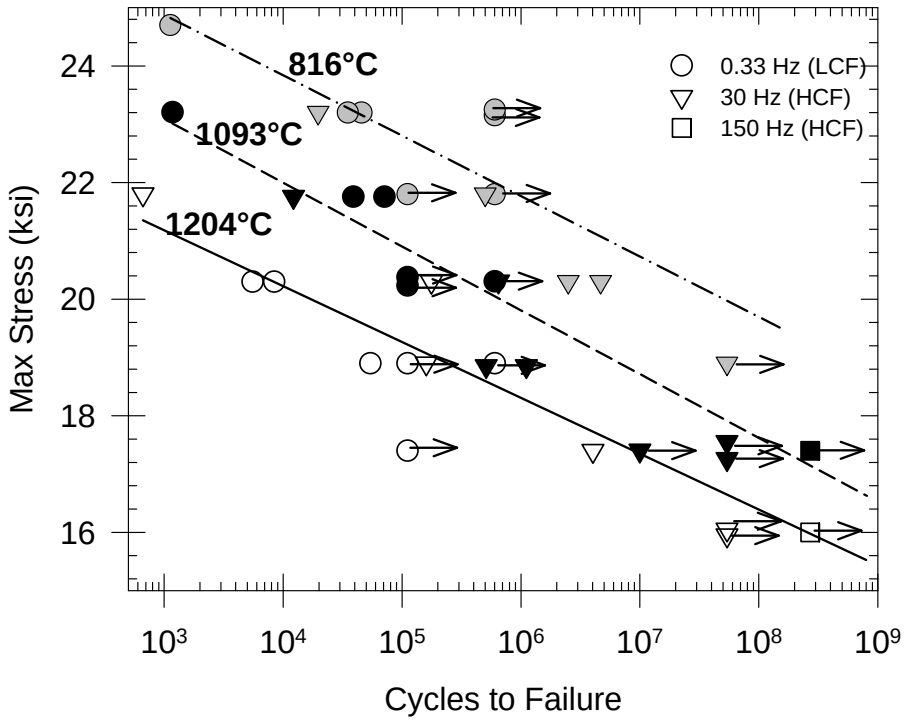

Figure 3-81. Combined LCF and HCF response for GE Prepreg MI composites made from Hi-Nicalon fiber with optimized GEGR configuration C fiber coatings. The gray symbols are the data points measured at 816°C, black symbols at 1093°C, and open symbols 1204°C. The data tend to give consistent trends when combined on the basis of cycles. The arrows indicate test run-outs.

Table 3-24. Summary of Residual Tensile Strength Measurements on Run-out Samples from the HCF Tests.

Sample	HCF Test Condition	Proportional Limit (MPa / change)	Ultimate Strength (MPa / change)	Strain to Failure (% / change)
1018 AsFab	-	158	290	1.11
1018-7	120MPa, 1093°C, 150Hz, 500h	181 / +15%	332 / +14%	0.88 / -21%
1018-6	120MPa, 1093°C, 30Hz, 500h	150 / -5%	307 / +6%	1.04 / -6%
1018-8	110MPa, 1204°C, 150Hz, 500h	154 / -3%	318 / +9%	1.07 / -4%
1019 AsFab	-	178	316	0.97
1019-2	130MPa, 816°C, 30Hz, 500h	143 / -20%	190 / -40%	0.33 / -66%
1019-6	120MPa, 1093°C, 30Hz, 92.6h	189 / +6%	348 / +10%	1.24 / +28%
1019-4	120MPa, 1093°C, 30Hz, 500h	145 / -19%	228 / -28%	0.12 / -88%
1019-7	110MPa, 1204°C, 30Hz, 500h	177 / -1%	334 / +6%	1.23 / +27%
1030 AsFab	-	167	313	0.87
1030-5	110MPa, 1204°C, 30Hz, 500h	168 / +0%	182 / -42%	0.09 / -90%
1030-8	100MPa, 1316°C, 150Hz, 500h	98 / -42%	256 / -18%	1.14 / +31%
1030-9	110MPa, 1316°C, 30Hz, 500h	27.6 / -83%	245 / -22%	0.97 / +11%

3.4.3.4 Creep Testing

Creep testing of the GE Prepreg MI composites was also conducted using the procedures described in Section 3.4.1.3. The creep data are summarized in Table 3-25, with the rupture curves shown graphically in Figure 3-82. Once again, the data for the GE Prepreg MI composites show a roughly 2 to 3 orders of magnitude increase in creep rupture life compared to the Goodrich slurry cast MI samples measured under the same conditions of stress and temperature. The creep rupture lives, at the same temperature and stress, are typically longer than under LCF or HCF testing conditions. Because the sample is constantly under the "maximum" stress during a creep rupture test whereas only a part of the time is spent at maximum stress during the cyclic fatigue tests, this result again indicates that cyclic loading is contributing to the sample failures beyond what would be expected from a simple time at stress criterion.

Creep rates at 816°C were below detectability, as would be expected. Only one rupture failure occurred at 816°C and 140MPa: however, two similar samples tested at these conditions were run-outs. All run-out samples were tensile tested to failure at room temperature following creep testing, and the results are given in Table 3-26. No degradation was observed in the tensile properties of the creep run-out samples at 816°C, suggesting that the one observed failure may have been caused by a defective test sample.

As with the Goodrich slurry cast material, creep rates did not reach steady state values during the creep experiments. The creep rates measured on run-out samples at the 1000 hour mark were consistently very low. However, the failure strains (or strain at 1000 hours for run-out samples) were considerably higher at 1093°C and 1204°C than one would expect from simple elastic loading of the specimens (on the order of 0.06 to 0.08%). These results indicate that there was a substantial primary creep regime where the initial creep rates were much higher than indicated in Table 3-25.

Run-out samples from the creep rupture test were tensile tested to failure in order to evaluate their residual strength properties. The results of these tests are summarized in Table 3-26. [Please note that the samples used for this testing were prepared in November-December of 2000, before the fiber coating deposition conditions were fully optimized, and thus the as-fabricated strengths of the composite panels were somewhat lower than those for fast-fracture testing in Table 3-20.] As with the LCF and HCF tests, sample strain to failure values tended to show the most degradation following creep testing. Three of the four run-outs creep tested at 1093° or 1204°C and then tensile tested at room temperature showed significant (>20%) reductions in the strain to failure. However, the remaining run-out at 1093°C actually showed an increase in strain to failure. None of the samples creep tested at 816°C showed significant degradation. The degradation of the run-out samples from the 1093°C and 1204°C creep rupture tests indicate that we have not yet determined if there is a stress below which creep damage would not occur. Additional testing at reduced stress levels would be required.

Table 3-25. Summary of the Tensile Creep Rupture Testing Results on GE Prepreg MI Composites Made in July – September, 2000 with GEGR Optimized Configuration C Fiber Coating on Hi-Nicalon™ Fiber. All Testing Was Performed in Air.

Specimen	Temp. (°C)	Creep Stress (MPa)	Rupture time[§] (h)	Failure Strain* (%)	Creep rate at 1000 hr (s^{-1})
730-1	816	125	>1000	0.07	$<10^{-11}$
704A-2[a]	816	140	460.2	0.05	-
732-2	816	140	>1000	0.08	$<10^{-11}$
717-2	816	140	>1000	0.08	$<10^{-11}$
704A-1[a]	1093	125	>1000	0.03	2.6×10^{-11}
704A-4[a]	1093	140	>1000	0.16	1.9×10^{-11}
732-3	1093	140	>1000	0.14	1.1×10^{-10}
732-7	1093	140	>1000	0.13	8.0×10^{-11}
717-1	1093	150	394	0.20	-
732-4	1093	150	190	0.14	-
704B-2[a]	1093	150	18.1	0.12	-
730-8	1093	160	15.4	0.12	-
704B-1[a]	1093	160	1.45	0.10	-
732-5	1204	125	>1000	0.25	3.0×10^{-11}
704B-5[a]	1204	125	>1000	0.20	8.0×10^{-11}
732-1	1204	140	>1000	0.31	2.3×10^{-10}
732-8	1204	140	454	0.28	-
732-6	1204	150	82.1	0.29	-
704A-5[a]	1204	150	0.32	0.18	-

[a] Panel 704 samples were slightly warped, possibly contributing to the relatively low fatigue lives.

§ A value of >1000 indicates a run-out, e.g. the sample survived the full 1000 hours without rupture.

* Strain at failure or strain at 1000 hr if sample was a run-out.

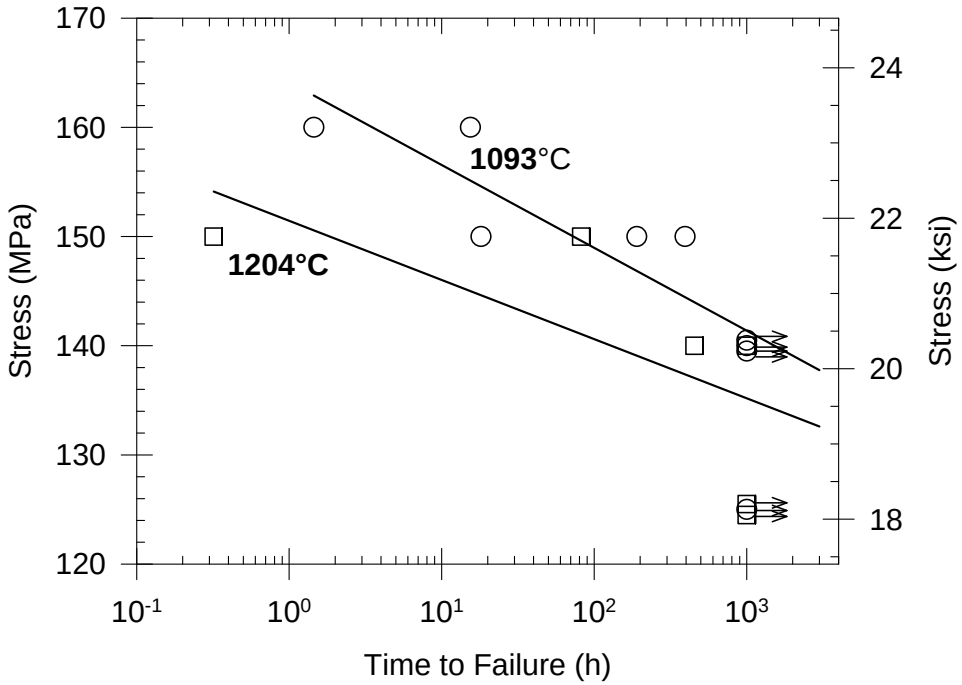

Figure 3-82. Creep rupture behavior in air for GE Prepreg MI composites made in July – September, 2000 from Hi-Nicalon™ fiber with optimized GEGR configuration C fiber coatings. The arrows indicate test run-outs.

Table 3-26. Summary of Residual Tensile Strength Measurements on Run-out Samples from the Creep/Rupture Tests on GE Prepreg MI Composites with Hi-Nicalon™ Fibers and Optimized GEGR Configuration C Fiber Coatings.

Sample	Creep Test Condition	Tensile Test Temp* (°C)	Proportional Limit (MPa / change)	Ultimate Strength (MPa / change)	Strain to Failure (% / change)
704 AsFab	-	RT	158	223	0.62
704A-1	125MPa, 1093°C	RT	170 / +8%	217 / -3%	0.47 / -25%
704A-4	140MPa, 1093°C	RT	165 / +4%	244 / +10%	0.72 / +16%
717 AsFab	-	RT	175	260	0.79
717-2	140MPa, 816°C	RT	194 / +11%	279 / +7%	0.74 / -6%
730 AsFab	-	RT	138	236	0.84
730-1	125MPa, 816°C	RT	180 / +30%	242 / +2%	0.82 / -2%
732 AsFab	-	RT	190	265	0.88
732-7	140MPa, 1093°C	RT	178 / -6%	220 / -17%	0.19 / -78%
732-5	125MPa, 1204°C	RT	155 / -18%	195 / -26%	0.21 / -76%
732-2	140MPa, 816°C	816	204	246	0.38
732-3	140MPa, 1093°C	1093	165	192	0.26
732-1	140MPa, 1204°C	1204	150	185	0.25

* Tests at RT were done at GE CRD, those at elevated temperatures were performed at Composite Testing and Analysis.

3.4.3.5 Hold Time Fatigue Testing

Hold time fatigue (HTF) testing was substituted for the pre-cracked oxidation and stressed oxidation tests done in the prior database efforts. This test is much like a creep rupture test, where the samples are held at temperature under constant load conditions until failure, except that every 2 hours the load is reduced to a low value (nominally ~4MPa) for 1 minute. This test was adopted from GE Aircraft Engines, where it was being used extensively for the evaluation of slurry cast composites with Sylramic™ fiber under the HSCT/EPM program. GEAE was also proposing to use HTF response as a critical material parameter for the design of CMC components. We wanted to be able to compare the performance of GE's prepreg composites made with Hi-Nicalon fiber with the slurry cast / Sylramic system. This test was performed at CTL using 152mm long, dogboned tensile specimens.

Table 3-27 gives the results of HTF tests conducted in air. Unfortunately the response to the HTF test was rather bi-modal in that nearly all of samples either failed during the 1st cycle or were full 500 hour run-outs. Only one specimen of the 16 tested had a lifetime between one and 250 cycles. These results make it practically impossible to establish a reliable HTF life curve.

Table 3-27. Summary of the 2-Hour Hold Time Fatigue Tests Performed on GE Prepreg MI Composites Made in June, 2001 from Hi-Nicalon™ fiber with the Optimized GEGR Configuration C Fiber Coatings. All Testing Was Conducted in Air.

Sample ID	Test Temp (°C)	Maximum Stress (MPa)	Life* (hours)
1066-4	816	179	1.33
1066-3	816	159	>504
1064-3	816	159	0.65
1064-1	816	138	>514
1066-1	816	138	72
1064-4	816	96.5	>506
1064-2	816	96.5	>504
1066-2	816	96.5	>500
1064-9	1204	179	failed at 173MPa
1064-8	1204	159	>514
1066-7	1204	159	>500
1064-5	1204	138	>502
1066-8	1204	138	>500
1066-5	1204	138	0.005
1064-7	1204	96.5	>540
1066-6	1204	96.5	>500

* A > sign indicates test run-out without sample failure.

The residual tensile strengths of all the run-out samples were measured at room temperature at CTL. The results of these tensile tests are given in Table 3-28. Data are also given for witness bars that were cut from each panel but not subjected to HTF testing

for comparison purposes. The strain to failure values showed the greatest effects of HTF exposure, just as it had in the LCF, HCF and creep tests; however the residual strength data had a smaller, more variable response. The overall changes in proportional limit and ultimate strength were mostly limited to ±20%, but were not entirely consistent. For instance, of the two samples HTF tested at 1204°C and 138MPa one sample (1066-8) showed reductions in ultimate strength and strain to failure of 24% and 64%, respectively, and the other sample (1064-5) showed less than 10% reduction in either property. Considering the samples tested at 96.5MPa, those tested at 816°C unexpectedly showed greater degradation in strain to failure than those tested at 1204°C, which actually showed increases in strain to failure.

These results would suggest that there is an intermediate temperature degradation mechanism that is not effective at higher temperatures. One such possible mechanism is oxidation of the fiber-matrix interfaces through matrix cracks. Such oxidation can occur largely unabated at 816°C, but at 1204°C the oxidation rate of the matrix surfaces in the matrix cracks would rapidly seal the cracks with silica, thereby preventing further oxidation. However, the relatively un-affected proportional limit stresses strongly suggest that no matrix cracking occurred during HTF testing. Another possibility would be oxidation of a carbon-rich fiber-coating interface. Although such layers have been observed in CVI composites, numerous TEM inspections of prepreg MI composites at ORNL have consistently failed to detect such carbon-rich interface layers.

Table 3-28. Summary of the Residual Tensile Strength Data Measured on the 2-Hour Hold Time Fatigue Test Run-out Samples.

Sample	HTF test conditions	Proportional Limit Stress (MPa / change)	Ultimate Strength (MPa / change)	Strain to Failure (% / change)
1064-w	none	174	287	1.08
1066-w, -10	none	186	275	0.80
1066-3	816°C / 159MPa	158 / -15%	260 / -5%	0.37 / -54%
1064-1	816°C / 138MPa	191 / +10%	298 / +4%	0.98 / -9%
1064-2	816°C / 96.5MPa	196 / +12%	296 / +3%	0.62 / -43%
1064-4	816°C / 96.5MPa	193 / +11%	304 / +6%	0.58 / -46%
1066-2	816°C / 96.5MPa	212 / +14%	242 / -12%	0.24 / -70%
1064-8	1204°C / 159MPa	†	293 / +2%	*
1066-7	1204°C / 159MPa	188 / +1%	268 / -3%	*
1064-5	1204°C / 138MPa	175 / +1%	271 / -6%	0.97 / -10%
1066-8	1204°C / 138MPa	189 / +2%	209 / -24%	0.29 / -64%
1064-7	1204°C / 96.5MPa	169 / -3%	305 / +6%	1.29 / +19%
1066-6	1204°C / 96.5MPa	160 / -14%	283 / +3%	1.30 / +62%

† No linear loading region was noted during the test – the sample matrix may have already been cracked.
* Extensometer slipping disturbed the measurement of strain data during the test.

3.4.3.6 JETS Testing

JETS testing of the GE prepreg MI composites, made in May, 2001 with optimized GEGR configuration C fiber coatings on Hi-Nicalon fiber, was conducted at MCL under the

supervision of GE Energy. Both thermal fatigue and thermal gradient testing were performed using the same procedures discussed in Section 3.4.1.4. Thermal fatigue testing was performed out to 2000 cycles, and thermal gradient testing to 2500 cycles. None of the prepreg MI samples was found to crack or show other damage for either test or for any of number of thermal shock cycles examined. Dynamic modulus measurements using a GrindoSonic instrument also showed no change after JETS exposure. This is in contrast to the Goodrich slurry cast MI composite measured earlier where nearly all of the test specimens showed some degree of edge cracking.

3.4.3.7 Thermal Property Measurements

Thermophysical property measurements performed on the GE Prepreg MI Composite included thermal diffusivity, heat capacity, thermal conductivity (calculated from thermal diffusivity, heat capacity and density), and thermal expansion. Where appropriate measurements were done in the thru-thickness (perpendicular to the fiber planes) and in-plane (parallel to one of the fiber directions) orientations. Samples for thru-thickness thermal diffusivity and in-plane thermal expansion were cut from standard 8-ply 0°-90° CMC panels. However, samples for in-plane thermal diffusivity and thru-thickness thermal expansion required samples that were at least 12mm long in the direction perpendicular to the fiber plies. In order to fabricate such specimens normal 8-ply panels were surface ground to a constant thickness and then sliced into bars. The bars were then stacked and glued together with a thin film of matrix slurry in order to get samples of the needed size and fiber orientation. These glued samples were put through a short second infiltration treatment to convert the matrix glue layers to the normal SiC-Si composition. Two sets of sample made from two separate starting panels (1067 and 1069) were tested, and all samples were made with the standard HGS matrix composition and Hi-Nicalon fibers coated with the optimized GEGR coating.

Concurrent Technologies Corp. performed the heat capacity measurements using a differential scanning calorimetry technique. The measured heat capacities for the two samples are shown in Figure 3-83. Over the complete temperature range measured the heat capacities from the two specimens agreed within 2%. The measured heat capacities also agree well with those calculated from standard JANAF thermodynamic tables and the average phase composition of the composites up to about 600°C, but above that temperature the measured values were substantially lower than the calculated values. Nevertheless the measured heat capacity values were used in the calculation of thermal conductivity described below. The use of the calculated heat capacity values would have increased the high temperature thermal conductivity values by 15-20%.

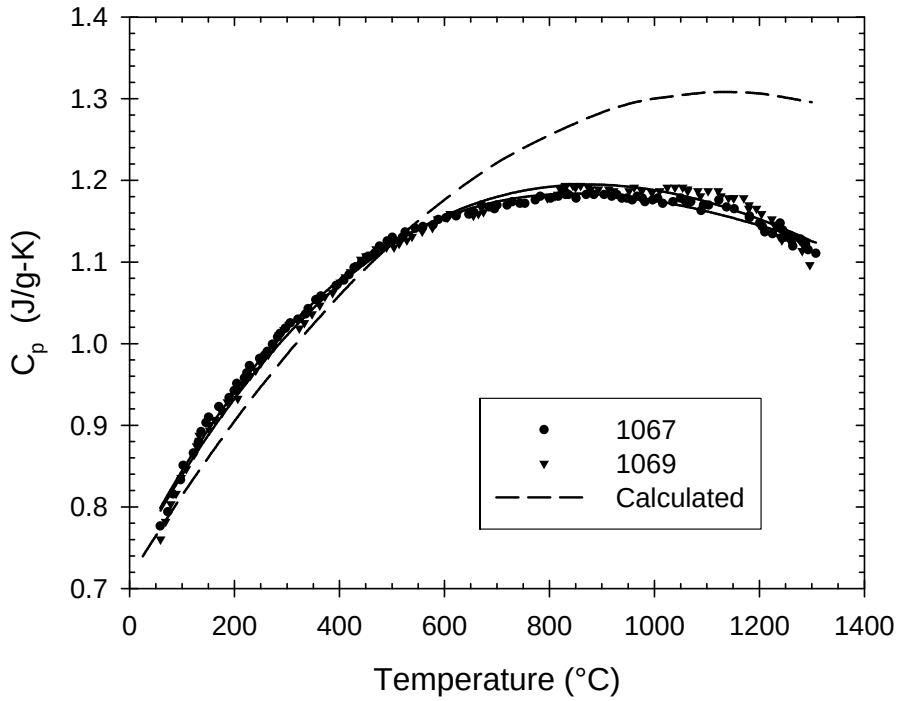

Figure 3-83. Heat capacity data measured on two GE Prepreg MI composite samples made in June, 2001 (data points and solid lines) compared to that calculated from standard thermodynamic tables (dashed line). Heat capacity is identical between the two measured samples within 2%.

Thermal diffusivity values were measured at GEGR using a laser flash technique. Prior measurement experience with ZrO_2-based TBC films had highlighted the need for an opaque surface layer on ceramic specimens due to the translucency of many ceramics, particularly in the IR wavelengths. Consequently the CMC specimen surfaces were coated with a 2μm layer of tungsten by sputtering to ensure surface opacity. The specimen was allowed to equilibrate for 10 minutes at each measurement temperature, and then three measurements were conducted at each temperature. Typical scatter in the three measurements at each temperature were only $\pm 0.2 mm^2/s$. The averages of these three measurements are shown as a function of temperature in Figure 3-84. The agreement in diffusivity values between the two samples was very good. The diffusivities measured in-plane (parallel to a fiber direction) were consistently ~25% higher than those measured thru-thickness (perpendicular to the fiber plies).

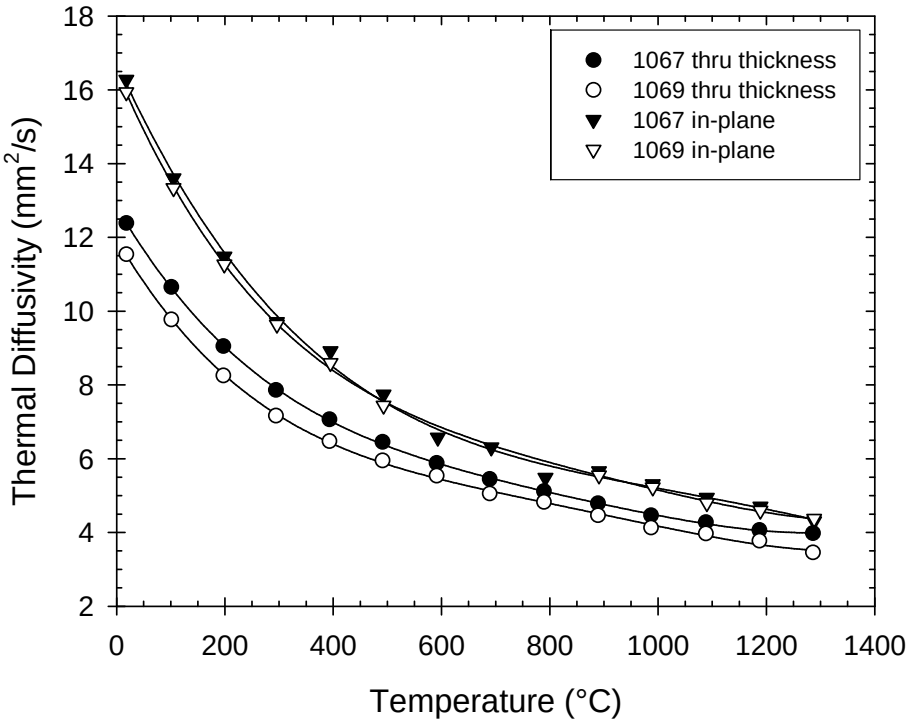

Figure 3-84. Thermal diffusivity as a function of temperature and measurement direction for GE Prepreg MI composite samples made in June, 2001 from HI-Nicalon™ fiber with optimized GEGR fiber coatings.

Thermal conductivity is simply the product of heat capacity, thermal diffusivity and density. Densities of the diffusivity samples were measured using Archimedes technique, which gave an average value of 2.783g/cc. Samples for the in-plane diffusivity measurements had slightly higher density values (~2%) than did samples for the thru-thickness measurement, which was due to the in-plane samples having gone through a second infiltration treatment during sample preparation. The actual density value for each of the diffusivity samples was used in the calculation of thermal conductivity. The density values were also adjusted for changes with temperature using the thermal expansion data to be discussed below.

The thermal conductivity values determined by this process are shown in Figure 3-85. Overall differences in conductivity values for the various samples were dominated by the changes in thermal diffusivity. Similar to what was observed in the diffusivity data, the thermal conductivity values were in fairly good agreement between the two panels, , particularly for the in-plane values. The in-plane conductivity values were consistently ~25% higher than the thru-thickness values, again similar to the trend observed with the thermal diffusivities.

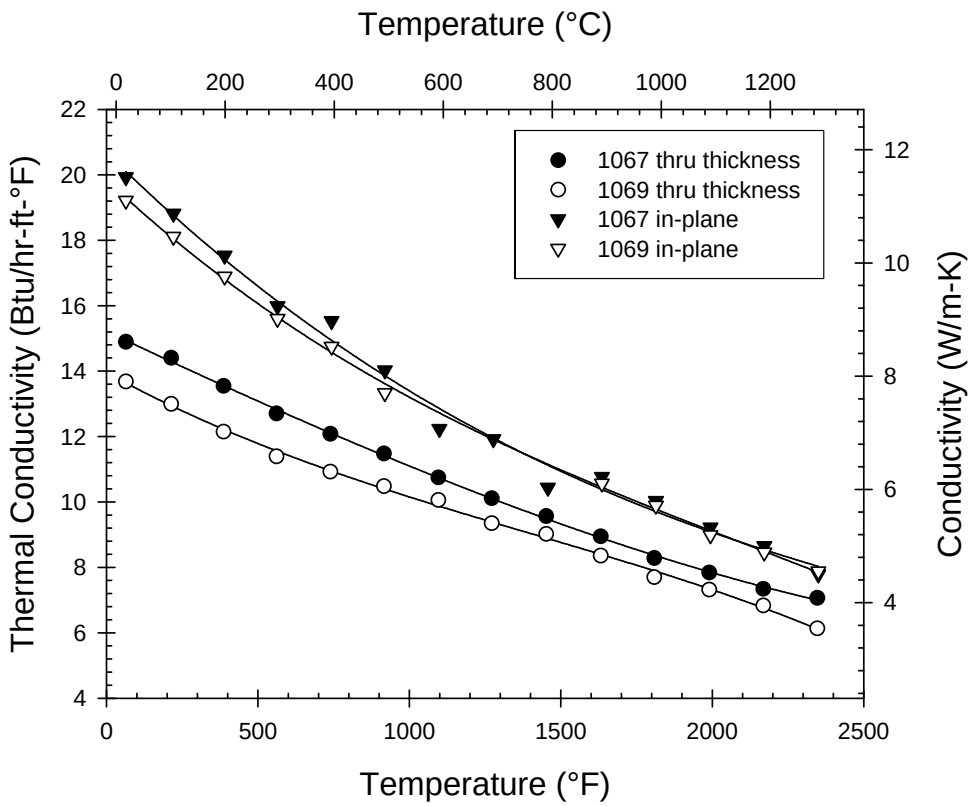

Figure 3-85. Thermal conductivity values as a function of temperature and sample direction determined for GE Prepreg MI composites made in June, 2001 from Hi-Nicalon ™ fiber with optimized GEGR fiber coatings.

Thermal expansion of the composite was measured at GEGR using a dual-rod contacting extensometer. Heating rate during the measurements was 7°C/min and all measurements were performed in air. Plots of the measured expansion vs. temperature are shown in Figure 3-86. All of the expansion curves are grouped quite closely, although there is a consistent trend in that the thru-thickness direction has a slightly higher expansion than does the in-plane direction.

The differences between the two panels (1067 and 1069) were so small that the expansion data was averaged to give a single curve for each orientation. The instantaneous (tangent) coefficient of thermal expansion (CTE) was calculated from the slopes of the expansion curves. These CTE values for the two orientations are plotted vs. temperature in Figure 3-87. The overall differences in CTE for the two orientations are rather small, which consistent with the close match in CTE between the fiber and the matrix.

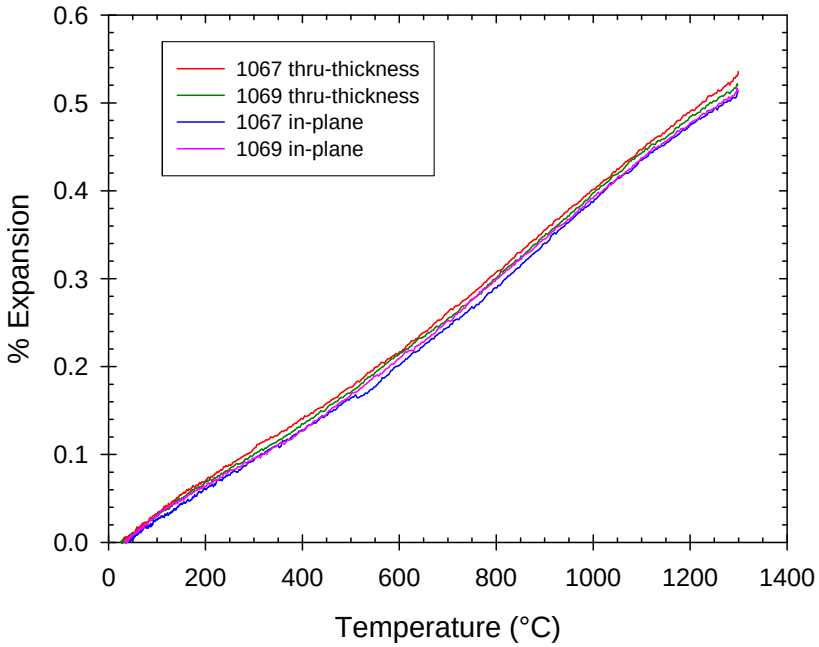

Figure 3-86. Thermal expansion behavior for GE Prepreg MI composites made in June, 2001 from Hi-Nicalon™ fiber with optimized GEGR configuration C fiber coatings. Data from two separate panels (1067 and 1069) are shown for two specimen orientations.

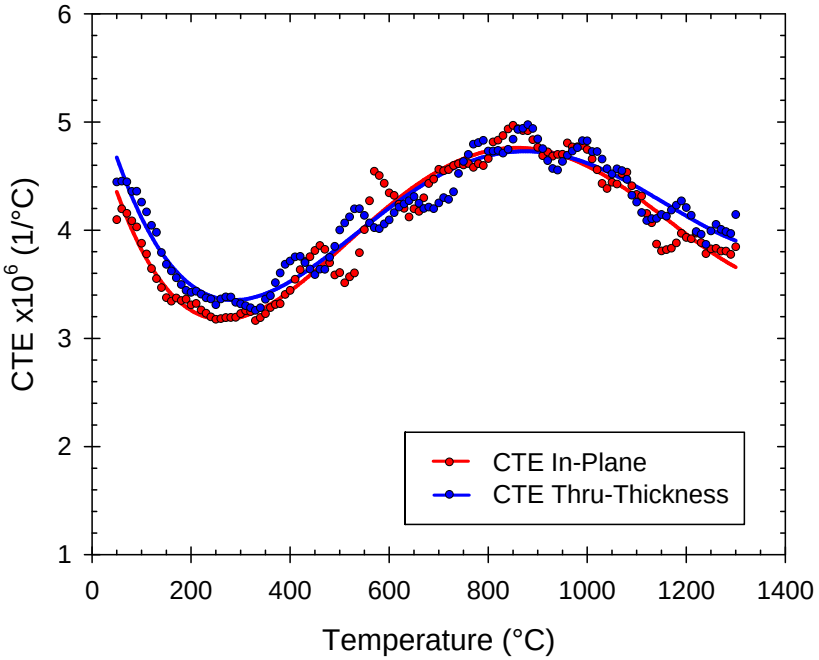

Figure 3-87. Coefficient of thermal expansion as a function of temperature for GE Prepreg MI composites made from Hi-Nicalon™ fiber with optimized GEGR configuration C fiber coatings.

3.4.3.8 Fiber Orientation Effects on Prepreg MI Composites

All of the previous material characterization and databasing was done on samples with balanced 0°-90° fiber architectures. However, one of the main advantages of composites is the ability to tailor the fiber architecture and engineer the material properties to fit the requirements of the application. Various mechanical models had been developed for predicting fiber architecture effects on the elastic and fracture properties of polymeric composites, but little work has been done on brittle matrix composite systems where the matrix modulus is comparable to, or greater than, that of the reinforcing fiber. We therefore needed to investigate the effects of fiber architecture on CMC modulus and failure behavior through experimentation. We also wanted to measure the elastic and fracture properties of unidirectional composites, from which individual ply properties could be derived for future use in developing optimized fiber architectures using ply-level laminate theory.

A series of CMC panels with varying fiber architectures were fabricated from a single fiber coating run. Where appropriate, individual test samples were cut from the same panel, but in different directions relative to the fiber direction, in order to minimize the effects of panel-to-panel variability. The resulting test bars had fiber architectures corresponding to 0° uniaxial, 90° uniaxial, balanced 0°-90° (equal number of plies in the 0° and 90° directions), unbalanced 0-90° (unequal number of plies in the 0° and 90° directions), balanced ±45° and unbalanced ±45°.

It should be noted that the panels prepared for this study were fabricated in September, 2002 from one of the best lots of Hi-Nicalon™ fiber that we had received over the entire course of this program. Processing of the test panels, with the exception of the very thick unidirectional panels used for ultrasonic modulus measurements, also went extremely well. Consequently practically all of the mechanical properties measured on this set of samples fell within the upper range of the distributions of properties normally seen, and thus the property values shown in the tables and graphs for the 0°-90° architectures are higher than those given in the previous database data sets. However, the property trends between the different architectures are still completely valid.

3.4.3.8.1 Mechanical Modulus Measurements

Modulus values were measured using two techniques. The first technique was based on measuring the slope of the stress-strain curves using a universal testing machine. Standard tensile bar type specimens were mounted into the testing machine and cycled between +70MPa and –70MPa stress under load control. The stress range of ±70MPa was chosen as to be safely below the proportional limit (i.e. matrix cracking) stress of the composite and yet large enough to give measurable values of strain.

The most problematic aspect of this technique was obtaining accurate strain values. Three methods of strain measurement were used, including face-mounted strain gages, an edge-loaded extensometer with knife-edge contacts (Instron model 2630-108), and an edge-loaded multiaxial extensometer with point contacts (MTS model 632.85b). A systematic difference was detected between the two faces of test bars when measured with the face-mounted strain gages. The exact cause of this difference was not determined, but

specimen misalignment in the testing machine was investigated and ruled out. In general, the edge-mounted extensometer with knife edges gave modulus values in between those measured with the strain gages, but was occasionally similar to one or the other of the strain gages. This result can be understood as a result of slight misalignment of the knife-edge contact of the extensometer arms on the sample, as illustrated in Figure 3-88, which would result in the extensometer preferentially contacting along one face of the sample. The multiaxial extensometer, which contacted the sample at points along the centerline of the thickness and automatically averaged reading from both edges of the sample, consistently gave strain results that agreed very well with the average of the two strain gages, and thus was used for the majority of room temperature testing. The multiaxial extensometer also measured the transverse strain across the width of the samples allowing for the measurement of Poisson's ratio. A diagram and photo of how the multiaxial extensometer contacted the test specimen are shown in Figure 3-89.

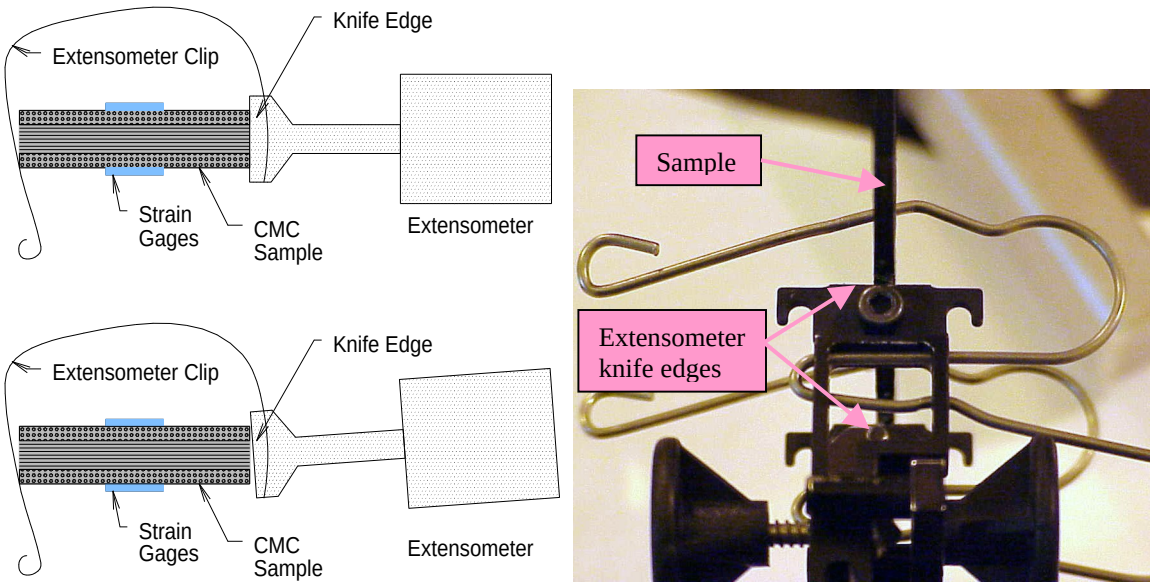

Figure 3-88. Illustration of the axial extensometer set up used for modulus measurements. The view is looking down the length of the test bar: Left Top – schematic showing proper alignment of the extensometer knife edge (view is looking down along the length of the test bar); Left Bottom – slight misalignment of the extensometer leads to preferential contact of the knife edges along one face of the sample; Right – photograph of knife edge to specimen contact during an actual test.

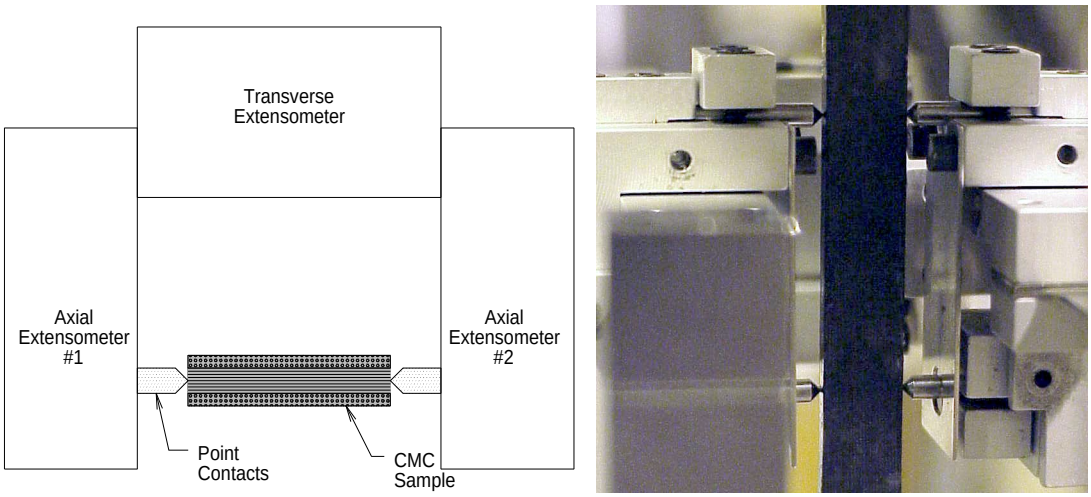

Figure 3-89. Illustration showing contact arrangement for the pointed extensometer arms of the multiaxial extensometer: Left – schematic representation where the view is looking down the length of the test bar; Right – photograph showing contact placement on an actual test sample.

The results of the mechanical modulus measurements are listed in Table 3-29 for each of the fiber architectures measured. The samples were all either 8-ply or 6-ply lay-ups as listed in the table, except for the 90° uniaxial samples, which were 20 plies thick. A very slight bow in the 8-ply 90° uniaxial panel, coupled with the relatively low strength in the 90° direction, caused all of the 8-ply 90° uniaxial samples to break during gripping in the test machine. A 20-ply panel prepared for ultrasonic testing, as will be discussed below, was therefore used for this testing since it was thick enough to allow the surfaces to be ground flat and parallel, thus avoiding fracture during loading into the test machine. In addition, the 90° uniaxial architecture samples were only measured in compression in order to avoid sample failures. All other architectures were tested over the full range of +70MPa to –70MPa. There was no evidence for any differences in modulus between tension and compression loading for any of the architectures tested. The data in Table 3-29 was all obtained using either the multiaxial or simple tensile extensometer. There were no systematic differences noted between the two extensometers.

Overall, the modulus data are fairly self consistent. The measured values of the transverse modulus (E_{22}) for the CMC composite system were particularly interesting. Mechanical and ultrasonic measurements both indicated a modulus of about 200Gpa for this orientation. Since the average reported fiber modulus for Hi-Nicalon is 279GPa and the average measured modulus of the SiC/Si matrix is about 372GPa, a transverse composite modulus with a value lower than either of the two main constituents would seem difficult to rationalize. However, the fiber coatings in this system have a substantial effect on the modulus of the composite. The modulus of the BN-based coating layers is particularly low – general handbook modulus values for CVD BN perpendicular to the deposition direction range as low as 2GPa. Even if the fiber coating has a thickness as low as 0.8 μm, properly accounting for the compliance of this material in the transverse micro-mechanical model leads to an expectation of a composite transverse modulus of about 200GPa. For thicker

coatings, this modulus is even lower. Physically, the reason why the low modulus coating is so important to the lowered transverse modulus is the fact that the high coating compliance effectively decouples the fiber from contributing to the transverse stiffness of the composite system. Micro-mechanically it is as if the composite has a hole where the fiber actually exists. The coating has a smaller impact on the fiber direction modulus (E_{11}), with micro-mechanical models predicting moduli between 310 and 345GPa depending on the thickness of the coating. Both of these micromechanical predictions are relatively consistent with the measurements of E_{11} and E_{22} made on unidirectional coupons in this test program (290GPa < E_{11} < 338GPa; 179GPa < E_{22} < 221GPa) . When laminate theory is applied using these moduli, the composite modulus of a balanced [0/90] laminate is predicted to be about 255GPa, a value that is almost exactly the historical average of data for GEGR prepreg MI composites.

The moduli for the 0°-90° lay-ups (both balanced and unbalanced) match reasonably well with simple laminate theory predictions. The moduli of the two types of unidirectional samples are somewhat lower than would be expected from the magnitude of the moduli of the 0°-90° lay-ups, which is likely a result of the difficulty in fabricating unidirectional samples and their qualitatively higher level of porosity.

Table 3-29. Summary of RT Elastic Modulus Data for Different Fiber Architectures Measured on Sample Fabricated in September, 2002.

Fiber Architecture	% of Fiber in Tensile Direction	In-plane Modulus (GPa)	Transverse Poisson's Ratio
0° unidirectional	100	304 ± 18 (5)	0.134 ± 0.006 (5)
90° unidirectional	0	200 ± 16 (3)	0.100 ± 0.011 (2)
[0-90-90-0]s	50	288 ± 15 (8)	0.114 ± 0.005 (3)
[90-0-0-90]s	50	277 ± 2 (3)	0.102 ± 0.005 (3)
[0-90-0]s	67	304 ± 6 (4)	0.124 ± 0.007 (4)
[90-0-90]s	33	263 ± 6 (4)	0.100 ± 0.010 (4)
[45 –45 –45 45]s	-	261 ± 6 (9)	0.175 ± 0.012 (6)
[45 –45 45]s	-	254 ± 9 (5)	0.173 ± 0.023 (5)

Values listed are in the form of "Average ± Standard Deviation (Number of Measurements)"

Measurements in the two in-plane directions of a 0°-90° lay-up (i.e. the [0-90-90-0]s and [90-0-0-90]s architectures) were statistically indistinguishable. Likewise the modulus values for 0° uniaxial and unbalanced 0°-90° with 67% of fiber in the measurement direction were also indistinguishable. However, modulus differences between any other subsets of the 0°-90° or uniaxial lay-ups were statistically significant. The difference between the 0°-90° and ±45° balanced lay-ups was also statistically significant.

3.4.3.8.2 Ultrasonic Modulus Measurements

The second method of measuring elastic moduli was through the use of an ultrasonic pulse-echo acoustic velocity measurement. Relatively thick (~5mm or 20-plies) samples

were needed for these measurements due to the size of the transducers and subsequent cross-sectional area required to effectively couple the transducers to the samples. Such thick samples require a significant amount of coated fiber, so only one uniaxial panel was fabricated at this thickness from which both 0° and 90° samples could be machined. Measurements were made with longitudinal, or compressive, waves for measurement of elastic modulus, and with transverse, or shear, waves for shear moduli.

Measurements were made on unidirectional samples in directions parallel to the fibers (E_{11}) and perpendicular to the fibers but still in the plane of the plies (E_{22}), but could not be performed perpendicular to the plies (E_{33}) due to the limited thickness of the samples. The moduli values determined from the sonic wave velocity measurements on unidirectional samples are listed in Table 3-30, and are compared to the moduli determined from the mechanical measurements. Overall the agreement between the moduli measured sonically or mechanically was fairly good. The sonic shear moduli G_{12} and G_{13} were practically identical, which would be expected from the symmetry of the samples.

Table 3-30. Average Elastic Moduli Calculated from Acoustic Wave Velocity Measurements on Unidirectionally Reinforced GE Prepreg MI Composites made in September, 2002 Compared to Values Obtained from Mechanical Measurements. All Values are in Units of GPa.

	E_{11}	E_{22}	E_{33}	G_{12}	G_{13}	G_{23}
Sonic	332 ± 4 (4)	196 ± 1 (2)	CNM	100 ± 3 (6)	101 ± 1 (2)	62 ± 3 (2)
Mechanical	304 ± 18 (5)	200 ± 16 (3)	CNM	111 ± 3 (6) †	CNM	77 ± - (1)‡

Values listed are in the form of "Average ± Standard Deviation (Number of Measurements)"
CNM = Could not measure

† Calculated from Young's moduli of 0°-90° and ± 45° samples

‡ Calculated from Young's modulus and Poisson's Ratio of a 90° unidirectional sample

3.4.3.8.3 Tensile Fracture Properties, 0°-90° Architectures

Following the modulus measurements most of the samples were tensile tested to failure at either room temperature or at 1204°C. The results of these tests are summarized in Table 3-31, and the room temperature tensile test results for the 0°-90° samples are shown in Figure 3-90. The trends in the fracture strength characteristics, including initial modulus, proportional limit stress, ultimate strength and strain to failure, as a function of the fraction of fiber in the tensile direction (as defined in Table3-29) are shown more clearly in Figure 3-91. Except for the 0° uniaxial sample, all of the parameters increased with increasing amount of fiber in the tensile direction. The reason that the observed ultimate strength and strain to failure did not continue to increase at 100% tensile fiber (i.e. with the 0° uniaxial sample) is because the fracture mode changed from primarily tensile failure to include a significant amount of shear failure with cracks running parallel to the fiber. This change in fracture mode can be observed in the photograph in Figure 3-92, which shows that the failure surfaces for the 0-90 samples were essentially perpendicular to the tensile axis, but a large portion of the failure surface runs parallel to the fibers for the 0° uniaxial sample.

Table 3-31. Summary of the Fiber Architecture Effects on the Tensile Fracture Behavior of GE Prepreg MI Composites Made in September, 2002.

Architecture	Test Temperature (°C)	Proportional Limit Strength (MPa)	Ultimate Strength (MPa)	Strain to Failure (%)
0° Uni	RT	247 ± 18 (2)	488 ± 15 (2)	0.63 ± 0.01 (2)
[0-90-0]s	RT	236 ± 19 (3)	497 ± 15 (3)	1.25 ± 0.11 (3)
[0-90-90-0]s [90-0-0-90]s	RT	197 ± 18 (2)	383 ± 17 (2)	1.10 ± 0.03 (2)
[90-0-90]s	RT	129 ± 2 (3)	234 ± 21 (3)	0.99 ± 0.20 (3)
[+45 –45 –45 +45]s	RT	173 ± 10 (2)	208 ± 4 (2)	0.57 ± 0.07 (2)
[+45 –45 +45]s	RT	152 (1)	154 (1)	0.14 (1)
0° Uni	1204°C	239 ± 41 (2)	292 ± 0 (2)	0.71 ± 0.10 (2)
[0-90-0]s	1204°C	239 (1)	390 (1)	0.85 (1)
[0-90-90-0]s [90-0-0-90]s	1204°C	169 ± 19 (2)	314 ± 20 (2)	0.88 ± 0.06 (2)
[90-0-90]s	1204°C	120 (1)	183 (1)	0.40 (1)
[+45 –45 –45 +45]s	1204°C	165 ± 2 (2)	202 ± 18 (2)	*
[+45 –45 +45]s	1204°C	121 (1)	163 (1)	*

Values listed are in the form of "Average ± Standard Deviation (Number of Measurements)"

* Could not be measured due to extensometer slippage

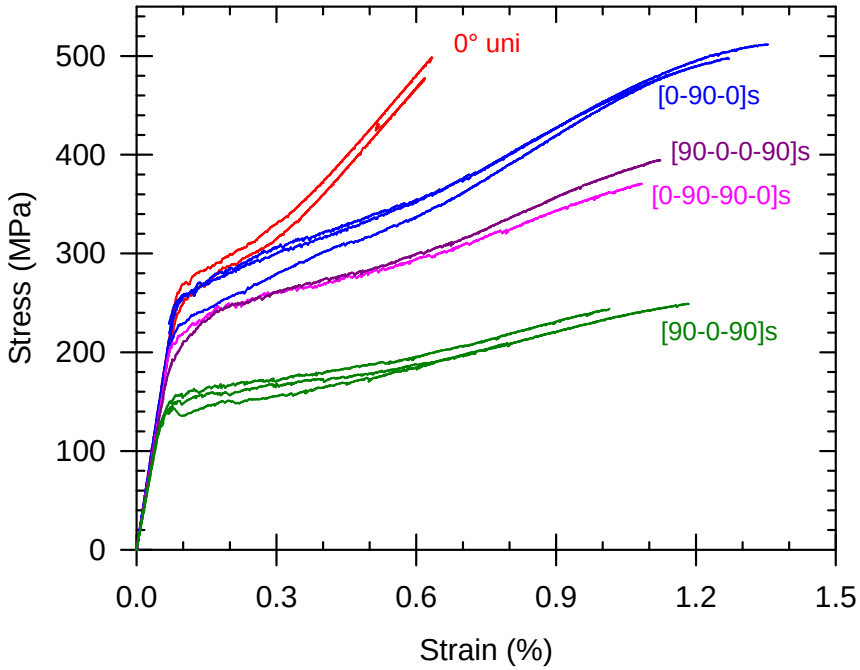

Figure 3-90. Tensile stress-strain behavior of GE Prepreg MI composites made in September, 2002 having various versions of 0°-90° fiber architectures.

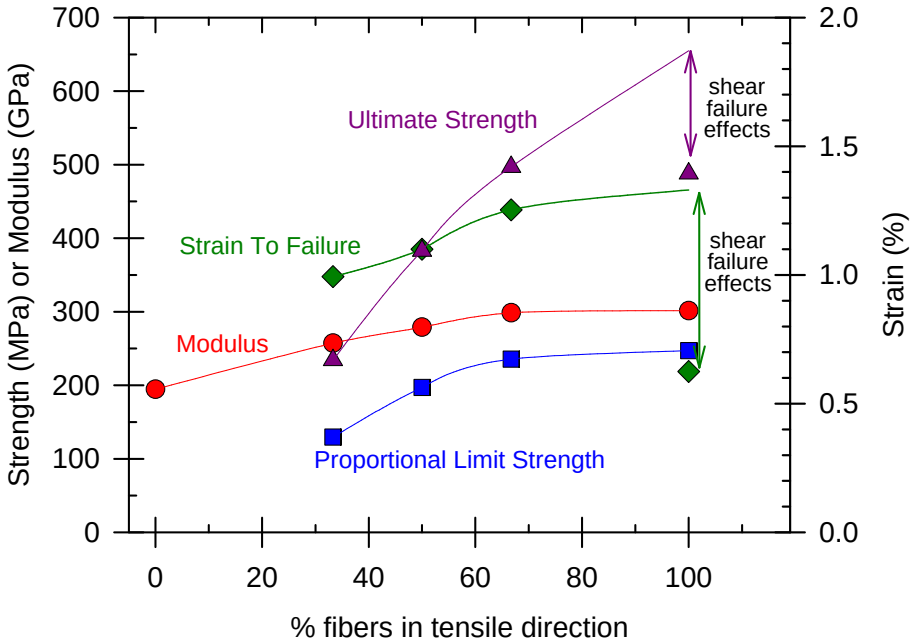

Figure 3-91. Tensile fracture parameters for GE Prepreg MI composites made in September, 2002 with 0°-90° fiber architectures as a function of the fraction of fiber in the tensile (0°) direction.

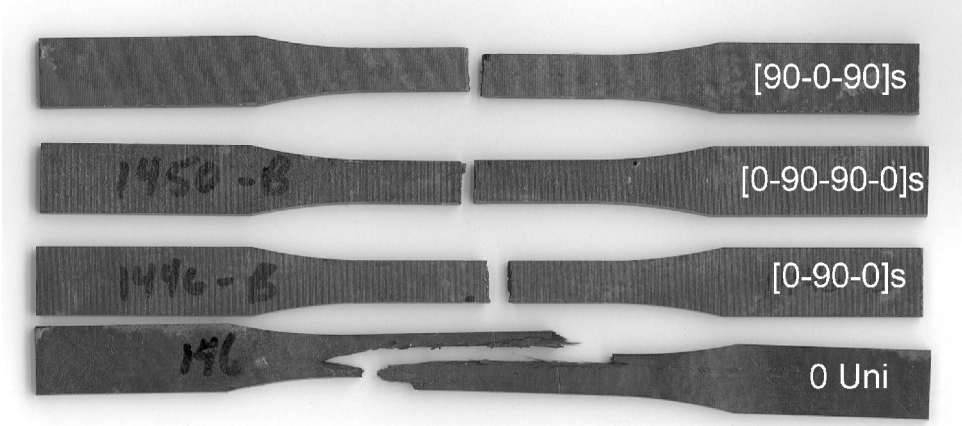

Figure 3-92. Photographs of fractured tensile samples with different 0°-90°-type fiber architectures. Samples including 90° plies showed fracture planes largely perpendicular to the tensile axis, indicative of tensile failure, whereas the 0° unidirectional sample shows a large amount of shear failure with the failure surface running parallel to the fiber direction.

3.4.3.8.4 Tensile Fracture Properties, ±45° Architectures

A similar effect of the influence of shear failures was noted in the samples with ±45° fiber architectures. Room temperature stress-strain behavior of both balanced, [45 –45 –45 45]s, and unbalanced [45 –45 45]s, ±45° lay-ups are shown in comparison to a balanced 0°-90° lay-up in Figure 3-93. The apparent ultimate strength and strain to failure of the ±45 samples were substantially reduced compared to the 0-90 orientation; however, this was again due to the change in failure mode from tensile to shear failure. The photograph in Figure 3-94 shows 0°-90°, balanced ±45 and unbalanced ±45 tensile bars after testing. The fracture surface of the ±45 balanced bar has a "jagged" appearance even down to the individual ply level due to the fracture surface locally running parallel to the fiber direction. This behavior indicates that each ply wanted to fail in shear but they were constrained from doing so globally by the influence of the adjacent plies. At best, this situation represents a mixed mode of tensile and shear failure. The fracture surface of the unbalanced ±45 sample is angled at about 30° to the tensile axis, tending to run parallel to the fibers in the majority of the plies. Having only 1/3 of the plies in the opposite orientation was not sufficient to prevent a mostly shear-type failure, and thus the relatively low strength and strain to failure values observed in the test. In retrospect, this change of failure mode with fiber orientation is not surprising. The impact of this shear failure mode on component designs is not clear since we have never observed that type of failure in any of the rig, engine and ballistic impact testing done on MI CMC components.

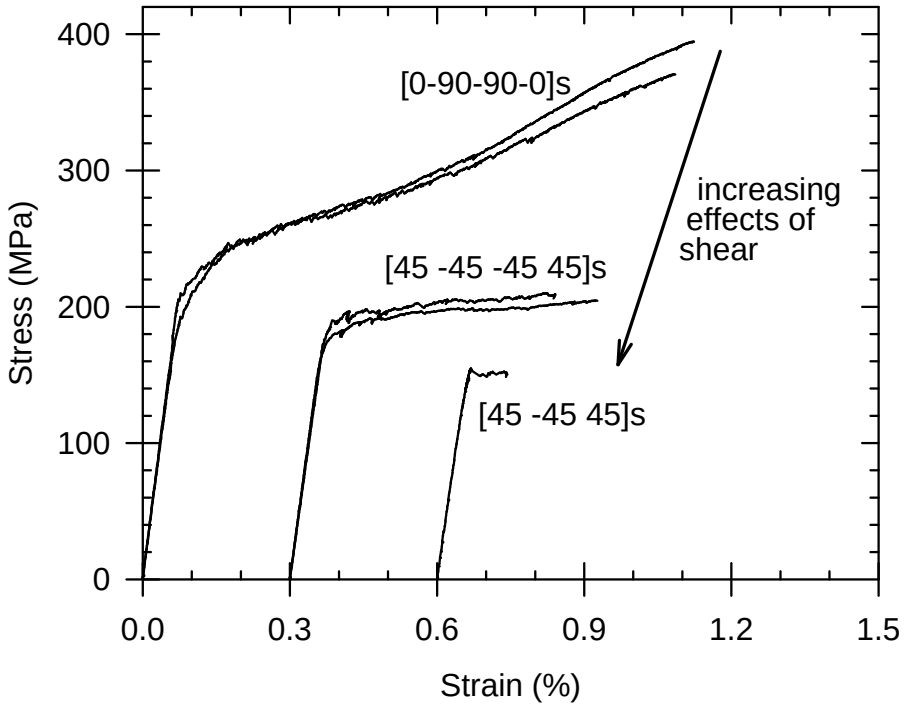

Figure 3-93. Tensile stress-strain behavior of balanced and unbalanced ±45 architecture samples of GE Prepreg MI composite compared to a balanced 0°-90° sample.

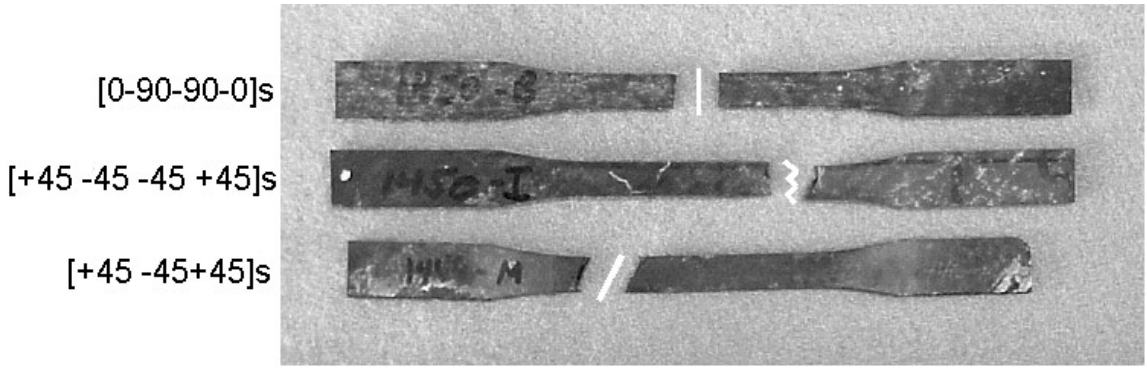

Figure 3-94. Photograph of failed tensile bars having balanced 0°-90°, balanced ±45° and unbalanced ±45° fiber architectures. The fracture surface of the 0°-90° bars run mostly normal to the loading axis. The fracture surfaces of the ±45° bars are at angles to the tensile axis either locally, in the balanced ±45° sample, or globally, as in the unbalanced ±45° sample.

3.4.3.8.5 High Temperature Fracture Behavior

High temperature (1204°C) tensile testing was conducted in air on a few remaining samples in order to verify that the trends observed at room temperature were repeatable at high temperature. A relatively fast strain rate (~2.5×10^{-3}/s) was used at 1204°C in order to minimize environmental (oxidation) effects. Results of these tests are summarized in Table 3-31. Overall there was a roughly 20% reduction in ultimate strength in the cross

ply composites when going from RT to 1200°C, which is consistent with the fiber strength reduction with temperature. The measured ultimate strength was actually higher at 1200°C than at RT for the unidirectional samples, but this was primarily a result of the change in failure mode to include less shear effects at high temperature, as evidenced by a more planar fracture surface. Strain to failure showed a similar trend, though the strain was particularly low for the [90-0-90]s biased lay-up. This result could be caused by the relatively low volume fraction of fiber in the tensile direction for this architecture (roughly 7.5 volume %), or it may be a result of extensometer slipping during the test, as suggested by the jagged nature of the stress-strain curve. On average, the proportional limit was relatively unchanged going from room temperature to 1204°C, and the initial Young's modulus dropped by about 8% on average.

The dependence of the high temperature fracture properties on the amount of tensile fiber for the 0°-90° architectures is shown in Figure 3-95. The trends for modulus, proportional limit and ultimate strength are very similar to the trends at room temperature. The drop in strain to failure at the higher % fiber in the tensile direction values was unexpected. This drop cannot be attributed to a change in fracture mode from tensile to shear, as was observed at room temperature, since the ultimate strength values did not show a similar drop.

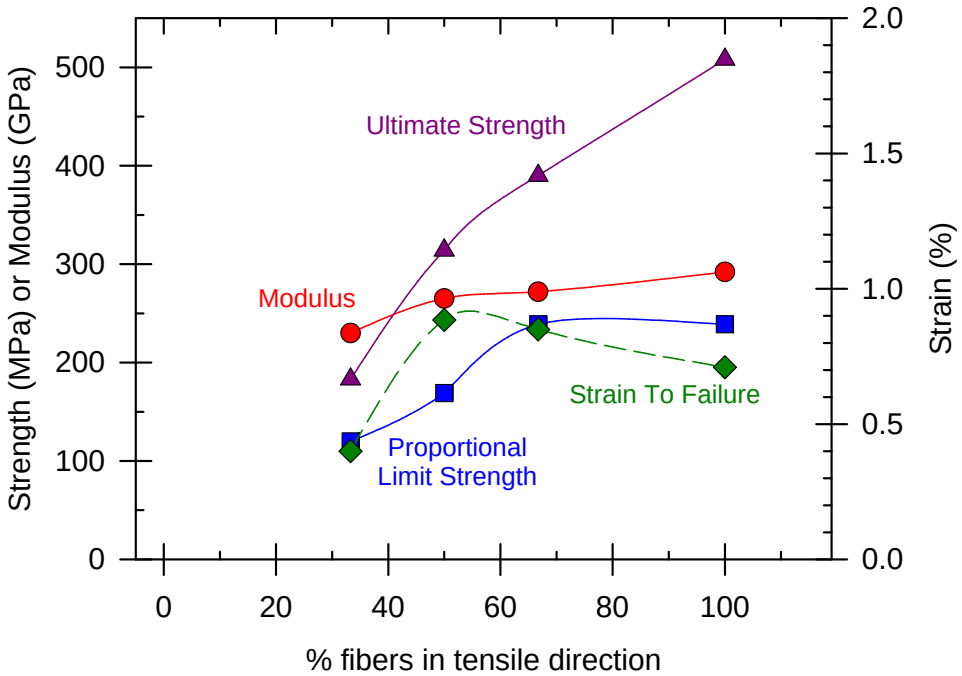

Figure 3-95. Tensile fracture properties of 0°-90° GE Prepreg MI composites measured at 1204°C as a function of the fraction of fibers in the tensile direction.

The data for the +/-45° lay-ups was not as conclusive, largely due to strain measurement errors introduced by extensometer slipping during the high temperature tests. There was substantial jitter in the extensometer signal beyond the proportional limit for all of the high temperature tests. About all we can conclude is that the Young's modulus dropped by

about 15% between RT and 1204°C, which was more than observed in the 0-90 lay-ups, and that the ultimate strength values were relatively unchanged.

3.4.3.8.6 Matrix Cracking Characterization

Obviously from the tensile test results discussed above, the ultimate strength and strain behavior of prepreg CMC's differ considerably when tested in the direction of the reinforcing fiber (i.e. 0°-90°) and tested at an angle to the fiber orientation (i.e. ±45°). However, the proportional limit strength was relatively unaffected by testing orientation. This would suggest that the matrix cracking behavior between the two orientations are also similar. Fluorescent penetrant inspection (FPI) was performed on fractured test bars with both balanced 0°-90° and ±45° orientations in order to check this supposition. Photographs taken with ultra-violet illumination following soaking in fluorescent penetrant dye are shown in Figure 3-96. The fluorescent dye highlights matrix cracks. In 0°-90° samples we observed the typical matrix cracking perpendicular to the tensile axis, which is also perpendicular to the fiber direction (Figure 3-96-A). Matrix cracks in failed ±45° samples also appeared to have matrix cracks running perpendicular to the loading direction, and therefore at 45° to the fiber orientation, but the cracking pattern was complicated by the final fracture surface that locally ran at 45° to the loading direction (Figure 3-96-B). An additional ±45° sample was loaded to 0.25% strain, which is well above the proportional limit strain but well below the strain to failure, and then characterized with FPI (Figure 3-96-C). This sample clearly showed matrix cracking running perpendicular to the loading direction, which is at a 45° angle to the reinforcement fibers. These observations confirm that the matrix cracking process is dominated by tensile fracture of the matrix regardless of the fiber orientation, which is why the proportional limit strengths were relatively unaffected by fiber orientation for balanced architectures.

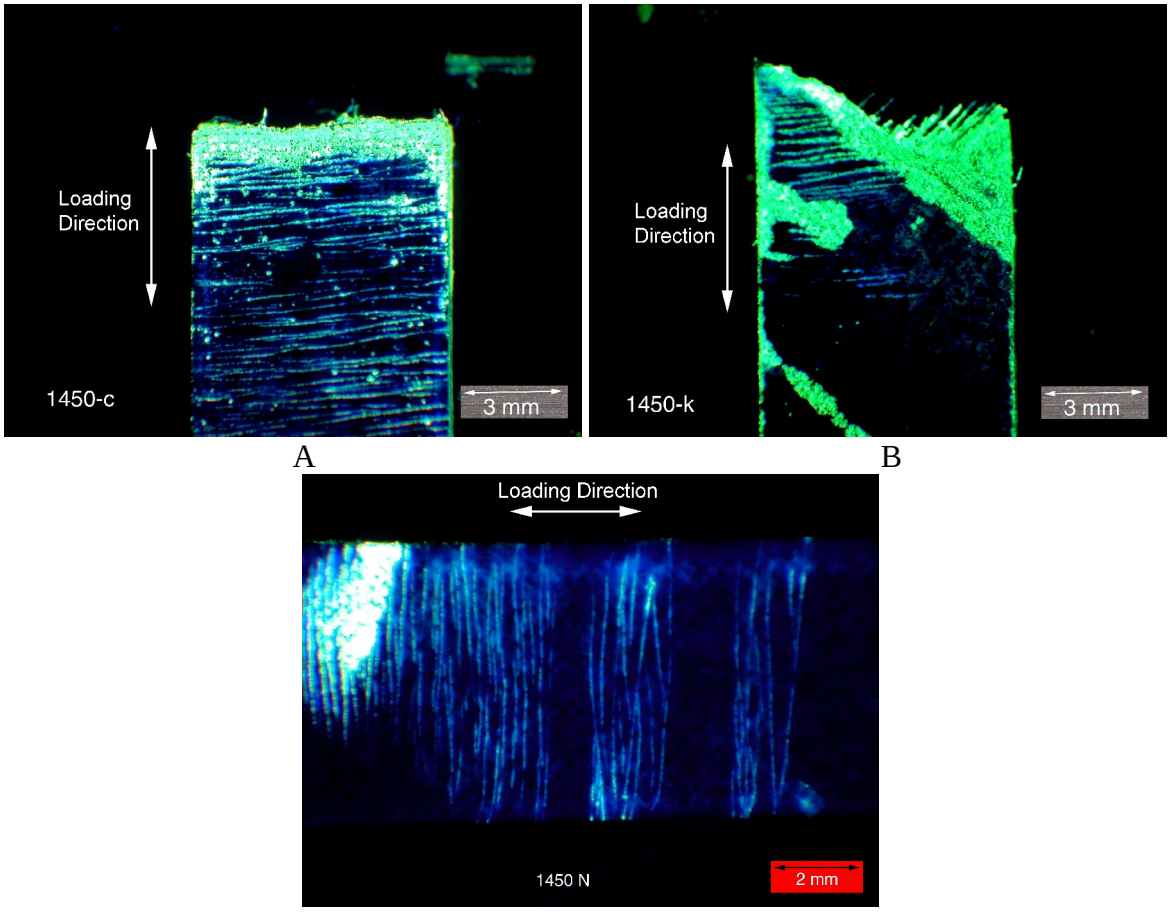

Figure 3-96. Fluorescent Penetrant Inspection photographs of GE Prepreg MI composites following mechanical testing. The light lines across the sample are decorated matrix cracks. A – a 0°-90° sample tested to failure; B – a ±45° sample tested to failure; C – a ±45° sample loaded only to 0.25% strain. In each case the matrix cracks primarily run perpendicular to the loading direction.

3.4.4 Characterization Under Steam Oxidation Conditions

There are two mechanisms by which CMC's can be degraded by exposure to high temperatures and high water vapor environments. The first mechanism has to do with oxidative attack of the fiber-matrix interface, particularly with regard to the BN-based fiber coatings. Under dry oxidation conditions the BN interface coatings of any exposed fibers simply oxidize to form B_2O_3 glass. The B_2O_3 (mixed with SiO_2 from oxidation of neighboring fibers and matrix) is a protective barrier against further oxygen penetration, and thus oxidation is limited to the near-surface region of the exposed fiber coatings. However, under conditions with water vapor present the B_2O_3 oxidation product hydrolyzes to form volatile $H_xB_yO_z$ compounds that readily evaporate from the surface. Fresh fiber coating is thereby continually exposed for oxidative attack, analogous to the oxidation of a carbon fiber coating when exposed to oxidation. The overall effect of such

an oxidation mechanism is that substantial volumes of the CMC can be rendered brittle even though there is little visible attack to the CMC surface.

The second mechanism whereby water vapor enhances oxidative degradation of Si-based ceramic composites is through volatilization of the bulk CMC itself. Silicon-based ceramics, such as SiC ,Si_3N_4 and $MoSi_2$, are generally accepted as having excellent oxidation resistance because of the formation of a stable, highly impermeable layer of SiO_2 oxidation product. However, under atmospheres with high water vapor pressure the SiO_2 layer becomes volatile from the formation of silicon hydroxide species[5,6]. Under such circumstances the protective SiO_2 layer is constantly volatilizing from the surface while new SiO_2 is being formed by oxidation of the substrate. The overall effect is a linear recession of the material surface with time, the rate of which is sufficient to compromise the integrity of a composite when exposed in gas turbine like environments, which can contain up to 1 atmosphere of H_2O.

In order to better understand the impact of these two mechanisms on the integrity of the ceramic composite materials being investigated, various materials tests were conducted in water-containing environments. Three general types of testing were performed: 1) exposure of samples to high temperature, high moisture environments with monitoring of sample mass in order to measure volatilization kinetics, 2) exposure of samples followed by tensile testing to evaluate the effects of exposure on retained mechanical properties, and 3) performance of the actual mechanical testing, including hold time and high cycle fatigue, under high water content conditions. This testing was performed under program task 3.2.b. Composite Property Measurement, subtask B - Steam Oxidation Characterization.

3.4.4.1 Volatilization Rate Measurements

Long-term steam oxidation exposures were performed in one of two sets of custom-built laboratory apparatus. A schematic diagram of the overall steam exposure systems is shown in Figure 3-97 House de-ionized water was further purified using a Millipore MilliQ Plus water purification system, and then fed using a metering pump into a steam generator furnace. All piping downstream of the steam generator is heated to above 120°C to prevent any condensation of the water vapor. Metered oxygen was then mixed into the steam flow and fed into the actual sample exposure furnace. Samples for exposure were hung from a linear slide mechanism on a high purity alumina rod using alumina and platinum fixtures. The linear slide would cycle the samples into and out of the exposure furnace with an ~30 second transit time. While the samples were inside the furnace the steam control valve directed the steam/oxygen flow into the furnace where it flowed upward past the samples. When the samples were translated out of the furnace the steam control valve bypassed the exposure furnace and directed the steam/oxygen flow directly to the exhaust. This was done to keep from flooding the laboratory with steam while the samples were in the out-of-furnace position.

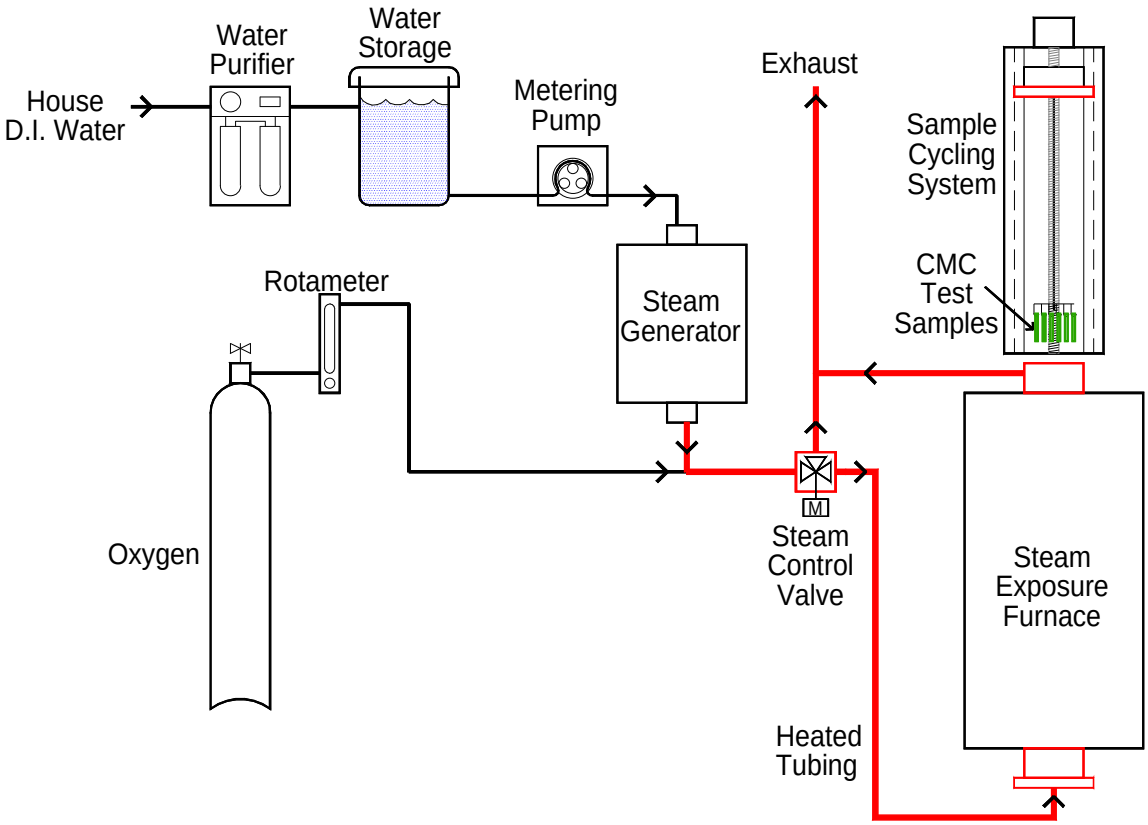

Figure 3-97. Schematic diagram of the steam furnace exposure apparatus used to perform environmental testing of CMC coupon samples.

Initial testing was started using a relatively small steam exposure furnace that limited both the number and size of the samples that could be accommodated. A second apparatus utilized a much larger furnace that allowed testing of a larger number of samples, which were also of sufficient size to allow for post-exposure tensile strength testing. The second apparatus was used for measuring oxidation/recession rates and for evaluating the effects of such steam oxidation treatments on the fiber-matrix interface coatings and their subsequent effects on the mechanical properties of the composites.

The first exposure run in the smaller furnace used twelve samples arranged in two layers, top and bottom within the furnace. The furnace cycle used was ~1 minute to insert the samples into the furnace hot zone, one hour and 50 minutes of exposure, ~1 minute to extract the samples out of the hot zone and ~8 minutes cooling in the room ambient. This overall cycle was repeated until the total desired hot exposure time was reached. The samples were periodically removed from the apparatus and weighed on a laboratory scale with 0.02mg repeatability in order to monitor the mass change with time. A cyclic exposure was used to see if any of the samples formed a non-adherent oxide layer that would spall during thermal cycling, and thereby greatly increase the mass loss rates. The test was run for a total of 500 cycles, or about 917 hours of hot steam exposure. The exposure temperature inside the furnace hot zone was 1204°C in an atmosphere of 90%

H_2O + 10% O_2 flowing at velocity of 4cm/s past the samples. The results obtained from the first run are shown graphically in Figure 3-98.

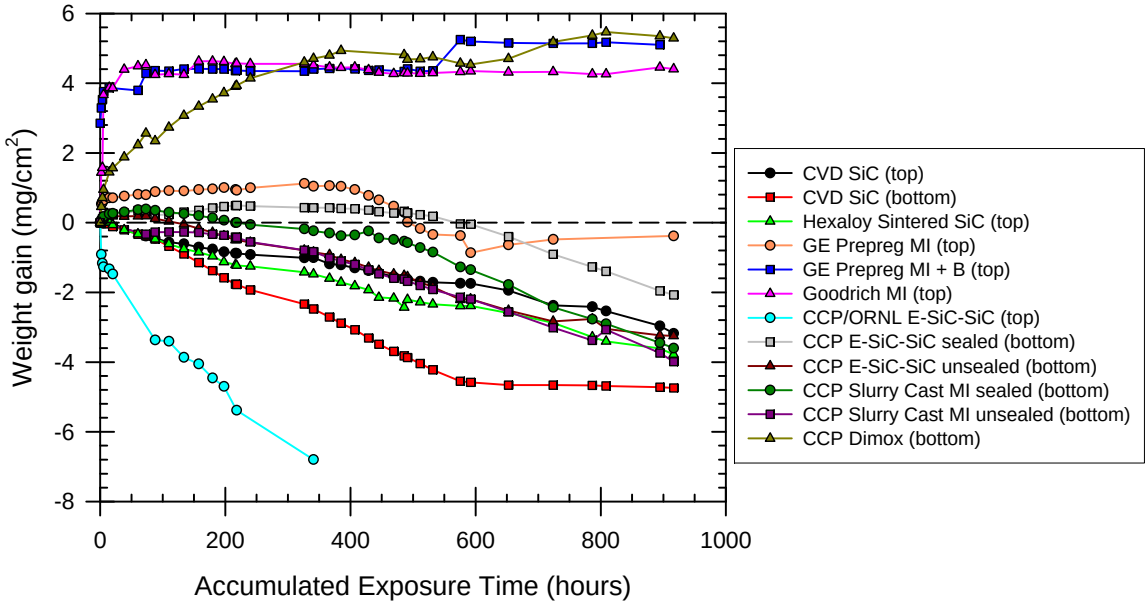

Figure 3-98. Mass gain or loss measured as a function of exposure time in the first steam exposure run in the small cyclic steam furnace. Exposure conditions were 1204°C in 90% H_2O + 10% O_2 flowing at 4cm/s with cycles to room temperature every 2 hours.

Two samples of high purity CVD SiC (Morton, Inc.) were included as reference standards for measuring the fundamental rate of SiC oxidation/volatilization. A sample of Hexaloy sintered SiC was also included to serve as a calibration standard against exposure treatments being done in the "Kaiser rig" at ORNL. The CMC samples in this run included a standard GE Prepreg composite, a GE Prepreg sample with the boron-doped matrix, a piece of CVI Enhanced SiC-SiC composite made by CCP (at the time known as Dupont-Lanxide Composites) obtained from ORNL, a piece of DIMOX composite made by CCP and a piece of slurry cast MI composite made by Goodrich. Two samples each of CCP CVI Enhanced SiC-SiC and CCP slurry cast MI composite (with Sylramic™ fiber) were included. These four samples had an external coating of CVD SiC to seal the surfaces of the composites, but one of each composite was machined after seal coating to re-expose fibers and fiber coatings at the edges of the samples, hence the "sealed" and "unsealed" designations.

This first steam exposure test was a practical learning experience in terms of identifying unwanted material interactions that impacted the mass loss data in unusual ways. Both of the GE Prepreg MI and the Goodrich slurry cast MI samples showed substantial initial mass gains on exposure. This was attributed to reactions between the samples and the

platinum wires from the sample support fixture, causing bonding between them and "sticking" of Pt to the sample surfaces when removing them from the fixtures for mass measurements. As these three samples lacked any seal coat, and would therefore have pure silicon phase at the sample surfaces, they were particularly susceptible to this interaction. The other samples that had only SiC or alumina in contact with the support wires did not show this interaction.

There was also a distinct trend in mass loss rates for samples in the bottom rank versus those in the top rank. This is clearly shown in the mass loss for the CVD SiC samples, where the mass loss in the top rank is only ½ that of the sample in the bottom rank. Other samples in the top rank, namely the GE Prepreg MI and the Goodrich slurry cast MI samples, showed very little mass loss. Recall that the steam/oxygen atmosphere flows upward in the furnace, passing over the bottom rank of samples first. These results strongly suggest that the atmosphere in the furnace was being saturated with $Si(OH)_x$ volatilizing from the bottom rank of samples, which then suppressed volatilization from the top rank of samples. The only sample in the top rank that showed rapid mass loss was the unsealed E-SiC-SiC sample obtained from ORNL. However, its mass loss rate was anomalous as it was more than 3X the rate for the bottom CVD SiC sample. Post-exposure microstructural analysis revealed that the rapid mass loss from this sample was caused by the oxidation and volatilization of the B-rich "enhancement" phase within the matrix and not by the volatilization of SiO_2 from surface oxidation.

Mass loss of the CCP E-SiC-SiC and slurry cast MI samples on the bottom rank also displayed some unexplained trends. Initially the mass loss rates for the sealed samples were lower than those from the unsealed samples, which could be explained by additional volatilization of exposed BN fiber coatings. However, the mass loss rates, at least initially, were still lower than that of the CVD SiC sample on the bottom rank. After about 500 hours of exposure the mass loss rates for these samples increased somewhat and became comparable to the overall average rate of the CVD SiC even though the mass loss rate from the CVD SiC decreased at about the same time. Mass loss rates for several of the samples are listed in Table 3-32. The rates listed for the CVD SiC and sintered SiC samples are the average rates over the total 917 hour exposure while those for the E-SiC-SiC and slurry cast MI samples are only for time beyond 500 hours. If the mass change is assumed to result solely from the oxidation/volatilization of SiC then a mass loss rate of 1 mg/cm^2-hr corresponds to a surface recession rate of 3.1μm/hr.

Table 3-32. Mass Loss Rates From the First Steam Exposure Run in the Small Cyclic Steam Furnace Apparatus

Sample Type	Position	Mass Loss Rate (mg/cm^2-hr)
CVD SiC	top	$3.09x10^{-3}$
CVD SiC	bottom	$6.27x10^{-3}$
Hexaloy Sintered SiC	top	$4.06x10^{-3}$
CCP E-SiC-SiC sealed	bottom	$5.74x10^{-3}$
CCP E-SiC-SiC unsealed	bottom	$4.01x10^{-3}$
CCP Slurry Cast MI sealed	bottom	$7.17x10^{-3}$
CCP Slurry Cast MI unsealed	bottom	$5.18x10^{-3}$
average of bottom samples	bottom	$5.67x10^{-3}$

The DIMOX composite sample showed nearly parabolic mass gain with exposure. This was attributed to oxidation of residual aluminum alloy in the composite matrix.

The most troubling observation from the first steam furnace exposure test was that the majority of specimens showed visibly noticeable, white oxidation product layers. Metallographic examination indicated that most of the CMC samples had porous, partially crystallized silica oxidation product layers on the surfaces with local thickness as high as 100μm. Under high SiO_2 volatilization conditions typical of a turbine we would expect a relatively thin (few microns at most), coherent, amorphous SiO_2 oxidation product layer. The thick, porous oxide is consistent with those observed on SiC-based materials exposed in the ORNL Kaiser rig, which has an essentially static atmosphere. Under these conditions the high water content acts to mineralize the silica oxidation layer, promoting its crystallization to form cristobalite with a porous morphology. The presence of the porous oxide indicated that the mass loss measurements were not indicative of a paralinear oxidation/volatilization mechanism, but of a much more complicated oxidation mechanism, and that determining a kinetic model for this situation would likely be impossible.

The most likely cause for the porous oxide mechanism was the low flow rate of gas in the steam furnace. Under low flow conditions and laminar flow there are boundary layers set up along any surface, including those of the test samples, that would impede the outward diffusion of the $Si(OH)_x$ species. Thus the volatilization rate would be dependent on the local flow conditions next to each sample, which could vary from sample-to-sample in the furnace.

Our initial attempt to get around this gas flow problem was to lower the number of samples in the furnace down to a single layer, and to arrange the samples more uniformly through the furnace cross section. Eliminating the second layer also eliminated the problem of $Si(OH)_x$ gas saturation affecting a second rank of samples. The sample holder assembly was also modified so that no platinum wire contacted any of the samples. The second exposure run was then done under identical cycle times, atmosphere composition and flow conditions as run #1. The mass change data from this run are shown in Figure 3-99.

Trends in the mass loss data for several of the samples were consistent with the first steam test. The mass loss rate for the CVD SiC sample was $4.19x10^{-3}mg/cm^2$-h, which is in reasonable agreement with the value measured in the lower rank of the first test. The sintered SiC sample had a mass loss rate of $10.2x10^{-3}mg/cm^2$-hr, or about 2.5X that of the first test, but in the first test it was in the top rank and was therefore affected by gas saturation. Nevertheless, the higher mass loss rate for the sintered SiC compared to that of the CVD SiC is not readily explained. The Goodrich slurry cast MI sample showed a mass loss rate similar to the CVD SiC sample, averaging $4.62x10^{-3}mg/cm^2$-hr. However, both the unsealed CCP CVI Enhanced SiC-SiC sample and the GE Prepreg MI sample showed mass gains with exposure. It was obvious from visual inspection that porous oxide was again forming on the composite samples, which explained the observed mass gains for these samples. Thick oxides were not observed on the SiC samples, and thus true paralinear oxidation/volatilization may have been achieved for these specimens.

The observed mass gains for the composite samples and the formation of the porous oxide layer again indicated that we had not achieved sufficient gas flow conditions to observe a strict paralinear oxidation/volatilization mechanism for these samples. A third test was therefore run at a higher gas flow rate. We had hoped to raise the flow rate by 2 orders of magnitude; however, at such high flows the furnace and specimen rack were being actively cooled by the incoming gas, making it impossible to adequately control the temperature of the samples. The highest practical gas flow rate where we could maintain control of sample temperature was determined to be 16cm/s, or in increase of 4X over the flow in the first two exposure tests.

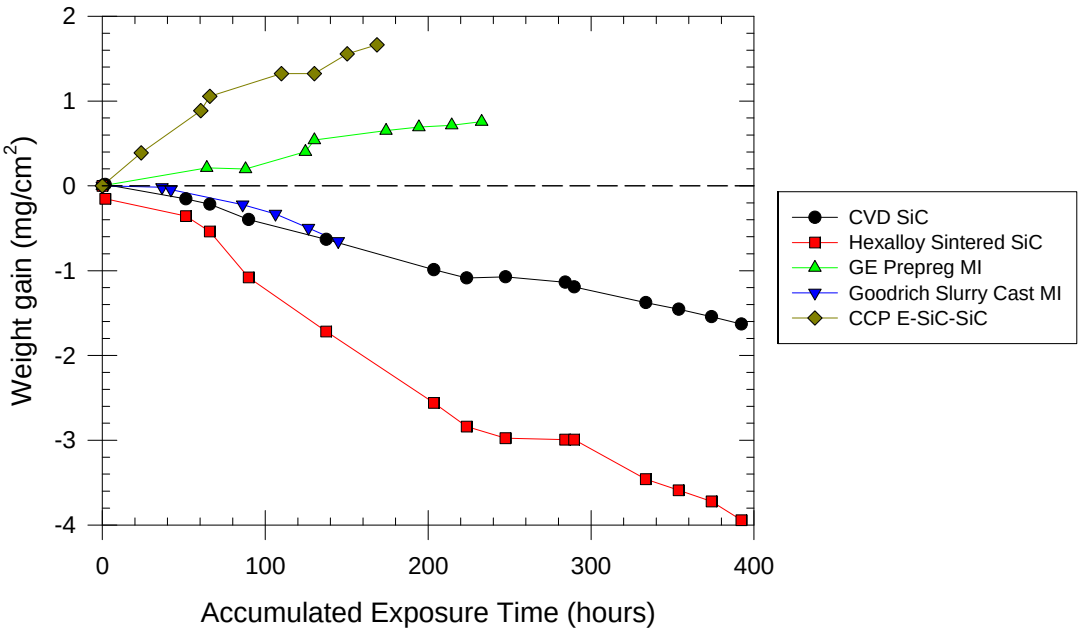

Figure 3-99. Mass gain or loss as a function of exposure time from steam exposure run #2 in the small cyclic steam furnace apparatus. Exposure conditions were 1204°C in 90% H_2O + 10% O_2 flowing at 4cm/s with cycles to room temperature every 2 hours.

Six new samples, including high purity CVD SiC, sintered SiC and four CMC specimens, were then exposed under this higher flow rate condition. Mass change data from this run are given in Figure 3-100. Although the SiC samples would appear to be showing paralinear mass loss, three of the four CMC samples were still showing an overall mass gain from exposure. The mass loss rates for the SiC samples were 1.8X those measured in exposure run #2, and the samples were relatively free of thick oxide. The CMC samples showing mass gains, however, still had localized regions of porous oxide formation.

In a semi-infinite flow field with no boundary effects a 4X increase in the flow rate would be expected to give a 2X increase in volatilization rate, which is close to the 1.8X observed for the monolithic SiC samples. However, in the small confines of the laboratory furnace the sample-to-sample spacing is influencing the thickness of the gas flow boundary layers around the specimens, so an increase of less than 2X is not surprising. GE developed a volatilization model based on first principal thermodynamic and gas flow principals. Under the conditions used for the laboratory tests this model predicts a mass loss rates for pure SiC between 0.003 and 0.012 mg/cm^2-hr depending on the flow rate and boundary layer assumptions used. These values correspond pretty well to the observed volatilization rates for the CVD SiC samples of 0.0042 to 0.0079 mg/cm^2-hr measured in runs #2 and #3, respectively.

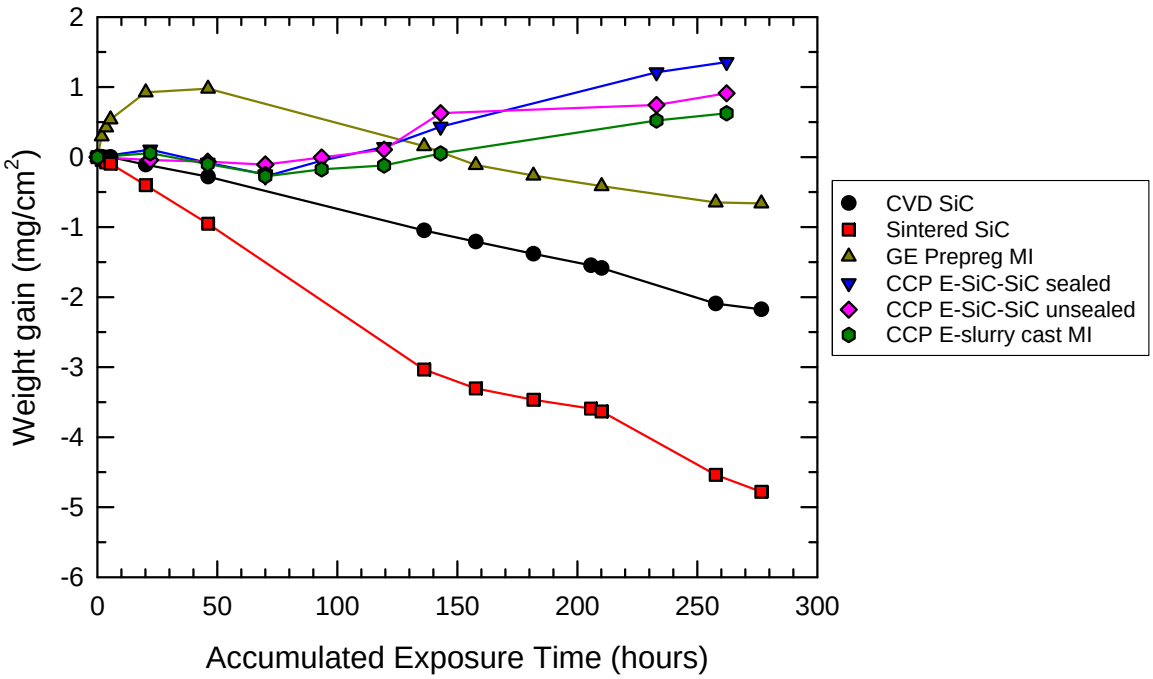

Figure 3-100. Mass gain or loss as a function of exposure time from steam exposure run #3 in the small cyclic steam furnace apparatus. Exposure conditions were 1204°C in 90% H_2O + 10% O_2 flowing at 16cm/s with cycles to room temperature every 2 hours.

Within the confines of achievable flow rates in the laboratory steam furnace apparatus, we were unable to obtain sufficient gas flow rates to clearly activate the paralinear oxidation/volatilization mechanism on the CMC samples. Moreover, actual gas turbine flow conditions would clearly be in a turbulent flow regime, and thus laboratory exposures limited to laminar flow regimes would not simulate real use conditions. For these reasons use of the laboratory steam furnaces for measuring recession rates was discontinued in favor of long-term combustion gas exposure tests to be described in Section 3.8.4. However, cyclic steam furnace exposure was still considered a useful tool for evaluating the effects of wet oxidative exposure on CMC mechanical properties. Since the most likely mode of mechanical degradation was through oxidative attack of the fibers and fiber/matrix interfaces, each of which are mostly internal to the CMC, the external gas flow rates would have minimal impact on the expected mechanical degradation. In order to tensile test the CMC samples following oxidative exposure minimum practical sample length of about 10cm was needed. We also wanted to be able to test a larger number of samples at a time for the sake of efficiency. It was for these reasons that the second cyclic steam apparatus with the larger sample exposure furnace was assembled.

3.4.4.2 Effect of Cyclic Steam Oxidation on Mechanical Properties

Sample exposures in the large cyclic steam furnace occurred during three separate campaigns. In the first campaign, from mid 1998 to early 1999, five separate runs were conducted. These runs included many different CMC materials and several different

exposure conditions. The main goals of these runs was to scope out the extent of any wet oxidation problems with the various CMC systems to help us in downselecting to a preferred set of materials for follow-up testing in 1999. The sample types and exposure conditions that were tested in the first campaign are listed in Table 3-33.

CVD SiC samples were inserted in most furnace runs to serve as a reference with regard to surface oxidation/volatilization. The overall observations on the CVD SiC samples, which were similar to the appearance of the SiC-based composite samples, was that the bottom 2cm of the sample showed thin glassy oxide and evidence of surface recession, whereas the upper 8cm of sample showed increasing accumulation of the porous oxide. Two phenomena contribute to the change in oxidation mechanism along the length: 1) the saturation of the gas phase with $Si(OH)_x$ and 2) the increase in thickness of the gas boundary layer with length along the samples. Consequently even the mass loss data from the CVD SIC samples were not really indicative of a pure surface oxidation/volatilization condition.

During the initial run in the large furnace four specimens were pulled from the steam furnace after 100 hours exposure and tensile tested. The results from these early samples are shown in Table 3-34, where they are compared to the tensile properties of test bars taken from the same source panels but tested with steam exposure. For three of the four composite systems tested the oxidation exposure had little effect on the mechanical properties. The GE prepreg MI material was essentially unchanged (the low matrix cracking stress of the as-fabricated specimen is due to that particular sample having a larger than normal warpage which introduced significant bending stresses). Both the Goodrich slurry cast MI and CCP Enhanced SiC-SiC samples showed minor reductions in ultimate strain and possibly ultimate strength. The DIMOX sample however degraded quite substantially with the ultimate strength dropping by 65% and the ultimate strain dropping by over 80%. These results indicated that the DIMOX system is particularly susceptible to degradation by steam oxidation. Although all of these samples had exposed fiber ends, the E-SiC-SiC composite, which has a similar fiber coating as does the DIMOX composite, did not show this severe degradation. This observation would suggest that the degradation of the DIMOX sample may not be caused by end-on attack of the fiber coatings but rather by oxidative degradation by oxygen or water penetration through the surfaces. Based on this result no further cyclic steam testing was performed on DIMOX composites.

Table 3-33. Summary of Samples Exposed in the "Large" Cyclic Steam Furnace Test in 1998 to early 1999.

Test Conditions	Exposure Time (hrs)	Material†	Sample Conditions*
Run #1	100	GE Prepreg / A	edges
1200°C	100	Goodrich MI	edges
90% H_2O + 10% O_2	100	CCP E-CVI	edges
4 cm/sec‡	100	CCP DIMOX	edges
	500	CVD SiC	as-fab
	500	GE Prepreg / A	as-fab, edges, precracked
	500	GE Prepreg + B / A	as-fab, edges, precracked
	500	GE Prepreg / C	as-fab, edges, precracked
	500	Goodrich MI	as-fab, edges, precracked
Run #2	500	CVD SiC	as-fab
1200°C	500	CCP MI / Sylramic	as-fab, edges, precracked
90% H_2O + 10% O_2	500	CCP E-MI	as-fab, edges
4 cm/sec	500	CCP E-CVI	as-fab
	500	CCP E-CVI sealed	as-fab, edges
	1000#	GE Prepreg / A	as-fab
Run #3	98	CVD SiC	as-fab
1200°C	98	CCP MI	as-fab
90% H_2O + 10% O_2	98	CCP CVI	as-fab
16 cm/sec			
Run #4	500	ACI MI, Hi-Nic	precracked
815°C	500	ACI E-SiC/SiC	as-fab
20% H_2O + 80% O_2			
16 cm/sec			
Run #5	500	GE Prepreg / A	as-fab, precracked
815°C	500	GE Prepreg / C	as-fab, precracked
90% H_2O + 10% O_2	50	CCP MI	as-fab, precracked
16 cm/sec	500	CCP MI	as-fab, precracked

† "Prepreg / A" is standard matrix GE prepreg MI composite with the configuration A fiber coating; "Prepreg + B / A" has additional B-containing phase added to the matrix and configuration A fiber coatings; "Prepreg / C is standard prepreg matrix with configuration C fiber coatings; "CVD SiC" is high purity monolithic SiC from Morton; "Goodrich MI" is slurry cast MI composite supplied by Goodrich Aerospace, Inc.; "CCP MI / Sylramic" is slurry cast MI composite supplied by CCP (then known as Allied Signal Composites, Inc.) reinforced with Sylramic™ fiber; "CCP E-MI" is slurry cast MI composite with an oxidation enhancement added to the matrix; "CCP CVI" is a CVI SiC-SiC composite supplied by CCP; "CCP E-CVI" is CVI SiC-SiC with a matrix oxidation enhancement supplied by CCP; "CCP E-CVI sealed" is enhanced CVI SiC-SiC with a CVD SiC seal coating supplied by CCP; "CCP MI" is slurry cast MI composite supplied by CCP; "CCP DIMOX" is an oxide matrix CMC made by CCP using the directed metal oxidation approach. All composites were reinforced with Hi-Nicalon™ fiber unless otherwise noted.

* "as-fab" means in the as-fabricated state with sample edges passivated during final densification and having no exposed fibers or fiber coatings; "edges" means that the sample edges were machined following final densification and therefore there were exposed fibers and coatings along the specimen edges; "precracked" means the samples were tensile tested to 0.2% strain to introduce matrix cracks into the specimens before exposure in the steam furnace; "faces exposed" means the large faces of the sample were machined, thereby exposing fiber and fiber coatings over the entire surface.

‡ Gas velocities are calculated from mass flows and are given as equivalent velocity at 25°C, 1 atmosphere conditions.

Two samples were exposed for 500 hours in Run #1 and 500 hours in Run#2, giving a total exposure of 1000 hours.

Table 3-34. Room Temperature Tensile Properties of Edge-Exposed Composite Specimens Before and After Steam Oxidation at 1200ºC for 100 Hours from Run #1 of the Large Cyclic Steam Furnace.

Material	Matrix Cracking Stress (MPa)		Ultimate Strength (MPa)		Ultimate Strain (%)	
	unexposed*	oxidized#	unexposed	oxidized	unexposed	oxidized
GE Prepreg MI	112†	174	306	307	1.07	1.17
Goodrich MI	135	141	317	275	1.01	0.70
CCP E-CVI	73	81	281	263	0.79	0.57
CCP DIMOX	104	95	327	114	0.58	0.10

* unexposed - composite tested without any steam oxidation exposure

oxidized - composite tested after 100 hours steam oxidation at 1200ºC

† The low value of matrix cracking for this sample was cause by specimen warpage.

Post-exposure mechanical properties of the other samples from Runs #1-#5 are listed in Table 3-35. Typically each type of composite was oxidized in three separate conditions: as processed (having all surfaces in the as-processed or seal coated condition with no fiber coatings or fiber ends initially exposed), with edges exposed (the sample had cut edges which exposed the fiber coatings and fiber ends at the specimen edges), or precracked (an otherwise as-processed or seal coated sample that had been pre-loaded to 0.2% strain to introduce matrix cracking prior to oxidation exposure). Instances where substantial degradation (more than 25% loss in a property compared to an unexposed sample from the same panel) was observed are highlighted in bold type.

The data for standard GE Prepreg composite with configuration A fiber coatings in Table 3-35 is somewhat unusual. The bar oxidized in the as-fabricated condition for 500 hours showed very substantial degradation in modulus, cracking stress, ultimate strength and strain to failure. This is in stark contrast with a similar bar tested after 100 hours that showed slight increases in strengths (see Table 3-34), and with the bar oxidized for 1000 hours, which showed substantial, but more modest, degradation. The samples oxidized precracked or with edges exposed showed much smaller degradation even though those conditions are expected to be more severe than oxidation as fabricated.

GE prepreg MI samples with the B-doped matrix and configuration A fiber coatings showed better property retention than the standard composition. Also, all of the oxidized samples show very similar behavior, indicating that there was probably very little preferential oxidation of the fiber-matrix interfaces in the edges exposed and precracked specimens. Even better behavior was seen in the standard GE prepreg MI composites made with configuration C fiber coatings. Here the data even more strongly suggests that there was no degradation from the oxidation treatment.

The data for the Goodrich slurry cast MI composite shows some degradation of the ultimate strengths between the as processed composite and those oxidized as processed or with edges exposed. The ultimate strength and strain to failure values drop even further

for the sample oxidized in the precracked condition. This would suggest that some enhanced interface oxidation occurred in the precracked bar.

Results for standard slurry cast MI composites made with Sylramic fiber by CCP, and tested in the as fabricated condition, were very poor. Moreover, even the unexposed composites of this composition tested rather poorly with low ultimate strength and strain to failure values. The sample oxidized as fabricated was essentially brittle. The specimen oxidized with edges exposed showed little difference from the as fabricated sample.

Results for CCP Enhanced MI composites (slurry cast MI composites incorporating the "oxidation enhancement" phase found used enhanced SiC-SiC CVI composites) were also marginal. For this material the unexposed properties were not very good with only a 240MPa ultimate strength and 0.45% strain to failure. Oxidation of the as-processed composite showed no effect on the tensile properties, but oxidation with edges exposed resulted in a substantial reduction in ultimate strength to about 193MPa. There were not enough samples of this particular composition to oxidize and evaluate a precracked specimen.

Within the limited data available, the CVI composites tested appear to have faired somewhat worse than the majority of melt infiltrated composites. All of the samples exposed at 1200°C showed substantial degradation in ultimate strength and strain to failure. There was less degradation in proportional limit, but these composites started with relatively low proportional limits before exposure. Degradation of the sample without a seal coating was slightly worse than for the same material with seal coating.

Overall, the results of steam exposure testing done in the first campaign indicated the following:

1. There was little or no degradation in properties in 100 hours exposure of all MI composites and CVI composites. However, the DIMOX composites were severely degraded.
2. After 500 hours exposure at 1200°C degradation starts in MI composites and CVI composites. Although we do not have enough statistical data, preliminary results show the following ratings of materials

Better ← → **Worse**

• GE Prepreg / C	• GE prepreg +B / A	• CCP E-CVI
	• GE Prepreg / A	• CCP MI / Sylramic
	• CCP E-MI	
	• Goodrich MI	

3. It was surprising that uncracked samples with unexposed fiber coatings at the edges still showed some degradation. It was also unclear as to why GE prepreg MI / B(Si)N showed no degradation in any of the conditions.

Table 3-35. Summary of Mechanical Property Degradation Measured Following Cyclic Steam Furnace Exposures During the First Testing Campaign in Mid 1998 to Early 1999. Properties Showing More Than 20% Degradation from the Furnace Exposure are Highlighted in Bold Type.

Material	Run #	Exposure Time (hr)	Condition	Initial Modulus (GPa)	Proportional Limit (MPa)	Ultimate Strength (MPa)	Strain to Failure (%)
GE Prepreg / A	1	0	unexposed	204	170	284	1.02
	1	500	as fab	163	**113**	**170**	**0.33**
	1 &2	1000	as fab	162	151	**193**	**0.63**
	1	500	edges	151	NA	**209**	0.83
	1	500	precracked	NA	NA	233	0.85
	3	0	unexposed	217	154	209	0.62
	3	500	as fab	212	170	208	0.90
	3	500	precracked	NA	NA	242	0.99
GE Prepreg +B / A	1	0	unexposed	199	154	288	0.90
	1	500	as fab	193	154	234	0.71
	1	500	edges	193	**114**	232	0.91
	1	500	precracked	NA	NA	230	0.90
GE Prepreg / C	1	0	unexposed	212	153	251	0.62
	1	500	as fab	203	169	252	0.81
	1	500	edges	202	180	247	0.75
	1	500	precracked	NA	NA	284	0.98
	5	0	unexposed	167	113	218	0.71
	5	500	as fab	192	125	247	0.98
	5	500	precracked	NA	NA	250	0.88
Goodrich MI	1	0	unexposed	191	142	331	0.75
	1	500	as fab	192	133	272	0.72
	1	500	edges	165	141	258	0.60
	1	500	precracked	NA	NA	**219**	**0.43**
CCP MI / Sylramic	2	0	unexposed	223	176	244	0.18
	2	500	as fab	214	161	**161**	**0.08**
	2	500	edges	205	139	216	0.19
CCP E-MI	2	0	unexposed	153	106	239	0.46
	2	500	as fab	172	108	231	0.37
	2	500	edges	150	90	187	0.39
CCP MI	5	0	unexposed	162	153	374	0.86
	5	500	as fab	187	145	309	**0.60**
	5	500	precracked	NA	NA	326	0.73
CCP E-CVI sealed	2	0	unexposed	174	59	281	0.79
	2	500	as fab	139	59	**185**	**0.57**
	2	500	edges	138	83	**175**	**0.25**
CCP E-CVI	2	0	unexposed	177	83	316	0.51
	2	500	as fab	174	93	**170**	**0.31**
	4	0	unexposed	181	102	315	0.50
	4	500	as fab	184	78	297	0.82

The second campaign of sample exposures in the large cyclic steam furnace was done in 1999-2000. The purpose of this effort was to further define the response of the samples to longer-term steam oxidation. Based on the poor response of the DIMOX and CVI

composites in the first round of testing only melt infiltrated composites (GE Prepreg MI with configuration A fiber coatings, CCP slurry cast MI with BN-based fiber coatings, CCP slurry cast MI with silicon-doped BN-based fiber coatings, and Goodrich slurry cast MI with BN-based fiber coatings) were studied in this second campaign. In order to better understand the relative contributions of thermal exposure, oxygen and water to the observed degradation additional heat treatments were also done in Ar and in air atmospheres for comparison to the steam exposure results. A minimum of two test specimens was run per each condition to better understand the variability of the results.

Results for this campaign of cyclic steam furnace testing is summarized in Table 3-36. The testing for this campaign was divided into two sets; the first set running in late 1999 that included air exposure to 500h and steam (90% H_2O + 10% O_2) exposure to 2000h, and the second set running in early 2000 including exposures in steam and Ar atmospheres for up to 500h. Samples used for the two sets of data were taken from different batches of each material, and thus different properties are given for the baseline "unexposed" samples from each set. Where the property of an exposed sample is more than 25% less than the property of the appropriate baseline sample the text is highlighted in bold type.

The following conclusions were drawn from the above results:

- The mechanical properties of GE prepreg with configuration A fiber coating are reduced by 20-25% on high-temperature exposure, independent of atmosphere and exposure time. Repeatability of this result from materials produced in 1998 (Table 3-35) to those produced in 1999 (Table 3-36) was good.
- Degradation of GE Prepreg with configuration C fiber coating appears to be worse in the 2000 data than in the 1999 data. However, this specimen was intentionally fabricated with fiber right at the specimen surface, in contrast to the slurry cast or CVI composites which typically have a 50-100μ thick layer of matrix at the surface, or even more if seal coated. The degradation seen was caused by oxidative consumption of ~75% of the tensile fiber plies at the specimen surfaces, as opposed to extensive internal oxidation noted in the CCP MI and CVI materials.
- The quality of CCP and Goodrich MI materials is variable lot-to-lot. The mechanical properties of CCP MI material with a BN fiber coating improved from 1998 to 1999, but then decreased again in 2000.
- The initial quality of CCP MI material with Si-doped BN fiber coatings was inadequate to assess whether this material is less susceptible to thermal and/or environmental exposure than similar material with undoped BN fiber coatings. Material supplied in early 1999 had very poor properties unexposed, yet even in late 1999 and in 2000, when the as-fabricated properties were very good, only 500h steam exposure at 1200°C was sufficient to severely degrade the composite because of extensive internal oxidation.

Table 3-36. Summary of the Cyclic Steam Furnace Exposure Results from the 1999-2000 Testing Campaign, Including Comparisons to Inert Atmosphere (Ar) and Ambient Air Exposures. All high temperature exposures were at 1200°C. Properties Showing More Than 20% Degradation from the Furnace Exposure are Highlighted in Bold Type.

Material	Year Tested	Exposure Conditions	Initial Modulus (Msi)	Proportional Limit Stress (MPa)	Ultimate Strength (MPa)	Strain to Failure (%)
GE Prepreg / A	1999	Unexposed	216±12	188±1	231±17	0.91±0.01
		500 h/air	191±5	145±10	179±7	0.92±0.28
		500 h/steam	221±28	148±4	184±34	0.69±0.11
		2000 h/steam	228±6	**132±2**	175±1	**0.67±0.01**
GE Prepreg / C	2000	Unexposed	228±19	119±17	260±21	0.68±0.09
		500 h/Ar	203±13	116±10	203	0.65
		500 h/steam*	171±24	**87±1**	**174±9**	0.70±0.01
CCP MI / BN	1999	Unexposed	188±8	162±4	390±7	0.78±0.02
		500 h/air	189±4	158±1	**290±47**	0.65±0.32
		500 h/steam	187±20	143±2	294±1	**0.58±0.00**
		2000 h/steam	187±10	**108±2**	**210±7**	**0.46±0.03**
	2000	Unexposed	233±54	132±8	252±4	0.51±0.11
		500 h/Ar	198±11	125±17	191	0.43
		500 h/steam	185	108	**182**	**0.32**
CCP MI / B(Si)N	1999	Unexposed	178±8	184±28	185±27	0.11±0.01
		500 h/air	184±13	**99±11**	**99±11**	**0.06±0.00**
		500 h/steam	163±1	**111±34**	**111±34**	**0.06±0.02**
		1000 h/steam	151±6	**58±9**	**90±29**	**0.06±0.01**
	1999	Unexposed	143±30	133±13	358±74	0.66±0.04
		500 h/steam	192±16	**97±0**	**114±3**	**0.07±0.01**
	2000	unexposed	194±29	127±2	361±18	0.67±0.02
		500 h/Ar	178±3	128±0	308	0.68
		500 h/steam	160±8	103±6	**214±46**	**0.48±0.22**
Goodrich MI / BN	1999	Unexposed	195±10	168±0	239±6	0.56±0.05
		500 h/air	192±12	148±5	187±30	**0.19±0.03**
		500 h/steam	201±17	135±13	**161±10**	**0.13±0.03**
		2000 h/steam	197±37	**108±2**	**137±4**	**0.14±0.01**
	2000	Unexposed	259±26	123±13	268±40	0.48±0.09
		500 h/Ar	228±25	108±13	295	0.61
		500 h/steam	219±15	115±17	291±20	0.63±0.03

- CCP MI material with a BN fiber coating has excellent properties as-fabricated, and the properties reduction upon 1200°C exposure for 500 h was roughly similar to that of GE prepreg material with BN fiber coatings, with an ~20-25% reduction in ultimate strength. Upon further exposure to 2000 h, however, the mechanical properties continued to decrease: the ultimate strength and strain to failure dropped by ~45% while the proportional limit dropped by ~30%. This decrease was the result of continuing internal oxidation of the material by water vapor.

- The 1998 Goodrich material showed ~20% degradation in ultimate strength and minimal degradation of strain capability and proportional limit after 500 hours (Table 4). However, the 1999 material showed much larger degradation in all three properties at 500 hours, and the degradation continued further on exposure for 2000 hours with the strain capability dropping by over 70%.
- In general, elastic moduli, proportional limits, and strains to failure of GECRD prepreg, CCP slurry-cast MI and Goodrich slurry-cast MI materials were not affected by exposure at 1200 °C for 500 h in argon. Ultimate tensile stresses of these materials were reduced by 15-25% except for the Goodrich material, which showed no decrease in properties after exposure. Although the Goodrich slurry cast MI samples had pore size and number distributions qualitatively similar to those of the CCP slurry-cast MI samples, they showed virtually no internal oxidation after 500h exposure in the high-steam environment.

At this point in the program the operation of the high pressure, high velocity coupon exposure combustion rig, to be discussed in Section 3.8.4, had been demonstrated. Since this rig exposes samples to a more realistic combustion atmosphere at high gas velocities, which more closely simulate the environment of a gas turbine engine, exposure testing of coupons was transitioned to this rig.

3.4.4.3 Mechanical Testing In Steam Environment

The above exposure testing was valuable in assessing the long-term thermal and oxidative stability of the composites in high water vapor atmospheres. However, all of the exposures were done with no stress applied to the composite samples. In real-world applications thermal and mechanical stresses would be imposed on the composites, which could accelerate the property degradation observed above. In order to assess the combined effects of mechanical stress and high temperature, high water environments on the degradation of CMCs several different long-term mechanical tests were run under steam environments.

The primary test done was a hold-time fatigue (HTF) test, which was performed in a steam atmosphere (90% H_2O + 10%O_2) for exposure times up to 100 hours. These tests were conducted on both CCP slurry cast MI composites and on GE Prepreg MI composites. Other tests performed included high cycle fatigue and creep rupture, which were done only on the GE Prepreg MI material. Testing procedures for these tests were described in Section 3.4.3.

3.4.4.3.1 HTF of Slurry Cast Composites

The steam HTF tests were limited to 100 hours exposure primarily since only one test frame at GEGR was modified to test under this environment, and thus all testing had to be done sequentially. It was unclear whether any degradation would be noted with only 100 hours exposure with intact CMC samples, so testing was also done on precracked composites. Testing precracked bars was also done to evaluate what magnitude of composite life could be expected should a crack occur in actual use. Precracking was done the same as for the precracked oxidation tests, namely the samples were loaded in tension to 0.2% strain at room temperature before being used for the hold time fatigue tests.

The choice of stress level for the hold time fatigue tests evolved with time as preliminary results were obtained and analyzed. Initial testing on CCP slurry cast MI composites with silicon-doped BN fiber coatings was done at maximum stress of 96.5MPa for uncracked specimens. Since little degradation was noted during these tests the stress level was raised to 122MPa for testing of CCP slurry cast MI composites with BN fiber coatings. When the GE Prepreg MI composites became available for testing the stress level for HTF testing was reduced back to 96.5MPa. Testing at these stress levels for the precracked samples was unrealistic since the major contributor to the stress state of real components is thermal strain. Thus in a matrix crack were to occur then the stress level would be reduced in the vicinity of the crack due to the increased compliance in the vicinity of the crack. It would be more realistic that the strain at the crack would remain at the level that existed before cracking. The stress levels for the HTF tests on precracked samples were therefore selected based on the observed loading and unloading stress-strain curves from the precracking treatment to give a sample strain of 0.05%, which roughly corresponds to approximately 96MPa in an uncracked CMC.

In all of the steam HTF testing the samples survived the full 100 hours of HTF exposure. Subsequently all samples were tensile tested to failure at room temperature after HTF testing and the residual tensile properties evaluated. The measured residual properties for CCP slurry cast MI composites with silicon-doped BN fiber coatings and for CCP slurry cast MI composites with BN fiber coatings are given in Tables 3-38 and 3-39, respectively. As was done above, when a residual tensile property of the HTF test bar falls more than 25% below that of the corresponding witness bar from the same panel then the property is highlighted in bold type.

Results of the uncracked HTF tests on the CCP slurry cast MI composites with silicon-doped BN fiber coatings, as summarized in Table 3-37, show no degradation, within experimental uncertainty, in subsequently measured ambient-temperature strength properties as a result of the combined environmental and stress exposures at either 1200° or 800°C. However, the modulus did show a uniform drop for all samples tested in hold time fatigue compared to the as-fabricated specimens. For comparison, uncracked HTF results on CCP slurry-cast panel containing BN coated Hi-Nicalon fibers show a significant degradation of subsequently measured ambient temperature strength properties (Table 3-38). The tests on samples with BN fiber coatings were performed under an applied stress that was approximately 85% of the ambient temperature proportional limit stress of 145MPa. It is possible that the applied stress in these tests was actually in excess of the proportional limit stress at the test temperature, and thus the samples with BN fiber coatings may have exhibited environmental attack through microcracks with a consequent degradation of ambient-temperature mechanical properties. The “uncracked” hold time fatigue results on CMC's with Si-BN, which were unlikely to have been cracked, and BN coated fibers, which may have been cracked at the same applied stress, are thus not directly comparable.

Table 3-37. Steam Environment Hold Time Fatigue Test Specimen Post-Test Tensile Properties for CCP Slurry Cast MI Composites With Hi-Nicalon Fiber and Si-Doped BN Fiber Coatings. Properties Showing More Than 20% Degradation from the Furnace Exposure are Highlighted in Bold Type.

HTF Test Condition*	Initial Modulus (GPa)	Proportional Limit (MPa)	Ultimate Strength (MPa)	Strain to Failure (%)
As-fabricated	219	139	378	0.652
As-fabricated	178	137	361	0.682
As-fabricated, precrack loading	236	150	-	-
As-fabricated, precrack loading	241	137	-	-
As-fabricated, precrack loading	228	143	-	-
As-fabricated, precrack loading	234	165	-	-
Uncracked, 1200°C, 96.5MPa	183	163	299	0.700
Uncracked, 1200°C, 96.5MPa	168	138	359	0.680
Uncracked, 800°C, 96.5MPa	186	182	356	0.670
Uncracked, 800°C, 96.5MPa	183	164	305	0.520
Precracked, 1200°C, 66Mpa	†	†	**181**	**0.205**
Precracked, 1200°C, 66Mpa	†	†	**190**	**0.220**
Precracked, 800°C, 66Mpa	†	†	**248**	**0.278**
Precracked, 800°C, 66MPa	†	†	**233**	**0.252**
Precracked, 800°C, 66MPa	†	†	**270**	**0.323**

* All HTF exposures were done in a 90% H2O + 10% O2 atmosphere for 100 hours. "Uncracked" means the sample was HTF tested in the as-fabricated condition and "precracked" means the sample was first stressed to 0.2% strain and then HTF tested. All properties listed here were from RT tensile tests done either before or after HTF exposure.

† Initial modulus and proportional limit stress are not meaningful measures of degradation because of the precracking treatment, and thus these values are not listed.

Table 3-38. Steam Environment Hold Time Fatigue Test Specimen Post-Test Tensile Properties for CCP Slurry Cast MI Composites With Hi-Nicalon Fiber and BN Fiber Coatings. Properties Showing More Than 20% Degradation from the Furnace Exposure are Highlighted in Bold Type.

HTF Test Condition*	Initial Modulus (GPa)	Proportional Limit (MPa)	Ultimate Strength (MPa)	Strain to Failure (%)
As-fabricated	183	146	357	0.754
As-fabricated	197	138	363	0.780
As-fabricated, precrack loading	193	149	-	-
As-fabricated, precrack loading	192	145	-	-
As-fabricated, precrack loading	234	148	-	-
As-fabricated, precrack loading	200	139	-	-
Uncracked, 1200°C 122MPa	181	181	316	**0.510**
Uncracked, 1200°C 122MPa	191	181	**252**	**0.307**
Uncracked, 800°C, 122MPa	Bad test	-	-	-
Uncracked, 800°C, 122MPa	251	134	**175**	**0.248**
Precracked, 1200°C, 55MPa	†	†	281	**0.398**
Precracked, 1200°C, 55MPa	†	†	**217**	**0.131**
Precracked, 800°C, 55MPa	†	†	**148**	**0.057**
Precracked, 800°C, 55MPa	Bad test	-	-	-

* All HTF exposures were done in a 90% H2O + 10% O2 atmosphere for 100 hours. "Uncracked" means the sample was HTF tested in the as-fabricated condition and "precracked" means the sample was first stressed to 0.2% strain and then HTF tested. All properties listed here were from RT tensile tests done either before or after HTF exposure.

† Initial modulus and proportional limit stress are not meaningful measures of degradation because of the precracking treatment, and thus these values are not listed.

The following conclusions have been drawn from the uncracked and precracked hold time fatigue tests on CCP slurry cast MI CMC's with Hi-Nicalon fibers tested in 90% H_2O + 10% O_2 atmospheres at 1200° and 800°C:

- Hold time fatigue testing of uncracked CMC's does not result in strength properties degradation after 100 h exposure, provided that the applied stress is low enough that the sample does not experience matrix cracking at temperature. An applied stress of 96.5Mpa does not pose a threat of environmentally assisted mechanical properties degradation, at least for relatively short exposure times.
- Hold time fatigue testing of precracked CMC's in high-steam environments at 1200° or 800°C invariably results in significant losses of subsequently measured ambient temperature mechanical properties in test times as short as 100h. Designing CMC turbine components to design stresses in excess of the matrix cracking (i.e. proportional limit) stress thus runs the severe risk of premature component failure under the combined challenge of environment and stress.
- Precracked, CCP slurry-cast MI CMC's with Si-BN fiber coatings show no advantage in durability under combined stress and high-steam environmental exposures with respect to CCP slurry-cast MI CMC's with BN fiber coatings.

3.4.4.3.2 HTF Testing of Prepreg Composites

Similar HTF measurements were conducted on GE prepreg MI composites, and the results to date are summarized in Table 3-39. All uncracked prepreg samples were exposed to 96.5MPa stress during HTF testing whereas the precracked specimens were held at 112 to 133MPa, corresponding to an initial strain level of 0.05%.

All samples survived the full 100 hour duration of the HTF test. In addition to the majority of samples with the configuration C fiber coating, two samples were tested that had a modified coating composition. [Please note that the samples used for this testing were prepared from fiber coatings deposited in November-December of 2000, before the fiber coating deposition conditions were fully optimized, and thus the as-fabricated strengths of the composite panels were somewhat lower than is typical of database material.]

The proportional limit stress of all of the uncracked specimens increased following HTF exposure. The ultimate strengths of the uncracked samples with configuration C fiber coating also showed no appreciable decrease in ultimate strength compare to as-fabricated samples, but uncracked samples with the modified fiber coating showed an average 20% reduction in ultimate strength when tested at 1200°C. The ultimate strength values of the precracked samples showed higher levels of degradation, reflecting the effects of atmosphere access to the fiber-matrix interfaces. Within the scatter of the data, the reductions in ultimate strength were comparable for the configuration C and modified coating systems at both 800°C and 1200°C.

As was seen with the cyclic fatigue and creep rupture specimens earlier in this report, strain to failure was the strength parameter that showed the most degradation from HTF exposure. Whereas uncracked samples with standard fiber coatings averaged only a 25% decrease in strain to failure, cracked samples with standard coating averaged a 65% decrease, with the degradation being worse at 800°C than at 1200°C. This observation is consistent with embrittlement by interface oxidation, since BN oxidation/volatility in steam is worse at 800°C than at 1200°C.

It was hoped that the samples with modified coatings would fare better with regard to interface oxidation. However, both uncracked and cracked samples with the modified coating showed greater degradation, particularly in strain to failure, following HTF testing than did samples with the standard coating.

Table 3-39. Steam Environment Hold Time Fatigue Test Specimen Post-Test Tensile Properties for GE Prepreg MI Composites With Hi-Nicalon Fiber. Properties Showing More Than 20% Degradation from the Furnace Exposure are Highlighted in Bold Type.

Fiber Coating Type	HTF Test Condition‡	Proportional Limit Stress (MPa)	Ultimate Strength (MPa)	Strain to Failure (%)
Configuration C	As fabricated	124	244	0.75
	Uncracked, 800°C, 96.5MPa	184	252	0.57
	Uncracked, 1200°C, 96.5MPa	146	210	**0.48**
	Uncracked, 1200°C, 96.5MPa	194	270	0.66
	Precracked, 800°C, 66MPa	†	**162**	**0.12**
	Precracked, 800°C, 66MPa	†	**183**	**0.14**
	Precracked, 800°C, 55MPa	†	207	**0.26**
	Precracked, 1200°C, 66MPa	†	216	**0.51**
	Precracked, 1200°C, 66MPa	†	206	**0.30**
Modified	As fabricated	146	274	0.61
	Uncracked, 800°C, 96.5MPa	173	275	**0.42**
	Uncracked, 800°C, 96.5MPa	170	243	**0.20**
	Uncracked, 1200°C, 96.5MPa	172	241	**0.29**
	Uncracked, 800°C, 96.5MPa	153	**201**	**0.12**
	Precracked, 800°C, 66MPa	†	**190**	**0.12**
	Precracked, 1200°C, 66MPa	†	**206**	**0.22**

‡ All HTF exposures were done in a 90% H2O + 10% O2 atmosphere for 100 hours. "Uncracked" means the sample was HTF tested in the as-fabricated condition and "precracked" means the sample was first stressed to 0.2% strain and then HTF tested. All properties listed here were from RT tensile tests done either before or after HTF exposure.

† Initial modulus and proportional limit stress are not meaningful measures of degradation because of the precracking treatment, and thus these values are not listed.

3.4.4.3.3 HCF and Creep Tests on Prepreg Composites

Other mechanical tests performed under high temperature steam environment were additional HCF and creep rupture tests on GE Prepreg MI composite done at 1315°C. Therefore there was a desire to investigate the standard GE Prepreg CMC material behavior in this higher temperature range to see whether a new generation of material would be needed for these applications. Only the GE Prepreg MI composites with optimized configuration C fiber coatings from the small reactor were evaluated so as to be comparable with the material previously used for the database measurements. Tests were run in a steam, namely 90% H_2O + 10% O_2, environment, and also in ambient air in order to have a comparison to the earlier HCF and rupture data that was run in air, but only up to 1204°C.

Results from the additional HCF tests are shown in Figure 3-101, plotted along with the prior data on prepreg MI composites measured in the 2001 database. As with the previous tests, the new tests at 1315°C were conducted with a stress R ratio of 0.05, with the majority of testing done at 30Hz. At 1315°C in air the response of the material was not dramatically different than that measured at 1204°C, within the scatter of the data. However, in the steam environment at 1315°C there appears to be a substantial knock-

down in the allowable stress, on the order of 15 to 30MPa compared to the 1204°C air data.

The new creep rupture data are shown in Figure 3-102, again including the original database data for comparison. Here the difference between 1204°C and 1315°C response was more significant, although the introduction of steam at 1315°C again results in a 20 to 30MPa knock-down in the allowable stress compared to the 1204°C air data.

The new HCF and creep rupture data were added to the material property database, and are being used to better understand and predict the effect of temperature and environment on the life of components.

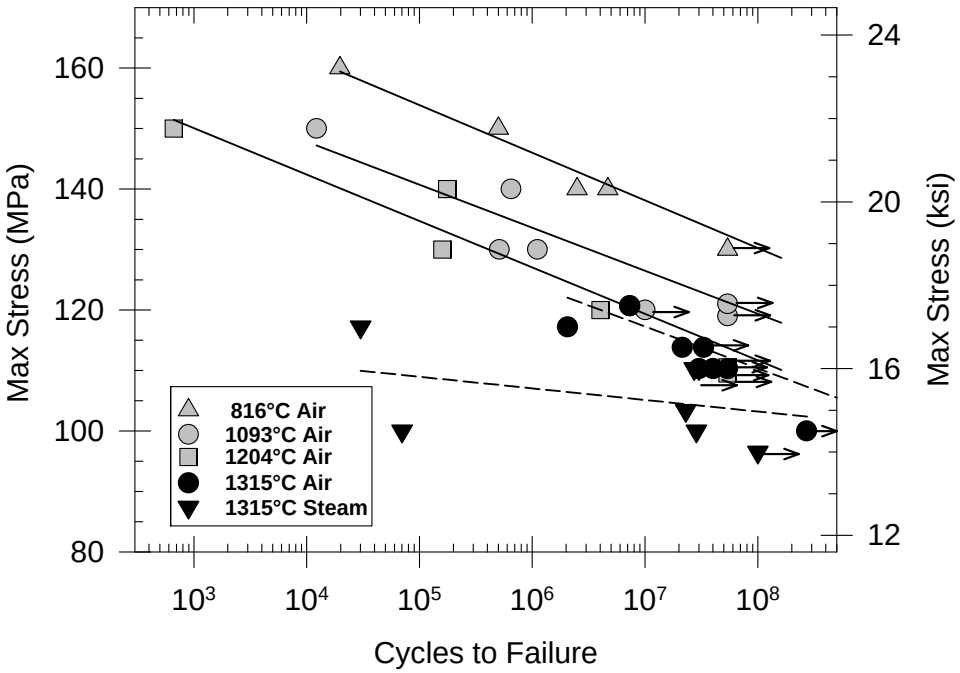

Figure 3-101. High cycle fatigue data (R=0.01, 30 Hz) on GE prepreg MI composites with Hi-Nicalon fiber and configuration C fiber coatings. Prior database data, all measured in air, are shown by the gray symbols with the new data at 1315°C in air and steam shown by the black symbols.

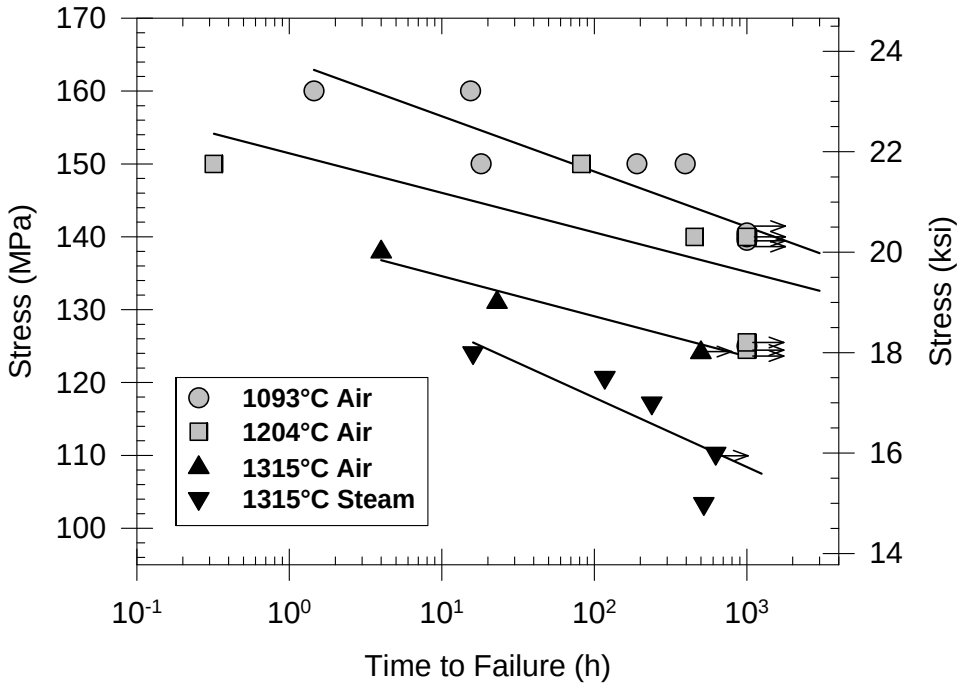

Figure 3-102. Creep rupture data on GE prepreg MI composites with Hi-Nicalon fiber and configuration C fiber coatings. Prior database data (all measured in air) are shown by the gray symbols with the new data at 1315°C in air and steam shown by the black symbols.

3.4.5 Characterization of Damage Tolerance

By and large, damage tolerance is the critical feature of continuous fiber ceramic matrix composites that allows them to even be considered for gas turbine engine applications. Monolithic ceramics are always susceptible to catastrophic failure due to their brittle fracture behavior. Although the monolithics can be made with very high as-fabricated strengths, and therefore low probabilities of failure, in real-world applications the components are subject to oxidation, volatilization, creep cavitation, erosion and impact by foreign objects in the gas stream, all of which introduce flaws that can severely reduce the monolithic ceramic strength. Thus such monolithic ceramics cannot be expected to maintain a low probability of failure over the lifetimes needed for application in large industrial gas turbines. CMC's, however, due to their pseudo-toughness that makes them much more tolerant of flaws and damage, are expected to have acceptable life in such applications.

Damage tolerance falls into two general categories: resistance to the initiation of damage and resistance to the propagation of damage. For the most part, the "damage" we are trying to prevent is a catastrophic failure. Although overstressing damage could be introduced in a variety of means, such as poor mechanical design of the component, improper design or operation or CMC-to-metal attachments, inadequate modeling of the

thermal environment leading to excessive thermal stresses, etc., there are two main sources for damage to turbine hardware that are largely out of the designers control. The first is damage caused by impact from foreign materials (sucked into the engine intake or from failing machine hardware upstream of the component of interest) that are present in the turbine gas stream. The second source, which is particularly applicable to a shroud component, is the occurrence of a blade tip rub. While the argument can be made that blade tip rubs can be prevented by proper turbine design, in reality the desire to minimize the blade tip gap in order to improve engine performance, and the fact that the rotor, buckets, shrouds and casing all heat up and cool at different rates during engine cycling, make blade tip rubs a common occurrence in practice. In smaller engines, where blade tip gaps have a disproportionate effect on engine performance, the design philosophy is often to have an abradable layer on the inside of the shroud with the intent to let the blades "rub into" the shrouds to minimize blade tip leakage during engine operation.

We have used ballistic impacts to simulate the types of damage expected in a turbine from foreign object collisions. Initial work was done to characterize the extent of damage seen from such ballistic impacts as a gage for resistance to damage initiation, and to serve as a base-line for subsequent environmental exposure testing. Impacted samples were also exposed to wet oxidation environments, using the laboratory cyclic steam furnace apparatus, in order to quantify the growth of the damaged regions under unstressed conditions. Damage propagation under stress was evaluated using hold time fatigue tests in steam on impacted samples.

Four types of CMC and two "monolithic" ceramics were used in this testing. Slurry cast MI composites from CCP reinforced with BN-coated Sylramic™ fibers or with BN-coated Hi-Nicalon™ fibers, and GE Prepreg MI composites with optimized configuration C fiber coatings on Hi-Nicalon™ or Hi-Nicalon Type-S™ fiber were the four types of CMC tested. Prepreg MI composites made without any fiber coating were initially used to simulate the behavior of a monolithic ceramic, but even this system showed evidence of toughness and fiber pull-out under the high velocity impacts even though they test as completely brittle in a normal tensile test. Subsequently impacts were also done on Kyocera SN-282 sintered silicon nitride to represent a typical monolithic structural ceramic material.

3.4.5.1 Slurry Cast Composites With Sylramic Fiber

The first of the CMC materials evaluated was slurry cast MI-CMC panels manufactured by CCP and reinforced with Sylramic fiber cloth. Four 7.6cm x 10cm panels and two 5cm x 15cm panels of this material were submitted to the University of Dayton Research Institute (UDRI) for foreign object damage (FOD) testing. Each sample was heated to 1200°C in the target area inside a hinged furnace. After the desired temperature was reached, the furnace was rapidly removed and a 4mm diameter chrome steel ball was shot at the center of each panel. Initial tests were at a nominal velocity of 427m/s, corresponding impact kinetic energy was 24J, and was sufficient for the projectile to completely perforate the sample in each case. Photographs, shown in Figure 3-103, of the front and back sides of a typical sample damaged at this higher impact energy show that the entry hole is the same size as the projectile and that exit hole is approximately twice the diameter of the

projectile. A CMC plug in the rough shape of a cone section has been removed by the impact.

Dummy specimens (sub-standard CCP slurry-cast material with Hi-Nicalon fiber reinforcements) were used to establish the lower impact velocity such that the projectile would damage but not pass through the sample. An impact velocity of 230m/s, corresponding to an impact energy of 7J, was still adequate to pass through the sample. When the impact velocity was reduced to 122m/s the projectile created a hemispherical cavity in the target, but did not pass through or cause material removal in a dummy sample. The back side of this sample showed fiber tearing and lifting, but no perforation. A slightly lower mean velocity of 116m/s was chosen as the lower impact velocity for the remaining six CCP Sylramic reinforced panels.

Results of impact testing of a typical Sylramic reinforced panel at 1200 °C and an impact velocity of 116m/s are shown in Figure 3-104. Although the projectile did not pass through the panel, a cone-shaped piece of material was removed by the impact. The diameter of this removed section on the impact side was approximately 75% of the diameter of the projectile, and the back side diameter of the removed section was approximately 125% of the diameter of the projectile.

All of the damaged samples were subjected to non-destructive evaluation (NDE) by infrared thermography, and the results compared to those of the samples prior to impact testing. Typical before-and-after results with a 427m/s impact velocity are shown in Figure 3-105. The impact damage zone (blue, pink, and black region in the center of the sample) is about twice the diameter of the projectile, consistent with the visual observation of the damage zone on the exit side. In addition, the porosity (orange indications) observed in the undamaged sample appears to have spread in the center section of the sample. The increase in apparent porosity in the Sylramic reinforced sample is probably a combined effect of the preexisting porosity and the imposed thermal gradients during impact testing. In several cases (see Figure 3-106 for an example), the visible impact zone was included in a large orange indication, which is probably a delamination caused by the joint effect of preexisting porosity, thermal gradients, and the impact itself.

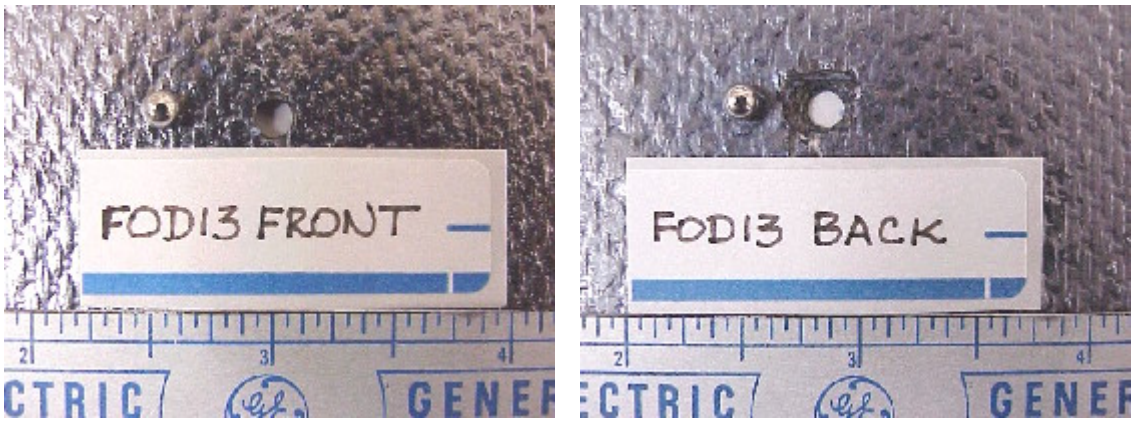

a **b**

Figure 3-103. Photographs of (a) the front (entry) side and (b) the back (exit) side of a CCP slurry-cast MI, Sylramic fiber reinforced 7.6cm x 10.2cm panel impacted with a 4mm chrome steel ball at 427m/s.

a **b**

Figure 3-104. Photographs of (a) the front side and (b) the back side of a CCP slurry-cast MI, Sylramic fiber reinforced 7.6cm x 10.2cm panel impacted with a 4mm chrome steel ball at 116m/s.

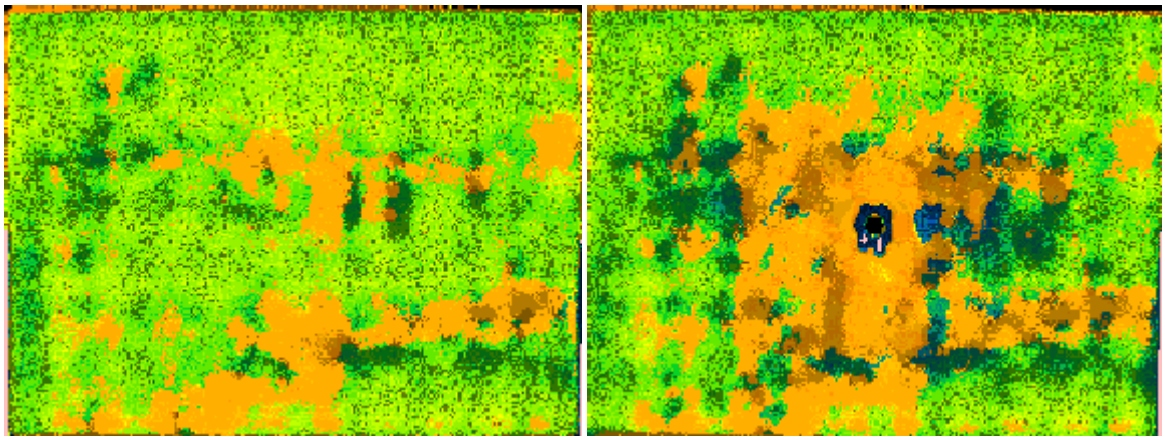

a **b**

Figure 3-105. IR thermography images of the front side of a CCP slurry cast MI, Sylramic reinforced sample (FOD13) impacted at 427m/s: (a) prior to impact testing; (b) after impact testing.

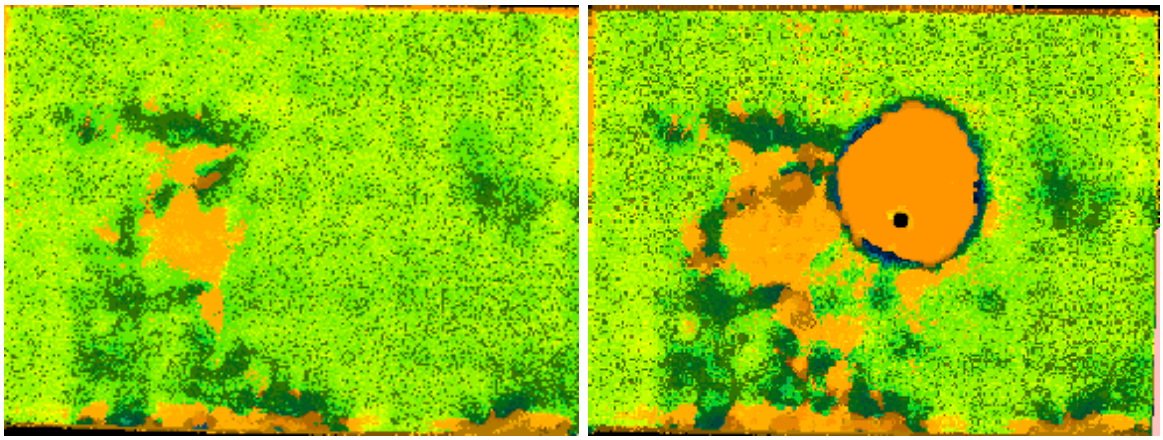

a **b**

Figure 3-106. IR thermography images of the front side of FOD15, a CCP Sylramic reinforced sample impacted at 125m/s: (a) prior to impact testing; (b) after impact testing.

Dye penetrant inspection was also employed on two of the panels (FOD13, impact velocity of 448m/s, and FOD17, impact velocity of 125m/s) to determine whether FOD created microcracks or other surface damage not visible to the naked eye. Dye penetrant imaging of the entrance side of FOD17 (Figure 3-107a) shows extensive surface microcracking in addition to the visually observable hole created by the impact event. Numerous microcracks radiate from the impact hole itself; in addition, there is a field of surface cracks in the lower right quadrant of the photograph that are connected to the impact hole by at least one microcrack. Since the remote microcracks are not radially symmetrical about the center of the impact hole, it is hypothesized that they were caused by an interaction between the shock wave created by the impact event and preexisting porosity within the composite. The effect of this interaction was to originate microcracks at the

internal porosity and propagate them to the surface. The damage visible in dye penetrant inspection of sample FOD13 (Figure 3-107b) is the same as the visually observable damage, with no additional microcracks. Dye penetrant inspection of the exit sides of the two samples likewise showed no features not observable to the naked eye.

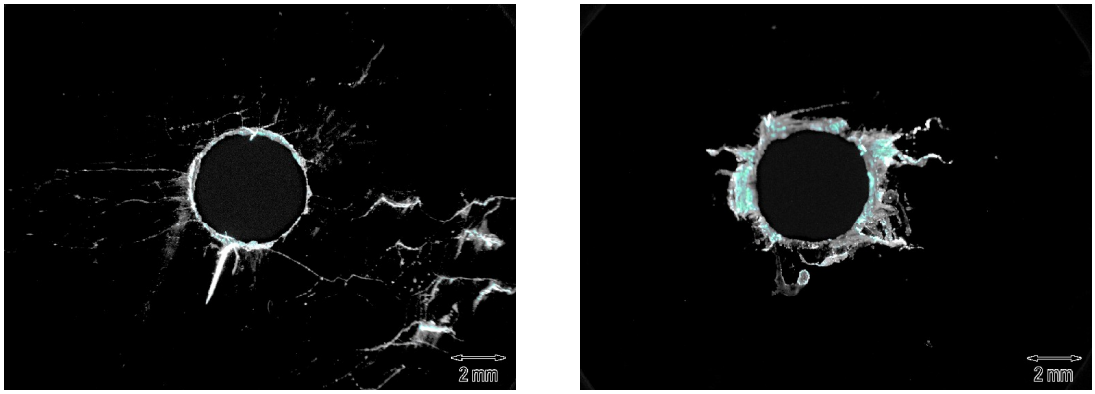

a **b**

Figure 3-107. Photographs under UV illumination following dye penetrant treatment of the entrance sides of FOD samples; (a) panel FOD-17, impacted with a 4mm steel ball at 125m/s and (b) panel FOD13, impacted with a 4mm steel ball at 448m/s.

Four of the eight 7.6cm x 10cm samples, two impacted with a steel ball at approximately 116m/s and two impacted at approximately 427m/s, were sectioned for determination of residual ambient temperature mechanical properties. Each sample was cut in two longitudinally through the center of the damage zone; one of the cut halves of each sample was further sectioned into three, approximately 1.3cm x 10cm bars for mechanical properties measurements.

Results of the mechanical property tests are summarized in Table 3-40. The –1 bar in each set contained one-half of the hole and/or damage zone along one edge. The –2 and –3 bars were outside the visually observed damage zone. The stress values, and therefore strengths, of the –1 bars were based on the estimated cross section of intact material next to the impact site. Strain during the tensile tests was monitored using the standard 25mm gage length extensometer; however, the presence of the half hole from the impact events would be expected to act as a stress concentrator to a localized region. Thus the actual strain, and stress, in the effective gage section next to the hole would be much larger than measured with the extensometer, which measured average strain over the entire 25mm gage length. There was no reliable way to correct the strength and strain values (and thus the modulus values as well) of the –1 bars to account for this stress concentration, so only the raw measured values are reported. The data for the –2 and –3 bars, which did not macroscopically include any of the impact damage, were not affected by these errors.

Ultimate strength and strain to failure values of the damaged –1 bars were reduced considerably in all cases with respect to the undamaged –3 bars. However, the modulus and proportional limit strength were practically unchanged, which would indicate that the

material not immediately affected by the visible impact damage remained intact and relatively free of microcracks. The mechanical properties of the –3 bars were similar in all cases to those of witness bar samples taken from the corresponding original 15cm x 23cm as-fabricated panels. Strains to failure of the bars containing half of the damage zone created by a 427m/s impact were slightly smaller than those containing damage from a 116m/s impact, possibly because the 427m/s damage zone is slightly larger. Two of the four –2 samples (FOD15-2 and FOD14-2) showed some apparent strength and strain to failure property reduction, whereas the remaining two did not. These results indicate that the real damage zone size was generally not much larger than the visually observed zone, at least insofar as it could be measured by in-plane tension test response.

Table 3-40. Summary of Post-FOD Residual Tensile Strength Properties of Slurry Cast MI Composites with Sylramic Fiber

Sample No.	Initial Modulus (GPa)	Proportional Limit Stress (MPa)	Ultimate Strength (MPa)	Strain to Failure (%)
Samples from panels impacted by a 4mm steel ball at ~427m/s				
FOD15-1	325	176	199	0.074
FOD15-2	250	162	316	0.310
FOD15-3	239	186	370	0.432
FOD18-1	299	188	217	0.089
FOD18-2	248	157	351	0.336
FOD18-3	209	159	350	0.364
Samples from panels impacted by a 4mm steel ball at ~116m/s				
FOD14-1	248	157	224	0.134
FOD14-2	229	178	294	0.257
FOD14-3	243	188	342	0.342
FOD19-1	298	171	237	0.105
FOD19-2	213	185	361	0.375
FOD19-3	179	147	356	0.343

In order to determine if the impact damaged regions would grow with environmental exposure, the other half-panels from the FOD tests were exposed for 500h at either 1200°C or 800°C in the standard 90% H_2O + 10% O_2 steam atmosphere in the large cyclic steam furnace apparatus described earlier. Mechanical properties of the environmentally exposed half-panels were determined in the same manner as the mechanical properties of the as-damaged half-panels, by sectioning each half-panel into –1 (damaged) and –2 and –3 (undamaged) test bars and testing at ambient temperature. Residual mechanical properties of damaged and environmentally exposed slurry-cast/Sylramic reinforced CMC's are summarized in Table 3-41. The damaged –1 sections in the slurry-cast panels, which exhibited significant losses in strain to failure after FOD testing, are now completely or almost completely brittle, with strains to failure of 0.04-0.07%. All of the undamaged –2

and –3 samples also show significant reductions in ultimate tensile strength and strain to failure in comparison with unexposed bars from otherwise similar panels. This result was consistent with previous steam furnace exposure tests on similar CCP slurry cast MI composites where degradation due to internal oxidation of the CMC was noted.

Table 3-41. Summary of Post-FOD Residual Tensile Strength Properties of Slurry Cast MI Composites with Sylramic Fiber Following Additional Exposure in a High-Steam Atmosphere for 500hr.

Sample No.	Initial Modulus (GPa)	Proportional Limit Stress (MPa)	Ultimate Strength (MPa)	Strain to Failure (%)
Impacted at 427m/s then exposed in 90% H_2O + 10% O_2 at 800°C				
FOD20B-1	322	146	146	0.043
FOD20B-2	249	177	265	0.190
FOD20B-3	240	159	276	0.224
Impacted at 427m/s then exposed in 90% H_2O + 10% O_2 at 1200°C				
FOD13B-1	285	159	171	0.072
FOD13B-2	243	145	205	0.132
FOD13B-3	230	143	199	0.132
Impacted at 116m/s then exposed in 90% H_2O + 10% O_2 at 800°C				
FOD16A-1	306	164	164	0.052
FOD16A-2	261	190	243	0.141
FOD16A-3	259	187	281	0.210
Impacted at 116m/s then exposed in 90% H_2O + 10% O_2 at 1200°C				
FOD17A-1	295	177	177	0.063
FOD17A-2	255	157	229	0.146
FOD17A-3	235	129	179	0.118

3.4.5.2 GE Prepreg Composites

Similar tests to those described above were also performed on GE prepreg MI-CMCs reinforced with Hi-Nicalon fiber. Six panels were impacted by a 4mm chrome steel ball at approximately 427m/s and six at approximately 116m/s in the same manner as described above

Photographs of the front and back sides of a typical prepreg sample impacted at 435m/s, corresponding to an impact energy of approximately 24J, are shown in Figure 3-108. The projectile has passed through the sample, leaving an entrance hole the same size of the projectile and an exit hole about twice the size of the projectile. A plug of material has been removed. The damage is similar to that imparted by a similarly energetic projectile in CCP slurry cast material with Sylramic fiber reinforcements.

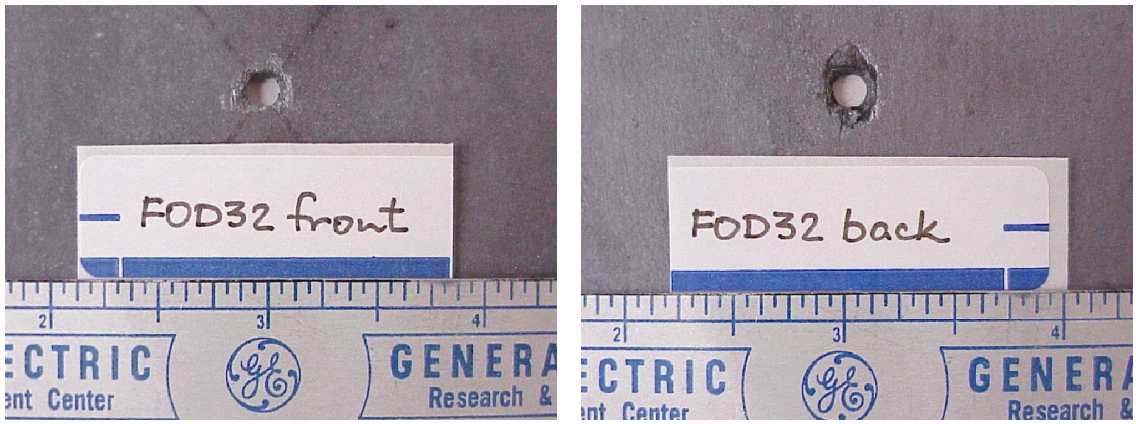

a **b**

Figure 3-108. Photographs of (a) the front (entry) side and (b) the back (exit) side of a GE prepreg MI, Hi-Nicalon fiber reinforced panel impacted by a 4mm chrome steel ball at 435m/s.

Results of impact testing of a GE Prepreg MI sample impacted at 118m/s, corresponding to an impact energy of approximately 1.8J, are shown in Figure 3-109. The ball has created an impact crater on the front side but has not removed any material. Although some of the composite has been flaked from the backside, several of the fiber layers have not been removed and are either intact or cracked. The overall backside damage zone is approximately 3 times the diameter of the ball, but much of the damage is to the unreinforced layer on the surface of the composite. Three of four 7.6cm x 10cm samples impacted at this lower velocity did not show any perforation, whereas the fourth sample showed a hole smaller than the diameter of the projectile. This latter appearance is similar to that of CCP slurry cast MI / Sylramic material impacted at the same velocity. The FOD resistance of GE Prepreg MI / Hi-Nicalon material is thus shown to be at least marginally superior to that of the slurry-cast / Sylramic material.

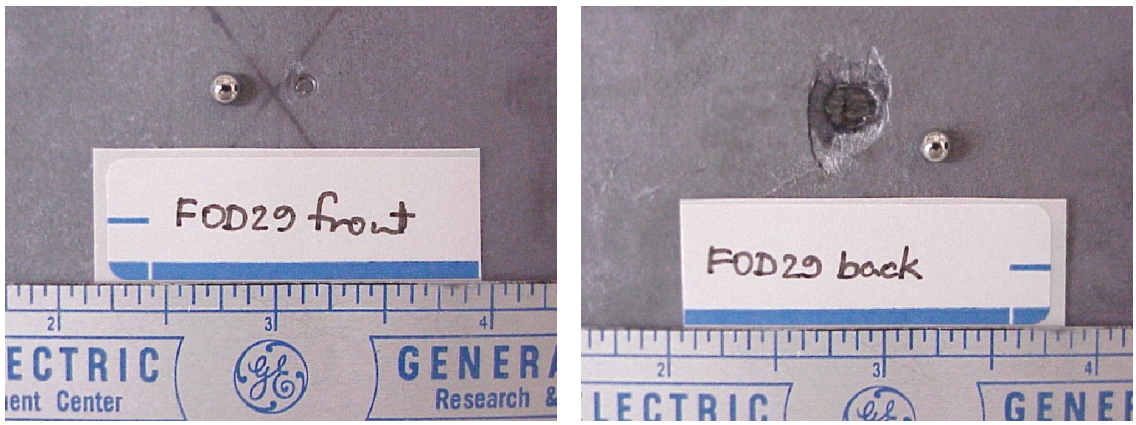

a **b**

Figure 3-109. Photographs of (a) the front side and (b) the backside of a GE Prepreg MI, Hi-Nicalon fiber reinforced panel impacted by a 4mm chrome steel ball at 118m/s.

All of the damaged prepreg samples were subjected to non-destructive evaluation (NDE) by infrared thermography, and the results compared to those of samples prior to impact testing. Typical before-and-after images on a sample damaged with an impact velocity of 435m/s are shown in Figure 3-110. The size of the damage zone as measured by NDE indications is approximately 2cm x 1.6cm, considerably larger than the visually observable damage zone diameter (comparing Figure 3-110 with Figure 3-108).

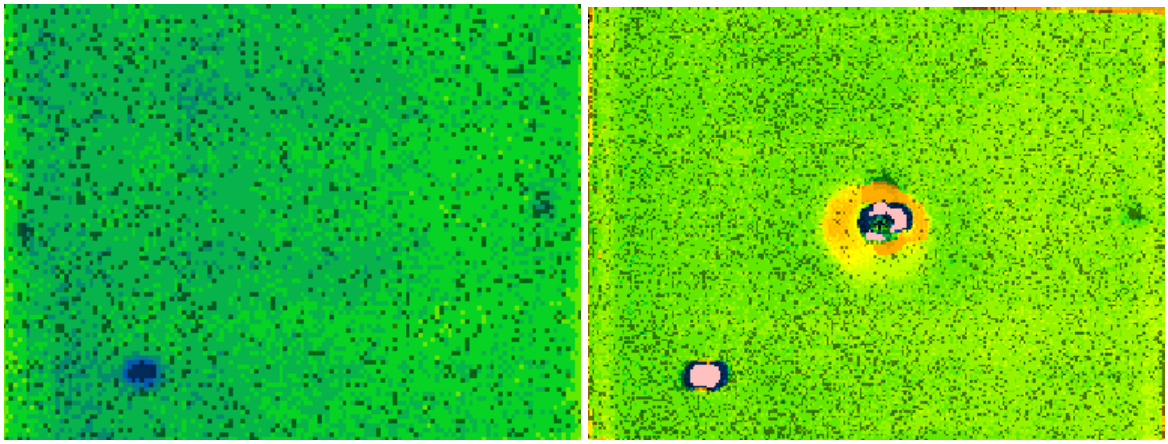

a **b**

Figure 3-110. IR thermography images of the front side of FOD32, a GE prepreg MI, Hi-Nicalon reinforced sample impacted at 435m/s: (a) prior to impact testing; (b) after impact testing.

Typical before-and-after NDE images on a GE Prepreg MI sample damaged with an impact velocity of 118m/s are shown in Figure 3-111. The apparent damage zone diameter as measured by NDE indication is approximately 1cm, in reasonable agreement with the visually observable damage zone diameter (compare Figure 3-111 with Figure 3-109). Evaluation of the remaining FOD panels shows a wide variation in damage zone size as measured by NDE. Several of the NDE damage zone diameters are about the same size as the visually observed damage, while others have NDE damage zone diameters up to 2.5cm or larger.

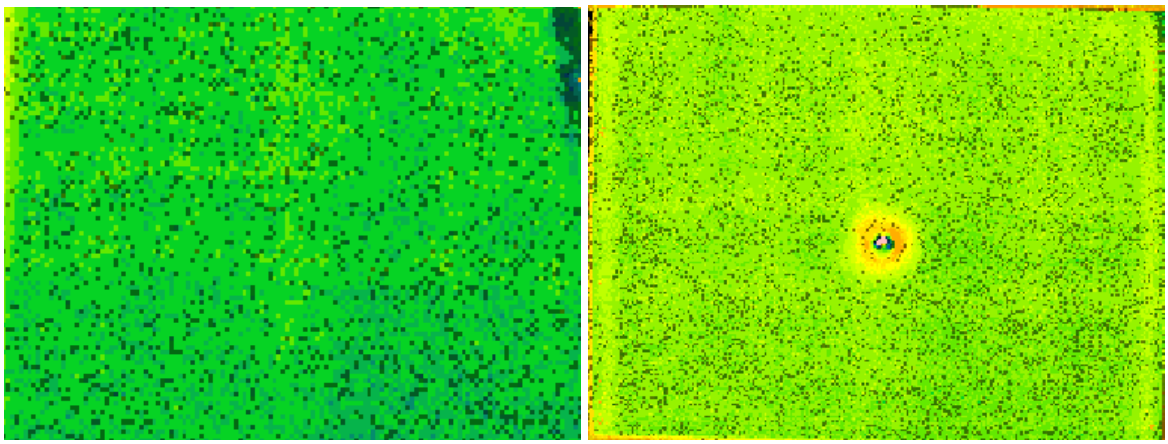

a **b**

Figure 3-111. IR thermography images of the front side of FOD29, a GE Prepreg MI, Hi-Nicalon reinforced sample impacted at 118m/s: (a) prior to impact testing; (b) after impact testing.

Four of the eight prepreg FOD samples, two impacted at approximately 116m/s and two impacted at approximately 427m/s, were sectioned for determination of residual mechanical properties. Preparation of test specimens was identical to that used for the slurry cast / Sylramic composites discussed above. The samples were bisected and one half of each panel was cut into three, 1.2cm x 10cm mechanical properties test specimens. The –1 specimen in each case contained half of the damage zone, whereas the –2 and –3 samples did not contain any of the visually observed damage zones.

Results of room temperature tensile strength tests on sectioned prepreg FOD samples are summarized in Table 3-42. Mechanical properties of the damaged –1 sections were reduced in all cases relative to those of the undamaged –2 and –3 sections; however, the extent of reduction was considerably less in all cases for the prepreg / Hi-Nicalon samples than for the slurry-cast / Sylramic samples. Two of the four damaged –1 prepreg samples exhibited strains to failure of 0.6-0.7% and the other two were in the 0.2-0.25% range, compared with 0.07-0.14% for the damaged –1 slurry-cast samples. The undamaged –2 and –3 prepreg samples generally exhibited full retention of ultimate strength and strain properties, although the unusual non-linear initial stress/strain behaviors of the –3 prepreg samples were not well understood.

Table 3-42. Summary of Post-FOD Residual Tensile Strength Properties of GE Prepreg MI Composites with Hi-Nicalon™ Fiber

Sample No.	Initial Modulus (GPa)	Proportional Limit Stress (MPa)	Ultimate Strength (MPa)	Strain to Failure (%)
Samples from panels impacted by a 4mm steel ball at ~ 427m/s				
FOD27-1	176	98	189	0.681
FOD27-2	294	158	283	0.875
FOD27-3	*	*	214	0.770
FOD30-1	319	110	183	0.233 †
FOD30-2	221	103	285	0.814
FOD30-3	*	*	276	0.809
Samples from panels impacted by a 4mm steel ball at ~ 116m/s				
FOD26-1	163	81	157	0.633
FOD26-2	212	123	299	1.10
FOD26-3	*	*	291	1.02
FOD31-1	314	115	178	0.213
FOD31-2	225	124	292	1.21
FOD31-3	*	*	283	1.05

† Sample continued to elongate at a stress of approximately 145MPa to a strain of 0.5% prior to breaking.
* Initial portion of stress/strain curve was nonlinear and thus reliable modulus and proportional limit values could not be determined.

The remaining half-panels of the GE prepreg MI / Hi-Nicalon FOD samples were exposed for 500h at either 1200°C or 800°C in the standard 90% H_2O + 10% O_2 atmosphere in the large cyclic steam furnace. The purpose of these exposures was to determine whether environmental exposures subsequent to foreign object damage would increase the size of the damage zone and/or further compromise mechanical properties in the damaged regions. Mechanical properties of the environmentally exposed half-panels were determined in the same manner as the mechanical properties of the as-damaged half-panels, i.e. by sectioning each half-panel into –1 (damaged) and –2 and –3 (undamaged) test bars and tensile testing at ambient temperature.

Residual tensile strength properties of damaged and environmentally exposed prepreg / Hi-Nicalon™ CMC's are summarized in Table 3-43. The damaged –1 sections show reduced strains in comparison with similarly damaged unexposed bars; however, all four of the exposed –1 samples retain some strain capability with strains to failure of 0.15-0.27%. The undamaged –2 and –3 samples exposed at 800°C exhibit no reduction in mechanical properties with respect to unexposed –2 and –3 samples, and the undamaged –2 and –3 samples exposed at 1200°C exhibit only modest reductions in ultimate tensile strength and strain to fail with respect to the corresponding unexposed –2 and –3 samples. In general, the exposure tests on FOD samples again demonstrated the superiority of GE Prepreg MI /

Hi-Nicalon™ CMC's compared to CCP slurry-cast MI / Sylramic CMC's in retention of damage tolerance subsequent to foreign object damage and environmental exposure.

Table 3-43. Summary of Post-FOD Residual Tensile Strength Properties of GE Prepreg MI Composites with Hi-Nicalon™ Fiber Following Additional Exposure in a High-Steam Atmosphere for 500hr.

Sample No.	Initial Modulus (GPa)	Proportional Limit Stress (MPa)	Ultimate Strength (MPa)	Strain to Failure (%)
Impacted at ~ 427m/s then exposed in 90% H_2O + 10% O_2 at 800°C				
FOD32B-1	323	125	187	0.153
FOD32B-2	202	112	261	0.812
FOD32B-3	*	*	295	0.929
Impacted at ~ 427m/s then exposed in 90% H_2O + 10% O_2 at 1200°C				
FOD25A-1	235	110	143	0.242
FOD25A-2	197	95	170	0.613
FOD25A-3	*	*	201	0.659
Impacted at ~ 116m/s then exposed in 90% H_2O + 10% O_2 at 800°C				
FOD28A-1	289	93	179	0.272
FOD28A-2	248	117	299	1.15
FOD28A-3	*	*	288	1.00
Impacted at ~116m/s then exposed in 90%H_2O-10% O_2 at 1200°C				
FOD29B-1	47.3	21.3	30.1	0.239
FOD29B-2	*	*	40.2	1.05
FOD29B-3	*	*	33.6	0.829

* Initial portion of stress/strain curve was nonlinear and thus reliable modulus and proportional limit values could not be determined.

While the above combined impact and steam exposure testing showed little growth of damaged zones with environmental exposure, those exposures were done in the absence of any applied stress. Applied stress was expected to increase the likelihood of damage propagation, and thus an exposure condition under stress was needed to investigate this possibility. Hold time fatigue testing under high temperature steam environment was selected as the most appropriate method to test for the propagation of impact damage under stress.

Four 5cm x 15cm GE Prepreg MI FOD panels were impact tested with a 4mm steel ball at sample temperature of 1200°C. Impacts were performed at approximately 116m/s and 430m/s, and the samples were then sectioned into 1.2cm x 15cm test specimens for hold time fatigue testing. Hold time fatigue tests were performed by subjecting the specimens to a maximum stress of 96.5MPa in an Instron mechanical test frame while simultaneously exposing their center sections in a furnace at 1200° or 800°C. A mixture of 90% H_2O + 10% O_2 was simultaneously passed through the furnace to simulate the water vapor concentration in a combustion atmosphere. The applied stress was cycled from 96.5MPa

to zero for 10 minutes every two hours, thus a 100-h hold time fatigue test corresponded to 50 load/unload cycles.

All of the specimens survived the environmental fatigue exposure. Ambient-temperature residual mechanical properties of the mechanically/environmentally exposed specimens were determined after the tests and compared to the mechanical properties of the mating bars, each of which contained the other half of the imposed foreign object damage.

Table 3-44 shows the mechanical properties of the damaged bars exposed to hold time fatigue, the corresponding damaged bars with no further exposure, and as-fabricated witness bars from the same original panels as the FOD panels from which the hold time fatigue specimens were cut. The modulus and stress data for the damaged bars were derived on the basis of the minimum cross-sectional areas of the bars in the damaged regions. The as-damaged bars showed reasonably good mechanical properties retention, with fracture stresses ranging from 63-67% of those of the as-fabricated CMC bars. Retention of strain to failure was more variable; the two as-damaged bars from panel 1045 (33B-1 and 34A-1) retained 83-89% of the original strain capability, whereas the two as-damaged bars from panel 1048 (35A-1 and 36B-1) retained 43-49%. Because of the small number of data points, it is not clear whether this represents a panel-to-panel variation or is fortuitous. In either case, the foreign object damage tolerance of GE prepreg material is seen to be good and similar to that for the 10cm long damaged samples described previously.

The damaged specimens exposed to hold time fatigue showed further decreases in mechanical properties, but significant retention of fracture stress and strain capability was noted in all cases. Retained fracture stress ranged between 45% and 66% of that in the as-fabricated samples, with the 1200°C hold time fatigue samples apparently showing better strength retention than the 800°C samples. Retained strain capability ranged between 26% and 59% of that in the as-fabricated samples. The general conclusion is that the GE prepreg CMC resists combined mechanical and environmental exposure reasonably well when damaged, at least for short times, between 800° and 1200°C.

Table 3-44. Effects of FOD Impact and Hold Time Fatigue Testing in Steam on Tensile Properties of GE Prepreg MI / Hi-Nicalon™ Composites

Sample ID	Condition†	Initial Modulus (GPa)	Proportional Limit Stress (MPa)	Ultimate Strength (MPa)	Strain to Failure (%)
As- Fabricated Witness Samples*					
1045-2	as fab	252	125	350	0.94
1048-2	as fab	237	126	334	1.16
1048-4	as fab	269	181	326	1.15
Samples Impacted at ~ 427m/s					
FOD33B-1	impacted	155	100	220	0.78
FOD33A-1	impacted + HTF @ 800°C	203	98	157	0.27
FOD36A-1	impacted	197	104	219	0.57
FOD36B-1	impacted + HTF @ 1200°C	225	124	218	0.38
Samples Impacted at ~ 116m/s					
FOD35A-1	impacted	234	128	221	0.49
FOD35B-1	impacted + HTF @ 800°C	221	107	178	0.30
FOD34B-1	impacted	204	108	230	0.84
FOD34A-1	impacted + HTF @ 1200°C	147	117	209	0.56

* Sample 1045-2 is the "as fabricated" witness bar for FOD samples 33B-1, 33A-1, 34B-1 and 34A-1, and Samples 1048-2 and 1048-4 are the "as fabricated" witness bars for FOD samples 36A-1, 36B-1, 35A-1 and 35B-1.

† All ballistic impacts were done at 1200°C with a 4mm chrome steel sphere projectile; all hold time fatigue (HTF) testing was done at a maximum stress of 96.5MPa for 100 hours in a 90% H_2O + 10% O_2 atmosphere.

3.4.5.3 Impact Damage Threshold

All of the prior ballistic impact testing was performed at very high impact velocity, and therefore energy, where the CMC panels are completely penetrated, or at an intermediate velocity just below the threshold of complete penetration. The question then arose as to what was the impact energy threshold below which no observable degradation would occur. In order to determine this threshold small (3.8cm x 5cm) samples of three CMC materials (CCP slurry cast MI composites reinforced with Hi-Nicalon™ fiber, CCP slurry-cast MI reinforced with Sylramic™ fiber, and GE Prepreg MI reinforced with Hi-Nicalon™) were impacted at ambient temperature with 4mm chrome steel balls at impact velocities ranging between 183 and 55m/s. Preliminary testing had shown these velocities to be just above and just below the threshold for full perforation of the CMC panels by the chosen impactor. The purpose of these tests was to determine which combination of processing method and reinforcing fiber yielded the best FOD resistance in the threshold regime. At impact velocities greater than about 180m/s, the impactor always perforated the CMC and differences in extent of damage among the various CMC types are relatively small.

Pictures of the front side and backside of the CCP/slurry cast/Hi-Nicalon samples after damage by impactors traveling at 171, 117, 91, and 54m/s, are shown in Figures 3-112 and 3-113, respectively. This material had better impact resistance than the other two materials

in that the impactor did not perforate the CMC even at the maximum impact velocity. As usual, the backside damage zone was larger than the front side damage zone; damage was limited owing to extensive tearing and lifting of the fiber layers in the damaged region, which effectively absorbed the impact energy. Damage was minor below an impact velocity of 91m/s, and essentially no damage was observed at the minimum impact velocity of 54m/s.

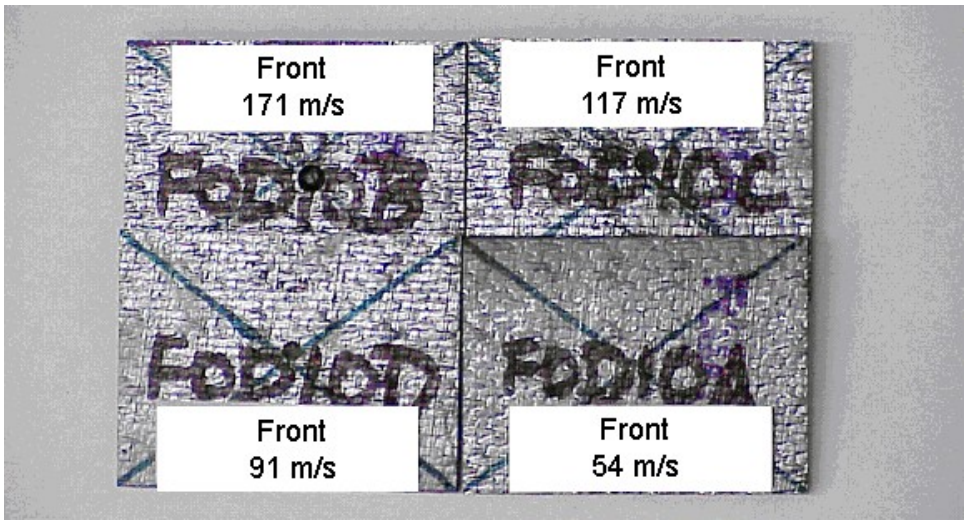

Figure 3-112. Photographs of front-side damage of CCP/slurry-cast/Hi- Nicalon CMC samples at near-threshold impactor velocities.

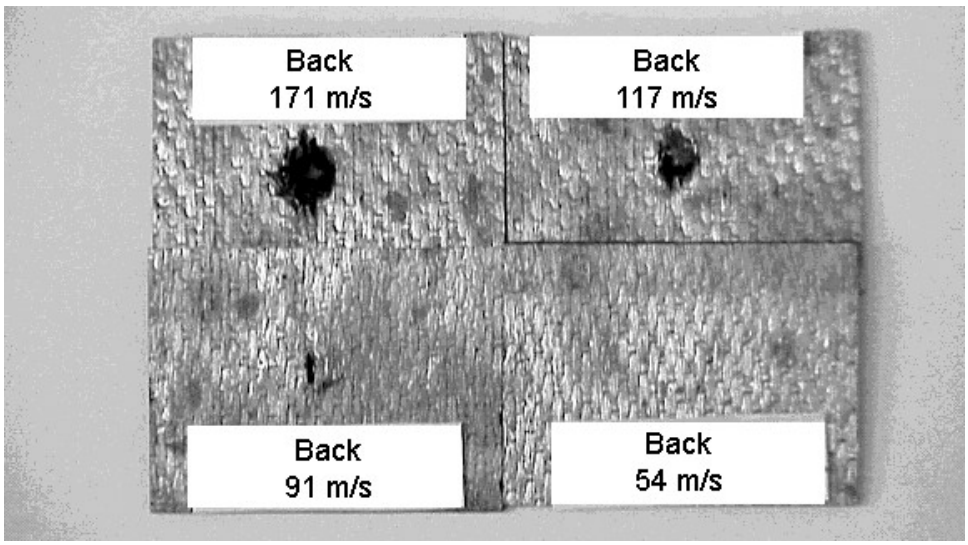

Figure 3-113. Photographs of backside damage of CCP/slurry-cast/Hi- Nicalon reinforced CMC samples at near-threshold impactor velocities.

Pictures of the front-side and backside of the CCP/slurry-cast/Sylramic™ samples after damage by impactors traveling at 180, 118, 99, and 56m/s, respectively, are shown in

Figures 3-114 and 3-115. This material had relatively poor impact resistance at the two highest impact velocities; the 180m/s impact perforated the sample, and the 118m/s impact created a hole in the material. Damage at 99m/s was more extensive than in the corresponding CCP/slurry-cast/Hi-Nicalon sample (compare the lower left sample in Figure 3-115 with the corresponding sample in Figure 3-113). No appreciable damage was noted at the lowest impact velocity of 56m/s. These results are consistent with FOD results on 7.6cm x 10cm panels impacted at 1200°C that were described earlier. The poorer impact resistance of Sylramic reinforced panels is probably related to the lower strain capability of Sylramic fiber with respect to Hi-Nicalon fiber.

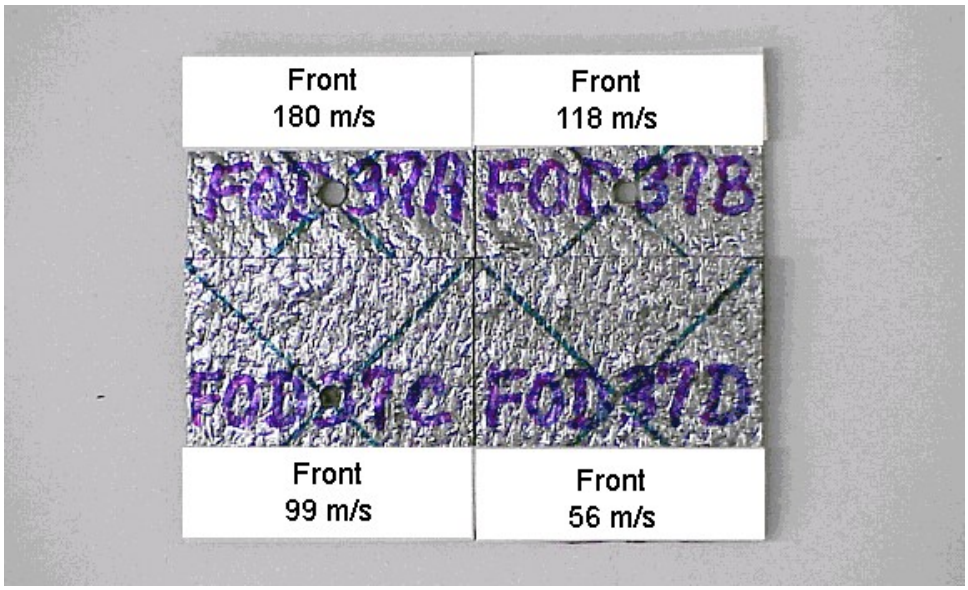

Figure 3-114. Photograph of front-side damage of CCP / slurry-cast / Sylramic CMC samples at near-threshold impact velocities.

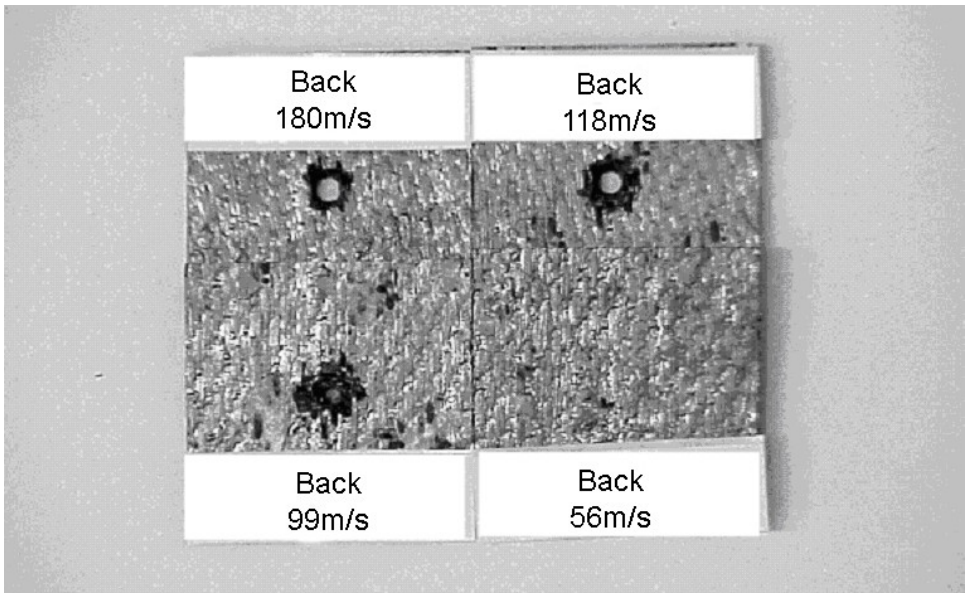

Figure 3-115. Photograph of backside damage of CCP/slurry-cast/Sylramic reinforced CMC samples at near-threshold impactor velocities.

Pictures of the front-side and backside of the GE Prepreg/Hi-Nicalon™ samples after damage by impactors traveling at 173, 111, 94, and 63m/s, respectively, are shown in Figures 3-116 and 3-117. The front-side damage of these samples is similar to that of the corresponding CCP/Sylramic samples, with 173m/s impact velocity being sufficient to cause perforation of the panel and 63m/s causing little or no observable damage. The backside damage of these samples was more extensive than that on either of the CCP sample types. Large sheets of the unreinforced surface layer were cracked away from the composite on the backside, especially at the lower impact velocities. In addition, it appears that at least one and perhaps more than one fiber layer were removed from the backside by the impact. This damage may result from the lower fiber volume fraction of this composite (25%) compared to the slurry cast materials (>35% fiber). The GE Prepreg was thus shown to be more sensitive to near-threshold FOD than the CCP slurry-cast material, especially with respect to backside damage.

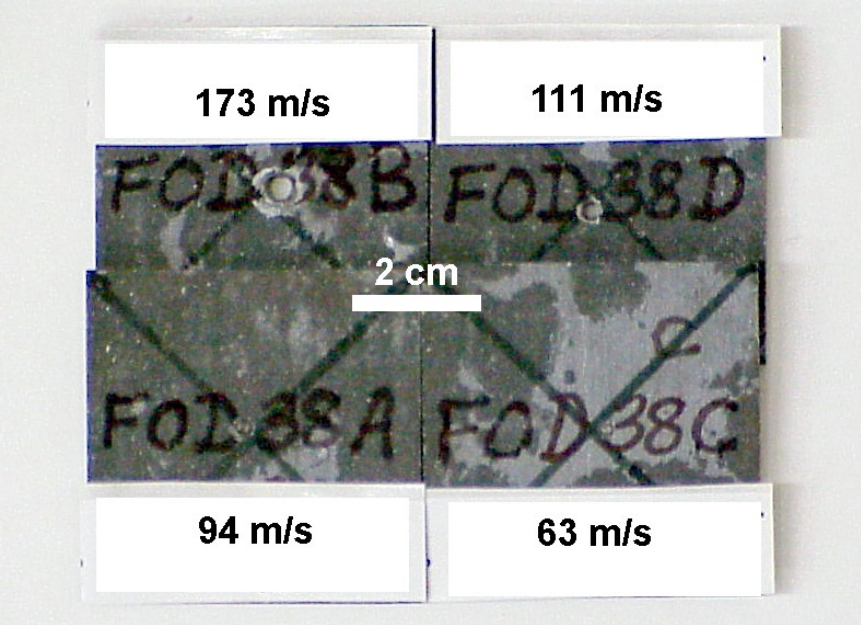

Figure 3-116. Photographs of front-side damage of GE Prepreg MI composites reinforced with Hi-Nicalon™ fiber following ballistic impact at velocities near the damage initiation threshold.

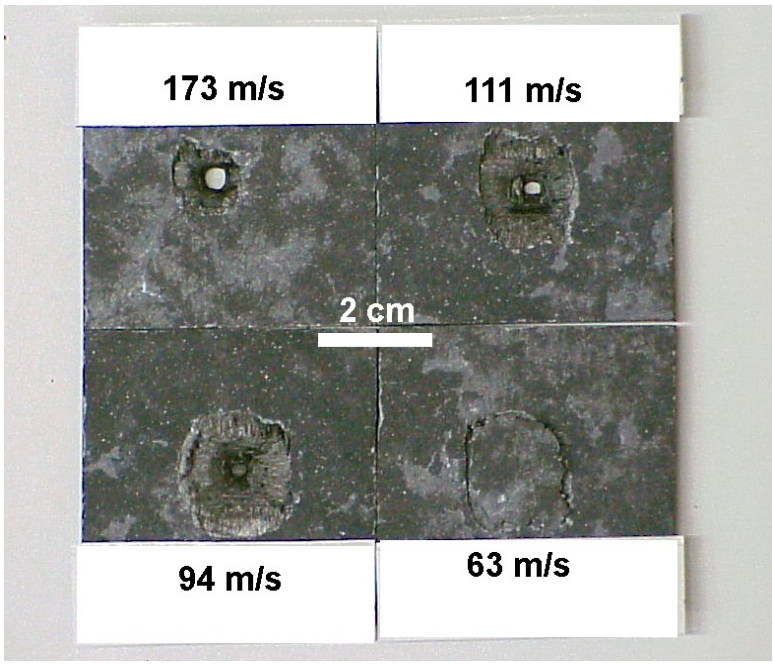

Figure 3-117. Photographs of backside damage of GE Prepreg MI composites reinforced with Hi-Nicalon™ fiber following ballistic impact at velocities near the damage initiation threshold.

3.4.5.4 Testing of Monolithic Ceramic Samples

Ballistic impact testing of two types of "monolithic" ceramic was conducted to serve as a benchmark for interpretation of the composite data. The main issue was how monolithic ceramics, with their higher strength but lower toughness than CMCs, would respond to the impact conditions being used for the CMC samples. The first material tested was GE Prepreg MI composite made with un-coated Hi-Nicalon fiber. The expected outcome was that the Hi-Nicalon fiber would be reacted with silicon during the melt infiltration and strongly bonded to the matrix, rendering a finished body that would behave as a monolithic siliconized silicon carbide. This material was initially impacted using the same procedures as the previous CMC impact tests, namely a 4mm chrome-steel ball projectile, sample temperature of 1200°C, and projectile velocities of nominally 427 and 116m/s, nominally.

The sample impacted at 427m/s displayed very similar behavior to the previously tested CMC samples, with a conical hole being punched through the panel. The holes on the "monolithic" and the CMC Prepreg samples were all roughly the same size as the projectile on the front (entrance) face. The exit holes on reinforced Hi-Nicalon and Hi-Nicalon type-S panels were both ~1.5X the size of the projectile whereas the exit hole on the panel made with uncoated fiber was larger (~3X the projectile) and more irregularly shaped. Nevertheless, the panel made with uncoated fiber did not shatter in a brittle fashion. Apparently there was a sufficient amount of un-reacted fiber cores still present in the sample made without fiber coatings to give it some degree of toughness under very high strain rates, even though it fractures in a brittle fashion during a normal tensile test.

At the lower impact velocity (116m/s) Hi-Nicalon and Hi-Nicalon type-S reinforced composite panels again performed very similarly; however, there was more damage to the uncoated fiber sample. Figure 3-118 shows photographs of the exit sides of the panels tested at 116m/s. The thru-hole on the panel made with uncoated fiber was larger than for either panel made with coated fiber. There was also a full width crack that occurred during the impact event; however, the panel did not separate fully into two pieces.

It was surprising that the panel made with uncoated fiber showed some degree of toughness and did not shatter in a brittle fashion. Previous testing at UDRI, performed at the request of GE Aircraft Engines, on sintered silicon nitride showed that this relatively high-toughness monolithic ceramic would shatter during ballistic testing at fairly low impact energies, much lower than those used in this study. We therefore decided to try impact testing of monolithic Si_3N_4 under the same conditions as used for the CMC tests.

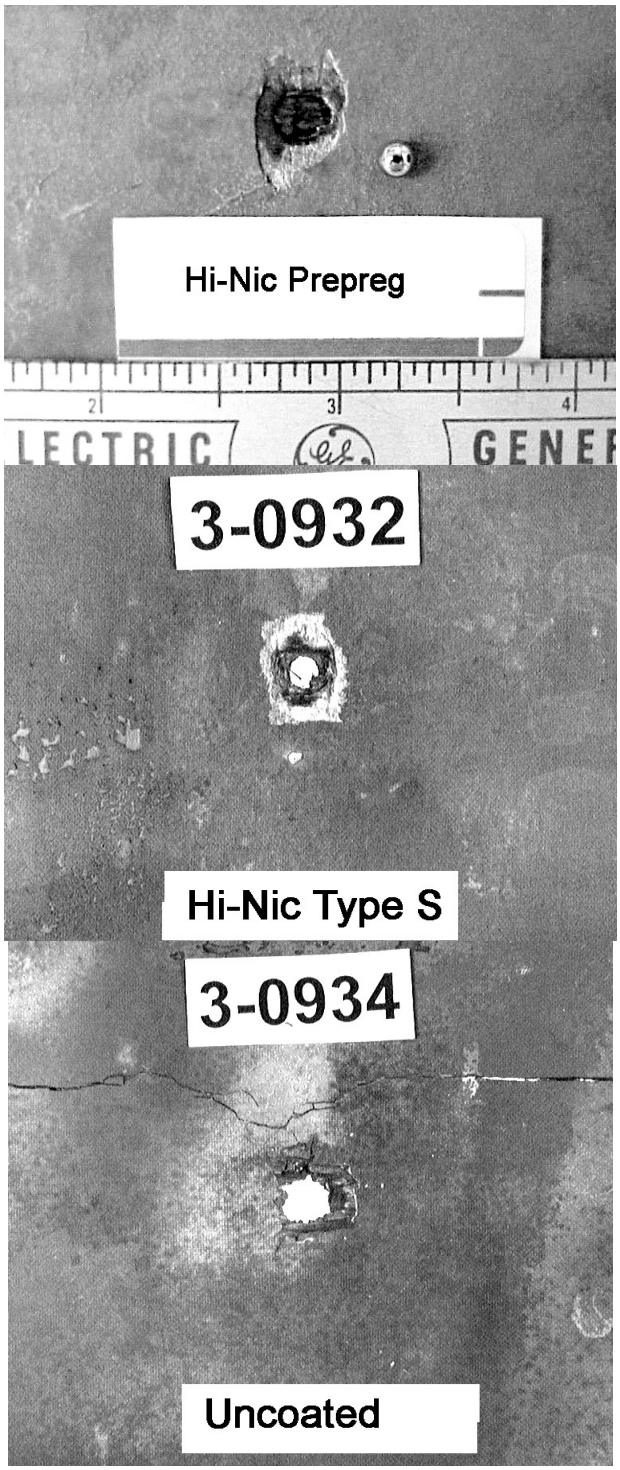

Figure 3-118. Photographs of prepreg CMC panels following ballistic impact testing with 4mm chrome steel balls at 116 m/s velocity. Fiber used in the panels is as follows: Top – coated Hi-Nicalon; Middle – coated Hi-Nicalon type-S; Bottom – uncoated Hi-Nicalon.

Plate specimens of Kyocera SN-282 sintered Si_3N_4 were procured for this testing. SN-282 is a moderate toughness, high strength silicon nitride that would represent a typical structural ceramic in consideration for small turbine components. These plates were ballistic impact tested at UDRI using the same procedures as described above, i.e. 1200°C, 4mm chrome steel ball and nominal impact velocities of 427 and 116m/s.

Two samples were impacted at each velocity, and all panels were observed to shatter on impact. Figure 3-119 shows photographs of one of the panels before and after impacting at a measure velocity of 121m/s. Typically the Si_3N_4 panels fractured into multiple pieces with a number of small fragments. The amount of fine debris increased significantly at the higher impact velocity of 438m/s, but the macrocracking patterns were similar. These investigations dramatically show the value in using CMCs as opposed to monolithic ceramics in applications where foreign object damage is possible. None of the CMC samples tested, with impact energies ranging from the threshold of observable damage up to complete penetration, displayed catastrophic damage, and yet all tests on monolithic sintered Si_3N_4 showed catastrophic failure at both energies tested.

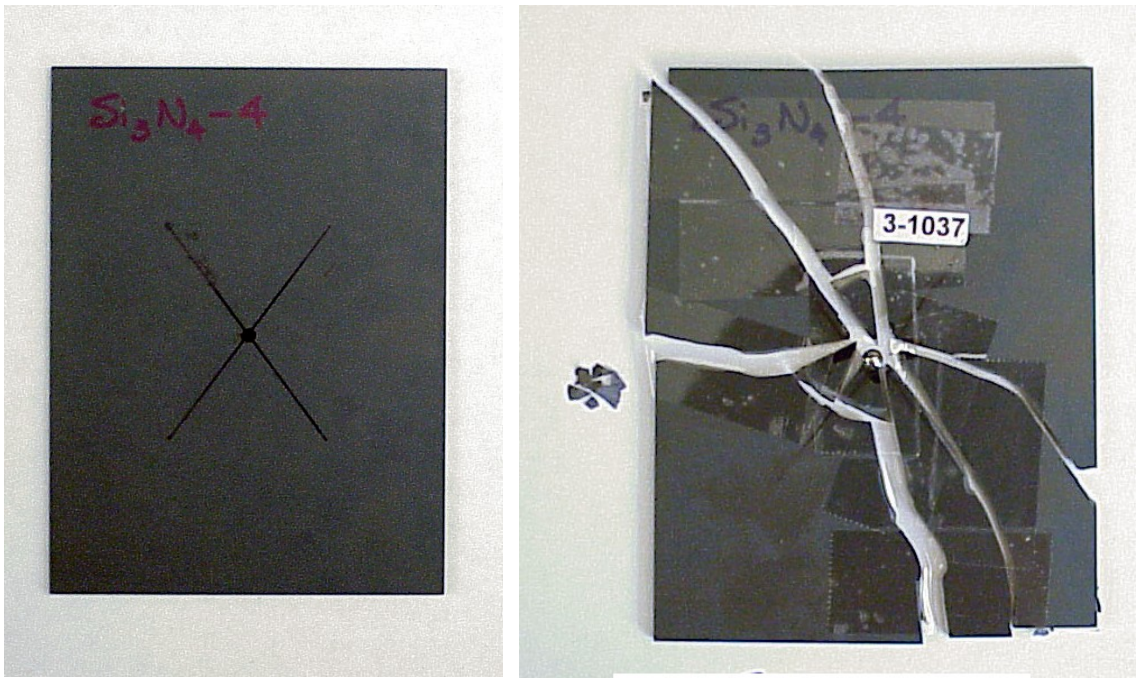

A **B**

Figure 3-119. Ballistic impact test results of Kyocera SN-282 sintered silicon nitride: A - before impact; B – after impact at 1200°C with a 4mm chrome steel ball at 121m/s. Cellophane tape, used to hold the fragments in relative position, is visible on the right photograph.

3.5 Composite Coating (EBC) Development

As noted previously in this report, oxidation of Si-based ceramics to form SiO_2 and the consequent volatilization of the SiO_2 as gaseous $Si(OH)_x$ species in environments with high water vapor pressures leads to a paralinear recession of the ceramic surface. The recession rate predicted for gas turbine like conditions is much too high for the intended large turbine applications targeted by this program. The prime remediation for this problem is to apply an Environmental Barrier Coating (EBC) to the ceramic, which blocks the access of water vapor to the substrate. In order to properly understand the function and durability of EBC coatings it is important to understand that an EBC does not stop the oxidation of the substrate (or bond coat as appropriate), but only prevents the reaction of the silica layer being formed by oxidation from being volatilized by water vapor.

An effective EBC system was developed under the NASA-sponsored High Speed Civil Transport (HSCT) program by a team including GE, NASA and United Technologies. The composition and configuration of the individual coating layers of the EBC were worked out during the HSCT program, and deposition of the coating onto slurry cast MI CMCs via plasma spraying was demonstrated. Ultimately it would be necessary to adopt this technology for the shrouds and combustors being investigated under the CFCC program in order to meet life goals, and thus there was a need to be able to coat the CMCs of interest to this program, namely GE's Prepreg MI composite, and to also better understand the performance of this coating to long-term steam environment exposures.

Work on the deposition and evaluation of EBC coatings was performed under program task 3.2.a.6 Composite Coating Development for Life Optimization. The purpose of this task was to adapt the environmental barrier coating technology developed under the HSCT program for use on GE prepreg MI composites, which included establishing coating deposition conditions, verifying coating mechanical durability via thermal cycling tests, and long-term environmental exposures to evaluate the efficacy of the coatings to eliminate the silica volatility problem.

The configuration of the HSCT EBC system is shown in Figure 3-120. The coating consists of three different layers. A primary consideration for any coating is the match of the coefficient of thermal expansion of the coating to the substrate. This is especially true for the EBC coating where coating cracking would not be acceptable. Consequently the choices of materials for use in the coating were highly limited.

The first layer, or bond coat, is silicon metal. The primary purpose of this layer is to serve as an oxygen barrier to prevent oxidation of the substrate CMC. This function is important since the CMCs of interest are mainly composed of SiC, which on oxidation forms SiO_2 and CO_2. The formation of silica is not, by itself, a major concern; however, the formation of CO_2 leads to the formation of pores at the CMC surface due to the inability of CO_2 to diffuse outward through the top coating layer. These pores grow, eventually linking up and leading to spallation of the EBC coating. Using a hermetic layer of silicon as the bond coat prevents any oxygen from reaching the CMC substrate and producing CO_2 bubbles. Oxidation of the silicon layer itself results in SiO_2 , but no CO_2 is formed. It was also

noted that the physical adherence of a silicon bond coat was better than what was achieved with direct coating of the oxide layers onto the CMC substrates.

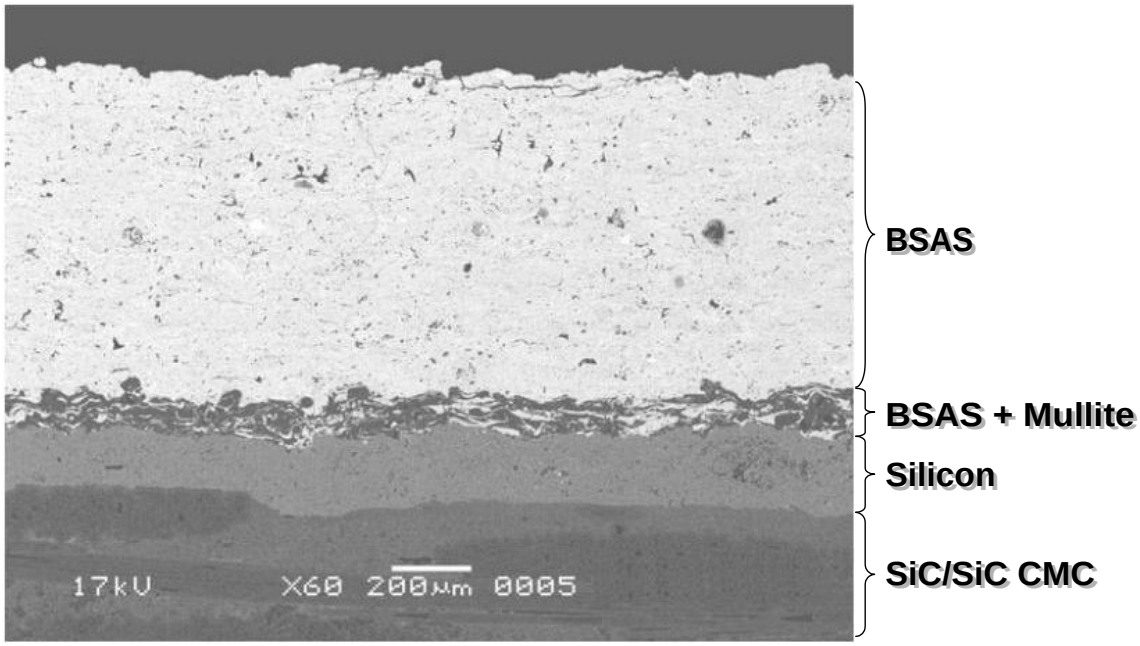

Figure 3-120. SEM photograph of a typical EBC coating on a SiC-based CMC substrate.

The second layer of the coating is a mixed layer of mullite ($Al_6Si_2O_{13}$) and barium-strontium-aluminosilicate (BSAS). Although mullite has a good CTE match to the CMC substrate, it had been shown that mullite did not have good chemical resistance to water vapor, as the silica in the mullite tended to be leached out and volatilized during high temperature, high water vapor exposures, leaving behind a porous alumina-rich material that was not an effective water barrier. Through extensive screening experiments it was found that BSAS had a good resistance to water vapor attack; however, when coated directly onto the silicon bond coat BSAS would crack due to its slightly worse CTE match with the CMC. A mixed layer of mullite and BSAS was then developed to serve as a transition layer between the bond coat and the BSAS top coat that had an intermediate CTE between the substrate and the BSAS top coat and also bonded well with the silicon bond coat and the BSAS top coat.

The third, or top, layer of the EBC is BSAS, which serves to prevent the volatilization reaction. The actual composition of this layer is that of the Celsian phase ($Ba_{0.5}Sr_{0.5}Al_2Si_2O_8$). The stable form of Celsian is monoclinic, however the plasma-sprayed coatings typically are amorphous as-deposited. A post-deposition heat treatment is therefore necessary where the coating crystallizes first to a hexagonal Celsian phase, and then to the monoclinic Celsian. Bansal[18] at NASA had been developing glass-ceramic CMC materials based on a Celsian matrix so the CTE compatibility of this material with SiC-based fibers was well known.

3.5.1 Deposition Onto Prepreg MI CMC Substrates

Processing trials of EBC deposition onto GE Prepreg MI CMC were carried out using 2.5cm x 1.2cm flat coupons cut from a large panel. The surface was first grit-blasted using 220-mesh alumina grit in order to clean and roughen the surface, and thereby enhance physical attachment of the coating. A three-layer EBC (Si / mullite+BSAS / BSAS) was deposited using air plasma spray (APS). The deposited coating was subjected to a heat-treatment at 1250°C for 24 hours to crystallize the mullite and BSAS phases. The cross-section of the as heat-treated coating is shown in the optical micrograph in Figure 3-121.

The coating resistance to H_2O and thermal shock was evaluated using the cyclic steam furnace exposure, as described in report Section 3.4.4.1. The exposures were done in a 90% H_2O + 10% O_2 environment, and samples were rapidly cycled from 1200°C to room temperature and back to 1200°C every 2 hours (150 minutes hot time and 10 minutes cold time). Samples were removed from testing after 96 and 230 cycles, corresponding to 176 and 421 hot hours, respectively, for microstructural examination. Figures 3-122 and 3-123 show optical micrographs of the cross-sections of these samples. Optically the silicon bond coat shows up as the white layer on top of the CMC; however, there is not enough contrast between mullite and BSAS to distinguish the mixed 2nd layer from the pure BSAS top coat.

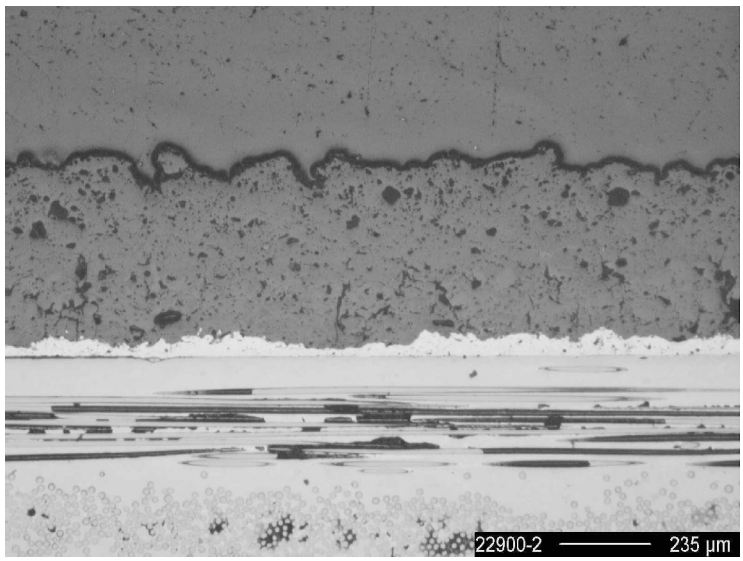

Figure 3-121. Optical micrograph of an EBC on a GE Prepreg MI composite following heat-treatment at 1250°C for 24 hours.

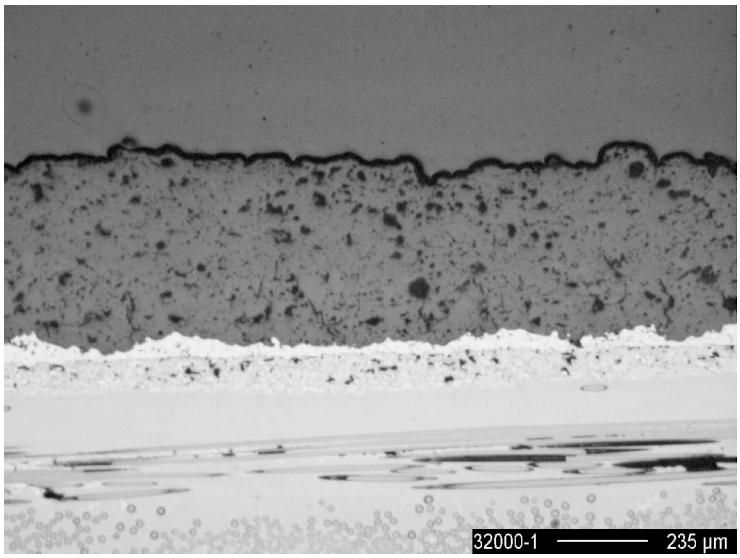

Figure 3-122. Optical micrograph of an EBC coated GE Prepreg MI composite after 96 cycles (176 hot hours) of steam exposure testing in the cyclic steam furnace at 1200°C.

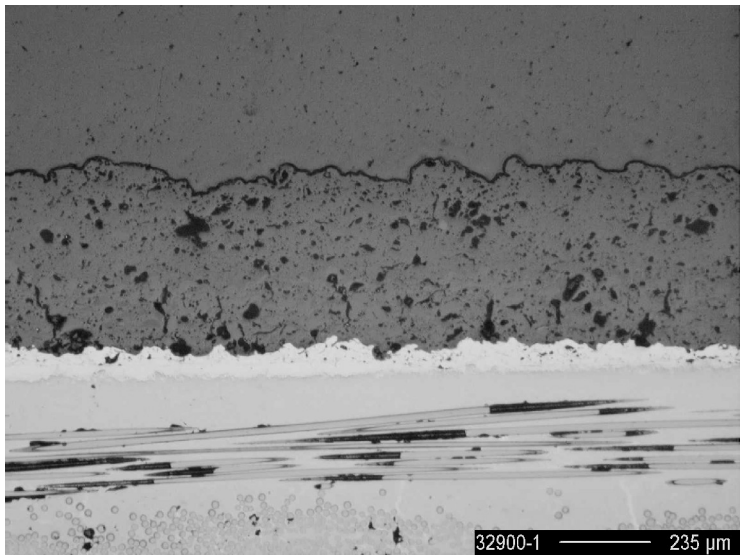

Figure 3-123. Optical micrograph of an EBC coated GE Prepreg MI composite after 230 cycles (422 hot hours) of steam exposure testing in the cyclic steam furnace at 1200°C.

It was seen that even after 230 cycles (421 hot-hours at 1200°C) the sample exhibited good bonding between the coating layers and between the coating and the substrate, there were no indications of EBC cracking, and that there was little interfacial oxidation. This result is comparable with EBC coated slurry-cast CMC tested under the HSCT/EPM program. Hence the feasibility of spraying EBC on GE Prepreg CMC had been demonstrated.

3.5.2 Bond Coat Oxidation Studies

In order to further characterize the long-term durability of the 3-layer EBC coating additional Goodrich slurry-cast MI and GE Prepreg MI samples, of 5cm x 5cm dimensions, were coated with EBC. The deposited EBC was subjected to a heat treatment at 1250 °C for 24 hours to stabilize the Celsian phase in the BSAS. X-ray diffraction analysis of the heat-treated coatings showed that the BSAS layer consisted of 100% Celsian phase. Typical microstructures of the cross-section and of the surface of these coatings are shown in the SEM micrographs in Figures 3-124 and 3-125.

Two EBC-coated GE Prepreg samples and two EBC-coated Goodrich slurry cast MI samples were exposed in a cyclic steam furnace in a 90% H_2O + 10% O_2 environment at 1200°C, but no cycling was used for this experiment. The samples were cycled to room temperature periodically (approximately every 100 hours) to allow for visual inspection of the EBC coatings. The initial intent was to expose the two pairs of samples for 4000 and 8000 hours. However, one of the Goodrich slurry cast sample developed a "blister" in the center of the coating after about 300 hours exposure. This blister was observed to grow in severity, leading to cracking of the EBC, with continued exposure. An additional coating blister also appeared at the edge of this sample after about 1000 hours, and also continued to grow at 1300 hours. Consequently the blistered slurry cast sample and one of the prepreg samples were removed from testing after 1300 hours for destructive characterization. Photographs of the surface of the two EBC coated CMC samples following 1300 hours exposure are shown in Figure 3-126.

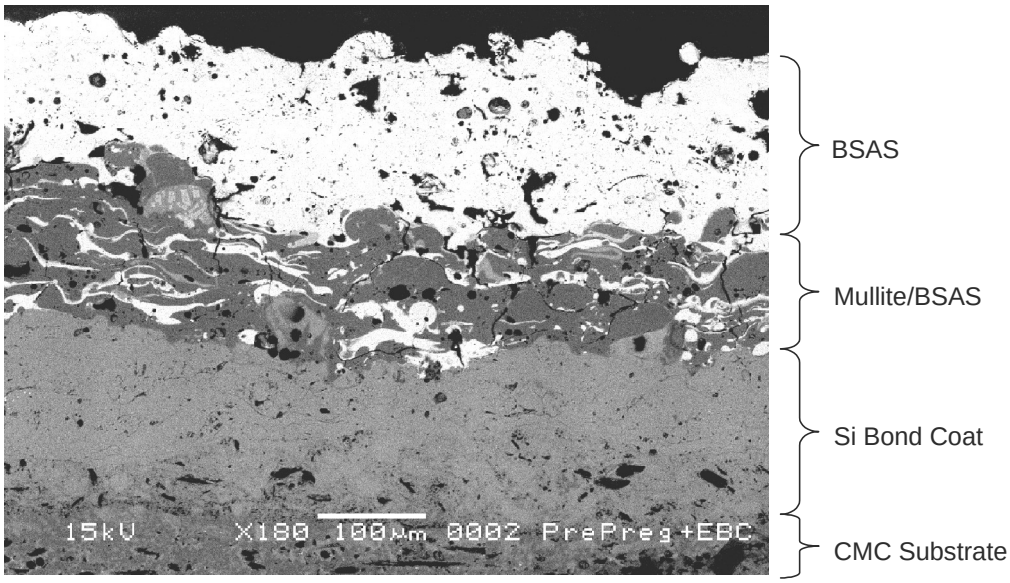

Figure 3-124. SEM micrograph of the cross-section of a three layer EBC on a GE prepreg CMC substrate. The silicon layer is above the micron marker, overlaid by the mullite + BSAS mixed interlayer and the BSAS top layer.

Figure 3-125. SEM micrograph of the top surface of a heat treated three-layer EBC on a GE prepreg substrate. The microstructure exhibits blade-like crystals typical of the BSAS Celsian phase.

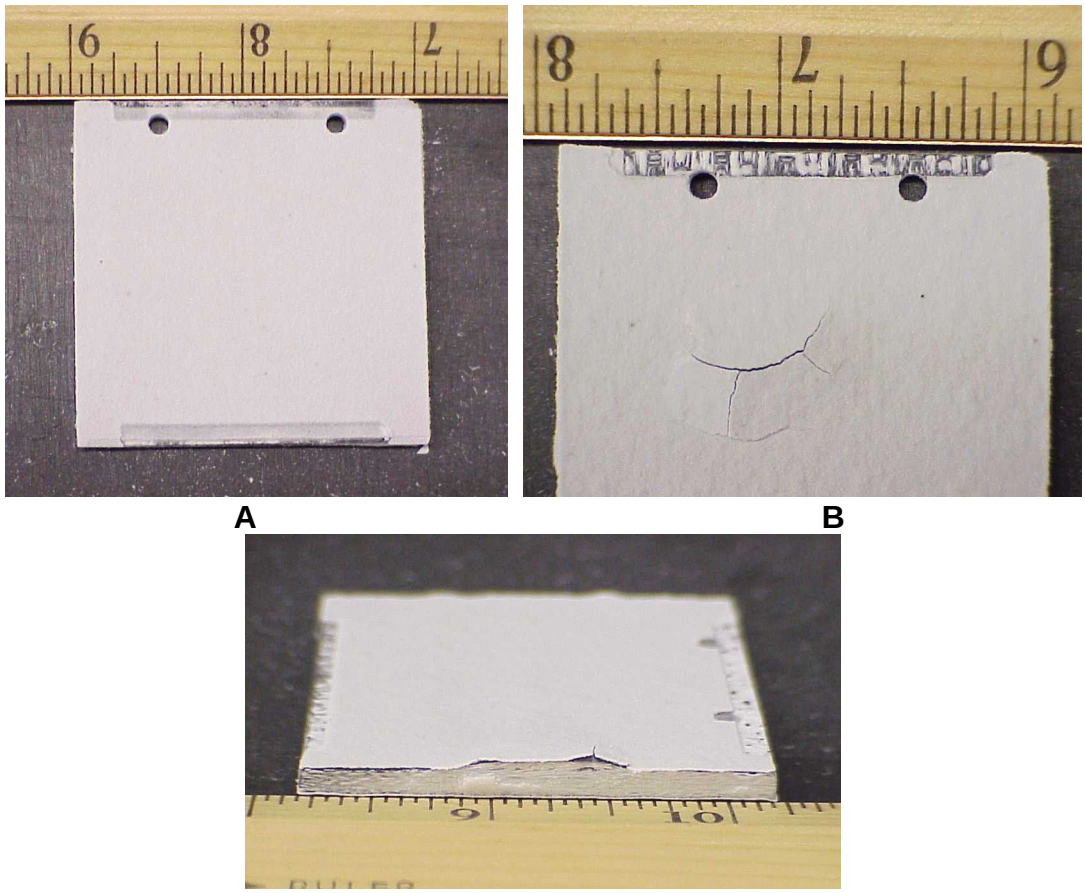

Figure 3-126. Photographs of the 5cm x 5cm CMC specimens with EBC after exposure for 1300 h: A – surface of the EBC on the GE Prepreg MI CMC substrate; B – surface of the EBC on the Goodrich slurry-cast MI CMC substrate surface; C – edge of the Goodrich slurry cast MI CMC. The blisters that formed on the surface and edge of the EBC on the slurry-cast CMC are visible in B and C, respectively.

The Goodrich slurry cast sample was cut up in such a way that the area where the EBC had blistered was exposed in cross-section, and the cut piece was mounted and polished. Examination of the polished surface by optical microscopy revealed that the blistering at the edge of the panel was caused by the oxidation of the underlying composite material. The growth of internal oxide, proceeding from the edge into the bulk primarily through interconnected porosity, caused the composite to expand (see Figure 3-127), which subsequently caused EBC near the edge of the panel to blister. The origin of the blister in the EBC in the middle section of the sample could not be conclusively determined from examination with an optical microscope.

Further analysis with SEM and EDS were performed to better understand the cause of blistering. Figure 3-128 shows SEM micrographs of the Goodrich slurry cast MI CMC sample in both a “normal” region and at the edge of the central blister. The EBC consists of a bond coat of Si, followed by a mixed layer of mullite and barium-strontium-

aluminosilicate (BSAS), and finally a BSAS top coat. The CMC substrate is visible at the bottoms of the micrographs.

In the "normal" region there appears to be a continuous layer of oxide at the interface between the Si bond coat and the mullite/BSAS EBC layer. This observation is consistent with oxidation of the Si layer to SiO_2 from oxygen diffusion through the EBC upper oxide layers. However, in the region of the blister there is substantial oxidation product formation at the bond coat – CMC substrate interface. There is also a delamination-like crack running through the oxidation product layer. The morphology of the oxide product between the bond coat and substrate is similar to that seen from internal oxidation of inter-connected porosity from earlier tests on non-EBC coated slurry cast samples. There also appears to be a vertical defect (vertical alignment of pores and/or cracks) near the edge of the blister.

The most likely scenario leading to this type of oxidation pattern is oxygen penetration from the sample edges through interconnected porosity in the bulk. Oxygen penetrating through the coating, either by solid diffusion or through a crack in the EBC, would tend to preferentially oxidize the Si bond-coat at the bond-coat to EBC interface. Even if the vertical crack extended through the bond coat, oxidation along the faces of the crack should seal the crack before substantial oxidation of the substrate to bond-coat interface could occur. However, it is still not clear whether the "blister" in the EBC existed before the test or whether it formed as a result of the bond-coat and substrate oxidation.

Characterization of the EBC on the GE Prepreg MI substrate gave very similar results to the un-blistered regions of the Goodrich slurry cast substrate. Oxidation was limited to the bond coat outer surface, and no EBC cracking, either horizontally or vertically, was noted. No evidence was found for internal oxidation of the Prepreg substrate, and thus no EBC blistering by oxidation at the substrate-bond coat interface was found.

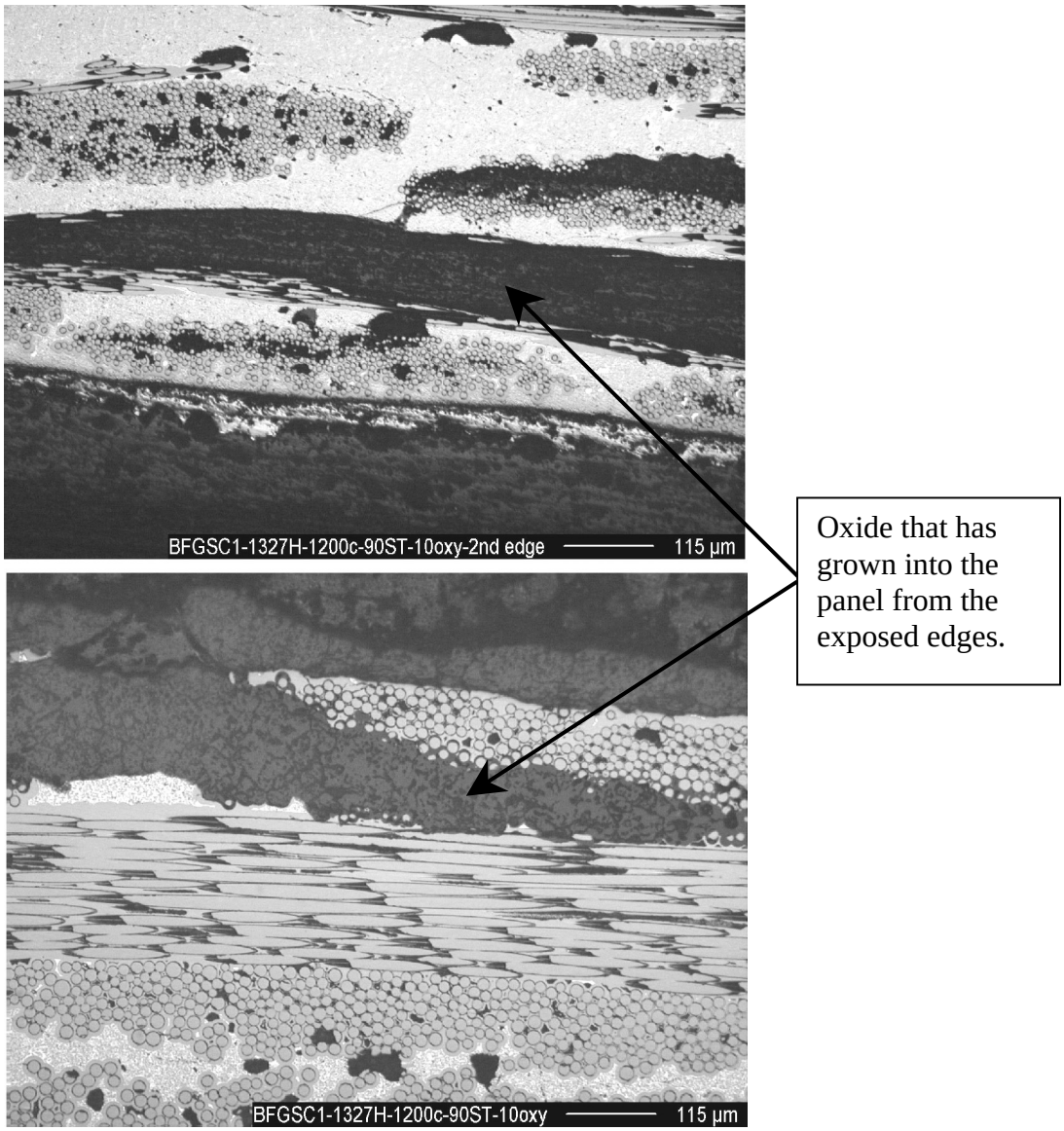

Figure 3-127. Optical micrographs of the cross section of the EBC-coated, Goodrich slurry cast MI-CMC sample which displayed coating blisters following 1300 hours of cyclic steam exposure at 1200°C. The arrows indicate the internal oxidation product (gray phase in both micro-photographs) formed by oxidation of composite matrix and fiber tows.

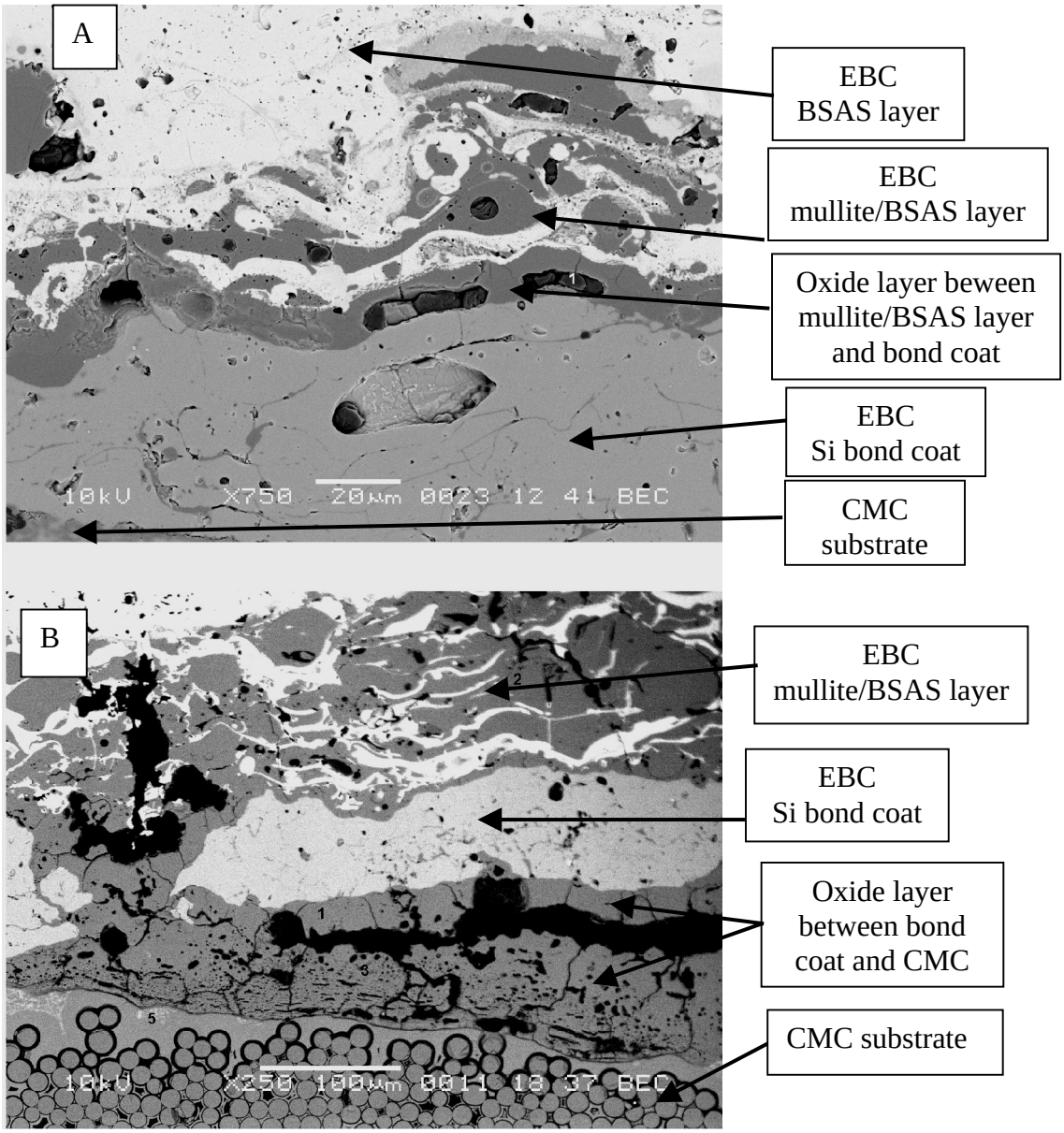

Figure 3-128. SEM micrographs of EBC-coated slurry cast MI composite following 1300 hours of cyclic steam furnace exposure at 1200°C. The micrographs are for an un-blistered (A) and blistered (B) region of the coating.

The remaining pair of EBC-coated samples were continued in steam oxidation exposure for a total of 4500 hours. Micrographs of the EBC cross section for these two samples are shown in Figure 3-129. The thermally grown oxide is clearly shown in the micrographs. Even with the formation of the silica layer, no EBC spallation was observed after 4500 hours.

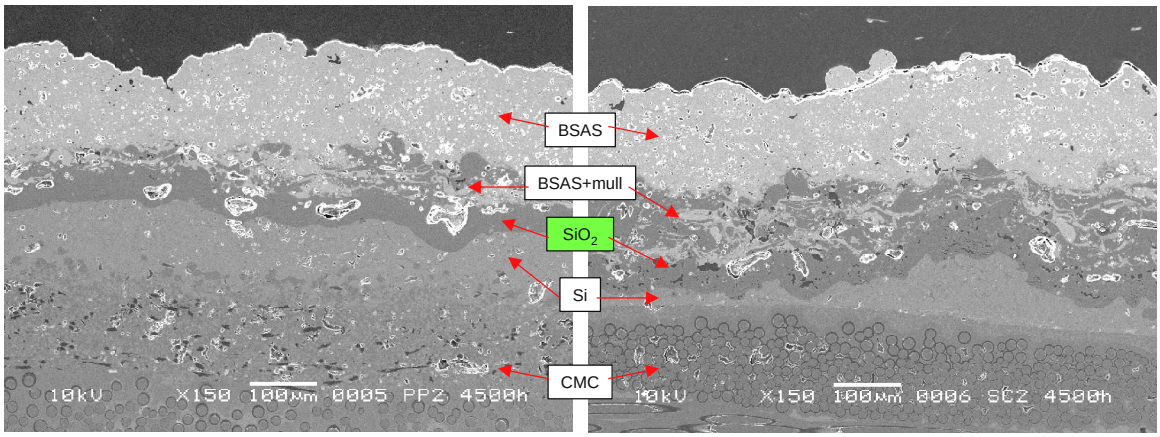

Figure 3-129. SEM micrographs of EBC cross sections on MI composite samples following 4500 hours of cyclic steam furnace testing: A – Goodrich slurry cast MI substrate, B – GE Prepreg MI substrate. The layers of the EBC, including the thermally-grown SiO_2 layer on top of the silicon bond coat, are indicated.

The oxidation rate of the EBC bond coat was determined based on estimates of oxide layer thickness obtained using SEM, energy dispersive x-ray spectroscopy (EDS) and optical microscopy. EDS dot mapping was used to define the location of the thermally grown silica layer. The oxidation layer analyzed composition was essentially pure silica at 1300 hours, but had a small amount of dissolved alumina from the mullite-BSAS transition layer at 4500 hours. Measurements of silica layer thickness from the SEM and via optical microscopy were in good agreement. The oxidation rate was determined from the average thickness of the oxide layer measured in the center region of each 5cm x 5cm panel in un-blistered regions to reduce the effects of edges and substrate internal oxidation.

Figure 3-130 shows a plot of the thickness of the silica layer versus steam exposure time. There were no statistically significant differences in the oxidation rate between the Prepreg or slurry cast CMC substrates. The relatively large error bars were a result of actual variation in the silica layer thickness, which could vary as much as 10X for a single sample, and not due to measurement errors.

One interesting phenomenon observed in the samples oxidized for 4500 hours was the formation of pores within the thermally grown SiO_2 layer. Figure 3-131 shows SEM micrographs of the silica layers in both prepreg and slurry cast MI samples after 4500 hours exposure. The mechanism of formation of the porosity is not currently understood.

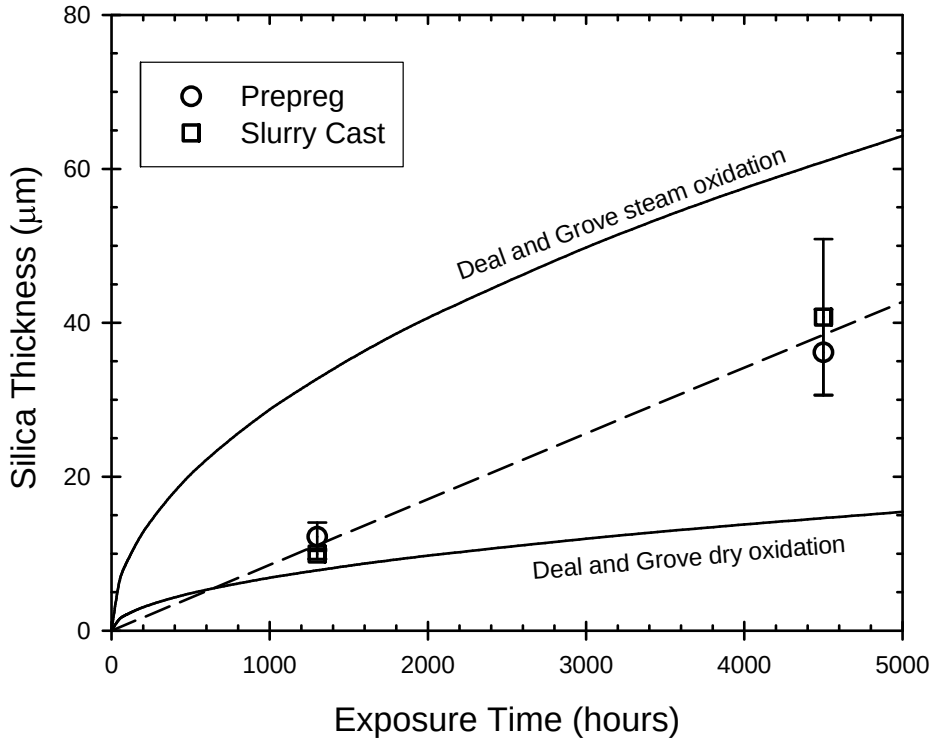

Figure 3-130. Relationship between the steam furnace exposure time and thickness of the thermally-grown SiO_2 layer within the EBC. The error bars represent ± one standard deviation. Calculated thickness trends for the oxidation of silicon in dry O_2 and steam based on the model of Deal and Groves[19] are shown for comparison.

K. More of ORNL reported at the June, 2001 ASME Turbo Expo meeting [20] that there was substantial reaction/decomposition occurring in the mullite/BSAS layer of the EBC coating on the slurry cast MI combustor liner that had been put through 14,000 hours of engine testing by SOLAR Turbines. The BSAS/mullite layer of the EBCs from the stream furnace test was examined in detail to look for evidence of similar composition changes. Figure 3-132 shows an SEM micrograph and EDS spectra from several regions within a representative mullite + BSAS layer. Even in close proximity to the thermally-grown silica layer, there were no detected compositional changes in the BSAS phase in this layer.

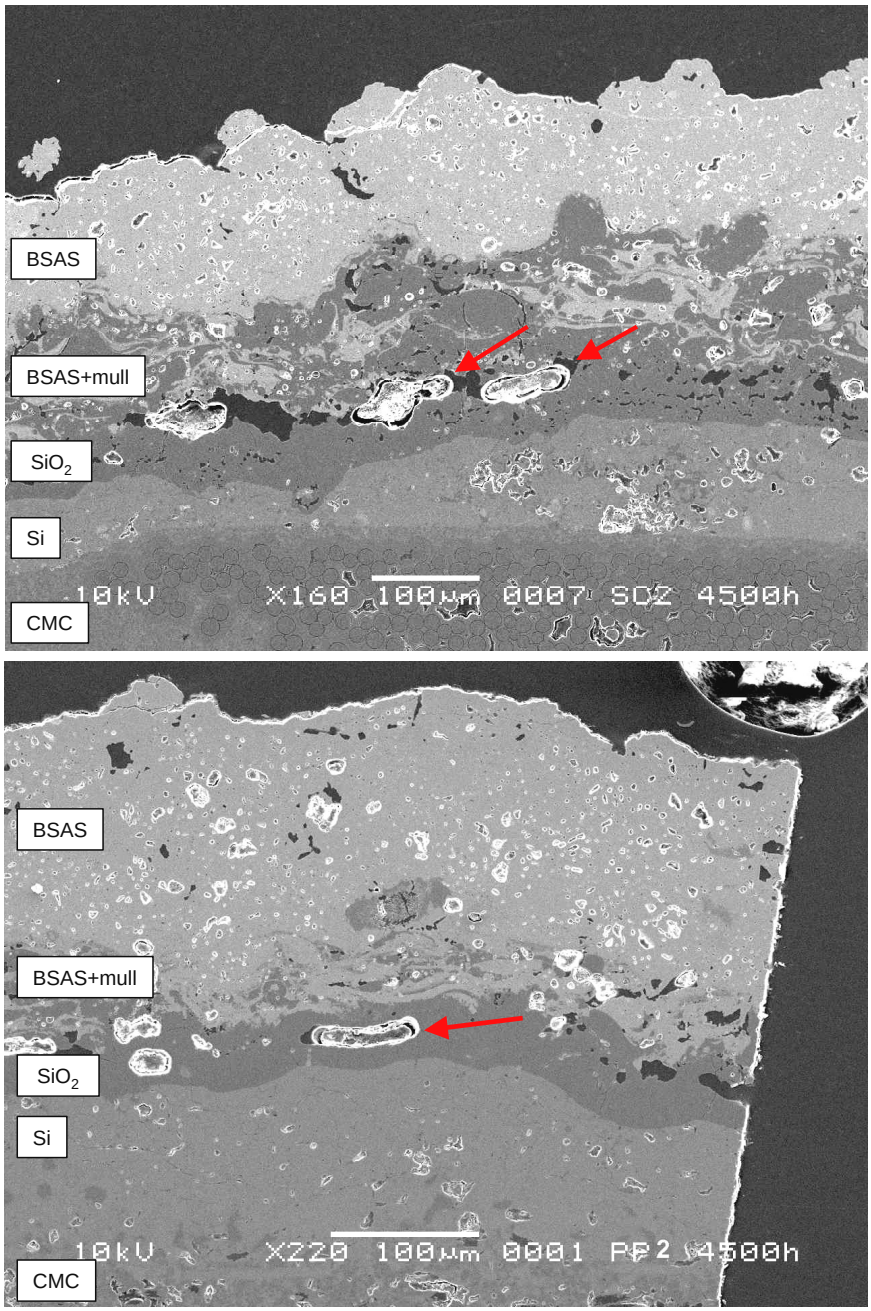

Figure 3-131. SEM micrographs showing the formation of pores in the thermally-grown silica layers formed by oxidation of the EBC silicon bond coat following 4500 hours steam exposure at 1200°C in the cyclic steam furnace. Top – Goodrich slurry cast MI substrate; Bottom – GE Prepreg MI substrate. The pores are indicated by the red arrows.

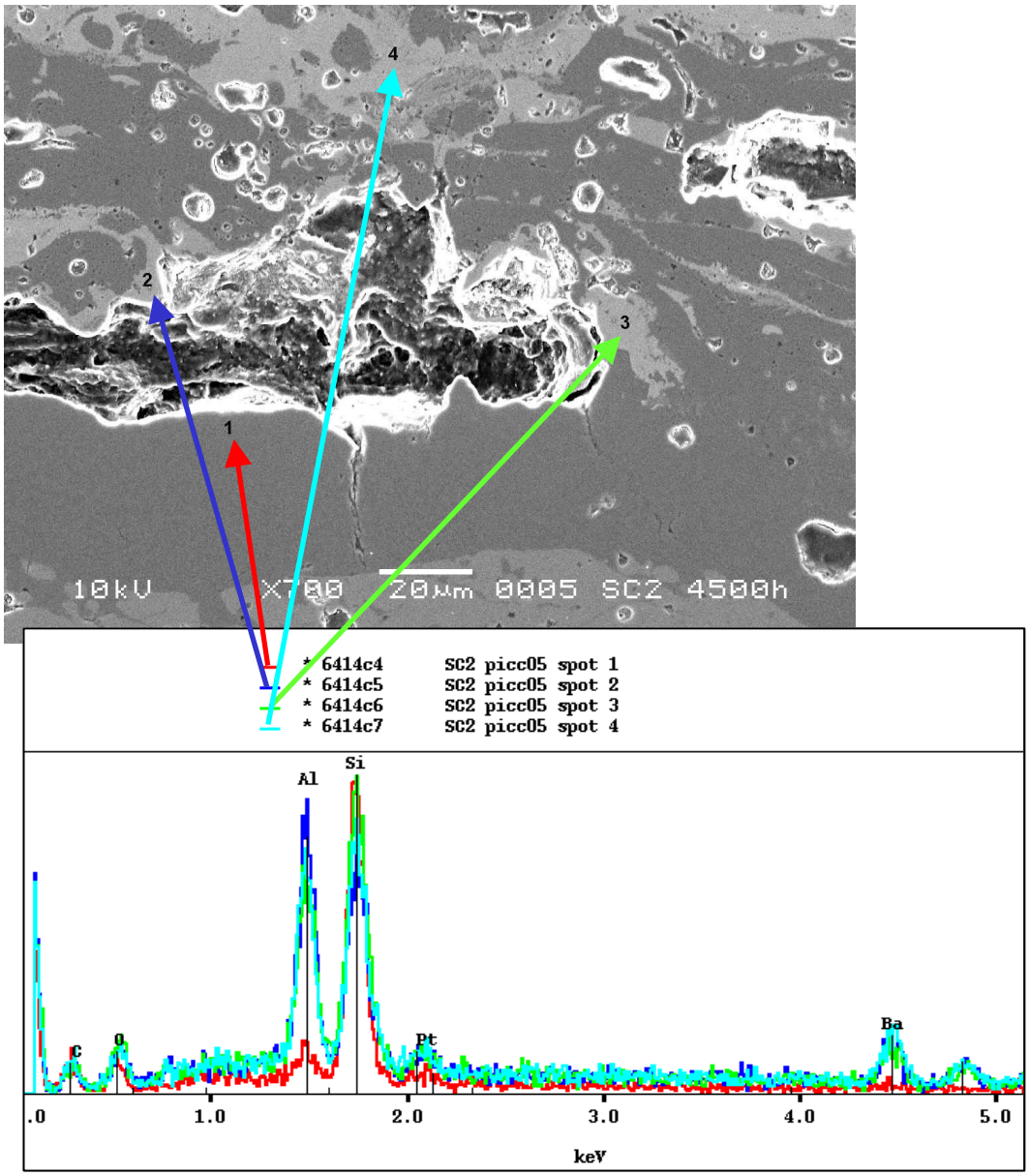

Figure 3-132. SEM micrograph and EDS patterns for several areas of the mullite + BSAS layer of the EBC coating following 4500 hours at 2200°F in the LTSF test.

3.5.3 Impact Testing of EBC-Coated CMCs

The above studies had demonstrated the stability of the EBC system to thermal and environmental exposures expected in a gas turbine. However, in an actual turbine application the EBC would be subject to mechanical damage from foreign object damage as well. Ballistic impact testing was therefore conducted on EBC-coated CMC samples to determine whether the EBC was more susceptible to impact damage than was the underlying CMC material.

Small (3.8cm x 5cm) samples of CCP slurry cast MI CMC reinforced with Hi-Nicalon were coated on both the front-side and backside with the standard 3-layer EBC. The samples were then impacted with the 4mm chrome steel ball at velocities of 435, 194, 107 and 93.6m/s.

A photograph of the backside of the damaged EBC coated samples are shown in Figure 3-133. Impacts at the two higher velocities were sufficient to perforate the samples. The diameter of the front-side damage zone was limited to about 1.5 times the size of the hole made by the impactor. At the two lower impact velocities, the front sides of the samples were pitted by the impactor but not otherwise damaged. There was no EBC damage noted in any region removed from the impact event. The backsides of all four of the samples showed more damage than the front sides, with damage zones in all cases of 2-2.5 times the diameter of the impactor. These results show that impact damage of EBC coated samples is limited in extent regardless of the velocity of the impactor, and is comparable to the damage zone size in the underlying CMC. Backside damage is more severe than front-side damage, especially at low impact velocities where little front-side damage occurs, but again is no more extensive than the CMC damage zone.

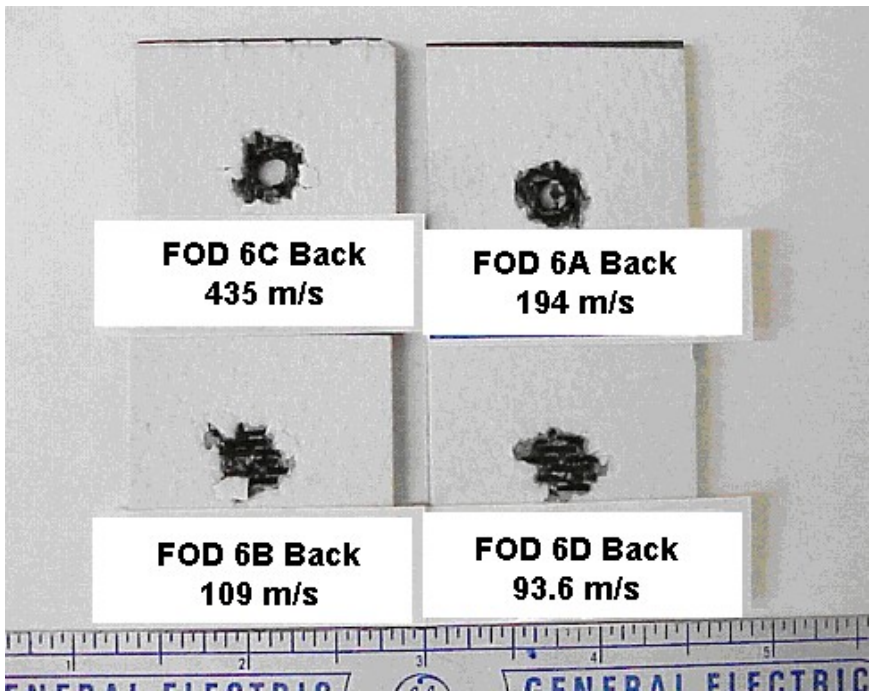

Figure 3-133. Photograph of backside (exit) damage of EBC-coated CCP slurry cast MI composites reinforced with Hi-Nicalon.

3.6 Process Understanding (Task 3.2.c)

The work in this section was performed under program task 3.2.c Process Understanding. The purpose of this task was to develop the necessary process capability to guide the scale-

up and optimization of the composite and component fabrication processes. Processing of large prepreg MI CMC components requires the scale-up of the pre-existing technology for the fabrication of small panels. To successfully process large components a model of the process is beneficial to avoid costly trial-and-error efforts and to better understand the robustness of the processing techniques. Experiments were also be done as needed to help develop our understanding of the fabrication process and help guide the scale-up activities.

Numerous activities were conducted under the Process Understanding task. Most of these efforts had direct impacts on the CMC fabrication process, and the implementation of their results, or the effects of their implementation, has already been discussed in previous sections of this report. The specific activities pursued under this task are listed and summarized below. More detailed descriptions of three of the efforts not covered elsewhere, namely the bend radius study, the shroud HIP repair study, and the CVD system leak study, are described in somewhat greater detail.

3.6.1 General Results

The drum winding process for monofilament fibers was investigated relative to the speed of winding and its effects on tape uniformity. A video-microscope was used to monitor the thickness and uniformity of slurry pick-up during drum winding of SCS-0 fiber. At all speeds the thickness of the slurry was even around the fiber as the hydrodynamic forces in the orifice tended to center the monofilament. At filament winding speeds between 8.5cm/s to 17cm/s the slurry thickness was uniform along the length and relatively independent of fiber speed up to 17cm/s. Below 8.5cm/s slurry instability was noted in that the slurry on the fiber would break up via Rayleigh waves, forming individual droplets on the fiber at very low speeds. The consequence of the slurry instability was that the wound tapes increased in roughness as the speed dropped below 8.5cm/s. These results were consistent with models of coating wire with enamel insulation.

The effect of boron additions to the silicon infiltration alloy on the reaction of silicon with carbon was investigated using several infiltration experiments. The effect of boron inhibiting the silicon-carbon reaction was first noted in monofilament-reinforced composites using the matrix slurry with crushed carbon felt, as discussed in report Section 3.2.1.4. Additional experiments were also done under this task to better quantify the effects of boron additions by examining the reaction fronts developed between highly aligned pyrolytic carbon samples and silicon-boron alloys of varying composition. As might be expected, reaction on the c-plane face of the pyrolytic graphite was limited regardless of the boron content of the alloy. However, reaction of the pyrolytic carbon on the a-plane face was much more aggressive and sensitive to boron content. Reaction on this surface with pure silicon led to deep penetration of the silicon into the carbon with "exfoliation" between the c-planes. When doped with >3wt% B the reaction on the a-planes was more uniform and planar in nature.

A new method of silicon infiltration was developed under this task with the advantage of being able to infiltrate complex shaped parts. Typically silicon infiltration had been performed by bringing the molten silicon alloy to the preform via a carbon cloth wick;

however, attachment of such wicks to complex shaped parts was not anticipated to always be possible. A new process was therefore developed wherein the preform is encased in a mixture of silicon, boron and boron nitride powders, either by dip coating or by spreading a slurry over the surface of the preform. Upon heating above the melting point of silicon the silicon and boron alloy would melt and react, and infiltrate into the preform via capillarity. The boron nitride would form a framework of porous solid around the preform that would keep the silicon alloy in contact with the preform and not allow it to simply "run off." Following the infiltration heat treatment the BN powder remaining on the surface of the preform, having been mostly depleted of silicon via the infiltration of the silicon into the preform, was very friable and could be easily removed from the infiltrated composite by physical scraping or grit blasting. This new infiltration technique, referred to as the "pack infiltration" process, eliminated the need for carbon wicks and any post-infiltration machining associated with removing the wicks where they were attached to the CMC. This technique was so successful on panels that it eventually became our standard process for infiltrating panels, and was used extensively for infiltration of shroud components, to be discussed in Section 3.8.1.3. Unfortunately this technique is not effective at infiltrating components with thick wall sections. In order to supply sufficient silicon alloy, the thickness of the powder pack increases in proportion to the thickness of the preform to be infiltrated.

As pack infiltration was largely ineffective for thick cross section items, infiltration studies were also done using wick infiltration of thick panels. Unidirectional reinforced panels 6.5mm thick were wick infiltrated in directions parallel and perpendicular to the fiber direction. After a 45 minute infiltration cycle the preform infiltrated parallel to the fiber direction was infiltrated to a depth of about 4cm whereas the preform infiltrated perpendicular to the fiber direction was only infiltrated to a depth of about 2cm. This information allowed us to set limits on the infiltration distances for thick components and helped define the optimum locations for wick attachment depending on the geometry and fiber architecture.

The processing of prepreg-like composites using three-dimensional fiber architectures was investigated under this task. An obvious weakness of 2-D laminate composites is the inherently low interlaminar strengths. Although GE's prepreg MI composites have the highest interlaminar strengths of any 2-D CMC material, there may be applications where additional interlaminar strength would be necessary. Plans were developed to evaluate both braiding and 3-D weaving of coated Hi-Nicalon™ tow into preform panels, which would be subsequently impregnated with matrix slurry and processed as typical MI composites. However, during negotiation with braiding and weaving vendors it was discovered that the amount of fiber lost to stringing up the machinery would greatly exceed the amount that actually got into the composite preforms. Subsequently a pin weaving process, whereby tow is manually wrapped around stationary pins, was used to prepare 3-D woven preforms. Several problems were noted with this approach, namely that the fiber packing was limited by the hand wrapping approach, that fiber coatings were damaged due to the tight bending around the pins, and matrix impregnation of even a loosely woven preform was problematic with poor wet-out and large intra-tow porosity. Following this experience work on 3-D architectures in prepreg composites was discontinued.

Wet and dry oxidation studies on silicon-doped BN samples was also done under this task, although the results have already been reported in Section 3.2.2.3. This work helped identify the optimum silicon doping level in the B(Si)N fiber coatings implemented under task 3.2.a.3.

Development of the tow coating technology was started under this task, which included the initial deposition studies used to identify proper CVD temperature/pressure/flow conditions to yield the desired thicknesses and uniformity of the various fiber coatings. Once these process parameters for the individual coating layers were identified the optimization of the multilayer coatings for use in CMC fabrication was transferred to task 3.2.a.

Many of the damage tolerance studies, including much of the ballistic testing described in report section 3.4.6. were actually conducted under the Process Understanding task.

In order to better understand and control the melt infiltration process, gas evolution from constituents of the composite preform, most notably the fiber, was studied by heating samples to 1400° – 1450°C and quantitatively analyzing the effluent with a mass spectrometer. Results varied considerably both from fiber lot to fiber lot as well as from sample to sample for a given length of fiber. It was concluded that sufficient gas (mainly CO) was generated from some samples to interfere with infiltration. Gas evolution became significant at ~1350°C (below the Si melting point), but would decrease with time to near zero after 1 to 2 hours. A 2-hour hold at 1350°C was therefore inserted into the infiltration furnace ramp to allow for any such out-gassing of preforms prior to introducing any molten silicon. Experience with this process has been positive with fewer components rejected due to poor infiltration following the institution of this temperature hold.

Effects of fiber architecture on the mechanical properties of prepreg MI composites has been discussed in section 3.4.3.8. The initial planning and sample fabrication for this effort was done under the Process Understanding task.

3.6.2 Bend Radius Study

A composite bend radius study was performed to test the limitation of the prepreg tapes to bending around sharp corners. Standard 8-ply “L-shape” panels, nominally 2.3mm thick, were fabricated by laying up tapes over right angle forms with various radii at the corner. The observations from this experiment are shown schematically in Figure 3-134. The CMC microstructure and thickness uniformity were maintained down to an inner radius of 6.3mm, but at smaller radii the corners were distorted as shown in the figure. As the allowable bend radius is expected to scale with the thickness of the composite, this result indicated that the tightest radius should be no smaller than 2X the thickness of the part.

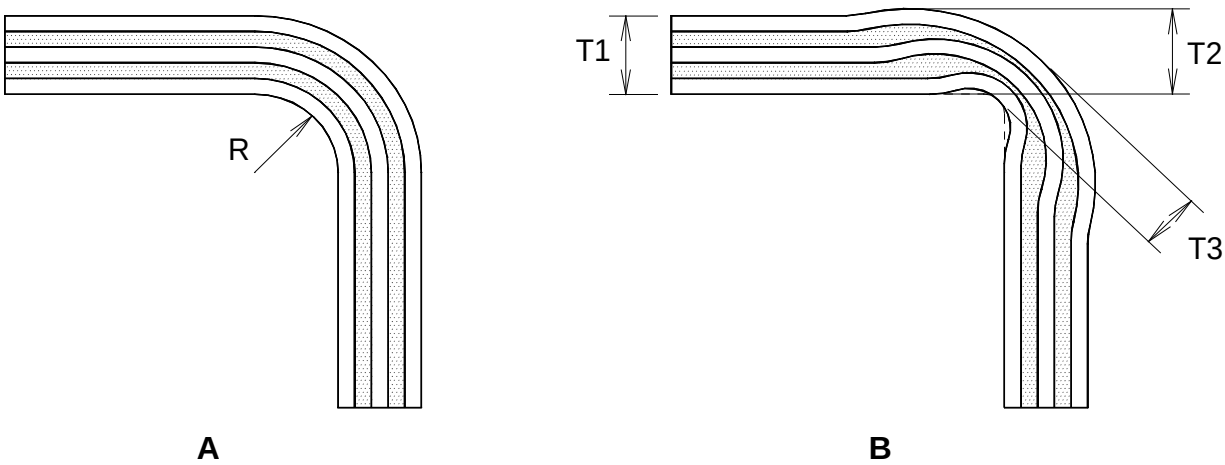

Figure 3-134. Simplified schematic representations of the 90° bend composite lay-ups. Composites with 12.7mm or 6.3mm inner bend radii (R) maintained uniform ply thickness around the bends, as shown in A. Composites with 3.2mm and 1.6mm inner bend radii displayed thickness variations around the bends, as shown in B, resulting from flow of material from the transverse plies (shaded) out to areas adjacent to the bends.

3.6.3 Shroud Repair Via HIP Processing

During the initial stages of shroud fabrication in the Advanced Materials for Advanced Industrial Gas Turbines (AMAIGT) program numerous shrouds with delamination and/or poor infiltration defects were produced. In a research environment such unsuccessful components can simply be scrapped; however, in a commercial production environment the ability to "rework" or repair such faulty parts would have a direct impact on the overall process yield. There was thus a desire to find a method for "healing" such defects in processed shrouds. The process evaluated was to hot isostatically press (HIP) the parts after infiltration.

Specimens of prepreg MI CMC with planar defects identified by Transient IR Analysis were taken from the AMAIGT program and sent to a vendor for HIP treatment. The initial experiment was to evaluate two HIP cycles; one above and one below the melting point of silicon. We anticipated that at 1350ºC the matrix should be plastic enough to deform and collapse planar defects offering the potential for silicon diffusion bonding within the matrix. In the event that silicon would not completely fill defects, a brief excursion above the melting point should further assist silicon infiltration.

The two HIP cycles described above were conducted. Both temperature and pressure were ramped linearly from the ambient to 1350ºC and 30,000psi, respectively. After a one-hour hold, one run was cooled to room temperature while the other run was rapidly heated to 1450ºC, held for 10minutes and then cooled to ambient. Transient IR analyses were performed on both specimens and compared to pre-HIP results. Neither trial showed significant improvement in the IR images. There were actually some indications that the

HIP treatment may have extended certain defects. It is possible that the pressure ramp could have produced stresses on the parts during heat-up before the Si was able to relax, thus extending the defects.

Microstructural examination of the above samples suggested that there may have been insufficient infiltration of the samples to form a sealed surface, and thus the HIP gas would be able to penetrate the porosity and not provide a compacting force to the composite. A third evaluation was therefore performed where the shroud was first completely coated with silicon using an air plasma spray process prior to HIPping. Following HIP treatment at 1450°C the surface silicon was found to have completely melted, as anticipated. However, NDE inspection showed essentially no change in the composite defects. Following these three unsuccessful attempts we decided to discontinue any further evaluations of HIPing treatment to heal defects in MI CMCs.

3.6.4 CVD Reactor Leak Study

The effects of CVD vacuum system leaks on the deposition of fiber coatings, and on the mechanical performance of composites made with these coatings, was also investigated under this task. During the May-August, 2003 time frame we experienced both water and air leaks in our larger CVD fiber coater. Unfortunately it took several weeks to months for us to recognize the problems and affect repairs. Consequently we wanted to better understand the effects of small water and air leaks on the behavior of the coated fiber, and subsequent processing and properties of the composites produced from such fiber. Such knowledge should help us to more effectively detect the occurrence of such leaks in the future. In addition, it would provide insight as to the tolerance for leaks during the CVD coating process.

Past experience suggests that air and water leaks during the CVD fiber coating process reduce the coating rate and lead to decreased mechanical properties in ceramic matrix composites (CMCs). It has been hypothesized that oxidized coatings give off CO and/or SiO at high temperatures during the melt infiltration process, causing a positive pressure in the porous perform. The pressure caused by out-gassing is thought to slow the wicking of silicon into the preform and thereby prevent full densification of the component. The potential for oxidized coatings can occur when an air or water leak is undetected during the CVD coating process.

A 2-factor 2-level Design of Experiments (DoE) was designed using air and water as the two factors. Controlled amounts of air and water vapor were introduced into the smaller CVD reactor to observe the effects on the coating rate, morphology, and mechanical properties of CMCs. During deposition of fiber coating configuration C controlled amounts of air and water were injected into the reactant stream of the CVD reactor. The lower air leak flow rate corresponded roughly to the detection limit of oxygen by the residual gas analyzer. The high air leak flow rate was 3X the low flow rate. Water flow rates for high and low leak rates were set to be equivalent to the O_2 component of the air leak flow rate, which would still give roughly ½ the amount of oxygen.

One response variable, weight gain during the coating process, was used as a measure of coating rate. The other primary response variables were the mechanical properties of the CMC including ultimate strength, modulus, strain to failure, and proportional limit stress. It should first be noted that the fiber lot used, #369, had a very high tensile strength (3450MPa) as measured by the fiber supplier, NCK. This was well above the historical average of about 2900MPa, and thus exceptional properties might be expected.

The air/water leak experiments were done in two sets, the first set being the initial design of experiments and comprising test samples 1818, 1801, 1816, 1844 and 1817 as listed in Table 3-45. The surprising result of the initial experiments, as indicated by the data in Tables 3-46 and 3-47, was that there was a beneficial effect of the leaks on the room temperature tensile properties, especially on ultimate strength but also to a lesser extent the on proportional limit stress, modulus, and strain to failure. The high water/high air leak condition, CVD 335B, showed a 23% increase in ultimate strength when compared to the baseline results with the same fiber lot, CVD 334A. The other 3 leak experiments, although having higher mechanical properties over the baseline run, showed much less improvement.

Results of the tensile tests done at 1204°C, summarized in Table 3-46, did not show the same trend observed at room temperature. The strain to failure of these samples averaged around 1% at the high strain rate. The decrease in strain to failure from RT to 1204°C averaged around 28%, which is typical for Hi-Nicalon™ composites. Overall, the oxidized coatings had no observable effect on the high temperature tensile properties.

Table 3-45. Tensile Properties of Samples from the CVD Air/Water Leak DoE Measured at Room Temperature

Sample	Fiber Lot	CVD Run	Water Flow Rate	Air Flow Rate	Ultimate Strength (MPa)	Strain to Failure %	Modulus (GPa)	Proportional Limit Stress (MPa)	Sample Thickness (mm)
1818	369	335B	high	high	463	1.58	257	187	2.26
1801	369	333A	high	low	405	1.44	239	182	2.34
1816	369	334A	No Leak:Baseline		376	1.19	229	159	2.36
1844	369	334B	low	low	340	1.07	243	188	2.51
1817	369	335A	low	high	391	1.45	220	177	2.21
1928	356	340	high	high	273	0.73	248	159	2.36
1679	356	305	No Leak; Baseline		264	0.77	247	137	2.50
1929	369	345	high	high	421	1.27	219	136	2.24
1930	369	345	high	high	258	0.78	212	127	2.46

Table 3-46. Tensile Properties of Samples from the CVD Air/Waterleaf DoE Measured at 1204°C using Low and High Strain Rates

		Low Strain Rate				High Strain Rate			
Sample	CVD Run	Ultimate Strength (MPa)	Strain to Failure (%)	Initial Modulus (GPa)	Proportional Limit Stress (MPa)	Ultimate Strength (MPa)	Strain to Failure (%)	Initial Modulus (GPa)	Proportional Limit Stress (MPa)
1818	335B	252	0.36	233	194	341	0.91	263	202
1801	333A	249	0.38	193	196	363	1.08	203	205
1816	334A	237	0.35	217	132	346	1.09	224	185
1844	334B								
1817	335A	247	0.32	224	181	319	0.94	214	198

The relative amounts of oxidation within the coating layers were confirmed with TEM and EELS of the two extreme conditions of the DoE (no leak vs. highest leak rates). As expected, the baseline sample, 1816, had no observable oxygen within the coatings. The BN coating within this sample was dense, large grained with the c-axes highly aligned perpendicular to the fiber surface, and had no oxygen at the fiber/BN interface. Sample 1818, the sample containing fiber coated under the highest air and water leak rate, showed oxygen levels greater than 10% within the BN and had significant oxygen within the other coatings as well. The BN is highly disrupted, turbostratic, and porous. The fiber/BN interface showed no oxygen or excess carbon. Although not characterized, the fibers coated with intermediate levels of air and water leak rates, namely samples 1801, 1844, and 1817, would be expected to have between 3-10% oxygen within the BN coating layers.

As noted above, sample 1818, containing fiber coated under the highest leak rate conditions, showed the highest tensile properties. However, the likely explanation for the increase in RT tensile properties observed in this sample may be totally unrelated to the oxidized coating. In low magnification optical microscopy, as shown in Figure 3-135, sample 1818 was observed to have a very dense matrix with well distributed fibers. The combination of excellent distribution of fibers and almost complete lack of porosity has proven to yield superior performing composites in the past. Two other samples from this study, 1816 and 1817, shown in Figure 3-136, had somewhat more tightly bundled fibers within the tensile plies as well as a small amount of porosity within the matrix. This improved fiber distribution and defect-free microstructure likely accounts for the superior tensile properties of sample 1818 when compared to the other samples in the DoE.

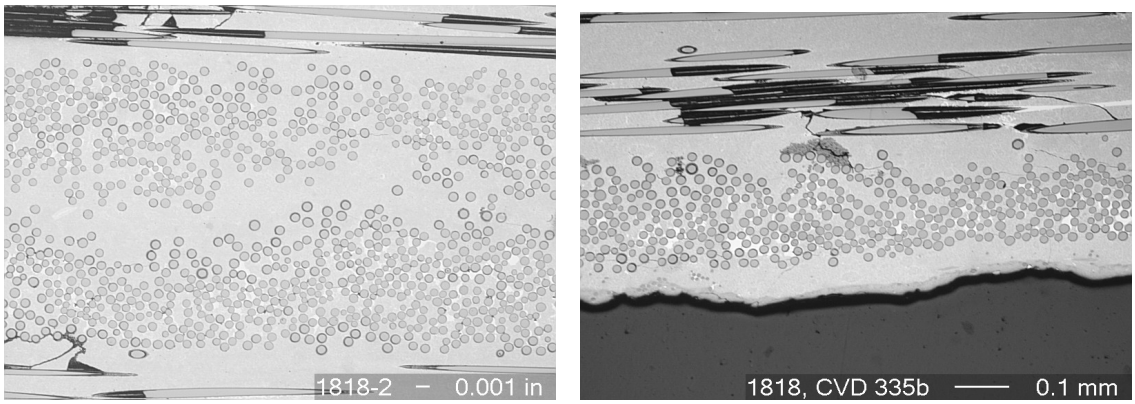

Figure 3-135. Optical photos of CMC sample 1818 containing fiber coated under high air/high water leak conditions. On left is the cross section of the inner two tensile plies. On right is an outer tensile ply.

Clearly the two expected results of the DoE experiments, decreased weight gains and decreased mechanical properties with increased reactor leakage rates, did not occur. Coating weight gains showed typical scatter suggesting that the leaks had little or no effect on coating rate. Also, based on the matrix properties, namely the proportional limit stress and modulus, it appears that infiltration was not inhibited. Because these results were so surprising we decided to reproduce the coating run at the highest air and water leak rates using the same fiber lot and also with a second more typical fiber lot, namely lot #356.

The room temperature tensile properties of the repeat samples, using fiber from lots 356 and 369 and coated under the high air/high water leak rate conditions, are included in Table 3-45. Samples 1929 and 1930 were direct repeats of sample 1818; however the mechanical properties of these two panels differed significantly. The tensile properties of the first sample, panel 1929, matched those of the baseline no-leak sample. The second panel, sample 1930, however, showed a substantial reduction in tensile properties, including drops in ultimate strength and strain to failure of 31% and 33%, respectively, compared to the sample made with no leaks.

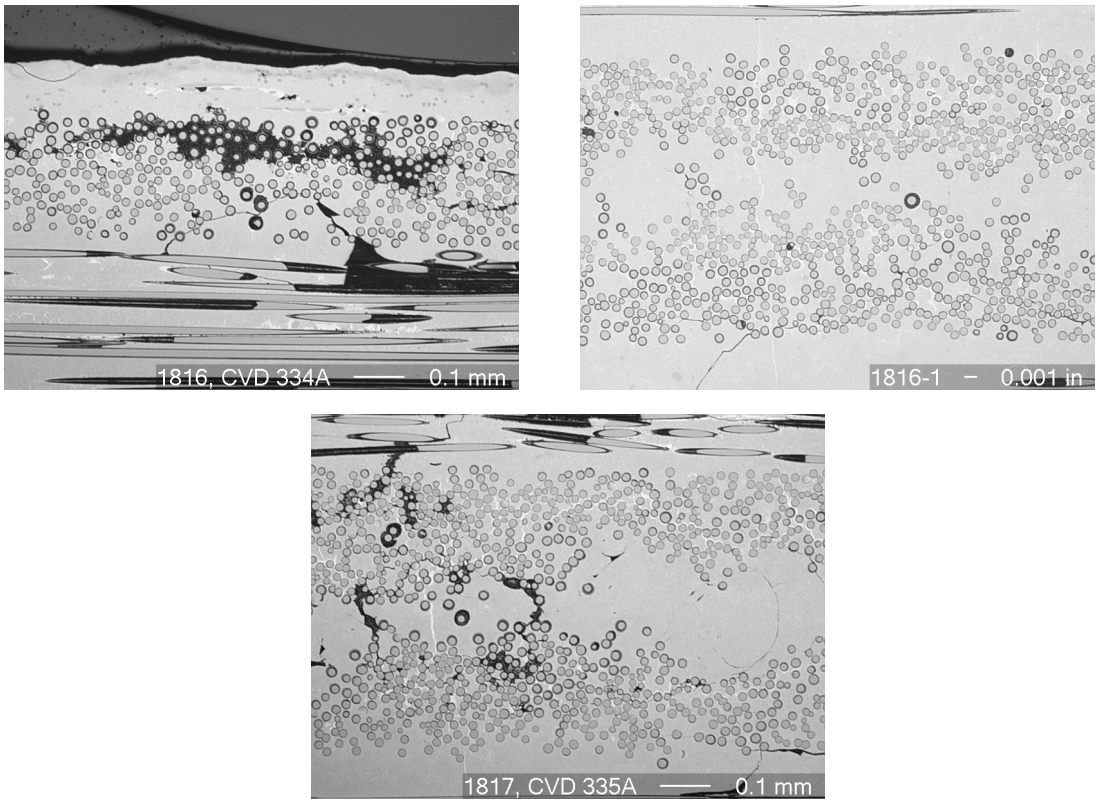

Figure 3-136. The two micrographs on the top are cross sections sample 1816 containing fiber coated under baseline conditions with no leaks. The bottom micrograph shows the cross section of the inner two tensile plies of sample 1817, which contains fiber coated under the high air/ low water leak condition.

A second repeat experiment of the high water/high air leak condition was conducted using a different fiber lot, #356, which had 25% lower tensile strength than lot #369. The resulting RT tensile properties for this sample (1828), which are included in Table 3-45, were rather mediocre compared to the lot 369 samples. Nevertheless they closely match the historic properties for this fiber lot, as evidenced by the results from sample 1679, which was fabricated ~one year earlier without any CVD reactor leaks.

Microstructural characterization of these repeat samples showed a higher amount of porosity within the tows of the tensile plies than was seen in the initial DoE samples. However, the degree of porosity did not correlate with the reductions in tensile properties as sample 1929 had more observed porosity than sample 1930 and yet still had better mechanical properties.

The overall result of these experiments is that there were no discernible effects of rather large water and air leaks in the fiber CVD coating operation on the fabrication and mechanical properties of prepreg composites. Even at the highest leak rates tested only one of four samples made showed any significant reductions in mechanical properties compared to baseline samples made from the same fiber lot but with no leaks during tow coating. Likewise, coating rates were not noticeably changed as a result of the presence of

these leaks. Oxygen contamination of the coatings was confirmed by TEM, and yet this oxygen content appeared to have no effect on the short-term mechanical performance of the composites. Coating morphology however, was changed by the presence of the water and air leaks during CVD coating. Whether this oxygen contamination would have detrimental effects on the performance of the composites during long-term thermal exposure or under fatigue conditions still needs to be determined. However, these preliminary results do indicate that the high temperature, low pressure CVD tow coating process is rather robust with regard to minor leaks in the CVD system.

3.7 Process Economics (Task 3.2.d)

This work was done under program Task 3.2.d Process Economics. The objective of this task was to estimate the costs of producing CMC gas turbine components on a commercial scale. However, estimating the cost of manufacturing involves rather detailed analysis of the process steps, which at this time is still considered highly proprietary information by GE and by other CMC manufacturers. Consequently the details of how the cost models are derived, and their predictions in absolute terms, cannot be discussed here. Rather results of the cost modeling will be described in general terms, with results presented only in relative terms.

Obviously, for any CMC component to be successful in the marketplace the cost to consumers needs to be attractive enough, compared to the expected benefits provided by that component, to warrant its purchase and utilization. Given the expected level of benefit to be derived from a CMC shroud system in a 7FA class engine, GE Energy marketing has indicated that the CMC shroud should be no more than 3X the price of current metal shroud technology. The question then becomes whether we believe a CMC shroud can be produced within this cost limit.

A detailed process cost model was developed by GEGR to evaluate the costs of producing CMC shroud components. The initial model analyzed the process steps as practiced at the laboratory scale of fabrication since that, at the time, was our experience base, and thus we could confidently assess the raw material and manpower needs and process step yields for this scale of process. The model was then expanded to include projections as to the process costs for a scaled-up production process. All of the material processing steps were maintained from the lab model, but allowances were made for the use of larger equipment and greater automation. Based on these models the relative contribution of each raw material and process step was evaluated as to its contribution to the overall cost to produce the component. The breakdown of costs for the lab-scale and production-scale processes are shown in the Pareto charts in Figure 3-137. Please note that the cost model included only fabrication of the CMC inner shroud, and did not include any additional metal hardware required for the shroud system or for EBC coatings.

The top chart in Figure 3-137, which is representative of the current lab-scale process, shows that fiber coating application is the highest cost step in current the process. This is not surprising since this process step is currently very labor intensive. At the lab scale the cost of fibers is only the third highest cost factor.

The bottom Pareto chart shows the results when the cost model is applied to a similar, but scaled-up, production process for prepreg MI shrouds. The overall cost of the shroud drops to about 10% of the current lab-scale cost at this production level. The labor-intensive process steps have all benefited from economies of scale; however, the fiber costs have not dropped by nearly as much at this volume level. Consequently the cost of fibers is projected to be roughly 50% of the total shroud cost.

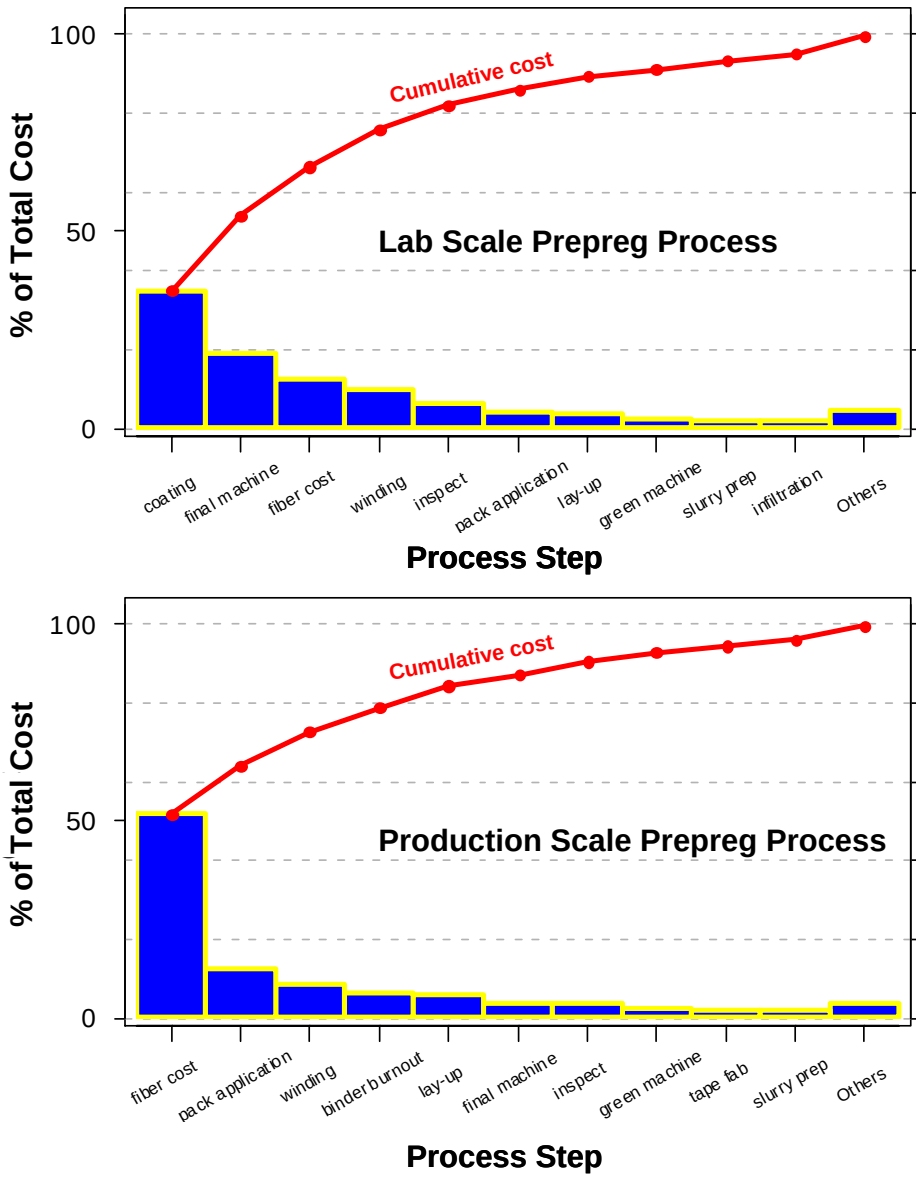

Figure 3-137. Pareto charts showing the relative contribution of the various process steps to the total cost of a prepreg MI-CMC shroud component using lab-scale (top chart) and production scale (bottom chart) processes.

A completely different cost model had been developed by GE Aircraft Engines for the fabrication of CMC combustor liners using the slurry cast MI process. This model more completely captured the contribution of investment costs, such as real estate, building and equipment purchases and write-offs, but nevertheless included much of the same analysis for the individual process steps as in the GEGR model. The GEAE model was updated to reflect the processing details for making a shroud rather than a combustor liner, and the GEGR model was then updated to include the investment costs. The various model assumptions, such as the scaled-up yields for the individual process steps, were then reconciled between the two models. These two models were then used to compare the production costs of CMC shroud components using the prepreg (GEGR model) or slurry cast (GEAE model) processes. Neither model included EBC coating costs, but these would be identical between the two materials. At a scaled-up production level of 10,000 shroud segments per year, the costs of the prepreg process were slightly (~ 15%) lower than those for the slurry casting process, which was largely attributable to the lower fiber volume fraction of the prepreg shrouds. The 15% difference is likely to be within the estimation errors of the cost models so that no real cost advantage can be claimed for either approach at this time. The absolute magnitude of shroud cost for the scaled-up process was only about ~2.5X the cost of a metal shroud, which was well within the initial cost target, even allowing for the additional cost of EBC coating.

3.8 Component Fabrication and Testing (Task 3.3)

The overall goal of this task was to design, fabricate and test turbine hardware made from the GE Prepreg MI CMC as well as other appropriate CMC materials. At this stage in the development process the designs were not intended to be fully engine-test ready, although some of the components did undergo engine testing, but to be sufficiently representative of actual hardware to result in a meaningful evaluation. Testing was to be done under turbine-like conditions, including appropriate temperatures, gas pressures, gas velocities and composition of the exposure atmosphere. The only methods available for meeting all of these requirements were high pressure combustion rig testing or actual engine testing.

While initial efforts in this task were directed mainly to testing of turbine components, namely shrouds (Sections 3.8.1 and 3.8.3) and combustor liners (Section 3.8.2), additional testing of material coupons under high pressure, high velocity combustion conditions was also performed. As noted previously in Section 3.4.4, laboratory exposures under steam-containing environments, though valuable for evaluating material oxidative stability, were not capable of simulating all of the degradation mechanisms that were likely to occur in real turbine applications. An automated combustion rig (Section 3.8.4) was therefore designed and constructed to allow long-term testing of material coupon samples under conditions that more closely simulated actual gas turbine conditions. This long-term exposure testing of coupons complemented the more short-term rig and engine testing of actual components discussed in Sections 3.8.1 through 3.8.3.

3.8.1 7FA Shroud Feasibility Testing

Two gas turbine hot section components were of particular interest for this program: the first stage shroud and combustor liner. The shroud forms the outer boundary of the hot gas

path surrounding the turbine buckets (blades). Shrouds, in large industrial engines, are typically segmented, although in smaller machines the shroud can sometimes be a continuous ring. In a 7FA size engine, which was the primary target engine for CMC component introduction for this program, has a segmented shroud consisting of 96 inner shrouds supported by 32 outer shroud blocks, which form the interface of the shroud system to the engine casing. A schematic diagram of the cross section of the turbine section of a 7FA engine is shown in Figure 3-138 with the inner and outer shroud components indicated.

3.8.1.1 7FA Shroud Conceptual Design

The geometric design restrictions for the shroud component were that the contour and position of the hot gas path face of the inner shroud needed to mimic the surface of the current metallic shrouds, and that the interfaces of the outer shroud block to the engine casing and to the 1st and 2nd stage nozzle components had to be preserved.

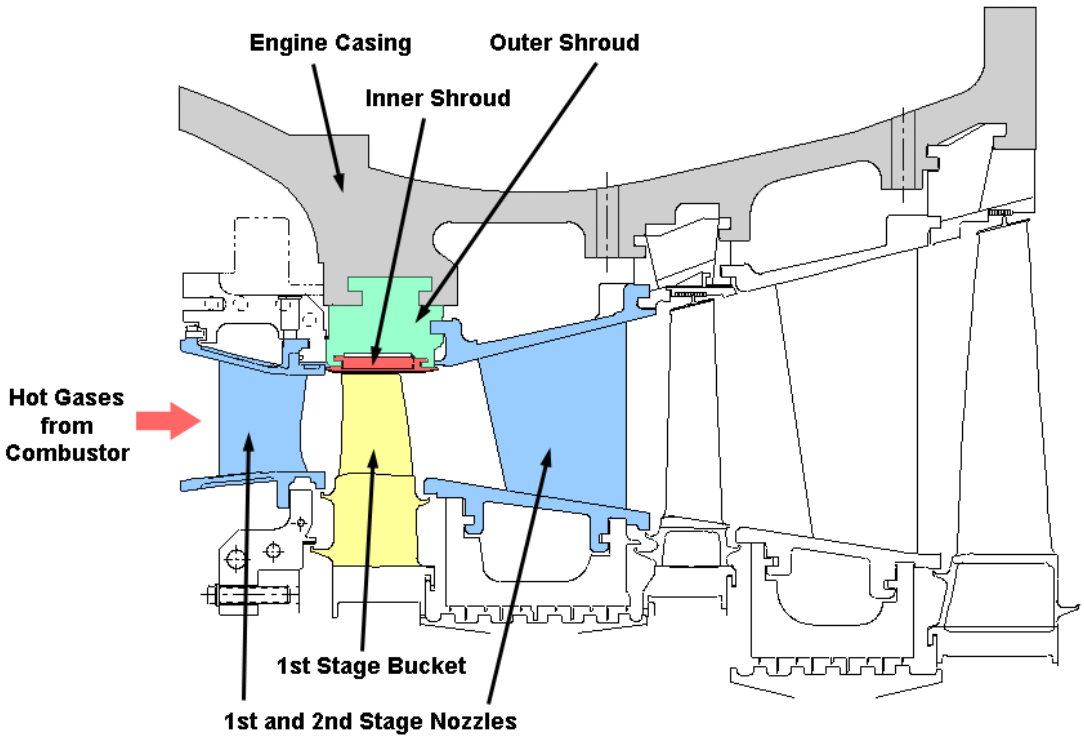

Figure 3-138. Simplified cross section of a 7FA turbine hot section showing the relative location of the 1st stage inner and outer shrouds.

An initial conceptual design for the inner shroud was developed during Phase 1 of GE's CFCC program. That design, shown in Figure 3-20, had several features that proved very difficult to fabricate, most notable of which were the sharp corners between the hot gas path face and side and end walls. Therefore a prime consideration for the new design was to make it more manufacturing friendly.

A second design consideration, which is critical to the success of any ceramic part used in conjunction with metallic structures, was to allow for the differential thermal growth between the CMC inner shroud and the metallic outer shroud block to which the inner shroud would be attached. This function was realized in the original concept by having the inner shroud hang from rods, inserted through the oval holes on the side walls, that passed circumferentially around the turbine and were held by the outer shroud blocks. This approach was later rejected as it did not provide for precise positioning of the inner shroud block in the axial and circumferential directions.

Several new conceptual designs were developed early in this task. The conceptual design team consisted of representatives from GE Power Systems Engineering, GE Power Systems Material & Processes Lab, GEGR, CCP (then known as DuPont-Lanxide, Inc.) as well as outside design consultants. Several of the concepts that were developed are presented here simply as examples, but there were numerous alternate concepts that are not presented in interest of brevity.

Several of the conceptual designs included flat, or nearly flat, plates of CMC as the inner shroud, such as shown in Figure 3-139A. Such designs had the benefit of having a very simple geometry for the CMC inner shroud, thus making CMC manufacture much easier than for Phase 1 design. However, such designs always had metallic support "hooks" to support the CMC inner shroud plate. These hooks would be subjected directly to the hot gas path temperatures and would still be required to hold the inner shroud in proper location against an inward-applied restraining force, usually applied by a spring mechanism. Adequately cooling these hooks to prevent excessive oxidation and to be able to support the attachment loads without creeping tended to eliminate much of the cooling air reduction benefits we were trying to achieve with the CMC shroud system.

An alternate geometry that held much potential was that of flat plate with the ends curled over by 180 degrees, commonly referred to as the "toboggan" design. This design had the advantages that only CMC would be exposed to the turbine hot gas path and that the location of the attachments to the outer shroud block were moved outward past the CMC inner shroud to a cooler location in the outer shroud block. The CMC part of this design is still a relatively simple shape, although having full 180° bends on both ends did present some challenges in tooling design and part lay-up. The remaining challenge was to devise a method of attachment that would maintain the position of the inner shrouds relative to the outer shroud block but still allow for thermal expansion mismatch.

Several attachment concepts for the toboggan shroud were investigated. One of them involved clamping one end of the shroud using a DAZE arrangement while letting the other end slide axially in a slot in the outer shroud block, as shown in Figure 3-139B. A DAZE attachment is a special type of dovetail geometry whereby the angle of the dovetail is chosen based on the thermal expansion differences between the parts being joined to minimize relative displacement of the parts. However, having a hard clamped attachment does not allow for differential circumferential growth of the inner shroud and outer shroud block. Also, due to the through-thickness thermal gradients, both the CMC inner shroud

and the outer shroud block would undergo thermal deformations that tend to curl the inner shroud ends and the clamp and slot in the outer shroud block, and thereby would overload the CMC in the attachment regions.

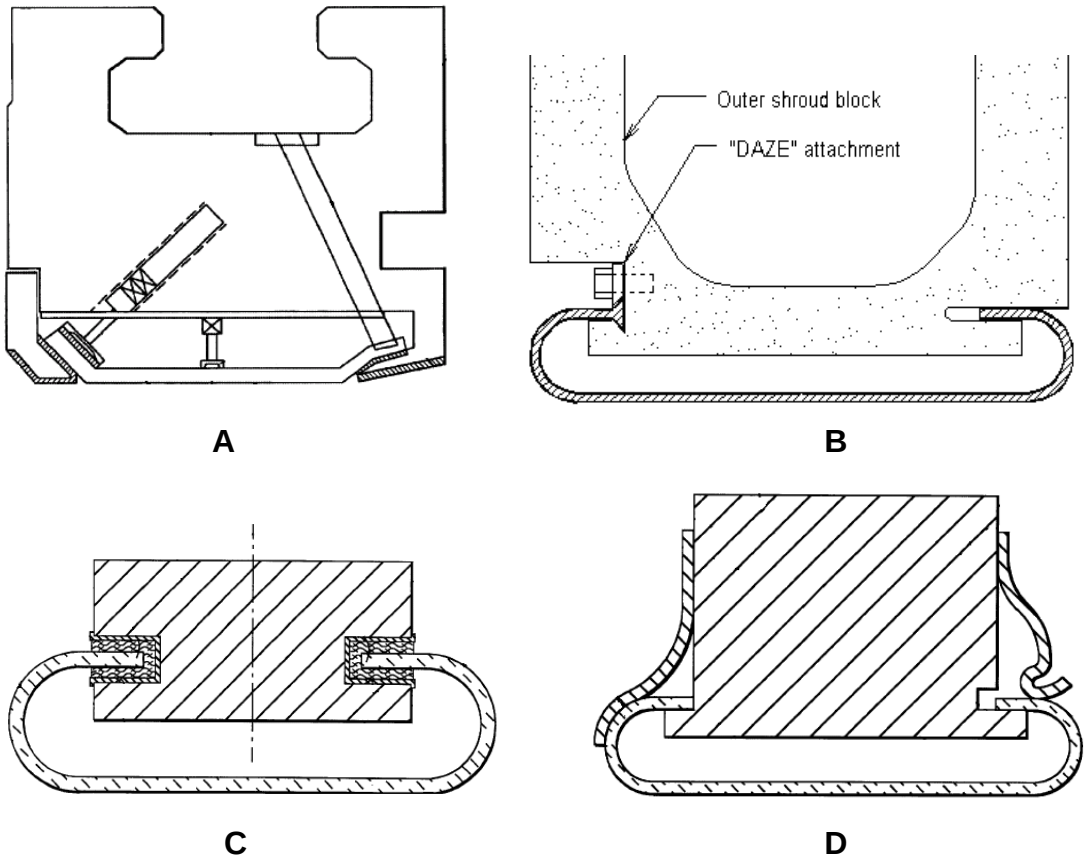

Figure 3-139. Various conceptual designs evaluated for use as CMC inner shroud:
A – bent plate inner shroud with metal hook attachments
B – curved "toboggan" shroud with front DAZE attachment
C – curved shroud with compliant slotted interface attachment
D – curved shroud supported on OSB ledges with leaf springs.

One attempt at making the attachments more compliant so it could be tolerant of such deformations was to capture the ends of the inner shroud in slots in the outer shroud block, but to line these slots with a compliant material, as shown in Figure 3-139C. The compliant material was anticipated to be a metal cloth similar to what is used in certain gas turbine seals. This approach was rejected mainly for reasons of creep relaxation of the compliant material, which would reduce the positional accuracy of the inner shroud with time. There were also concerns with wear of the compliant material against the CMC due to vibrations and thermal cycling.

The design that was eventually adopted for rig testing included the toboggan-shaped CMC inner shroud that was hung on ledges in the outer shroud block. The inner shroud was held against the outer shroud block using metallic leaf springs. The front spring wrapped partly down around the curved end of the shroud, pushing the shroud downward (toward the hot gas path) and rearward in the axial direction so that the inner shroud was firmly seated against the outer shroud block ledge. The spring on the rear curve provided only downward force, but would easily flex to allow for axial displacement of the inner shroud relative to the outer shroud. Aerodynamic and pressure differential forces would also tend to push the inner shroud rearward in the turbine, helping to maintain contact with the outer shroud block along the stop of the front ledge. This shroud configuration is shown schematically in Figure 3-139D.

3.8.1.2 Shroud Design Analysis

Various analyses of the designs were performed while trying to select the best design for rig testing. Two-dimensional finite element modeling (FEM) analyses were used to estimate temperature profiles for the designs and thermal stresses. Previous 3-D solid model analyses of the standard metallic shroud system were also reviewed to gain insights into the temperatures and deformations to be expected in the outer shroud block. A full 3-D solid model was then generated for the design in Figure 3-139D, which was analyzed using ANSYS FEM to determine the detailed temperature and stress distributions within the CMC inner shroud and outer shroud block for this design. By including the appropriate material properties for the CMC inner shroud into this model we could quantitatively predict the differences in behavior of the various CMC systems under consideration.

The physical properties used as inputs to the FEM analyses were selected to simulate the behavior of the following composite systems: (1) prepreg MI with Hi-Nicalon fiber or slurry cast MI with Sylramic fiber, (2) slurry cast MI with Hi-Nicalon fiber, (3) Enhanced SiC-SiC CVI, (4) standard SiC-SiC CVI, and (5) DIMOX Al_2O_3-SiC. The primary difference between data sets 1 and 2 is that the prepreg MI with Hi-Nicalon fiber and slurry cast MI with Sylramic fiber composites have a somewhat higher thermal conductivity than slurry cast MI composites with Hi-Nicalon fiber. Likewise, the only differences between Enhanced SiC-SiC and standard SiC-SiC are that the standard SiC-SiC has higher values of elastic modulus and thermal conductivity. Although we only tested Enhanced SiC-SiC shrouds in this program the available data set for standard SiC-SiC was more complete and judged to be more reliable. We were least certain of the input data for the DIMOX system. We utilized available literature and specification sheet data where available and estimated properties that were not available. Repeated requests were made to DuPont-Lanxide Composites for a more thorough data set, but we received no response. The material physical properties used in the model are listed in Table 3-47. All materials were assumed to be transversely isotropic so directional properties are only listed for two directions. Values for some of the properties of the Prepreg MI and Slurry cast systems may not correspond to those given in report section 3.4 since this analysis was carried out prior to the majority of the material property database effort.

The hot gas path thermal boundary conditions, as well as the boundary conditions for the outer shroud blocks to the adjacent nozzles and turbine casing, were taken from GE's standard design practice for shrouds in a 7FA engine. However, details of the cooling air leakages in the outer shrouds were not included in the models since the optimum amount of cooling flow for the overall CMC shroud system had not yet been determined. No active cooling was applied to the shrouds, but they were passively cooled via conduction, convection and radiation heat transfer to the cooler outer shroud block. Please note that both the temperature and stress distributions are strong functions of the boundary heat transfer conditions, which are only known approximately for the turbine engine or the shroud test rig. The boundary conditions used in the "standard design practice" generally overestimate the heat transfer coefficients on the hot-side and under-estimate those on the cool-side in order to ensure that the components will survive under thermal conditions which are beyond those seen in normal engine operation. Thus the absolute values of the predicted temperatures and stresses are likely to be higher than the actual values. Nevertheless, the relative rankings of the materials with regard to temperatures, temperature gradients and stresses should still be valid.

Table 3-47. Material Property Data for the Five Composite Systems Used in the ANSYS FEM Shroud Analyses* †.

Property	Prepreg MI	Slurry Cast MI	Enhanced SiC-SiC	Standard SiC-SiC	DIMOX
density (g/cm^3)	2.82	2.68	2.46	2.46	2.91
specific heat (J/g-K)	0.741 / 1.31	0.741 / 1.31	0.615 / 1.15	0.615 / 1.15	0.75 / 1.34
in-plane modulus (GPa)	243 / 191	243 / 191	221 / 187	263 / 223	123 / 162
interlaminar tensile modulus (GPa)	207 / 172	207 / 172	177 / 142	211 / 178	76.5 / 112
in-plane shear modulus (GPa)	91.7 / 64.1	91.7 / 64.1	116 / 98.6	116 / 98.6	90.3 / 134
interlaminar shear modulus (GPa)	88.3 / 60.7	88.3 / 60.7	112 / 94.5	112 / 94.5	30.3 / 44.8
in-plane Poisson's ratio	0.19	0.19	0.15	0.15	0.10
out-of-plane Poisson's ratio	0.21	0.21	0.18	0.18	0.19
in-plane CTE ($x10^{-6}$/°C)	3.87 / 4.68	3.87 / 4.68	2.52 / 4.73	2.52 / 4.73	3.78 / 5.4
interlaminar CTE ($x10^{-6}$/°C)	4.30 / 4.30	4.30 / 4.30	2.52 / 4.73	2.52 / 4.73	4.86 / 11.2
in-plane therm. cond. (W/m-K)	33.9 / 16.2	21.3 / 11.5	11.0 / 8.65	12.8 / 9.23	8.65 / 5.48
thru-thickness therm. cond. (W/m-K)	30.8 / 14.7	19.3 / 10.5	8.65 / 6.06	11.5 / 8.22	8.65 / 5.48

* Please Note that these material properties were considered representative of the various materials at the beginning of the design effort, before the extensive properties characterizations in Section 3.4 were completed.

† Where two values are given for any property the first value is for room temperature and the second is for 1200°C, except for the DIMOX composite where the second numbers are for 1093°C.

The boundary heat transfer, temperature, pressure, etc., conditions were held constant for the ANSYS analyses and only the physical properties of the CMC inner shroud material

was varied. The analyses then predicted the temperature, strain and stress distributions in the shrouds. Results of the temperature predictions from the ANSYS model for the three of the CMC systems are shown in Figure 3-140. In general, the FEM results for the Slurry cast MI / Hi-Nicalon™ composites were intermediate between the Prepreg MI and Enhanced SiC-SiC composites. Similarly, the results for the CVI standard SiC-SiC were slightly worse (e.g. higher stresses) than for the Enhanced SiC-SiC composites. Consequently the results for Slurry Cast / Hi-Nicalon and standard SiC-SiC composites are not shown in the figures. The 3-D plots in Figure 3-140 are for half models of the CMC inner shrouds where the far edge of the 3-D plots is actually the shroud axial center line. Overall the maximum temperatures, typically falling in the center of the hot gas path region, were very similar for the different systems and close to the gas temperature of 1176°C, as would be expected from the high heat transfer coefficients from the hot gas path and limited cooling applied to the shrouds.

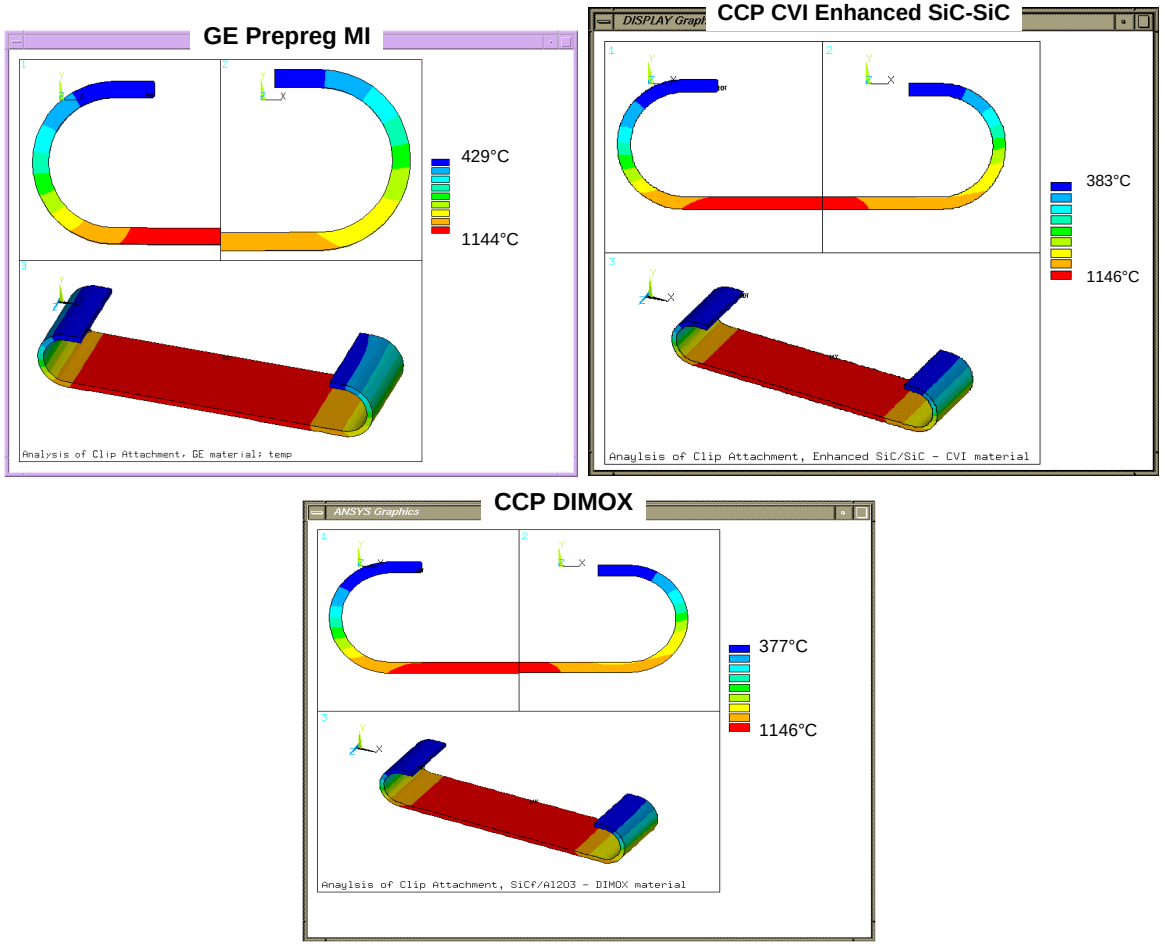

Figure 3-140. ANSYS analysis results, using identical thermal boundary conditions, for temperature distribution within the CMC inner shroud for the GE Prepreg MI (top left), CCP CVI SiC-SiC (top right) and CCP DIMOX (bottom) composite systems.

The coolest regions of the shroud, which occur at the ends of the curls where the CMC inner shroud mates to the metallic outer shroud, varied in temperature more than the hottest regions. This effect is primarily due to the varying in-plane thermal conductivity of the systems and how well the heat is transmitted around the curved ends. The GE Prepreg MI material, which has the highest thermal conductivity of the CMCs evaluated, the highest minimum temperature, whereas the DIMOX inner shroud had the lowest minimum temperature. The lower minimum temperature may be an advantage in helping to keep the shroud attachments cool, but it also creates a larger thermal gradient between the hot gas path surface and ends of the forward and rear curves, which in turn tends to increase the thermal stresses in the inner shroud.

Plots of the in-plane stresses in the turbine axial direction are shown in Figure 3-141. In the analyses the reference axes actually wrap around the curled ends of the shroud so that the plots represent true in-plane stresses in the direction of the fibers within the composites. The maximum tensile stress was in the range of 100 to 110MPa. For the Prepreg shroud the max stress location was near the transition between the flat hot gas path face and the forward curl along the shroud backside edge. For the CVI and DIMOX systems the stress was actually slightly higher near the mid-point of the aft curl along the backside edge.

Similar results were obtained for transverse in-plane stress, interlaminar tensile and shear stresses, and in-plane shear stresses. The results of the thermal/stress analyses are summarized in Table 3-48. In general, the magnitude of the stresses were inversely proportional to the material thermal conductivity, as would be expected for components where the primary stresses are thermal gradient driven.

Based on best estimates of material properties, the in-plane tensile stresses were closest to the material limits (proportional limit strength). Whereas the MI materials maintained some property margin for in-plane stress (GE and Goodrich MI shroud witness coupons proportional limits measured consistently over 135MPa and CCP MI coupons average 121MPa) the SiC-SiC and DIMOX shrouds would be expected to crack under these conditions (Enhanced SiC-SiC witness coupons showed proportional limits from 91 to 239MPa and DIMOX coupons averaged 94MPa). However, remember that the calculated stresses are for boundary conditions that are more severe than what we expect for the rig tests so that these results did not necessarily predict failure in the rig tests. The other stresses (interlaminar tension and interlaminar and in-plane shear) did not exceed the material strengths even for the severe boundary conditions modeled. Please note that for a real engine component design the material property values used are those at three standard deviations below the nominal value (-3σ), so that these positive margins based on nominal properties may not be sufficient when accounting for statistical variation in the properties.

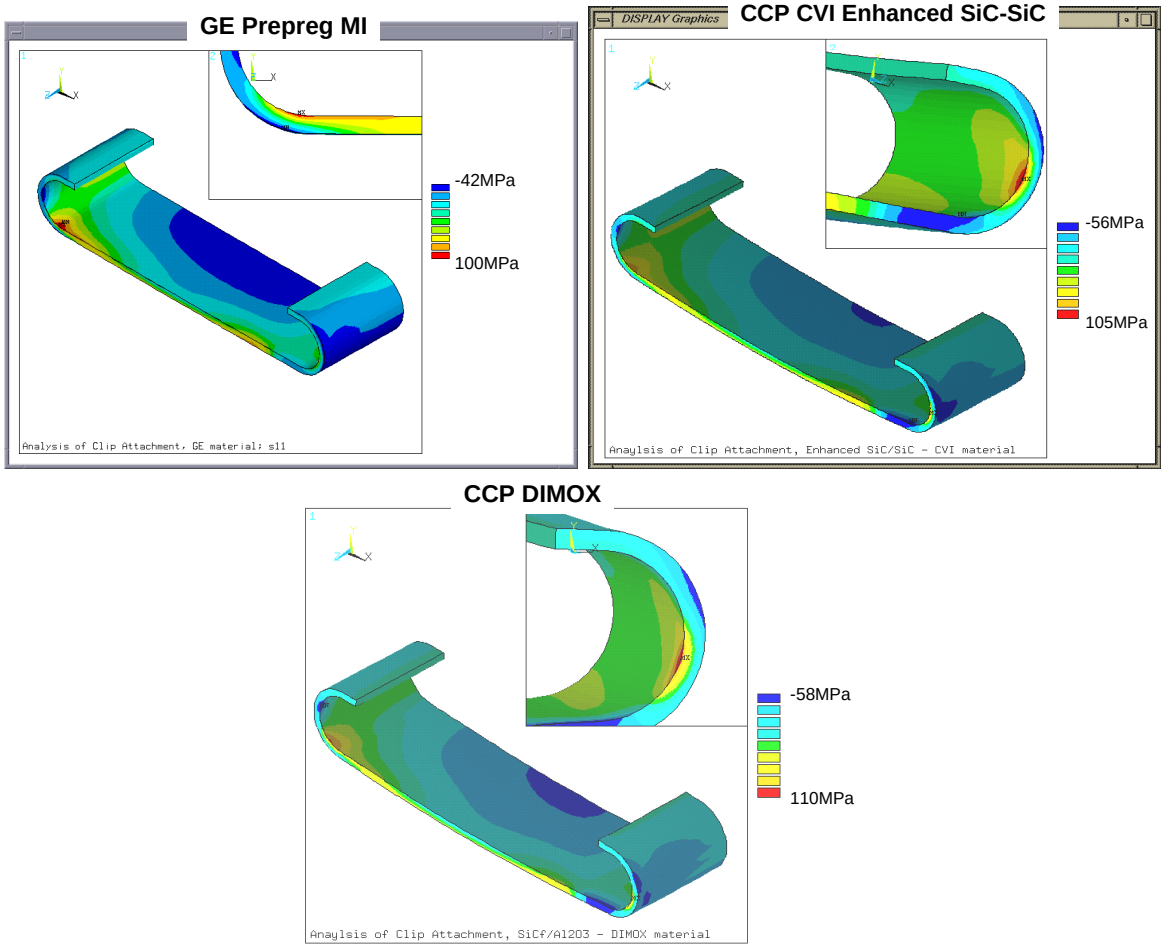

Figure 3-141. In-plane axial stress contour plots for CMC inner shrouds made from GE Prepreg MI (top left), CCP CVI SiC-SiC (top right) and CCP DIMOX (bottom) composite systems.

Table 3-48. Summary of the ANSYS FEM Analysis Results for the Five CMC Inner Shroud Material Systems.

Property	Prepreg MI	Slurry Cast MI	Enhanced SiC-SiC	Standard SiC-SiC	DIMOX
max Temp. (ºC)	1144	1145	1146	1146	1146
min Temp. (ºC)	429	396	383	386	377
max temperature differential (°C)	715	749	763	760	769
thru-thickness thermal gradient in hot gas path region (°C/mm)	5.7		16.4		18.6
max axial in-plane tensile stress (MPa)	100	104	105	116	110
max transverse in-plane tensile stress (MPa)	64.1		72.4		66.9
max interlaminar tensile stress (MPa)	3.4	4.1	3.4	4.1	6.2
max in-plane shear stress (MPa)	26	29	39	43	48
max interlaminar shear stress (MPa)	12	15	20	22	19

There was some disagreement within the design team regarding whether the distribution and magnitude of the calculated stresses were determined mostly by the thermal profiles and geometry of the shrouds versus the inherent anisotropy of the CMC material systems. ANSYS analyses were therefore performed on a shroud using isotropic thermal and elastic properties equal to the in-plane properties of the Prepreg MI system. These results were then compared to the standard model of the prepreg system that included material anisotropy (modeled as orthotropic) to evaluate the influence of material anisotropy. Examples of the calculated temperature and stress distributions for the anisotropic and isotropic analyses are shown in Figure 3-142. As can be seen the thermal and stress distributions were practically identical The equivalence of these results was interpreted as indicating that the stress distributions were primarily determined by the thermal boundary conditions and shroud geometry.

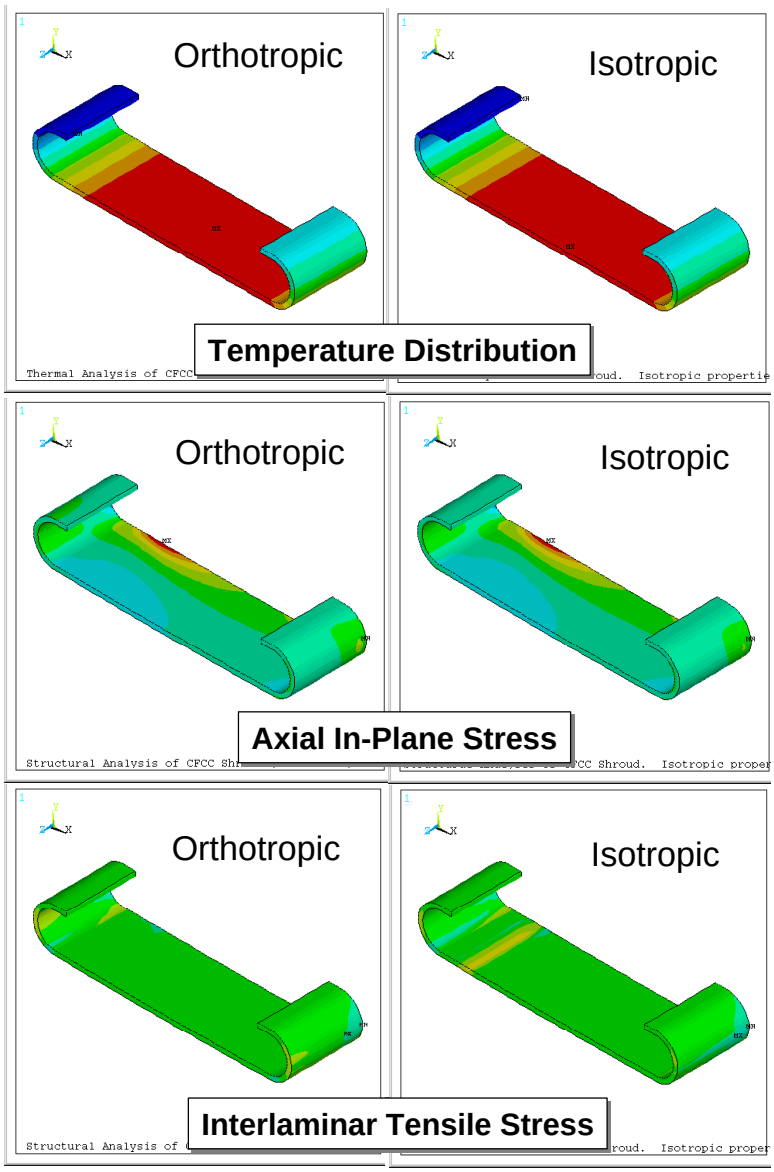

Figure 3-142. Comparison of ANSYS thermal and stress analyses results for a CMC shroud with normal orthotropic thermal and elastic properties with a similar shroud with isotropic material properties. The transverse in-plane stress and shear stresses were also similar for the two sets material properties.

3.8.1.3 CMC Shroud Fabrication

GE Prepreg MI shrouds were fabricated using the standard HGS and the boron-doped HGS matrix compositions. Hi-Nicalon™ fiber coated with a configuration A fiber coating in the ACC 3-line coater system was used for all shrouds. Fiber coating and tape winding processes were identical to those used for making standard test panel samples.

All but one of the Prepreg shrouds were laid up using a [0-90-0-90]s 8-ply configuration, with the one exception being done as a 9-ply [0-90-0-90-0-90-0-90-0] configuration for

comparison. The target thickness was 2.5mm, though most of the shrouds were slightly thinner than this target. The lay-up was done in a three-piece stainless steal female mold. Autoclave lamination and curing was done at the same conditions as standard panel samples. Following cure the shrouds were hard enough to allow green machining of the preforms to the final shroud shape. The dimensions of the shrouds were very stable through binder burn-out and infiltration, with no noticeable changes in dimensions from the as-laminated condition. Figure 3-143 shows photographs of a typical as-fabricated Prepreg MI shroud.

Figure 3-143. Photographs of a typical GE Prepreg MI shroud in the as-fabricated state.

Overall 18 GE Prepreg MI shrouds were fabricated in this program. The first seven, many of which were made with uncoated fiber, served as processing trial parts, allowing the processing parameters to be optimized. One of the shrouds was incorrectly machined in the green state, and was subsequently used as a demonstration part. Likewise one of the infiltrated shrouds was retained for show-and-tell purposes. The remaining nine shrouds were used in rig testing, and included six shrouds with the standard matrix and three shrouds with the boron-doped matrix.

In addition to the Prepreg MI shrouds fabricated at GEGR, shrouds of several other composite systems were procured for rig testing. Eight slurry cast MI shrouds were purchased from CCP (then known as DuPont-Lanxide Composites), five of which were made with Hi-Nicalon™ fiber and three with Sylramic™ fiber. Five slurry cast MI shrouds were also purchased from Goodrich Aerospace. DuPont-Lanxide Composites also had their own contract within the CFCC program, and they manufactured several shrouds under their contract by CVI and DIMOX processes for testing by GE. These "donated" DuPont-Lanxide shrouds were all fabricated with Hi-Nicalon™ fiber, and included six CVI Enhanced SiC-SiC shrouds and six Al_2O_3-SiC DIMOX shrouds.

All shrouds were put through a variety of pre-test inspections, including IR NDE by W. Ellingson and J.G. Sun at Argonne National Lab, CMM dimensioning measurements at GEGR, and acoustic modal response measurements at GEGR. Witness coupons were

processed along with every shroud. In GE's case the shrouds were made slightly over-sized and the witness coupons were cut directly from the flat section of the shroud during green machining. These bars were then burned-out and infiltrated in the same furnace runs as the shroud component from which they were fabricated. Room temperature tensile testing of the witness coupons served as a process check on the quality of the shrouds, and also provided "as-fabricated" material data for comparison with post-test destructive characterization results. The witness coupons were also used as samples for microstructural evaluations. A summary of the results from RT tensile tests done on the witness bars is given in Table 3-49, and the NDE images of as-received shrouds are shown in Figure 3-144.

The prepreg system shrouds, particularly with the standard matrix composition, tended to have the highest proportional limits and strain to failure values of all the different types of shrouds that were evaluated. The CCP shrouds, whether slurry cast MI or CVI, tended to have the highest ultimate strength values. The Goodrich slurry cast MI had proportional limit stresses much better than the CCP shrouds, and almost on par with the GE Prepreg shrouds, and also had ultimate strength values comparable to the GE shrouds. The CCP slurry cast MI shrouds with Sylramic fiber™ displayed tensile behavior very close to a brittle material, having only moderate ultimate strengths and very low strain to failure values. The CCP DIMOX shrouds had fairly high ultimate strength values, but their strain to failure values were only about ½ that of the GE Prepreg shrouds. The DIMOX shrouds also tended to have gradually curving stress-strain curves, making it very difficult to delineate any "linear" loading regime. Consequently the proportional limit and initial modulus values of the DIMOX shrouds should be considered as only approximations. It is likely that the DIMOX material is microcracked even before loading due to the large thermal expansion mismatch between the SiC fiber and alumina matrix, and therefore a strict proportional limit, or "first matrix cracking" stress really did not exist for these shrouds.

Table 3-49. Summary of CMC "Toboggan" Shroud Witness Bar Tensile Test Data.

Material System*	Shroud ID	Proportional Limit Stress (MPa)	Initial Modulus (GPa)	Ultimate Strength (MPa)	Strain to Failure (%)
GE Prepreg Standard Matrix	G1A-1	153	254	280	1.01
	G1A-2	210	263	385	0.97
	G1A-3	165	230	332	1.03
	G1A-4	168	224	289	1.00
	G1A-5	-	-	-	-
	G1A-6	145	210	310	1.22
GE Prepreg B-Doped Matrix	G1B-1	124	205	325	1.05
	G1B-2	203	275	268	0.73
	G1B-3	142	221	300	1.15
CCP Slurry Cast MI	G2A-1	133	163	401	0.84
	G2A-2	123	170	399	0.73
	G2A-3	138	308	410	0.64
	G2A-4	120	160	336	0.80
	G2A-5	112	158	177	0.27
CCP Slurry Cast MI / Sylramic	G2B-1	83	241	190	0.11
	G2B-2	41	247	203	0.14
	G2B-3	117	-	121	0.04
Goodrich Slurry Cast MI	G2C-1	150	236	295	0.73
	G2C-2	163	241	301	0.70
	G2C-3	159	257	321	0.74
	G2C-4	165	286	267	0.60
	G2C-5	145	257	278	0.63
CCP CVI Enhanced SiC-SiC	D1-1	91	162	364	0.63
	D1-2	93	141	332	0.63
	D1-3	92	153	354	0.61
	D1-4	125	150	345	0.62
	D1-5	121	163	373	0.66
	D1-6	115	159	379	0.72
CCP DIMOX†	D2-1	104	171	328	0.58
	D2-2	110	179	374	0.65
	D2-3	79	121	269	0.49
	D2-4	94	143	277	0.45
	D2-5	83	164	295	0.48

* All systems were reinforced with Hi-Nicalon fiber unless otherwise indicated.

† The stress-strain curves tended to be smooth curves with very poor definition of any initial linear loading region, and thus the proportional limit stress and initial modulus values are only approximate for the DIMOX material.

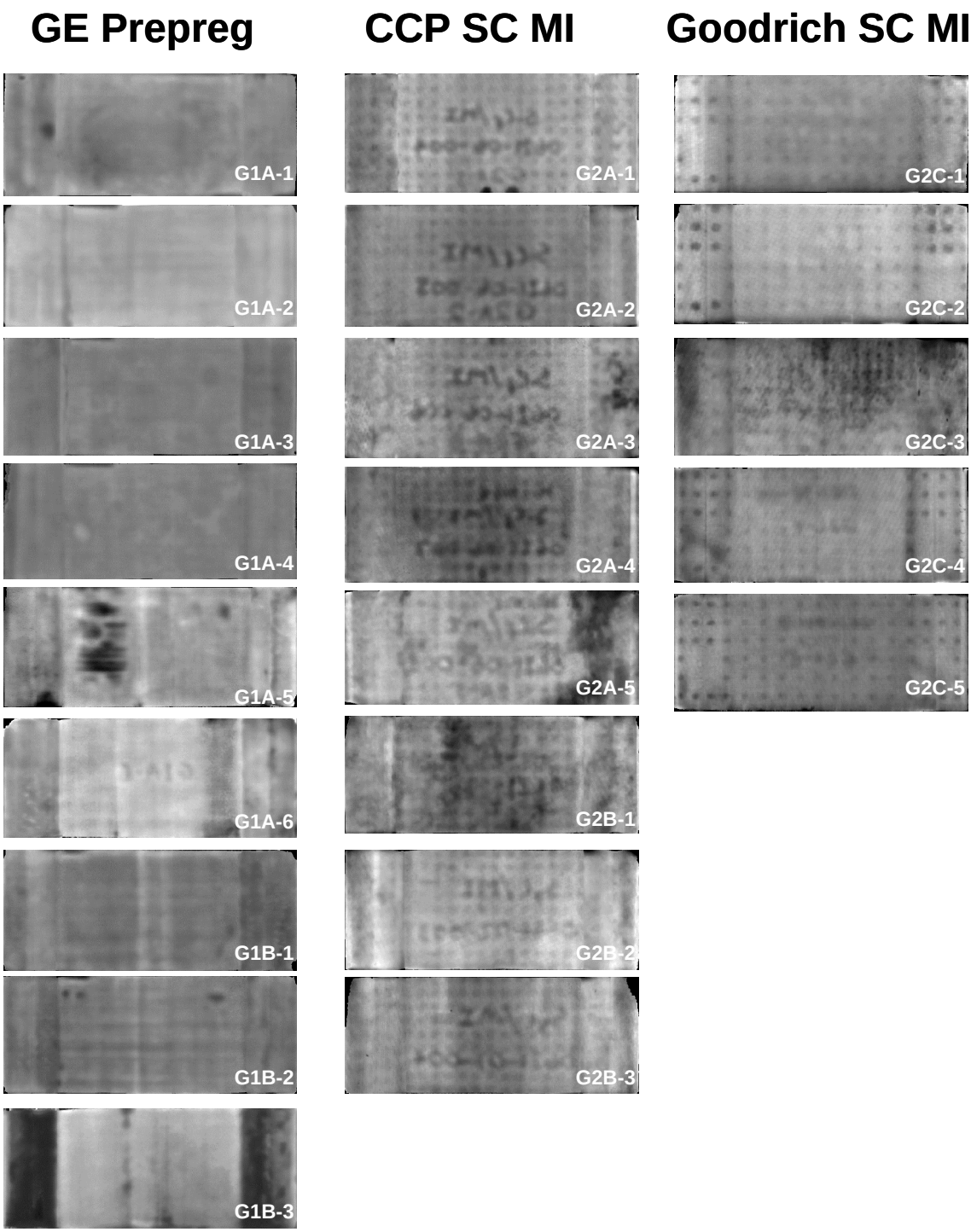

Figure 3-144. Transmission IR NDE images of thermal diffusivity for melt infiltrated shrouds from GE, CCP and Goodrich, in the as-fabricated condition. The absolute diffusivity scale varies for each image so comparisons between images may not be valid.

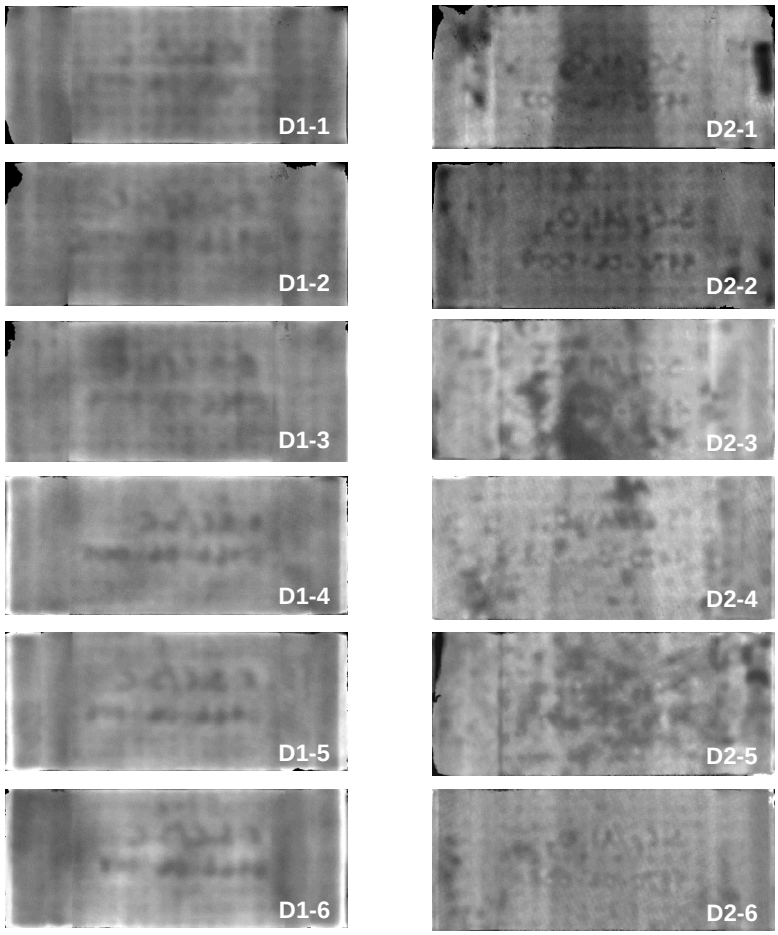

Figure 3-144, Continued. Transmission IR NDE images of thermal diffusivity for CVI Enhanced SiC-SiC and DIMOX shrouds from CCP in the as-fabricated condition. The absolute diffusivity scale varies for each image so comparisons between images may not be valid.

3.8.1.4 Test Rig Design and Fabrication

The high-pressure combustion test rig used for this study was designed and assembled at GEGR. GEGR had an established combustion test facility incorporating two large-scale piston compressors and one large axial rotary compressor with a combined capacity of 4.5 kg/s of air mass flow at 1.2MPa pressure, a compressed gas pre-heater capable of heating this flow to 350°C, a natural gas compressor for fuel delivery, ASME certified pressure vessels and piping, and an exhaust gas handling system. The facility is divided into 7 independent test cells, each with independent process control and data-logging systems.

The primary goal of the rig was to be able to expose the CMC shroud components to a combustion gas environment of temperature, flow and pressure as close to the expected 7FA engine conditions as possible. ANSYS FEM modeling of the shrouds using 7FA engine boundary temperature and heat transfer conditions had indicated that the CMC shrouds were expected to run at temperatures close to 1200°C, so attaining CMC shroud

temperatures of 1200°C was an important consideration. This requirement also proved to be a significant rig design and operational challenge due to the difficulties in reliably delivering sufficiently hot combustion gases to the shroud test section without thermally damaging other metallic hardware in the test cell. Accommodation of more than one shroud at a time was also highly desirable to increase the productivity of the tests. In addition to steady-state exposures of up to 200 hours at a time, the rig should also be capable of exposing the shrouds to multiple, meaning hundreds of, thermal cycles without major overhauls.

3.8.1.4.1 Rig Overview

The rig design that was developed is shown schematically in Figures 3-145 and 3-146. The entire combustion apparatus would be contained in an existing pressure vessel that was piped for counter-flow gas flow (i.e. the compressed gas enters the pressure vessel near the exhaust end of the vessel, flows around the outside of the test hardware to the front of the pressure vessel (right to left in Figure 3-145), and then turns to enter the premixer/combustor, and the combusted gases flowing inside the test hardware from the combustor, through the transition piece and shroud test sections, and then to the exhaust (left to right in Figure 3-145)). This flow pattern simulates the flow arrangement in a typical can-annular combustor system, which was what this test cell was originally designed to accommodate, and allows the compressed air to be used for rig cooling. A separate cooling air circuit was set up to deliver precisely measured cooling flow to the test section that was intended for exclusive cooling of the CMC inner shrouds.

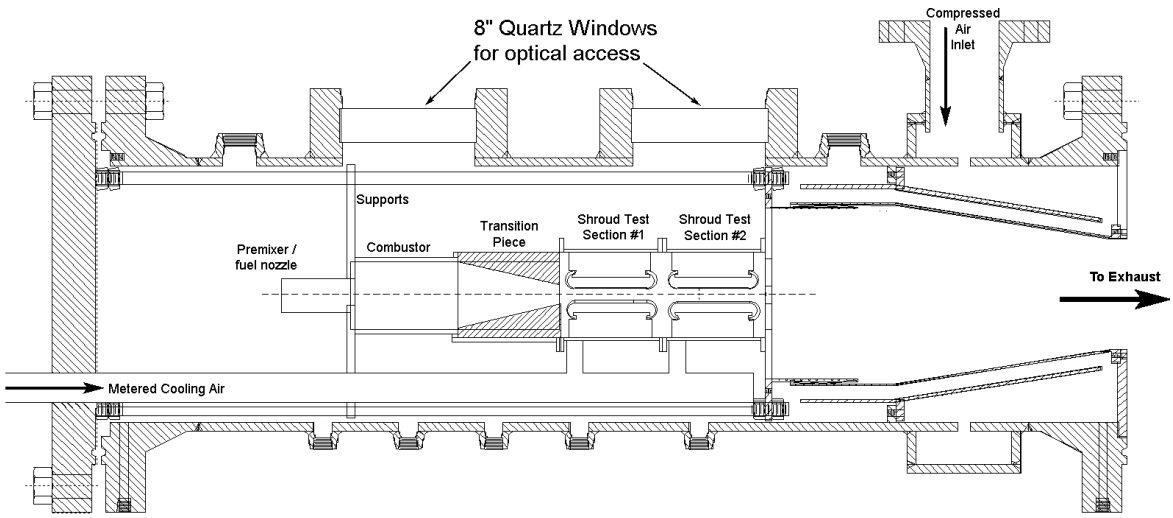

Figure 3-145. Schematic diagram of the shroud combustion test rig showing the overall configuration of the pressure vessel. The test sample exhaust exposure section of the internal hardware is not shown.

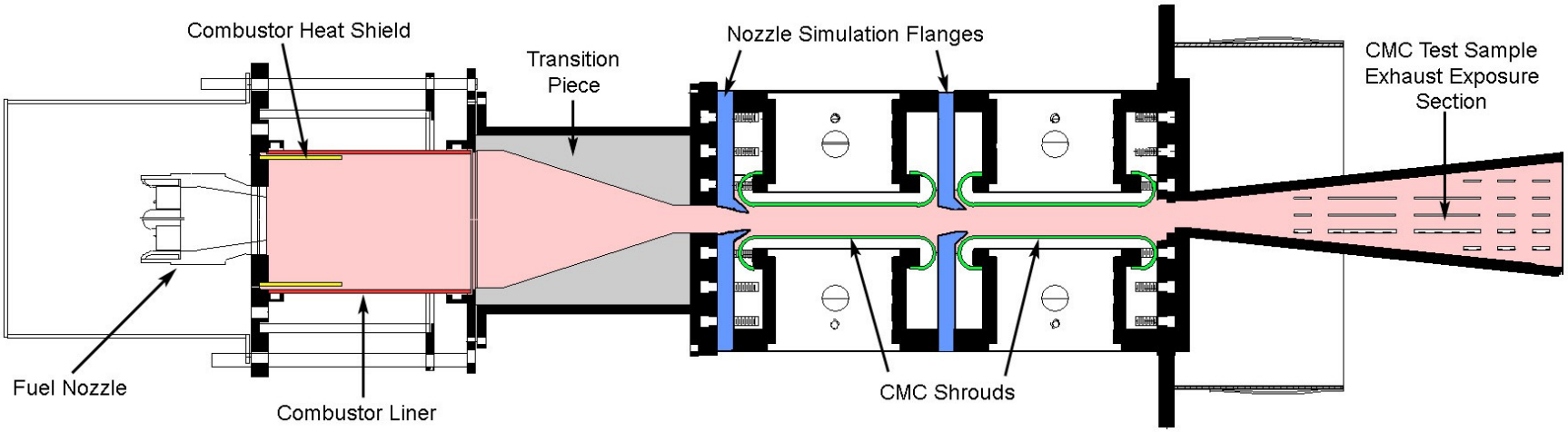

Figure 3-146. Schematic drawing of the internal hardware in the shroud combustion test rig. The hot gas path, from the combustor through to the exhaust, is marked in pink.

Overall the hardware internal to the pressure vessel, which made up the actual shroud test rig, was divided into four main sections. Each section was relatively independent of the others, with the sections being bolted together using metallic flanges at the ends of the sections to form the whole test rig. The rig was fixed to the pressure vessel using rods that extended from the end flange of the pressure vessel. The entire rig internal structure was supported on these rods, and mated to the exhaust duct inside the pressure vessel via a hula seal. The only location firmly bolted on the rods was the flange at the exit end of the shroud test section. All other flanges were supported by the rods through holes in the flanges, but were allowed to slide axially along the rods in order to accommodate the thermal growth of the rig.

The gas premixer/fuel nozzle was a design borrowed from a GE LM6000 aero-derivative engine combustor. The combustor itself included a superalloy heat shield (shown in yellow in Figure 3-146) between the fuel nozzle and combustor liner wall to shield the liner from excessive heat load from the gas flame. A ring of holes through the cap of the combustor between the heat shield and combustor liner allowed compressed air to flow along the backside of the heat shield to prevent overheating. Such a construction is standard in the LM6000, and was adopted for the rig. The initial design of the combustor liner (shown in red in Figure 3-146) was a simple stainless steel cylinder with both backside impingement cooling and front side film cooling provided by the ring of holes mentioned above.

The combustor liner was cylindrical in shape, roughly 10cm ID x 15cm long, for symmetry with the premixer/fuel nozzle because it is easier to obtain stable flame conditions in such a geometry. The flow path in the shroud test section, however, was rectangular in shape, roughly 8cm x 1.3cm in size. Thus the flow path had to be transitioned from the circular exit of the combustor to the rectangular inlet of the shroud test section through a transition piece. Due to the need for shaping the gas flow, the hot combustion gases would be impinging on the walls of the transition piece, making it too hot for use of an uncooled metal. Film cooling of the transition piece was not viable since the film established on the transition piece walls would carry over into the shroud test section, diluting the combustion gases and making it even more difficult to get the desired CMC shroud temperatures. For these reasons an uncooled ceramic transition piece was selected, made by casting a high-alumina castable refractory mix (shown in gray in Figure 3-146) into a stainless steel shell. Such a construction had been used successfully in previous combustion rig projects, although not under conditions of severe thermal cycling as were anticipated for this rig.

The shroud test section of the rig was a shape consisting of four simulated outer shroud blocks arranged as two in line on opposite sides of the central hot gas path. In this way four CMC inner shrouds (shown green in Figure 3-146) could be exposed simultaneously. The outer shroud blocks were designed to be hollow with fused quartz windows at the outer walls and at a position just behind the CMC inner shrouds. The inner window behind the shrouds was supported by a series of bars, such that the view through the windows was like that of looking through a picket fence. The bars were present to support the quartz windows against the pressure drop from the outside to the inside of the rig and

also incorporated cooling air holes to direct impingement cooling air onto the back of the CMC inner shrouds. By lining up the position of the rig with the location of one of the quartz windows on the side of the pressure vessel it was possible to have visual access to at least one of the shrouds during testing. Visual access was desirable for safety reasons in that we would be better able to detect a shroud failure if it were to occur. It also allowed the monitoring of the CMC shroud temperature using an optical pyrometer.

Just ahead of each shroud position within the shroud test section was a nozzle simulation flange that was intended to simulate the flow trip coming off of the first stage nozzle outer platform (shown in blue in Figure 3-146). In order to simulate this flow trip these flanges extended into the combustion gas flow path by about 5mm, and consequently were subject to a very high heat load. The original construction of these flanges was of stainless steal with air cooling passages and thermal barrier coatings. As will be described in Section 3.8.1.5, these flanges caused some severe durability problems during rig testing, and were eventually replaced with a redesigned version that included a Prepreg MI CMC plate bolted to the front of the flange.

Photographs of several sections of the internal rig hardware during fabrication and assembly are shown in Figure 3-147. The top photo shows an end view of the transition piece with the alumina castable refractory lining clearly visible, and the partially assembled combustor section showing the stainless combustor liner. The bottom photo shows a side view of the shroud test section with the two outer quartz windows on one side of the test section indicated.

3.8.1.4.2 Shroud Rig CMC Combustor Liner Fabrication

High-pressure combustion rig testing of any component is a fairly expensive proposition. Safety concerns dictate that the tests be continuously monitored by at least two operators. The amount of electricity used to compress and pre-heat the air, in addition to the natural gas used during the test, contribute to rather high energy usage costs. Consequently there is a strong incentive to get the most data possible from each test, which in this case means exposing as much CMC hardware to the combustion environment as possible. One way to increase the amount of CMC under test would be to build other parts of the rig, in addition to the shrouds, from CMC. An obvious candidate, especially since it was one of the component of interest for this program, was the combustor liner. The initial design called for an impingement cooled stainless steel liner, but two Prepreg MI liners were also fabricated for use in the rig. The process development and processing trials for fabrication of these liners provided valuable experience for the fabrication of the larger Frame 5 liners to be discussed in report section 3.8.2.

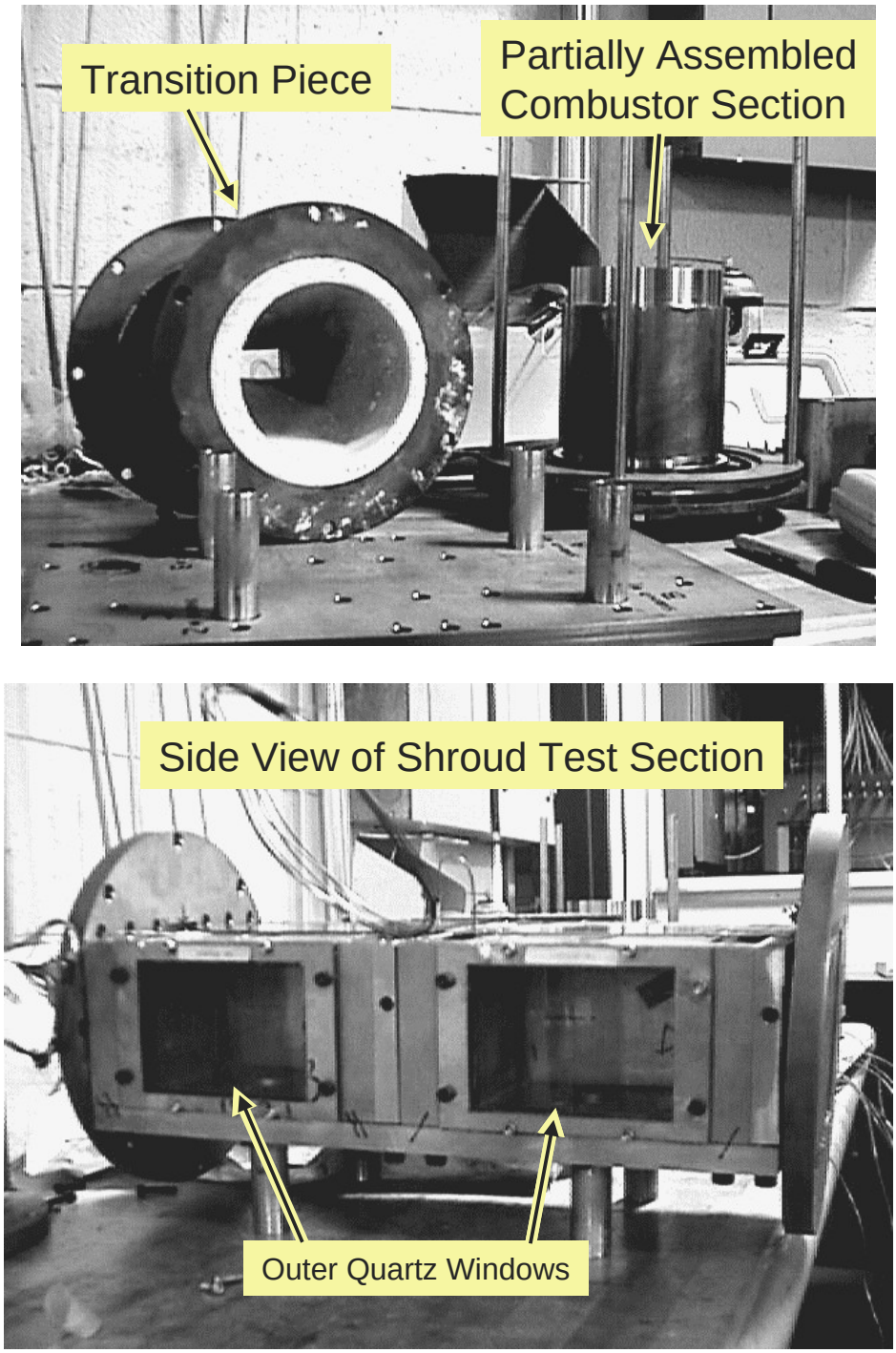

Figure 3-147. Photographs of sections of the shroud test rig internals during assembly.

Two combustor liners were fabricated for use in the shroud test rig using the process described above. Although the intermediate debulk treatments helped to minimize the amount of fiber buckling, it did not completely eliminate it. Consequently some surface wrinkles and delaminations still occurred in the combustor liner cylinders. Photographs of these liners are shown in Figure 3-148. Transmission IR NDE was performed on the liners

at ANL, and the thermal diffusivity images obtained are shown in Figure 3-149. The dark strips running top to bottom in the images represent wrinkles that were formed on the liners during autoclave lamination, whereas the more diffuse areas of dark gray indicate possible delaminations or porosity. Air-coupled ultrasound inspections and X-ray CT scans were also performed on the liners that corroborated the presence of delaminations and/or low density regions corresponding to the locations of the defects in the IR images. Despite the obvious microstructural defects in these liners, they were still used successfully in the shroud rig tests.

Figure 3-148. Photographs of the Prepreg MI CMC liners made for the shroud combustion test rig.

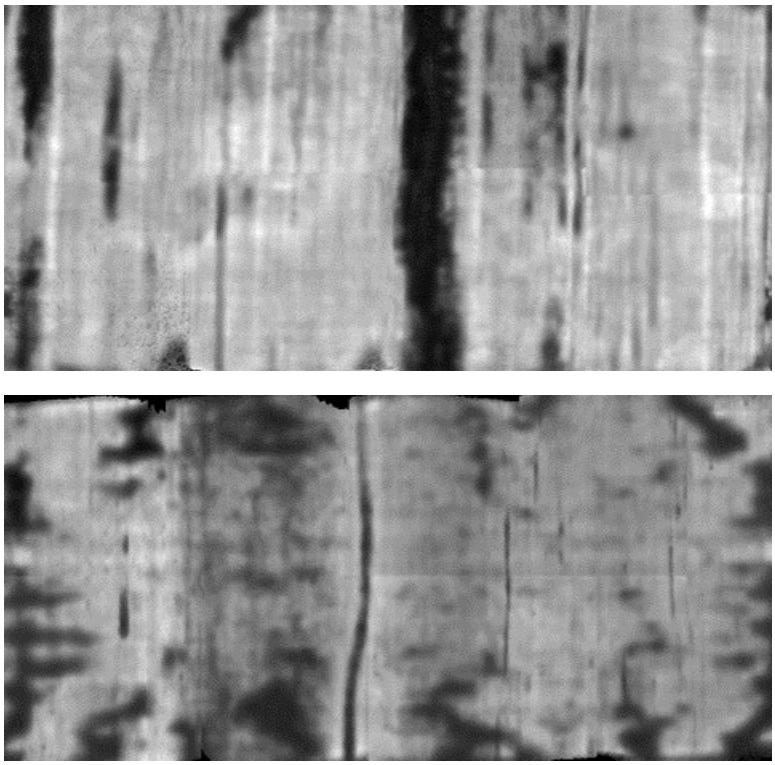

Figure 3-149. Transmission IR thermal diffusivity images of the small combustor liners made for use in the shroud combustion test rig. The darker areas indicate low thermal diffusivity associated with delaminations or porosity. The continuous stripes top to bottom in both images indicate the presence of surface wrinkles.

3.8.1.4.3 Shroud Rig CMC Coupon Test Section

As mentioned previously, combustion rig testing is expensive so maximizing the amount of material exposure data that could be obtained from the rig was a prime consideration. Besides the shroud exposure data to be derived from the tests, the other major product of the combustion rig is a large quantity of hot, high pressure combustion gases. It was highly desirable to find a way to utilize this by-product for additional material exposure testing. The way that this was done was to add an exhaust diffuser onto the end of the shroud test section, and to make this diffuser capable of holding CMC test bars within the exhaust gas stream. In this manner multiple CMC coupons could be exposed to the high pressure, high velocity combustion gas environment while the shroud exposure testing was being conducted.

The exhaust diffuser was simply a set of divergent plates and a set of parallel plates welded together in a wedge shape with the entrance to the wedge being bolted up against the exit of the shroud test section. The angle of the divergent walls was limited to 11 degrees from the gas flow direction in order to prevent flow separation. Roughly 13 cm back from the entrance of the diffuser parallel walls were welded in, forming a rectangular channel roughly 4.5cm x 8.4cm. Slots were cut into the two parallel walls through which CMC test bars could be inserted. This arrangement exposed the center 8.4cm of the test bars to the rig exhaust gases, while ~3.4cm of each end of the test bar extended outside of the exhaust

flow. End caps were then bolted over the sample ends, thereby trapping them within the diffuser. This section of the test rig is indicated in the diagram in Figure 3-146.

3.8.1.5 Shroud Rig Exposure Testing

Due to the large number of shrouds to be tested, and to the varying conditions at which the tests were to be conducted, it was necessary to break up the exposure testing into numerous short test runs. The overall test plan for the rig was to prove out operation of the rig and troubleshoot any combustion stability or hardware issues using all metallic hardware, including a metallic combustor liner and metallic shrouds. One of the metallic shrouds was outfitted with ten thermocouples at various locations, and was used to plot out the temperature gradients at the inner shroud locations. CMC shrouds would then be introduced for exposure testing at reduced temperature conditions in order to validate that the rig was still working adequately with CMC shrouds in place.

The exposure testing of the CMC shrouds was then to be performed using three types of tests. In all of the testing the overall pressure was kept constant at a nominal value of 1.2MPa in the shroud test section, dropping to ~1MPa in the exhaust diffuser. In the first type of test the temperature of the rig would be increased in stepped increments from a relatively low firing temperature of about 600°C up to a final firing temperature of 1177°C (2150°F). (The term "firing temperature" refers to the adiabatic gas temperature calculated from the combustion of the measured gas and air flows. Calculated values of firing temperature were validated using combustion gas sampling and analysis. The actual gas temperature within the rig starts at the firing temperature in the combustor region but then decreases through the shroud test section with the introduction of cooling gas flows and expansion of the combustion gases.) Such "step tests" were done to look for infant mortality failures of the shrouds at temperature levels where severe damage to the rig would not occur, even in the event of a full shroud failure.

The second type of test was to expose the shrouds to a series of 100 rapid thermal cycles to simulate turbine trip events. (A "trip" is when the turbine is shut down for an emergency, and involves a rapid shut off of the fuel supply while the turbine is still running at full speed. Such an event has the effect of subjecting the turbine hardware to a sever thermal shock as the turbine flow suddenly changes from full operating temperature (~1250°C) to the compressor discharge temperature (~400°C) in a few milliseconds.) Nominally the shrouds would be cycled between a shroud temperature of ~1200°C down to the lowest temperature that the combustor system would operate at without blow-out.

The cycles would then be followed by 100 hours of steady state exposure at a nominal shroud maximum temperature of 1200°C for any shrouds that survived the thermal cycles. Both the cyclic and steady state exposures were broken into two segments to allow the shrouds to be switched between the front (upstream) and rear (downstream) positions. Due to the ingress of cooling air from the shrouds and nozzle simulation flanges the temperatures at the rear (downstream) shroud locations were expected to ~50°C lower than those in the front (upstream) locations, which was verified using the instrumented metallic shroud. The cyclic and steady state tests were therefore divided into two separate runs so

that the shrouds in the front and rear positions could be switched, thereby ensuring that all shrouds saw the same overall test environment.

3.8.1.5.1 Shroud Testing Under Reduced Temperature Conditions

Fabrication and assembly of the shroud combustion rig was completed in early 1998. Following a pressurization safety check, the rig was fired up for the first time on January 13, 1998. Six tests were conducted using only metallic hardware in order to be sure the rig was fully operational before the introduction of any CMC components. A listing of all of the rig runs, including these initial test runs, is given in Table 3-50. During this initial testing several issues with cooling flow and hardware durability were observed and fixed. For instance, the throat region between the transition piece and the shroud test section showed excessive thermal degradation during these tests. Fortunately this section was originally designed and built to have a removable metallic insert in the throat region to allow for just such a modification. A higher temperature alloy was substituted for the initial throat insert and additional cooling air was introduced on the back of the insert. Other minor modifications to the outer shroud blocks were also needed to allow for the incorporation of additional temperature monitoring thermocouples.

During testing of the thermal cycling ability of the rig it was discovered that rapidly quenching to a relatively low temperature was difficult due to flame blow-out. Re-lighting the combustor, typically done using a spark gap, proved unreliable after about ten starts. Subsequently a small hydrogen torch was added to the fuel nozzle assembly. The hydrogen torch provided a small stable flame even under conditions where the natural gas flow was completely shut off. The flame size of the hydrogen torch could be made sufficiently small that it only contributed about a 25°C rise to the incoming compressed air, and thus allowed for rapid thermal cycling of the rig from ~1150°C to ~450°C in a few seconds by simply turning the natural gas flow on and off.

The rig shakedown tests ran through early March, 1998, at which point the rig was considered ready for testing of CMC shrouds. As this was the first ever combustion rig test of CMC hardware in this facility only two CMC shrouds were included in the very first CMC exposure run on March 13. The step-wise exposure test was truncated at a maximum rig firing temperature of only 1010°C in order to allow for inspection of the rig and CMC shrouds before proceeding to the full 1177°C firing temperature goal during test run 8.

As noted earlier, the pressure vessel and shroud test rig outer shroud block modules were equipped with fused quartz windows allowing for visual access to the back side of 2 shrouds during rig testing. A video camera was set up in the test cell to record the images of the backside of the shrouds on the left side of the rig. Figure 3-150 shows a still image from the video taken during run 8 and shows the glowing shrouds through window support/shroud cooling air bars.

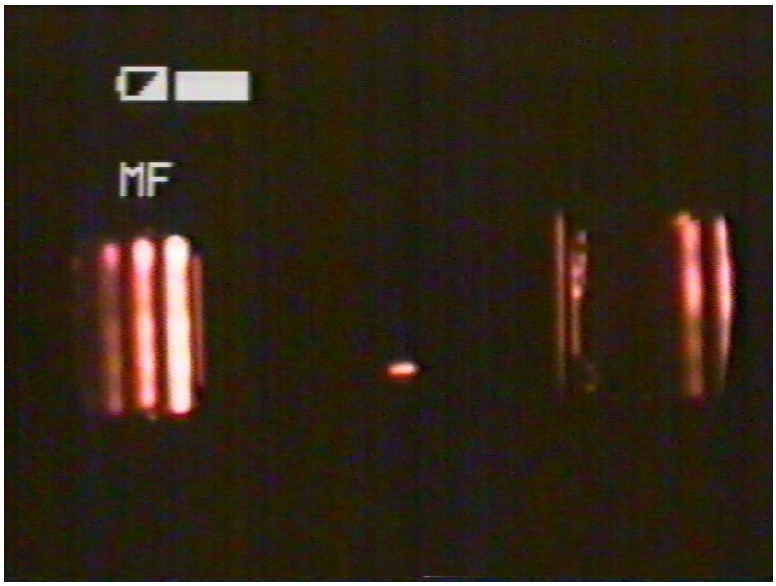

Shroud A: (Fwd Left) G1A-3 Shroud B: (Aft Left) Metal (1 TC)

Figure 3-150. Video image of the shroud test section during step test run 8 in the shroud rig. The image is of the back sides of two shrouds as viewed through fused silica windows on the pressure vessel and test rig. The bright vertical bars are the actual hot shrouds (there is no external illumination) showing between the impingement cooling bars (the dark vertical stripes).

Table 3-50. Summary of All Shroud Combustion Rig Tests Conducted from Jan. 13 Through Dec. 30, 1998.

Test	Start Date	Shrouds* by Position in the Rig: front left	rear left	front right	rear right	Test Summary
1	1/13/98	none				1st rig test; check fuel nozzle
2	2/5/98	none				Combustor shake down
3	2/10/98	none				Check combustor turndown limit
4	2/17/98	SS	inst	SS	SS	Check temperatures in shroud assembly
5	3/2/98	SS	inst	SS	SS	Shakedown test to check cooling air modifications
6	3/5/98	SS	inst	SS	SS	Shakedown test at full air flow and pressure conditions
7	3/10/98	G1A-3	inst	D1-1	SS	Step test to 1010°C. First test with CMC shroud components
8	3/13/98	G1A-3	inst	D1-1	SS	Continue run 7 step test to 1177°C.
9	3/19/98	G2C-1	D2-1	G1B-1	G2B-1	Step test to 1177°C on 4 new CMC shrouds.
10	3/26/98	G2C-1	D2-1	G1B-1	G2B-1	First cyclic test at 1177°C; stopped at 38 cycles due to gas sample probe failure; 62 remaining cycles completed on 3/28; G2B-1 cracked
11	4/2/98	G1A-3	G2C-1	D1-1	G1B-1	Second 100 cycle test at 1177°C
12	4/7/98	D2-1	D1-1	G1A-3	G2B-2	Third 100 cycle test at 1177°C
13	4/16/98	G1B-2	D2-2	G2C-2	D1-2	Start first endurance test at 1177°C and check out CMC combustor operation
14	4/19/98	G1B-2	D2-2	G2C-2	D1-2	Finish first 50 hour endurance test
15	4/29/98	D2-2	G1A-2	D1-2	G2B-3	Check out combustor heat shield modification and exhaust coupon exposure hardware
16	5/7/98	D2-2	G1A-2	D1-2	G2B-3	Check further modifications to heat shield and fuel mixing optimizations
17	5/12/98	D2-2	G1A-2	D1-2	G2B-3	Installed ceramic coupons in exhaust section, start second 50-hour endurance test at 1177°C, shroud G2B-3 cracked
18	5/17/98	D2-2	G1A-2	D1-2	G2A-1	Finish out second 50-hour endurance test
19	6/2/98	G2A-1	G1B-2	G1A-2	G2C-2	Third 50-hour endurance test at 1177°C
20	6/25/98	G1A-6	D1-3	G2A-2	G2C-3	Increase firing temperature to 1260°C, impingement air blocked to two shrouds
21	7/7/98	D2-3(i)	D1-3	G2B-3(i)	G2C-3	Increased firing temperature to 1371°C, cooling air removed from all shrouds, installed shrouds with embedded TC's

* "metal" refers to stainless steel shrouds used for rig shake down testing; "inst" is a stainless steel shroud instrumented with ten thermocouples, "CMC" refers to the various ceramic composite shrouds; and "HS-188" refers to a metallic shroud made of Haynes HS-188 cobalt-based superalloy used for comparison to the CMC shrouds. The shrouds are listed according to their position in the test rig in the order front left - rear left - front right - rear right.

(i) This shroud was instrumented with an embedded thermocouple for direct measurement of CMC shroud temperatures.

Table 3-50. Continued

Test	Start Date	Shrouds* by Position in the Rig				Test Summary
		front left	rear left	front right	rear right	
22	7/10/98	D2-3	D1-3	G2B-3(i)	G2C-3	Increased firing temperature to 1454°C
23	7/20/98	D2-3	D1-3	G2B-3(i)	G2C-3	Increased firing temperature to 1482°C, added combustor liner cover
24	7/22/98	D2-3	D1-3	G2B-3(i)	G2C-3	Gas sample probe failure, calculated firing temp. reached up to 1650°C
25	7/24/98	D2-3	D1-3	G2B-3(i)	G2C-3	20 thermal cycles at 1565-1593°C firing temperature
26	8/20/98	D2-3	D1-3	G2B-3(i)	G2C-3	tested new NSF† shields and increase rig air flow; firing temp of 1427°C, shrouds ran to ~1093°C
27	8/25/98	D2-3	D1-3	G2B-3(i)	G2C-3	new NSF and backside heat shields; firing temp of 1504°C, shrouds ran to 1200°C
28	9/15/98	HS-188-1	G2A-3	G1A-1	D1-4	1st 50 cycles on shroud configuration 1, firing temp of 1467°CF, shrouds ran to ~1200°C
29	9/30/98	D1-4	G2C-4	G2A-3	D2-4	1st 50 cycles on shroud configuration 2, firing temp of 1497°C, shrouds ran to ~1200°C
30	10/2/98	D1-4	G2C-4	G2A-3	D2-4	2nd 50 cycles on shroud configuration 2, firing temp of 1496°C, shrouds ran to ~1200°C
31	10/28/98	D2-4	G1A-1	G2C-4	HS-188-2	100 cycles on shroud configuration 3, firing temp of 1482°C, shrouds ran to ~1200°C
32	10/31/98	G2C-4	G2A-3	D1-4	G1A-1	2nd 50 cycles on shroud configuration 1, firing temp of 1468°C, shrouds ran to ~1200ºC
33	10/31/98	G2C-4	G2A-3	D1-4	G1A-1	50 hours steady state, firing temp of 1468°C, shrouds at ~1200ºC, G1A-1 and G2C-4 shrouds cracked
34	11/14/98	G2A-4	G2C-5	G1A-6	D1-5	1st 50 hour steady state test at firing temp of 1371°, done in two separate runs of 24 and 26 hours
35	12/10/98	D1-5	G1A-6	G2C-5	G2A-4	2nd 50 hour steady state test at firing temp of 1371°C
36	12/29/98	D1-5	G1A-6	G2A-4	G2C-5	100 thermal cycles at 1371°C firing temp

* "metal" refers to stainless steel shrouds used for rig shake down testing; "inst" is a stainless steel shroud instrumented with ten thermocouples, "CMC" refers to the various ceramic composite shrouds; and "HS-188" refers to a metallic shroud made of Haynes HS-188 cobalt-based superalloy used for comparison to the CMC shrouds. The shrouds are listed according to their position in the test rig in the order front left - rear left - front right - rear right.

† NSF = nozzle simulation flange

(i) This shroud was instrumented with an embedded thermocouple for direct measurement of CMC shroud temperatures.

Both of the CMC shrouds and the test rig metallic hardware survived the initial tests with little signs of distress so that during run 9, which was the first run with all four positions having CMC inner shrouds, the step test was conducted directly to 1177°C. A plot of the thermal ramp in the rig for run 9 is shown in Figure 3-151. Although thermocouples were not imbedded within the shrouds, an attempt was made to monitor the shroud backside temperatures with thermocouples "glued" to the backside surfaces with an alumina-based potting cement. However these thermocouples consistently read rather low temperatures compared to what was expected for the shrouds due to the insulating nature of the cement and to the influence of cooling air on the back sides of the shrouds.

The CMC shrouds that had survived the thermal ramp test were then used in thermal cycling tests. The test procedure was to first establish rig operation at nominally 1150°C firing temperature and then to cycle the rig firing temperature between 1150°C and about 450°C by rapidly shutting and opening the fuel inlet valve in 2 minute cycles (i.e. 1 minute with fuel on followed by one minute with fuel off). The thermal history of such a cyclic test rig run is shown in Figure 3-152. The response of the change in combustion gas temperature (Tfire) was extremely fast, with the full 700°C temperature swing occurring in less than 5 seconds. What little lag that was present was believed to be caused by heat capacity of the combustor and transition piece hardware. The shroud temperatures, as measured by thermocouples attached to the back faces, fully responded to the thermal cycles within 15 seconds. Undoubtedly the hot gas path face of the shrouds experienced and even more severe thermal shock.

Rig runs 10-12 were the first set of thermal cyclic tests. The original plan was to perform the cyclic tests on six shrouds using 3 rig runs where each shroud would be exposed for 100 cycles in a front position and 100 cycles in a rear position. However, after the first 100 cycle exposure a crack was observed in shroud G2B-1. Rather than risk possible crack propagation and shroud failure during the second set of cycles, shroud G2B-2 was substituted for G2B-1 in run 12.

The original test plan called for the step tests, thermal cycle tests and 100 hour steady state durability tests to be run on the same set of shrouds. However, doing so would mean that if any shroud degradation was found in post-test characterization that the primary reason for the degradation, whether from the thermal cycling of from the longer-term steady state exposure, would be lost. Consequently the shrouds that had seen 200 cycles in rig runs 10-12 were pulled from testing and evaluated. A different set of six shrouds was then used for the 100 hour exposures in rig runs 13-19.

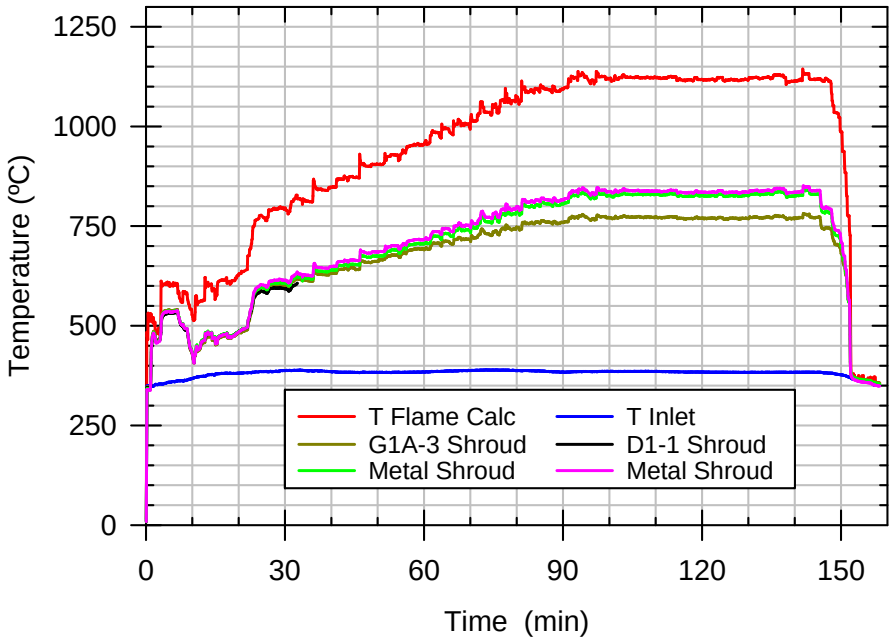

Figure 3-151. Temperature vs. time during rig test run 9.

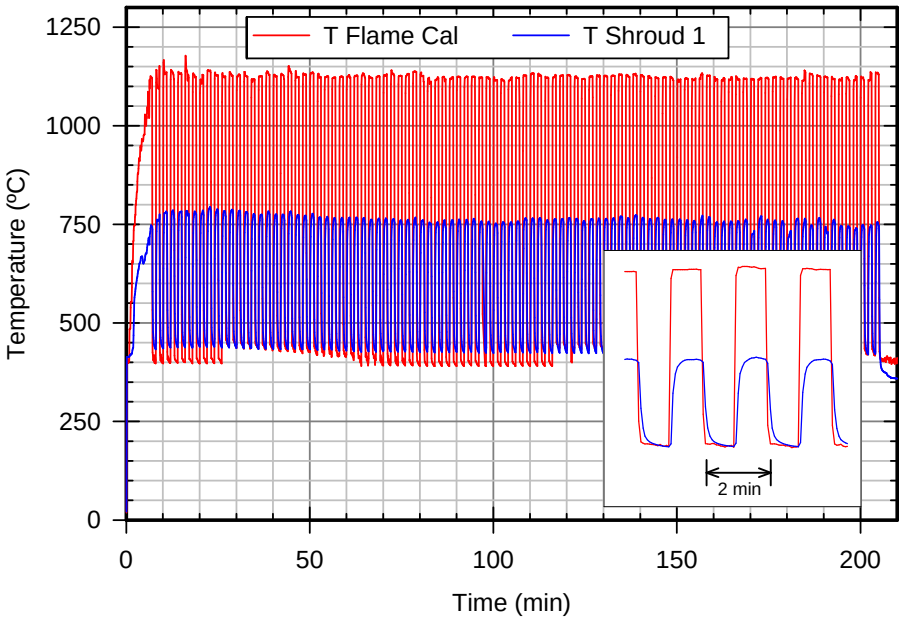

Figure 3-152. Temperature vs. time plot for the rig firing temperature and one of the shroud thermocouple temperatures during a thermal cycle rig test run. The inset shows the rapid nature of the thermal cycles, where firing (hot gas) temperature varied between the extremes in less than 5 seconds and the shroud thermocouple temperatures cycled between the extremes within ~15 seconds.

As with the cyclic test, the 100 hour exposure test was broken into 50 hour segments so that the shrouds could be switched between the front and rear rig positions. The first CMC combustor liner was also introduced into the rig for run 13 since the starting metallic liner

had been significantly damaged by the cyclic tests. Consequently run 13 was shortened so the CMC combustor liner could be inspected after ~2 hours to ensure it was holding up well. After this inspection showed no issues with the CMC liner the remainder of the first 50 hour exposure was completed in run 14.

Although the CMC combustor liner was operating well, after run 14 is was noted that the heat shield in the combustor was oxidizing and warping to the extent that it had contacted the ID of the CMC liner and partially reacted with it locally. Consequently the first liner was removed from the rig and the second CMC liner was installed. With a CMC combustor liner present there was less of a concern with overheating of the liner, so the heat shield was shortened for run 15. The exhaust diffuser assembly for holding test coupons on the exhaust end of the shroud test section was also added. At the start of run 15 there were problems with flame stability in the rig, likely caused by increased mixing of the cooling air from the outside of the heat shield that was prematurely diluting the air/fuel mixture. The test was stopped early to allow for inspection of the combustor heat shield and the exhaust diffuser hardware, both of which were in good condition.

Prior to run 16 the ring of dilution holes used to cool the heat shield were partially plugged in order to improve flame stability on the combustor. With reduced cooling the durability of the heat shield was suspect, so it was essentially eliminated. Run 16 was a short-duration run of a few hours with the main goal of testing the heat shield and cooling air modifications on the flame stability. The rig performed well during this test so that the second 50 hour exposure test was started in run 17. CMC coupon samples were also installed in the exhaust diffuser for the first time during run 17. There was a concern that there would be reaction between the test coupons and the metallic support plates in the exhaust diffuser, and consequently run 17 was stopped after only 4 hours to allow for inspection of the test coupons. As no issue with the coupon samples was found the remainder of the 50 hour exposure was completed in run 18. However, after run 17 shroud G2B-3 was found to be cracked after only ~6 hours total exposure from runs 15-17. This was the second of the CCP slurry cast / Sylramic™ fiber shrouds to have obviously cracked during testing. In both cases the cracks were arrested after propagating inward from an edge about 2cm, and neither shroud failed completely. Shroud G2A-1 was then substituted for G2B-3 for run 18. Rig run 19 then completed the third of the three 50 hour endurance tests. Runs 13 through 19 thus yielded 5 shrouds that had been exposed to 100 hours and one shroud (G2A-1) that had been exposed for ~76 hours, in addition to the G2B-3 that was cracked after ~24 hours.

3.8.1.5.2 Shroud Testing Under Very High Temperature Conditions

Shroud test rig runs 20-27 were a series of short runs that were done in order to get the CMC shroud material temperature up to the desired 1150°-1200°C range. The shroud thermocouple data from runs 7-19 strongly suggested that the CMC inner shrouds were running considerably cooler than was anticipated from the engine condition analyses. The most likely cause of the low CMC shroud temperatures was overcooling of the shrouds from the backside impingement cooling air. In order to test the effects of the cooling air the impingement cooling air was blocked in two of the shroud positions for rig run 20. When the rig was first fired at the “standard’ 1177°C firing temperature the shrouds with

no impingement cooling were still running considerably cooler than the hot gas path temperature, so that the rig firing temperature was raised to 1260°C to try to bring the temperature of the shrouds up to 1200°C; however, the shrouds still ran considerable cooler than 1200°C as measured by the backside thermocouples.

The shroud backside thermocouples had several operational issues, including the insulating effect of the alumina cement used to attach them to the shrouds and poor reliability of this cement bond. Optical methods of measuring the shroud temperature using IR thermography and optical pyrometry proved unsuccessful due to clouding of the windows during a rig run. Given the uncertainties with the existing thermocouple measurements it was felt that the only way to get a more reliable measure of the actual shroud temperatures was to instrument one of the CMC shrouds with an embedded thermocouple. This was to be accomplished by cutting a 1.3mm deep, 1.3mm wide slot into the back side of a shroud with a diamond saw, into which a 0.8mm thermocouple would be cemented. By having the thermocouple bead embedded in the shroud only 1mm from the hot gas path face we expected to get a much more accurate assessment of the actual CMC shroud temperature. There was a risk to cutting such a slot into the back side of a shroud in that the slot could act as a crack source, thereby introducing damage unrelated to the rig exposure and ruining the shroud for further testing and evaluation. For this reason, and because the slurry cast MI / Sylramic system was the one of the highest thermal conductivity CMC systems under study, shroud G2B-3, which had already been cracked in rig run 17, was selected for instrumentation. Shroud D2-3 was also instrumented in a similar fashion, and was selected since it represented the system (DIMOX) with the lowest thermal conductivity. For all rig runs from 21-27 the shroud temperatures quoted are based on the measured temperature of instrumented shrouds G2B-3 and D2-3.

Since blocking of the impingement cooling had not caused any notable distress on the CMC shrouds during run 20 the impingement cooling channels were also blocked for the remaining two shrouds. Thus for rig runs 21 and beyond there was no active cooling on any of the CMC shrouds.

Rig test 21 was a short run to test the response of the instrumented shroud. The firing temperature was gradually increased to 1371°C, yet the shroud temperature only reached ~1000°C. Moreover the temperatures of the instrumented shrouds were found to be in reasonable agreement with the normal backside thermocouples used up to this point. This result indicated that the backside thermocouples were indeed indicating actual shroud backside temperatures, ranging from 760° to 815°C in runs 7-20, and that the hot gas path temperature of the shrouds probably never exceeded 900°C during these early runs. Run 21 was stopped to allow for inspection of the rig metallic hardware out of fear that the higher firing temperatures could be damaging the rig. Luckily rig damage was limited to the replaceable insert in the throat of the shroud test section inlet and some cracking in the castable refractory of the transition piece.

The intent of rig test 22 was to continue increasing the rig firing temperature until a CMC shroud temperature of 1200°C was attained. However, as the firing temperature reached

~1450°C combustion dynamics became fairly severe and the rig test was stopped. with shroud temperatures having only reached ~1050°C.

Up to this point the rig combustor had been operated primarily in the lean pre-mixed combustion mode, i.e. the fuel and air were being mixed within the premixer upstream of the combustion zone. This mode was selected since it represented the manner in which most modern combustors are operated. However, the fuel nozzle also had allowances for running in a diffusion flame mode. A "diffusion flame combustion" is where the fuel is simply injected into the air stream without premixing and immediately combusted, which is the historic manner in which most combustors operated prior to the introduction of low NOx combustion technology. In general, diffusion flame combustion is less prone to give combustion dynamics than is lean premixed combustion. In order to address the combustion dynamics issue observed in rig run 22 the fuel nozzle was re-configured to utilize a combination of ~2/3 premixed combustion and ~1/3 diffusion combustion.

There was also a concern that part of the problem with getting high shroud temperatures was traceable back to the combustor liner cooling. Up to run 23 the combustor liners had all had backside convective cooling. It was believed, and backed up by thermocouples measurements, that because of this cooling that the combustor walls were running substantially cooler than the combustion gas temperature. This situation led to the possibility that the cool combustor wall was also cooling the combustion gas near the edges of the combustor and that this cooler region was not completely mixing out of the flow prior to the shroud test section. In order to minimize the possible cooling effects of the combustor liner a flow shield was added outside of the CMC combustor liner that blocked all backside convective cooling to the liner.

The reconfiguration of the fuel nozzle was largely successful, as increasing the firing temperature of the rig to 1482°C produced no excessive combustion dynamics. The flow sleeve around the combustor liner was also successful in that the liner temperature increased to ~1000°C. Unfortunately the shroud temperature was still limited to ~1050°C. The rig was shut down at this point to allow for inspection of the combustor liner to ensure that it was not being overheated from the elimination of cooling air. The combustor was still in good shape following this run, but the shroud test section replaceable flange throat insert and the nozzle simulation flanges were both showing thermal damage.

Rig run 24 was intended to increase the rig firing temperature further in an attempt to get a CMC shroud material temperature of 1200°C. Early in the run, however, the gas sample probe failed. The gas sample probe is connected to oxygen and CO_2 analyzers, and the measured ratio of CO_2 to O_2 in the combustion gases is used as a second method of back-calculating the rig firing temperature as a check on the firing temperature calculated from the upstream air and fuel flows. The sampling probe failure caused the rig temperature based on gas sampling to be erroneously low, so that the rig was mistakenly turned up to a firing temperature of ~1650°C, attaining a shroud temperature of ~1200°C, before the probe problem was discovered. Inspection of the rig after shut down indicated little effect on the CMC hardware, but the metallic rig hardware was showing increasing signs of

oxidation distress. Similarly the transition piece refractory lining was increasingly cracked and with some small regions having been eroded.

Rig run 25 was conducted with the repaired gas sample probe. Rig firing temperature was increased to ~1580°C, which gave a measured shroud temperature of ~1200°C. At that point 20 thermal cycles were run in order to test the operability of the combustor at this extreme temperature and to evaluate the effects of such extreme temperature cycles on the durability of the test rig.

Unfortunately, the shroud rig accumulated serious damage during runs 24 and 25. Parts of the refractory lining of the transition piece were lost (It is likely that the higher temperatures in the refractory caused increased glassy phase formation, which on thermal cycling caused cracking and spalling of the refractory). Also the inlet flange to the shroud exposure section and the two forward nozzle simulation flanges, which were air cooled, TBC-coated stainless steel, partially melted. Photographs of the damaged flanges are shown in Figure 3-153. (The photographs were take after the flange was cut for repairs, to be described below, and only show the end exposed to the hot gas path.) Despite the higher exposure temperatures, pieces of the transition piece flying downstream and likely impacting the CMC shrouds, and the shrouds being hit by molten metal coming from the melting nozzle simulation flanges, no structural damage was noted on the CMC shrouds. There was a build-up of surface oxide "glaze" on the shrouds, but it is not clear if this oxide was a product of oxidation of the shrouds or a glassy phase coming from the over-heated transition piece and accumulating on the shrouds.

The shroud rig required considerable repairs following run 25, including rebuilding of the transition piece liner and of the shroud test section inlet flange. The nozzle simulation flanges were modified by bolting plates of Prepreg CMC to the front of the flanges. Shroud G1B-3 was cut to yield two flat plates of GE prepreg MI composite. The melted ends of the nozzle simulation flanges were cut off and new ends with cooling channels were welded in place. The flange was then machined to allow the mounting of the CMC plates onto the forward face of the flanges where the hot gases directly impinged. The CMC plates were then simply bolted into a cut-out on the front of the flanges.

During the rig re-build some of the air by-pass holes on the rear side flange of the shroud rig were plugged, thereby forcing more compressor air through the combustion rig itself. This was done because room temperature flow testing of the rig performed during the re-building process had indicated that there was more leakage than expected around the aft hula seal where the shroud rig mated to the test cell exhaust pipe. It was hoped that the extra flow through the rig, and the consequently higher surface heat transfer coefficients in the shroud test section, would help increase the shroud temperature toward the 1200ºC goal with a rig firing temperature below 1500°C. The initial rig test following rebuild, run 26, was therefore a short test to validate the operation of the rig under these new flow conditions. There were also concerns about the durability of the new nozzle simulation flanges due to the large thermal expansion mismatch of the CMC plate and metal substrate, which could lead to cracking of the CMC plate insert. During this test the rig was run up to a firing temperature of 1427°C and a measured shroud temperature of 1093°C. The rig

performed in a very stable manner and post-test rig inspection showed the nozzle simulation flanges to be intact and functional.

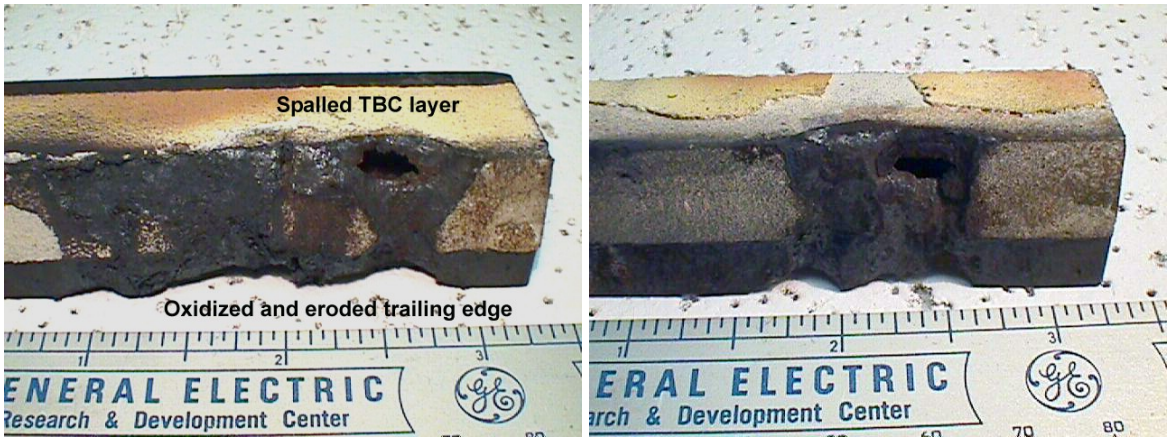

Figure 3-153. Photographs of the two front nozzle simulation flanges following rig test 25 showing spallation of the TBC and melting of the flange ends. The photographs were taken after the flanges had been cut for repair purposes so only the flange faces that extended into the hot gas path are shown.

Despite the improvements made in run 26, it was still feared that it would require pushing the shroud rig firing temperature to around 1550°C in order to attain the 1200°C shroud temperature goal. There were substantial concerns about rig durability when operating under these conditions, particularly for the cyclic tests. It was highly desirable to limit the firing temperature to the 1430°-1480°C range if possible to limit rig thermal damage. One-dimensional heat balance calculations were performed for the shroud components and they indicated that just radiative heat flux from the CMC inner shrouds to the very cold (<500°C) outer shroud blocks could alone be sufficient to keep the inner shrouds from reaching the 1200ºC temperature goal at these firing temperatures. Radiation heat shields were therefore added to the shroud blocks to limit the amount of radiative cooling.

Although the radiative cooling was hindering the attainment of the desired shroud test temperatures, it would have a positive impact for an actual shroud application in an engine. Normally, radiative cooling effects in current metal shrouds are not important because of the relatively high amounts of convective and film cooling used, because the metal shrouds are much thicker with a larger temperature drop across them, and because of the relatively low emissivity of the metal. The fact that radiative cooling of the higher emissivity, thin-walled CMC shrouds is so effective means that they may require even less cooling air in an engine application than previously thought, thereby giving an even greater engine cycle benefit.

In rig run 27, with no cooling air to the CMC inner shrouds and with heat shields in place to limit radiative heat loss, the goal of a 1200ºC shroud temperature was attained at a rig

firing temperature of 1504°C. Although slightly higher than the value desired, this level of firing temperature was considered low enough to proceed with the normal shroud testing.

Inclusion of an instrumented shroud in all following rig tests, in order to have a direct confirmation of the shroud temperatures, was not feasible. The instrumented shroud would displace a normal test shroud, and thus increase the number of tests needed to complete the test plan. The temperature distribution for the entire rig during run 27 was therefore used as a calibration point for measuring the shroud temperatures in all following rig runs, the assumption being that if the overall rig temperature distribution from run 27 could be reproduced without any hardware changes that it would be a sufficient indication that the CMC inner shrouds were indeed running at close to the 1200°C target.

With all of the data collected during the highly instrumented rig runs, where the combustor liner, shrouds and exhaust diffuser section all had gas stream temperature measured by either thermocouple or gas probe analysis, the actual exposure conditions within the shroud rig could be estimated fairly closely. The combustion conditions defined by rig test 27, and then duplicated in runs 28-33, gave the following environment conditions for the different sections of the test rig: in the combustor section the gas temperature was ~1500°C with a mass flow of 0.75kg/s at a velocity of 41m/s and pressure of ~1.3MPa; in the front shroud position the gas temperature was ~1400°C with a mass flow of 0.9kg/s at a velocity of 207m/s and a pressure of ~1.2MPa; in the rear shroud position the gas temperature was ~1370°C with a mass flow of 0.95kg/s at a velocity of 210m/s and a pressure of ~1.1MPa; and in the exhaust diffuser section the gas temperature was ~1200°C with a mass flow of 1.2kg/s at a velocity of 119m/s and a pressure of ~1.0MPa.

With the rig firing temperature in the range of 1500°C the normal gas temperature conditions of an actual engine had been substantially exceeded. Consequently it was not clear how a metallic shroud would behave under similar exposure conditions, and the performance of the CMC shrouds relative to a metallic shroud was an important evaluation criterion. A metallic shroud made to the CMC shroud configuration was therefore included in the next test as a gage of how severe the testing conditions really were. The normal metallic engine shrouds are made of cast Inconel 718. Unfortunately this material was not available in time for the next planned test, and so a shroud made from Haynes HS-188 sheet stock was used instead. This alloy has similar oxidation behavior to the Inconel material, and was therefore expected to have a similar response to rig exposure since the mechanical stresses on the shroud are negligible.

Normally the thermal cycling tests would be run in three 100-cycle tests while rotating individual samples in and out of the rig so that each shroud would accumulate 200 thermal cycles. However, because of the extreme firing temperature conditions being used each run was limited to only 50 cycles to allow for rig inspection and repair between runs.

During rig run 28 the thermal conditions of run 27 were matched at a rig firing temperature of 1467°C. The rig was then rapidly cycled 50 times to ~450°C and back with a one minute hold at the two extremes between cycles. The HS-188 shroud showed very severe degradation following these 50 cycles. The shroud was warped, heavily oxidized, and had

a thermal fatigue crack from the exposure. A photograph of the tested HS-188 shroud is shown in Figure 3-154. The backside temperature measured on the HS-188 shroud was roughly 1300°C, which was about 100ºC higher than that measured on any of the ceramic shrouds. The higher measured temperature could have been the result of several factors: 1) the HS-188 shroud was thinner than the CMC shrouds and had a higher thermal conductivity in this temperature range so that the temperature drop across the shroud would be smaller, 2) the thermocouples on the HS-188 shroud were embedded in the shroud rather than being glued on to the back side and were thus more representative of the front-side temperatures, and 3) the emissivity of the CMC shrouds is much higher than HS-188 and thus they are more effectively cooled by radiative cooling, which was the dominant cooling mechanism since all impingement and convective cooling air on the backs of the shrouds had been eliminated.

Figure 3-154. Photograph of the HS-188 shroud following rig test exposure in rig run 28. Shroud warping, oxidation and thermal fatigue cracking are evident.

Following this same 50 cycle test none of the CMC shrouds included in the test showed any signs of degradation. Because of the severe damage to the HS-188 shroud it was removed from the test rig and a different configuration of 4 CMC shrouds was used for the next two tests (runs 29 and 30). Again, the CMC shrouds all survived the total of 100 thermal cycles without incident, but parts of the test rig were damaged. The cast monolithic ceramic transition piece was losing material because of thermal shock during the cyclic tests. This allowed the hot gases to directly impinge on the flange throat inserts at the inlet to the shroud test section, severely oxidizing and/or melting parts of the inserts. The nozzle simulation flanges within the shroud section, which had been previously fitted with front face shields made of GE prepreg MI composite, still showed damage to the metal part of the flange. Unfortunately the last rebuild had blocked some of the cooling air passages in the metal and caused a reduction in the cooling air flow to these parts, causing them to overheat. The flanges consequently showed severe oxidation and cracking following the cyclic test. Despite the cracking and warping of the metallic section, the ceramic shields on the front of the flanges were still intact and functioning. New nozzle simulation flanges, which incorporated the CMC heat shields and modified cooling passages to return to the original levels of cooling air flow, were therefore fabricated for

further rig tests. Repairs were also made to the shroud section inlet flange and to the castable refractory lining of the transition piece.

During rig run 31 a second HS-188 shroud was run in a rear rig position, which typically sees about 40°C lower temperature gases than the front positions, for 100 cycles. The full 100 cycles were run with the shrouds in the same rig positions, rather than stopping at 50 cycles and rearranging the shrouds, due to rig scheduling constraints. Again the HS-188 shroud was severely oxidized and warped, as shown in Figure 3-155. Throughout all of these cyclic tests (runs 28-31) all of the CMC shrouds were undamaged and dimensionally stable.

Figure 3-155. Photograph of the second HS-188 shroud following rig testing in a rear position during run 31. The shroud hot gas path face was highly warped and heavily oxidized after ~2 hours exposure and 100 thermal cycles.

The HS-188 shrouds oxidized and warped so badly during the cyclic tests, which had a total exposure time of only 1-2 hours, that it was decided not to include such shrouds in the steady state exposure tests. This left 5 CMC shroud materials to test but only 4 rig positions for testing. Based on the degradation seen in the CCP DIMOX shrouds following the lower temperature rig testing, this material was withdrawn from further testing. Instead of performing the steady-state exposure on the D2-4 shroud it was sectioned after the cyclic tests and two test bars from the shroud were placed in the rig exhaust section during the steady state exposure tests.

Again due to rig scheduling constraints it was necessary to perform the last set of 50 thermal cycles (run 32) followed immediately by the first 50 hours of steady state exposure (run 33) without a rig shut-down and inspection. During this run two of the CMC shrouds, the Goodrich slurry cast MI shroud G2C-4 and the GE Prepreg MI shroud G1A-1, were

found to have cracked. Photographs of the cracked shrouds after exposure are shown in Figure 3-156. The cause of these failures was believed to be related to rig degradation because the rig components upstream of the shrouds were again very heavily damaged during the run. The transition piece, which was heavily damaged in the earlier cyclic tests, continued to erode and thereby exposed the front flange and front nozzle simulation flanges of the shroud testing section to direct hot gas impingement. This caused the shroud test section inlet flange and nozzle simulation flanges to partially melt, exposing some of the internal cooling passages. The changes in cooling air flow caused by the failure of these metallic rig parts caused severe lateral thermal gradients in the Goodrich and GE shrouds and caused the observed cracking. This interpretation is supported by the fact that the oxidation patterns on the surfaces of these shrouds were very non-symmetric. In both materials the cracks were arrested within the shrouds and neither experienced a catastrophic failure. The CCP MI and CVI E-SiC-SiC shrouds, which had a more uniform oxidation pattern indicating that they saw less of a lateral thermal gradient, withstood the exposure intact.

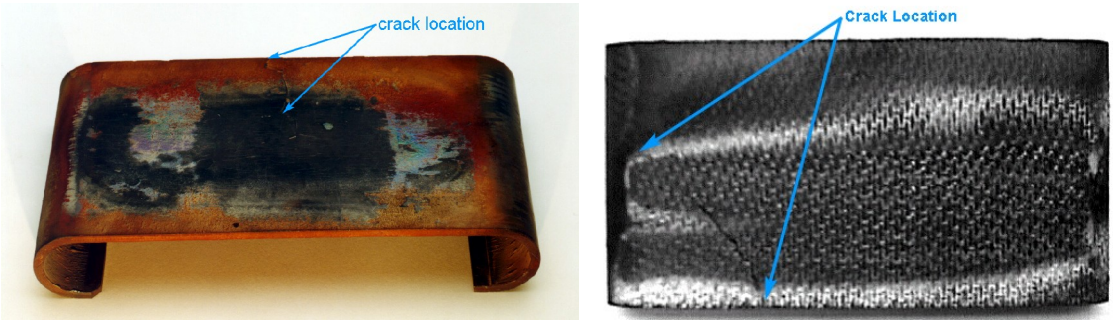

Figure 3-156. Photographs of GE Prepreg MI shroud G1A-1 (left) and Goodrich slurry cast MI shroud G2C-4 (right) following rig test 33. The locations of the shroud cracks are indicated. The red tint on the shroud is from the deposition of iron oxide from upstream metallic hardware. (The photograph on the right is black& white and thus does not show the iron deposits.)

In order to verify that the shroud cracking noted following rig tests 32 and 33 was caused by the rig hardware degradation an ANSYS analysis was performed on the cracked G2C-4 shroud. This shroud displayed very clear surface markings from enhanced oxidation/volatilization that corresponded precisely with regions that had been lost from the transition piece and shroud test section inlet flange. The hypothesis was that the disruption of gas flow caused by the transition piece and flange damage caused hot streaks that impinged on the shroud surface. There were very likely also cold streaks caused by the increased cooling air coming from the damaged inlet flange. The extra thermal gradients caused by these hot and cold streaks then led to increased thermal stresses that cracked the shrouds. Based on the oxidation markings on the shroud an estimated combustion gas temperature pattern was derived as shown in the top plot of Figure 3-157, where the gas temperature peaked locally at two locations across the shroud width.

Placing this type of gas temperature gradient into the shroud analysis boundary conditions and running the thermal and stress analyses yields the results shown in Figure 3-157.

With the normal, uniform temperature boundary conditions the shroud temperature is uniform across the width, as shown in Figure 3-140. However, with the temperature gradient in the hot gas boundary conditions the thermal profile of the shroud becomes non-symmetric, as shown in the middle plot in Figure 3-157. This change in thermal gradient in turn increases the axial tensile stress in the shroud along the edge near the hot streak, with the maximum stress occurring at the precise location where the shroud crack initiated (marked by the magenta circles on the photograph and stress plot of Figure 3-157). Obviously the magnitude of the thermal gradient, and therefore of the added tensile stress, would depend on the magnitude of the hot and cold streaks. The results in Figure 3-157 are for high, medium, and low temperatures in the temperature-position plot of 1540°C, 1315°C, and 1090°C, respectively. Similar analyses were also performed for the cases of an even more severe combustion gas temperature gradient and for no gradient. A comparison of the results of these calculations is given in Table 3-51. Since the Goodrich slurry cast MI material has a matrix cracking stress of about 120MPa at these temperatures the analysis predicts that shroud cracking should occur for either of the hot-streak conditions, but not for the uniform gas temperature condition. It is believed that similar thermal gradient effects also caused the cracking of shroud G1A-1; however, due to the lack of a clear oxidation pattern on this shroud a pattern for the combustion gas gradient could not be estimated, and therefore an analysis could not be performed.

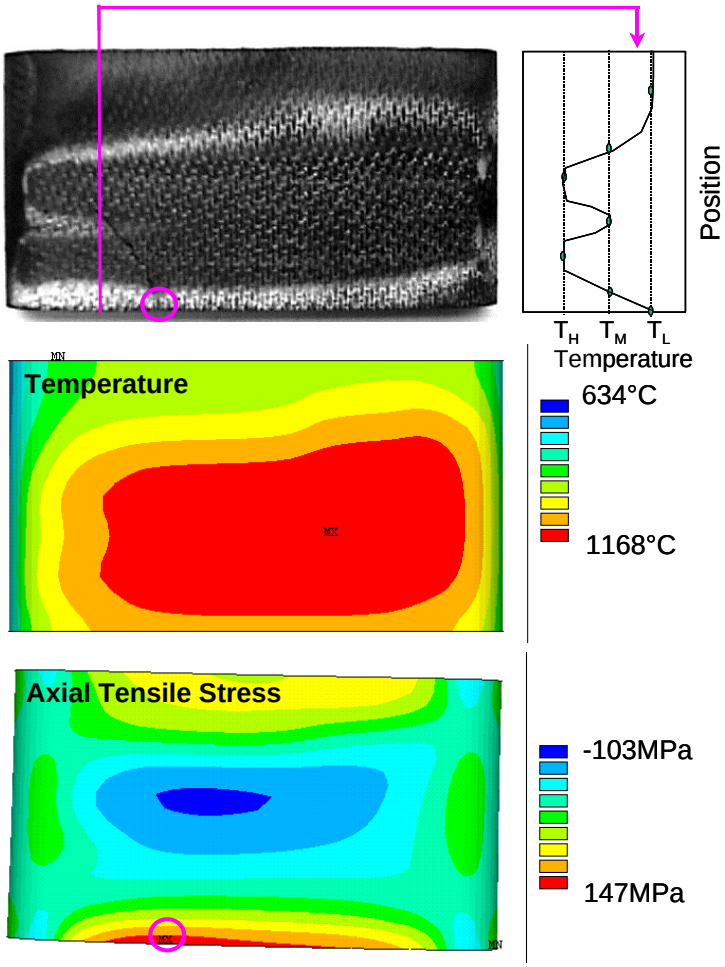

Figure 3-157. Ansys FEM analysis results for cracked shroud G2C-3.
Top – photograph of the shroud and shape of the combustion gas profile derived form the oxidation markings
Middle – temperature distribution in the shroud caused by the combustion gas gradients
Bottom – axial tensile stress distribution caused by the non-symmetric thermal gradients.

Table 3-51. Comparison of the ANSYS Analysis Results for the Thermal Streak Conditions on Shroud G2C-3 in Rig Runs 32-33.

Assumed Combustion Gas Temperatures*			Maximum Shroud Temperature (°C)	Maximum Shroud Tensile Stress (MPa)
T_H (°C)	T_M (°C)	T_L (°C)		
1540	1540	1540	1176	113
1540	1315	1093	1168	147
1650	1371	1093	1222	163

* The high, middle and low temperatures correspond to the three temperature levels in the assumed combustion gas gradient as indicated in Figure 3-157.

3.8.1.5.3 Shroud Testing Under Intermediate Temperature Conditions

The extreme damage caused to the rig in runs 32 and 33, and its subsequent influence on the cracking of the shrouds, made it apparent that long term testing under such severe temperature conditions was not appropriate for this rig. It was decided to reduce the rig firing temperature to approximately 1370°C and repeat the exposure tests. It was also noted in the prior tests that the most severe rig damage, particularly to the cast refractory transition piece, tended to occur during the thermal cyclic tests. Therefore for the next set of tests the steady state exposure runs were performed first in the hope that minimal rig repair would be needed before starting the cyclic test. In order to minimize the number of additional rig runs needed it was decided to not test the DIMOX shrouds further, but to only include GE Prepreg MI, CCP slurry cast MI, Goodrich slurry cast MI and CCP CVI E-SiC-SiC shrouds.

Test runs 34-36 were completed using a 1370°C rig firing temperature, and included 100 hours of steady state exposure followed by 100 thermal trip cycles. During these tests the backside shroud temperatures varied between 1065°C and 1120°C. A small crack was found in the Goodrich MI shroud after run 35, with a location similar to that in the cracked shroud from run 33. Despite the crack this shroud was exposed for an additional 100 thermal shock cycles in run 36 with no observed propagation of the crack.

Following run 36 very small cracks were found in the GE Prepreg MI and the CCP slurry cast MI shrouds as well. These cracks were so small that they could only be seen under magnification and may have been missed in earlier examinations, and may therefore have originated during runs 34 or 35. The appearance of these small cracks prompted a more detailed reexamination of the previously tested shrouds. Under visual examination with a stereomicroscope it was found that there was a very small crack in the CCP slurry cast MI shroud (G2A-3) from rig runs 28-31 as well. Cracks were not visually observed in the CCP CVI E-SiC-SiC shrouds, but these shrouds tend to have much rougher surfaces compared to the MI shrouds, which would tend to hide the very small cracks seen in some of the MI shrouds.

The second GE Prepreg MI combustor liner had been in place in the test rig since run 19. This liner had successfully survived nearly 200 hours of service at rig firing temperature of up to 1650°C, including over 400 thermal trip cycles. During rig re-build after run 32 it was noticed that there were some small (1-2mm) metallic balls adhering to the inner surface of the liner. EDAX analysis of one of the balls showed it to be silicon. The "sweating" of silicon to the surface of MI-type materials when heated above the melting point of silicon (1410°C) is a commonly observed phenomenon. The presence of the Si balls indicated that part of the combustor liner got to at least 1410°C. Even at these very high temperatures the liner remained intact and dimensionally stable.

The third CMC "component" in the test rig was the leading edge of the nozzle simulation flanges. As noted previously the flanges had been a major reliability problem with the rig. The original design was TBC-coated stainless steel with active air cooling. This design worked satisfactorily for the lower temperature runs (runs 1-19), but the flanges were

severely damaged (oxidation, cracking and in some cases actual melting) during the higher temperature runs (see Figure 3-153). This severe damage prompted a redesign of the flanges utilizing a GE Prepreg MI composite plate on the leading edge to act as a heat shield for the rest of the structure. The rather crude implementation was to simply mill out a section of the front face of the flange and bolt the CMC plate into position. Despite the thermal expansion mismatch the CMC plates remained intact and greatly reduced the damage to the flange leading edge. A picture of one of the CMC-modified flanges is shown in Figure 3-158 after it had been used in runs 26-33. There was some erosion of the exposed edge of the CMC plate, but it remained intact through testing that would have completely destroyed a metallic flange. In fact the stainless steel trailing edge of the flange behind the CMC plate was still being oxidized and eroding during rig operation. The stainless steel structure of the nozzle simulation flanges actually had to be remanufactured between runs 33 and 34, but the same CMC plates were used for both rebuilds, attesting to the durability of the Prepreg MI CMC. Photographs of one of the re-fabricated flanges following rig test 36 are also shown in Figure 3-158.

No further shroud rig testing was performed. The rig damage that accumulated through the high temperature tests had become quite extensive. Simple rebuilds of the nozzle simulation flanges, transition piece and several support flanges in the rig were no longer possible so that continuing testing would have required manufacturing totally new components at considerable cost. Moreover, more shroud testing had already been completed (over 300 hours of rig operation) than in the original program plan (200 hours).

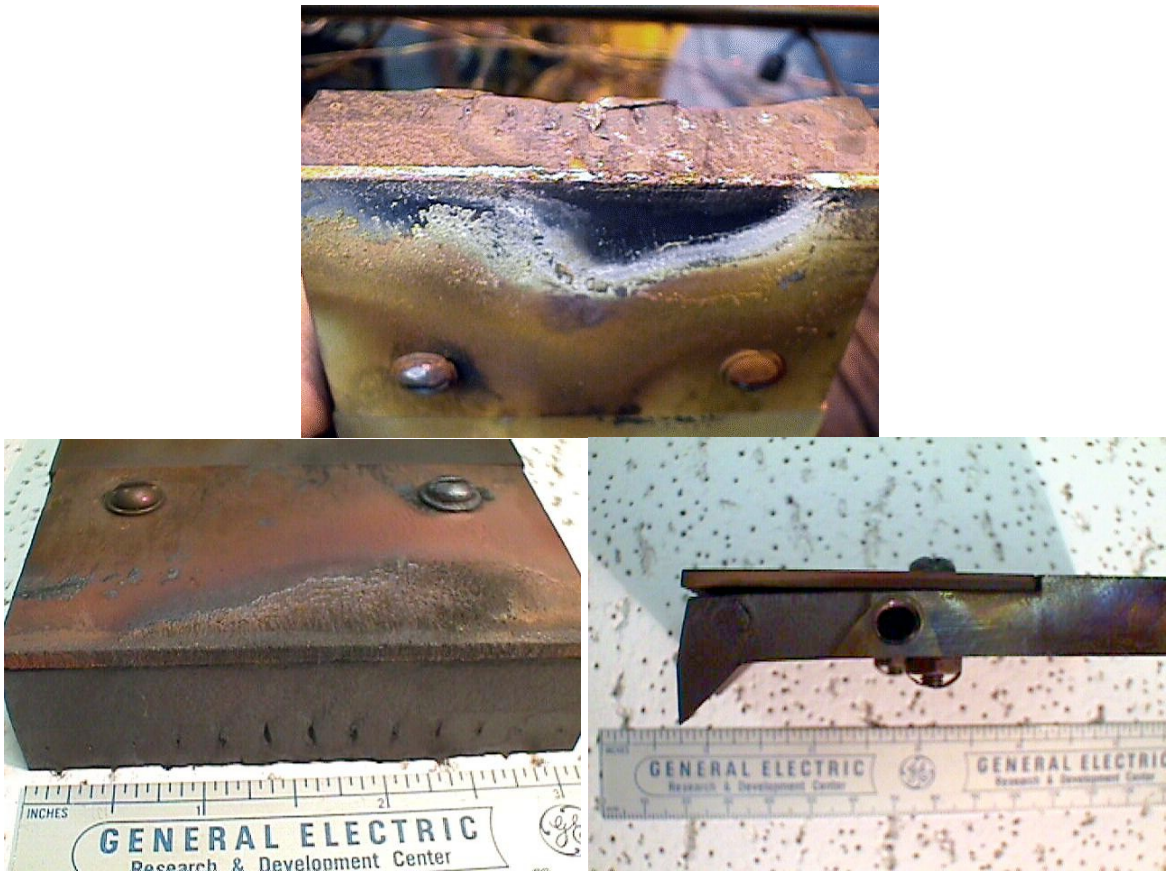

Figure 3-158. Photographs of two of the modified nozzle simulation flanges incorporating the bolted-on CMC plate on the leading edge. The reddish appearance of the CMC plates is from iron oxides that deposited during rig testing.
Top – condition of the flange following rig run 33.
Bottom – One of the rebuilt flanges following at the conclusion of shroud rig testing (after run 36).

3.8.1.6 Shroud Post-Test Characterization

Post-test characterization of the shrouds was performed under program task 3.4. Component Evaluation.

3.8.1.6.1 Non-Destructive Characterization

All of the shrouds used for rig testing went through post-test nondestructive evaluation (NDE), and most of the shrouds were also subject to destructive evaluations. Pre-test NDE relied most heavily on IR thermography inspections by Dr. W. Ellingson and Dr. J.G. Sun at Argonne National Laboratory. For example, pre-test and post-test thermal diffusivity images of the shrouds used in the initial rig testing (rig runs 7-19) are shown in Figure 3-159. Other than the crack observed in shroud G2B-1 there were no significant changes in the diffusivity images as a result of rig testing. This observation was not surprising in that the shroud temperatures, and therefore also the thermal stresses, during these runs were relatively low.

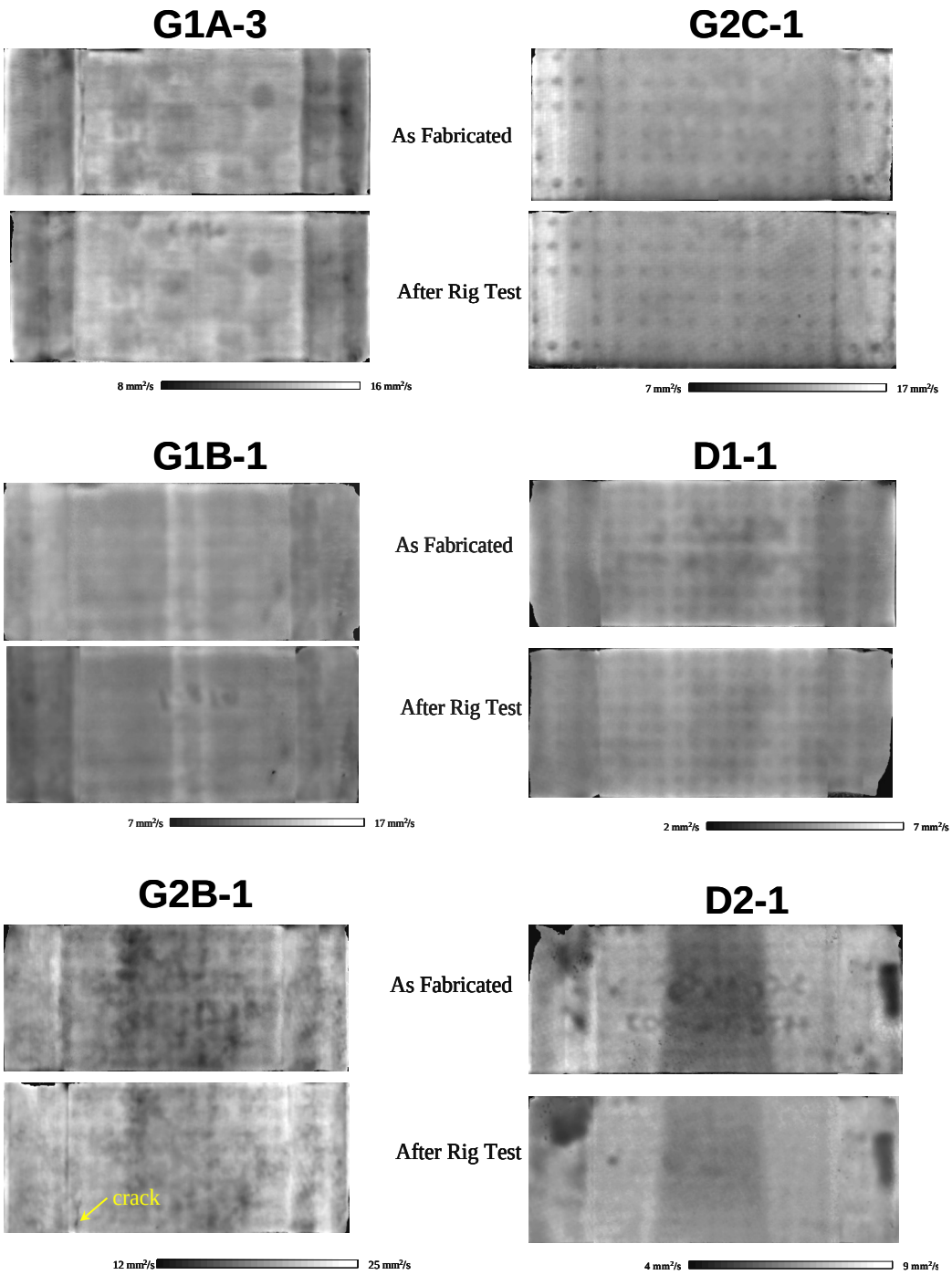

Figure 3-159. Comparison of pre-test and post-test thermal diffusivity images of the shrouds used in rig runs 7-19. Other than the crack in shroud G2B-1 there were no significant changes in the NDE images. The shroud identities are as listed in Table 3-49.

Shrouds tested in rig runs 28-36, under more severe thermal conditions, did often show changes in the NDE images. Examples of several of these changes in the IR diffusivity images are shown in Figure 3-160. The preliminary interpretation of the image changes, as suggested by the NDE team, are indicated on the images.

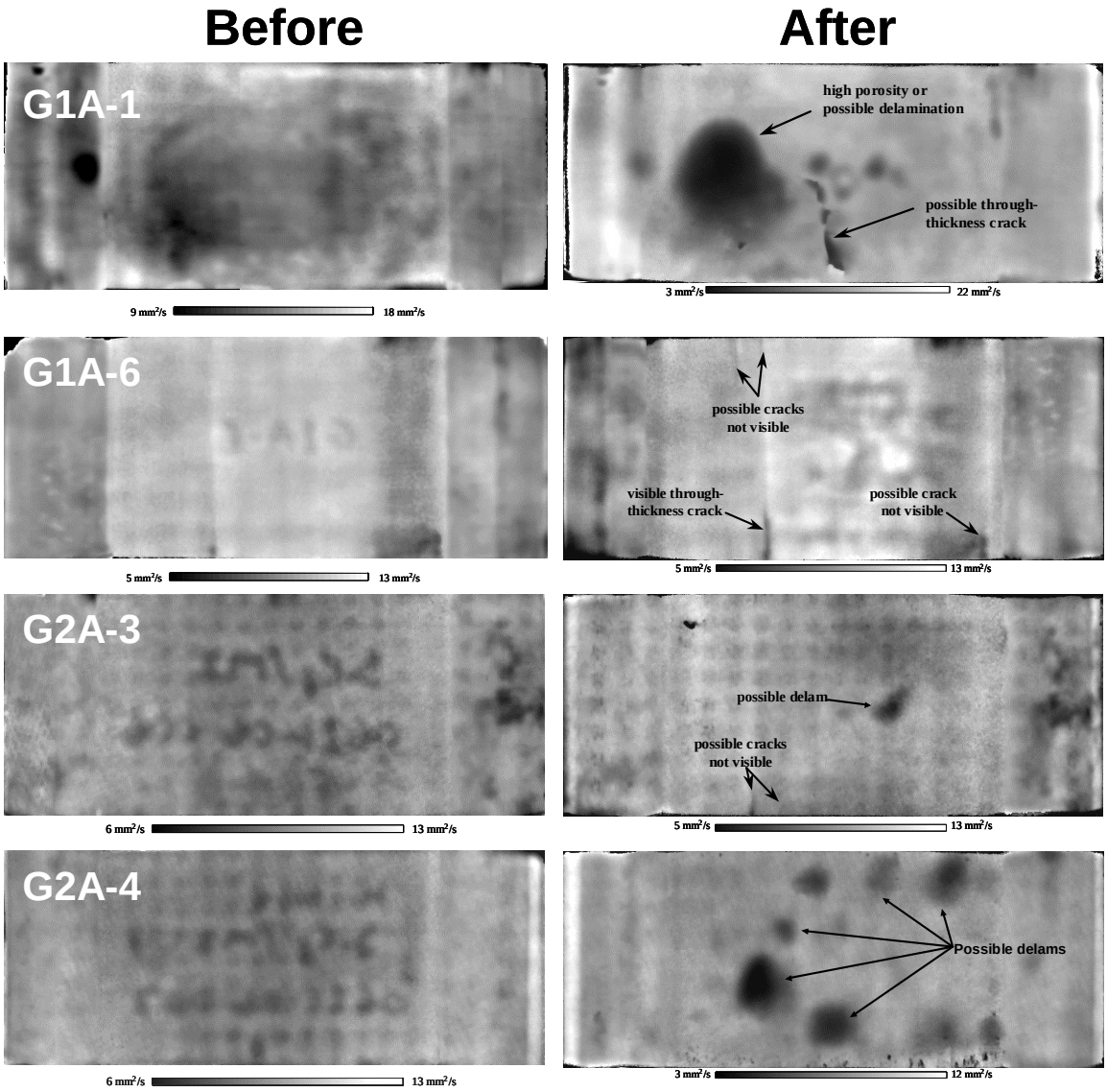

Figure 3-160. IR thermal diffusivity images from shrouds used in rig runs 28-36.
Left – images of the as-fabricated shrouds;
Right – images of the shrouds after rig testing.
The shroud identities are as listed in Table 3-49.

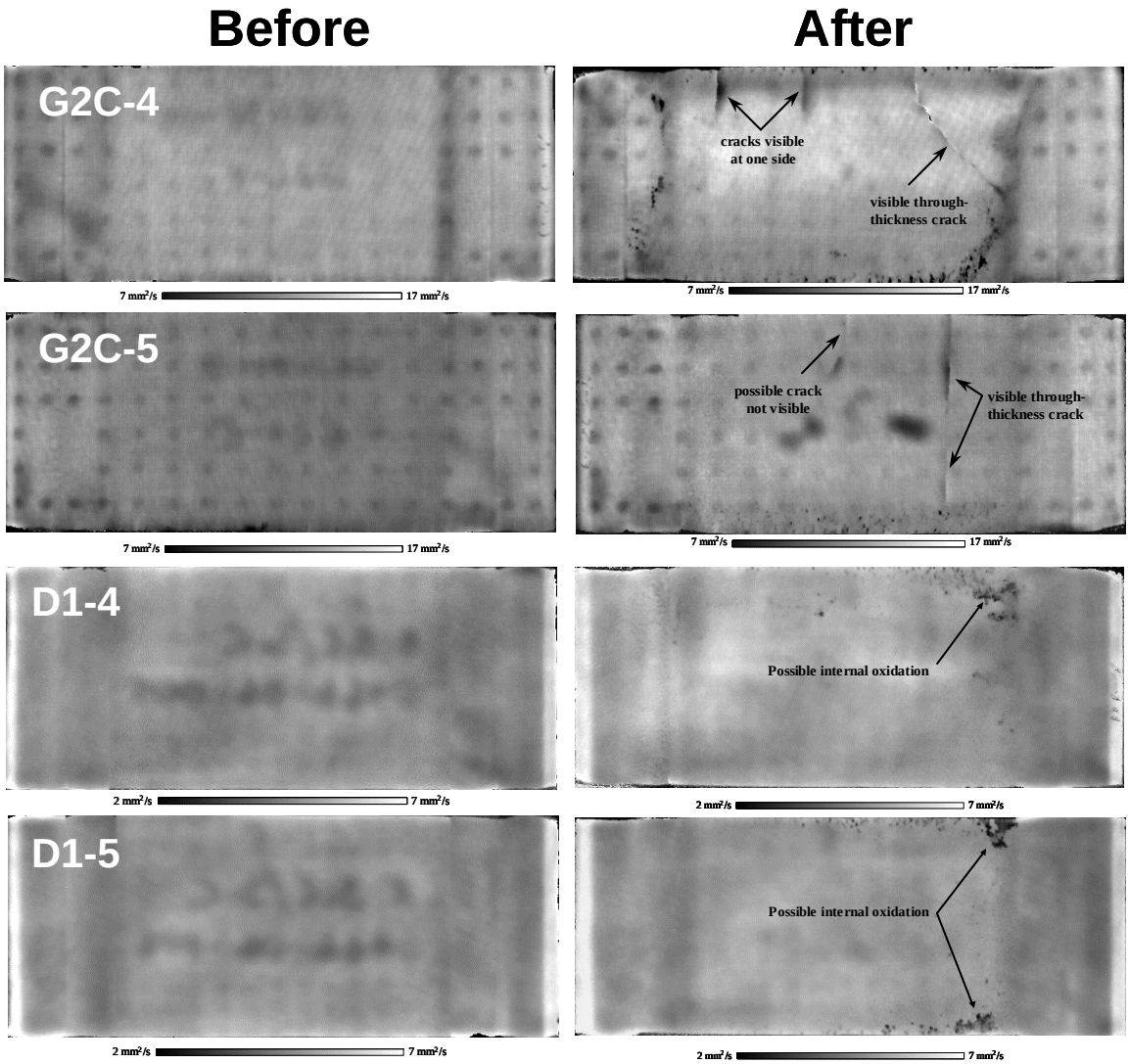

Figure 3-160, Cont'd. IR thermal diffusivity images from shrouds used in rig runs 28-36.
Left – images of the as-fabricated shrouds;
Right – images of the shrouds after rig testing.
The shroud identities are as listed in Table 3-49.

Other potential NDE techniques were also evaluated using shroud G1A-6 since this shroud had known matrix cracks. The alternate techniques tested included water-coupled ultrasound at ANL, reflection transient IR (time-of-flight) imaging, laser-coupled ultrasound, optical holography (shearography), and eddy current detection at GEGR. Figure 3-161 shows images generated for shroud G1A-6 from several of these techniques. The alternate techniques were used to examine only the flat hot gas path face of the shrouds whereas the transmission IR image includes the end curls as well. Overall, transmission IR as practiced at ANL produced the clearest, most easily interpreted images at this time, although reflection transient IR showed promise for inspecting complex shapes.

The front-flash "thermal time of flight" measurement done at GE CRD uses flash lamps to pulse heat one side of the shroud and an IR camera measures the time dependence of the temperature of that same surface. By deconvoluting the temperature decay curve one can detect both the presence and depth below the surface of any defect that influences heat conduction. Again this technique is most sensitive to porosity or delamination cracks. This technique also detected the larger of the two cracks, and also picked up the edge delamination; however, it also missed detecting the smaller of the two through-thickness cracks.

Another technique evaluated was laser ultrasound. In this technique a medium-powered laser is pulsed on the sample surface. This pulse generates very local and very rapid surface heating. The expansion of the heated surface spot effectively launches an acoustic wave into the material. A second low-power laser, focused on a spot nearby to the excitation laser, picks up the movement of the surface in response to the acoustic wave. By rastering both the pulsing laser and detection laser across the surface of the sample an image can be obtained. By choosing the shape of the excitation laser "spot" and by time and frequency analysis of the detected acoustic waves both the longitudinal and shear waves for through-thickness and surface propagation can be detected and analyzed. Figure 3-161 shows an image obtained using the laser ultrasound technique. Using this technique the larger edge crack was clearly detected and the smaller edge crack may have been detected, though with much less certainty. The edge delamination was not detected. The cause of the periodic "spots" in the image was not fully understood, but it was not believed to be an artifact of the test or data reduction technique. Images could not be obtained from the other types of shrouds (other than prepreg MI) because of the larger amounts of surface roughness and subsequent variable reflectivity.

Figure 3-161 also shows a shearography photograph of a section of the edge of the shroud near the larger through-thickness crack. The shearography technique looks at the interference pattern between two laser-generated images of the shroud. The first image is recorded with the shroud in an unstressed state and then compared to a real-time laser image with the shroud under a slight stress (finger pressure). Movement of the shroud in response to the stress caused interference fringes on the image, each of which represents movement of ½ the wavelength of the laser light (about 300 nm). Discontinuities in the fringes indicate features that are reacting to the stress differently than the surrounding material, such as cracks. Because of limitations of the shearography equipment at GE CRD only a portion of the shroud could be imaged at any given time. Figure 3-161 shows a part of the edge of the shroud containing the larger through thickness crack. In fairness, the quality of the image as seen in real time is much better than what was captured by the video camera. This technique was able to detect the larger edge crack, but did not detect the smaller crack or the delamination crack.

Eddy current measurements were also used to generate images of the shrouds, but because of the relatively low electrical conductivity and poor coupling of the composite to the field coil no meaningful information was obtained.

As mentioned earlier, the appearance of very fine cracks in some of the shrouds tested late in the program justified a more detailed inspection of all of the rig-exposed shrouds. The shrouds were visually inspected using a stereo optical microscope, and for several shrouds very fine through-thickness cracks were found extending inward from the edges. The positions and approximate depths of the cracks as determined by visual inspections are noted in Table 3-52, where the dimensions refer to the origin of the crack along the edge of the shrouds as shown in Figure 3-162. Although no cracks were found in NDE that had not been found during detailed visual examination, the full depths of the cracks were not easily determined without sectioning of the shrouds. During shroud sectioning for the extraction of tensile test specimens, to be discussed below, any tensile bar that contained a crack across the entire width simply fell apart after cutting. Extensive oxidation of the crack interfaces was noted with no evidence of intact bridging fibers.

Following visual inspections the thermal images were re-examined to see if the visible cracks could be seen in the NDE images. Whereas most of the cracks were not obviously depicted on the images, there were features on the thermographs corresponding to the visually observed cracks in all but one of the shrouds. The thermography images also indicated the presence of delaminations and/or high porosity regions in two of the shrouds, and possible internal oxidation in the CVI shrouds. During sectioning of the shrouds for mechanical testing the existence of the delaminations and their positions and sizes were confirmed.

One surprising outcome of the visual and NDE inspections was that no matrix cracks were detected in the CCP Enhanced SiC-SiC CVI composite shrouds. Previous thermo-mechanical modeling of the shrouds indicated that this material should have thermal stresses about 25% higher than the MI composites for similar thermal conditions. Given that the matrix cracking stress for this composite system is typically 15% to 40% lower than for the MI composites, based on shroud witness coupon data, cracking would have been expected in the CVI SiC-SiC composites before seeing it in the MI composites. It should be noted that rig hardware degradation during the tests, particularly of the transition piece and nozzle simulation flanges, subjected the shrouds to non-uniform temperature distributions, and thus the thermal stresses in the shrouds and tendency for cracking would have been dependent on the shroud's position in the rig.

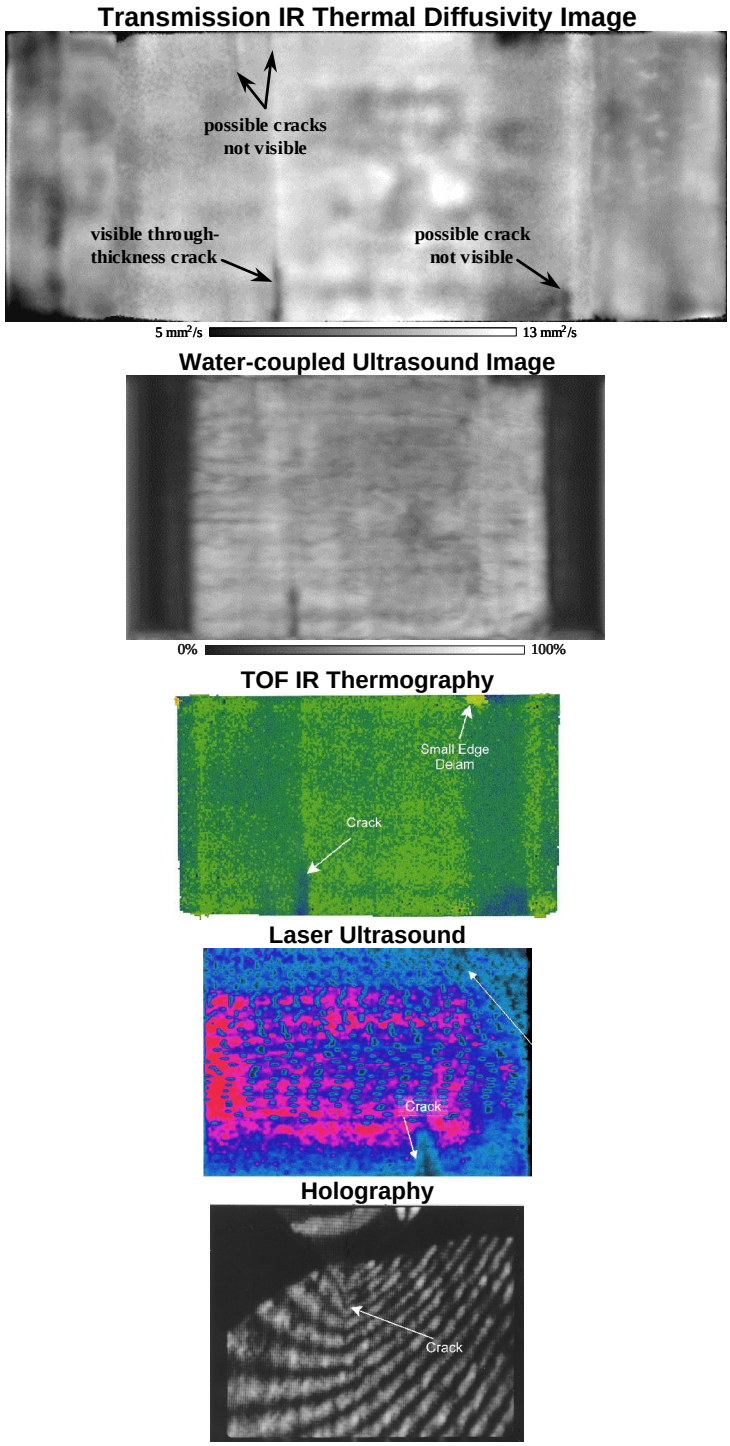

Figure 3-161. Various NDE images of shroud G1A-6 following rig testing done to compare the effectiveness of the various techniques for finding cracks and delaminations in the CMC shroud. The laser ultrasound image is flipped left-to-right relative to the other images.

Table 3-52. Summary of Visual Inspection Results on Shrouds from Rig Runs 28-36 and Comparison to NDE Thermal Diffusivity Imaging Results

			Visual Inspection Results			NDE – Transmission Thermography		
			Crack Position				Interlaminar	Interlaminar
Shroud	Type	Rig Test Run#	L	d	Edge	Crack Detected?	Defect Detected?	Defect Confirmed?
G1A-1	GE MI	28-33	2.8”	1.5”	A	Yes	Yes	Yes
			3.6”	0.2”	B			
G2C-4	Goodrich MI	28-33	1.8”	1.5”	A	Yes	None	
			3.2”	0.75”	A	Yes		
			4.6”	0.75”	A	Yes		
G2A-3	ACI MI	28-33	1.6”	0.4”	A	Yes	None	
D1-4	ACI CVI	28-33	None				None	
G1A-6	GE MI	34-36	2.8”	0.8”	A	Yes	None	
			1.6”	0.8”	B	Yes		
G2C-5	Goodrich MI	34-36	1.3”	3”	A	Yes	None	
			3”	1”	A	Yes		
G2A-4	ACI MI	34-36	1.2”	0.3”	A	No	Yes	Yes
			1.2”	0.6”	B	No		
D1-5	ACI CVI	34-36	None				None	

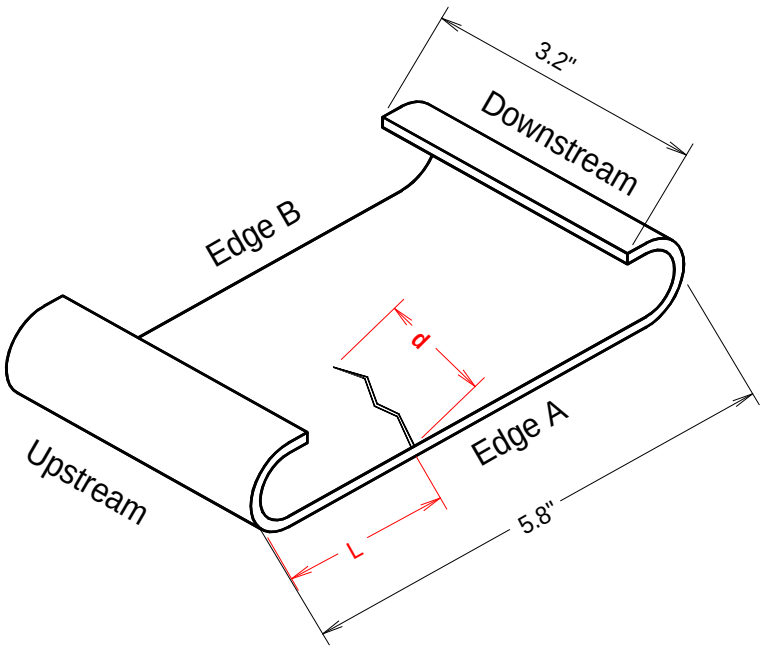

Figure 3-162. Schematic diagram of a cracked shroud showing how the distances “L” and “d” in Table 3-52 were defined.

A second unusual aspect of the CVI shrouds was that they were found to have deformed somewhat during rig testing. Shroud D1-4, which saw exposure at the highest temperature

conditions, had an upward bowing of the gas path surface (bowed away from the hot gas path) of roughly 0.3mm. A schematic diagram, showing the pattern of the shroud bowing exaggerated 10X for clarity, is given in Figure 3-163. The bowing on shroud D1-5, which was tested at somewhat lower rig temperatures, was about 0.2mm. This observation suggests that the CVI shrouds experienced stress relaxation via creep, which may have helped prevent cracking of this material. All of the MI shrouds had less than 0.05mm change of the hot gas path face, which is within the measurement errors caused by surface roughness and/or oxidation effects.

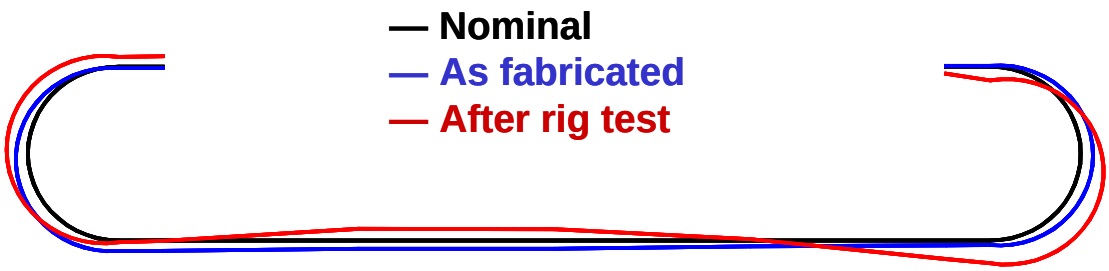

Figure 3-163. Schematic representation of the deformation of shroud D1-4 following rig testing as determined by CMM measurement. The deviations from nominal dimensions are shown exaggerated 10X for clarity.

In addition to the NDE and CMM inspections, shroud modal frequency analysis was performed after rig testing. It was anticipated that the introduction of cracks or delaminations would lead to changes in the modal frequency response of the shrouds, and that this technique may one day prove to be a valuable field technique for assessing shroud damage. Free-state modal frequencies were measured by supporting the shrouds on elastic bands and striking them with an electromechanical actuator (i.e. the striker from an electric door bell). A microphone place close to the shroud flat surface picked up the acoustic amplitude vs. time response of the shrouds, which was converted via FFT analysis to the amplitude vs. frequency domain.

Modal analysis was found to confirm the initial visual observations in that shrouds with relatively large distinct cracks did indeed show changes in the frequency response; however, shrouds with the very small cracks observed only under stereomicroscopic examination did not show a significant effect on modal response. Examples of the modal response for an uncracked shroud (G2A-4) and for shrouds with relatively large cracks (G1A-6 and G2C-5) from rig runs 34-36 are shown in Figure 3-164. The response of shrouds with very fine cracks were similar to that for G2A-4 in that no appreciable change in the modal frequency response was noted. Shrouds with large, visually obvious cracks, such as G1A-6 and G2D-5, did show substantial response changes. It was encouraging that the modal response corroborated the visual inspections, but disappointing that it was less sensitive to fine cracking than the microscopic inspection.

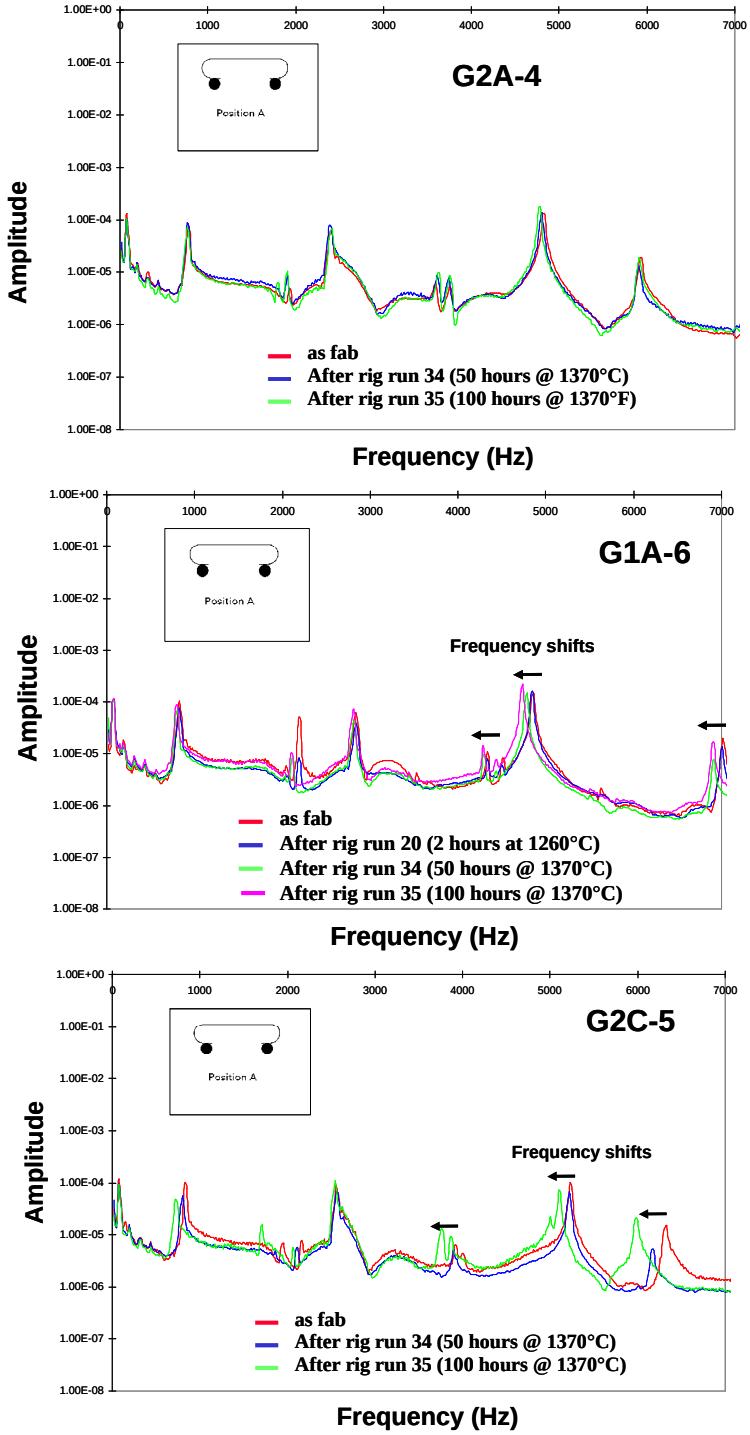

Figure 3-164. Examples of modal frequency response measured on shrouds tested in rig runs 34-36. G2A-4 (top) showed no observed cracking whereas shrouds G1A-6 (middle) and G2C-5 (bottom) had visually observable cracks following run 35. Shroud identities are as listed in Table 3-49.

3.8.1.6.2 Destructive Characterization

Destructive characterization of the shrouds included mechanical testing and microstructural evaluations. Tensile testing was performed on straight-sided tensile bars cut from the hot gas path face flat section of the shrouds according to the diagram in Figure 3-165. C-ring bend tests were also performed on some of the shrouds by slicing the forward bend section and loading them to failure as shown schematically in Figure 3-166.

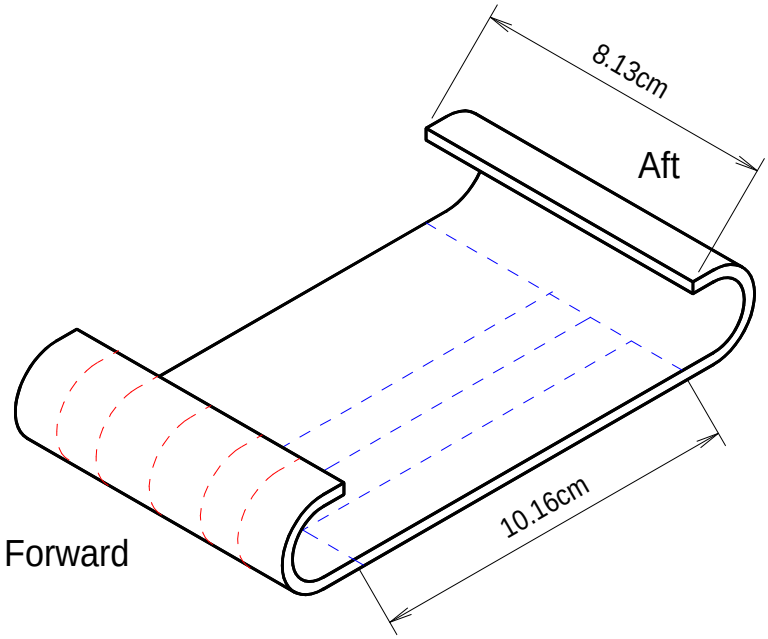

Figure 3-165. Diagram of the sectioning done on CMC inner shrouds after rig testing.

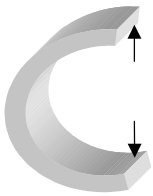

Figure 3-166. Schematic representation of the C-ring bend tests performed on samples cut from the front bend section of selected shrouds.

The purpose of the mechanical testing was two fold: first to evaluate the shrouds for thermal or oxidative degradation as a result of the exposure in the combined high temperature, water vapor, gas velocity and pressure environment, and secondly to look for evidence of otherwise undetected matrix cracking since matrix cracking under such an environment would be expected to lead to rapid degradation. However, many of the samples early in the testing were exposed for relatively short times, such as the cyclic tests in runs 10-12 where any given sample would have been exposed to high temperature for only ~7 hours. Fiber-matrix interface oxidation and degradation may not occur in such a short time frame, making it difficult to detect if matrix cracking may have occurred.

Consequently additional steam furnace exposures at 1200°C for 100 hours were conducted on the larger panels cut from the shroud hot gas paths to ensure oxidative degradation should there be any matrix cracking. This panel was then sectioned into individual test bars and tensile tested along with the bars cut from the shroud but not exposed to steam.

The measured stress-strain behaviors for shrouds exposed in the first round of step and cyclic testing (rig runs 7-12) are shown in Figures 3-167 to 3-172. Overall the melt infiltrated composites showed excellent property retention with no significant degradation observed. The same was true for the Enhanced SiC-SiC CVI shroud. (Although the ultimate strengths of the exposed shroud bars are slightly lower than the witness coupon strengths for the Enhanced SiC-SiC and for the GE prepreg MI shrouds, this was probably not the result of any degradation, but caused by the witness coupons for these shrouds having higher strengths than are normally observed for these materials.) The CCP MI with Sylramic fiber shroud, which was known to have been made from "sub-standard" fiber and was relatively weak with low strain to failure, and which actually cracked during the cyclic test, showed slightly higher strengths in the exposed shroud bars than it did for the witness coupon. The tensile properties of these exposed shrouds, even after an additional 100 hours of steam furnace exposure, was good enough that testing of the bars cut after only rig testing was not a high priority.

The only shroud which showed appreciable degradation following the rig tests and steam furnace exposure was that made from the CCP DIMOX Al_2O_3-SiC material. However, it was not clear whether the degradation seen in this shroud was caused by the rig exposure or by the steam oxidation treatment since exposure of as-fabricated bars of DIMOX Al_2O_3-SiC in the steam oxidation furnace also causes degradation of mechanical properties. Therefore an additional test bar was cut from the as-exposed DIMOX shroud and tensile tested without the steam oxidation treatment. The results of this test are also shown in Figure 3-172 along with the stress-strain data for the rig and steam furnace exposed samples from this shroud. The amount of degradation in the un-oxidized bar was less than seen in the bars which had gone through the steam oxidation treatment, but the initial modulus, matrix cracking stress, ultimate strength and strain to failure were all lower than the witness coupon bar. This result indicated that the DIMOX shroud had undergone some amount of degradation just from the rig exposure.

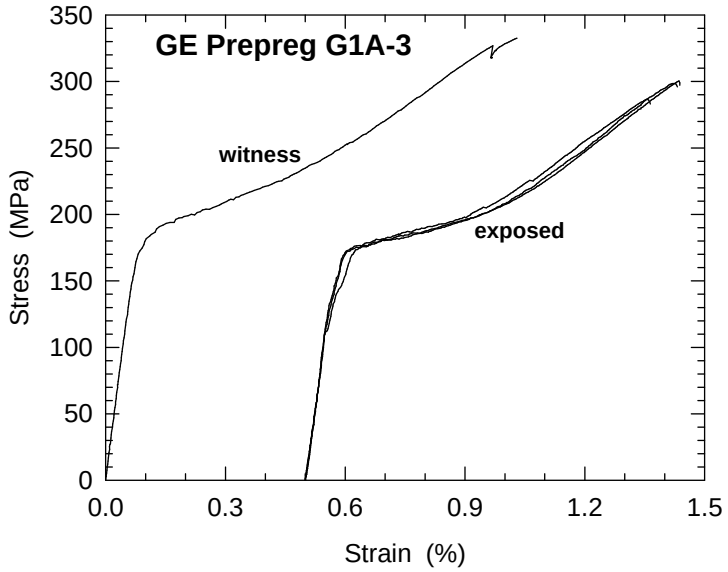

Figure 3-167. Tensile behavior of samples taken from shroud G1A-3 after rig testing in rig runs 9-12 plus an additional 100 hours of steam oxidation exposure (1200°C, 90% H_2O + 10% O_2) compared to a witness bar tested in the as-fabricated condition. Curves are offset for clarity.

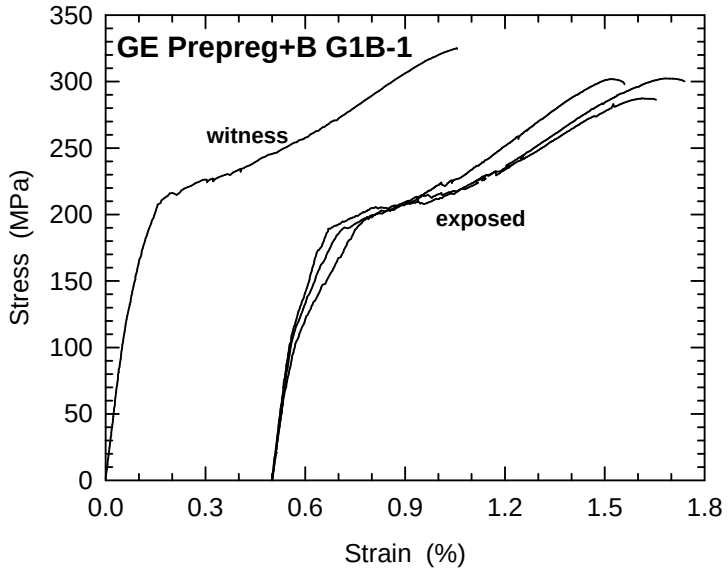

Figure 3-168. Tensile behavior of samples taken from GE Prepreg+B shroud G1B-1 after rig testing in rig runs 9-12 plus an additional 100 hours of steam oxidation exposure (1200°C, 90% H_2O + 10% O_2) compared to a witness bar tested in the as-fabricated condition. Curves are offset for clarity.

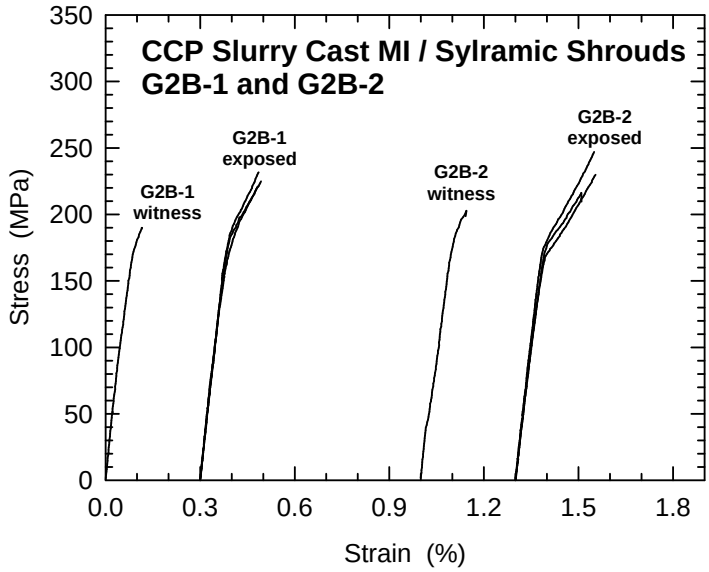

Figure 3-169. Tensile behavior of samples taken from CCP Slurry Cast / Sylramic shrouds G2B-1 and G2B-2 after rig testing in rig runs 9-10 (G2B-1) or rig run 12 (G2B-2) plus an additional 100 hours of steam oxidation exposure (1200°C, 90% H_2O + 10% O_2) compared to a witness bars tested in the as-fabricated condition. Curves are offset for clarity.

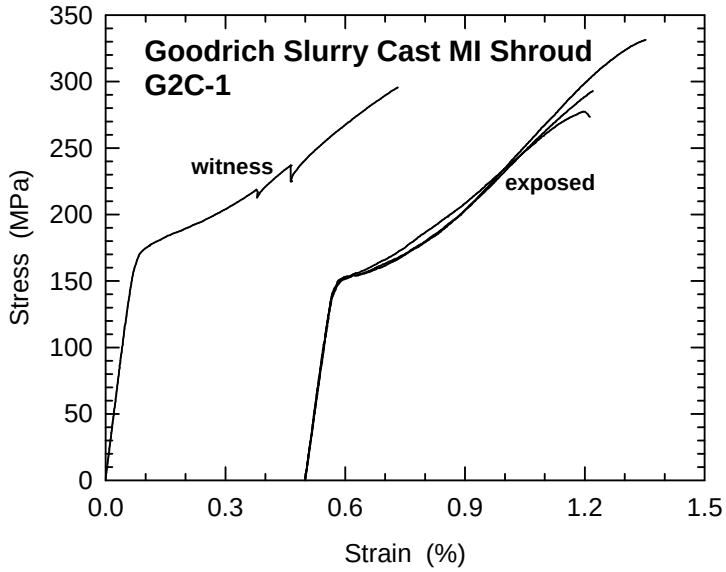

Figure 3-170. Tensile behavior of samples taken from Goodrich Slurry Cast MI shroud G2C-1 rig testing in rig runs 9-12 plus an additional 100 hours of steam oxidation exposure (1200°C, 90% H_2O + 10% O_2) compared to a witness bars tested in the as-fabricated condition. Curves are offset for clarity.

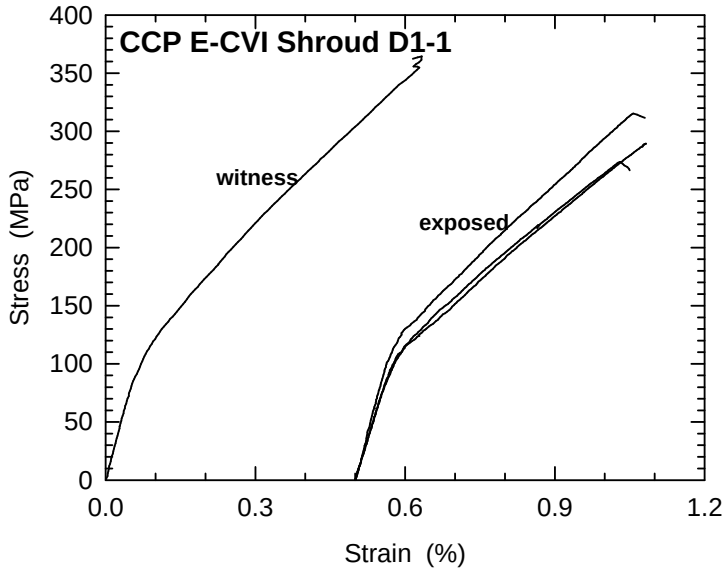

Figure 3-171. Tensile behavior of samples taken from CCP Enhanced SiC-SiC CVI shroud D1-1 after rig testing in rig runs 7-12 plus an additional 100 hours of steam oxidation exposure (1200°C, 90% H_2O + 10% O_2) compared to a witness bars tested in the as-fabricated condition. Curves are offset for clarity.

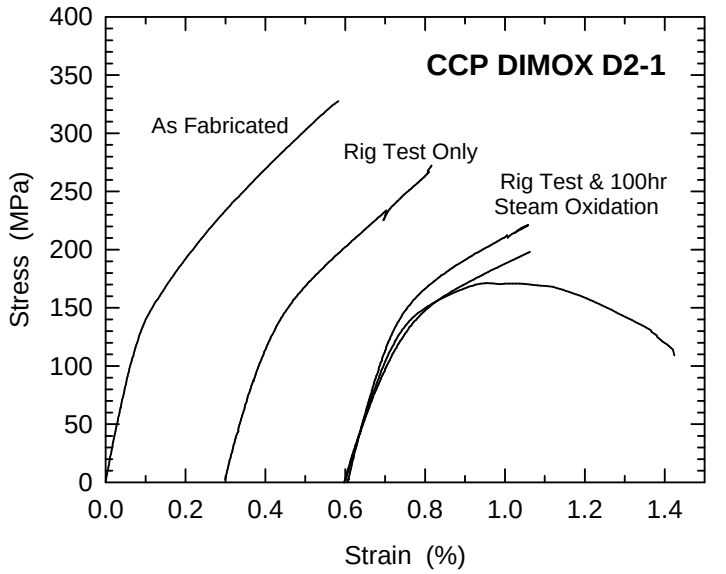

Figure 3-172. Tensile behavior of samples taken from shroud D2-1 after rig testing in rig runs 9-12 and after additional 100 hours of steam oxidation exposure (1200°C, 90% H_2O + 10% O_2) compared to a witness bar in the as-fabricated condition. Curves are offset for clarity.

Shrouds from the second set of tests (rig runs 13-19; 100 hours steady state exposure at a rig firing temperature 1177°C) all came through testing relatively unharmed. It was recognized that the actual shroud temperatures in these runs were well below 1200°C.

Also, the majority of shrouds tested in rig runs 7-12 showed no significant degradation even after an additional 100 hours of steam furnace oxidation at 1200°C. It was therefore highly unlikely that the shrouds would have experienced any mechanical degradation from this set of rig tests. Consequently these shrouds were retained for use as "show-and-tell" pieces and were not destructively characterized.

Similarly the next set of rig tests (runs 20-27) were primarily intended to push the capabilities of the rig to attain inner shroud temperatures of 1200°C. This series of short tests spanned a considerable range of test temperature, including an extreme over-temperature condition in run 24. This highly variable and irregular thermal history that these shrouds experienced in the rig tests would make interpretation of any testing results highly ambiguous. Consequently this set of shrouds was not destructively characterized either.

Shrouds exposed in rig runs 28-33 did attain the desired 1200°C material testing temperature. Despite the rig degradation problems discussed earlier, which lead to the hot/cold streak conditions that are believed to have cracked shrouds G1A-1 and G2C-4, these shrouds were destructively characterized. The post-rig test tensile data from these shrouds is compared to the witness bar tensile data in Table 3-53. Note that the data in Table 3-53 is only for bars cut from the shrouds where no noticeable cracking had occurred. Table 3-53 also includes the post-test tensile data for shrouds rig tested in runs 34-36.

Table 3-53. Summary of Room Temperature Tensile Test Data from CMC Shrouds Exposed in Shroud Rig Tests 28-33 and 34-36 and Compared to the Shroud Witness Bar Tensile Data.

		Initial Modulus (GPa)		Proportional Limit (MPa)		Ultimate Strength (MPa)		Strain to Failure (%)	
Shroud	Rig Runs	As-Fab	Tested	As-Fab	Tested	As-Fab	Tested	As-Fab	Tested
G1A-1	28-33	254	257	155	150	280	250	1.00	0.85
G2C-4	28-33	286	325	165	159	267	176	0.60	0.16
G2A-3	28-33	170	230	138	144	410	263	0.64	0.37
D1-4	28-33	150	217	125	129	345	323	0.62	0.38
D2-4	28-31	141	124	97	68	278	161	0.46	0.22
G1A-6	34-36	210	292	145	178	310	298	1.20	0.95
G2C-5	34-36	257	273	145	161	278	245	0.65	0.62
G2A-4	34-36	160	231	120	112	336	207	0.80	0.29
D1-5	34-36	159	199	115	158	378	349	0.70	0.41

The initial modulus values of all the shrouds, except for the DIMOX shroud D2-4, increased with rig exposure, which is a phenomenon that was not fully understood. Other than this increase in initial modulus, the GE prepreg MI shrouds, G1A-1 and G1A-6, showed no appreciable changes in cracking stress, ultimate strength or strain to failure. (The strain to failure values of rig tested bars were somewhat lower than the as-fabricated samples, but this was most likely because these specific as-fabricated samples had

unusually high values for this property. The strain to failure values of the rig tested shrouds were still relatively high and well within the normal range for as-fabricated bars.)

The Goodrich slurry cast MI shroud faired much better in runs 34-36 than in runs 28-33, with only a small reduction in ultimate strength and strain to failure values in the later tests but a substantial reduction in these properties in runs 28-33. This would tend to indicate that the Goodrich slurry cast material was somehow affected by the somewhat higher exposure temperatures during runs 28-33. However, shroud G2C-4 did have a large crack after runs 28-33, and this could have allowed for internal oxidation of the composite beyond the crack front and into the uncracked material that was tested.

The CCP slurry cast MI shrouds, G2A-3 and G2A-4, again showed significant reductions in both ultimate strength and strain to failure for both sets of rig tests. The CCP CVI Enhanced SiC-SiC shrouds, D1-4 and D1-5, also showed significant reductions in strain to failure, although the ultimate strength values decreased only slightly.

During sectioning of the shrouds into test bars any bar that had a severe (visually obvious) crack running across its entire width simply fell apart along the crack, indicating that no bridging fibers remained intact. Examining the crack front surfaces under magnification revealed that a relatively thick layer of oxide was formed on the crack faces. There were no fibers bridging the cracks or even just penetrating through the oxide layer. This indicates that any bridging cracks had been completely oxidized during the shroud exposure. A detailed description of the observations from one sample, GE prepreg MI shroud G1A-1, is given below.

A bar containing a crack was cut from the edge of shroud G1A-1. A small piece containing part of the crack surface was then cut from the bar and mounted such that the thickness of the shroud and the crack surface could be seen edge on. The exposed surface was polished and coated with a conductive material for scanning electron microscopy (SEM) examination. Figure 3-173 shows SEM micrographs of the cracked surface. The crack surface was covered with an approximately 3-4 μm thick layer of oxide (labeled A in Figure 3-173(A). As indicated by the white arrows in this figure the coatings on the fibers near the cracked region were also oxidized. However, the penetration of oxidation does not appear to exceed a few tens of microns (<30 μm, area labeled B in Figure 3-173(B)). The results of X-ray energy dispersive spectroscopy (EDS) analysis at the surface of a fiber perpendicular to the cracked surface showed the presence of some oxygen up to a depth that closely matched the observations in SEM micrographs.

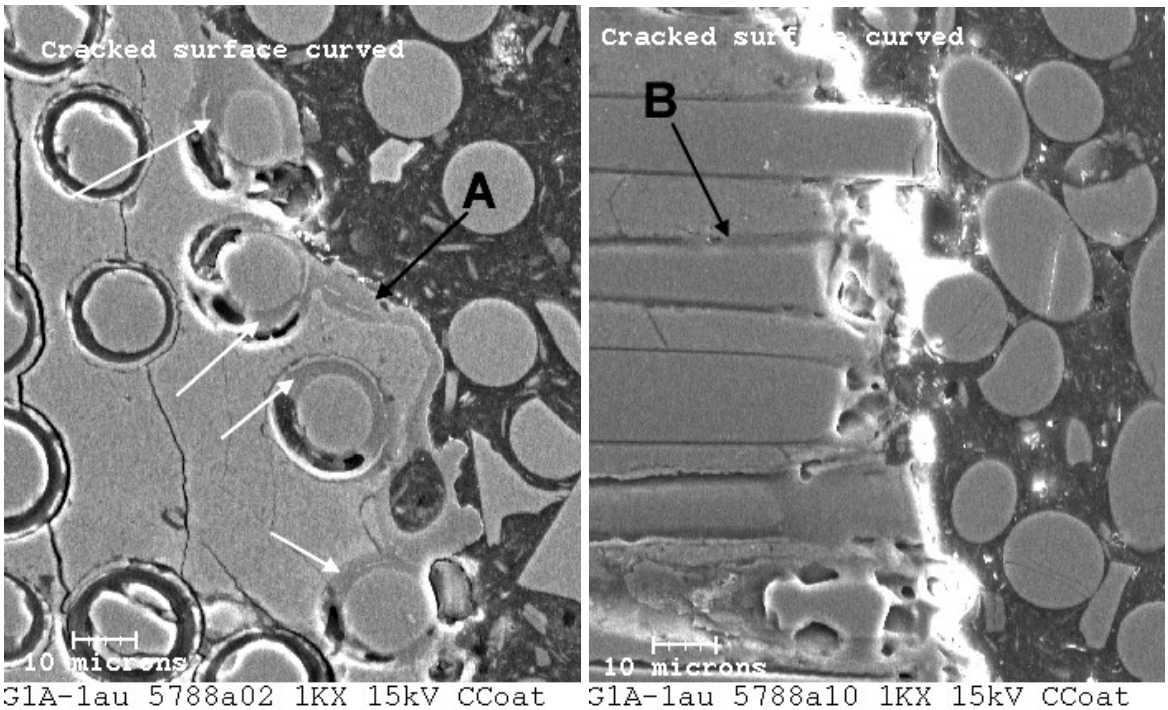

(A) **(B)**

Figure 3-173. SEM micrographs of a polished section of the crack face taken from shroud G1A-1. (A) shows that oxidation of the fiber coatings occurred only for fibers very close to the crack face, as indicated by the white arrows. Oxidation of fiber-matrix interfaces intersecting the crack face was on the order of 30μm maximum, as shown in (B).

NDE of two of the shrouds (G1A-1 and G2A-4) suggested the presence of delaminated areas. However, examination of the edge surface of tensile test bars cut from the same areas revealed that these were not delaminations by the commonly accepted definition. Normally a delamination is thought of as a crack or large penny-shaped pore occurring between composite plies. In shroud G1A-1 the "delamination" was found to be a very narrow, intra-ply crack running parallel to the surface of the shroud. A piece of material from G1A-1 was polished such that the cracked region could be observed edge-on. Figures 3-174 shows SEM micrographs taken from the polished region. The absence of any apparent oxidation layer at the crack surface suggests that the crack did not extend to any of the composite surfaces. The area was examined at higher magnifications, but no indications of oxidation could be found. The absence of oxidation in this shroud was not surprising given that the matrix material is dense and would prevent the diffusion of oxygen into the interior. It is worth noting that the tensile bar that contained this intra-ply crack fractured away from the cracked region during tensile testing. This result suggests that the intra-ply crack did not strongly affect the in-plane strength of the shroud.

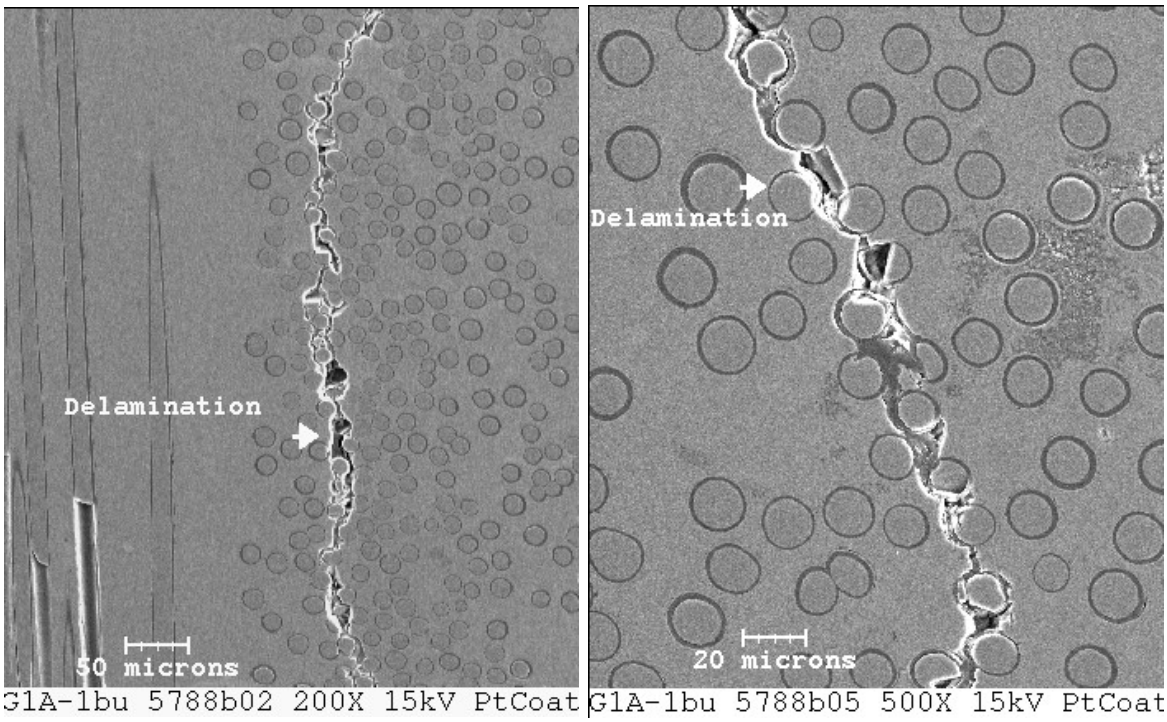

(A) **(B)**

Figure 3-174. SEM micrographs of a polished section through shroud G1A-1 showing the intra-laminar crack.

In the case of shroud G2A-4, examination under an optical microscope showed that the "delamination" was actually a high concentration of inter-ply porosity just under the first composite ply. The internal surfaces of this porosity were oxidized, indicating interconnectivity of the pores with the shroud surface. Furthermore, a tensile bar containing this "delamination" fractured in shear along the high-porosity layer when subjected to mechanical testing. Oxidation of the "delamination" in this shroud, and not in the prepreg MI shroud, is probably a result of the higher matrix porosity of the slurry cast MI material compared to prepreg MI. Also, the porosity in the slurry cast MI material tends to be more interconnected than in prepreg MI materials, thus providing internal paths for rapid oxygen penetration.

The fracture surfaces from the tensile bars cut from the shrouds exposed in rig runs 28-33 and 34-36 were examined using SEM, and the results are described below.

a) G1A-1 and G1A-6 (GE prepreg MI)

- No internal oxidation detected.
- Relatively short fiber pullout (2 to 10 fiber diameters). Fibers pulled out singly.

b) G2C-4 and G2C-5 (Goodrich slurry cast MI)

- Fracture surfaces showed some signs of internal oxidation.
- Relatively short fiber pullout (2-20 fiber diameters). Fibers pulled out singly.

c) G2A-3 and G2A-4 (CCP slurry cast MI)

- Relatively long fiber pull-out (5-100 fiber diameters) with possible matrix crumbling during fracture. Fibers pulled out mostly individually.
- Fracture surface showed some internal oxidation with some small embrittled regions (no fiber pull-out) noted.

c) D1-4 and D1-5 (CCP E-SiC-SiC CVI)

- Fibers pulled out as bundles. Relatively long bundle pull-out (5-50 fiber diameters).
- In D1-4 fracture occurred across a region where noticeable internal oxidation took place. It was evident that the fiber coating was oxidized in this region. Internal oxidation was also noted in D1-5.

The above observations can be used to at least partially explain some of the trends in residual strength properties observed in the shrouds, as summarized in Table 3-53. The internal oxidation seen in G2A and D1 type shrouds, especially the embrittled regions in G2A-4 and coating oxidation seen in D1-4, would explain the loss of failure strain for these materials after rig testing. The relatively good strength retention of the G1A (GE prepreg MI) type shrouds can be attributed to their high density, and thereby their resistance to internal oxidation damage. However, the loss of ultimate strength and failure strain of the G2C (Goodrich slurry cast MI) samples was more severe than the microstructural changes would seem to indicate. It was also not yet clear how much of the internal oxidation can be attributed to the shroud through-thickness cracks and how much to simple penetration of oxygen from the sample surfaces.

It is well known that the strength of fibers in a composite can be estimated using fiber fracture mirror size measurements and empirical relations [21]. There was an interest in determining the fiber strength distribution in two of the rig-tested shrouds, G1A-1 and G2A-4, in order to do a preliminary comparison of how the two MI processes effect fiber strength. In each sample fiber fracture mirror size measurements were taken from the SEM micrographs of at least 40 fibers on each fracture surface. Only fibers which showed fiber-matrix debonding and pull-out were used for these measurements. In addition to the mirror size estimation the micrographs reveal the origin of fiber failure. A change in the location of the fracture mirrors from volume to near surface locations would suggest that surface damage might be taking place.

While examining the fracture surfaces it was noted that more of the fibers in G2A-4 exhibited failure origins near the surface than in G1A-1, suggesting that fiber weaving and lay-up of the slurry cast process may damage fibers. This observation is consistent with the fiber strength distributions calculated from the fracture mirror measurements, as presented in Figure 3-175, that show the fiber residual strength of the G1A-1 shroud to be measurably higher than that for the G2A-4 shroud. However, residual fiber strengths from both shrouds were still rather high, suggesting that fiber strength degradation is not an important factor over the time frame of the shroud rig tests. (The fiber fracture strengths in Figure 3-175 are much higher than the 2.6GPa nominal fiber strength reported for Hi-Nicalon. The high strengths are a result of the very short effective gage length in a

composite fracture test, which is defined by the matrix crack spacing. Generally quoted single fiber strength data is typically based on a 2.5cm gage length.)

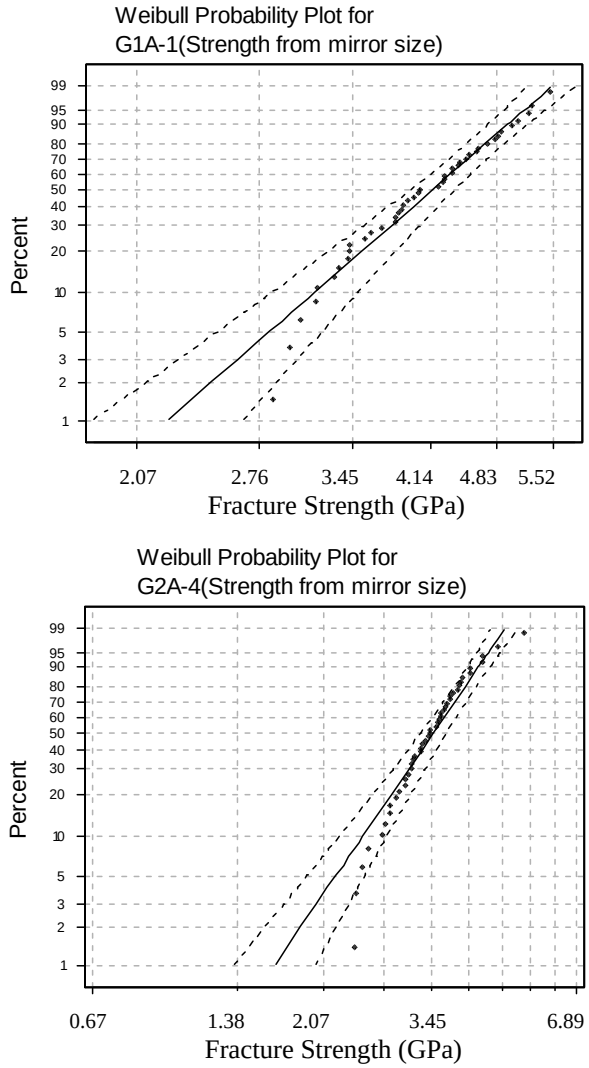

Figure 3-175. Weibull probability plots of fiber strength (calculated from fiber fracture mirror size) from the fracture surfaces of bars cut from shrouds G1A-1 (top) and G2A-4 (bottom). Median fiber strengths for the G1A-1 and G2A-4 shrouds were 4.14GPa and 3.38GPa, respectively. The high strength values, as compared to typically quoted fiber strength values of 2.62GPa, are a result of the very short fiber gage length tested (equivalent to the matrix crack spacing).

Tensile bars were obtained from several of the cracked shrouds that included part of the crack front and yet still had limited intact CMC. The stress-strain curves for these bars did not exhibit fracture behavior typical of MI composites, as shown in Figure 3-176 for shrouds G1A-1 and G2A-3. For samples with little remaining intact cross sectional area both the strength and particularly the strain to failure were greatly reduced relative to

uncracked bars from the same shrouds. (Please note that the strain to failure of the uncracked specimen taken from the CCP slurry cast MI shroud was already substantially reduced relative to as-fabricated material.) In bars with greater amounts of intact (i.e. uncracked) cross section the stress-strain curves tended to look more like those for uncracked bars with higher strain to failure values. These results suggest that the fiber and/or fiber-matrix interface were degraded near the crack tip regions.

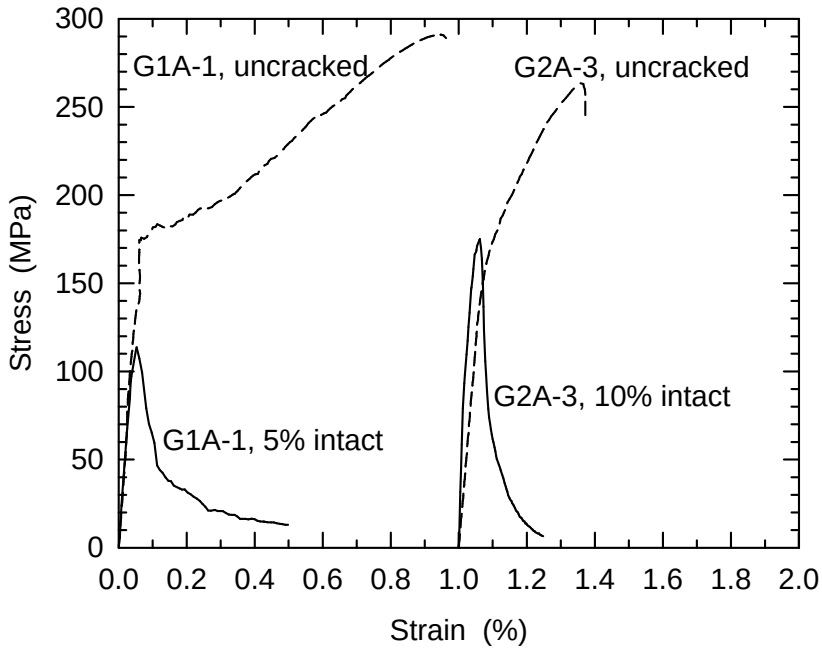

Figure 3-176. Tensile stress-strain behavior of test bars cut from cracked shrouds G1A-1 and G2A-3 having a limited amount of intact CMC remaining in the test bar. Stress values for the cracked bars are calculated from the estimated amount of intact cross section measured on the fracture surface after failure.

The shroud post-rig test tensile test data measured on uncracked test bars is summarized in Table 3-54 for reference. In many instance more than one bar was tested so the values reported in the table are the averages. Shroud samples exposed in rig runs 28-33 or 34-36 and then exposed to steam furnace oxidation typically exhibited some additional, though usually minor, property degradation compared to the samples exposed only in the rig runs.

Table 3-54. Results of Mechanical Tensile Tests on Uncracked Bars Cut From the Rig-Tested CMC Shroud Components

Material	Shroud ID	Shroud Exposure History‡	Initial Modulus (GPa)	Proportional Limit Stress (MPa)	Ultimate Strength (MPa)	Strain to Failure (%)	Comments
GE Prepreg MI	G1A-3	W	225	167	332	1.03	
		A	225	129	295	0.91	
	G1A-6	W	216	139	310	1.07	
		B	314	132	296	0.94	
		C	316	179	268	0.70	
	G1A-1	W	254	155	280	1.01	
		D	252	151	250	0.89	
		E	152	123	221	0.73	
GE Prepreg MI with B	G1B-1	W	200	126	325	1.05	
		A	178	105	297	1.12	
CCP MI with Hi-Nicalon	G2A-4	W	159	120	336	0.80	
		B	234	117	262	0.29	
		C	263	119	192	0.32	
	G2A-3	W	311	138	410	0.64	
		D	230	150	263	0.36	
		E	228	148	268	0.25	
CCP MI with Sylramic	G2B-1	W	241	138	190	0.12	
		A	214	162	226	0.18	100 cycles only
	G2B-2	W	247	179	203	0.14	
		A	204	169	231	0.24	100 cycles only
Goodrich MI	G2C-1	W	239	157	295	0.73	
		A	215	141	301	0.76	
	G2C-5	W	257	145	278	0.66	
		B	266	157	245	0.62	
		C	275	132	239	0.60	
	G2C-4	W	276	154	267	0.60	
		D	313	157	169	0.16	
		E	287	138	175	0.15	
CCP CVI E-SiC-SiC	D1-1	W	160	90	364	0.63	
		A	150	99	293	0.56	
	D1-5	W	163	121	374	0.66	
		B	202	156	349	0.41	0.2mm bow†
		C	158	112	263	0.37	0.2mm bow
	D1-4	W	149	125	345	0.61	
		D	224	116	323	0.38	0.3mm bow
		E	200	98	268	0.36	0.03mm bow
CCP DIMOX	D2-1	W	165	109*	328	0.58	
		A	112	89*	214	0.45	
	D2-4	W	141	97*	278	0.46	
		D	124	68*	154	0.22	cycles only
		F	121	88*	137	0.18	

‡ Rig test conditions were as follows:

W – as-fabricated witness bar to be compared to the exposed samples directly beneath

A – 200 flame off/flame on thermal shock cycles in rig runs 9-12 followed by 100 hours furnace exposure at 1200°C in steam (90% H_2O + 10% O_2)

B – 100 hours steady state rig exposure plus 100 flame off / flame on thermal shock cycles in rig runs 34-36

C – same as B but with additional 100 hours steam furnace exposure at 1200°C

D – 200 flame off / flame on thermal shock cycles followed by 50 hours of steady state rig exposure in runs 28-33; rig hardware failures caused severe lateral thermal gradients during the steady state exposure

E – same as D but with an additional 100 hours steam furnace exposure at 1200°C

F – 200 cycles as in D, but with 150 hours extra exposure in the rig exhaust section in runs 33 and 36

† Shroud hot gas path faces were found to have deformed outward (away from the hot gas path) by the indicated amount.

* DIMOX test bars showed continuously curving loading curves, suggesting that the matrix already contained microcracks. The proportional limit values listed therefore do not imply a 1st matrix cracking stress.

It can be recalled that the C-shaped hook ends of the shrouds were cut off in order to prepare tensile bars from the flat part of the shrouds (see Figures 3-165). The hook ends have an outer radius of curvature of 12.7mm. C-ring test specimens that were ~12mm wide were cut from the leading (upstream) hook of several shrouds. A schematic representation of the loading of the C-ring during the test was given in Figure 3-166. In the loading configuration shown in the figure both in-plane and through-thickness (interlaminar) tensile stresses as well as interlaminar shear stresses are induced in the specimen. Therefore, the C-ring test introduces failure modes such as delamination.

In almost all the tested samples failure occurred by delamination in the central region of the C-ring. This mode of failure is caused by through-thickness normal and shear stresses. The average interlaminar tensile stresses at failure, as calculated from the test results, are summarized in Table 3-55, although because of the mixed mode of failure these values should not be taken as direct measurements of either interlaminar tensile strength or interlaminar shear strength.

During testing it was noted that the location of the delamination failure did not depend on the presence of processing defects such as poorly filled areas. The C-rings from the shrouds subjected to the most severe testing conditions (rig tests 28-33) were found to fail at higher average stresses compared to those subjected to less severe conditions (rig tests 34-36). Shrouds tested at the lowest rig temperatures (rig tests 7-12) showed intermediate values of interlaminar strengths. The reasons for this variation with test condition were not understood. Another surprising result was that CVI shroud samples gave some of the highest C-ring test results even though the interlaminar strengths of CCP CVI material has generally been found to be inferior to those of MI composites.

Table 3-55. Results of C-Ring Tests on Previously Rig-Tested Shroud Specimens

Shroud Type	Shroud ID	Rig-test Runs	Interlaminar Tensile Stress at Failure[1] (MPa)
GE MI	G1A-3	7-12	22.8 ± 0.7
	G1A-1	28-33	31.7 ± 0.7
	G1A-6	34-36	16.5 ± 4.8
Goodrich MI	G2C-1	9-12	20.0 ± 0.1
	G2C-4	28-33	22.1 ± 1.2
	G2C-5	34-36	19.3 ± 1.5
CCP MI	G2B-1	9-12	20.7 ± 1.4
	G2A-3	28-33	26.9 ± 3.4
	G2A-4	34-36	11.7 ± 1.4
CCP E-CVI	D1-1	9-12	24.8 ± 2.1
	D1-4	28-33	32.4 ± 4.1
	D1-5	34-36	20.0 ± 4.1

[1] Limits are ± one standard deviation for measurements on 2-3 specimens.

3.8.1.7 CMC Shroud Rig Combustor Post-Test Characterization

Two GE Prepreg MI CMC combustor liners were fabricated and used in the shroud combustion rig testing. The first liner was introduced during rig run 13 and was removed after rig run 14. The second liner was present from rig run 15 through the end of testing.

The CMC liners were utilized for two reasons: first to allow for the accumulation of additional CMC exposure experience in the test rig, and second to replace a stainless steel liner that had failed after rig test 12. The stainless liner had been through various rig shakedown tests, most of which were done at reduced rig firing temperatures, and through the initial step and cyclic tests. The liner had accumulated 12 completed start-stop cycles and 300 flame on – flame off "trip" cycles, but only had ~15 hours accumulated at a rig firing temperature of ~1177°C, all with backside convection cooling. The first CMC liner was used only for rig runs 13 and 14, but had accumulated 2 start-stop cycles and 50 hours of exposure at the same firing temperature. A photograph of the stainless liner and the 1st CMC liner is shown in Figure 3-177. The stainless liner exhibit pronounced deformation and oxidation damage, with an oxidation fatigue crack having breached the wall of the liner. The CMC liner was relatively unscathed, showing only minor signs of thermal tinting from oxidation on the outer surface. On the inner surface the CMC liner showed two regions of enhanced oxidation caused by the deformation of the heat shield that in turn caused hot streaks in the liner.

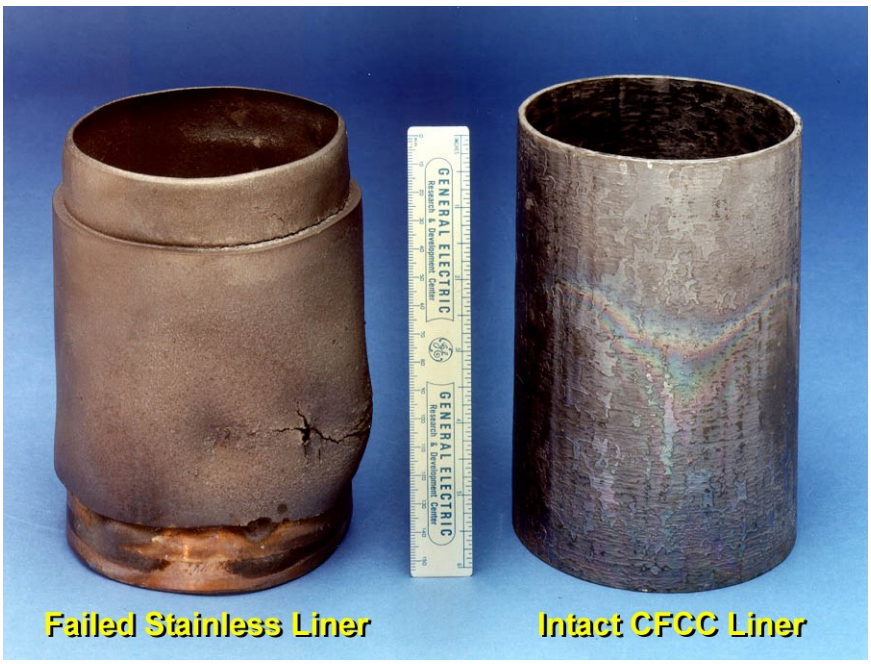

Figure 3-177. Photograph of the failed stainless steel combustor liner and the 1st GE Prepreg CMC liner used in the shroud combustion rig tests.

The 2nd CMC liner, having been present in the liner for many more tests, accumulated approximately 104 hours at a rig firing temperature of ~1177°C, 12 hours at firing

temperatures from 1260°-1650°C, 60 hours at a firing temperature of ~1480°C, 54 hours at a firing temperature of ~1371°C, 22 full start-stop cycles, and 400 simulated turbine trip cycles. Moreover, the majority of these exposures (rig run 24 and beyond) were done with no active backside cooling at all on the combustor. Despite this rather lengthy and demanding thermal exposure the liner remained intact and functional throughout. Photographs of the OD and ID of the 2nd CMC liner are shown in Figure 3-178 after rig testing had been completed. On the ID photos in Figure 3-178 there are several areas of enhanced oxidation (whitish areas) and surface recession (black areas inside the whitish areas).

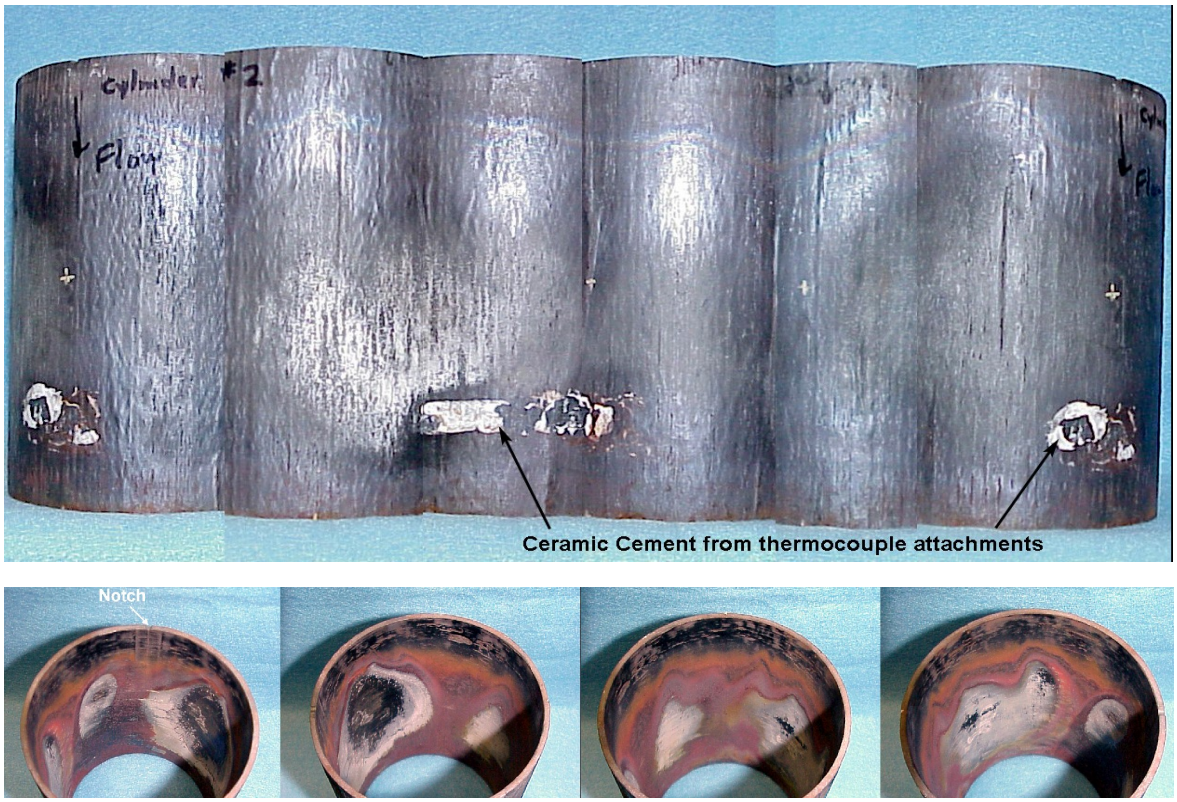

Figure 3-178. Photographs of the 2nd CMC combustor liner used in the shroud combustion rig tests.
Top – montage photograph of OD surface
Bottom – photographs of the ID surface from different angles showing the regions of enhanced oxidation and recession. The brownish-red tint on the ID is from iron oxides that deposited on the surface of the liner during rig operation.

Both CMC combustor liners were subjected to NDE inspection at ANL. Transmission IR thermography and air-coupled ultrasound inspections were done on the liners both before and after exposure in the shroud rig. The NDE images obtained are shown in Figures 3-179 to 3-182.

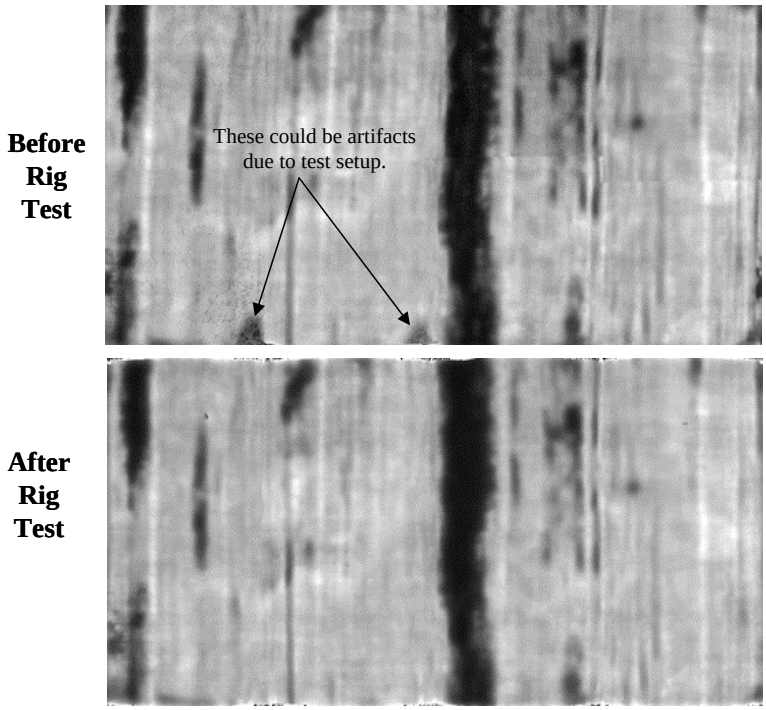

Figure 3-179. Thermal diffusivity image of the 1st CMC liner both before (top) and after (bottom) use in the shroud combustion test rig. There was no appreciable change in the NDE images caused by use in the test rig.

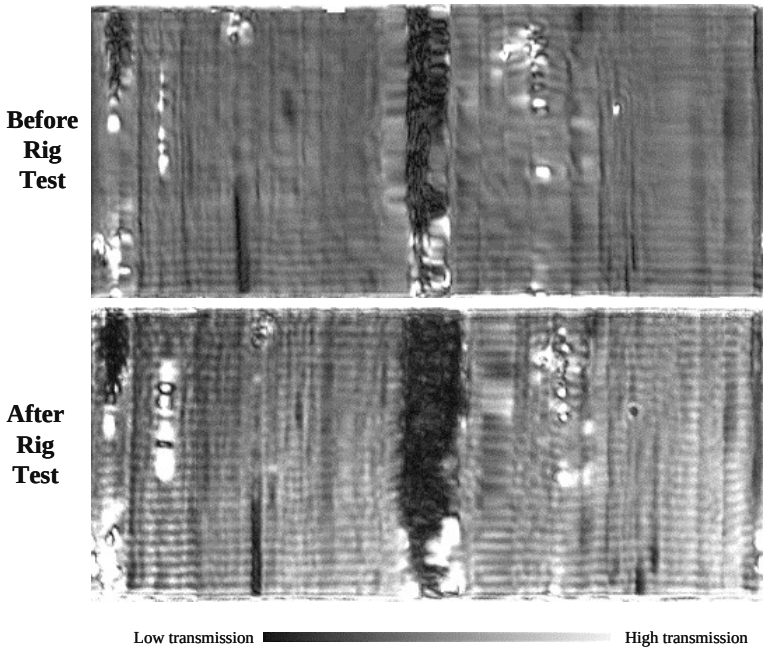

Figure 3-180. Air-coupled ultrasound image of the 1st CMC liner both before (top) and after (bottom) use in the shroud combustion test rig. Differences in the images are believed to be caused by sight differences in transducer calibration between images.

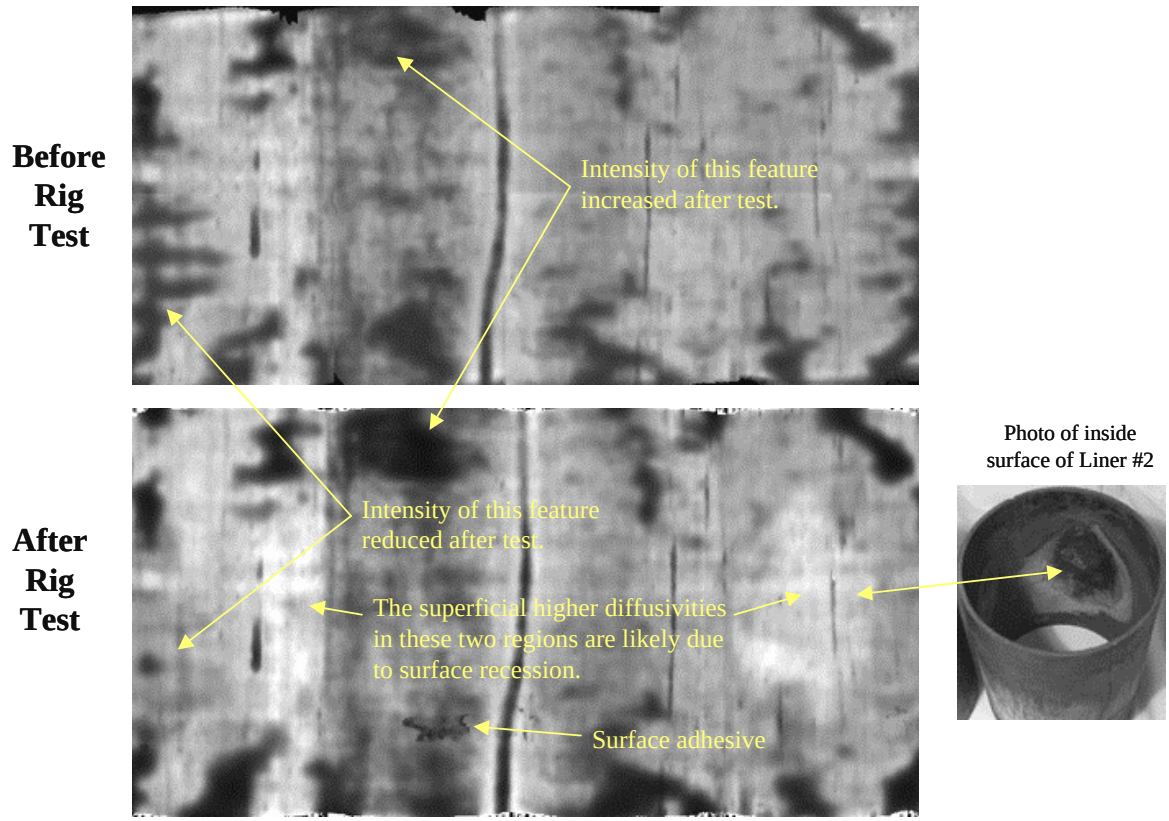

Figure 3-181. Thermal diffusivity image of the 2nd CMC liner both before (top) and after (bottom) use in the shroud combustion test rig. There were some minor changes in the intensities of some image features, some of which were attributable to recession of the interior of the liner, and therefore thinning of the wall locally.

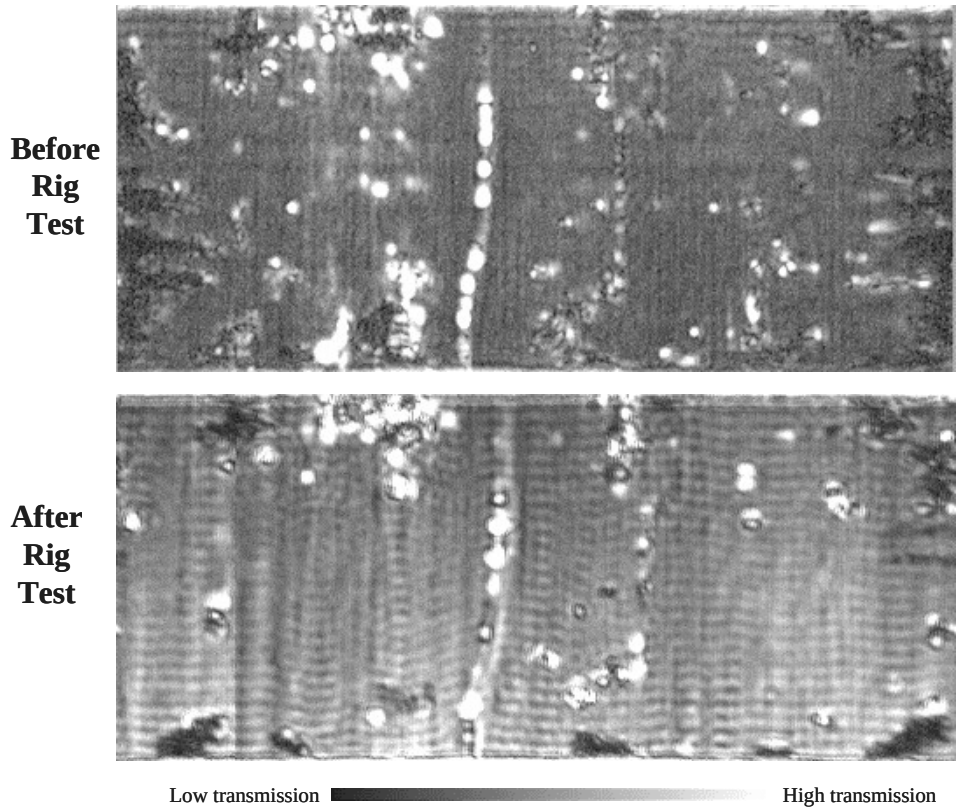

Figure 3-182. Air-coupled ultrasound image of the 1st CMC liner both before (top) and after (bottom) use in the shroud combustion test rig. Differences in the images are believed to be caused by differences in transducer calibration between images.

In an attempt to evaluate whether the prolonged exposure to rig combustion conditions had any impact on the mechanical properties of the 2nd liner, the liner was sectioned into a series of rings to allow for burst testing. Figure 3-183 shows photographs of the liner after sectioning.

Rings 1, 3, 5 and 7 from the 2nd liner, along with somewhat thinner rings trimmed from both liner 1 and liner 2 during machining to final dimensions for the rig tests, were sent to Dr. E. Lara-Curzio at ORNL for burst testing.

The test specimens were infiltrated using Dow Corning's Silastic RTV silicone rubber using molds of ultra-high molecular weight polyethylene that were machined to conform with the dimensions of the rings to insure uniform infiltration and parallelism of the rubber surfaces. The rubber inserts were allowed to cure at ambient temperature for 24 hours. To pressurize the test specimens, stainless steel pistons were fabricated to conform with the ID dimensions of the specimens. The radial displacement on the outer surface of the test specimens was measured using a pair of LVDTs located at opposite sides of the specimen.

Figure 3-183. Photographs of the 2nd shroud rig combustor liner following sectioning for burst tests. Left – with the rings stacked in their original positions; Right – with the rings splayed apart to show the individual pieces. The arrows mark the direction of gas flow during rig operation.

The pressure was calculated as

$$P_{\max} = \frac{4T_{\max}}{\pi d_i^2} \tag{9}$$

where d_i is the ID and T_{max} is the peak load. The maximum hoop stress was calculated according to

$$\sigma_\theta^{\max} = \frac{P_{\max} d_i^2}{d_o^2 - d_i^2}\left(1 + \frac{d_o^2}{d_i^2}\right) \tag{10}$$

where d_o is the outer diameter.

Figures 3-184 and 3-185 show the hoop stress versus hoop strain results from the evaluation of the as-processed rings "A" and "B", which were taken from the 1st and 2nd liners, respectively. During some tests problems were experienced recording the signals from the LVDTs, and therefore the strain data in these Figures should be considered with some reservations. Furthermore, specimen "B" had to be tested twice because the first test was interrupted when the specimen started to be loaded in a non-uniform manner due to its short height. Therefore, the difference in the shape of the stress-strain curve with respect to that in Figure 3-184 for ring "A", and the lower stiffness recorded in the initial region of the test, are probably indicative of the damage induced during the first test. The hoop strength results from the rest of the tests have been summarized in Table 3-56.

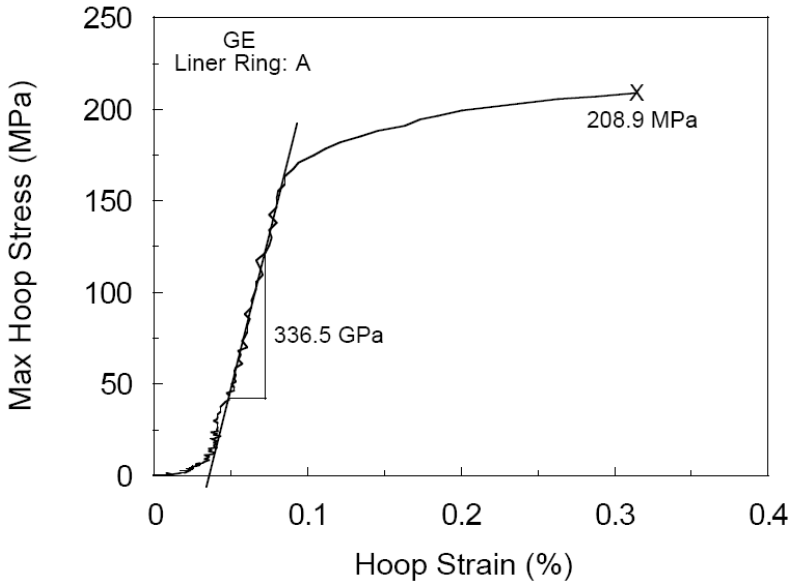

Figure 3-184. Stress-strain behavior of the as-fabricated ring specimen from the first shroud rig CMC combustor liner.

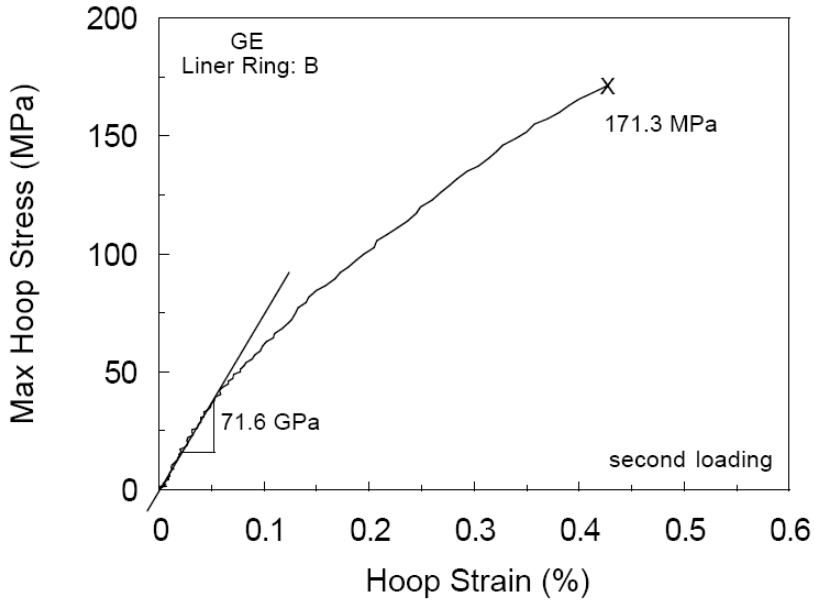

Figure 3-185. Stress-strain behavior of the as-fabricated ring specimen from the second shroud rig CMC combustor liner.

Table 3-56. Summary of Shroud Combustion Rig CMC Combustor Liner Ring Burst Tests Done at ORNL.

Specimen ID	Identity *	Maximum Hoop Stress (MPa)
A	1st (as fabricated)	208.9
B	2nd (as fabricated)	171.3
B1	2nd (ring #1)	198.7
B3	2nd (ring #3)	199.6
B5	2nd (ring #5)	141.5
B7	2nd (ring#7)	222.5

* The sample identity is either from the 1st or 2nd rig combustor liner with the ring numbers as shown in Figure 3-183.

Despite the fact that the test of sample B (the as-fabricated ring from the 2nd liner) was somewhat problematic, there is no indication of any appreciable material degradation of the liner from these tests. Ring #5 from the 2nd liner (sample B5) was from the location of the liner that included part of the largest, and most severe, region of surface recession on the ID, which may explain the slightly lower strength of this ring compared to the others.

3.8.1.8 Coupon Exposure Testing in the Shroud Rig

Considering the expense of performing high pressure combustion rig tests, it was important to obtain as much CMC material exposure time as possible while running the shroud combustion test rig. As described in section 3.8.1.4.1, an exhaust diffuser was added onto the exit of the shroud section of the test rig that allowed the introduction of test coupons in the rig for exposure to high pressure, high velocity combustion gases.

The exhaust diffuser, without samples, was added to the test rig for run 15. During rig runs 15 and 16 the air flows were adjusted to account for any added pressure drop caused by the diffuser and the durability of the assembly was verified. The first set of exhaust test coupons were then inserted into the rig during runs 17 through 19, accumulating 100 hours of rig exposure. Due to the expansion of the flow and mixing in of cooling air from the shroud test section the exposure conditions in the exhaust section were at reduced gas temperature and velocity compared to the conditions in the shroud test section. Thermocouples inserted into the exhaust section showed the exhaust section to be running ~200° to 300°C below the rig firing temperature, with the temperature varying somewhat depending on position in the diffuser. However, because there is no cooling of the coupons and they extend directly across the hot gas path flow the temperature of the test section of the coupons is roughly equivalent to the gas temperature. Thus in runs 17-19 the coupons were exposed for 100 hours at ~950°C at a gas pressure of ~1MPa and gas velocity of ~119m/s.

A second set of exhaust samples was exposed during runs 32-35, although not all of the samples were available at the start of run 32 and so only saw exposure in runs 34 and 35. The estimated exhaust bar exposure conditions for this set of runs was 52 hours at ~1200°C including 50 thermal trip cycles, plus 100 hours at ~1090°C, all at a gas pressure of ~1MPa and gas velocity of ~119m/s.

During the first exhaust exposure set the test bars were exposed in the as-fabricated condition (edges of the bars were sealed during final densification or by a CVD SiC overcoat), or with edges exposed (the sample had freshly cut edges that exposed the fiber ends and fiber coatings to the environment), or after precracking the bars to 0.2% strain. Limited quantities of some CMC material systems prevented them from being tested in all conditions. A complete list of the sample types exposed in the 1st set of exhaust exposures is given in Table 3-57. The position of the samples within the exhaust diffuser as given by the diagram in Figure 3-186, although position in the exhaust section was not expected to result in significant differences in the exposure conditions.

After exposure the bars were removed from the rig for evaluation. The purpose of the high purity CVD SiC was to serve as a reference material for evaluating the material recession rate from SiO_2 volatilization. One of two high purity CVD SiC bars was found to have broken during exposure, but all of the composite bars were intact. All of the bars, including the surviving CVD SIC sample, had a brownish deposit on the surfaces (shown to be primarily Fe_2O_3 by EDAX and X-ray analysis), and most of the bars showed some chipping of the corners at the positions where they passed through the diffuser side walls, thereby making any mass change measurements meaningless.

Tensile tests of the bars were done at room temperature. The results of these tests are given in Figures 3-187 through 3-193. Each of these figures includes the stress-strain behavior of an "unexposed" reference bar, which was cut from the same starting panel as the rig exposed bars and tested without any rig exposure, for comparison to the post-exposure data. The GE prepreg MI composites exhibited somewhat unusual behavior in this test. For both the standard and B-doped prepreg materials with configuration A fiber coatings the samples exposed in the as-fabricated condition showed a substantial reduction in strengths and strain to failure compared to unexposed samples. However, for samples with exposed edges the amount of degradation was much smaller. Little or no degradation of prepreg samples with exposed edges might be expected since the fibers exposed are the 90º fibers which do not have good connectivity with the 0º, or tensile, fibers. Thus environmental attack of the fiber coatings exposed on the 90º plies may not affect the 0º plies much, and thus the residual tensile strength should not degrade much. However, an explanation for the substantial degradation of the samples exposed as processed was not determined. Similar degradation did not occur in the samples with configuration B-2 fiber coatings, as shown in Figure 3-189. (Note that these test samples were fabricated before the fully optimized configuration C fiber coating system had been developed.)

Looking at the pre-cracked prepreg bars, the standard matrix sample again degraded quite substantially, the sample with the B-doped matrix degraded to a lesser extent and the sample with the standard matrix and Si-doped BN fiber coating showed no degradation at all.

Table 3-57. Summary of the Sample Types Used in the First Shroud Rig Exhaust Section Exposure Test

Material Type	Condition*	Rig position
Morton CVD SiC	as fab	2
	as fab	24
GE Prepreg MI	as fab	1
standard matrix	cracked	9
Configuration A fiber coatings	edge exposed	16
GE Prepreg MI	as fab	12
B-doped matrix	cracked	17
Configuration A fiber coatings	edge exposed	20
GE Prepreg MI	as fab	8
standard matrix	cracked	15
Configuration B-2 fiber coatings		
CCP Slurry Cast MI	as fab	4
Enhanced Matrix	cracked	11
	edge exposed	19
CCP Slurry Cast MI	as fab	22
Sylramic fiber	cracked (0.15%)	23
Goodrich Slurry Cast MI	as fab	6
	cracked	13
	edge exposed	21
CCP CVI Enhanced SiC-SiC	as fab	7
no seal coat	cracked	14
CCP CVI Enhanced SiC-SiC	as fab	3
with CVD SiC seal coat	cracked	10
	edge exposed	18

* "as-fab" refers to the as-fabricated condition with the edges of the bars were sealed during final densification; "edge exposed" refers to samples with machined edges that exposed the fiber ends and fiber coatings to the environment; "cracked" refers to bars that had been precracked to 0.2% tensile strain, unless otherwise noted.

The Goodrich slurry cast MI bars exposed in the rig exhaust showed no evidence of degradation, even in the precracked bar. This lack of degradation, as shown in Figure 3-190, is in direct contrast to the steam furnace oxidation results, discussed in section 3.4.4, where all of the oxidized samples showed evidence of degradation. The results on the CCP slurry cast MI bars with Sylramic™ fiber in 3-191 suggest that no degradation occurred from the rig exposure, but the results were not conclusive due to the very poor strength and strain to failure values of the as-processed bars.

Testing results for CCP Enhanced SiC-SiC CVI composites with and without CVD SiC seal coatings are shown in Figures 3-192 and 3-193, respectively. Here again there was no clear evidence of any degradation having occurred in any of the bars as a result of the shroud rig exposure.

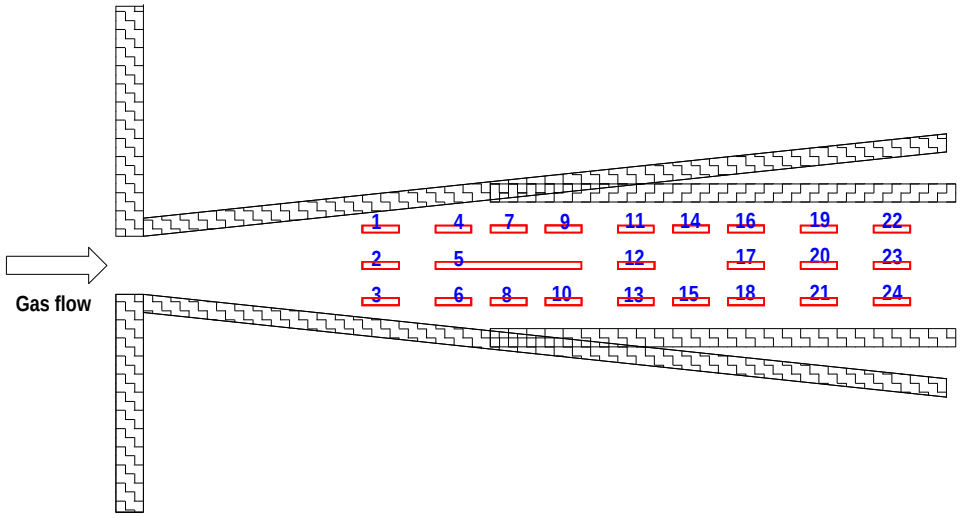

Figure 3-186. Diagram showing relative position of exhaust diffuser test samples as numbered in Table 3-57.

In summary, results of first set of exhaust rig tests indicated that little or no degradation was observed in 100 hours in MI samples prepared by Goodrich and CCP, CVI samples prepared by CCP and GE prepreg MI samples with Si-doped BN fiber coatings. The results on the standard prepreg and B-doped prepreg MI composites with BN-based fiber coatings were unexpectedly poor. The results of this test served to further push the development of silicon-doped BN fiber coatings for GE Prepreg MI composites, as has been discussed in section 3.2.6.2.

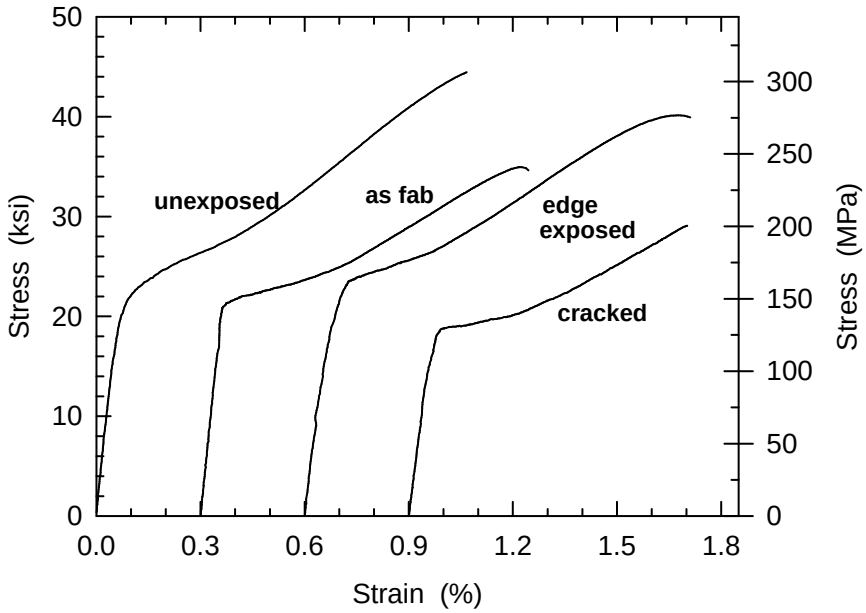

Figure 3-187. Tensile stress-strain behavior of GE standard prepreg MI composite bars made with configuration A fiber coatings before and after exposure in the shroud rig exhaust section during rig runs 17-19. Curves are offset for clarity.

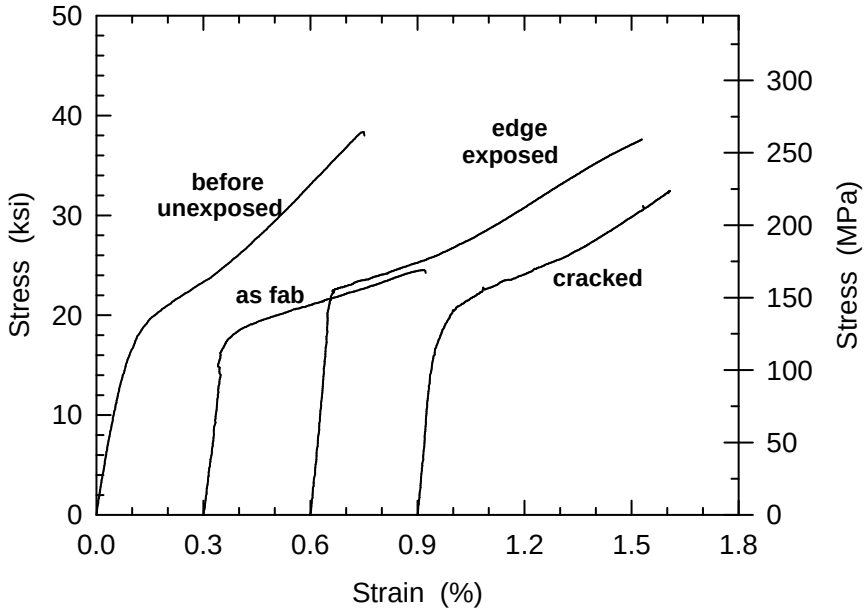

Figure 3-188. Tensile stress-strain behavior of GE B-doped prepreg MI composite bars made with configuration A fiber coatings before and after exposure in the shroud rig exhaust section during rig runs 17-19. Curves are offset for clarity.

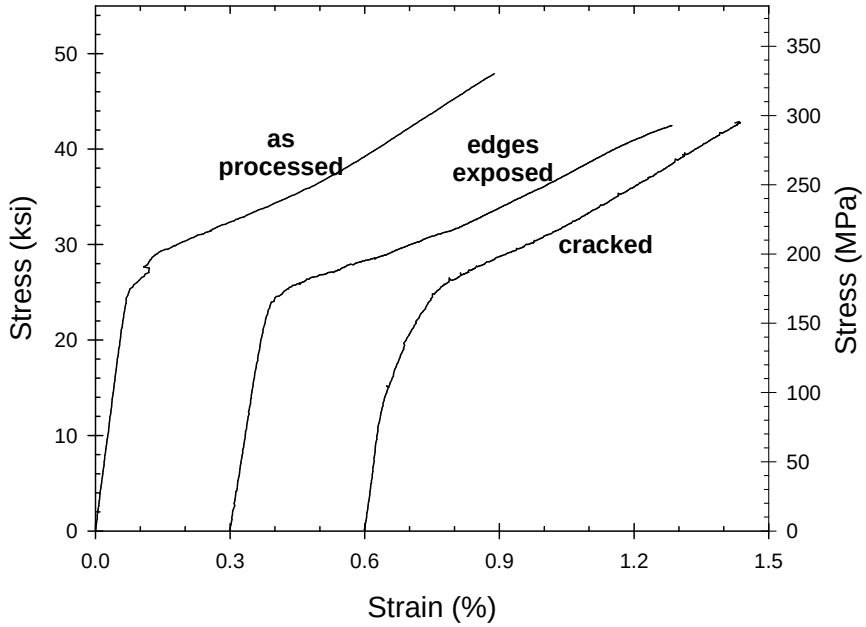

Figure 3-189. Stress strain behavior of GE standard prepreg MI composite bars made with configuration B-2 fiber coatings before and after exposure in the shroud rig exhaust section during rig runs 17-19. Curves are offset for clarity.

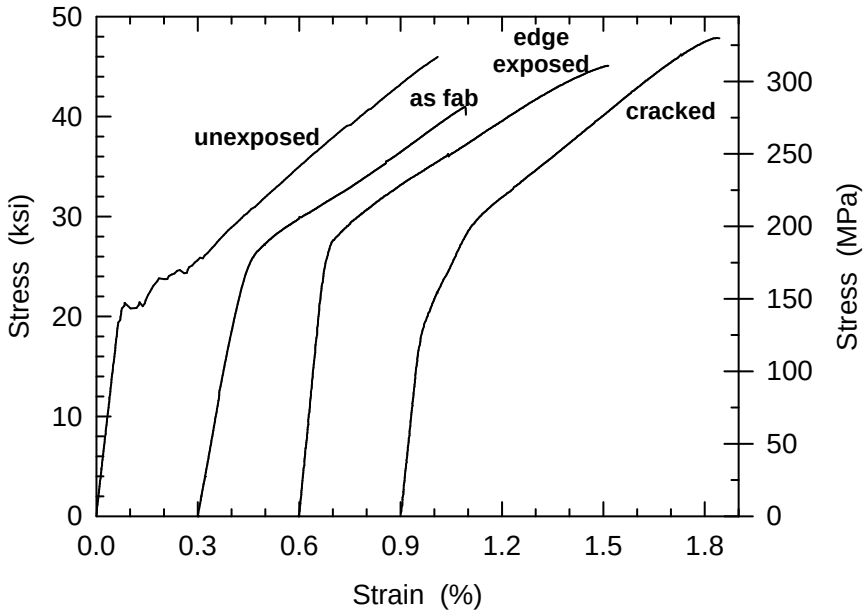

Figure 3-190. Stress strain behavior of Goodrich slurry cast MI composite bars before and after exposure in the shroud rig exhaust section during rig runs 17-19. Curves are offset for clarity.

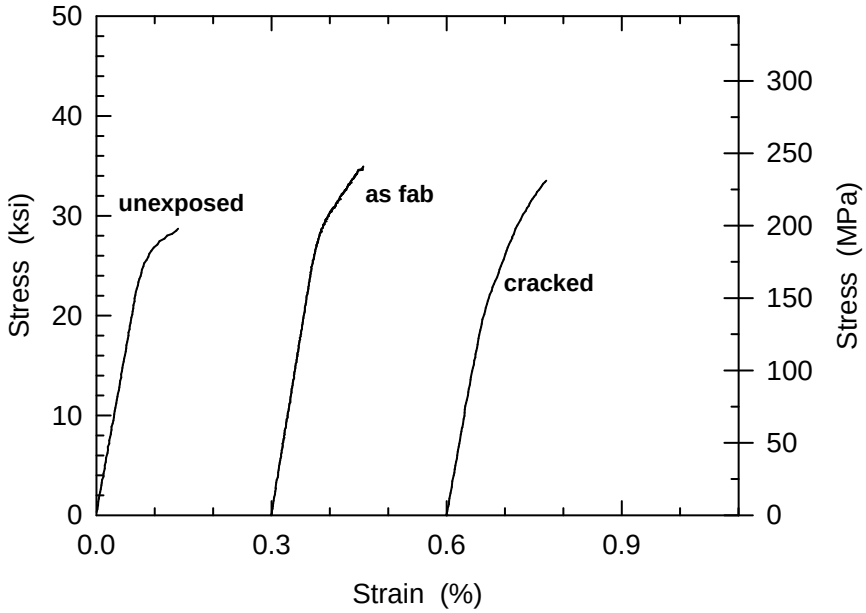

Figure 3-191. Stress strain behavior of CCP slurry cast MI composite bars reinforced with Sylramic™ fiber before and after exposure in the shroud rig exhaust section during rig runs 17-19. Curves are offset for clarity.

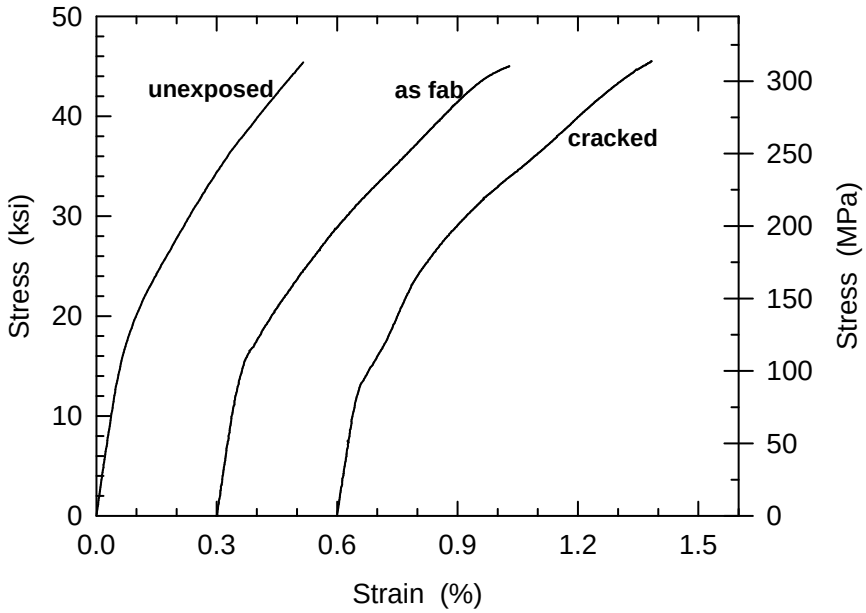

Figure 3-192. Stress strain behavior of unsealed CCP CVI Enhanced SiC-SiC composite bars before and after exposure in the shroud rig exhaust section during rig runs 17-19. Curves are offset for clarity.

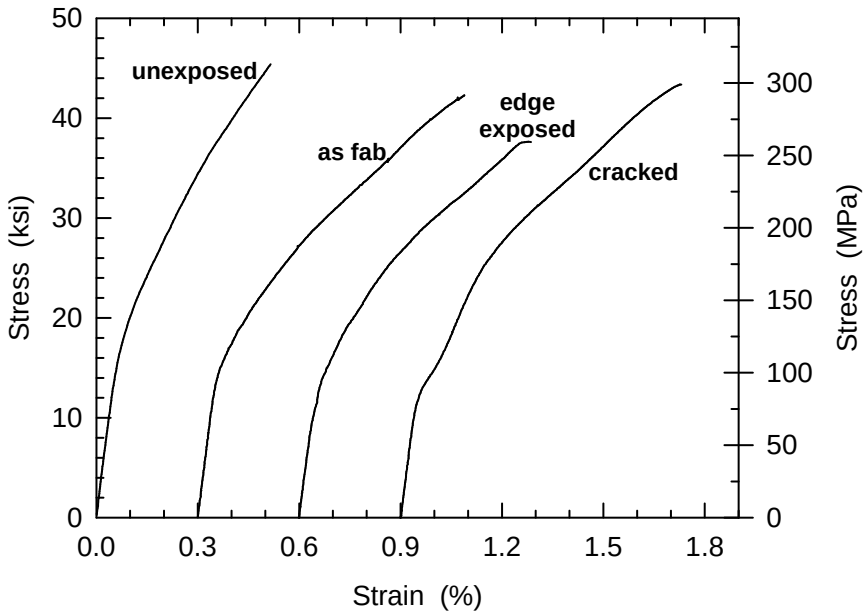

Figure 3-193. Stress strain behavior of CCP CVI Enhanced SiC-SiC composite bars with CVD SiC seal coatings before and after exposure in the shroud rig exhaust section during rig runs 17-19. Curves are offset for clarity.

Prior to the second set of exhaust bar tests the exhaust diffuser was modified. During the high temperature test and cyclic runs (rig runs 20-31) the interior top and bottom wall plates in Figure 3-186 were overheated and badly oxidized. There was also a desire to include a larger number of test samples in the exhaust exposure test. Consequently the interior parallel plates were removed from the diffuser and additional specimen slots were cut in the side walls. The sample numbering arrangement for the modified diffuser used in the 2nd exhaust sample exposure test is shown in Figure 3-194.

A complete listing of the samples used in the 2nd exhaust bar exposure test is given in Table 3-58. Following exposure in the shroud rig the bars were removed from the exhaust diffuser and visually inspected before tensile testing. Both mass and thickness measurements were made before and after exposure; however, the measurement were not of much value. During exposure a film of iron oxides was deposited on the samples, giving them a reddish hue and confounding the thickness measurements. There was also substantial erosion of the leading edges of many of the bars, probably at least partially caused by impact from pieces of the upstream rig that oxidized and/or melted during the runs. In addition to the leading edge erosion and chipping, there were wear marks on several of the bars caused by abrasion against the edges of the sample slots in the stainless steel side walls of the diffuser. In fact, most of the wear was noticed in positions where the mounting slots had been modified and the wall thickness of the exhaust diffuser contacting the samples was only 3.1mm thick rather than the normal 9.5mm thick contact regions for most positions.

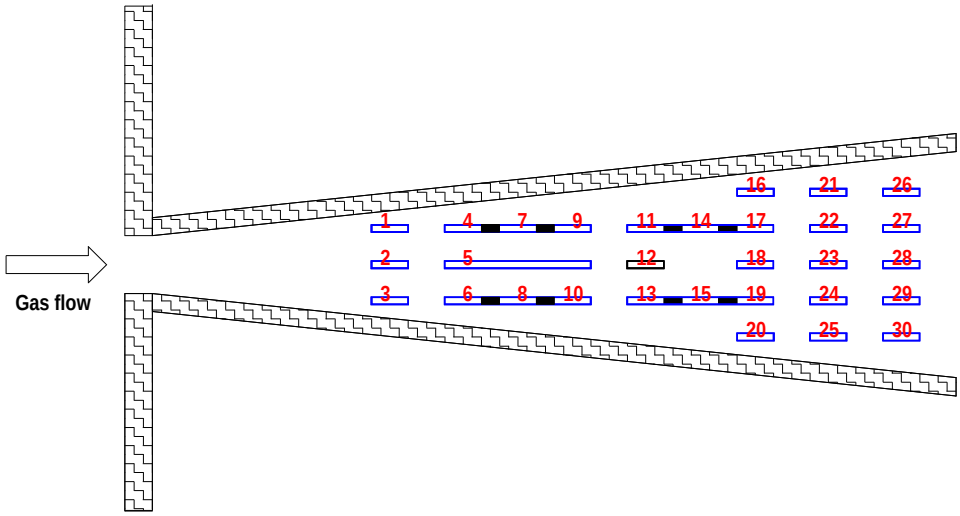

Figure 3-194. Diagram of the shroud rig exhaust sample exposure section as configured for the 2nd exhaust exposure test in rig runs 32-35.

Three samples failed during the exposure test: the Morton monolithic CVD SiC, the Composite Optics oxide-oxide CMC and one of the CCP slurry cast MI bars. Failure of the monolithic SiC bar is not surprising given the amount of rig damage that occurred during these runs and the high probability of impact damage from debris liberated from the upstream rig components. The Composite Optics sample, which was not introduced into testing until run 34, failed during the first 24 hours of run 24. This bar also had the most severe erosion of any of the test samples, having been completed eroded through the width. This result strongly suggested that the low density (high porosity) of the Composite Optics oxide-oxide system gave it insufficient toughness and erosion resistance for a turbine application. The third bar that failed, a CCP slurry cast MI bar in the precracked condition, will be described below.

All of the surviving samples were tensile tested at room temperature to measure the effects of the exposure on mechanical properties. Results for the standard GE Prepreg MI coupons with configuration A fiber coatings are shown in Figure 3-195. Coupons from two different batches of samples were included: Run 333 which was also used in the first set of shroud rig exhaust samples that were exposed at somewhat lower temperatures, and a newer Run 396. The run 333 bar showed similar degradation after this set of exposures as did the similar bar from the first set of exposures. In the earlier test the run 333 bar exposed in the as-fabricated condition showed greater degradation than did either the precracked bar or the bar with fibers exposed along the edges. Somewhat different behavior is seen in the run 396 bars. The as-fabricated strengths of these bars was substantially lower than for the run 333 bars, but the strengths and strain to failure values both increased following rig exposure.

Table 3-58. Listing of CMC Test Samples Exposed During the Second Shroud Rig Exhaust Exposure Test During Rig Runs 32-35.

Type	Condition	Rig position
CVD SiC	as fab	12
GE Prepreg MI	as fab (333)	17
configuration A fiber coatings	as fab (396)	27
	cracked (396)	22
	edge exposed (396)	23
GE Prepreg MI	as fab	29
configuration B-2 fiber coatings	cracked	28
	edge exposed	24
CCP Slurry Cast MI	as fab	8
	cracked	9
	edge exposed	2
Goodrich Slurry Cast MI †	as fab (surf ground)	1
	cracked	10
	edge exposed	3
CCP CVI SiC-SiC	as fab	13
no seal coat	cracked	14
	edge exposed	4
CCP CVI SiC-SiC	as fab	11
with CVD SiC seal coat	cracked	15
	edge exposed	6
CCP DIMOX	as fab	
	cracked + edges	19
	edge exposed	7
CCP DIMOX Shroud	edge exposed	21
D2-4	edge exposed	25
Composite Optics oxide-oxide CMC‡	as-fab	18
GE Prepreg MI FOD panel	impacted	5

* "as-fab" refers to the as-fabricated condition with the edges of the bars were sealed during final densification; "edge exposed" refers to samples with machined edges that exposed the fiber ends and fiber coatings to the environment; "cracked" refers to bars that had been precracked to 0.2% tensile strain; "cracked + edge" refers to a bar that had both exposed edges and had been precracked.

† The Goodrich MI samples were not ready in time for exposure in runs 32 and 33, and thus were only exposed in runs 34 and 35.

‡ The Composite Optics sample was introduced to the rig at the start of rig run 34, but was failed by the 24 hour point of this run.

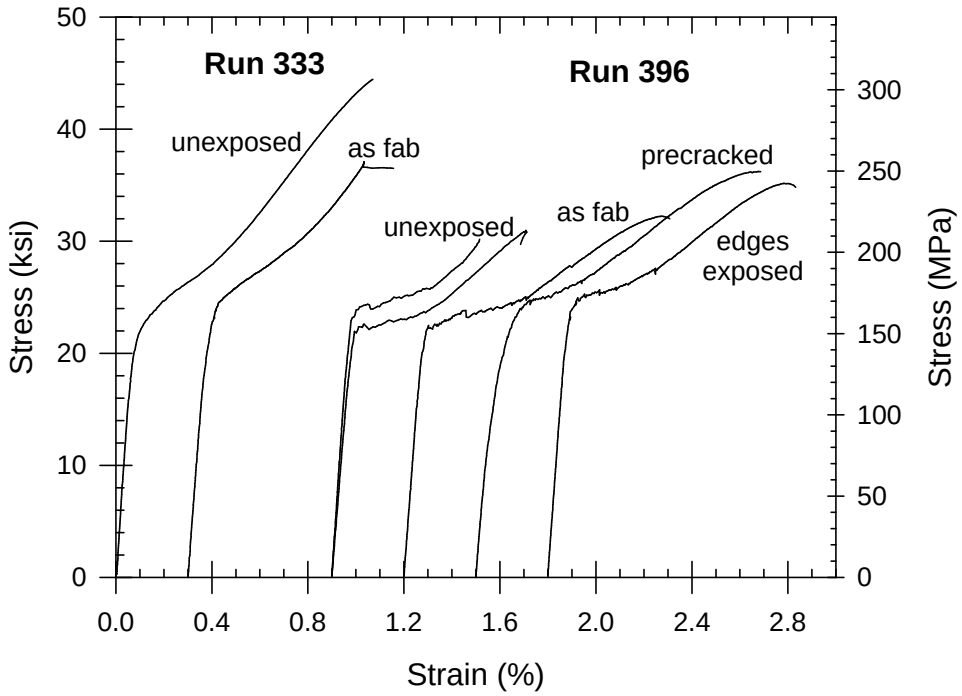

Figure 3-195. Tensile strength behavior of standard GE Prepreg MI bars before (unexposed) and after (as fab, precracked and edge exposed) high temperature, high pressure combustion gas exposure in the shroud test rig exhaust. Samples were exposed during shroud rig runs 32-35, which included 50 thermal cycles and 50 hours exposure at a maximum temperature of roughly 1200ºC plus 100 hours exposure at a maximum temperature of roughly 1090ºC. Test coupons from two batches of composite (Run 333 and Run 396) were included.

Tensile strength data for the GE Prepreg MI samples made with configuration B-2 fiber coatings are shown in Figure 3-196. The results for this set of coupons is also similar to those from bars exposed in the first exhaust exposure test: no observable degradation of the exposed bars compared to the unexposed bars. These results along with the results above on run 396 bars suggested that the amount of degradation may be related to the starting strength of the coupons with high strength coupons showing degradation and low strength coupons not showing any degradation.

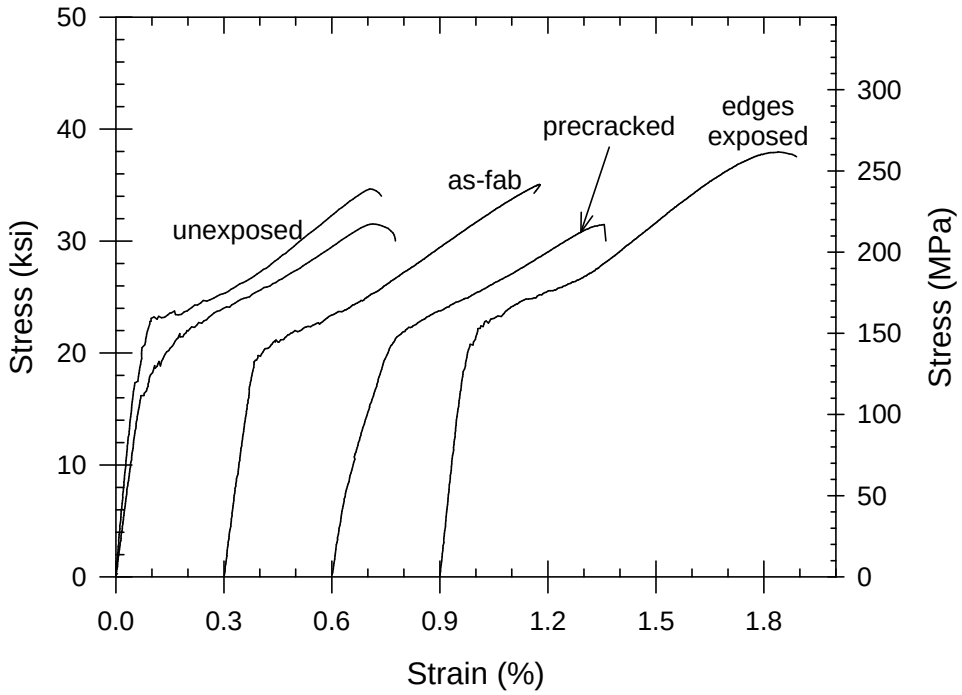

Figure 3-196. Tensile strength behavior of GE Prepreg MI bars made with configuration B-2 fiber coatings before (unexposed) and after (as-fab, precracked and edge exposed) high temperature, high pressure combustion gas exposure in the shroud test rig exhaust. Samples were exposed during shroud rig runs 32-35, which included 50 thermal trip cycles and 50 hours exposure at a maximum temperature of roughly 1200ºC plus 100 hours exposure at a maximum temperature of roughly 1090°C.

Results for the CCP slurry cast MI bars were somewhat surprising in that the exposed bars displayed very substantial degradation, as shown in Figure 3-197. The bars exposed as-fabricated and with edges exposed both had over 40% reductions in ultimate strength and strain to failure, and the bar exposed in the precracked condition actually failed in the rig. The failure of this bar was unusual in that it both broke transversely and split by delamination. The surfaces exposed by the delamination had very little MI matrix on them. The bar exposed in the as-fabricated condition also showed delamination cracks along the edges. Subsequent microstructural examination showed that these bars had several plies that were completely un-infiltrated, and rapid oxidation along the interconnected porosity in this ply eventually caused swelling and delamination of the bars. These observations indicated that these particular bars had very little MI matrix in them prior to testing, and that their poor behavior was a result of this major processing flaw and probably not representative of normal CCP MI material.

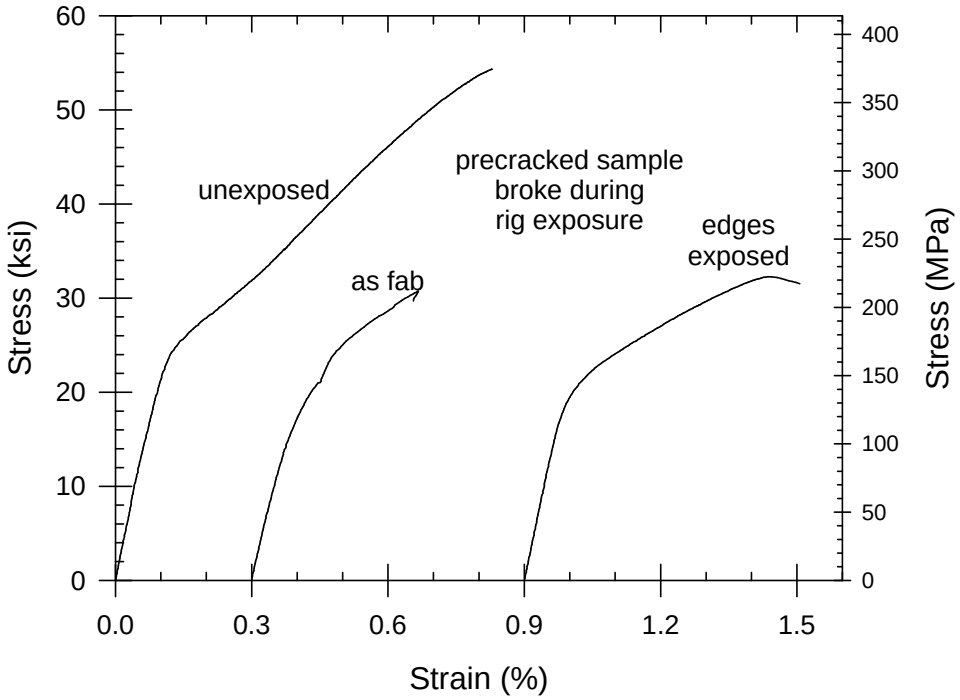

Figure 3-197. Tensile strength behavior of CCP slurry cast MI bars made with HI-Nicalon fiber before (unexposed) and after (as-fab and edges exposed) high temperature, high pressure combustion gas exposure in the shroud test rig exhaust. Samples were exposed during shroud rig runs 32-35, which included 50 thermal trip cycles and 50 hours exposure at a maximum temperature of roughly 1200ºC plus 100 hours exposure at a maximum temperature of roughly 1090ºC. The bar that was exposed in the precracked condition failed in the shroud rig.

The tensile test results on the Goodrich slurry cast MI samples, shown in Figure 3-198, were much closer to what was expected. The bars exposed in the as-fabricated condition or with edges exposed showed no degradation in ultimate strength or strain to failure; however, the bar exposed after precracking to 0.2% strain displayed substantial strength reduction. (The tensile data shown for the edges exposed bar was from a second tensile test since during the first test there was a datalogging error that was not noticed until the bar had been loaded to above matrix cracking, thus explaining the low proportional limit and initial modulus measured during the re-test data in the figure.) This behavior is similar to what we would have expected, i.e. no degradation for the case where fiber coatings are not exposed and little or no degradation for the case where only fiber ends are exposed, but potentially larger degradation when most of the load-bearing fibers and coatings are exposed to the atmosphere through the matrix cracks. Please note that the Goodrich bars were exposed only during rig runs 34 and 35, and thus did not experience the 50 thermal shock cycles and 50 hours at 1200ºC (32 and 33) runs as did most of the other test bars.

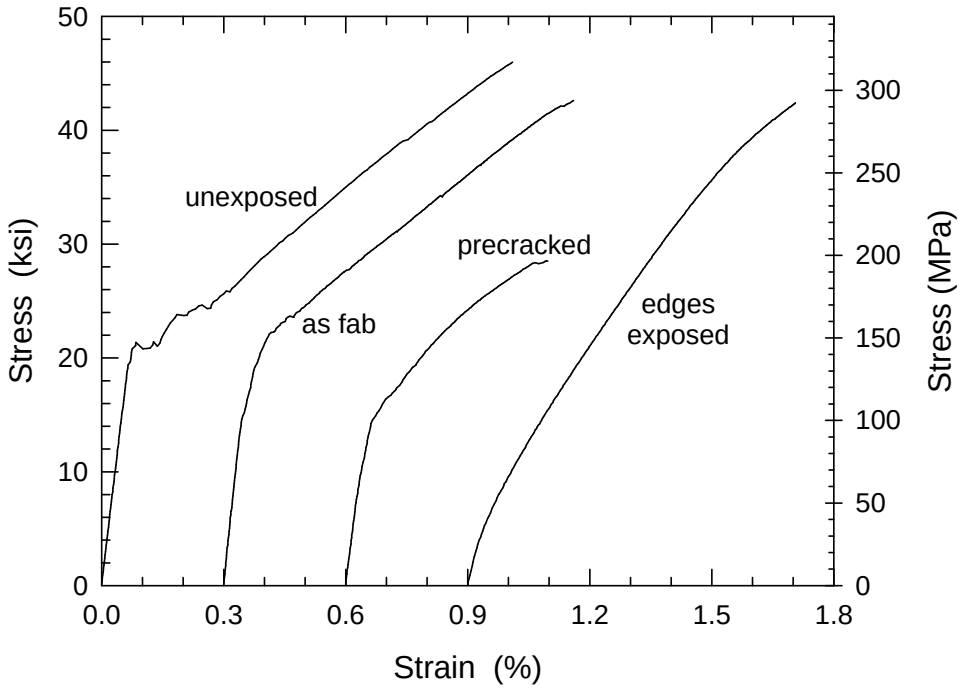

Figure 3-198. Tensile strength behavior of standard Goodrich slurry cast MI bars before (unexposed) and after (as-fab, precracked and edges exposed) high temperature, high pressure combustion gas exposure in the shroud test rig exhaust. Samples were exposed during shroud rig runs 34 and 35, which consisted of 100 hours exposure at a maximum temperature of roughly 1090°C.

The rig exposure results for the CCP CVI SiC-SiC composites were very good, as shown in Figures 3-199 and 3-200. Essentially no degradation was observed for bars exposed in the as-fabricated condition or after precracking to 0.2% strain for both seal coated and non-seal coated bars. Both bars that were tested with exposed edges did show about 20% degradation in ultimate strength, but the magnitude of the ultimate strength remained above 275MPa. The observation that the CVI SiC-SiC bars were more susceptible to edge-on oxidation than the MI bars could possibly be explained by the higher amount of interconnected internal porosity that would be exposed along the bars edges; however, it is not clear why there was no degradation of the precracked bars.

Tensile testing results for the DIMOX Al_2O_3-SiC bars exposed in the shroud rig exhaust section are shown in Figure 3-201. As was the case for previous steam oxidation exposures of both coupons and bars cut from shrouds, the DIMOX bars displayed significant degradation for both precracked and edge exposed conditions. (No DIMOX bars with sealed edges, or the "as-fabricated" condition, were available for testing.)

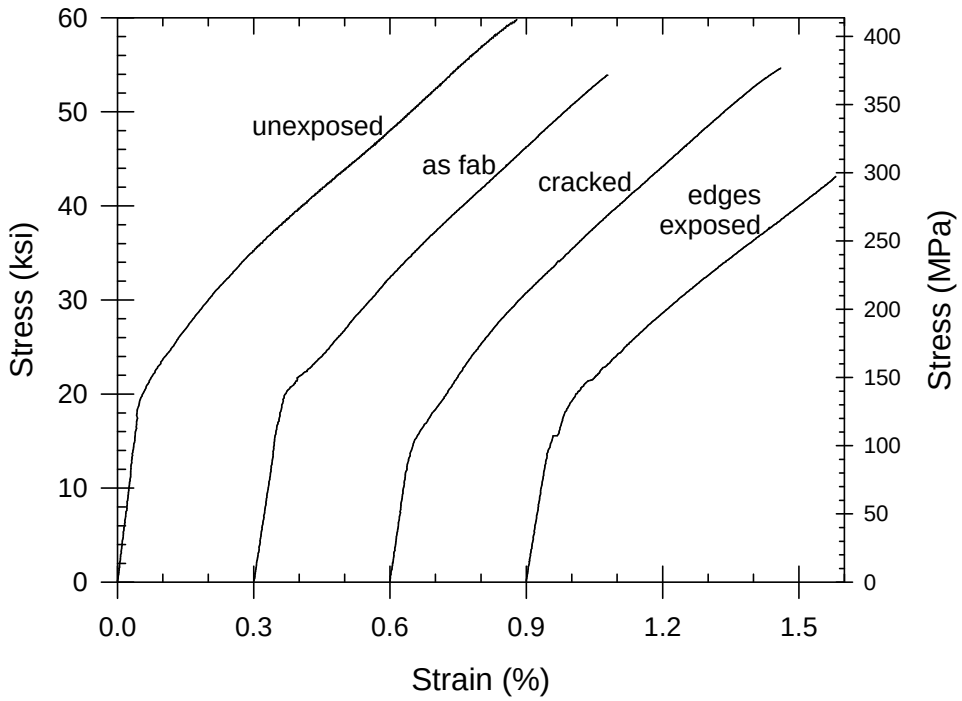

Figure 3-199. Tensile strength behavior of standard CCP CVI SiC-SiC bars with CVD SiC seal coat before (unexposed) and after (as-fab, precracked and edges exposed) high temperature, high pressure combustion gas exposure in the shroud test rig exhaust. Samples were exposed during shroud rig runs 32-35, which included 50 thermal trip cycles and 50 hours exposure at a maximum temperature of roughly 1200ºC plus 100 hours exposure at a maximum temperature of roughly 1090°C.

Bars that had been cut from DIMOX shroud D2-4 were also exposed in the second shroud rig exhaust exposure test. This shroud was previously used in rig runs 29-31, but was then dropped from testing. Subsequently the shroud was then sectioned into test bars and two of the bars were then run in the exhaust diffuser section of the shroud rig during runs 32-35 to accumulate additional environmental exposure. Tensile test results for the shroud witness bar, for bars tested after the shroud testing in runs 29-31, and for bars tested after additional exposure in the rig exhaust section in runs 32-35 are shown in Figure 3-202. Following rig exposure as a shroud the material showed a nearly 50% decrease in ultimate strength and strain to failure values relative to the original shroud witness coupon. A slight further decrease in these properties occurred during additional exposure as test bars in the rig exhaust section.

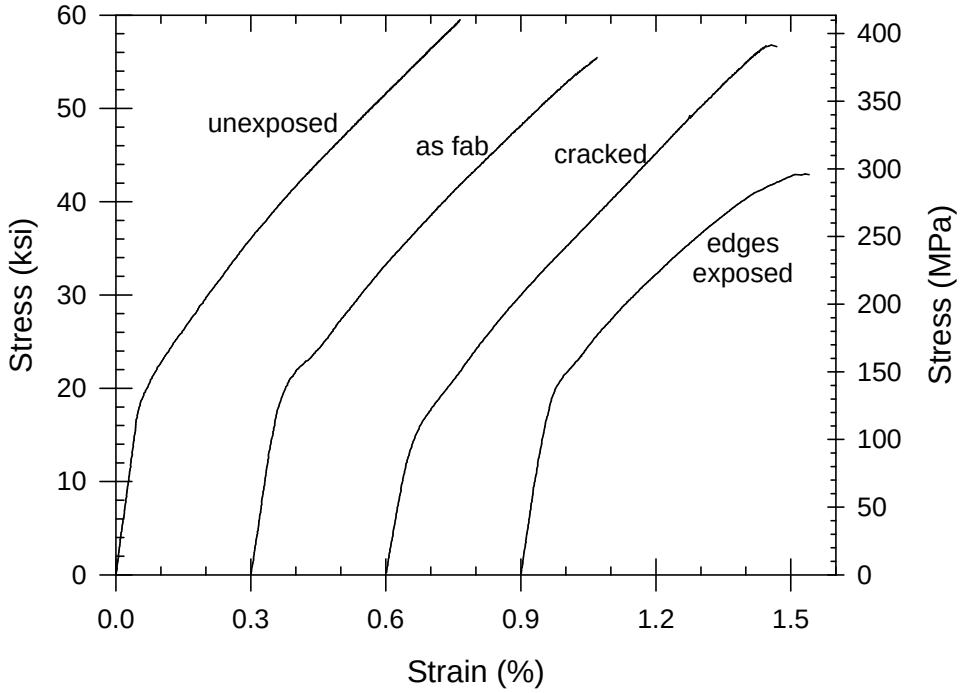

Figure 3-200. Tensile strength behavior of standard CCP CVI SiC-SiC (no seal coat) bars before (unexposed) and after (as-fab, precracked and edges exposed) high temperature, high pressure combustion gas exposure in the shroud test rig exhaust. Samples were exposed during shroud rig runs 32-35, which included 50 thermal trip cycles and 50 hours exposure at a maximum temperature of roughly 1200ºC plus 100 hours exposure at a maximum temperature of roughly 1090°C.

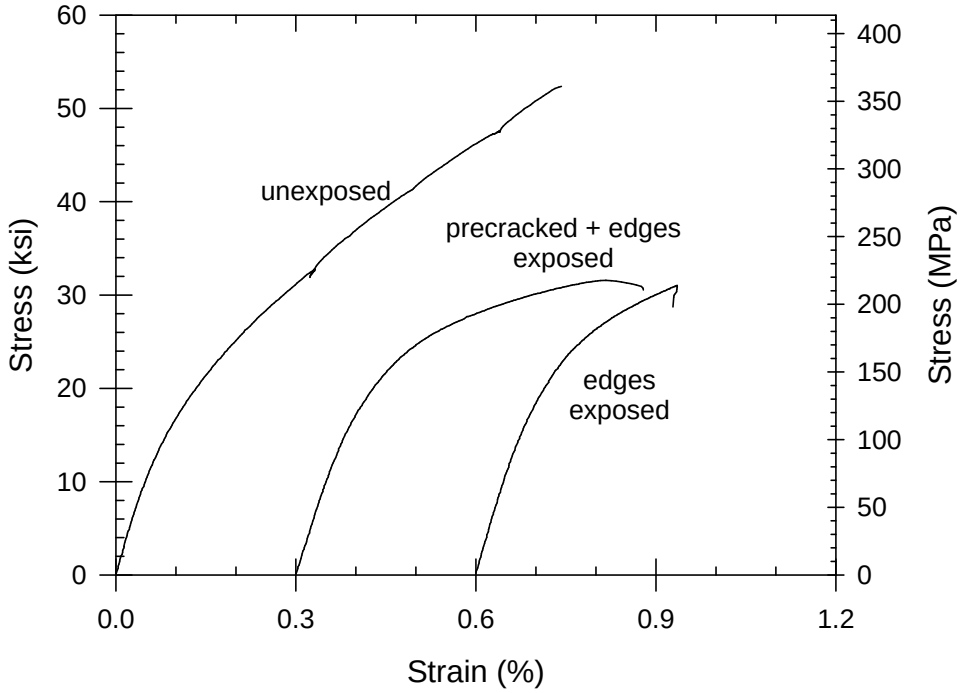

Figure 3-201. Tensile strength behavior of CCP DIMOX Al_2O_3-SiC bars before (unexposed) and after (precracked + edges exposed and edges exposed) high temperature, high pressure combustion gas exposure in the shroud test rig exhaust. Samples were exposed during shroud rig runs 32-35, which included 50 thermal trip cycles and 50 hours exposure at a maximum temperature of roughly 1200ºC plus 100 hours exposure at a maximum temperature of roughly 1090°C. Because of sample supply limitations there were no bars available without exposed edges.

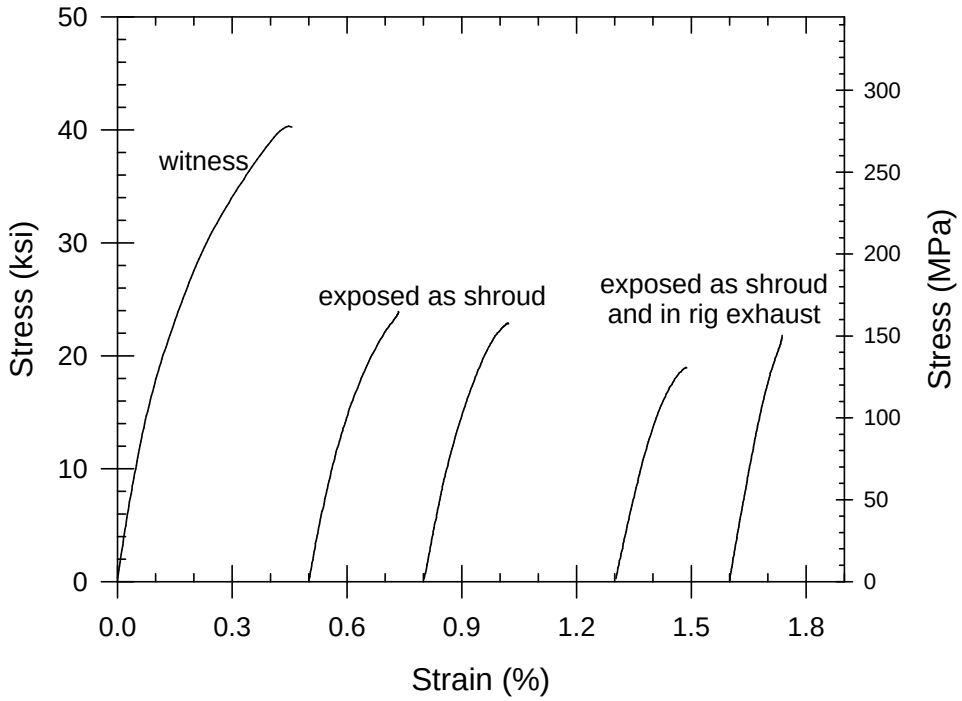

Figure 3-202. Room temperature tensile stress-strain behavior of samples from CCP DIMOX shroud D2-4. The behavior of a witness coupon processed with the shroud is shown for comparison. The shroud was exposed in rig runs 29-31 and was then sectioned into test bars. Two of the bars were then run in the exhaust diffuser region of the shroud rig during runs 32-35 to accumulate additional environmental exposure.

In general the ultimate strength and strain to failure were the tensile properties that were most affected by shroud rig exhaust exposure, similar to the observations of steam furnace exposed samples. The relative reduction in these properties for the various samples exposed in the second rig exhaust test, as a percentage of the values determined from the unexposed bars from the same sample panels, are listed in Table 3-59. This data gives a somewhat more quantitative assessment of the degree of degradation that might not be obvious from the above graphs.

Table 3-59. Summary of Tensile Results from Second Exhaust Rig Exposure Tests

Sample Type	Exposure Condition	Relative Ultimate Strength# (%)	Relative Strain to Failure# (%)
GE Prepreg MI	as fabricated (run 333)	84	80
standard matrix	as fabricated (run 396)	105	154
configuration A fiber coating	cracked (run 396)	118	165
	edge exposed (run 396)	115	143
GE Prepreg MI	as fabricated	106	116
standard matrix	cracked	95	100
configuration B-3 fiber coating	edge exposed	115	130
ACI MI	as fabricated	56	45
standard matrix	cracked	0	0
with Hi-Nicalon fiber	edge exposed	59	73
Goodrich MI	as fabricated	93	85
standard	cracked	62	50
	edge exposed	92	80
ACI CVI SiC-SiC	as fabricated	93	100
standard, not seal coated	cracked	95	113
	edge exposed	72	83
ACI CVI SiC-SiC	as fabricated	90	89
standard with seal coat	cracked	91	98
	edge exposed	72	77
ACI DIMOX Al_2O_3-SiC	cracked and exposed edges	60	78
uncoated	edge exposed	59	46

Relative values are the percentage of the same property measured on un-exposed bars from the same sample batch or panel.

3.8.1.9 FOD Coupon Exposure Testing

One of the most demanding aspects of developing a material worthy of turbine use is having it survive instances of foreign object damage, or FOD. FOD can be caused by objects that get sucked into the engine intake, from objects accidentally left inside the engine during assembly or servicing, or by debris coming from upstream compressor, combustor or turbine hardware. Since the flow vector for the combustion gases through the turbine section is largely parallel to the shroud hot gas path face the shrouds are not typically subjected to large amounts of FOD. However, debris entering the turbine can be impacted by the spinning buckets and thrown outward against the shrouds. Consequently the ability of a CMC shroud to survive such an impact event is critical to its overall the success.

There are generally three aspects to consider when evaluating foreign object damage. The first is the effects of the damage immediately caused by the impact event. Clearly traditional monolithic ceramics have had a poor reputation in this regard due to their brittle nature and tendency to fail catastrophically from high velocity impacts. Thus the CMC needs to first simply survive the impact event without catastrophic failure.

The second aspect is the effect that any impact damage may have on the operability of the component, and thus on the engine itself. For instance, a large FOD event on a highly

cooled component, such as a nozzle, could lead to substantial local cooling air leakage paths. The effects of this additional cooling leakage could mean that other components on the same cooling air circuit are now starved of cooling air, and thus overheat and degrade to the point of failure. The extra cooling would also lead to a cold streak condition that could add to the thermal stresses on downstream hardware. Further the flow irregularities caused by the leakages could cause pressure fluctuations that would excite resonant frequencies in buckets, leading to high cycle fatigue failures. Depending on the type of damage, instead of cooling air leaking outward one could also have the situation where hot combustion gases are ingested into the cooling air circuit. Subsequently much of the underlying or supporting hardware, which is typically made of cheaper, less thermally capable alloys, would be at risk. Unfortunately most of these issues are addressed by the overall design of the turbine systems and detailed design of the individual turbine components. The only requirement of the material is to try to minimize the susceptibility to damage so as not to overwhelm the safe guards built into the designs.

The third aspect of FOD damage has to do with how the damage grows with continued operation of the turbine engine. There are few active sensors on most turbine hardware, so FOD events typically go un-noticed by the engine operator. It is therefore possible that a component that has suffered FOD damage will be required to operate until the next engine inspection interval, which could be up to 24,000 hours depending on the component. Materials where impact damage leads to an acceleration of the normal thermal/oxidative/stress degradation mechanisms may not survive over this period.

FOD evaluations of CMC coupons were discussed in section 3.4.5 as a method characterizing damage tolerance. The projectile impact testing followed by steam furnace exposure helped to characterize both the resistance to damage initiation (which was poor for CMCs relative to metals but still much better than monolithic ceramics) and damage growth. However, steam furnace exposures do not simulate the high pressures and gas velocities of a real combustion test. The shroud rig exhaust diffuser section provided a valuable opportunity to do exposure of a FOD-damaged CMC in a more realistic combustion environment.

Two 7.6cm x 15.2cm prepreg MI composite plates were fabricated at GEGR using Hi-Nicalon fiber with configuration A fiber coatings from ACC. Each panel was subject to a room temperature ballistic impact test at GE Aircraft Engines. A compressed gas air rifle was used to “shoot” each panels with a 4.45mm hardened stainless steel ball projectile at a velocity of over 305m/s. The impact energy of 18J was sufficient to punch a hole completely through each plate. The entrance side showed only a round hole with no indications of cracking beyond the impact site. On the exit side there was some enlargement of the hole and indications of delamination, but the observable damage extended to only about two to three times the diameter of the projectile itself. Photographs of one of the as-impacted panels, along with close-up photos of the impact zones, is shown in Figure 3-203.

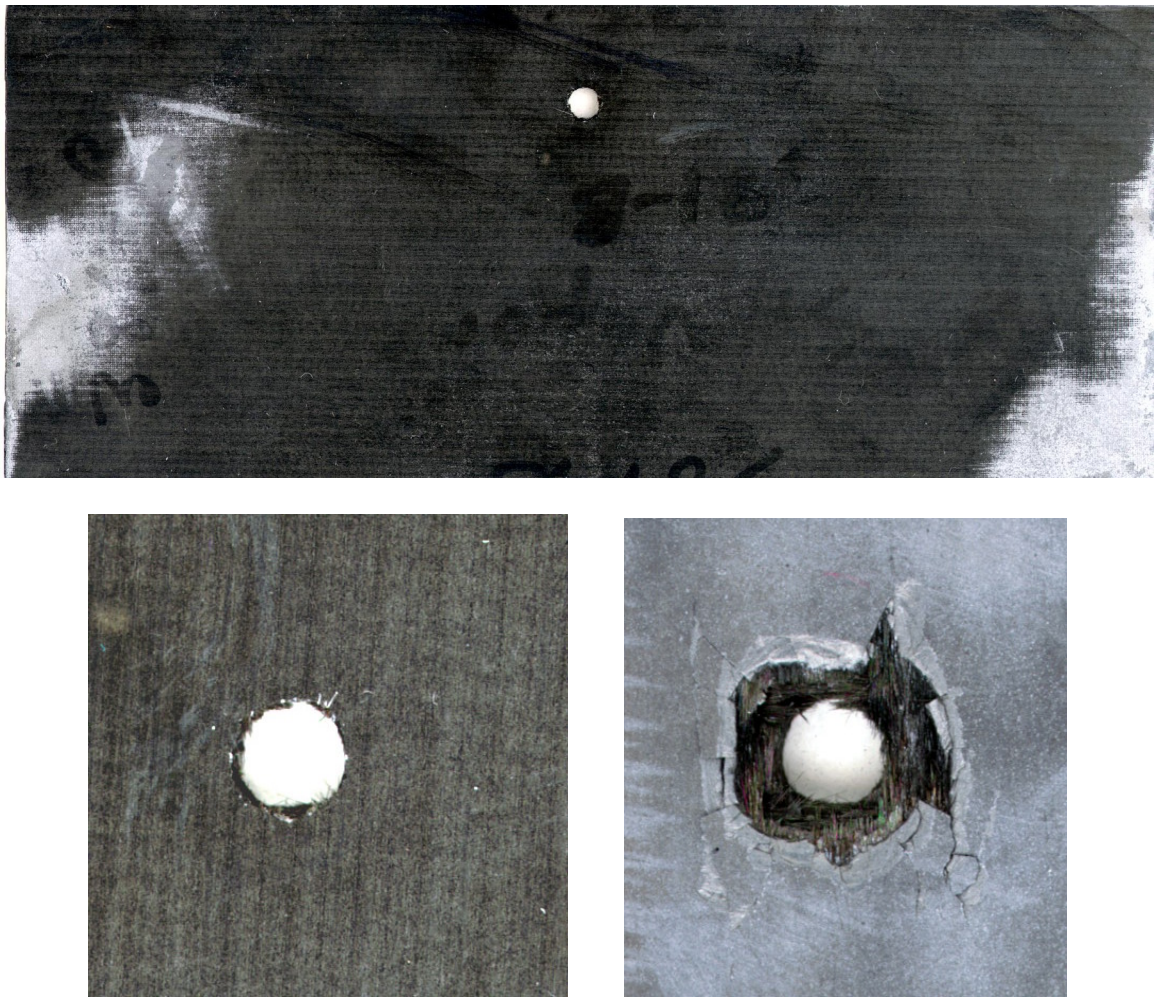

Entrance **Exit**

Figure 3-203. Photographs of a GE Prepreg MI composite panel after ballistic impact testing. Top – overall view of panel showing impact location near one edge. Bottom – close-up views of the projectile entrance and exit sites.

One of the panels from the impact test was then exposed in the shroud rig exhaust diffuser during rig runs 32-35. The edge nearest the impact hole was in the upstream position in the rig, and was thus directly impinged with combustion gas during the exposure. Figure 3-204 shows photographs of the panel after rig exposure along with close-up photos of the impact entrance and exit sites. Following over 150 hours exposure in the shroud rig exhaust section there was no visible extension of the impact damaged region.

Both of the impacted panels were then sectioned into 0.4" wide bars for tensile testing, as shown by the cut lines in the top photo of Figure 3-204. The results of the tensile tests are given in Figure 3-205 for the panel that was impacted but not exposed in the rig, and in Figure 3-206 for the panel that was impacted and then exposed in the shroud rig exhaust section.

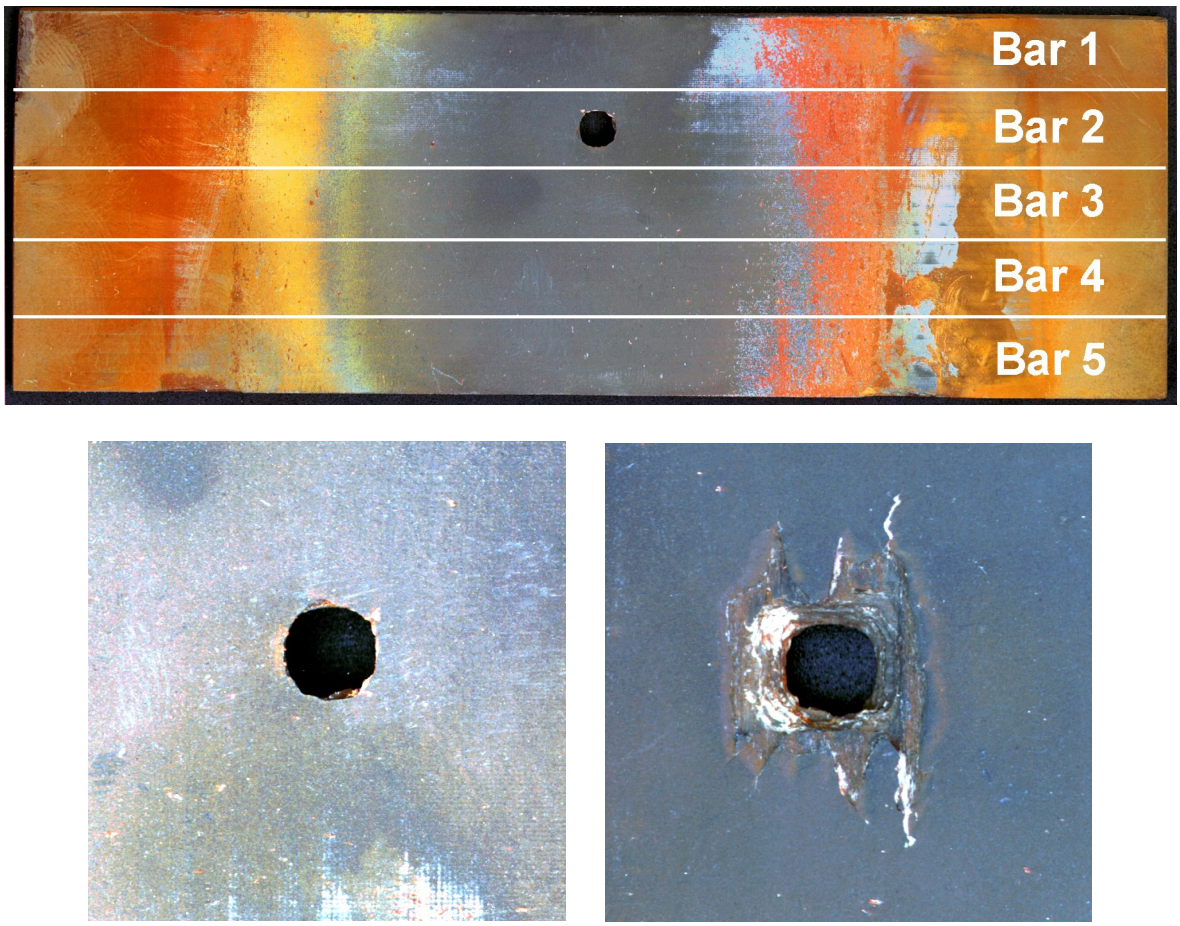

Figure 3-204. Photographs of the FOD panel that was exposed in the shroud rig exhaust section during rig runs 32-35. The white lines in the top photograph show how the FOD panels were sectioned for tensile testing. The bar labels give the position of the bars relative to the impact hole and are used to label the tensile test results in Figures 3-205 and 3-206. Bar #1 was on the leading edge of the exposed panel. The photographs on the bottom show close-up views of the impact site.

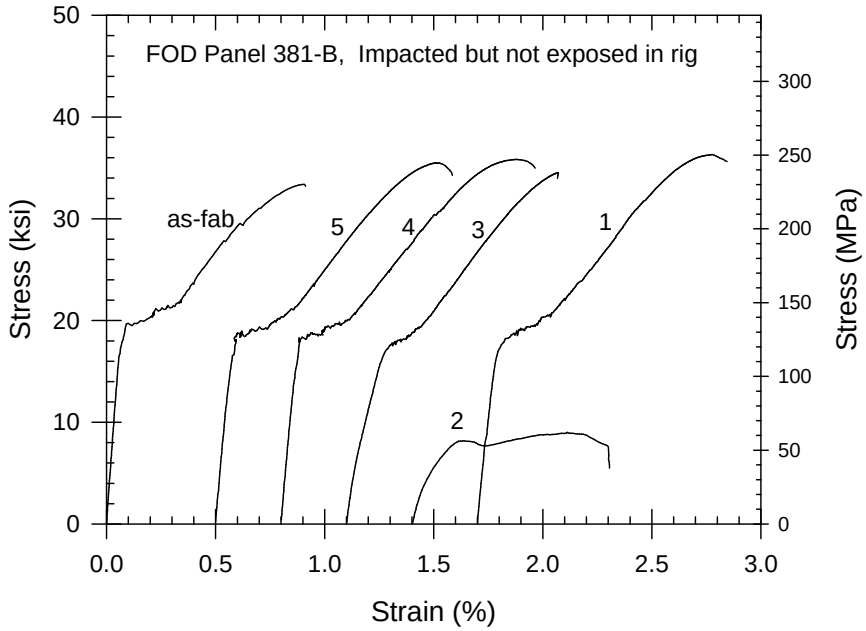

Figure 3-205. Tensile test results from the GE Prepreg MI composite panel following ballistic impact to simulate foreign object damage. The as-fab bar was cut from the panel prior to the impact event. The labels for curves 1-5 indicate the positions of that bar in the panel relative to the impact region, as shown in Figure 3-204.

The results in Figure 3-205 show the extent of damage caused by the impact alone. The damage appears to be very localized near the impact area since test bars immediately adjacent to the impact region show no degradation in ultimate strength or strain to failure. Bar #3 did show a lowered initial modulus and non-linear loading curve suggesting that some of the matrix cracks from the impact probably extended into this bar. The lack of change of the ultimate strength and strain to failure indicate that no appreciable fiber damage occurred away from the immediate impact zone. (Please note that the cross-sectional area for bars #2 in Figures 3-205 and 3-206 are not corrected for the presence of the impact holes so that the actual strength of the remaining material is much higher than indicated by the bar #2 curves.)

Figure 3-206 shows the stress-strain behavior of the panel that was exposed in the shroud test rig. Again, compared to the bar cut from the as-fabricated panel none of bars 3-5 showed any degradation. Since bar 3 is adjacent to the impact zone this indicates that even with high temperature, high pressure combustion gas exposure the damage zone did not propagate appreciably in 150 hours. The other bar adjacent to the damaged zone, bar #1, did show reductions in ultimate strength and strain to failure; however, this degradation appears to have been caused by end-on effects of the leading edge. The leading edge of the panel had some substantial chips and erosion that exposed fiber coatings during the rig test. The fracture surface of bar #1 has normal fiber pullout except for about 1.5mm next to the leading edge of the bar where there is very little pull-out. This suggests that at least part of the degradation seen in bar #1 was caused by edge effects rather than growth of the impact damage zone.

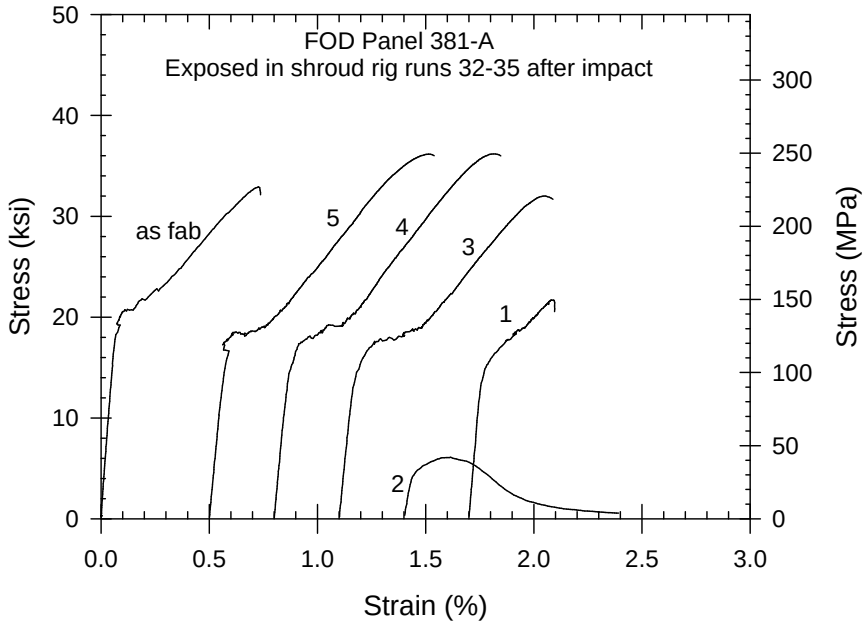

Figure 3-206. Tensile test results from the GE Prepreg MI composite panel following ballistic impact to simulate foreign object damage and then exposed in the shroud test rig for over 150 hours and 50 thermal cycles during rig runs 32-35. The as-fab bar was cut from the panel prior to the impact event and did not undergo rig exposure. The labels for curves 1-5 indicate the positions of that bar in the panel relative to the impact region, as shown in Figure 3-204.

These results on the FOD panels were very encouraging. They indicated that foreign object damage, at least for ballistic damage at 305m/s, is very localized in the composite. Moreover, the damaged region did not grow appreciably after over 150 hours of combustion environment exposure. The possibility of foreign object damage is one of the concerns limiting the application of monolithic ceramics to turbines, as demonstrated by the results in section 3.4.5.4. These preliminary FOD results indicated that CMC materials fulfill their promise of being much more damage tolerant.

3.8.1.10 Next Generation 7FA Shroud Preliminary Design

Following the successful combustion rig tests of the "toboggan" 7FA shroud components, and the success of the GE-2 engine shroud tests to be discussed in section 3.8.3, there was a commitment on the part of GE Energy management to pursue a field engine test of the 7FA shroud. While the toboggan shroud had been a good start, the design process that led to that configuration had not been as rigorous as is required for actual engine hardware. Consequently there was a need for additional shroud design work in order to bring the design up to normal design practice standards. There was also a need to modify and improve the overall shroud system design based on the observations of the shroud rig test. Program Task 3.3.i Large Turbine Component was therefore added to the program as part of the Phase II+ proposal, with work on this task starting in the Spring of 1999.

Overall the CMC inner shrouds were considered to have performed very well in the rig test campaign. However, parts of the metallic attachment features required substantial revision. To some extent, the design of the CMC inner shroud was driven by the need to develop a robust attachment method.

Initially five conceptual designs were developed, which were then reduced to one primary design candidate. Details regarding the shroud component design and configuration are proprietary information of General Electric, and thus are not presented here.

One of the major design considerations was the width of the CMC shrouds. Currently F-class turbines use 3 metallic inner shroud pieces per each outer shroud block. Using fewer inner shroud pieces, such as 2 or 1 per outer shroud block, would decrease sealing leakages between the shrouds. However, because the attachment areas are intentionally cooler than the gas-path face the shrouds tend to curl in the transverse direction from this thermal gradient. This thermal deformation and the stresses induced by it increase with increasing shroud width. Thermal and structural FEM analysis of the expected deformations indicated that increasing the width of the shroud to be one CMC inner shroud per outer shroud block would cause excessive thermal deformation and thermal stresses. At three inner shrouds per outer shroud block the stresses were considerably lower and could be kept within material strength limits.

The GE design team had been focusing on a 7F class turbine component for possible engine testing, and several 7FA engines had been identified as potential testing sites. However, the availability of engines for such testing depends on several factors beyond GE's control, such as engine maintenance schedules and customer willingness to participate in the test. For these reasons eventual testing in a 7F class machine could not be guaranteed, and thus allowances had to be made use of an alternate test vehicle. GE has a large installed fleet of E-class turbines (7E and 6E) which could also serve as suitable sites for a shroud rainbow test; however, the current metallic shrouds in these machines, and thus the design constraints applied to the CMC shroud design, differ from those of the 7F class of engines. Thus the design of a CMC shroud for an E-class machine would necessarily differ from that of an F-class machine. Rather than dilute the manpower, and thus the effort, assigned to the 7F shroud design the design of a 7E shroud using was pursued using external design resources. The 7E shroud design effort was directed by design engineers at GE Power Systems, but the model generation and FEM analyses were done by an external engineering service. The particular engineering service selected had considerable experience in designing turbine components using CMC materials from previous work done under the NASA-sponsored HSCT program. Because much of the design work done for the 7F shroud also applies to the 7E shroud concepts, and because testing of a 7E shroud is only being considered as a potential back-up to the testing of a 7F shroud, the design effort needed on the 7E shroud was smaller than what had been needed for the 7F shroud.

Continuous refinements to the design were made throughout 1999. A preliminary design review for the CMC 7FA shroud system was held with the GEPS Chief Engineer's Office on December 13, 1999. Detailed heat transfer and cooling flow models were developed to

predict the gas velocities and temperatures throughout the inner and outer shroud regions. The results of these models were used to define the boundary conditions for the ANSYS finite element analyses. Combined thermal and structural analyses were done using a constant CMC component geometry and the material physical properties of GE's prepreg MI composite.

Following the preliminary design review additional design modifications were made to the CMC shroud design. Most of the excessive thermal stresses in the preliminary design were related to the larger thermal gradient around the leading edge of the shroud. The leading edge was subsequently modified to reduce the thermal gradient by modifying the shroud shape and attachment configuration. These changes also made the CMC inner shroud easier to fabricate.

This revised design was reviewed by the GE Energy Chief Engineering Office in April 2000. At that review the general shape and function of the CMC shroud design, including the new attachment scheme, was approved. Approval of the shroud design by the Chief Engineers' office marked the completion of program milestone 70.

At this point in the CFCC program GE had submitted a separate proposal to DOE-EE under the "Advanced Materials for Advanced Industrial Gas Turbines" program to carry forward with the design and testing of a 7F shroud component. Consequently no additional design work on the shroud was done under the CFCC program.

3.8.2 Frame 5 Combustor Fabrication and Testing

The purpose of this task was to design, fabricate and combustion rig test a combustor system incorporating a CMC combustor liner. This work was done under program Task 3.3.b Combustor Liner Fabrication and Testing, which was added to the CFCC Phase II contract in 1997.

The particular combustor system selected was that of a "Frame 5" size gas turbine engine, which was selected for several reasons. The first reason had to do with the potential benefits and market for such a combustor system while minimizing technical risk to the program. Although substantial benefits are possible by introducing ceramic components in large industrial gas turbines, to reduce the risk of their introduction it was at that time considered likely that ceramic components would first be introduced in smaller industrial machines, primarily as a vehicle for upgrades in older machines. GE has a large fleet of industrial gas turbines worldwide, including about 3500 Frame 3 and 5 machines with a power output of less than 40MW. These machines incorporate thirty year old combustor and turbine technology which results in high NOx emissions and low fuel efficiency compared to current gas turbine standards. This installed base represents a good opportunity for firing temperature up-rates to improve efficiency and increase output power. There is also the opportunity to greatly reduce the NOx emissions with modifications to the combustor system.

Secondly, the Frame 5 combustor was also a reasonable size and shape component to attempt. As discussed in Section 3.8.1.4, small (~10cm diam. x ~15cm long) cylindrical combustor liners were fabricated and used with great success in the shroud combustion test rig. The next step in combustor development would be to do a larger combustor liner, but to maintain the simple cylindrical shape for ease of fabrication. A Frame 5 liner, being essentially a cylinder 28cm in diameter by 112cm long, was still substantially longer than would be convenient to fabricate at that time. However, combining the new CMC liner with improved Dry Low NOx (DLN) fuel nozzles/premixers would allow the combustor liner to be shortened to ~30cm, making it feasible to be made from CMC. Also, the shorter liners were less expensive to fabricate, and allowed for the simultaneous testing of two CMC liners in the combustion test cell.

The third reason had to do with the existing combustion testing capability at GEGR. The Frame 5 liner was at the limit with regard to size of what could be accommodated in combustion tests at GEGR. Moreover, a concurrent combustion testing program was ongoing with metallic Frame 5 liners. Testing of the CMC liners could be "piggybacked" on this metallic liner testing effort, thereby minimizing the amount of extra combustion test hardware that would be needed.

Therefore, the goals established for this task were to fabricate and rig test combustor liners equivalent in diameter to the Frame 5 combustion cans (~28cm diam.), but only 25.4cm long. An existing Frame 5 combustor liner was to be modified to accept two cylindrical CMC test liner sections for the purposes of rig testing. The CMC Liners would be fabricated by GEGR using the Pre-Preg MI approach, and by CCP (then know as DuPont-Lanxide Composites, Inc.) using the slurry casting MI approach, both with Hi-Nicalon™ reinforcing fibers. These material systems were selected based on the good results these materials were giving in the steam furnace testing and in the shroud rig tests. Also, DuPont-Lanxide Composites also had its own CFCC program at the time that was used to support the fabrication of the slurry cast liner. The testing goal was to do exposure testing in the high pressure combustor rig for up to 200 hours under typical gas turbine operating conditions.

3.8.2.1 Testing of Baseline Metallic Combustor

The objective of this task was to generate aerothermal design models for GE MS5002 (or "Frame 5") gas turbine combustors using high pressure rig and field data. The data, such as metal temperatures, NOx and CO emissions, air flow splits and pressure drops, and the models were critically needed to effectively design and test the shorter ceramic combustors (25.4cm in comparison to 112cm for the metallic combustor). The performance data was also needed to provide a baseline for a Frame 5 liner against which the performance of the CMC liners could be judged and projected to actual performance in the field.

The MS5002B turbine used in field testing had a pressure ratio of about 8.5:1, a compressor discharge temperature of about 290°C and a net power output of about 28MW. It had 12 combustors arranged in a can-annular configuration. The base load combustor exit temperature is 953°C (1747°F) at ISO conditions.

A combustion test rig was designed and built capable of accommodating a standard, full size Frame 5 combustor. As shown in Figure 3-207, this rig utilized as many standard Frame 5 gas turbine components as possible, including a Frame 5 combustor casing and endcover as parts of the pressure vessel. The fuel injector, fuel supply, air supply, exhaust and data acquisition system were all custom built to connect with existing laboratory facilities. The CMC liner rig also used a standard Frame 5 combustor casing and endcover. Construction and set-up of the CMC liner rig was therefore much easier since interfacing issues for connecting these components to the existing laboratory facilities had already been solved.

The Frame 5 combustor facility was used both to map out the aerothermal operation of two different baseline configurations and to generate baseline performance data for the metallic combustors. A standard and a "Lean Head End" (LHE) combustor were tested at two different pressures over a range of combustor exit temperatures. The LHE liner is a new, reduced NOx combustor developed by GE that is very similar to the standard metallic liner but with a different effective area distribution. A selection of test points and results for the standard liner are shown in Table 3-60. Both the baseline and LHE combustors were tested at a variety of pressures, air flow rates and fuel flow rates so as to measure their performance over a wide range of operating conditions. This also allows for extrapolation of the rig data to engine operating conditions.

Important performance parameters that were measured included liner temperatures (which are critical to predicting liner life), emissions of oxides of nitrogen (NO_x) and carbon monoxide (CO). Figure 3-208 shows that the metallic liner, which utilizes conventional film cooling, typically operates with metal temperatures that are substantially (~380°C) lower than the bulk average combustor exit temperature. While these low temperatures ensure long liner life, they can result in significant CO emissions due to the cold liner walls. Metal temperatures do not vary significantly with combustor pressure.

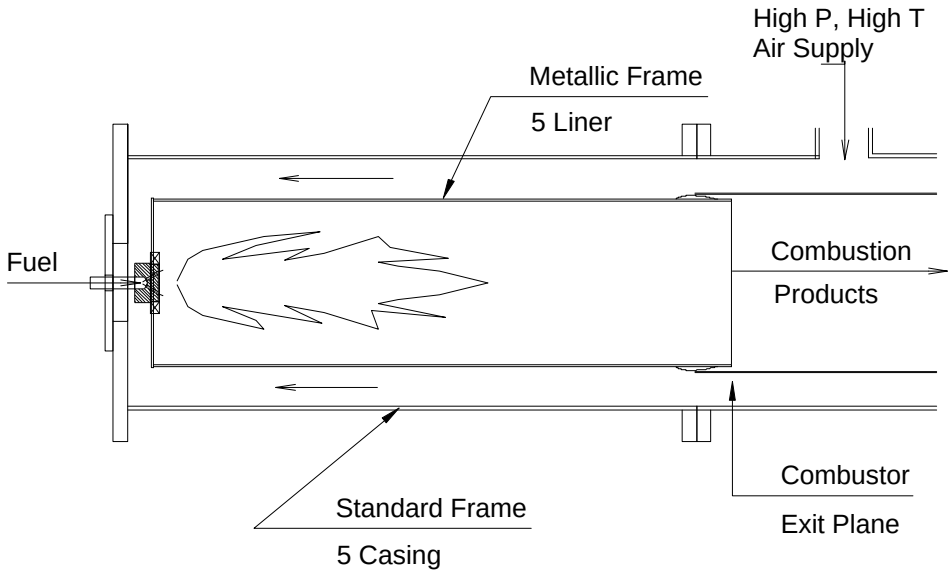

Figure 3-207. Schematic of the high pressure Frame 5 test rig, used for both baseline metallic Frame 5 combustors and the CMC Frame 5 combustors.

Table 3-60. Test Conditions for the Baseline Metallic Frame 5 Combustor.

Pressure (bar)	Air Flow Rate (kg/s)	Fuel Flow Rate (kg/s)	Equivalence Ratio	Combustor Exit Temperature (°C)
4.59	5.35	0.054	0.164	707
4.69	5.35	0.059	0.180	748
4.78	5.35	0.064	0.195	783
4.87	5.35	0.068	0.212	821
4.95	5.35	0.072	0.225	852
5.05	5.35	0.078	0.245	893
5.16	5.35	0.085	0.265	938
5.23	5.35	0.089	0.277	966
5.30	5.35	0.093	0.292	998
5.37	5.35	0.144	0.305	1023
5.43	5.35	0.150	0.317	1049
2.78	3.27	0.047	0.165	706
2.83	3.27	0.051	0.178	737
2.93	3.31	0.056	0.190	767
2.98	3.31	0.060	0.205	801
3.03	3.31	0.065	0.221	836
3.07	3.31	0.069	0.234	865
3.12	3.31	0.073	0.247	895
3.17	3.36	0.076	0.257	918
3.20	3.31	0.080	0.270	946
3.26	3.31	0.083	0.284	977
3.27	3.31	0.086	0.292	994
3.32	3.31	0.090	0.304	1019
3.37	3.31	0.094	0.321	1056

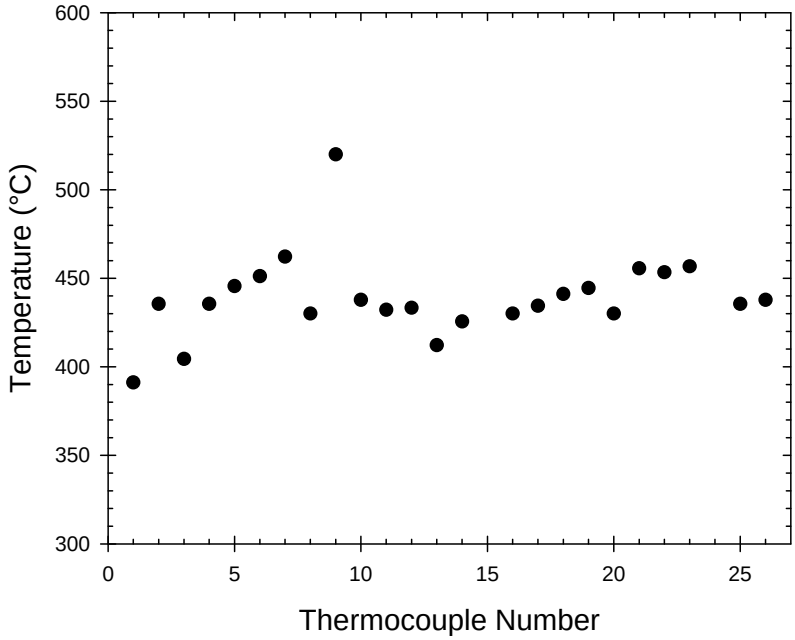

Figure 3-208. Typical measured temperatures of baseline metallic Frame 5 combustor.

Figure 3-209 shows NOx produced during the laboratory rig tests (in parts per million, dry, corrected to 15% O_2) as a function of combustor pressure and exit temperature. The corresponding CO versus exit temperature curve is shown in Figure 3-210. Each combustor was tested at two different total flow rates and pressures, because the total air flow through an MS5002 engine combustor (about 9.5 kg/s or 21 lbm/s at base load) exceeds the capacity of the laboratory air compressors. This is not a significant problem as standard design practice is to scale the emissions results from these lower pressure tests to full pressure conditions. In general, laboratory NOx emissions are proportional to p^n, where p is the absolute pressure and $0.3 < n < 0.5$. Through testing at two different pressures, we can determine the pressure exponent n for each combustor and scale lab NOx emissions to full flow and pressure. A regression analysis of the data in Figure 3-209 resulted in pressure exponents of $n = 0.36$ for the standard combustor and 0.40 for the LHE combustor. Laboratory CO emissions are generally found to be insensitive to pressure and do not require scaling. This can be seen clearly in Figure 3-210, which shows no variation of CO with pressure.

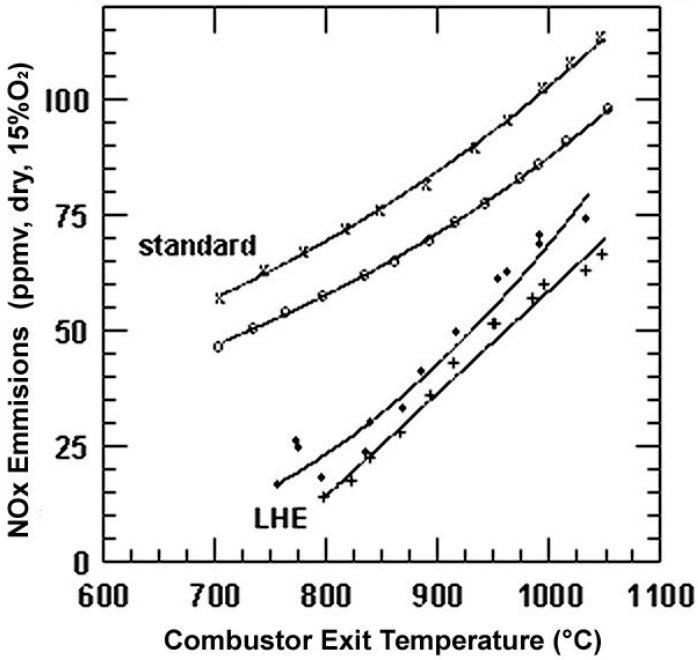

Symbol	Combustor	Air Flow (kg/s)	Pressure (bar)
x	standard	5.4	5.0
o	standard	3.3	3.1
*	LHE	6.0	5.4
+	LHE	4.2	3.8

Figure 3-209. Typical NOx variation with combustor exit temperature for baseline and "Lean Head End" (LHE) metallic Frame 5 combustors during laboratory rig testing.

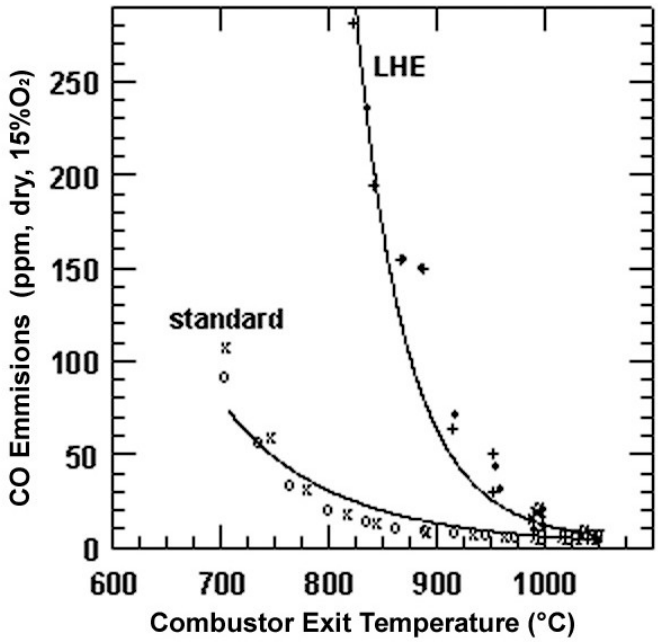

Figure 3-210. Laboratory measurements of CO emissions from standard and "Lean Head End" (LHE) combustors at the same conditions as shown in Figure 3-209.

In order to confirm the relationship between the performance data measured in the lab and those actually found in an operational gas turbine, 2 trips were made to an MS5002B gas turbine operating on the north slope of Alaska. Performance data were measured for standard metallic liners during the first trip and for the LHE liners during the second trip. Figures 3-211 and 3-212 show the NOx and CO emissions from the MS5002B turbine. Also shown on Figure 3-211 are the NOx emissions predicted from the laboratory data. The agreement is quite good.

These tests were a valuable precursor to the CMC combustor tests. The test rig design, test procedures, data acquisition system, and data reduction practices developed during the course of this task were used to perform testing of the CMC Frame 5 liners. The aerothermal models and the performance data were used to help design the CMC combustor. The lab to field relationships were used to predict CMC combustor performance during actual gas turbine operation.

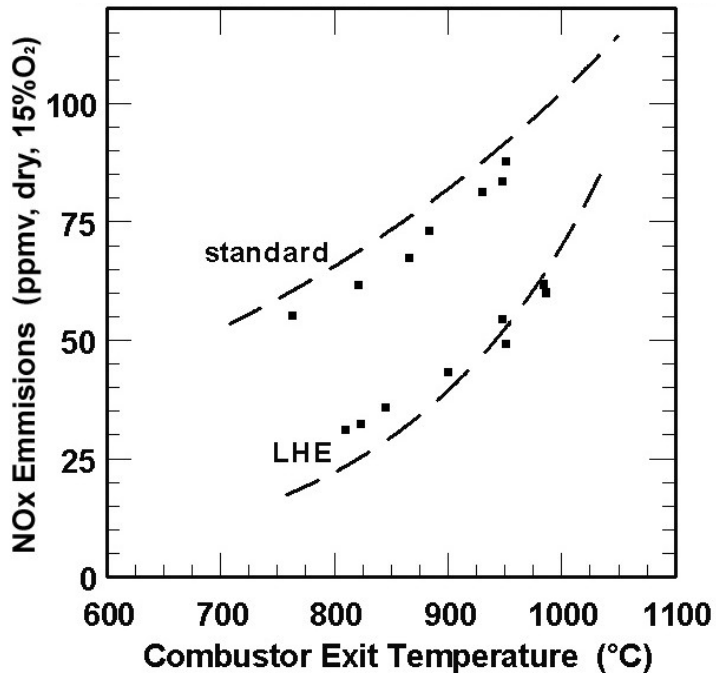

Figure 3-211. NOx emissions from an MS5002B turbine equipped with standard and "Lean Head End" (LHE) combustors. Compressor discharge temperature = 269 ± 9°C for all points. Symbols represent field measurements, while dashed lines represent expected values, based on laboratory measurements corrected to field fuel composition, pressure and compressor discharge temperature.

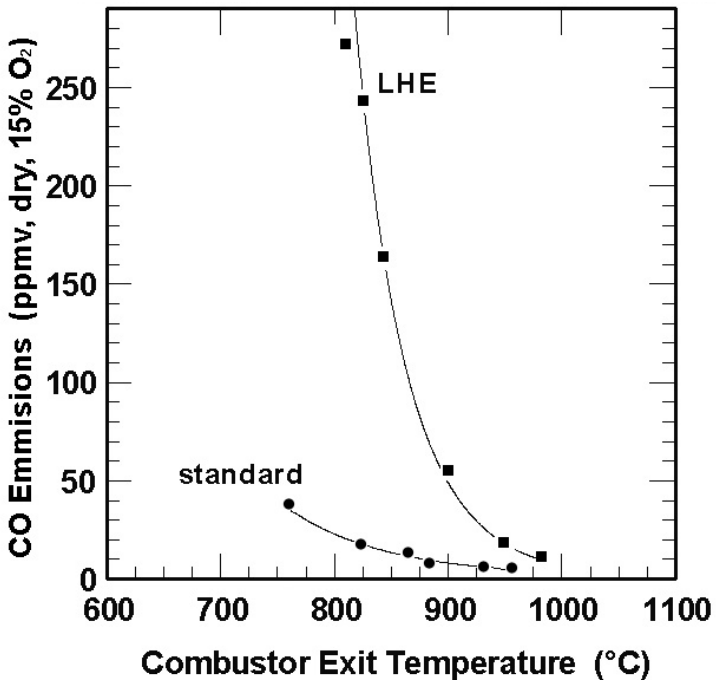

Figure 3-212. CO emissions from an MS5002B turbine equipped with standard and "Lean Head End" (LHE) combustors at the same conditions as shown in Figure 3-211.

3.8.2.2 Combustor Design and Analysis

Overall the CMC Frame 5 combustor liner needed to accommodate two short CMC liner segments and still fit into the combustion test cell that was already equipped to handle a metallic Frame 5 liner. The Frame 5 combustor is a typical can-annular design where the compressed air from the compressor flows along the outside of the liner from the combustor exit end toward the "head end" where the fuel nozzle(s) are located. The air then turns180° to enter the inside of the combustor liner through the combustor cap / fuel nozzle assembly. (In the existing Frame 5 combustor configuration air also enters the inside of the combustor liner through various dilution and film cooling holes in the cap and liner itself, but such dilution holes would be largely eliminated in a low NOx combustor system.) The most straightforward approach to meeting these needs was to actually cut apart an existing metal liner and modify it to hold the two CMC liner segments. In this way all of the attachments, seals and liner-to-pressure vessel interfaces of the metallic liner could be retained in the rig test liner without complicating the design of the CMC parts. Thus the only requirement on the CMC liner segments was that they match in dimension the ID surface of the metal liner, resulting in a simple straight cylinder shape for the CMC liner segments.

The overall liner design concept that was developed is shown schematically in Figure 3-213, which shows the liner as it would be positioned inside the combustion test cell pressure vessel. As with an actual engine combustor, the compressed air would enter near the exhaust end of the pressure vessel and then flow back (right to left in Figure 3-213) around the outside of the combustor liner to the head end of the combustor. The compressed air would then enter the combustor through the fuel nozzle and combustor cap. The liner cap was modified to accommodate either a diffusion flame type fuel nozzle or a premixed DLN-type fuel nozzle. The natural gas fuel would then be burned with the combustion gases flowing inside the combustor liner to the exhaust plenum (left to right in Figure 3-213).

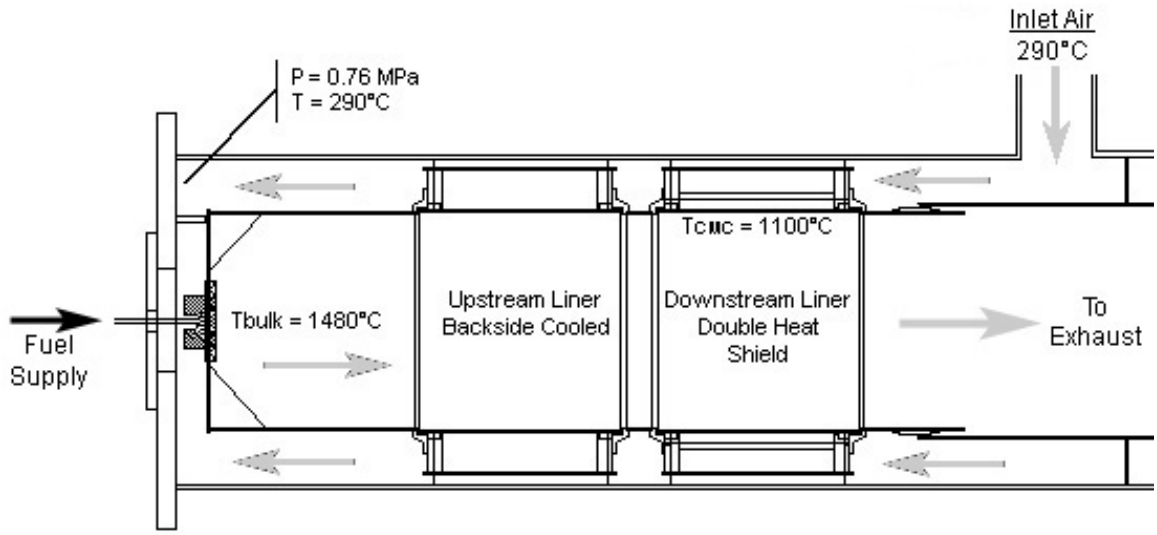

Figure 3-213. Schematic diagram of the CMC-modified Frame 5 combustor liner inserted into the combustion test cell.

One important consideration was the amount of cooling to apply to the CMC liners. Allowing the compressed air to flow along the outside of the CMC liners and provide convective cooling would impose no performance penalty, in the form of increased pressure drop, on the combustor. With this convective cooling of the liner the CMC would run at relatively low temperatures, thereby ensuring long liner life. However, part of the benefit of using CMC liners would be from the elimination of cool liner walls, which lead to flame quenching near the walls and increased CO emissions. Thus elimination of backside cooling from the CMC liners would help to maintain a high combustor wall temperature and decrease CO. In order to test the CMC liners under both the cooled and uncooled conditions a double-walled flow and heat shield was added to the downstream liner position to prevent the compressed gas flowing outside the liner from actually contacting the liner. In the other, upstream position no heat shields was used, thereby allowing full convective liner cooling. The two CMC liners to be tested could be exposed under both conditions by simply changing their positions within the combustor.

The main challenge in the design of the combustor, as it is with most ceramic components, was the attachment between the CMC liners and the metallic support structure. The attachment had to accommodate the large differences in thermal expansion of the CMC and metallic parts and yet constrain the liners adequately to prevent excessive vibration or leakage of the compressed air through the liner wall. The design that was developed was to trap the liner axially between metallic flanges and to use external seals near the ends of the CMC sections to hold the liner in place radially, and yet still allow for differential thermal growth. A more detailed schematic drawing of the liner attachment scheme is shown in Figure 3-214.

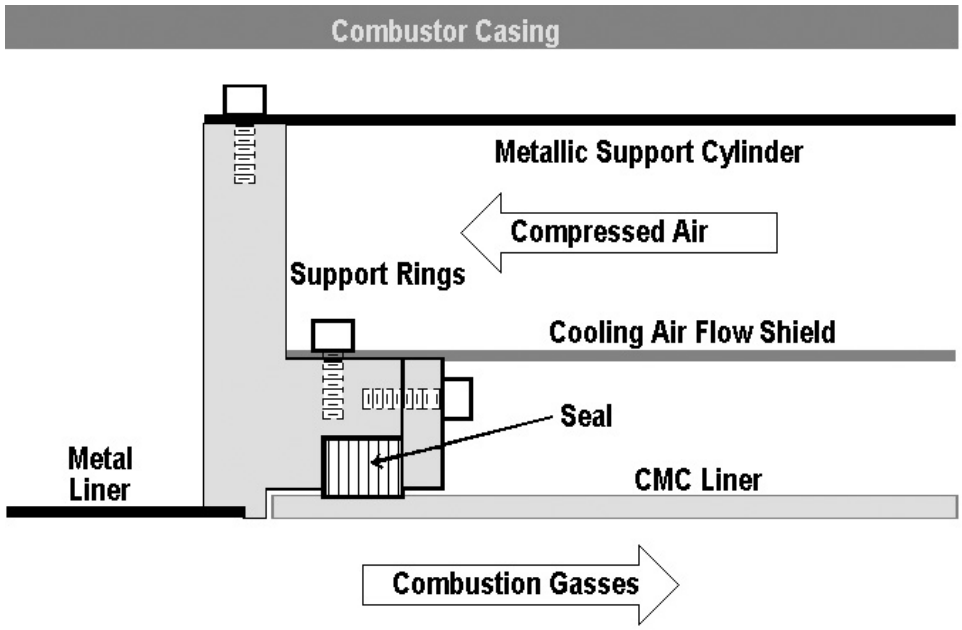

Figure 3-214. Schematic drawing of the liner attachment configuration in the CMC Frame 5 test combustor.

Several seal concepts were considered for use in the combustor. Simple metallic leaf "C" or "W" seals were rejected due to insufficient elasticity at temperature. During combustor operation the temperature of the seal could climb as high as 1000°C. Creep relaxation and oxidation of a metallic seal at these temperature would lead to a reduction in seal effectiveness. Rope seals consisting of carbon fiber in a nickel wire overbraid had been used previously in the combustion test facility with other programs, but the lack of oxidation resistance of this rope limited its use to temperatures and times much lower than were needed for this combustor. A rope seal of braided Nextel™ fiber was also evaluated. This material had sufficient temperature capability and the compliance of the rope could be controlled by the configuration of the braid. It also had a relatively low thermal conductivity, which was advantageous in minimizing thermal gradients in the liner. However, there were concerns about the abrasion durability of this rope during thermal cycling, and the cost was rather prohibitive.

The seal configuration finally chosen for the liners was to use a set of nested rings, similar to piston rings, that alternately contacted the CMC liner or the outer metallic support ring. A close-up schematic of this type of seal is shown in Figure 3-215. The larger rings are compressed to fit into the metallic support ring, and the smaller rings are expanded slightly to fit over the CMC liner. The rings are then loosely captured in a channel in the metallic support ring so that the rings can expand outward at independent rates during thermal excursions. Axial thermal growth is accommodated by sliding between the inner rings and the CMC liner surface. The temperature of the seal rings is moderated somewhat by any leakage air, but it still required that the rings be made of a high temperature alloy, namely Hastelloy X. The inner surfaces of the rings that contacted the CMC liners were also

coated with ZrO_2-based TBC to further reduce the temperature of the rings and to serve as a reaction barrier between the metallic rings and MI CMC.

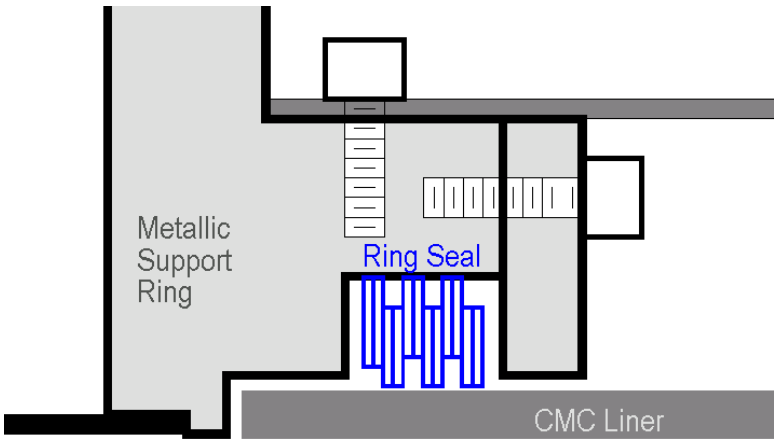

Figure 3-215. Close-up schematic of the nested ring seal design.

ANSYS FEM analysis was used to predict the temperature and stress distributions in the ceramic liners. The four main factors affecting both distributions were the combustion gas temperature profile, the heat transfer coefficients from the hot combustion gas to the liners, whether backside convective cooling was or was not applied to the liner, and the amount of leakage air flowing through the ring seals. Surprisingly, the temperature and heat transfer coefficient profiles had not been well characterized even for standard metallic Frame 5 combustor liners. Consequently 3-D Computational Fluid Dynamic (CFD) and Flownet calculations were required to define the combustion gas heat load to the liners. An example of the CFD calculation results for heat transfer coefficient on the combustor surface using a 1/3 sector and DLN fuel nozzle is shown in Figure 3-216.

The combustion gas temperature profile depends on the type of fuel nozzle used and on whether the combustion dilution holes in the metallic sections of the liner remained open or were plugged. Calculations of the bulk average combustion gas temperature as a function of axial distance along the combustor are shown in Figure 3-217. With diffusion flame combustion the peak in the temperature distribution is higher than for premixed combustion, which is as expected and is the reason for the lower thermal NOx produced by the premixed combustion configuration. However, once the air from the first row of dilution holes gets mixed in to the diffusion flame the gas bulk gas temperature drops back to the level of the premixed combustion configuration. Normally in the metal liners there is a second set of dilution holes that would correspond in axial position with the section of metal liner in between the two CMC liner sections. If these holes were allowed to remain open the extra dilution air would further depress the combustion gas temperature at the downstream CMC liner position. If the second row of dilution holes was plugged, however, the gas temperature decreased only slightly along the remaining length of the liner due to normal heat loss to the liner.

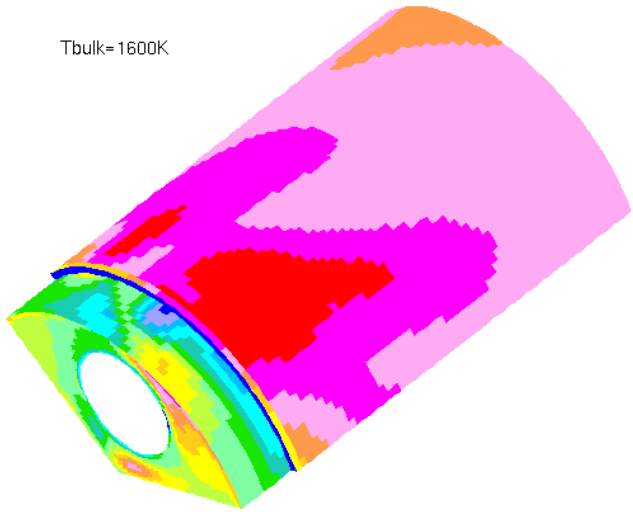

Figure 3-216. Example of 3-D CFD computation results for the heat transfer coefficient on the inside of a Frame 5 combustor using DLN type premixer/fuel nozzle. A one third sector is shown.

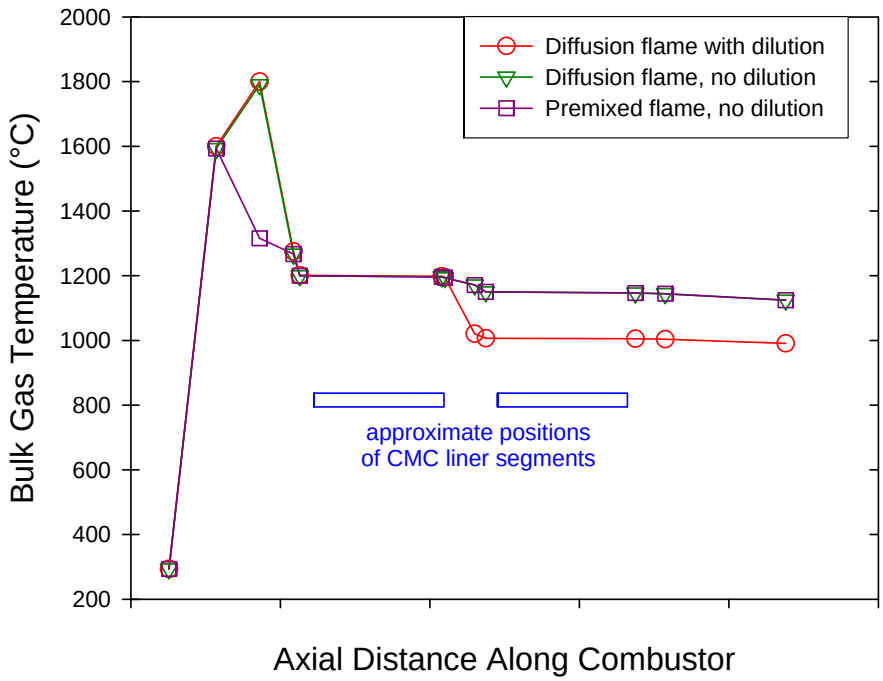

Figure 3-217. Combustion gas temperature profile along the axial direction of the test rig combustor for diffusion flame, both with and without blocked dilution holes between the CMC liner position, and for premixed flame conditions.

The ANSYS analyses were run by mapping the calculated gas temperature and heat transfer profiles onto the inner surface of the combustor liner, applying the pressure loads resulting from the pressure drop from the outside to the inside of the combustor liner, and then calculating the thermal and stress distributions for the CMC liner segments. Whether or not backside convective cooling was applied to the CMC liner had a large impact on the liner temperatures, but did not have a substantial impact on the calculated stresses. The main factor affecting the thermal stresses in the CMC liners was the amount of heat extracted from the liners at the attachment/seal locations. The cooling of the ends of the liner segments from the heat losses set up axial thermal gradients that induced high tensile hoop stresses at the ends of the CMC liners. In these regions the temperature of the liner was a strong function of the assumed leakage of the seal and the amount of thermal conduction allowed through the rings. Using a "tight" seal would minimize cooling from air leakage, but increase cooling from thermal conductivity through the rings. Using a "loose" or leaky seal reduced conductive heat loss, but increased the cooling of the ends of the CMC liner segments from the leakage air. A tradeoff study indicated that minimizing air leakage through the seal was the most beneficial situation for reducing liner thermal stresses. Applying TBC coating to the inner surfaces of the rings that contacted the CMC liners also minimized the heat loss via conduction through the seal rings.

3.8.2.3 Combustor Rig Fabrication

As noted earlier, the majority of the hardware for the combustor testing facility had already been installed and instrumented as part of a previous GE study on metallic Frame 5 liners. The only hardware that needed to be fabricated for the CFCC program was the modified Frame 5 metallic liner and the CMC liner segments themselves. The metallic portion of the Frame 5 test combustor liner was fabricated by cutting sections out of a standard metallic liner and welding in the metallic support rings. The support rings were bolted to "metallic support cylinders" outside of the CMC liners that provided the mechanical integrity to the overall liner that was lost by cutting out the liner wall sections. A photograph of the modified CMC test liner is shown in Figure 3-218.

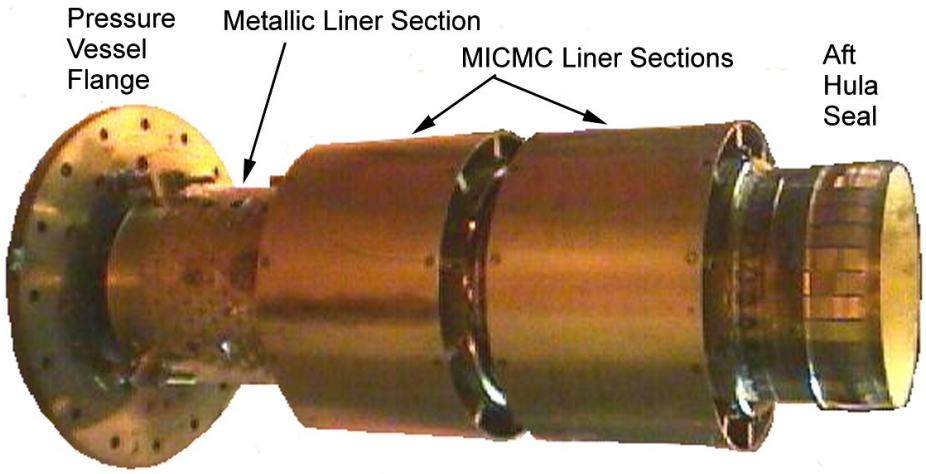

Figure 3-218. Photograph of the modified CMC Frame 5 combustor liner fully assembled and mounted onto the test cell pressure vessel flange.

3.8.2.4 CMC Combustor Liner Fabrication

Two CMC combustor liners were fabricated for rig testing. One of the liners was obtained from CCP (then known as DuPont-Lanxide Composites, Inc.) as part of their separate CFCC program. This liner was made using Hi-Nicalon™ fiber, in the form of 5-harness satin cloth, and the slurry cast MI process. The second liner was made at GEGR using Hi-Nicalon fiber and the prepreg MI composite process. The fiber used for this liner was coated in GEGR's small tow coater using coating configuration A.

Developing a fabrication process, and in particular the infiltration procedures, for making this liner required several experiments. The lay-up process was similar to what was used for the small shroud test rig liner in that the hoop plies were directly wound onto a cylindrical mold, and the axial plies were pre-wound and then laid onto the cylinder by hand. A photograph of the drum winding process for one of the hoop plies of a trial liner is shown in Figure 3-219.

Successful fabrication of dense prepreg liner with good mechanical properties required several processing trials. Attaining complete infiltration was particularly challenging, and required performing infiltrations using a large (1.2m x 1.2m x 1.4m working volume) vacuum furnace at GE Lighting, Quartz and Chemical Products in Cleveland, OH. Temperature control modifications and calibrations needed to be done on this furnace in order to reproduce the infiltration conditions of the furnace at GEGR. Success of this effort is demonstrated by the data in Figure 3-220, which shows the tensile properties of witness coupons infiltrated at GEGR and infiltrated in the GE Lighting furnace during calibrations and during infiltration of the final Frame 5 liner component.

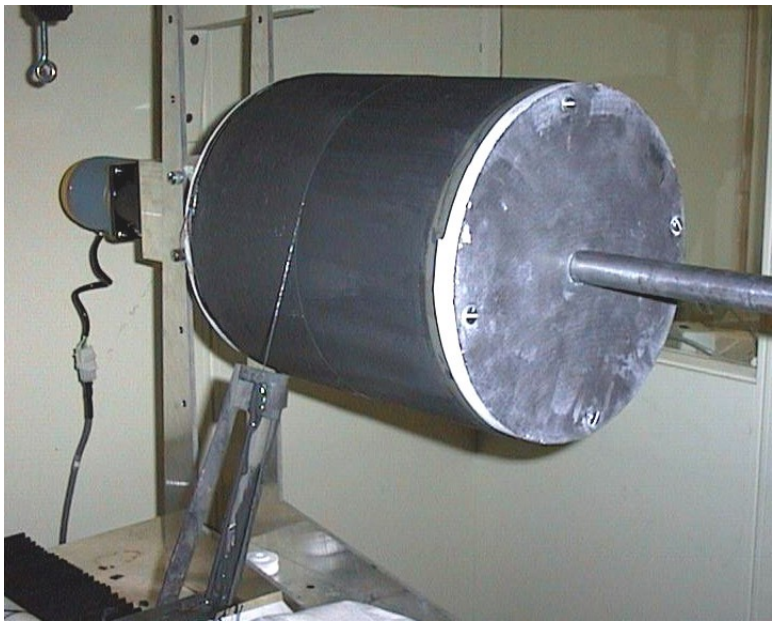

Figure 3-219. Photograph of drum winding process for applying hoop-oriented plies to a Prepreg MI Frame 5 combustor preform. This particular liner was built on a carbon mandrel with BN spray coating (white) on the surface.

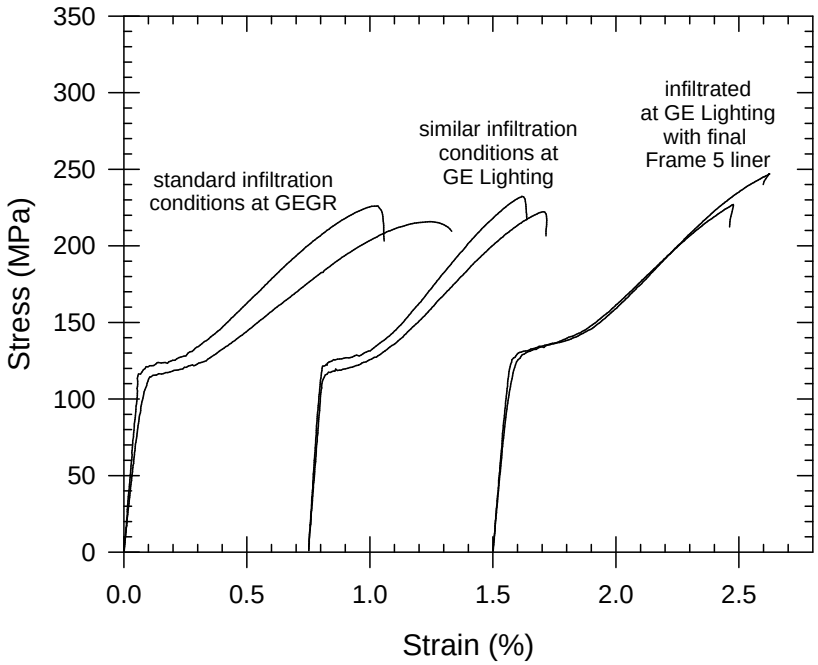

Figure 3-220. Tensile stress-strain behavior of Prepreg MI composite test samples from a single panel that were infiltrated at different times and in different furnaces. The bars infiltrated in the GE Lighting furnace showed comparable or better properties than equivalent bars infiltrated at GEGR, thereby indicating the attainment of comparable infiltration conditions at both locations.

Both the GE Prepreg MI and the CCP slurry cast MI liners were sent to Argonne National Lab for NDE inspection. The Prepreg liner was inspected by transmission IR thermography, air-coupled ultrasound and water-coupled ultrasound. The slurry cast liner was inspected only by IR thermography and air-coupled ultrasound. The images generated from these inspections are shown in Figures 3-221 and 3-222 for the prepreg and slurry cast liners, respectively.

The IR image of the Prepreg liner shows some localized defects along the top edge, most of which correspond to minor delaminations induced by ply wrinkles. However, none of these defects extends the full width of the liner. The vertical stripes on the Prepreg liner water-coupled ultrasound image are a result of localized thickness variations caused by the infiltration mandrel surface modification that was used to enhance infiltration and do not represent actual material defects.

The NDE images for the slurry cast liner show a distinct periodic pattern probably caused by localized variations in density. The pattern is not related to the weave of the cloth used for fabrication of the liners as the size and periodicity of the features is an order of magnitude larger than the pattern of the weave. Rather the pattern in the NDE images correspond to the spacing of holes in the CVI tooling used during fabrication of the liner. The extent of SiC vapor infiltration thus varies in the composite according to the pattern of the tooling holes, and this variation apparently carries over to the local density of the material in the final part even after melt infiltration.

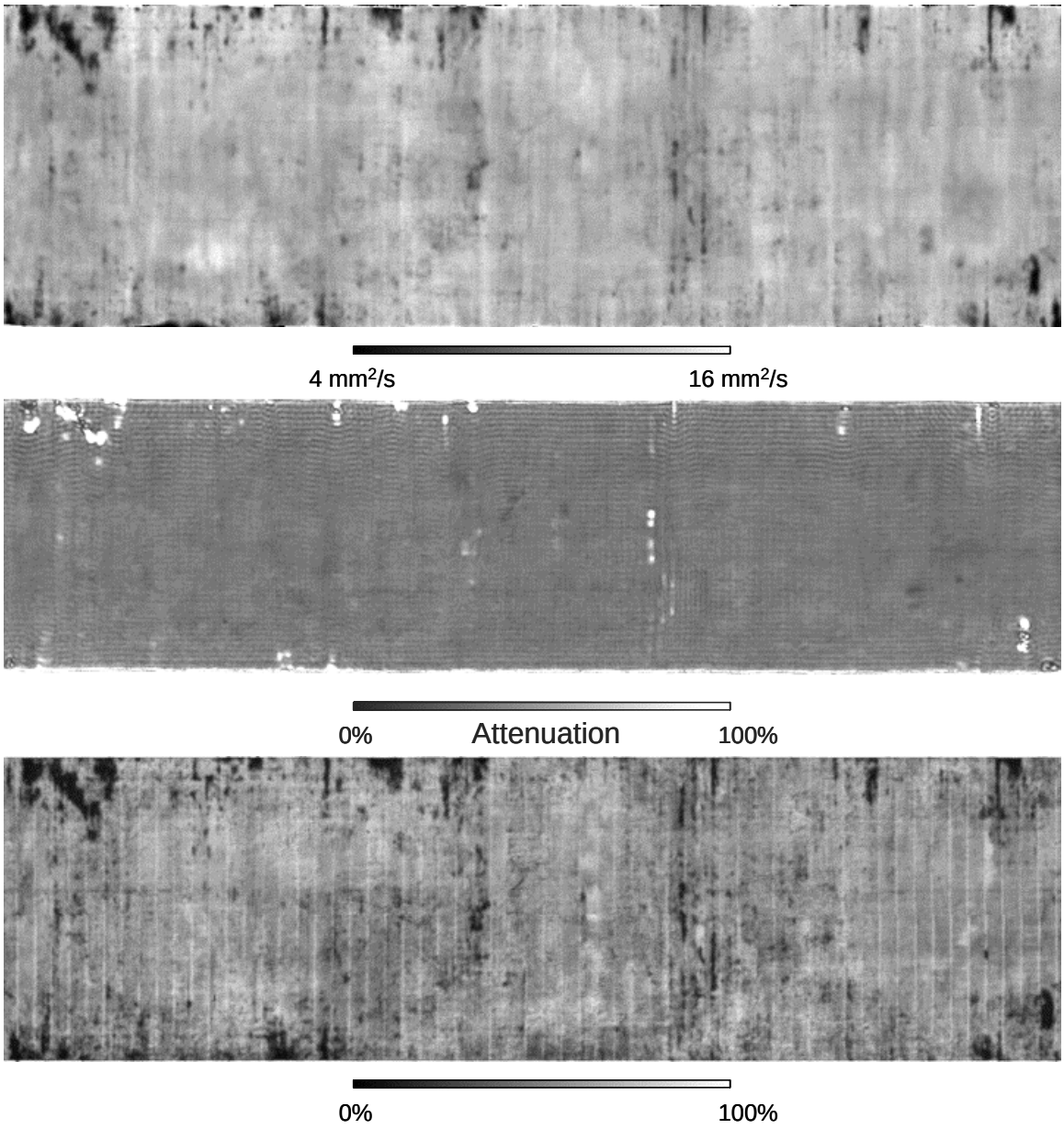

Figure 3-221. NDE images of the GE Prepreg MI Frame 5 combustor liner segment prior to rig testing: Top – transmission IR thermal diffusivity image; Middle – air-coupled ultrasound attenuation image; Bottom – water-coupled ultrasound transmission image.

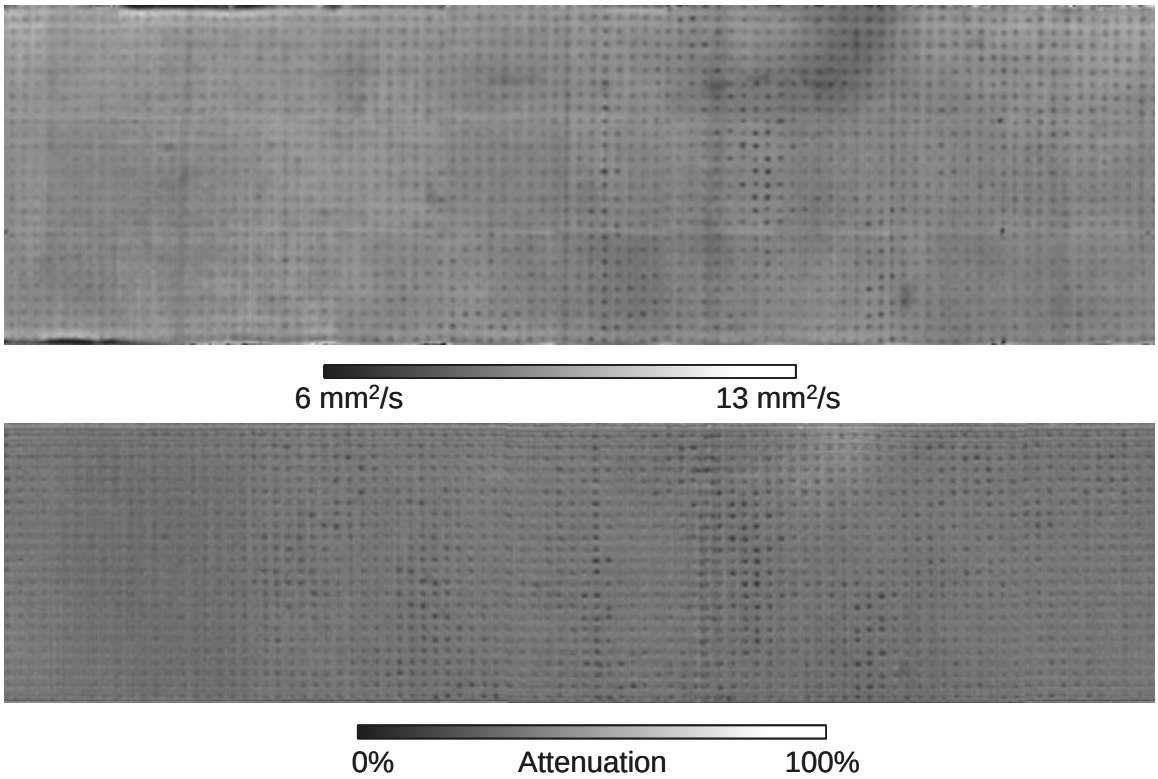

Figure 3-222. NDE images of the CCP slurry cast MI Frame 5 combustor liner segment prior to rig testing: Top – transmission IR thermal diffusivity image; Bottom – air-coupled ultrasound attenuation image.

3.8.2.5 Combustor Rig Testing

The overall test plan for the CMC Frame 5 liner segments initially called for 300 hours of rig testing split into two testing phases, each including several individual rig test runs. The first phase of the testing (150 hours) was to be done under "lean head end" diffusion flame combustion conditions, followed by a second phase (also 150 hours) using premixed, DLN-like combustion conditions. The testing in each phase would include 20 thermal trip cycles with the remainder of time at steady state conditions. The target rig firing temperature (i.e. the calculated adiabatic bulk average combustion gas temperature immediately after the flame) for the first phase of testing was 1430°C. This value exceeds the normal firing temperature of a Frame 5 engine, but based on the firing temperature to component temperature lag seen in the shroud test rig this firing temperature was expected to get the uncooled CMC liner segment up to its expected operating temperature in an actual engine (~1100°C). The reason that an engine liner would run at a higher temperature than would a rig test liner at the same firing temperature is due to the higher gas flow rate, and therefore higher surface heat transfer coefficients, in the engine compared to what is achievable in the rig.

Assembly of the combustor test liner was completed in August of 1998 and initial rig operation tests were run using instrumented metal liners in place of the CMC liner

segments. A complete listing of all of the CFCC-related combustion tests performed in the Frame 5 combustor test rig are listed in Table 3-61.

The first test of the rig was a cold flow test to check the flow splits and pressure drops within the rig and to verify operation of the data logging system. During these tests a relatively high pressure drop across the combustor cap was noted compared to the drop in a standard Frame 5 liner. The increased pressure drop was caused by the elimination of several dilution holes and many louvered cooling holes in the liner due to the substitution of the solid liner sections. Thus more air was being forced to flow through the combustor cap, leading to the larger than normal pressure drop. In order to compensate for this high combustor cap pressure drop the area of the exhaust back pressure orifice was reduced. The back pressure orifice is a constriction in the exhaust line downstream of the combustor liner test section that partially blocks the gas flow to raise the pressure in the combustor test section, thereby simulating the presence of turbine section in a real engine.

Three additional test runs were done in August-October of 1998 where further adjustments to the rig pressure drop were instituted by change the effective area of the metallic support rings around the CMC liner test sections. Several iterations were required, but the liner pressure drop was adjusted to match that typical of Frame 5 LHE combustors (dP/P ~ 3%). It was also noticed that the fuel line pressure drop during these tests was higher than desired, leading to pressure and temperature oscillations. The size of the fuel line was therefore increased to minimize the pressure drop in the fuel line. A rough calibration was also determined between rig firing temperature and the actual test liner segment temperature using the instrumented metallic liners. However, the temperature limit of the metallic liners was only ~1000°C so a full calibration up to the 1100°C desired liner temperature could not be done.

In addition to monitoring the temperature of the test liners with imbedded thermocouples, it was also desired to have a better mapping of the temperature distribution within the liners. This information was considered critical to being able to diagnose any CMC liner failures that may occur during rig testing since hot streak thermal conditions were known to have caused shroud cracking in the shroud combustion rig tests. Thermal indicating paint was applied to the metallic liners prior to test 3. Figure 3-223 shows a photograph of one of the liners after application of the thermal paint. The color change of the paint was intended to give an indication of the temperature distribution throughout the liners in both the cooled and uncooled positions.

After run 4 the liners were removed from the rig and inspected. Figure 3-224 shows montage photographs of the entire outer surface of each liner where the temperature of the liner is indicated by the different shades of color, with the color sequence being red to yellow to tan to pink to brown with increasing temperature. The paint had a useful temperature indication range up to ~900°C, and in regions of the uncooled liner that exceeded that value the paint charred to a black color.

Table 3-61. Summary of the CFCC Program Frame 5 Combustor Rig Tests

Test	Date	Liners/Positions*	Description/Result
1	8/6/98 - 8/10/98	Metal	Flow checks and debug data acquisition system (no combustion)
2	8/13/98	Metal	First Diffusion Combustion & Shakedown Test: Sheet metal rollups (2 TCs/rollup) in place of the CMC liners. Liner pressure drops were too large, and there was inadequate fuel flow due to fuel line pressure drop. Firing temperature = 1260°C, max. liner temperature = 953°C
3	10/8/98	Metal	Diffusion Combustion - Shakedown and Thermal Paint Test New metal rollups with multiple TCs and thermal paint to map liner temperature distribution under diffusion combustion conditions. Lost burst disk (a standard safety release) while adjusting liner pressure drop.
4	10/13/98	Metal	Diffusion Combustion - Shakedown and Thermal Paint Test Same test as before with replacement burst disk. Liner pressure drop now set correctly. Still too much pressure drop in fuel line to get desired maximum temperatures (firing temperature = 902°C, want 1430°C)
5	6/17/99	Metal	Check fuel flow fixes and rig operational stability Fuel pressure oscillation, combustion dynamic and temperature gradient issues were identified. Maximum liner temperature was 1010°C (the metal limit) at a firing temperature of 1293°C.
6	7/22/99	Metal	"Cold" flow test to check fuel pressure oscillations: Reduced fuel regulator pressure, which also lowered fuel/air ratio.
7	7/23/99	Metal	Fix for fuel pressure oscillations checked out. Combustion dynamics still present. Maximum liner temperature of 980°C at 1343°C firing temperature.
8	7/30/99	prepreg – cooled slurry cast - uncooled	First CMC liner test: Firing temperature to 1480°C; Uncooled liner reached 1110°C and the cooled liner 800°C; No detectable hardware damage; cycles not run due to igniter failure; Total exposure time of 3 hours.
9	8/6/99	slurry cast – cooled prepreg – uncooled	Second CMC liner test: Firing temperature of 1480°C, 10 thermal shock cycles, total exposure time of 3 hours; No detectable hardware damage
10	8/11/99 – 8/13/99	slurry cast – cooled prepreg – uncooled	Third CMC liner test: Firing temperature of 1480°C, 72 hours duration, test interrupted 3 times to remove deposits from exhaust orifice plate.
11	8/25/99 – 8/27/99	prepreg – cooled slurry cast - uncooled	Fourth CMC liner test: Firing temperature of 1480°C, 72 hours duration, 10 trip cycles at end of test for missed cycles in test 8.

* The upstream , or "cooled," liner had normal convective backside cooling, and thereby high heat flux and thermal gradients. The downstream, or "uncooled," liner had a double heat shield assembly to block backside convective and radiative cooling, and thus had higher material temperatures with smaller thermal gradients.

Figure 3-223. Photograph of one of the instrumented metallic liner segments following application of the temperature-indicating paint.

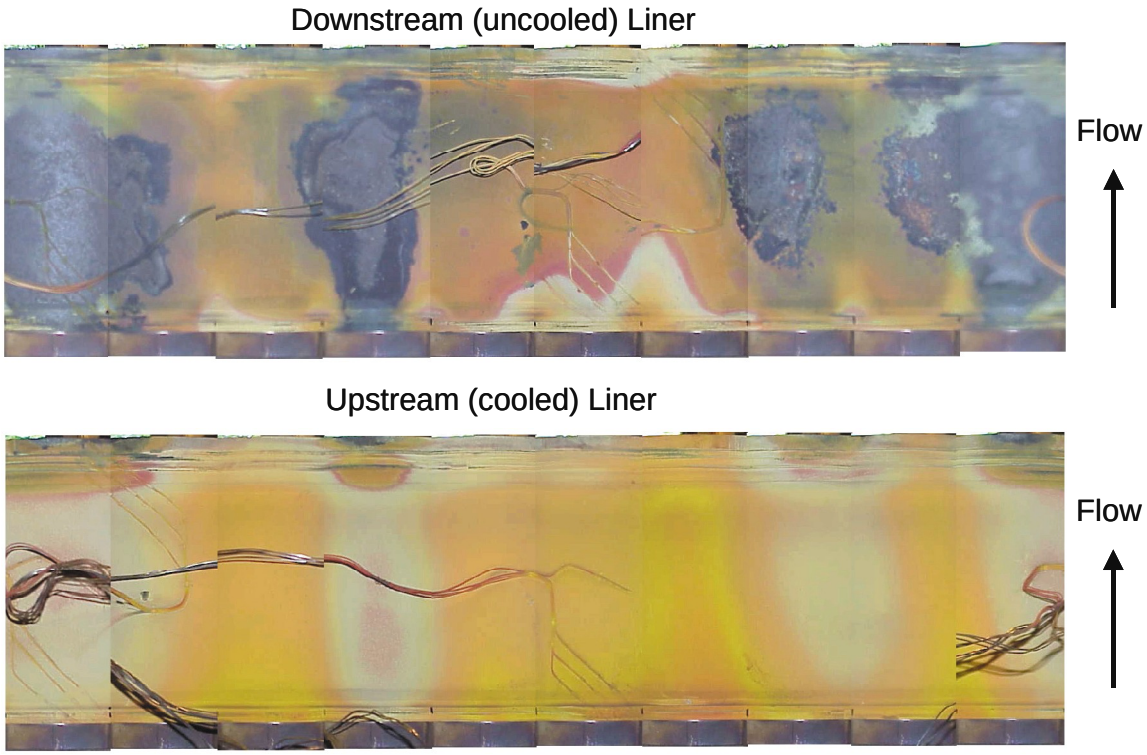

Figure 3-224. Photographic montage of the outer surface of the metallic combustor segments after rig test 4 showing the changes in color of the temperature indicating paint.

After rig run 4 the operation of the rig was judged to be satisfactory to begin rig testing of the CMC liners. However, due to the liner infiltration problems described previously, the prepreg liner was not available for rig test until June of 1999. An additional rig

shakedown run was needed to ensure proper operation of the rig after such a long period of inactivity. Unfortunately a few minor combustion problems were identified during this test run. First, and most importantly, combustion dynamics at 200 Hz with a mean fluctuation of 7-10kPa and peak fluctuations of up to 14kPa, were observed during the test. Normal operating procedures for Frame 5 turbines allow for up to 17kPa of combustion dynamics, so its occurrence in this test rig is not unexpected. A 14kPa combustion gas pressure fluctuation would roughly correspond to a 1.5MPa cyclic hoop stress being introduced into the liners. Since this stress only about 2% of the thermal stress calculated to be in the liners it is not expected to cause any durability problems with the CMC liners.

Also during the run a combustion gas temperature oscillation of about 50°C with a period of about 1 minute was observed. The cause for this oscillation was pressure variations from the fuel compressor, which was a facility problem rather than a problem with the combustor rig. This oscillation was not considered to be significant problem since the liner temperatures were found to oscillate by only 5°C for the 50°C oscillation in gas temperature. Nevertheless the fuel pressure regulator was re-built to alleviate this problem.

Working through these combustion dynamic and pressure fluctuation issues and validating the fixes required two additional rig runs. In rig test 7 the fuel pressure oscillations were eliminated, but combustion dynamics were still present, though at a reduced level from run 5. There were still concerns, however, as to whether the desired CMC liner exposure temperature of 1100°C could be achieved, especially considering the increased radiative cooling of CMC components relative to metallic components as previously seen in the shroud rig. Up to this point the uncooled liner position only had a single heat shield installed. In order to minimize heat loss of the uncooled liner section via radiation the second heat shield was added after run number 7. With this fix in place the rig was now ready to do exposure testing on the CMC liner segments.

The first rig tests with the CMC liners was run 8. That test was a relatively short (3 hour) run to ensure that the rig was operating properly with the CMC liners in place and that there were no premature failures of either liner caused by the attachments. This first test was also intended to include 10 thermal trip cycles, but these could not be performed due to an igniter failure.

Temperature of the CMC liners was monitored using four thermocouples per liner attached to the outer surface. Three of the thermocouples were in a line axially along the liner at one location, and the other was in the center of the liner 180° from the first three. These thermocouples were mounted to the liners by machining a shallow notch into the liner surface with a diamond saw, placing the thermocouple probe tip in the notch, and then covering the thermocouple with an alumina-based cement. A photograph of the prepreg liner showing three of the four thermocouples attached to the outer surface is shown in Figure 3-225.

During rig test number 8 it was found that the uncooled CMC liner reached a maximum temperature of about 1110°C at a rig firing temperature of 1480°C. The cooled liner

reached 800°C. Temperatures of the metallic rig hardware were all within safe ranges during this test, so that the firing temperature, gas flow rates and rig pressures from this test were used as the target values for subsequent tests.

Following test 8 the rig was disassembled and the liners and attachments were inspected. There was no apparent damage to either liner; however, some of the larger "bumps" in the CCP liner did show some wear in the seal region. (The bumps are caused by the loops in the fiber weave sticking up slightly into tooling holes that are needed for the CVI fiber coating process.) Montage photos of the outer surfaces of the liners following this first rig test are shown in Figure 3-226. Slight coloration of the slurry cast liner in particular was noted as a result of oxidation (reflected light interference effects from the thin oxide layers formed during the test).

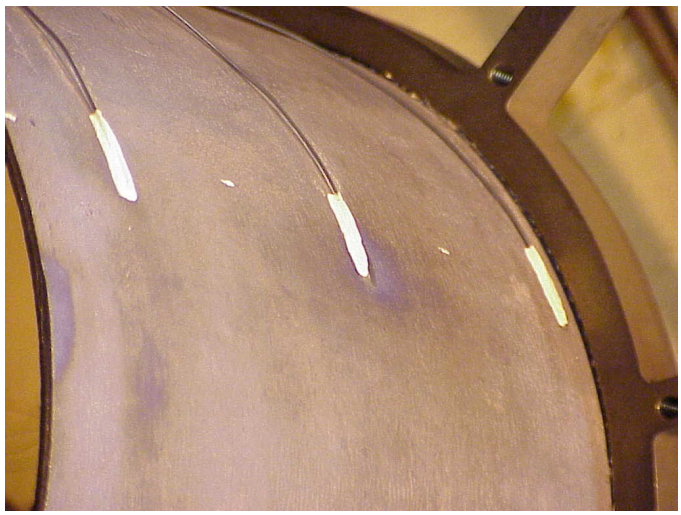

Figure 3-225. Photograph of the outer surface of the prepreg CMC combustor liner segment showing three of the four bonded thermocouples used for liner temperature monitoring during the rig tests.

For the second CMC liner exposure test, rig run 9, the liner positions were switched (see Table 3-61) and the rig was again run for only 3 hours. The thermocouple on the hottest section of the uncooled liner failed very early in this test, so that rig conditions were adjusted to be like those in run 8 rather than trying to control to a maximum temperature on the liners. No rig operational problems were noted during this test, and the 10 thermal trip cycles were run successfully. Following test 9 the rig was only partly disassembled and the CMC liners examined visually. There was no indication of any distress to either liner. Thermocouples were re-attached to the liners and the rig was re-installed in the pressure vessel for rig test 10.

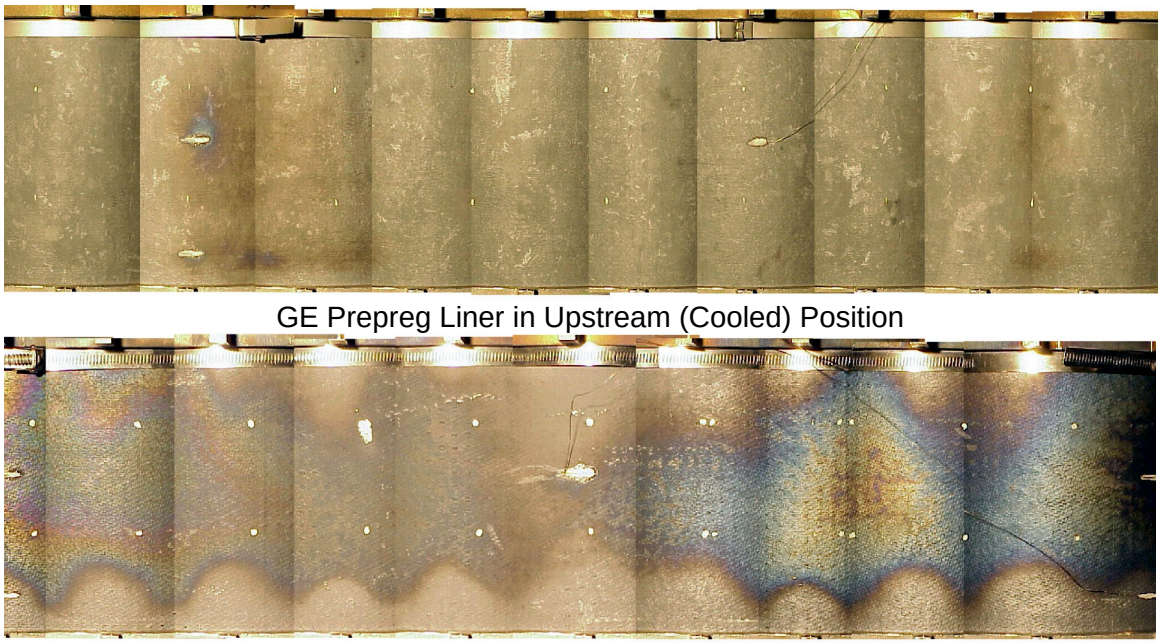

Figure 3-226. Montage photographs of the CMC Frame 5 liner segments following rig test 8. Flow direction of the combustion gases would be top to bottom relative to the liner pictures (cooling air on the outside of the liners would be flowing bottom to top).

Test 10 was the first long-time (72 hours) steady-state exposure test. Again, the thermocouple at the maximum temperature condition of the uncooled liner failed early during this test so that rig operation was controlled to give firing temperatures, pressures and flow rates as much like test 8 as possible. Within the rig there is an "orifice plate" at the back end of the pressure vessel that is used to control the overall pressure in conjunction with the compressed air flow rate. Because the orifice plate lies directly in the combustion gas stream it is necessary to cool the combustion gases ahead of the orifice plate using a water spray. During the test the water spray caused a build-up of lime on the orifice plate, which would restrict gas flow too much and lower the pressure drop through the combustor. Consequently the rig had to be shut down three times in order to remove the lime. After test 10 the rig was again fully disassembled and inspected. Montage photographs of the two liners after test 10 are shown in Figure 3-227. Please note that the color differences in the liners between Figures 3-226 and 3-227 are a result of different lighting conditions when the photographs were taken and do not indicate any major change in the appearance of the liners. The only noticeable change between the two photography sessions was a slight increase in the interference colors of the oxide films caused by liner oxidation during exposure.

The liner positions were again switched back to their original positions as in test 8 and the rig re-assembled. The final test run was test 11. This test included an additional 72 hours of steady state exposure, plus the 10 thermal trip cycles that were missed in test 8. Lime build-up on the orifice plate also occurred during this run, as evidenced by a slow decrease

in the rig pressure drop with time. However the lime apparently broke away from the orifice plate on its own since the pressure drop would periodically and abruptly drop back to the starting value with no other changes in the rig operating parameters. Following this final run the rig was disassembled and the liners inspected visually. There was still no evidence of liner cracking or other distress.

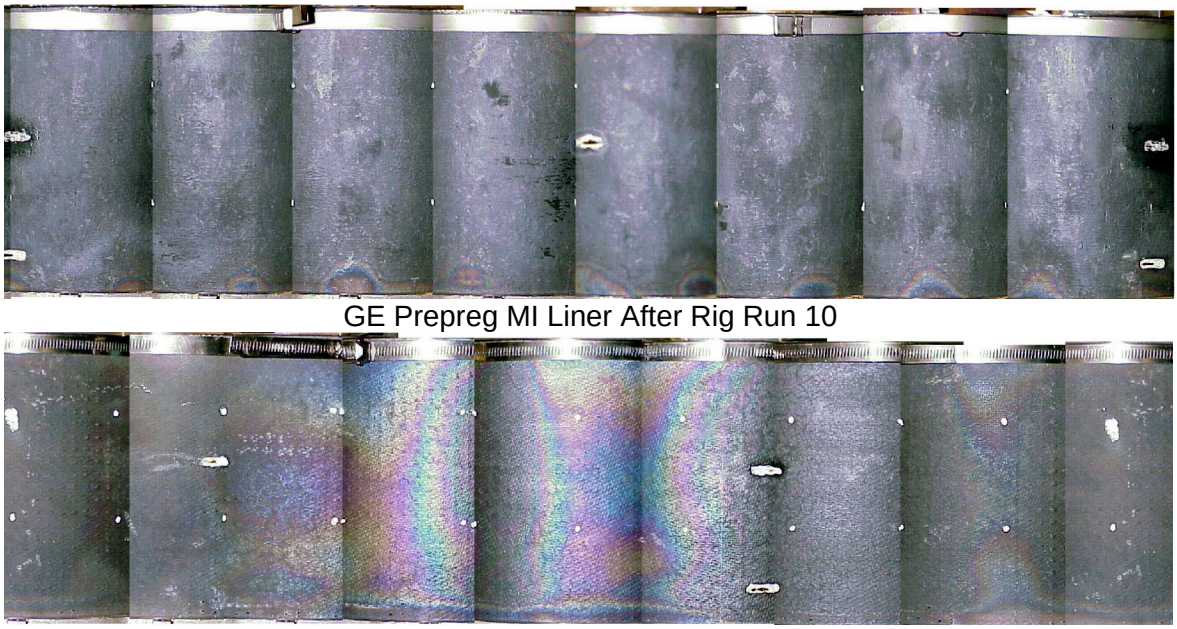

Figure 3-227. Montage photographs of the CMC Frame 5 combustor liner segments after rig test 10.

During the 4 rig test runs on the CMC liners the liners had accumulated 150 hours of rig exposure, consisting of 75 hours and ten thermal trip cycles in each of the cooled and uncooled liner positions. This set of experiments was considered adequate to have demonstrated the feasibility of using CMC liners for retrofit Frame 5 engine applications.

The original test plan had been to modify the Frame 5 combustor system to incorporate a premixed, DLN fuel nozzle assembly as used in the F and H class engines. However, such a modification would be an extreme change in the operation of the combustor system, and there was no guarantee that the combustor could be made to operate in a stable manner. The prospect of needing multiple combustion tests just to get the new combustor system operational was not considered an optimum use of program resources, and so testing under DLN combustion conditions was dropped from the program. Rig test 11 therefore completed the rig testing of the Frame 5 combustors.

3.8.2.6 Combustor Post-Test Characterization

Post-test NDE inspections of both liners were again performed at ANL, and included transmission IR thermography, air-coupled ultrasound transmission and water-coupled

ultrasound. Post-test images of the GE prepreg MI liner and CCP slurry cast MI liner are shown in Figures 3-228 and 3-229, respectively. The only difference noted in the before-to-after NDE images was a slight increase in the intensity of one of the edge defects of the prepreg MI liner (shown in the inset comparison in Figure 3-228). Due to the complete lack of observable damage on the CMC liner segments, either visually or by NDE, and to the fact that the liners had been exposed to rather mild conditions (~1100°C maximum for ~75 hours), there was little incentive to perform detailed destructive analyses.

3.8.3 2MW Turbine Shroud

While working on the development of the toboggan shrouds and Frame 5 combustors it was apparent that an engine testing opportunity in a large industrial gas turbine was going to be very unlikely. Despite the success of the material development efforts and of the shroud and combustor rig tests, the liability for lost generating capacity that would be incurred if a CMC component were to fail in the field was just too high for large engines. It was therefore recognized early in the program that a small test engine opportunity would be needed in order to demonstrate the durability of the CMC materials in a real engine environment. However, at the start of the Phase 2 program such an opportunity had not been identified.

In early 1997 GEGR began discussions with Nuovo Pignone in Florence, Italy, regarding the potential for a joint CMC component development program. GE had been a majority owner of Nuovo Pignone (NP) for some time and was, at that time, in the process of acquiring them wholly. NP is now a division of GE Energy, and known as GE Oil and Gas. NP had several small gas turbine engines in their portfolio, ranging in power output from 2 to 25 MW. They had also been manufacturing GE Frame 5 (up to 30MW) and Frame 6 (up to 70MW) gas turbines for the European market under a royalty agreement with GE. The attractiveness of NP as a partner for developing a turbine component was that they had company-owned test engines on site that could be used for component testing without the risk of lost revenue that would be associated with a customer engine in the field.

Throughout 1997 and 1998 GEGR and GE Power Systems worked with the NP on the design of a second stage CMC shroud ring for a PGT-2 (now called GE-2) gas turbine engine. Fabrication of the shroud rings for engine testing was started in 1998, and 100 hours of engine testing was completed in late 1999. All of this work was done using internal GE funds. However, the success of this work prompted a follow-up effort on the design, fabrication and engine testing of a stage 1 shroud ring for this same engine. The efforts on the stage one shroud, excluding the actual running of the engine exposure tests, which were still done entirely with GE funds, was added to the CFCC program contract during Phase 2+, starting in March of 1999, as program Task 3.3.f. The stage 2 shroud work was also included in the Phase 2+ program, as Task 3.3.e, but at no cost to DOE as it was still internally funded by GE. In order to give an overall account of the PGT-2 engine testing efforts the work done on the stage 2 shroud outside of the CFCC program is described here along with the work on the stage 1 shroud.

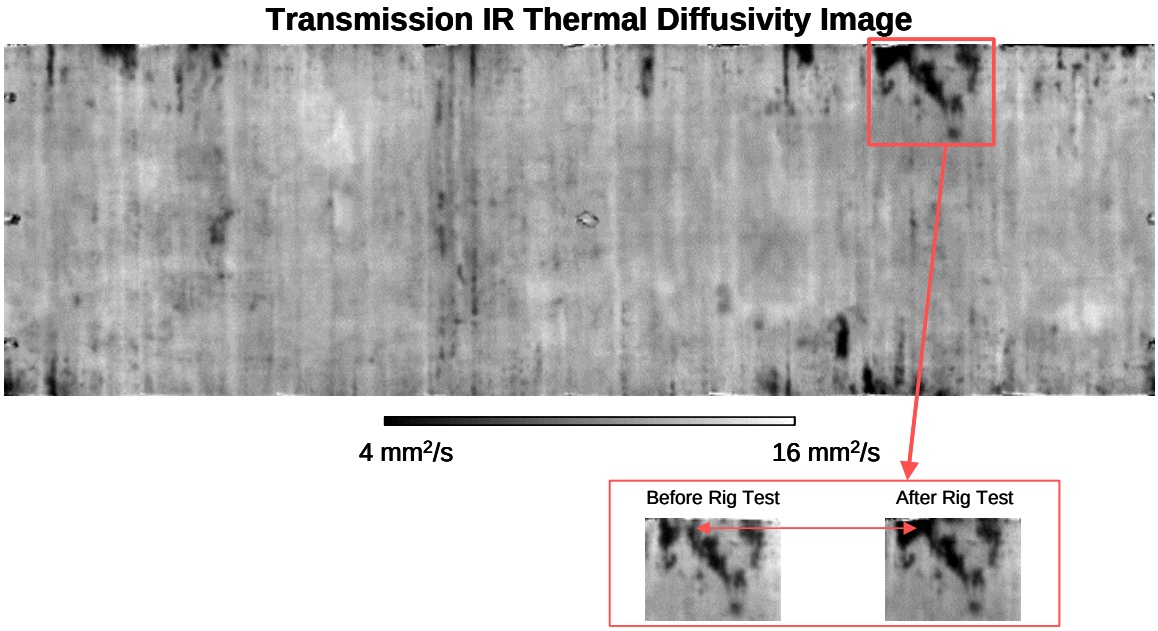

Figure 3-228. NDE images of the GE Prepreg MI combustor liner following combustion rig testing.

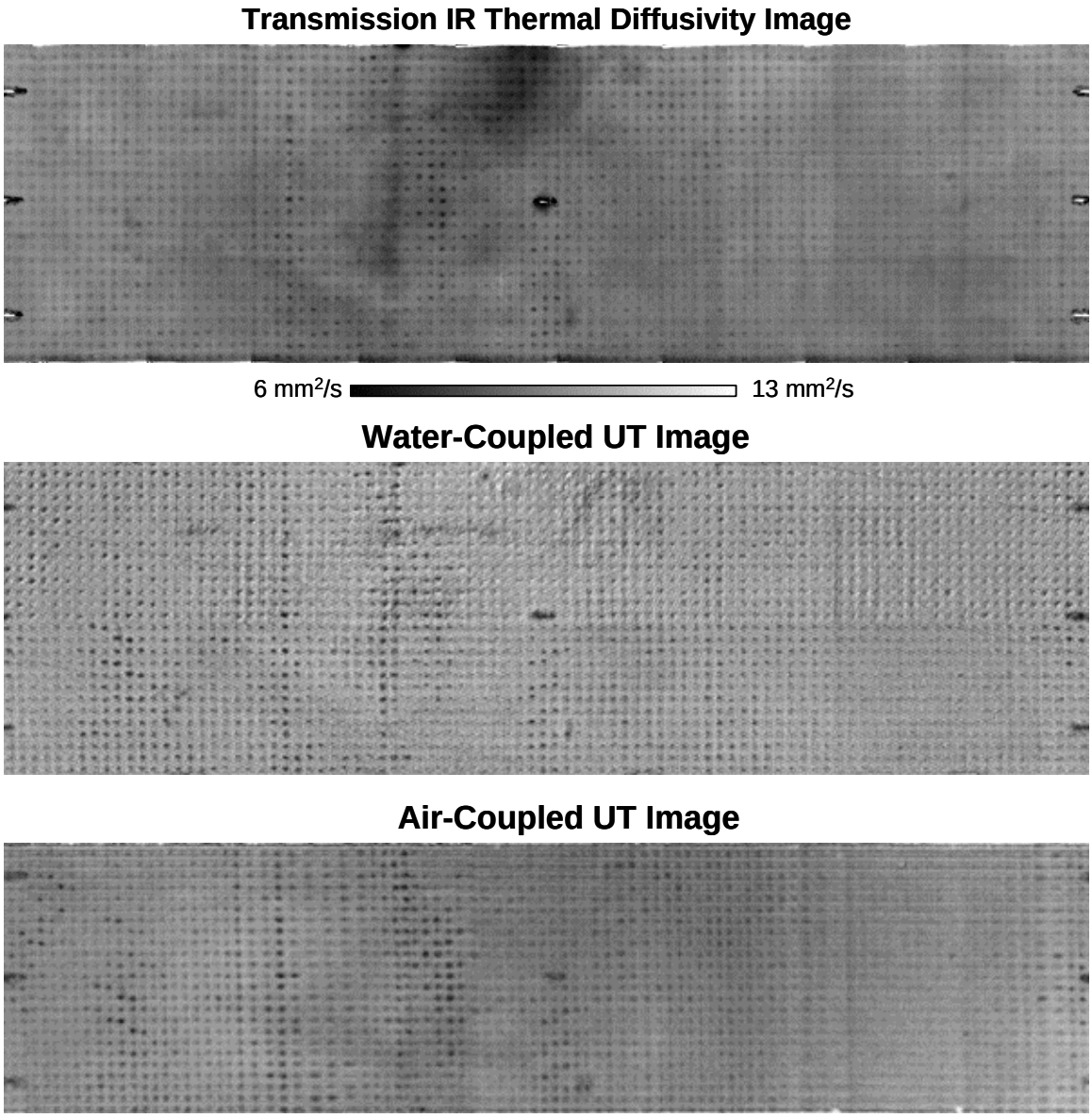

Figure 3-229. NDE images of the CCP slurry cast MI combustor liner following combustion rig testing.

The PGT-2 (GE-2) engine is a 2MW gas turbine typically used as a generator drive in small power/heat cogeneration facilities. The turbine has a 2-stage centrifugal compressor, a single can combustor, and a 2-stage axial turbine section. A cross-sectional diagram of a PGT-2, not showing the combustor can, is given in Figure 3-230. A close-up of the turbine section highlighting the positions of the shrouds is show in Figure 3-231. The PGT-2 has a turbine inlet temperature of roughly 1010°C with a gas temperature of ~775°C in the vicinity of the second stage shroud and ~980°C in the vicinity of the first stage shroud. The existing metallic shroud is an uncooled, segmented design made from Hastelloy X. A segmented shroud is used to accommodate thermal growth differences between the shroud and the turbine casing and thermal stresses within the shrouds

themselves. The differential thermal growth also dictates that the shroud segments have a single point attachment to the casing. However, this shroud and attachment design allows the shroud segments to become slightly misaligned during turbine operation. This misalignment in turn causes increased blade-tip clearances, which lower turbine efficiency, or could even lead to blade tip rubs against the shroud segments. In order to eliminate these issues of the segmented shroud, the replacement CMC shroud components were to be single piece shroud rings. Having single piece shroud rings would allow for reduced tip clearance, and therefore better efficiency and power output, while lessening the chance for tip rubs.

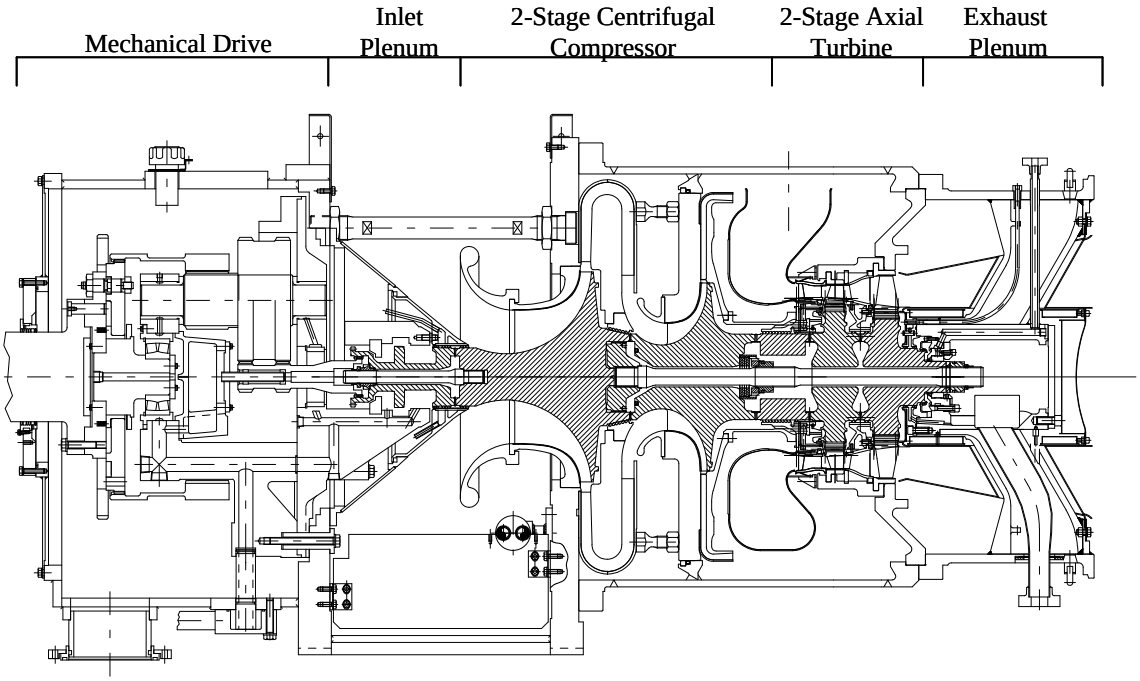

Figure 3-230. Cross section diagram of the PGT-2 (GE-2) gas turbine.

3.8.3.1 Stage 2 Shroud

3.8.3.1.1 Stage 2 Shroud Design

The purpose of this effort was to design, fabricate and engine test a second stage shroud component for a GE/NP PGT-2 turbine engine. As noted above, the majority of the shroud design effort had been completed prior to this effort being included in the CFCC program. The design for the CMC shroud and attachment hardware that was developed is shown in Figure 3-232. The shroud ring was trapped between a forward and rear retaining flanges with the aerodynamic and pressure loads expected to keep it pressed against the aft flange. The seal on the backside of the shroud ring was a nested metal ring configuration similar to that previously described for the Frame 5 combustor seals. There were four cut-outs on the aft edge of the shroud ring that engaged radial bosses on the aft retaining flange, which controlled the radial position of the shroud relative to the turbine case.

The initial design of the CMC shroud ring is shown in Figure 3-233. The shroud ring was a thin walled (2.4mm thick) right cylinder with an inner diameter of 466.2mm and an axial length of 57.5mm. The main processing challenge for fabrication of this shroud ring was maintaining the ID dimension, which had a dimensional tolerance of +/- 0.2mm with a total out-of-roundness of 0.3mm. Even using an infiltration mold, this was a much tighter tolerance than the prepreg MI process had demonstrated on previous components. Consequently some post-densification machining of the ID and OD would likely be required.

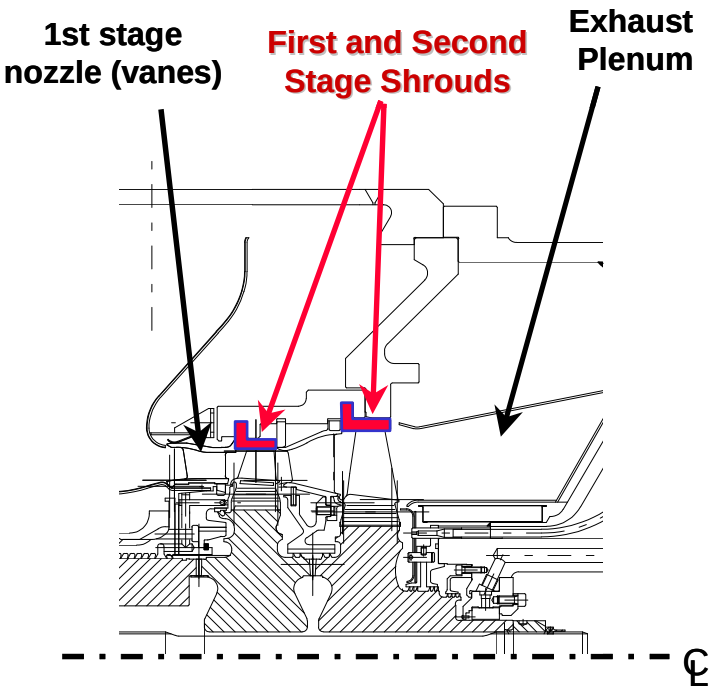

Figure 3-231. Diagram of PGT-2 (GE-2) engine turbine section showing the positions of the 1st stage and 2nd stage shrouds.

Nuovo Pignone engineers performed ANSYS FEM analysis of the shroud. The results of these analyses indicated that the maximum shroud temperature would be 802°C along the leading edge, with temperature dropping to about 550°C along the trailing edge. There was also a temperature gradient in the hoop direction around the turbine caused by the single combustor can configuration that produced a roughly 50°C gradient in the hoop direction of the shroud ring. The steady state stresses caused by these gradients were all very low, with maximum tensile axial, hoop and radial stresses in the CMC ring of 0.9, 9.5, and 0.33MPa, respectively. Analyses were also run for start-up and shut-down transients, in which case the maximum axial, hoop and radial stresses increased to 1.4, 25, and 1.2MPa, respectively. All of these predicted temperatures and stresses were well below the design limits for the prepreg MI composite material.

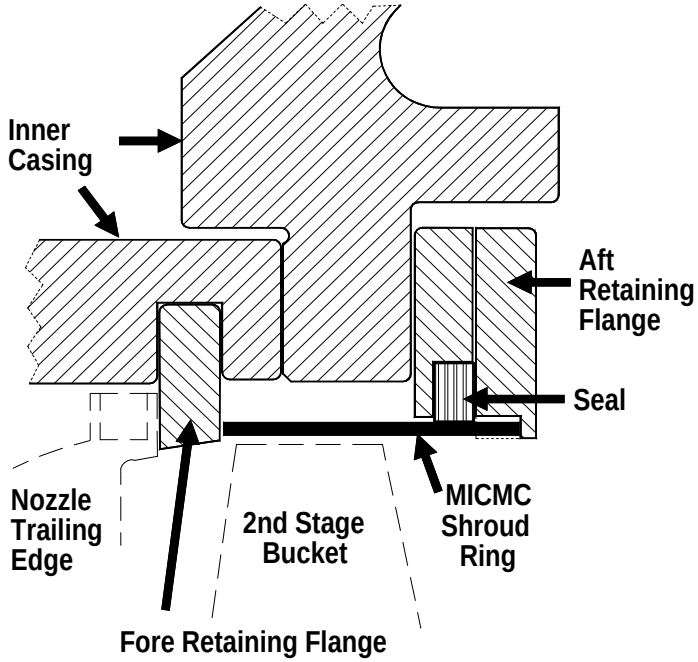

Figure 3-232. Schematic of the PGT-2 CMC 2nd stage shroud ring attachment and interface design in the as installed in the engine.

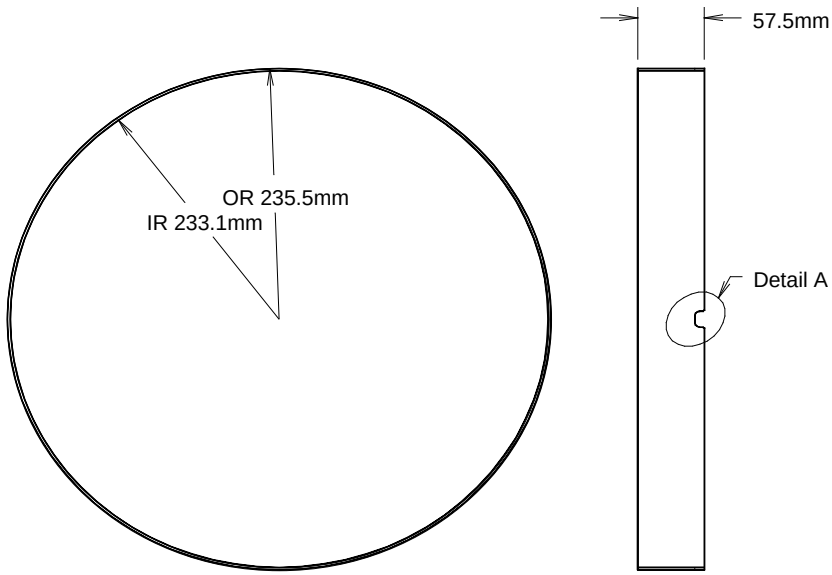

Figure 3-233. Drawing of the CMC PGT-2 stage 2 shroud ring.

3.8.3.1.2 Shroud Fabrication

The fabrication process of the 2nd stage shroud rings was very similar to that used for the Frame 5 combustor liners. Hoop oriented plies were applied to a cylindrical form via

direct winding. Axial plies were then laid in by hand from pre-wound tapes. The shroud ring was too large to fit into the infiltration furnace, so the melt infiltration step was done at GE Lighting in Cleveland, OH, at the same time as the Frame 5 combustor liner infiltrations. Overall, three shroud rings were fabricated with the intent to choose the best ring for use in the engine tests. A photograph of the second shroud ring to be fabricated, following melt infiltration but before machining, is shown in Figure 3-234.

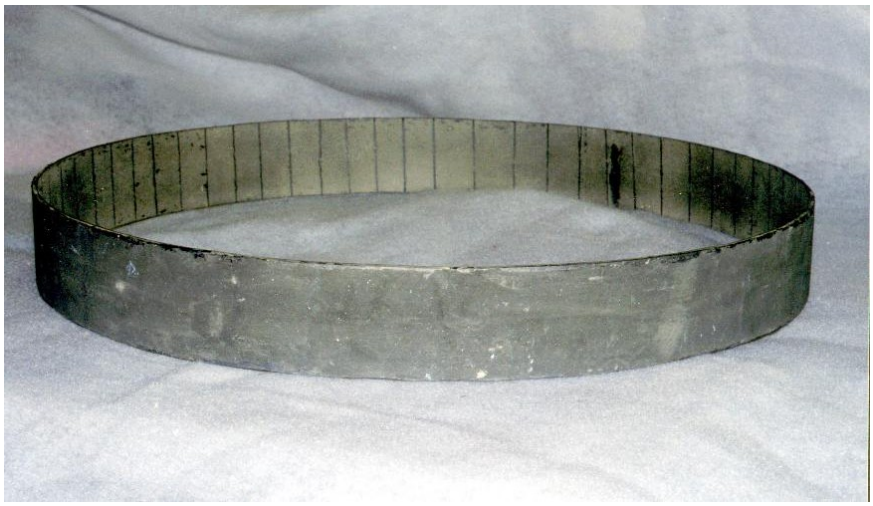

Figure 3-234. Photograph of the second PGT-2 (GE-2) second stage shroud ring in the as-infiltrated condition. Ring outer diameter is ~23.6cm.

Machining of the shroud rings was done at two ceramic machining vendors. The first ring was sent to Bomas Machine Specialties in Sommerville, MA for grinding to final dimensions. Unfortunately the part became dislodged from the machining fixture during OD grinding. Repositioning of the piece in the grinding fixture was not very precise and the final piece had significant non-concentricity of the OD and ID with a varying wall thickness. Because of the poor machining this shroud was considered unsuitable for further testing.

The second shroud ring was also sent to Bomas for machining. The second shroud was fabricated with extra length in the axial direction to allow for more secure fixturing during machining. The as-fabricated ID of this shroud ring was slightly larger than the desired dimension so that very little grinding of the ID was needed. However, grinding of the OD was once again more extensive than had been desired. Explicit instructions were communicated to Bomas that grinding of the OD should be stopped at the first sign of fiber exposure. Despite this the OD of the liner was ground quite deeply in two locations, extending into the second ply of the composite. A photograph of the shroud following machining is shown in Figure 3-235.

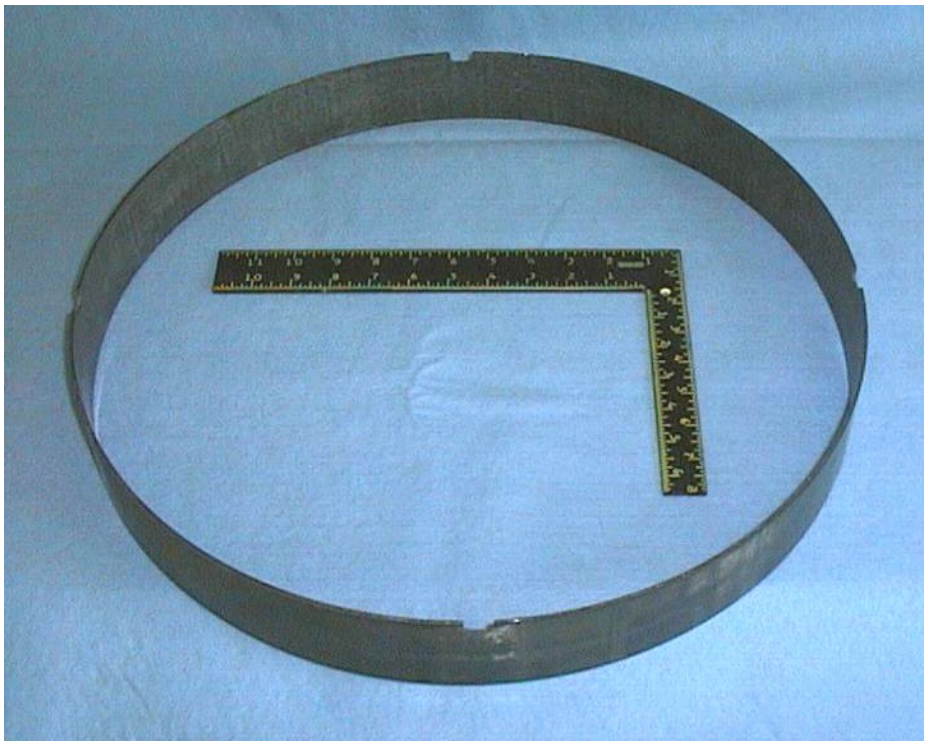

Figure 3-235. Photograph of the 2nd PGT-2 stage 2 shroud ring following machining.

The height of the shroud ring was made substantially over-size to allow for trimming away of uneven edges from the hand lay-up procedure. Unfortunately insufficient material was removed from the first edge before the overall ring was cut to length, leaving one edge with a rough appearance. On casual visual inspection the roughness appears similar to delaminations, but is really due to the internal plies not extending completely to the edge in localized spots. Despite the excessive removal of material from the OD and the rough trailing edge, the shroud ring was in good physical condition and could possibly be acceptable for engine testing.

This shroud was subsequently sent to Argonne National Lab for NDE examination following machining. Transmission IR thermography and water- and air-coupled ultrasound examinations were performed, and the images derived from these tests are shown in Figure 3-236. In both the thermal diffusivity and water-coupled ultrasound images there appeared to be more defects near the top of the ring (the trailing edge of the shroud) as compared to the bottom edge. This was consistent with the ply drop-off defects seen visually following machining. The light area on the bottom left side of the IR image is the region where the ring was ground too thin from the OD. The vertical lines, or vertical rows of "spots", that appear in both the thermal and water ultrasound images were generally associated with small wrinkle defects or axial ply seams. Interpretation of the air-coupled ultrasound image was somewhat more tenuous.

Although this shroud ring met the NP dimensional specifications, substantial fractions of the outer plies of the composite were removed during machining. There were concerns

that this improper machining may cause thermal distortions in the shroud ring that could lead to blade rubs. Thermal-mechanical FEM analysis was done on the shroud ring to compare thermal distortions and stresses introduced by the machining damage. A full shroud ring solid model with all 8 plies was first built and the temperature distribution derived from previous thermal analyses at NP was then mapped onto the ring. The structural analysis was then run to determine the displacements and stresses in a "perfect" shroud. The two outer plies of the composite were then removed from the model over a 90° arc segment and the analysis was done again. The radial displacements and stresses for the "defective" shroud model were within 1% of the base model. These results indicated that the over-machining of shroud #2 should not cause dimensional instability during the engine test.

A third 2nd stage shroud ring was fabricated and infiltrated at GE Lighting. The infiltration of this ring was essentially complete except for two dime-sized regions on the inner surface where the innermost layer of unreinforced material was not completely infiltrated. This ring was sent to a new machining vendor (Chand Kare Technical Ceramics) for CMM examination and machining. CMM inspection of the ring at Chand Kare indicated that the average as-fabricated ID (the ID was the most critical dimension for the shroud ring) was roughly 0.15mm undersize, which represents only a 0.03% error from the 466.2mm target dimension.

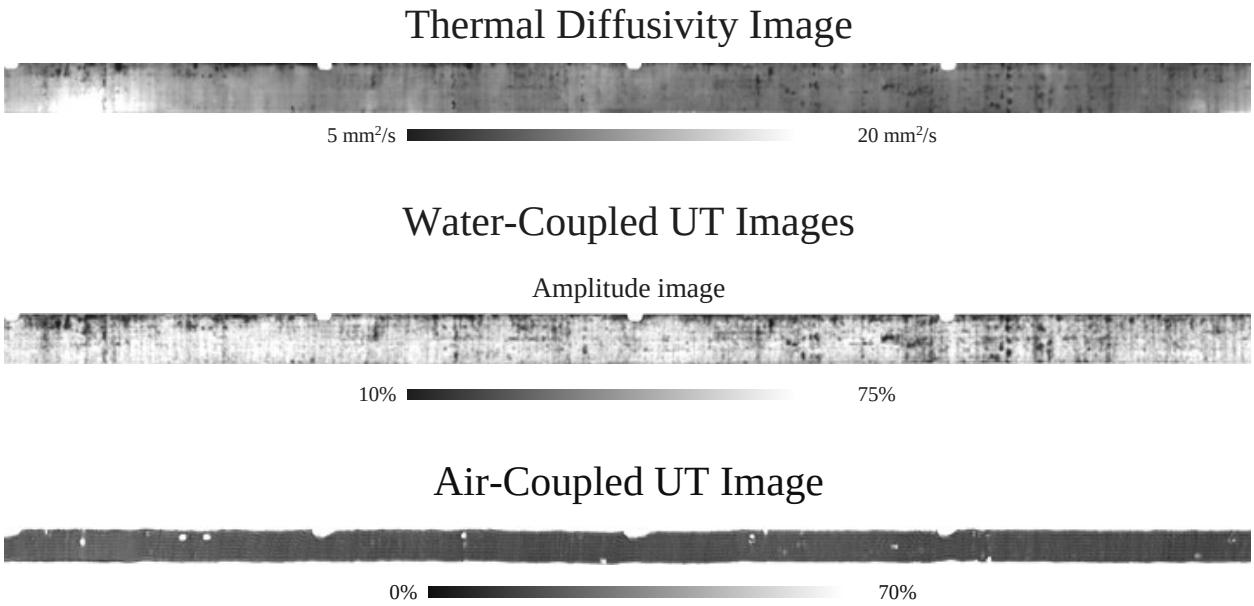

Figure 3-236. Pre-test NDE images of PGT-2 (GE-2) shroud ring #2. Both thermal diffusivity imaging and water-coupled ultrasound indicate greater defect concentration near the upper (trailing) edge of the shroud ring, which is consistent with the visual inspection following machining. Vertical lines in the thermal and water-coupled ultrasound images indicate small buckles or seems in the composite plies.

Visual inspection of the 3rd shroud ring following machining at Chand Kare Technical Ceramics showed it to be in much better condition than either of the two earlier shrouds machined at Bomas. Exposure of fiber on the inner surface of the shroud was very minimal, and also very minor on the OD as well. The shroud wall thickness was also much more uniform than in the earlier shrouds. A photograph of this shroud ring is shown in Figure 3-237.

This shroud was also sent to ANL for NDE inspection. IR and ultrasound NDE images of the 3rd shroud ring are shown in Figure 3-238. The two dark spots near the left edge of both the IR and ultrasound images were the locations of the uninfiltrated regions noted on the shroud ID. The dark spots along the bottom of the images at the far right correspond to a region that had a local delamination that was observable on the shroud machined edge.

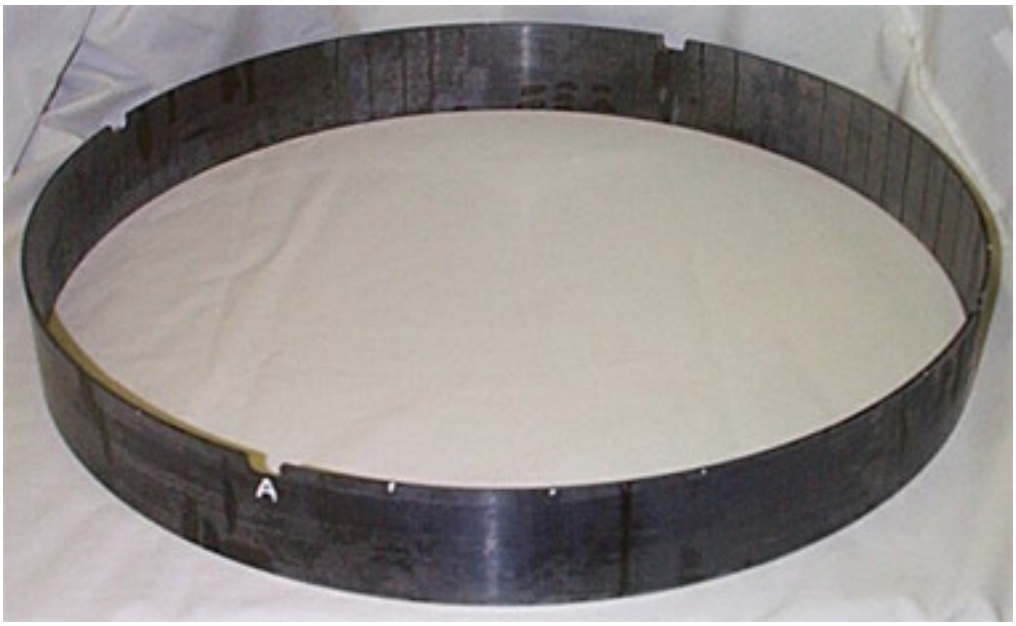

Figure 3-237. Photograph of the 3rd stage 2 shroud ring following machining.

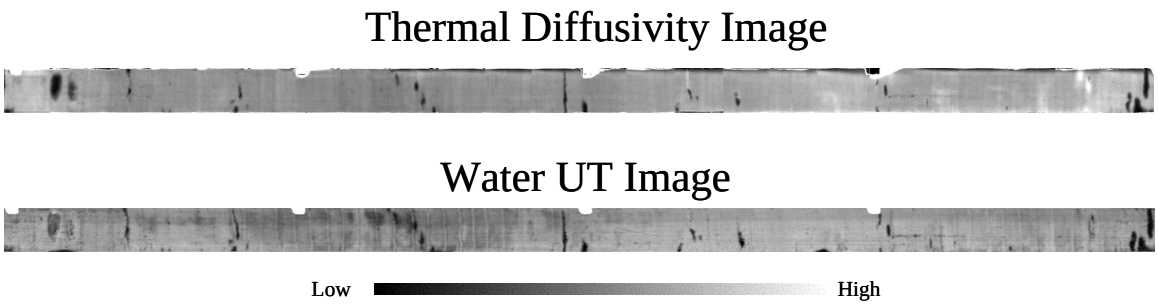

Figure 3-238. NDE images of the 3rd stage 2 shroud ring.

Despite the improved machining of ring 3, shroud ring 2 was selected for use in the engine tests primarily for two reasons. First, there was concern about the depth of the uninfiltrated regions in shroud ring 3 and their potential impact on the oxidation resistance of the shroud. Second, engine assembly had started using shroud ring 2 due to schedule constraints, and the quality of ring 3 was not judged to be sufficiently superior to that of ring 2 to justify the tear-down and rebuild of the full 2nd stage shroud assembly.

3.8.3.1.3 Engine Testing

Detailed test and instrumentation plans were put together for the PGT-2 stage 2 shroud engine tests. Instrumentation possibilities were somewhat limited because of space constraints imposed by the engine casing. Spring-loaded thermocouples were mounted in the inner casing that pressed against the backside of the CMC shroud ring in 8 places. In order to keep the thermocouples in contact with the shroud they were spring loaded with a nominal contacting force of about 2N. Two thermocouples were also located in the space

behind the CMC shroud ring, and additional thermocouples attached to the metallic inner casing ring. The locations of the thermocouples were chosen to allow measurement of both the axial and radial temperature distribution in the shroud and surrounding structure. Two dynamic pressure gage taps were also placed in the cavity behind the CMC shroud ring and used to look for acoustic resonances of the shroud ring.

Pre-assembly of the shroud ring within the inner turbine casing was done at Nuovo Pignone in order to check the fit of the shroud and to verify the positioning and operation of the instrumentation. A photograph of the inner casing assembly with the CMC shroud ring in place is shown in Figure 3-239. Also visible in this photograph are the first stage nozzle and segmented shroud. As depicted in the photograph, the Prepreg MI CMC shroud ring was captured between two metal retaining rings, and was held in the proper radial position by four metal tabs that engage the slots on the shroud ring. This arrangement was intended to maintain proper centering of the shroud ring while allowing for differential thermal growth radially of the ceramic shroud and the metallic inner casing.

Figure 3-240 shows a photograph of the shroud pre-assembly with the second stage rotor in place. The rotor was added in order to check the blade tip-to-shroud gap height before engine assembly. Figure 3-241 shows the instrumented inner casing section after installation into the test engine. The second stage nozzle, rotor and shroud are not yet installed.

Final assembly of the PGT-2 engine with the prepreg MI CMC 2nd stage shroud was completed in early October, 1999. The first engine start-up with the CMC shroud was attempted on October 11; however, combustor control system problems (not related to the CMC shroud) prevented the attainment of full-speed, full-load (FSFL) conditions. During this time the turbine was tripped from full-speed, no-load conditions four times while trying to start the engine. The control system problems were subsequently resolved and the engine was run up to FSFL conditions on October 12 for 2 hours. During operation there were no unusual engine operation parameters noted.

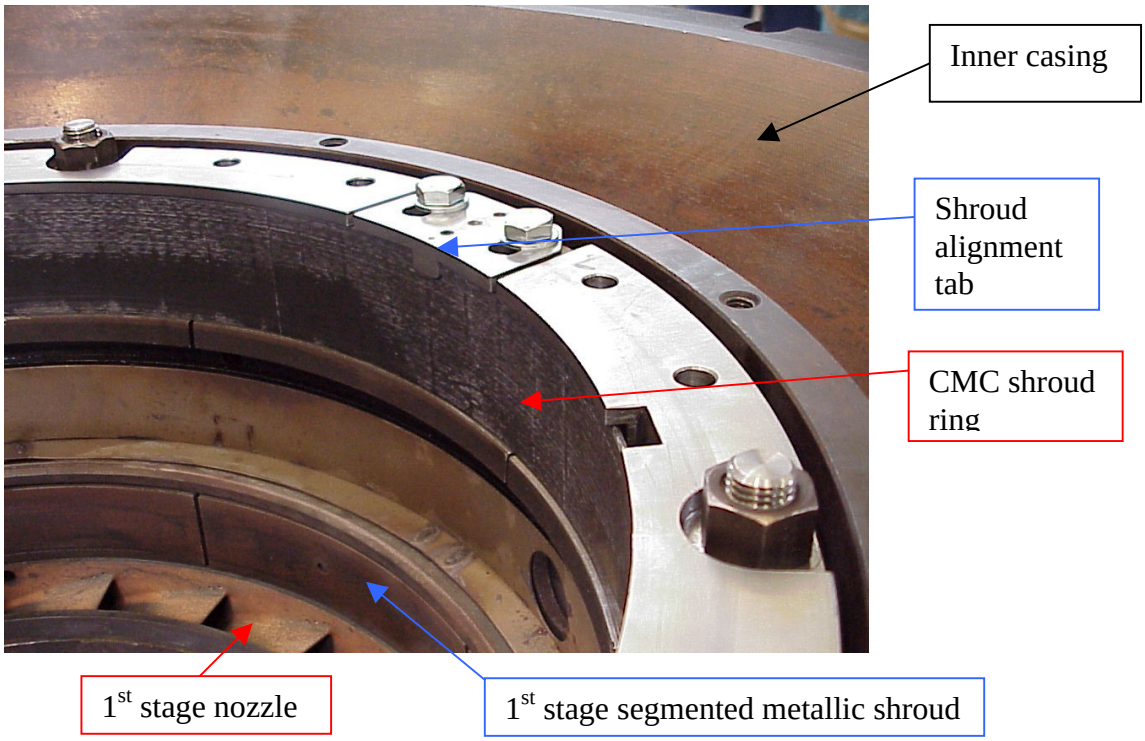

Figure 3-239. Photograph of the pre-assembly of the CMC second stage shroud ring within the PGT-2 inner casing.

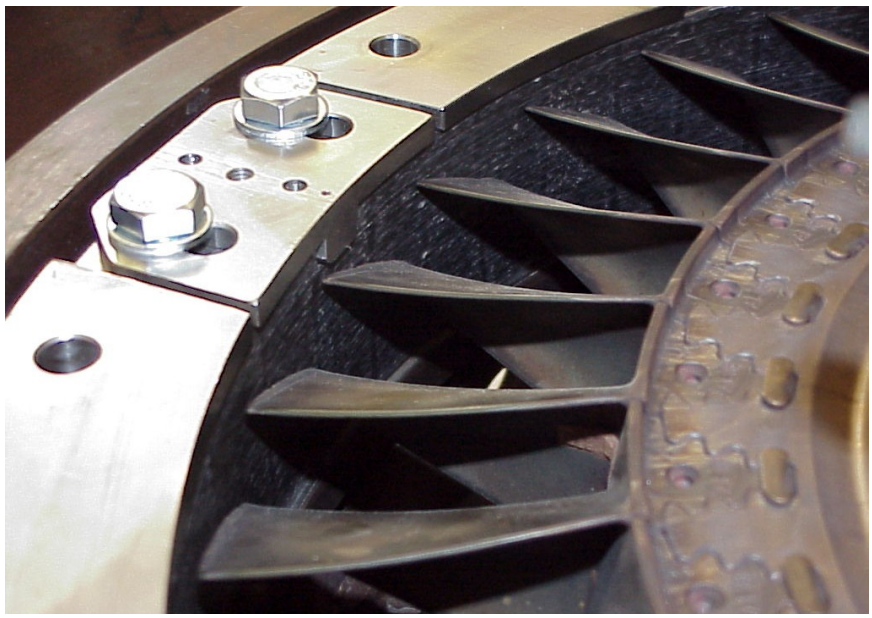

Figure 3-240. Photograph of CMC shroud pre-assembly with the second stage rotor assembly in place.

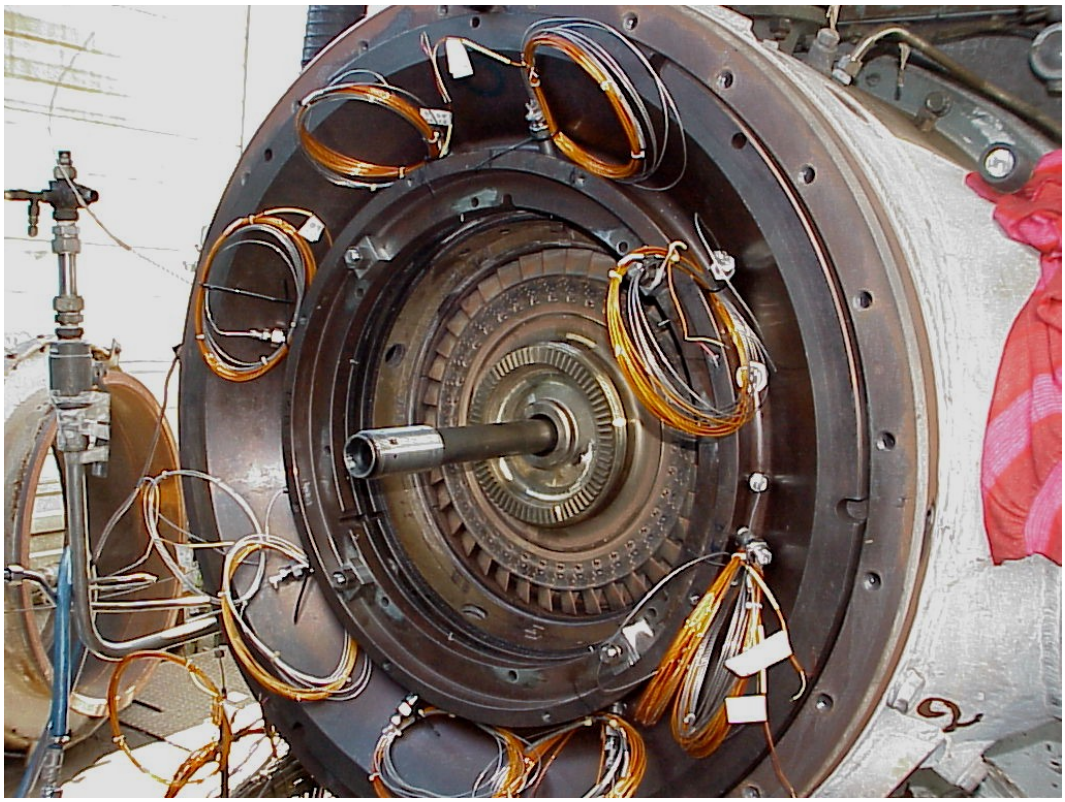

Figure 3-241. Photograph of the instrumented inner casing after installation within the PGT-2 outer casing. The second stage nozzle, CMC shroud, seals and retaining rings have not yet been installed. The eight wire bundles are for the spring-loaded thermocouple probes.

On October 13 the aft expansion joint on the engine exhaust was removed so that the shroud could be inspected visually and by borescope. During this inspection it was believed that a crack was detected in the shroud and there was evidence of a blade tip rub. Figure 3-242 shows the blade rub region as seen from the exhaust plenum of the engine. Consequently the aft section of the turbine was disassembled and the shroud removed for closer inspection.

On closer visual inspection outside of the engine it was realized that the crack-like feature seen by borescope was not actually a crack, but a seam in the inner layer of unreinforced matrix material. However, the blade tip rub indications were quite real. Figure 3-243 shows a photograph of the rub region after the shroud had been removed from the engine. The light colored regions are actually a thin layer of metal from the blade tips that had been “smeared” over the surface of the shroud, as shown further in the close-up photo in Figure 3-244. The shroud itself showed very minor abrasion in the rub region with a maximum penetration depth of only 0.1-0.2mm. No fibers were exposed by the rub and there were no signs of cracking caused by the rub.

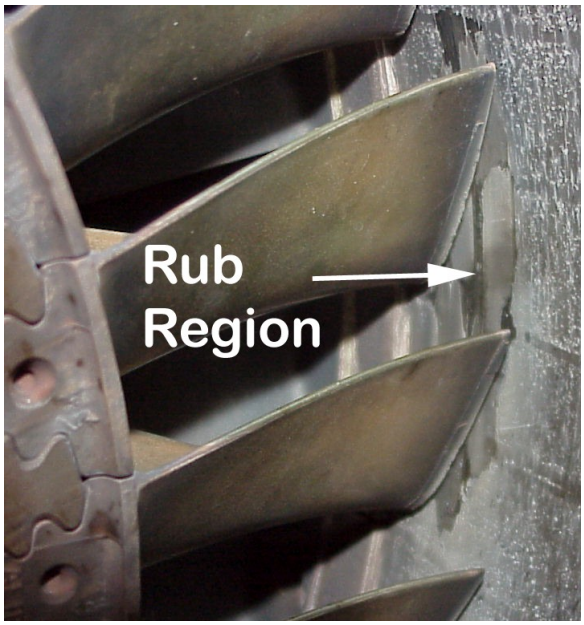

Figure 3-242. Photograph of the blade tip rub region on the prepreg MI CMC stage 2 shroud ring as seen from the rear of the PGT-2 engine.

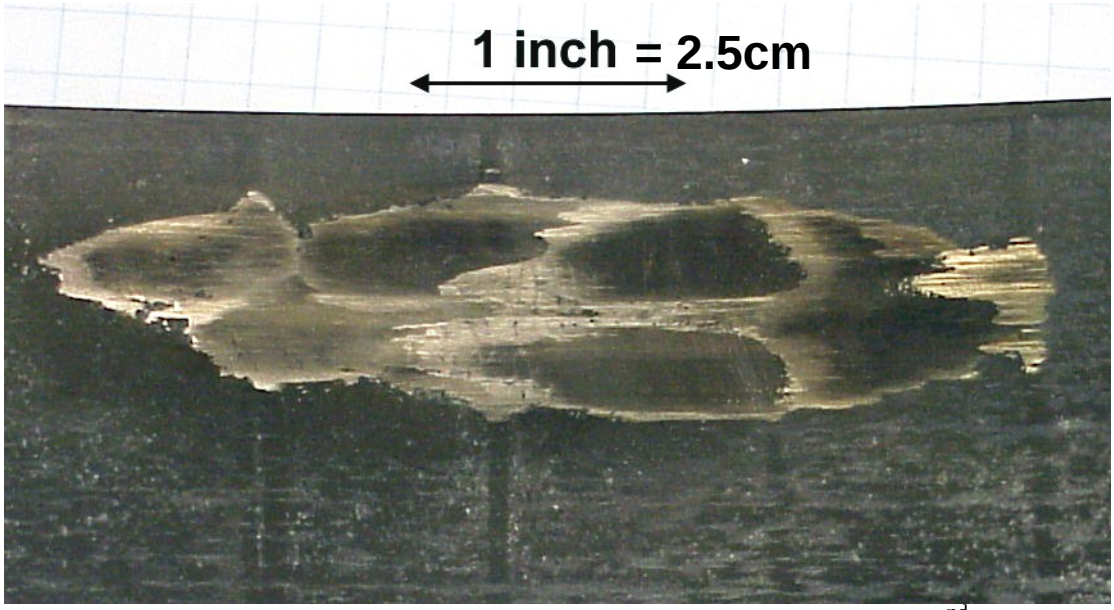

Figure 3-243. Photograph of the blade tip rub on the prepreg MI CMC 2nd stage shroud following the first 2 hours of engine testing. The light, silvery markings are blade alloy smeared over the surface of the CMC shroud.

Figure 3-244. Close-up photograph of the edge of the blade rub region showing the metal from the blade smeared over the CMC shroud. Little to no abrasion of the CMC was noted.

Some minor chipping of the shroud ring was noted along the trailing edge where the shroud rests against a metallic retaining ring. As noted earlier, the trailing edge of the shroud ring was not entirely uniform before engine testing because of a machining error. In areas where the trailing edge surface was not completely flush some chipping of the inner composite ply occurred. A photograph of the largest such chipped region is shown in Figure 3-245. Although the machining defects are believed to be the greatest contributor to the chipping damage, the excessive vibration that would come from a blade tip rub probably also contributed.

The survival of the shroud through a blade tip rub was both a good and bad result. From a material development perspective the survival of a rub was very positive in that it clearly demonstrated the damage tolerance and toughness of the composite to "abusive" exposure conditions. Coming into this engine test the possibility of a blade tip rub, and the unknown consequences that would result, was one of the biggest risks that was faced. The MI CMC composite shroud ring came through such an event apparently unscathed.

On the other hand, the fact that a blade tip rub occurred at all was a negative result with respect to the shroud design. Considerable effort was taken to develop a shroud attachment/mounting system that should have controlled the radial position and circularity of the shroud so that it remained concentric with the turbine casing, and thereby with the rotor. The CMC shroud ring also had a 1mm greater ID than the nominal segmented metallic shroud in order to minimize the possibility of a blade rub during these initial tests. Nonetheless, the fact that a blade tip rub occurred indicated that either the shroud attachment scheme was not operating as planned and the shroud concentricity with the rotor was not being maintained or that the engine itself had thermal distortions during

operation that are causing the rotor and casing to loose concentricity. Determining which was the true cause of the blade tip rub would require additional information. Linear Variable Differential Transformer (LVDT) sensors were procured for use in later testing to get a better indication of the position of the shroud ring during engine start-up, operation and shut-down.

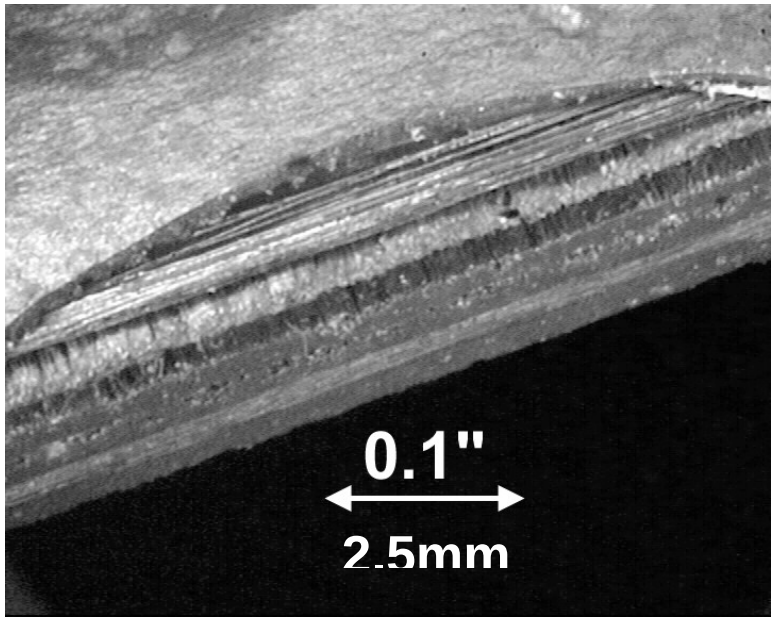

Figure 3-245. Oblique photograph (roughly at 45°) of the trailing edge of the CMC shroud following the first engine test showing the largest occurrence of surface chipping damage.

Since no visible damage was found during the inspection this same shroud ring was re-assembled into the engine and engine testing resumed. The next stage of the engine test plan was to run 64 hours of "steady state" FSFL exposure using eight 8 hour engine runs. The engine was started in the morning, run during the normal 8-hour plant shift, and then shut down and allowed to cool overnight. Following the total 64 hours of exposure the engine was again disassembled and the CMC shroud ring removed for inspection. Visual inspection of the shroud indicated that additional blade tip rubbing had occurred in the same location on the shroud, and that a new rub occurred at a different location. Again, the depth of rub was very small with no visible damage to the CMC shroud. Additional chipping of the shroud trailing edge was also noted, but again the extent of chipping and potential impact on shroud performance were small.

This same shroud ring was subsequently re-inserted into the engine for the completion of this stage of engine testing. The final part of the test plan consists of 32 hours of cyclic testing, including 6 cold starts, 12 hot starts, 13 normal stops and 5 turbine trips. This testing was completed in December, 1999. Overall the test was quite successful, with the shroud ring surviving the full 100 hours with only very minor chipping of the shroud

trailing edge. More importantly, the shroud survived at least 3 separate blade tip rub events without failure.

The results of the engine tests were so positive that Nuovo Pignone decided to do additional engine testing not in the original test plan. Although the shroud ring survived the blade rubs, the shroud ring, seals and attachments were designed to prevent such rubs from occurring. The fact that they occurred indicates that at least one of these features is not operating as expected. Each of the blade rubs occurred adjacent to an alignment slot in the shroud ring, suggesting that the shroud was "sticking" on the alignment pins and thus could not grow radially during heat up of the engine. However, free radial growth of the back-side seals was also being questioned.

As a preliminary design modification the number of alignment slots was doubled. The shroud ring was fairly large in diameter, but had a relatively thin wall section, causing it to be fairly compliant mechanically. Consequently the shroud ring could be easily elastically deformed beyond the out of the roundness specification by rather modest localized forces. The additional alignment slots would provide more physical constraint to hold the shroud ring to a circular shape. Conversely, the compliance of the ring would also have allowed it to deform if "sticking" at the alignment slots or seals had occurred, thereby limiting the induced mechanical stress. The extra constraint added by the additional slots could cause much higher stresses if such sticking were to occur again.

The lvdt sensors mentioned above were also installed into the inner casing of the engine so that the position, diameter and circularity of the shroud ring could be monitored during engine operation. This data was needed to better understand the operation of the seals and attachments, and was critical to the design of the stage 1 shroud since similar seals and alignment features were also being considered for that application. Verifying proper operation of these features in the stage 2 shroud was necessary before finalizing the stage 1 shroud design.

The Additional engine testing of the PGT-2 stage 2 shroud ring was performed during April and May of 2000. Approximately 20 additional test hours were run with the new configuration. The installed displacement sensors indicated that the shroud ring was not deforming (i.e. going out-of-round) during engine operation. Post-test inspection of the ring indicated no new rub events. Subsequent to this test the stage 2 shroud was re-assembled with only 1/2 of the alignment slots being used so that the attachment was similar to that used in the initial engine tests in 1999. During this test an increase in the variability of the radial displacements was noted, indicating greater shroud out-of-roundness. These results indicated that the temperature-induced ovality of the inner shroud, which led to the blade tip rubs in the 1999 tests, was prevented by the increase in the number of shroud alignment slots.

Up to this point the stage 2 shroud had seen 135 hours, including 25 normal starts and 15 turbine trips, of engine exposure. The original testing plan had called for an additional 900 hours of engine exposure testing at a field site. However, 1000 hours of engine testing of the stage 1 shroud, to be discussed below in Section 3.8.3.2, was also pending. NP

management decided to continue the shroud testing using the on-site test bed engine rather than incurring the cost of additional shut downs of a customer engine, and also because the performance of the shrouds could be more closely monitored with the on-site engine. Consequently the additional 900 hours of engine test of the stage 2 shroud was done in conjunction with the testing of the stage 1 shroud, and is discussed in Section 3.8.2.3.3.

3.8.3.1.4 Post-Test Characterization

Between the preliminary testing done on only the stage 2 shroud and the combined long-term testing of both the stage 1 and stage 2 shrouds, the prepreg MI CMC stage 2 shroud ring accumulated 1035 hours of testing under full speed, full load conditions, including 61 normal starts, 34 normal stops and 27 trip stop cycles. The measured backside temperatures during steady state operation averaged about 660°C with a spread of +10/-20°C depending on exact location. Early heat transfer calculations of the shroud indicated expected shroud temperatures to vary from 735-585°C (the large temperature variation is caused by the circumferential temperature distribution resulting from the use of a single combustor can plus the fore-to-aft temperature drop through the second stage). The measured shroud temperatures were consistent with these predictions.

One additional blade tip rub was noted beyond the three rubs that occurred during the first 100 hours of testing. In all cases the rubs did not appear to cause any cracking of the shroud. The rubs were characterized by a slight removal of material from the shroud surface coupled with smearing of blade tip alloy over the shroud surface adjacent to the rub. In two of the rub locations the rubs were deep enough to expose the reinforcing fiber.

3.8.3.1.4.1 Non-Destructive Characterization

Following engine exposure the shroud was put through various nondestructive and destructive analyses. NDE analyses, including transmission IR thermography, water-coupled ultrasound and air-coupled ultrasound inspections, were performed at ANL. Additional NDE characterization, including reflective IR thermography and fluorescent dye penetrant inspection, were done at GEGR.

Water-coupled ultrasound transmission images for the CMC stage 2 shroud before engine testing, after 100 hours of preliminary engine testing, and after the full 1035 hours of engine testing are shown in Figure 3-246. (The pre-test image is offset so that the image features line up vertically.) Note that only 4 alignment slots are on the pre-test image, whereas the images after 100 hours and 1035 hours show 8 alignment slots. A significant indication became apparent after the first 100 hours of testing, but did not appear to grow at all during the subsequent 935 hours of engine exposure testing. It was not clear whether this defect was introduced during the actual engine testing or during engine assembly and disassembly.

Transmission IR thermography images from before and after testing are shown in Figure 3-247. (The IR camera at ANL was broken during the inspection period after 100 hours exposure so that no image was obtained by thermography at that testing interval.) The thermography images corroborated the observations of the ultrasound quite well.

Particular attention was paid to the regions of blade tip rubs during the NDE inspections. Figure 3-248 shows a detailed IR thermography image of the location on the shroud ring that had the most severe blade tip rub. Despite the blade rub, there was no damage or defect detected.

Reflection, time-of-flight, IR imaging was also performed on the shroud at GEGR. Figure 3-249 shows the defect depth image determined for the section of the shroud ring that included the delamination-like defect that occurred during engine testing. The size and shape of the defect in reflection match those determined by the transmission IR inspection. The IR reflection technique gives added information as to the depth of the defects relative to the object thickness. The image in Figure 3-249 is a false color image with the color correlated to the depth of the defects detected. This analysis indicated that the delamination that formed during testing was ~1mm below the outer surface of the shroud ring.

Fluorescent dye penetrant testing was performed to look for the presence of through-thickness cracks. Areas considered to have higher probability of developing such cracks, particularly the areas of blade tip rubs and the attachment slots, were examined closely. Figure 3267 shows the results of the dye penetrant inspection performed at the most severe blade rub areas. Although a large number of surface scratches were highlighted by the penetration of the dye, none were found to be cracks that propagated through the wall of the shroud. Inspection at attachment slots did not reveal any through-thickness cracks either.

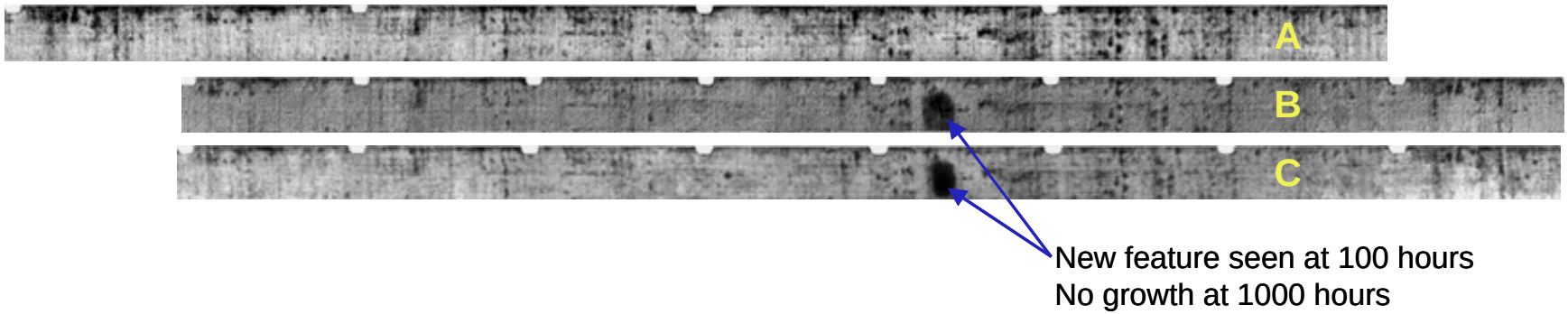

Figure 3-246. Water-coupled ultrasound images of the prepreg MI CMC PGT-2 stage 2 shroud ring.
A – as fabricated condition before engine testing;
B – after 100 hours of rig testing and re-machining of additional alignment slots;
C – after 1035 hours of engine exposure testing.

Figure 3-247. IR transmission thermography images of the PGT-2 CMC stage 2 shroud both before and after engine testing.

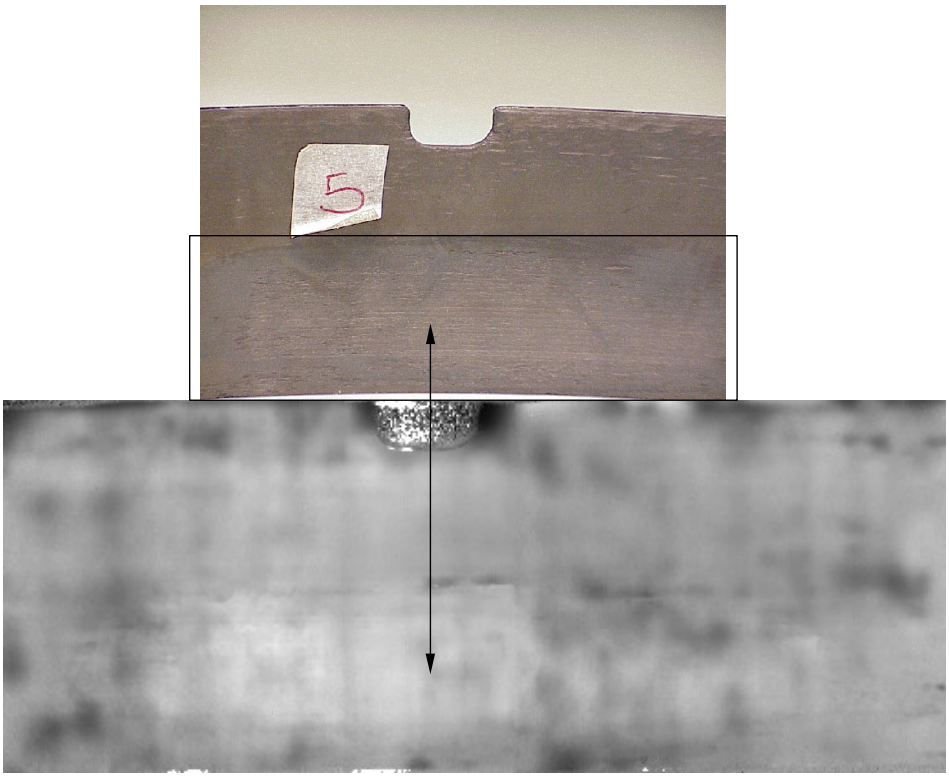

Figure 3-248. Photograph (top) and detailed IR thermography image (bottom) of the region of the stage 2 shroud having the most severe blade tip rub event.

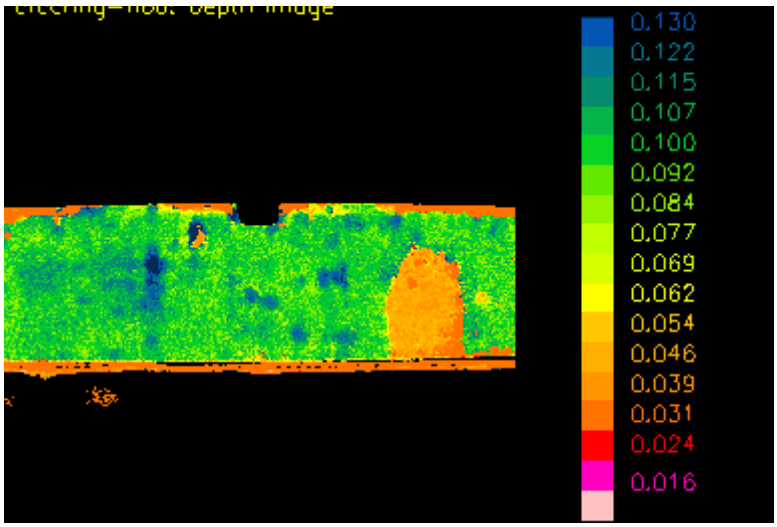

Figure 3-249. Reflection IR depth image showing the location of the delamination-like defect that developed during engine testing. This image shows the defect to be ~1mm below the outer surface of the shroud ring.

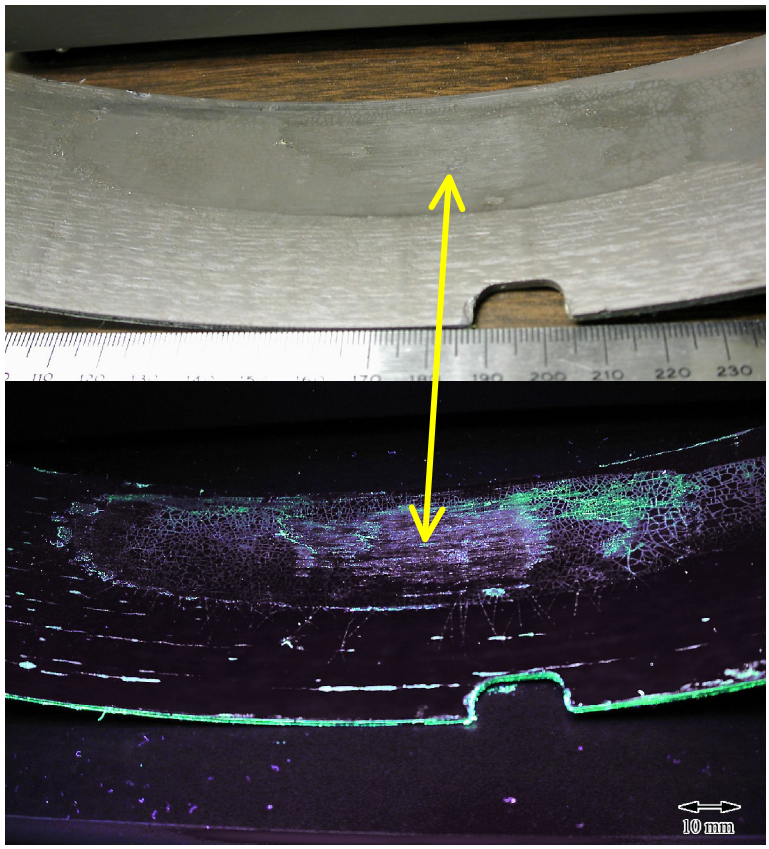

Figure 3-250. Photograph (top) and black light photograph (bottom) following fluorescent dye penetration of the section of the PGT-2 stage 2 shroud that had the most severe blade tip rub.

3.8.3.1.4.2 Destructive Characterization

Limited destructive analyses were done on the stage 2 shroud ring. One of the first issues of interest was whether there was any residual strain (stress) in the shroud as a result of the engine exposure. Four micro-strain gages were mounted on the surface of the ring before it was cut. Two of these were mounted on the inside surface while the other two were mounted on the outside surface. The difference between the readings of the strain gages before and after the shroud was cut gave a direct measure of the residual strain in the shroud.

The strain gage readings were initially set to zero. The stability of the readings was monitored over a period of four hours. It was found that after an initial warm up period of 10 minutes, the readings were stable. Readings taken from the strain gages after 24 hours showed a drift of only ± 0.0002 % strain demonstrating that the strain gages had adequate stability and could be used to do the measurements. Figure 3-251 shows the location of the strain gages and the relative position of where the initial cuts were made on the shroud. The numbers in the drawing refer to the positions of attachment slots.

The results of residual strain measurement are given in Table 3-62. The strain gage readings were taken after the shroud was cut at the two locations indicated in Figure 3-

251. The measured values show that the residual strain in the shroud ring was very small. To put the values in perspective it is worth mentioning that the average value of strain measured at matrix cracking in pre-preg MI CMCs is ~0.06 %. It was interesting to note that the results indicated that the outer surface of the shroud was in compression while the inner surface was in tension. This observation suggested that the shroud might have gone through a net shrinkage during fabrication and/or the engine test.

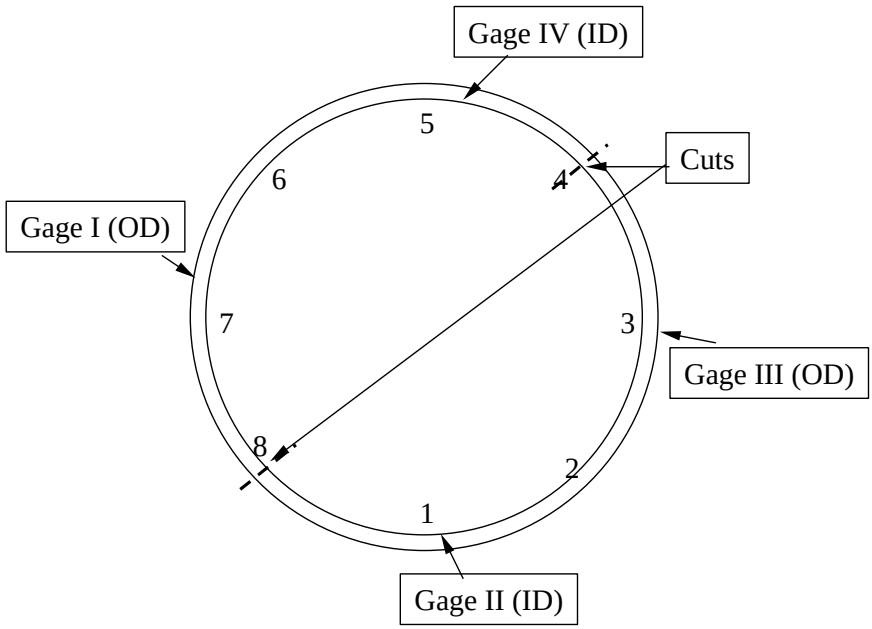

Figure 3-251. Schematic showing the positions of the strain gages bonded to the PGT-2 stage 2 shroud ring prior to cutting.

Table 3-62. Residual Strain Measured from Strain Gages Bonded to the PGT-2 Stage 2 Shroud Ring After Cutting the Ring for Destructive Analysis.

Strain Gage ID	Location	Surface	Reading (microstrain)	Reading (%)
I	between slots 6 & 7	outer	40	0.004
II	between slots 1 & 2	inner	-24	-0.0024
III	between slots 2 & 3	outer	60	0.006
IV	between slots 4 & 5	inner	-60	-0.006

Retained mechanical properties of the stage 2 shroud after the engine test were measured by sectioning several ~13mm wide strips with edges parallel to the ring axis for tensile testing. The strips were cut from specific areas of interest such as blade rubs and areas where internal defects were detected by NDE. The cutting scheme is shown in Figure 3-252, which is a detailed thermal diffusivity image of the shroud. The test bars could not be directly gripped in a tensile test machine that has flat grips because of curvature across

their width. In order to overcome this problem, rectangular pieces of copper were cut from a 3.2mm thick plate that were then machined to get profiles that matched the curvature in the bars. The copper pieces were used as spacers between the bars and the hydraulic grips during the tensile tests. In addition, the ductile nature of the copper would allow it to deform and accommodate any surface roughness in the CMC bars that might otherwise cause stress concentrations. Figure 3-253 shows an illustration of how the copper spacers were used during testing.

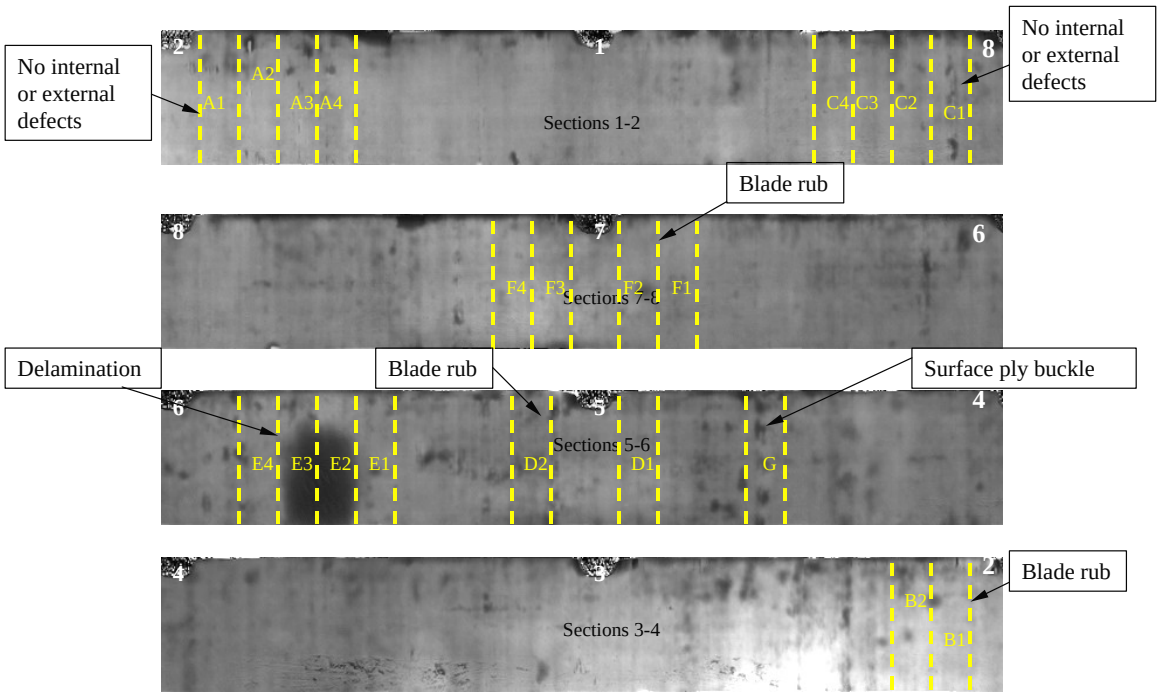

Figure 3-252. Detailed thermal diffusivity image showing the cutting scheme for tensile bars that were used to characterize the post-engine test mechanical properties of the PGT-2 2nd stage shroud. Test bars were cut from different locations of interest such as blade rubs and areas with internal defects.

The length of each tensile bar was only 57mm, which corresponds to the height of the shroud ring. Approximately 19mm on each end of the bar had to be used for gripping during the tensile test. This requirement made it impossible to get direct strain measurements using a standard extensometer that normally requires a 25mm gage length. Instead, micro-strain gages were mounted on opposite surfaces of the bars and were used to monitor strain during the tensile tests.

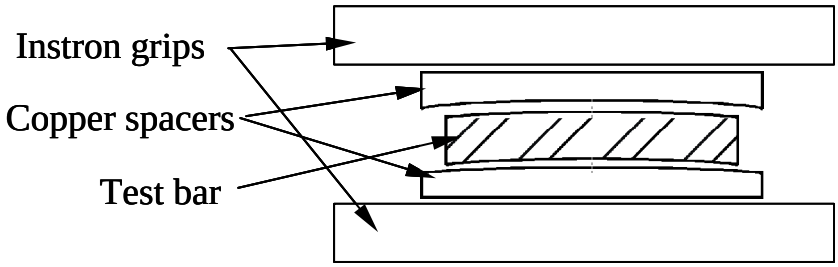

Figure 3-253. Schematic representation of the gripping method used to test the bars cut from the shroud ring. The copper spacers were machined to fit the curvature of the bars in order to avoid creating stress concentrations.

Tensile test results from the bar strips cut from the stage 2 shroud are summarized in Table 3-63. The properties measured on a witness bar that was processed at the same time as the shroud rings are also included in the table for comparison. One interesting observation from the values in the table is related to material properties measured in the areas where blade rubs occurred. A close examination of these bars revealed that material removal in some places was as deep as the second or third ply. However, as seen in Table 3-63, the properties measured from these bars were as good as properties measured in bars that were cut from sections of the shroud where there was no apparent damage. Another interesting observation was that the elastic portion of the stress-strain curves corresponding to bars cut from blade rub areas was not linear. Non-linearity in CMC materials is typically caused by cracks present in the matrix prior to the tensile test. As described in the section on NDE results, the presence of surface cracks at blade rub locations was evident from the results of dye penetrant inspection.

Table 3-63. Summary of Retained Tensile Strength Properties of Test Bars Cut from the PGT-2 Second Stage Shroud*

Sample condition	Proportional Limit (MPa)	Ultimate Strength (MPa)	Strain to Failure (%)
Witness panel	152	201	0.62
Shroud – no apparent defects	130 ± 9	198 ± 30	0.62 ± 0.14
Shroud – blade rub area	123 ± 10	203 ± 19	0.61 ± 0.10
Shroud – internal defects	107 ± 21	138 ± 9	0.26 ± 0.11

* ± limits represent one standard deviation for 4 to 6 tests

In bars cut from areas where there was no apparent damage and bars cut from blade rub areas the average values of the measured properties were mostly comparable with properties measured in witness bars that were processed at the same as the shrouds. The only difference was the slightly lower value of the proportional limit stress in the bars cut from the shroud. It is important to note that despite the obvious surface damage and material removal caused by the blade rub, the CMC material exhibited graceful failure

during the tensile test with no degradation of ultimate strength or strain to failure. This result shows that the material was able to retain reasonable damage tolerance characteristics.

Bars cut from areas of the shroud that contained delaminations or ply wrinkles did exhibit property knockdowns relative to the witness bars. The stress-strain curves obtained from testing these bars were typically characterized by extended strain deformation at a constant stress after the initial matrix cracking (see Figure 3-254). Failure in these bars was characterized by a stepped fracture surface that coincided with the plane of delamination. The results obtained from these bars demonstrated that , as expected, delaminations could have deleterious effect on the mechanical properties of a component.

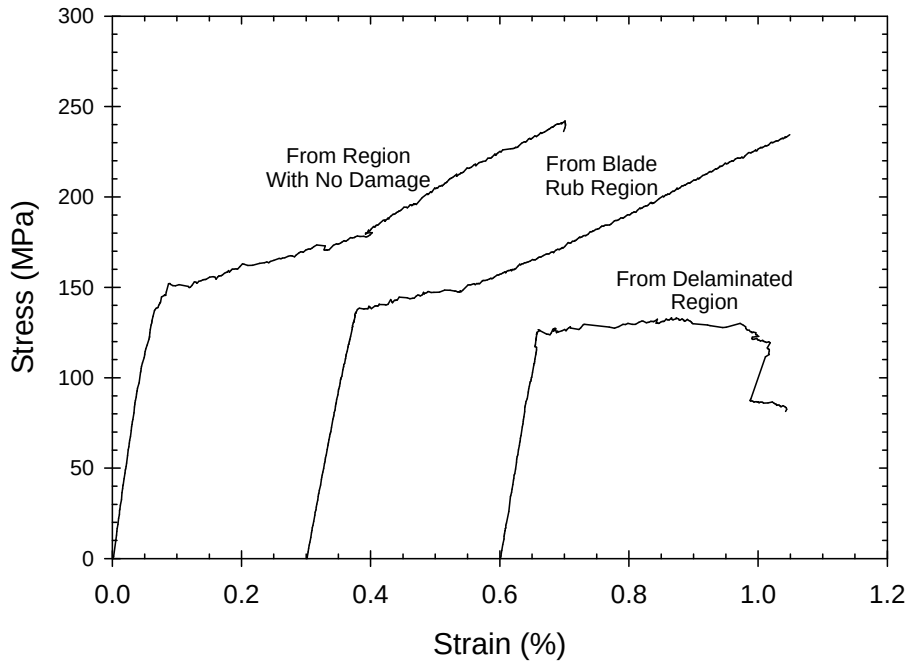

Figure 3-254. Representative tensile stress-strain behavior of several samples cut from the PGT-2 stage 2 shroud ring after 1035 hours of engine testing.

3.8.3.1.4.3 Microstructural Characterization

Figure 3-255 compares optical micrographs taken from polished metallography specimens prepared from as-fabricated and post-engine test material pieces cut from the PGT-2 stage 2 shroud. The micrograph of the post-engine test material was specifically taken from a region where there was no apparent damage. Comparing the two micrographs no noticeable difference could be found. Figure 3-256 shows a micrograph from a sample cut from a region of the shroud where both thermal and water UT imaging suggested the presence of a delamination. It can be seen that there is indeed a delaminated region in the middle longitudinal ply of the shroud. There was good agreement between the actual size of the delamination measured after cutting and the size determined from NDE. Furthermore, the depth at which the delamination is located with

respect to the shroud wall was in good agreement with the result of the reflection IR NDE imaging.

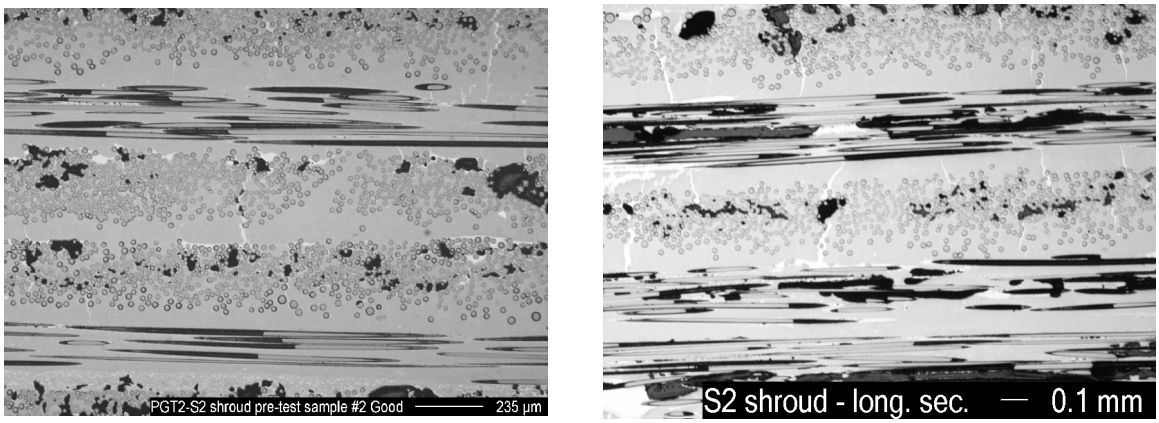

Figure 3-255. Optical micrographs of samples cut from the PGT-2 stage 2 shroud before engine testing (left) and after 1035 hours of engine testing (right).

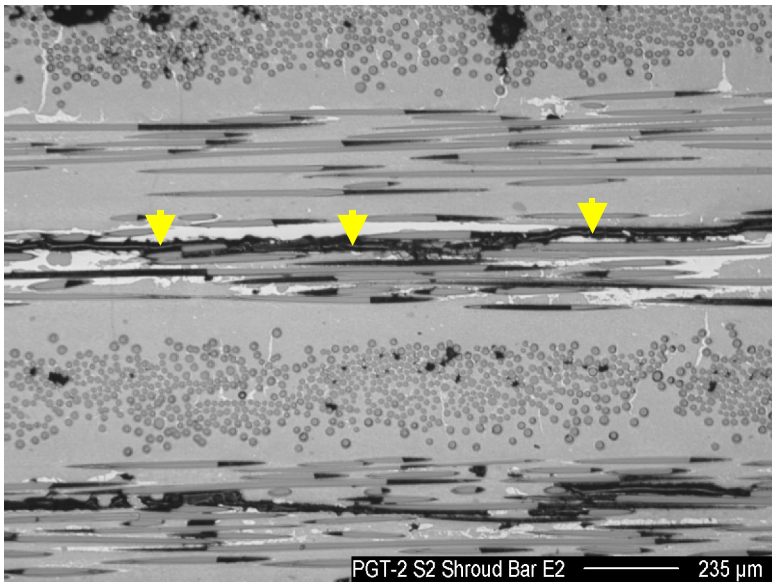

Figure 3-256. Optical micrograph of a sample cut from a region of the stage 2 shroud where NDE inspection suggested the presence of a delamination-type defect. An actual intra-ply crack / delamination was found and is indicated by the arrows.

Samples cut from blade rub regions were mounted and polished such that the shroud could be examined in cross section. Figure 3-257 shows an edge-view photograph of such sections taken from the blade tip rub regions showing the partial wall thinning due to abrasion during the rub. Optical microscopy of these samples revealed that matrix cracking had occurred to a limited depth, such as shown in Figure 3-258. Cracks were

not found elsewhere in the shroud away from the blade rub areas. These observations were in good agreement with the results of the dye penetrant inspections that revealed a large concentration of surface scratches and/or cracks at the blade rubs (see Figure 3-250).

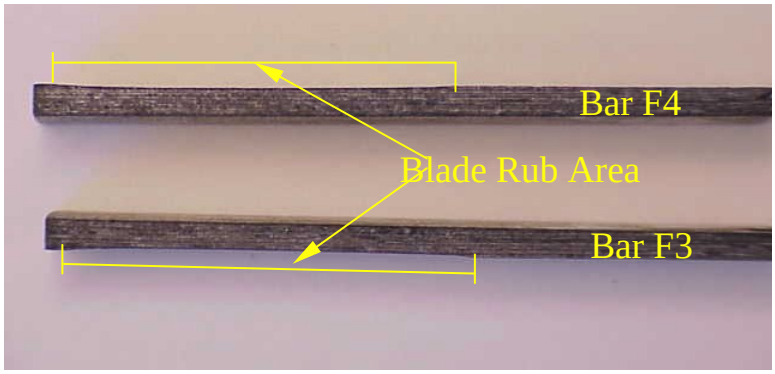

Figure 3-257. Photograph of sections cut from the PGT-2 stage 2 shroud in the blade rub regions showing slight wall thinning due to abrasion during the blade rub.

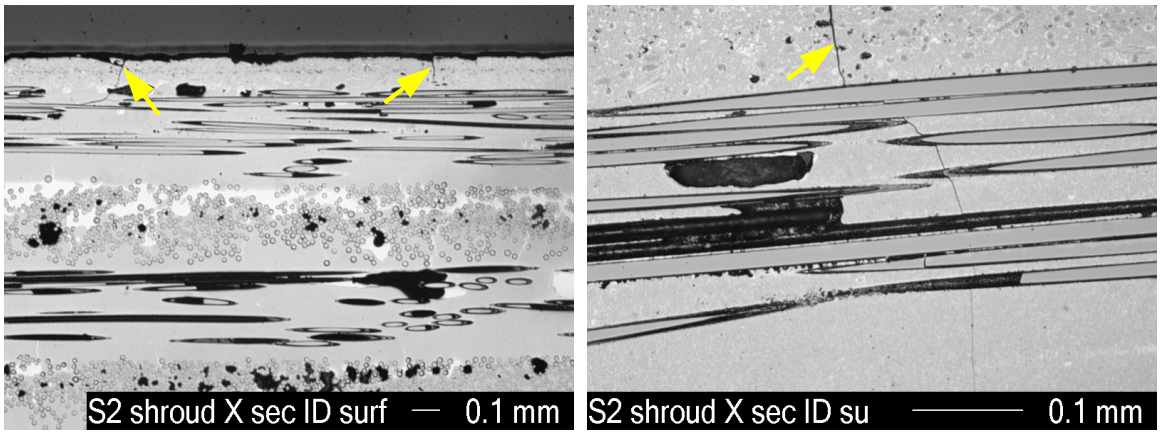

Figure 3-258. Optical micrographs of the PGT-2 stage 2 shroud in a region where a blade rub had occurred during engine testing. Surface matrix cracks were found and are indicated by the arrows. The cracks seldom penetrated any further than the first ply of the composite.

Another feature found at the blade rub areas was the presence of what appeared to be embedded metallic particles in the shroud surface. These particles were believed to be chunks the blade tips that abraded into the shroud during the rub events. In order to confirm this the sample was further examined by SEM. Figure 3-259 shows SEM micrographs taken at the surface of an area where a blade rub had occurred. The lower magnification image shows that a ~100μm wide band of material that has a lighter contrast compared to the SiC matrix was present at the surface of the shroud. As seen in the higher magnification image the large particles were embedded in what appeared to be a mixture of the light and dark contrast phases.

The composition of several embedded particles was analyzed with energy dispersive x-ray spectroscopy (EDS). A typical example of the spectra collected is shown in figure 3-260. The spectrum contains strong peaks corresponding to Si, Ni, Cr, Ti, Co, and Al. If the Si is ignored, the EDS spectrum suggests that the embedded particles have a composition that corresponds to the turbine blade alloy. Although there was no direct evidence, the cause for the strong Si peak might have been from SiC that was mixed in with the metallic particles during the blade rub, or from diffusion of matrix Si into the alloy particles during engine exposure.

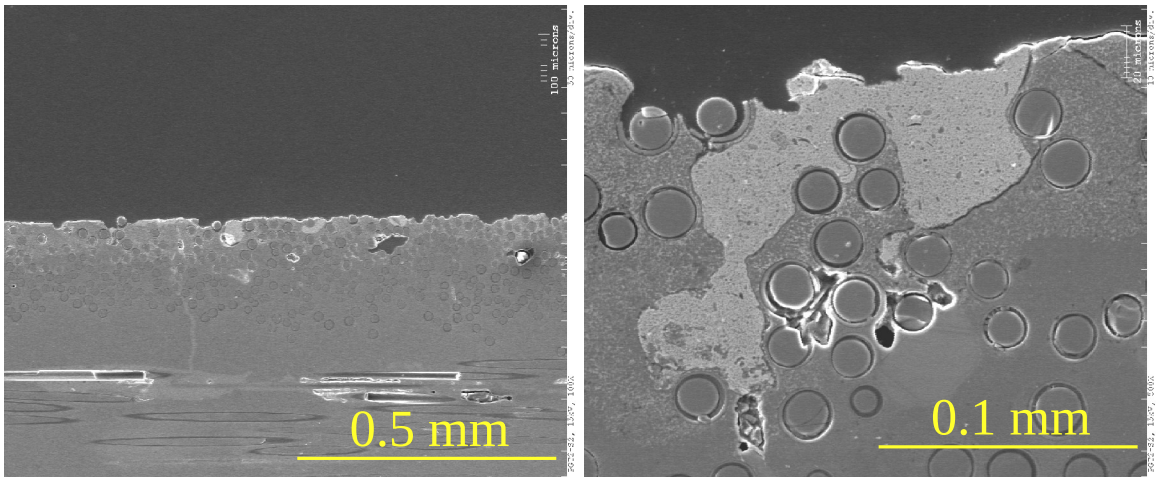

Figure 3-259. SEM micrographs from a blade rub on the inner wall of the PGT-2 stage 2 shroud. The lighter gray phase embedded in the surface asperities are foreign material that was probably embedded in the wall during the blade rub.

Surrounding each of the embedded particles was a region of the composite matrix that had an unusual light and dark contrast in the SEM. Figure 3-261 shows an EDS spectrum that was collected from the composite matrix nearby to one of the embedded particles. The spectrum showed mainly Ni and Si and contained only small or zero amounts of the other elements found in the larger embedded particles. Figure 3-262 shows another EDS spectrum collected from a phase found at the interface between one of the large embedded particles and the composite matrix. It can be seen that this phase contains significantly smaller amounts of Ni compared to the spectra presented in Figures 3-260 and 3-261.

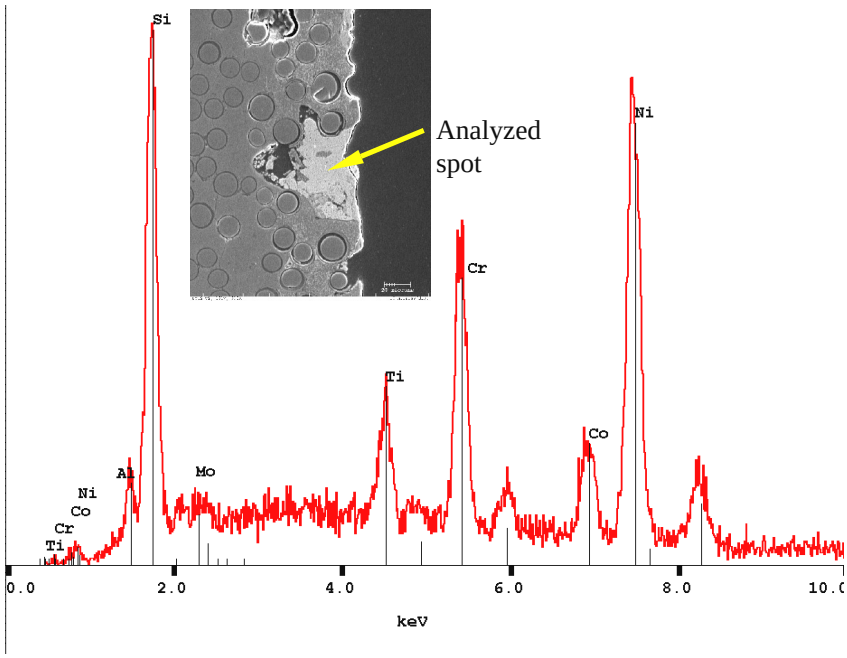

Figure 3-260. EDS spectrum acquired from an embedded particle in the surface of the PGT-2 shroud ring in a region where a blade rub had occurred. The Ni, Cr, Ti, Co, Al and Mo peaks correspond to the blade tip alloy.

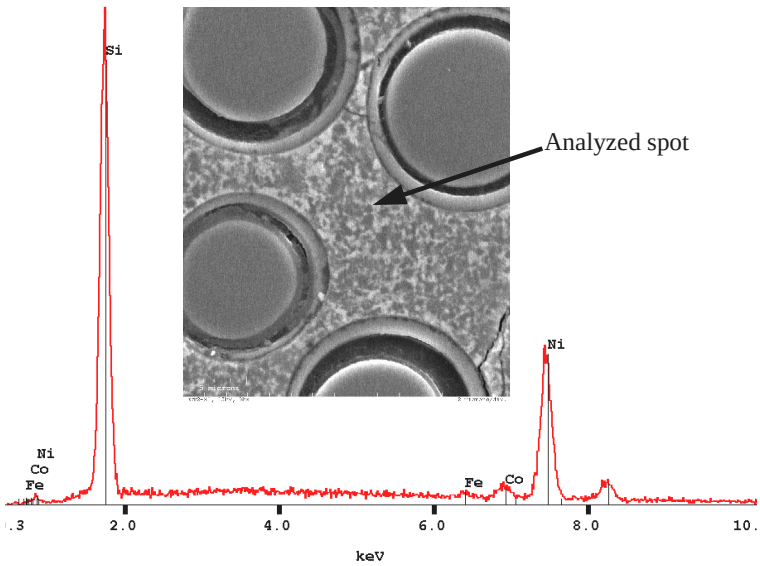

Figure 3-261. EDS spectrum acquired from the composite matrix phase surrounding one of the embedded particles in a blade rub region of the PGT-2 stage 2 shroud. This spectrum contains strong peaks only for Si and Ni.

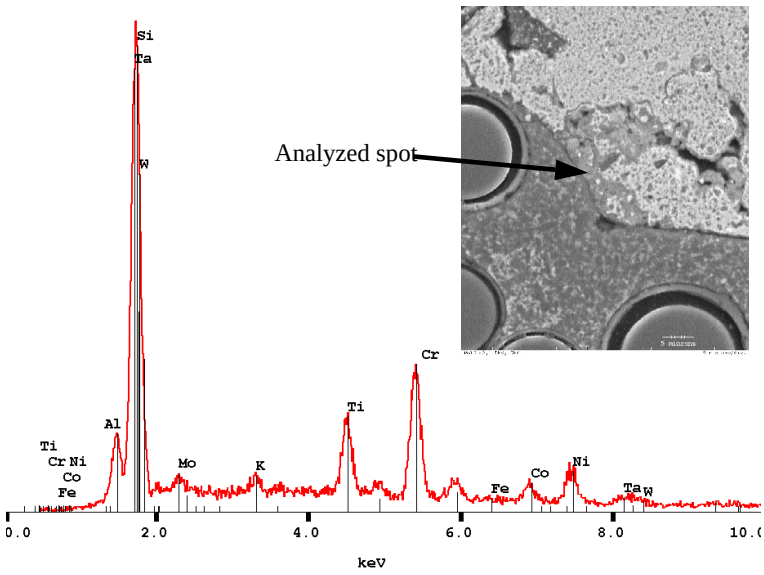

Figure 3-262. EDS spectrum acquired from phase found at the interface between a surface embedded particle and the composite matrix in a blade tip rub region of the PGT-2 stage 2 shroud ring. The spectra shows many of the elements of the blade alloy with reduced levels of Ni compared to the embedded particles.

These observed differences in composition around the embedded particles indicated that the incorporation or formation of the secondary phase network in the ring surface could not have occurred by a simple abrasion process. Rather the results suggest that the embedded particles of blade tip alloy interdiffused and reacted with the composite SiC-Si matrix to form nickel silicide in the composite matrix and a Si-rich, Ni-depleted phase at the particle-matrix interface. The Ni-Si system contains a eutectic that melts at ~ 965°C, that would be further reduced by the presence of the other alloy constituents. It is not unreasonable to assume that melting of this eutectic could explain the distribution of the secondary phase. Such a scenario may seem unlikely when one considers the relatively low temperatures measured in the ring wall during the engine test (575°C-665°C); however, a transient higher wall temperature could have occurred during the blade rub event due to frictional heating that could have been sufficient to cause the melting of the eutectic.

3.8.3.2 Stage 1 Shroud

Work on the PGT-2 stage 1 shroud was performed under contract Task 3.3.f 2MW Turbine Stage 1 Shroud. The purpose of this task was to design, fabricate and engine test a first stage shroud component for a Nuovo Pignone PGT-2 (now called GE Oil & Gas GE-2) turbine engine. The PGT-2 had a turbine inlet temperature of roughly 1010°C with a gas temperature of ~980°C in the vicinity of the first stage shroud. The higher gas temperature and pressure, tighter blade tip clearance and greater risk of turbine damage should a failure occur all made the 1st stage shroud component more challenging to design than the 2nd stage shroud. Fortunately considerable practical experience was gained from the 2nd stage shroud tests that helped to guide the design and fabrication efforts for the 1st stage shroud.

3.8.3.2.1 Stage 1 Shroud Design

Several conceptual designs for the PGT-2 first stage shroud were generated and reviewed. Several of these concepts are shown in Figure 3-263. All designs included a single piece CMC shroud ring backed by a "piston ring" seal and held in location using metallic pins or tabs engaging slots in the CMC ring. Based on the difficulty of fabrication, machining requirements, and the anticipated magnitudes of the thermal gradients and stresses, design concept C from Figure 3-263 was chosen for detailed thermal and structural analysis. The initial design of the CMC shroud ring corresponding to the selected concept is shown schematically in Figure 3-264A.

The CMC part of the 1st stage shroud design C is a 424mm diameter, single-piece ring with varying cross section. The increased thickness of the aft section of the ring was intended to provide additional stiffness compared to the 2nd stage shroud ring design. Radial alignment and free thermal growth was accomplished by using eight radial slots in the CMC ring. Unlike the 2nd stage shroud, the slots in the 1st stage shroud extended only part way through the thickness so that none of the metallic outer shroud assembly would be exposed to the hot gas path. Considerations were made to spring load the alignment pins, but this option was rejected due to concerns over spring relaxation and possible seizing of the pins due to oxidation.

Although concept "C" gave good results in the design analyses there were some remaining concerns about the flexibility of the thin, forward section of the shroud ring and the subsequent ability to seal well to this surface. Also, based on the observations of the 2nd stage shroud ring deformations during engine testing there was a desire to make the stage 1 shroud as stiff as possible to prevent such deformations. Somewhat later in the design process a different shroud ring design was developed to address these concerns. The main difference in the designs was that the newer design had a larger thickness in both the forward and aft ends of the ring with a machined circumferential slot in the CMC for location of the seals. This improved shroud system design "E" is shown schematically in Figure 3-265, and the drawing for the CMC shroud ring for this design in shown in Figure 3-264B.

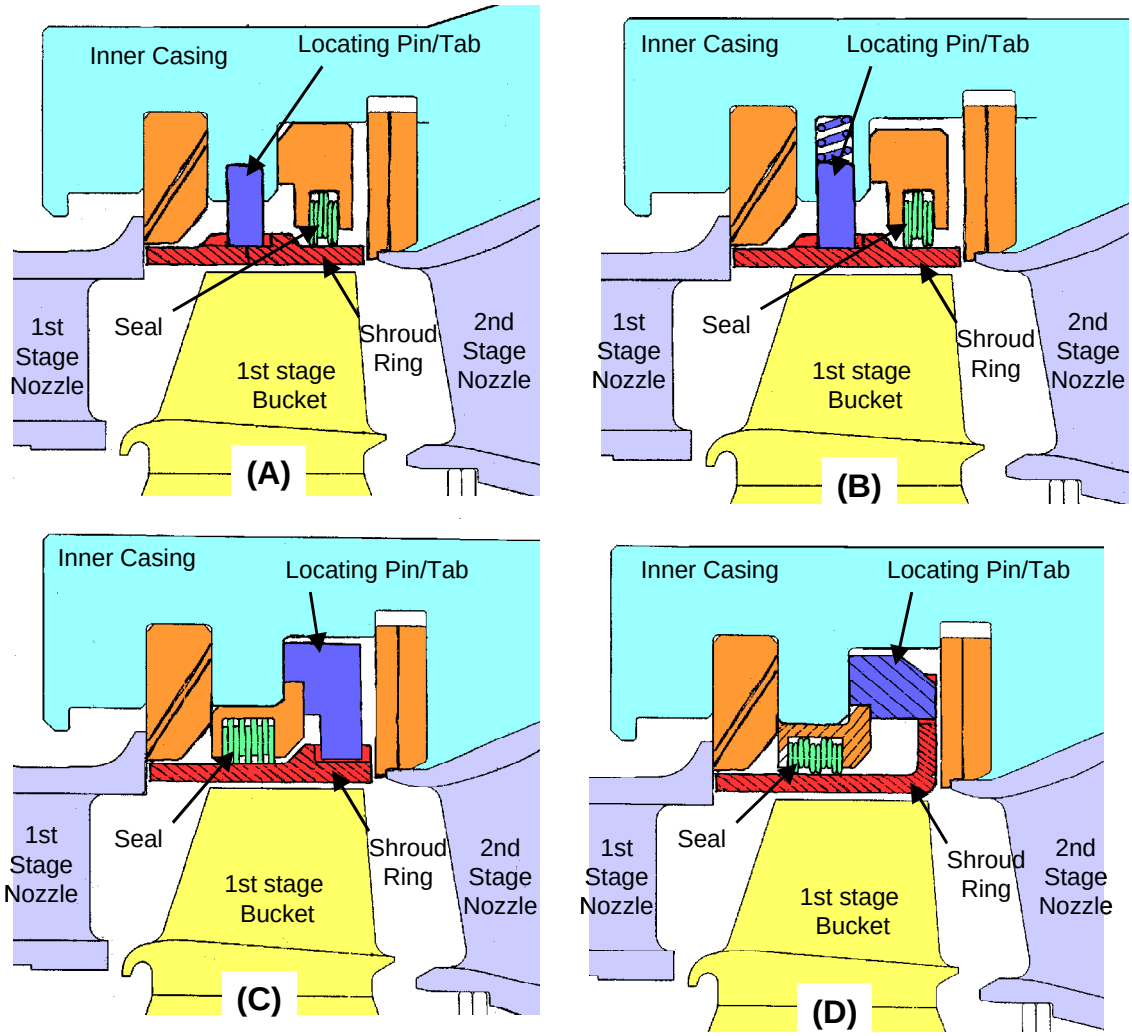

Figure 3-263. Schematic drawings of various PGT-2 stage 1 shroud conceptual design options that were considered.

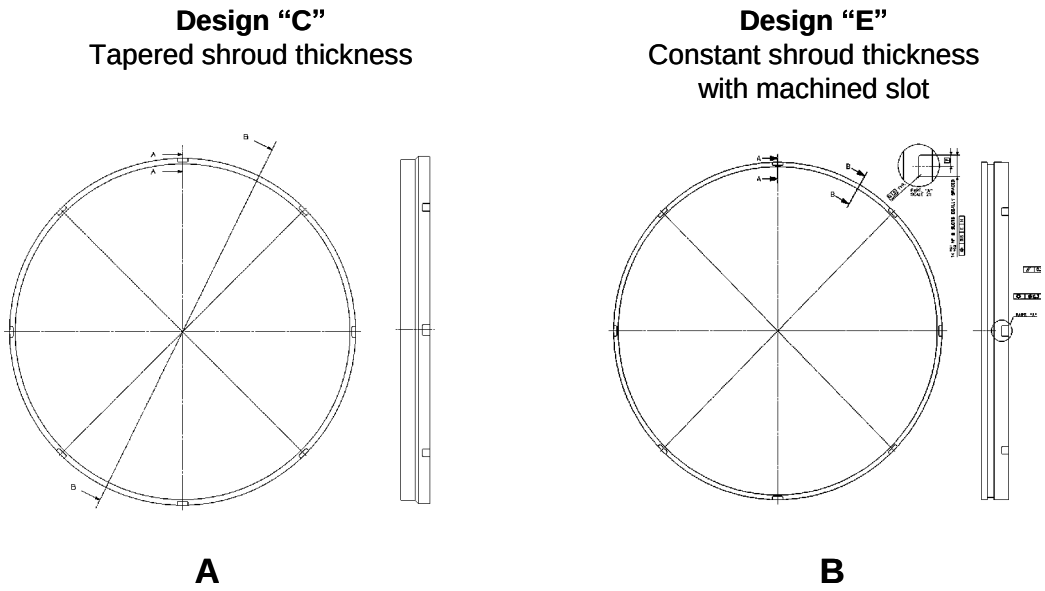

Figure 3-264. Drawings of the CMC ring component for the PGT-2 1st stage shroud design concept "C" (A) and concept "E" (B).

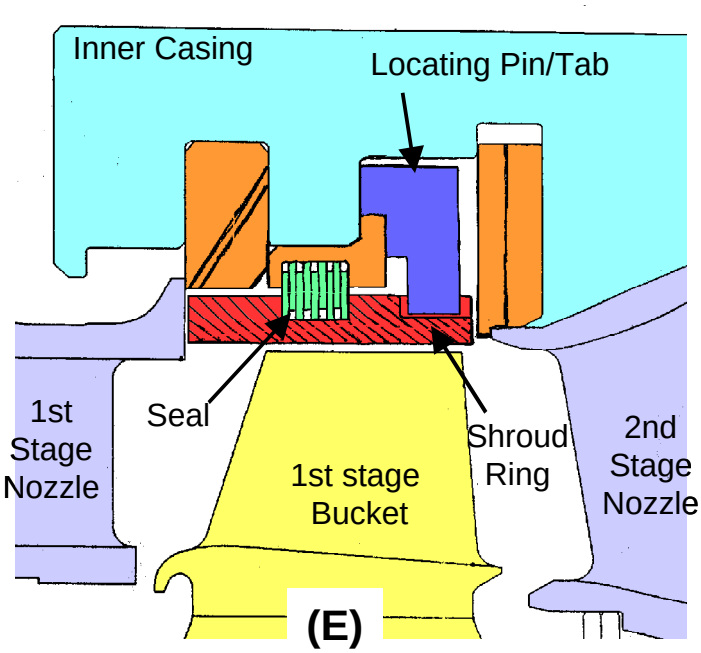

Figure 3-265. Schematic representation of the PGT-2 stage one shroud system design "E" incorporating a constant thickness CMC shroud ring with a circumferential slot for engagement with the seal.

For the 1st stage shroud the ANSYS thermal and structural analyses were done largely by the engineering team at Nuovo Pignone. The overall result was that the temperature and

stresses in the stage 1 shroud design “C” and “E” were both within the material design limits.

3.8.3.2.2 Stage 1 CMC Shroud Fabrication

Initial fabrication trials were done on shroud design “C”. This design incorporated a stepped wall thickness, which was a new feature that had not been previously fabricated. Three fabrication trials were made, two being sub-scale and one being full-scale, to verify that such a feature could be fabricated and infiltrated. The initial trial pieces showed a tendency to form delaminations at the boundary between the thick and thin wall sections; however, slight modification to the lay-up process were effective at minimizing this problem.

The first stage 1 shroud for engine testing, which utilized the last remaining inventory of “good” coated fiber from Advanced Ceramics, was subsequently fabricated in March, 2000. The ID dimension requirements of this ring had a tolerance of 422.4+/-0.15mm with a circularity of 0.3mm. The ring fabricated at GEGR had an average measured ID of 422.3mm, but showed a deviation of +/-0.55mm. This ring was sent to the machining vendor, Chand Kare Associates, Inc., for grinding of the ID surface, grinding of the OD surface in the seal mating area, machining of the eight alignment slots, and cutting the ring ends to length. A photograph of this shroud ring following machining is shown in Figure 3-266. Visual examination of the edges of the machined shroud showed numerous delaminations, particularly in the end with the increased wall thickness. A photograph of one of the most severe delaminations is shown in Figure 3-267. The shroud was then shipped to Nuovo Pignone for dimensional inspection via CMM. The most critical dimension of the shroud, the ID, was found to be 422.36mm, which was well within the specification of 422.4 +/- 0.15mm. All straightness, circularity and perpendicularity requirements were also met.

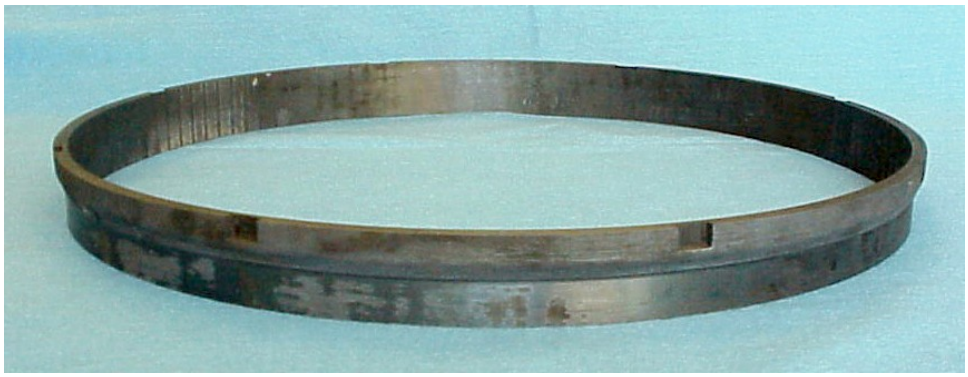

Figure 3-266. Photograph of the PGT-2 stage 1 shroud ring #1, made to design “C” with a stepped cross section thickness, following machining. The ID of the shroud ring 422mm.

Figure 3-267. Photograph of the thick edge of stage 1 shroud ring #1 showing the presence of the ply delaminations.

It was during the time period when stage 1 shroud #1 was being fabricated that Nuovo Pignone developed the design concept "E" described above. This design was expected to be somewhat simpler to fabricate because of the constant wall thickness, but it did require a greater volume of material overall. Since either design, "C" or "E", could be installed in the PGT-2 engine with minimal changes in the metallic support structure it was decided to build a second shroud ring to design "E".

Actually two shroud rings were fabricated according to design "E", designated as ring #2 and ring #3. Ring #2 was a trial ring using poor quality, archived fiber, and ring #3, which was intended to be used for possible engine testing, utilized newly-coated fiber from GEGR's in-house small tow coater. Both rings were sent to Chand Kare Associates for machining, and a photograph of ring #3 following machining is shown in Figure 3-268.

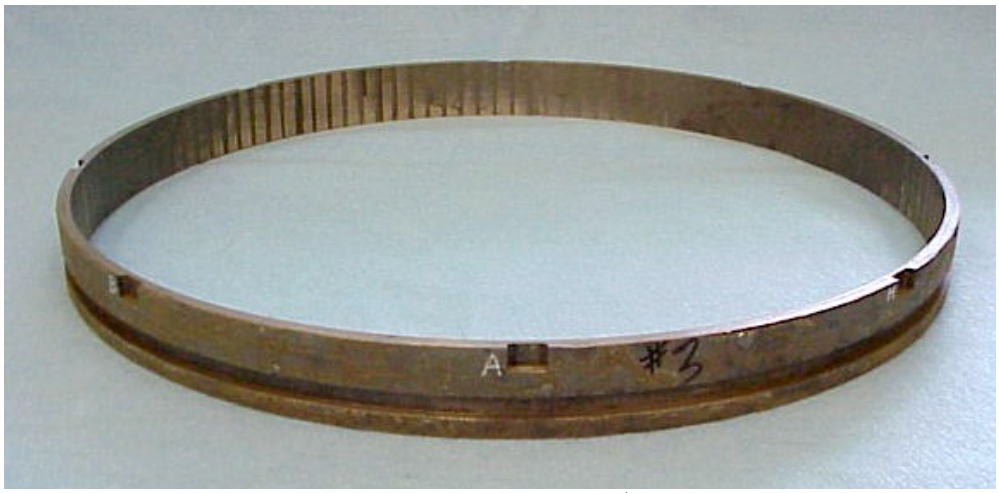

Figure 3-268. Photograph of the PGT-2 CMC 1st stage shroud ring #3 following machining.

Visual inspection of the machined features indicated that shroud ring #3 had fewer internal defects than either the first or second stage 1 shroud rings. Consequently only the third ring was sent to ANL for NDE inspection. Results of the IR thermal diffusivity measurements are shown in Figure 3-269. The thickness differences caused by the machined circumferential slot, introduced by diamond grinding from the outer surface, requires that the thermal diffusivity images be re-scaled to be able to see the features in both the ground (thin) and un-ground (thick) areas. Features seen in the images scaled for the thicker sections are less distinct because of in-plane thermal conductivity effects. This loss of resolution with thicker walls is typical for both transmission IR and ultrasound NDE techniques. Although substantial variations in through-thickness thermal diffusivity were evident, the overall quality of shroud ring #3 was judged to be good enough to proceed with engine testing.

3.8.3.2.3 Stage 1 Shroud Engine Testing

The prepreg MI CMC stage 1 shroud ring #3 was fitted into the metallic inner casing, and the PGT-2 engine was re-assembled with the CMC stage 1 shroud in place. Figure 3-270 shows the shroud ring being assembled into the turbine inner casing prior to installation into the engine. Installation and instrumentation work was completed, and the engine was started on October 4, 2000. After about 8 hours, including 2 start-stop cycles, a borescope inspection of the stage 1 shroud was performed. No changes in the shroud were detected so engine testing was resumed.

The initial stage of testing, consisting of 115 hours of total exposure with 10 normal start-stop cycles and 12 turbine trips, was completed on October 10. During this time the engine ran with very little performance penalty caused by the CMC shroud despite the somewhat larger blade tip clearance used. With additional reductions in blade tip clearance an efficiency and power output gain compared to the standard metallic shrouds could be expected.

The engine was then disassembled to allow visual inspection of the stage 1 shroud. Figure 3-271 shows a photograph of the shroud during engine disassembly. The shroud ring displayed no signs of distress or damage, except for some minor scratches as shown in Figure 3-272. Initially it was believed that these scratches were caused by a minor blade tip rub; however, there was no evidence of any blade tip alloy adhering to the shroud surface as had been seen in the earlier 2nd stage rubs. However, upon closer inspection it was shown that these “scratches” were simple machining marks created during the ID grinding of the ring and that they became more visible due to slight surface oxidation and decoration by impurities in the turbine atmosphere.

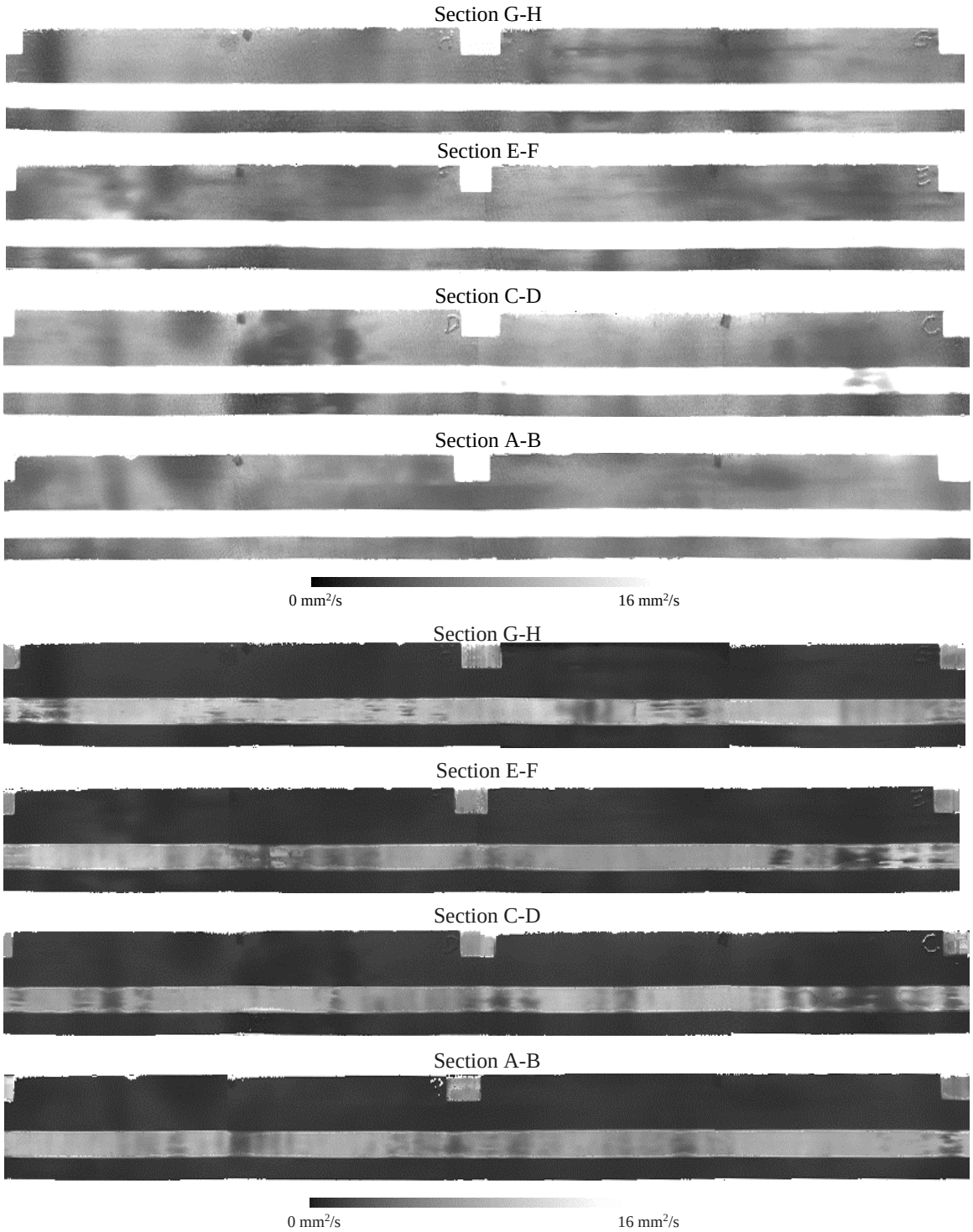

Figure 3-269. Detailed thermal diffusivity images of GE PGT-2 Stage 1 Shroud Ring #3 scaled for the thick, un-ground sections (top) and for the thin, ground sections corresponding to the circumferential slot and the attachment pin slots (bottom).

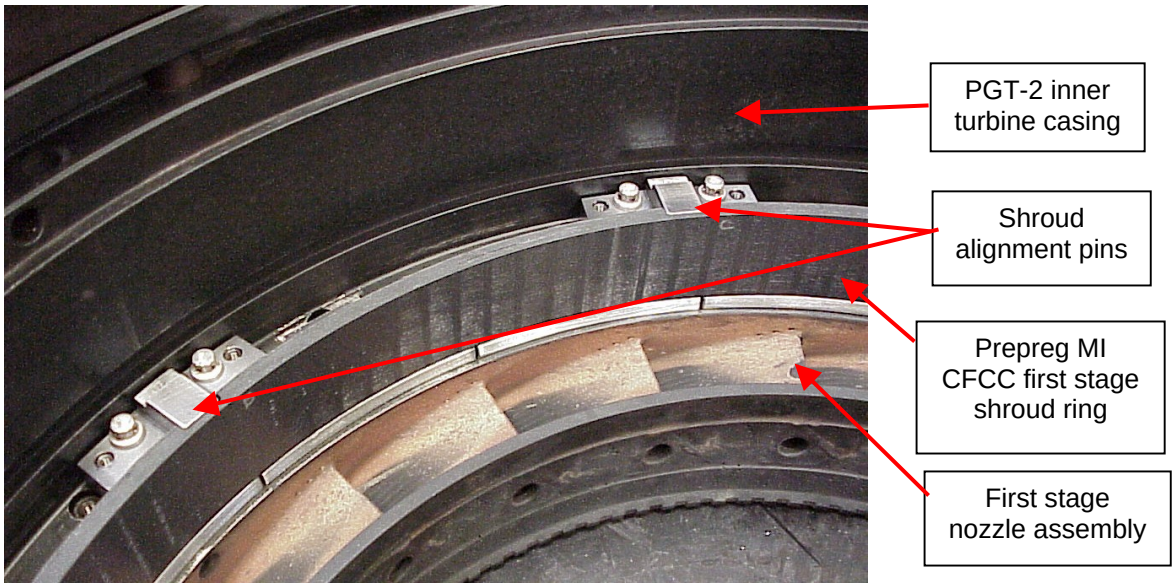

Figure 3-270. Photograph of the PGT-2 turbine inner casing (aft looking forward) during assembly with the CMC first stage shroud ring.

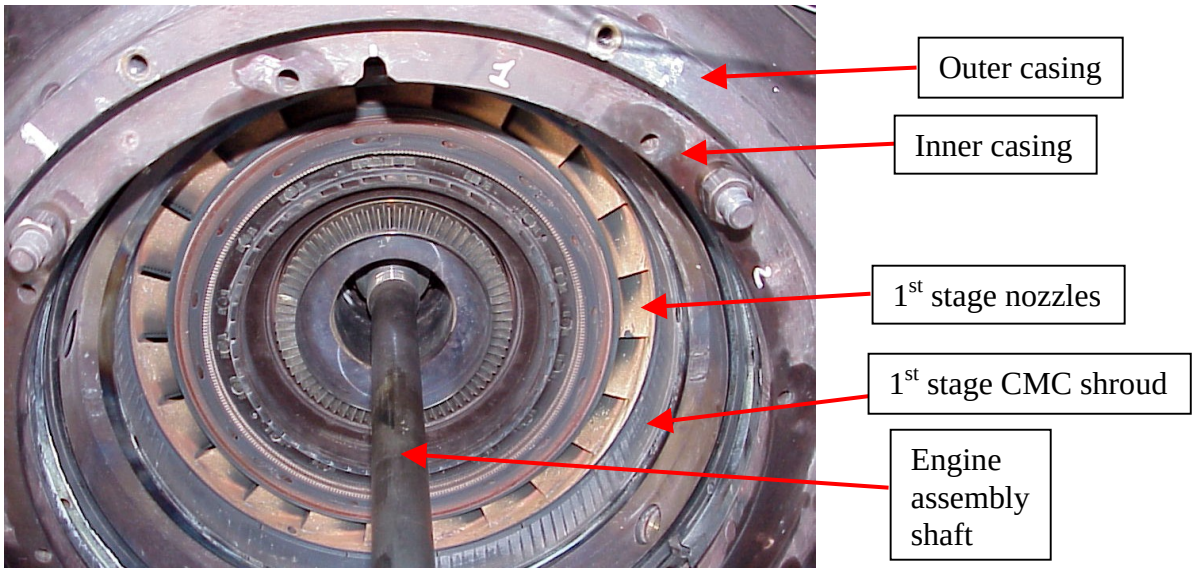

Figure 3-271. Photograph (from aft of engine looking forward) of the partially disassembled hot section of the PGT-2 engine following the initial 115 hours of stage 1 CMC shroud testing. The aft shaft bearing, 1st and 2nd stage blades/disks and 2nd stage shroud have been removed.

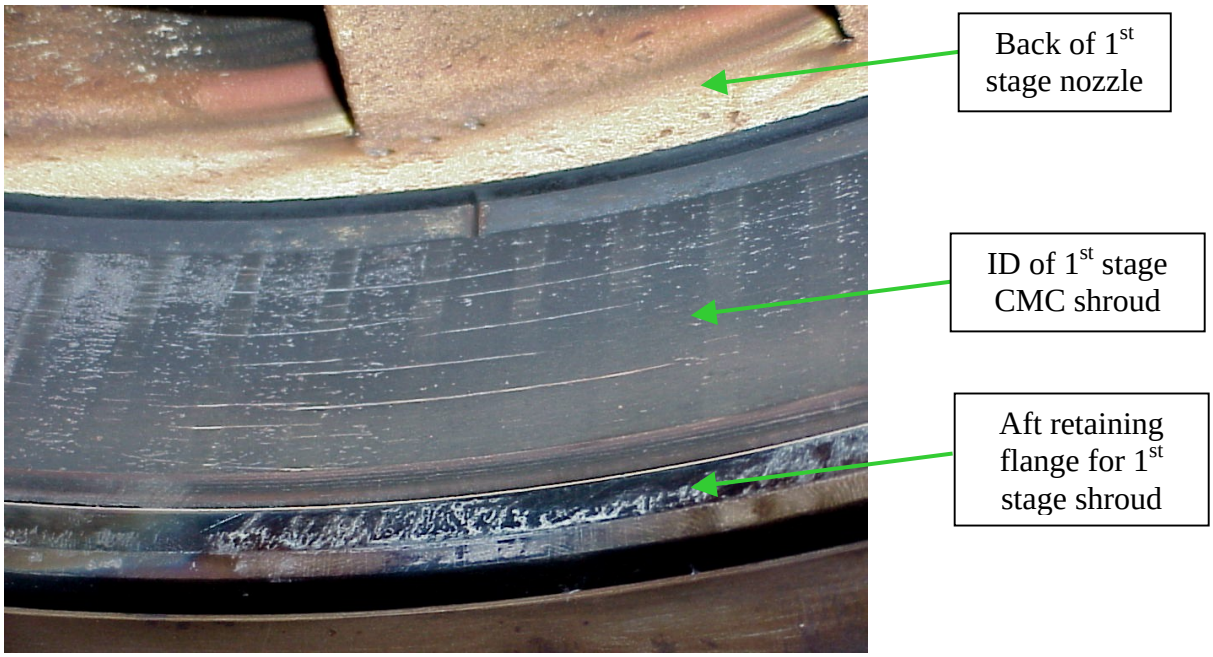

Figure 3-272. Close-up photograph of part of the 1st stage CMC shroud ring following the 115 hour initial engine test. The circumferential scratches on the ID surface were machining scratches decorated by turbine impurities.

The PGT-2 engine was then re-assembled with both the 1st and 2nd stage CMC shrouds in place on October 19, 2000, and the "long-term" engine test was started. At the start of this test the 1st and 2nd stage shrouds had already seen 115 hours and 135 hours, respectively, of accumulated engine operation. (The second stage shroud had additional engine time compared to the 1st stage shroud because of the tests of the attachment design modifications done in April, 2000.) The test plan was established for continuous operation 6 days a week (Monday mornings through noon Saturday) with 2 or 3 start-stop or turbine trip cycles per week in order to simulate real operating conditions.

The long-term shroud engine test was successfully completed on December 22 after 900 hours of turbine operation. The stage 1 shroud ring had accumulated 1015 hours of engine exposure at full-speed, full-load conditions, including 46 normal starts, 22 normal stops and 24 trip stops. CMC shroud component temperature measurement was severely limited by the space constraints within the engine. Four spring-loaded thermocouples were pressed against the outer aft (coolest) surface of the shroud ring. The temperatures measured from these thermocouples ranged from 680-815°C during steady-state operation (The large variation is caused by the use of a single combustor can, resulting in a large circumferential temperature gradient in the turbine).

The relatively low measured temperatures on the shrouds resulted from a combination of reasons. First, the thermocouple placement was limited to the aft section of the shroud ring, downstream from the 1st stage buckets. Because of the expansion through the turbine 1st stage the mean gas temperature in this region is on the order of 850°C, which

is considerably lower than the nominal firing temperature. In addition, cooling air from the combustor liner, transition piece and 1st stage nozzles, as well as leakages, create a radial temperature profile that is peaked at the center of the hot gas path and cooler along the inner and outer surfaces of the turbine annulus. Also, the 1st stage buckets are air cooled with the cooling air being discharged radially out the blade tips. This bucket cooling air effectively impingement cools the shroud, further decreasing its temperature. Combining all of these factors means the shroud temperatures, which were measured downstream of the 1st stage buckets, were fairly consistent with expectations. The forward edge of the shroud ring, upstream of the 1st stage buckets, was likely to have reached over 900°C.

3.8.3.2.4 Stage 1 Shroud Post-Test Characterization

The shroud ring was returned to GEGR for further post-test characterization. The first characterization performed was a detailed visual inspection. A photograph of the stage 1 shroud ring following engine test is shown in Figure 3-273. One blade rub was noted on the stage 1 shroud, although it is not clear at which point in the testing the rub occurred. The size and depth of this rub were both smaller than the rubs seen in the 2nd stage shroud, suggesting that the thicker cross section was effective at resisting out-of-round deformations caused by thermal or mechanical stresses. There were no signs of shroud damage beyond the immediate rub area, and all damage appeared to be limited to the abrasive removal of a small amount of ceramic from the CMC surface.

The radial pin and slot attachment scheme did lead to minor delamination cracking of the shroud on the edges of the slots, resulting in the loss of small amounts of CMC from the edges of the slots near the shroud OD. Examples of this material loss are shown in Figure 3-274. It is not clear if this was a clearance problem between the pins and the slots, or was caused by vibration and thrust loading between the pins and slots. Because the slots were machined into the shroud after infiltration the slot surfaces exposed the edges of the composite plies. Any loading from the alignment pins onto the CMC slots would effectively apply interlaminar shear stresses onto the CMC at the slot faces. Although this attachment scheme worked very well for maintaining alignment of the shroud ring while minimizing mechanical forces on the shroud, a more robust pin/slot configuration would be desirable for longer-term operation.

There were also a few, very minor losses of CMC from the OD along the trailing edge of the shroud. These were likely cause by “scraping” of the shroud against the aft metallic retaining flange during thermal transients. Material removed by chipping was two to six plies deep from the surface. All of the observed damage to the CMC shroud was very minor in extent and was in no way considered to be a threat to the performance or life of the component.

Figure 3-273. Photograph of the PGT-2 stage 1 shroud ring #3 following 1035 hours of engine testing at Nuovo Pignone.

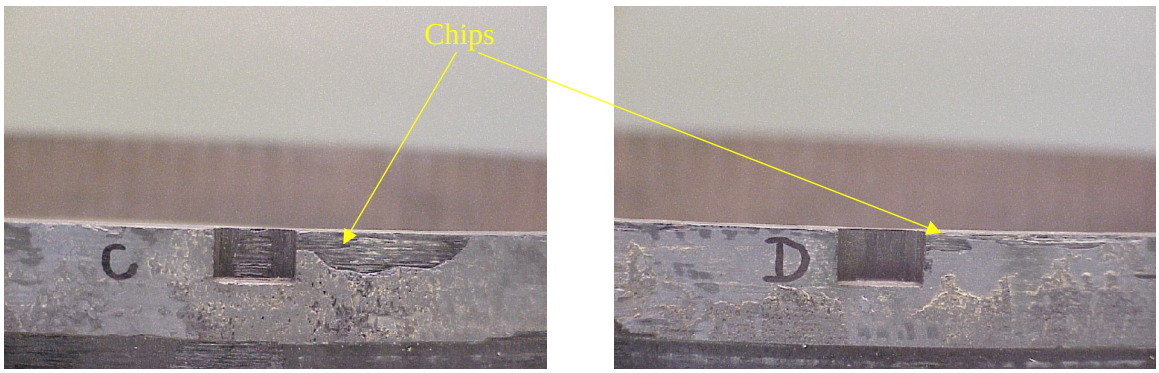

Figure 3-274. Photographs showing chipping of the outer surface of the PGT-2 stage 1 shroud near the attachment slots.

Post-test NDE was performed at ANL to look for any internal damage that might have developed during the engine test. Post-test IR thermography images are shown in Figure 3-275. Pre-test NDE data collected from the shroud rings was used as a baseline in interpreting the post-test NDE data. Virtually no internal damage was detected in the stage 1 shroud from the IR NDE results. Inspections were also performed with water-coupled and air-coupled ultrasound that corroborated the results seen in IR.

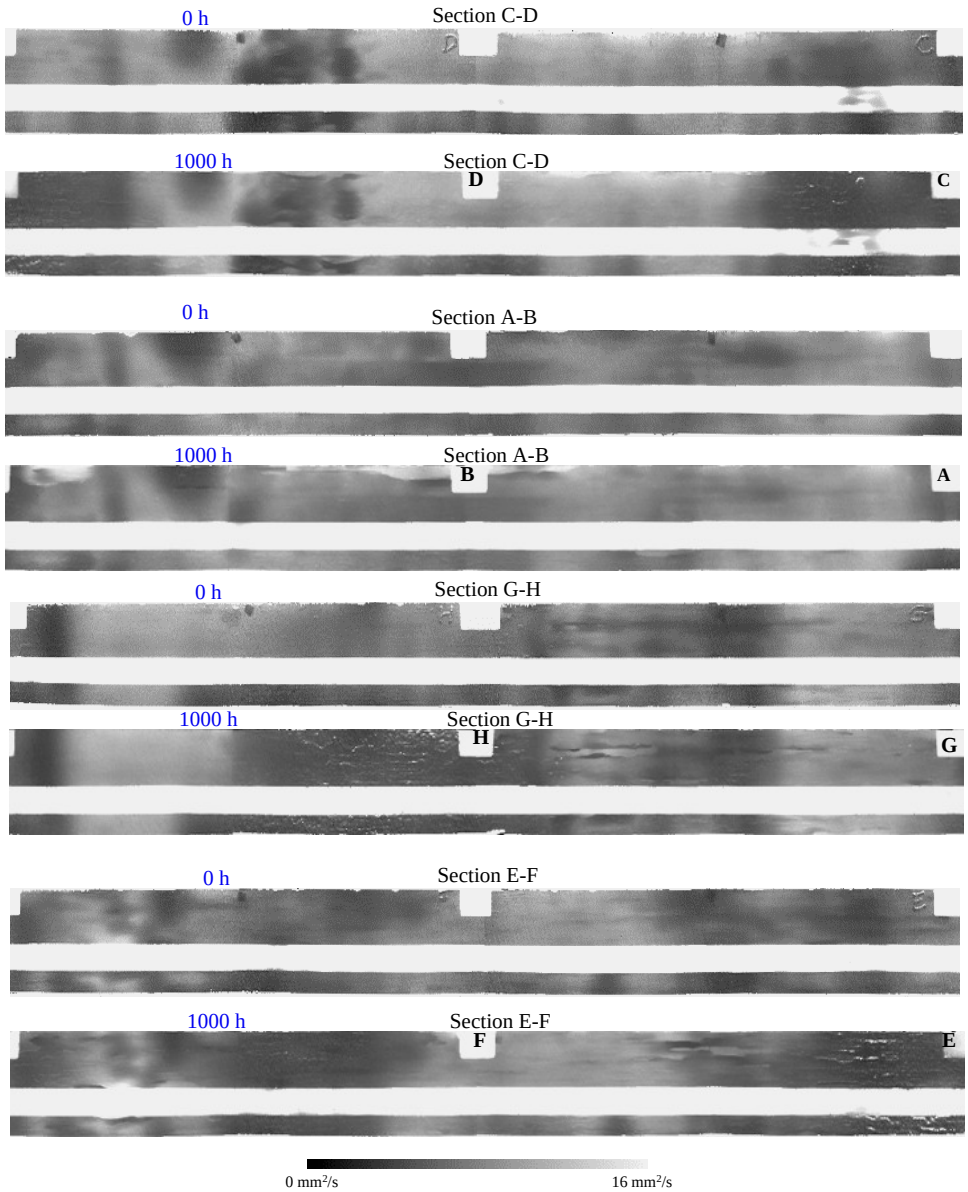

Figure 3-275. Comparison of pre-test (0 h) and post-test (1000 h) IR thermography images taken from the prepreg MI CMC PGT-2 1st stage shroud ring.

The thickness of the shroud, the short axial length, and the presence of the circumferential slot for the seal all made it impossible to extract meaningful mechanical property test specimens from the shroud. Substantial interlaminar defects were know to be present in the shroud ring prior to testing, but none of the NDE inspections suggested that any of these defects grew or changed, and thus there was little incentive to perform detailed microstructural analyses. The effects of the blade tip rubs were evaluated on the stage 2 shroud and did not need to be repeated for the stage 1 shroud. All of these combined reasons gave little incentive to perform any post-test destructive analyses on the 1st stage shroud ring.

3.8.3.3. 2MW Turbine Shroud Summary

Overall the shroud development and testing effort in the PGT-2 engine was very successful. This task represented the first actual engine test experience for a CMC component at GE. Valuable experience in the design and fabrication of the CMC components, design of the attachments and of the sealing configurations was also gained. Although the exposure temperatures were rather low compared to the larger, advanced industrial gas turbine conditions, the testing indicated that the CMC material was robust enough to withstand the full flow and vibration environment of an actual engine. One of the biggest unknowns going into the engine tests was what the response of the CMC shrouds would be to extraordinary events, such as blade tip rubs. The fact that the CMC shroud rings, which had significant pre-existing defects from the fabrication process, survived multiple blade tip rubs with no adverse effects was a strong indicator of the suitability of the Prepreg MI CMC material for gas turbine applications.

3.9 Long-Term Coupon Rig Testing

As discussed in Section 3.4.4, material exposure tests in steam-rich environments had been very valuable in identifying long-term oxidative degradation mechanisms in the various CMC materials tested. However, furnace steam tests are necessarily conducted at relatively low gas velocities where one of the major degradation mechanisms, namely the paralinear oxidation/volatilization of Si-based ceramics by the formation of $Si(OH)_x$ species, proceeds at a very slow rate. The various combustion rig and engine tests performed on shroud and combustor liner components were able to approach the high gas velocities of an actual engine; however, performing such tests is very expensive due to the safety requirement that the tests be constantly monitored by multiple operators, and by the cost of the fuel used during these tests. The rig tests have the additional costs of running the large air compressors needed to feed the test rigs. Consequently the duration of the rig tests has been limited to a few hundreds of hours in total. The PGT-2 engine test, where the engine supplies its own compressed air, was run for over 1000 hours, but still at a significant expense in fuel and operator time. The only existing method for attaining long-term material exposure data to turbine-like environments was to perform actual field engine testing. Unfortunately, despite the good successes of the rig and PGT-2 engine tests, GE Energy was not ready to commit to a field engine test without more long-term material data. Thus there was a strong need for a testing vehicle that could attain turbine-like conditions (primarily temperature, pressure, gas velocity and gas chemistry) and be run economically for extended periods, i.e. thousands of hours.

GE's solution to this problem was to develop a unique, automated combustion test facility for the exposure of CMC material coupons. The facility utilized infrastructure already present in the GEGR combustion test lab, such as existing air and fuel compressors, piping and exhaust ducting, in order to minimize fabrication costs. Design, fabrication, assembly, debugging and operation of this test facility, referred to as the "long-term" rig, was done under the CFCC program Task 3.3.d Long Term Rig Testing.

3.9.1 Rig Design and Fabrication

There were various unique features incorporated into the rig in order to allow it to operate economically and reliably. First, a computer-monitored control system was developed for the rig that would continuously monitor rig conditions, such as gas temperature, air and fuel pressures, air and fuel flow rates, rig pressure drops, etc., and adjust the fuel flow automatically to maintain proper temperature. If the operating parameters of the rig varied too far from baseline conditions a sequence of alarm conditions would occur. During the first level of alarm the computer controller was set up to automatically notify an operator via a wireless pager. This would allow the operator to check on the conditions of the test rig and make an assessment of the problems and institute any manual corrections that were necessary. If the rig operating parameters remained outside of the baseline conditions for an extended time, or if the parameters were substantially outside the desired ranges as to threaten the validity of the test or the safety of the rig operation, the rig would be automatically shut down by stopping the fuel flow. By utilizing this control system it was possible to operate the rig round-the-clock for extended periods of time without requiring constant operator monitoring, thus helping to minimize labor costs associated with rig operation.

The second unique feature of the long-term rig was the use of dedicated air and fuel compressors and exhaust system. Other test cells already present in the combustion laboratory all utilized a set of compressors that could be ganged and the outputs directed to any of the test cells, and the exhausts of the test cells all fed to the same exhaust gas handling system. This arrangement limited the lab to operating only one test cell at a time. Operating the long-term rig under this restriction would not have been possible. The use of dedicated compressors and a separate exhaust stack was therefore necessary. Fortunately independent small gas and fuel compressors and exhaust stack, which were originally installed for an atmospheric pressure test facility that was very infrequently used, were already available. The stand-alone air compressor was an Atlas-Copco unit capable of delivering ~0.5kg of air per second at up to 860kPa. A separate natural gas compressor, with a capacity of ~15g of natural gas per second, was also utilized for the rig. This fuel flow rate was capable of generating a firing temperature in excess of ~1300°C at the full flow capacity of the air compressor. Although these compressors were available and well matched to each other, their relatively low flow capacities dictated that the area of the rig sample exposure section be kept fairly small in order to simultaneously attain the desired pressure and gas velocity conditions.

Another unique feature of the long-term rig was that the internal hot gas path of the rig was made entirely of CMC components. This was done for two reasons: to maximize rig durability and to minimize variations in the exposure conditions within the rig. It was clear from the earlier shroud rig testing experience that nearly all of the rig durability issues were caused by failures of the metallic hardware or of the cast ceramic transition piece while the CMC shrouds held up extremely well. Also, the exposure conditions for all of the samples in the rig ideally would be identical in terms of temperature, pressure, gas composition and gas velocity, with sample temperatures running very close to the rig firing temperature. The only was to meet these requirements was to minimize any air

leakage into the rig and heat leakage out of the rig, which essentially dictated that the rig internal hardware not be cooled. Metallic hardware would not be capable of long-term operation at the desired 1200°C exposure temperature, and thus CMC hardware was required.

A design for the long-term rig that met all of these requirements was eventually developed, and is shown schematically in Figure 3-276. The rig was a vertical design with a circular cross section in the sample exposure section. The compressed air and natural gas fuel were fed through a pre-mixed combustion type fuel nozzle and then combusted within the combustor liner at the bottom of the rig. The hot gasses are then accelerated through a transition piece (actually integral with the combustor liner) and straightened with a bottom spacer tube before contacting the specimens within the main sample tube. Tensile bar specimens, nominally 102mm x 12.7mm x 02.5mm, lined the walls of the main sample tube and were held in place using "sample retaining rings" made of prepreg MI CMC. A final upper spacer tube then directed the hot gases to a pressure rated, water-cooled exhaust pipe. All of the rig internal hardware exposed to the hot combustion gases, including the combustor liner, transition section, combustion gas retaining tube, spacer tubes and sample retaining rings, were made of CMC.

The stack of CMC hardware was held in a vertical orientation inside an inner pressure vessel, all of which was enclosed in an outer pressure vessel. The space between the main sample tube and the inner pressure vessel was filled with alumina fiber thermal insulation to limit the heat loss from the sample exposure section. The purpose of the inner vessel was to support the CMC hardware and insulation, to allow for a cooled metal structure internal to the rig to prevent overheating of the outer pressure vessel, and to mitigate any gas pressure loads on the CMC hardware. A fraction of the compressed air fed into the bottom of the rig bypassed the combustor on the outside of the inner pressure vessel, thereby cooling it and the outer vessel. The inner pressure vessel also included rope seals at the junctions between the fuel nozzle cap and the combustor liner/transition piece, between the combustor/transition piece and the main sample tube, and between the sample tube and the inner pressure vessel. These seals were designed to allow for differential axial growth of the rig sections and yet minimize leakages into or out from the combustion gas path. The hot combustion gases would flow up through the rig and out the top through a pressure-rated, water-cooled elbow before the combustion gases were quenched by water injected at a back-pressure orifice (not shown in the diagram).
The combustor/transition piece was made as single piece from GE Prepreg MI CMC using Hi-Nicalon™ fiber. As was done for earlier combustor liners, the hoop plies in this part were direct wound and the axial plies were laid in by hand. The tapered transition section required numerous wedge-shaped cuts in the axial plies, but continuous fiber was maintained through the entire length of the combustor/transition piece. The main sample tube was made by CCP using the slurry cast MI process and Hi-Nicalon™ fiber.

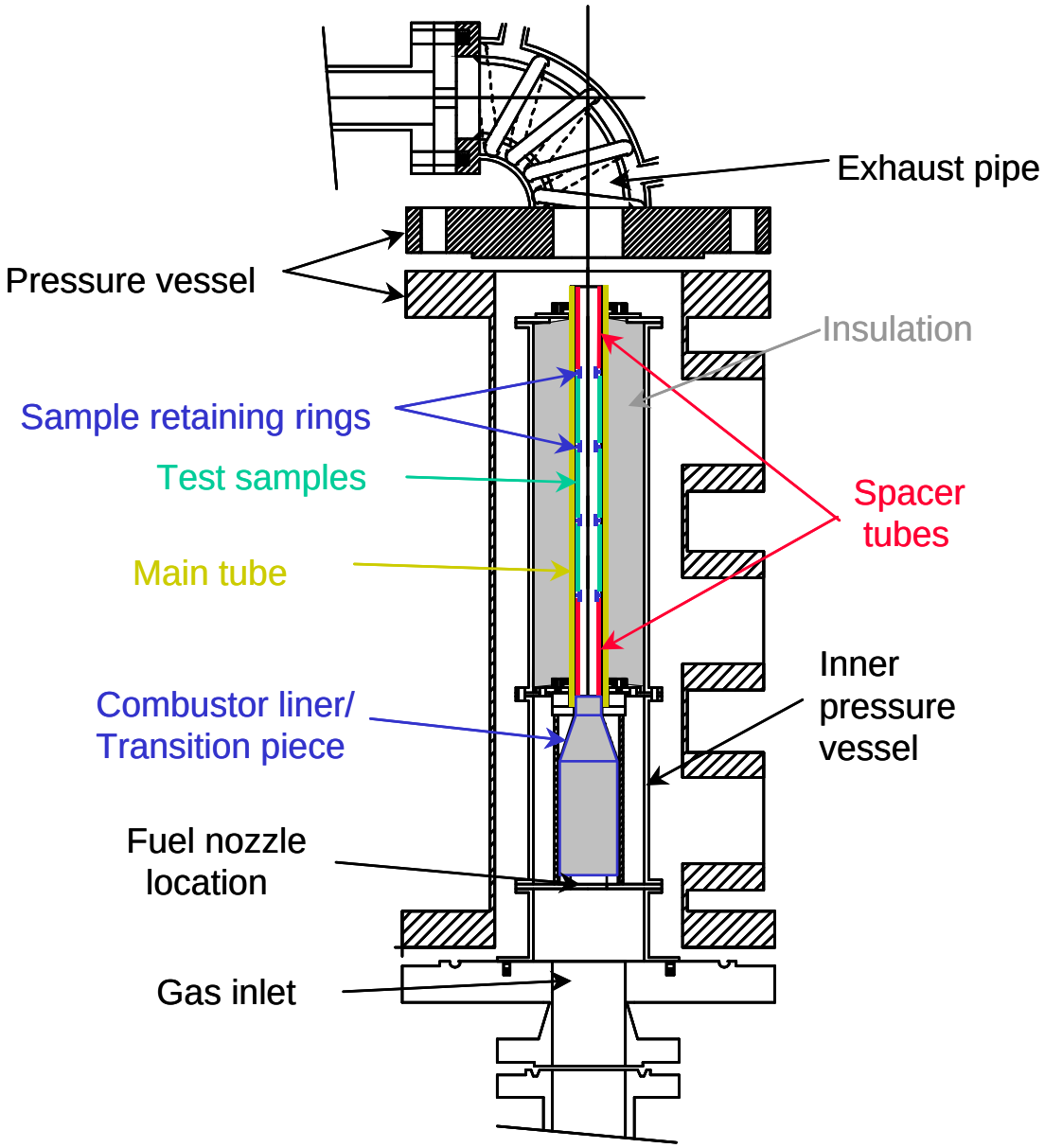

Figure 3-276. Schematic diagram of the long-term coupon exposure rig. The locations of the CMC components are indicated by colors (combustor liner/transition piece and sample retaining rings in blue, spacer tubes in red, main tube in yellow and coupon samples in green).

The arrangement of samples inside the sample tube is shown by the diagrams in Figure 3-277. Seven individual test bars were held in contact with the inside wall of the sample tube by the sample retaining rings. Although the diagram shows a circular OD on the retaining rings where they contacted the samples, the varying thickness of the test bars made it necessary in practice to custom machine the OD surfaces of the rings to an irregular heptagonal shape based on the thicknesses of the actual samples to be used.

Figure 3-276 shows three layers of test samples followed by a spacer tube at the exit end of main tube; however, for most of the rig tests an additional layer of samples was substituted for the top spacer tube, giving room for a maximum of 28 samples during a rig run.

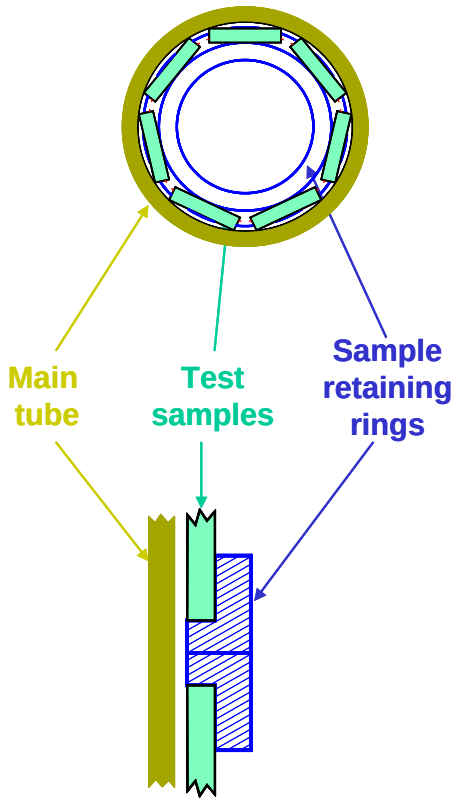

Figure 3-277. Diagram of how the test coupons were held inside the sample tube in the long-term combustion rig using the sample retaining rings.

3.9.2 Rig Build and Shakedown Testing

Although the conceptual design of the rig was completed in March 1999, detailed design, fabrication or acquisition of all of the rig parts, and making the necessary infrastructure changes to the combustion lab required nearly a year. A vessel support structure was fabricated and the pressure vessel, water cooled elbow and air inlet and exhaust piping were installed. The internal metallic components of the rig were then assembled (including metallic surrogates for the CMC hardware) to allow for cold flow testing of the rig. This required the installation of the data acquisition system and calibration of the flow and pressure sensors. The instrumentation system was checked using a cold, low flow (using house compressed air) testing.

Prior to full-flow (high pressure) testing of the rig several facilities upgrades were required. Orifice flanges were installed in the air supply line to better measure the air

flow rates. The natural gas delivery line was modified and instrumented to allow for independent control of the diffusion and pre-mixed sections of the combustor nozzle. (A relatively small diffusion flame was used for ease of lighting the rig and to help maintain a stable flame, whereas the majority of fuel was burned using the premixed flame in order to provide for a short, hot flame while minimizing NOx formation.) Computer-controlled solenoid valves were also added to the natural gas and two cooling water supply lines. These valves were pneumatic, and so required some minor modification to the house compressed air lines. An explosive gas sensor was installed in the test bay as recommended in a safety review. Photographs of the completed test rig and data acquisition system are shown in Figure 3-278.

Reduced pressure flow testing was then followed by full-pressure flow testing. The prepreg MI CMC combustor/transition piece, alumina gas containment tube, and thermal insulation were inserted into the rig and thermocouple instrumentation added. An alumina containment tube was being used in the initial shakedown tests of the rig to prevent any damage to the slurry cast MI CMC tube to be used during actual sample testing. With all of the components in place, a successful full flow, full pressure (using the dedicated air compressor) cold flow test was performed in order to confirm that the desired mass flows and pressures could be attained. Final leak checking of the pressure vessel and leak and flow checking of the natural gas lines were required before starting any fired flow tests.

Quite a bit of rig operation experimentation and debugging was necessary to get the long-term rig fully operational, as would be expected of any totally new combustion system. The initial fired test was run only to moderate rig temperatures in order to check rig lighting, flame stability and gas flow balances. During this test the alumina sample tube, which was being used as a surrogate for the slurry cast MI CMC tube, cracked and failed. An alumina “donut plate”, which was being used in the combustor to protect the dome plate from heat radiated from the flame, was also found to have cracked due to thermal gradient stresses or vibration. Fortunately there was no damage to the other parts of the rig. Subsequent tests were run using the MI-CMC sample tube, and the alumina donut plate was replaced with an all stainless steel structure.

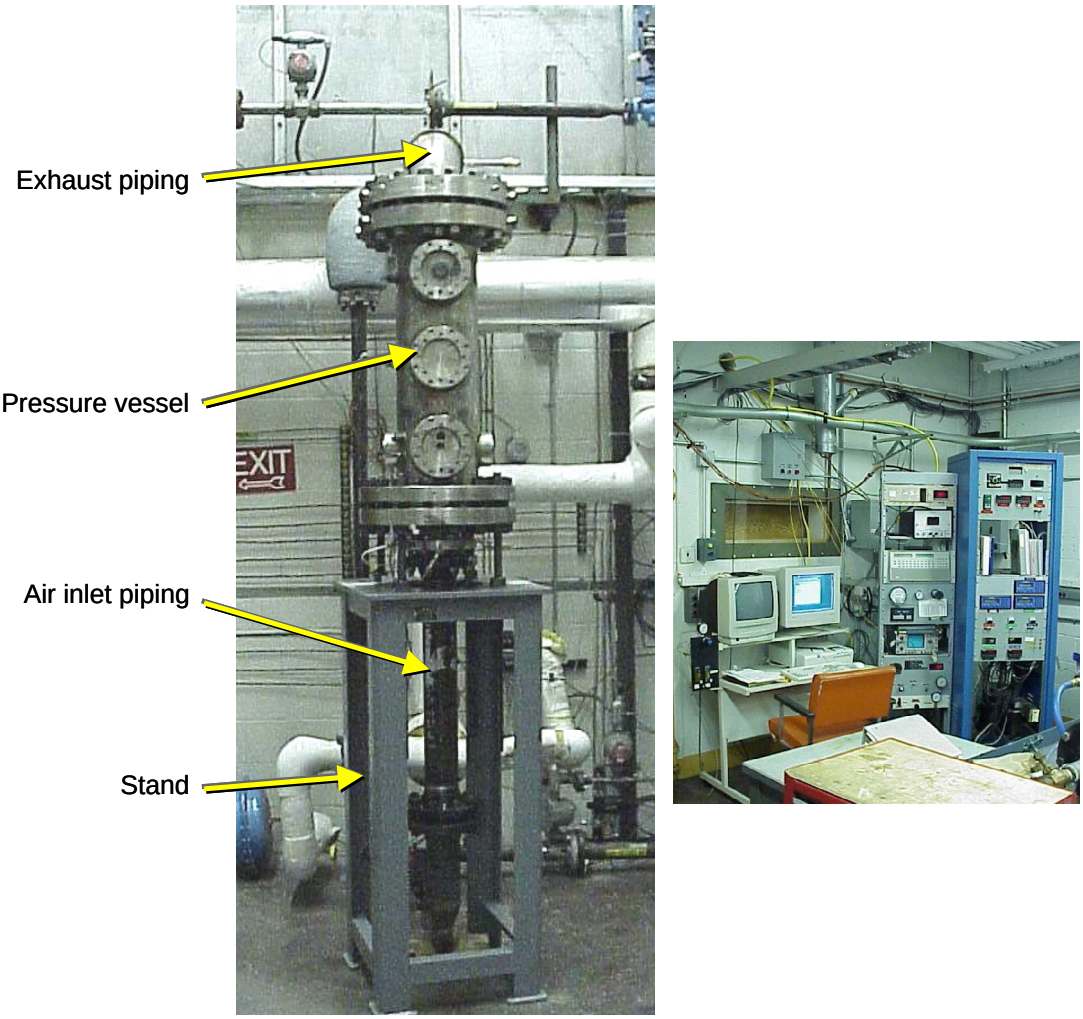

Figure 3-278. Photographs of the long-term combustion test rig: Left – set-up of the pressure vessel and piping; Right – PC-based rig monitoring and control system.

The subsequent rig firing test went to a rig gas temperature of 1150°C for 2 hours. There was sufficient air flow and fuel supply margins that rig firing temperatures in excess of 1380°C were judged to be easily obtainable. Unfortunately during this test the stainless steel "donut" plate mentioned above melted. This support plate was originally designed to have no air cooling so that the air flows coming into the rig combustor could be carefully characterized and controlled. Adding cooling air to the plate would have added some uncertainty regarding the air flow conditions within the combustor and possibly led to flame stability issues. However, the radiative heat load on the combustor dome was obviously too high, causing the plate to overheat, and eventually melt. One of the main functions of the donut plate was to limit air leakage around the front edge of the combustor liner. When the donut plate melted premixed air/fuel leaked around to the outside of the combustor, ignited, and burned a hole in the inner pressure vessel wall. A photograph of the inner pressure vessel with the burned through hole is shown in Figure 3-279. Despite the overheating and melting of the donut plate, and the flame passing outside the combustor liner to the extent that it could burn a hole in the inner pressure

vessel, none of the CMC rig parts (combustor liner/transition piece and sample tube) were damaged.

The inner pressure vessel was subsequently repaired and a new dome plate with air cooling was fabricated. Additional purge air channels were also added to the dome plate to direct more air to the inner pressure vessel in order to minimize the likelihood of any combustion gas leakage out of the combustor. The air for the added dome cooling holes came from the rig feed, such that the flow through the premixer (fuel nozzle) was reduced. Unfortunately these changes, particularly the addition of cooling air to the dome plate, caused unexpected combustion stability problems. Several attempts were made to initiate and maintain combustion during full pressure, full flow combustion tests, but the flame would not remain lit for more than a few minutes at a time. This situation necessitated a more detailed examination of the operation of the fuel nozzle/combustor using an "open flame" testing facility.

Figure 3-279. Photograph of the inner pressure vessel shell showing the hole that was burned out due to the failed fuel nozzle dome plate.

The first combustor modification evaluated in the open flame facility was to add a heat shield assembly between the cooling air holes in the dome plate and the premixed fuel nozzle. This setup operated well without the combustor liner / transition piece in place; however, when the combustor liner / transition piece was added to the test setup flame instability ensued. The interpretation of this result was that the large constriction of the

combustor liner / transition piece (from 76mm ID in the combustor section to 30mm ID at the exit of the transition piece) was accelerating the gas flow too quickly, thereby preventing flame holding within the combustor.

Two potential solutions were envisioned to deal with the flame stability problem: adding a flare flame to the premixed fuel nozzle, or use of a standard Frame 5 fuel nozzle (or "injector") that produces more of a diffusion flame condition. A series of eight flame stability tests were then run in the open flame facility aimed at evaluating these two concepts.

Retrofitting the premixed fuel nozzle with a flare flame circuit required additional machining, so the tests of the diffusion flame fuel nozzle were started while these modifications were being made. Tests run on the diffusion flame nozzle indicated that it would operate in a stable manner with the liner / transition piece in place, but that the temperature profile was highly peaked. The temperature profile across the exit of the transition piece is shown in Figure 3-280. Such a highly peaked temperature profile would be unacceptable for the coupon test rig where a uniform temperature distribution is needed.

These initial diffusion flame nozzle tests were performed at relatively low firing temperatures (below 600°C) because of limitations of the K-type thermocouples present in the test facility. It was expected that the temperature profile would flatten at higher firing temperatures (higher fuel to air ratio) and so a B-type thermocouple was installed. Unfortunately the combustor repeatedly experienced rich blow out when the temperature was raised above 1100°C.

Since the diffusion flame nozzle was not able to obtain over 1100°C testing was switched to the premixed nozzle with an added center body flare. The premixed fuel nozzle (DACRS-type) contains fuel circuits for both diffusion and premixed combustion flame conditions. The diffusion circuit is typically used for engine light-off and to help stabilize the flame at partial load operation conditions. Under normal full load condition only the premixed fuel circuit is used to reduce NOx emissions. A "flare", which is a fuel injector tube with a flared end capable of flame holding, was added to the diffusion fuel circuit of the premixed nozzle, as shown in Figure 3-281. The purpose of the flare was to act a "pilot" flame, thereby stabilizing combustion of the premixed gasses under conditions where they would normally blow out.

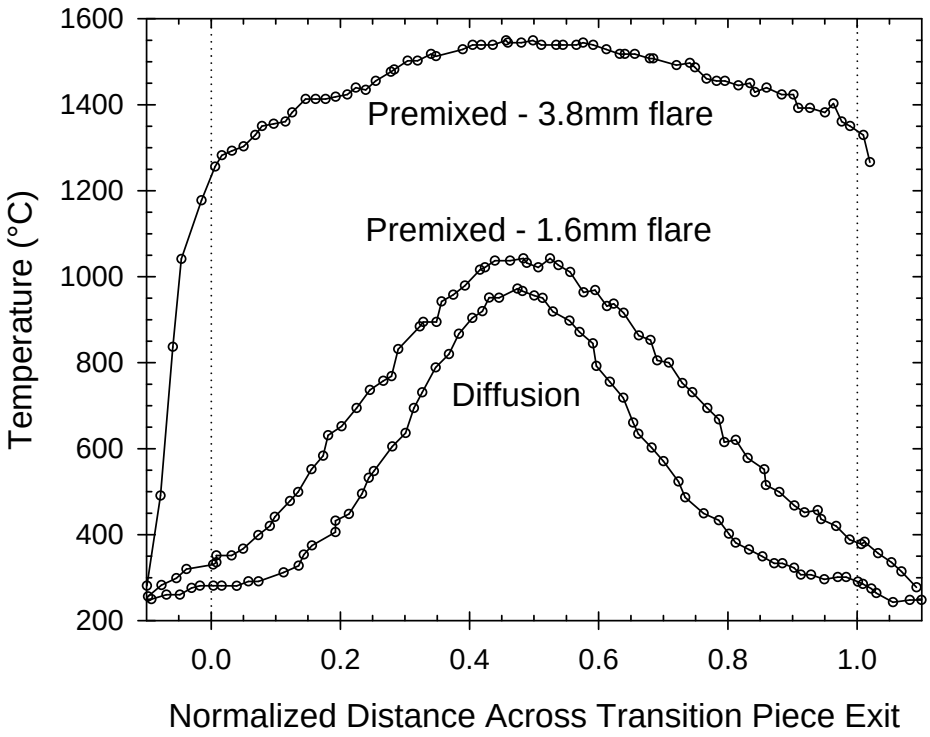

Figure 3-280. Temperature profiles measured in the open flame test facility for the long term rig combustor/transition piece fitted with different fuel nozzle configurations. The vertical dotted lines roughly correspond to the positions of the ID walls of the transition piece exit.

The amount of flare fuel fed to the system was controlled by adjusting the diameter of the flare fuel tube. During initial tests with this fuel nozzle, using 1mm or 1.6mm flare tubes, there was insufficient flare fuel to stabilize the flame to the desired overall temperature. Also, these smaller flare tubes still gave quite a narrow temperature profile, as shown in Figure 3-280. With 2mm and 3.8mm flare tubes the flame stability became better. By adjusting the ratio of premixed fuel to diffusion fuel and by using the 3.8mm flare tube stable, high temperature combustion conditions were obtained while still maintaining a relatively flat temperature profile across the transition piece exit. The temperature profile from this last test is shown as the top line in Figure 3-280.

Successful operation of the reconfigured combustor system in the long-term test rig was first verified under manual control, and then again using full automatic control for a relatively short (6 hours) rig test. During this later test run the rig operating conditions were pushed to the limit of mass flow available from the compressor without problem.

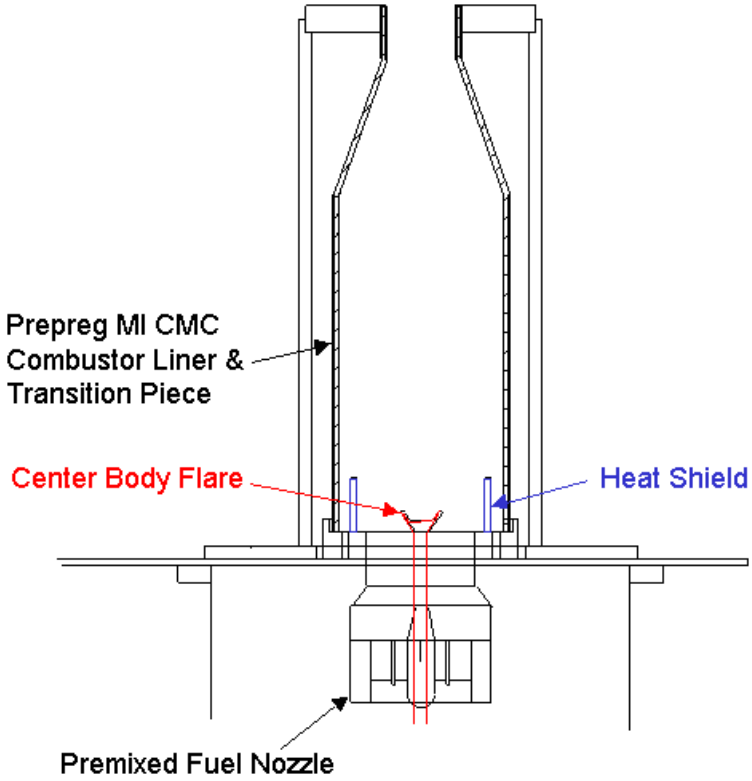

Figure 3-281. Schematic of the combustor arrangement in the open flame stability test facility, shown with the modified premixed fuel nozzle including the added center body flare.

Before starting the actual sample exposure tests the automatic operation of the rig during the overnight hours was needed to make sure there would be no issues with fuel or electricity supplies due to off-hour load changes. During this run the main sample tube was fitted with spacer tubes and sample retaining rings to simulate the full effects of having samples in the rig. The original design called for the sample retaining rings to be made of monolithic SiC-Si material (essentially un-reinforced prepreg MI composite matrix); however, the monolithic Si/SiC material was found to have inadequate fracture resistance for this use. All four rings cracked, with three of the four being broken into numerous small pieces. It was unclear whether the cracking was caused by normal rig operation or the possible back-flow of exhaust quench water during rig shut-down, which would have thermally shocked the rings. None of the CMC rig parts were damaged. As a result of this test the design of the retaining rings was modified to be a hybrid structure of CMC and monolithic. The inner 1/3 of the ring would be made of prepreg MI CMC in order to provide it with damage tolerance and thermal shock resistance, while the outer 2/3 of the ring would still be made of the monolithic matrix only for ease of machining in the green state. Once the new hybrid sample retaining rings were fabricated, and the rig passed the remaining safety inspections for long-term, unattended operation, the initial test run with CMC test samples was attempted.

Mounting the samples in the test rig proved to be somewhat of a challenge. The samples had to be slid into place inside a relatively long (~60cm) tube, which required some clearance between the samples and the tube walls. However, vibration or "fluttering" of the samples in the high velocity gas stream of the rig could not be allowed due to wear and sample failure concerns. The solution was to pre-assemble the samples into "cartridges" that made up one level of samples in the rig. The assembly of the cartridges, each consisting of seven test samples and two retaining rings, is shown in Figure 3-282. The samples were cemented onto the flats of the retaining rings using an alumina-silica heat-setting cement. Once the cement was set the cemented ends could be shaped by grinding to allow the assemblies to slip fit into the CMC main tube of the rig. During a rig run the cement served to lock the samples in place by filling the space between the samples and the main tube (there was no cement on the sample faces exposed to combustion gas within the rig), and thereby prevented sample movement or vibration. Typically one of the samples in the top layer and one in the bottom layer would have embedded thermocouples for measurement of actual material temperature in the rig. During a rig run, the operating parameters would then be adjusted to yield the actual sample temperatures that were desired.

The first rig run with CMC coupon samples in the rig took place on October 30, 2000, and utilized four spacer tubes and only one layer of samples. The run conditions were adjusted to yield a mean sample temperature of 1200°C as measured by the embedded thermocouples. Combustion dynamic pressure variations of up to ~70kPa, but changing the relative fuel flows between the premixed and diffusion flames minimized this variation. Upon rig disassembly, two types of contaminants were observed on the samples, as shown in Figures 3-283 and 3-284. The first was a generalized reddish-brown discoloration of the samples, particularly of the EBC-coated samples. The second contaminant was the irregular, localized deposition and/or build-up of a glassy phase on the retaining rings and sample surfaces.

Fourth (top) rank of samples
assembled onto retaining rings
for combustion rig run #1

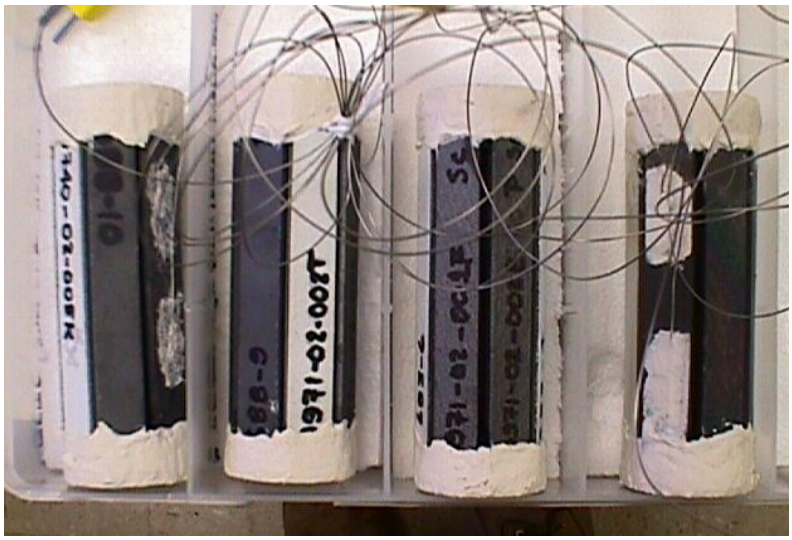

Figure 3-282. Top - Photograph of a single sample "cartridge" assembly consisting of seven test bars and two retaining rings; Middle – Photograph of four cartridges showing the alumina-silica cement used to hold the sample ends securely to the retaining rings; Bottom – one spacer tube and four sample cartridges (left to right) inside a glass tube to show the arrangement of samples as they would be inside the long-term combustion rig main sample tube.

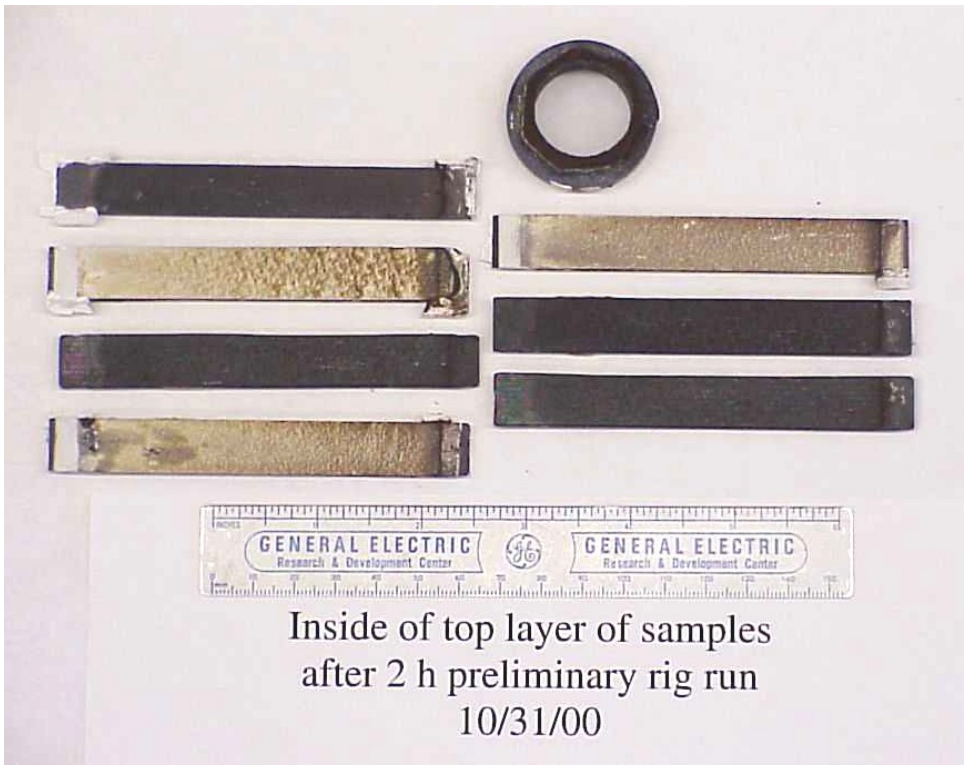

Figure 3-283. Photograph of the CMC samples and one retaining ring as used in the preliminary 2-hour rig test on Oct. 30, 2000. The inside surfaces (those in contact with the hot gas flow) of CMC samples are shown following exposure at 1200 °C for 2h.

Figure 3-284. Close-up photograph an EBC-coated sample from the 2h rig run at 1200°C, showing deposition of a glassy contaminant on the sample surface.

Analysis of the contaminants by SEM showed that the generalized discoloration was mainly iron oxides, similar to what had been seen in the previous shroud combustion rig tests. The iron had been transported by the air flow from a section of piping that had rusted owing to water accumulation. Thorough cleaning of this pipe section and installation of a drain sharply reduced iron contamination of the samples in later rig runs. The dark glassy contaminant was found to be a calcium iron aluminosilicate. This

material had evidently been transported by the gas flow as liquid droplets. It was found on ring surfaces that protruded into the flow as well as on the samples in gas eddy regions near the sample/ring attachment areas. Although overheated insulation was originally believed to be the cause of this type of deposit, it reappeared even after the insulation had been replaced by a higher-temperature type. This type of deposit is typical of dust that is ubiquitous in the atmosphere and is often seen on TBC-coated hardware pulled from engines. Consequently such deposits were considered to be typical of what the CMC would see in real engine applications so no further efforts were made to remove it.

Overall nineteen combustion trials, either done in the actual long-term rig or in the open-flame combustion facility, over an 8 month period were required to get the rig operation to the point where CMC sample testing was possible.

3.9.3 Rig Exposure Testing of CMC Coupons

The initial program plan called for 2000 hours of long-term rig exposure testing on a variety of CMC coupons. However, such environmental exposure data was considered so critical to the CMC component design efforts that this testing program was extended to 6000 hours of total rig exposure time under the CFCC program. The very long component life goals, up to 72,000 hours for a set of shrouds, required that material degradation data from exposure to turbine-like environments be collected over as long a time period as possible. The long-term combustion rig proved to be the most efficient method of performing the needed exposures.

A complete listing of the long-term combustion rig runs is given in Table 3-64. Additional details of the operation of the rig during these runs are discussed below, and the post-exposure characterization of the samples exposed during these tests is discussed in Section 3.9.4.

The first attempt to run the rig with the full complement of samples was made on November 3, 2000. The rig was found to exhibit excessive combustion dynamics that extinguished the flame after a period of operation of 30 seconds to 10 minutes. A careful diagnosis of the problem showed that it was caused by acoustic coupling between the gas flow in the sample retaining tube and the incoming airflow in the feed line. Placement of an orifice in the air feed line effectively de-tuned the acoustic resonance and permitted smooth operation of the rig with a full sample load. After this problem had been solved, a full safety review was undertaken to permit long-term unattended operation.

Further modifications were made to more accurately measure and control the gas temperature and radial temperature profile in the vicinity of the top layer of samples. The relationships among the temperatures measured by the type K thermocouples on the sample, a type B thermocouple inserted in the flow level with the top end of the top layer of samples, and the calculated flame temperature were established. These relationships were used to maintain the rig conditions constant even after the embedded thermocouples in the samples had failed (typically after 10-15 h of rig operation).

The first full 500 hour rig run (rig run #1) with a full complement of 28 samples (four cartridges with seven samples each) was started on November 30 and was completed on December 22. The total run was actually accomplished in a series of shorter individual runs. The shorter individual runs were used to allow for occasional rig and sample inspections, or were caused by rig operational issues leading to shutdowns. This first rig run was started with a 24hr "attended unattended" segment. During this time period, an attendant was present to monitor the rig and respond to any unexpected problems, but did not manually adjust any of the operating parameters. Once this segment had been completed, the rig was restarted in a fully unattended operating mode.

This first rig run was interrupted twice for borescope inspections. At 24 hours the sample retaining rings and aluminosilicate cement assemblies were found to have held the samples firmly in place. Iron oxide deposition was seen as a red coating on the first (lowest or farthest upstream) rank of samples only. The CVD SiC seal coat had partially spalled from two samples in the second rank. None of the other samples showed significant damage. At 225 hours two or three of the EBC coated samples showed minor chipping. The two samples with spalled seal coats showed further spalling, up to 50% of the area exposed to the high-velocity gas stream being now uncoated. A third sample next to the two that had exhibited early seal coat spalling also showed such spalling over 10-20% of its surface area.

Throughout this test the rig ran very smoothly with very consistent, controllable conditions. The operating parameters of the rig were as follows: sample temperature = 1199±20°C; total pressure = 880kPa (9.0 atm); water vapor partial pressure, P_{H2O} = 100kPa; and gas velocity = 213m/s. However, the thermocouples embedded in samples in the first rank (nearest the combustor) indicated a temperature of approximately 1120°C during rig operation, whereas the fourth-rank thermocouples (farthest downstream from the combustor) showed a temperature of approximately 1200°C. This difference may account for the lower rate of volatilization and greater Fe oxide deposition on samples in the first rank as compared to those of samples in the upper ranks. This temperature pattern was observed in practically all subsequent rig tests, with the first rank of samples running approximately 80°C cooler than the samples in ranks 2 through 4. The cause of this irregularity was incomplete mixing of the cooling air from the combustor dome plate with the combustion gases at the first rank level. However, due to the trips in the flow path caused by the sample retaining rings, the combustion gases became fully mixed and uniform by the 2nd rank and beyond.

Table 3-64. Summary of the Long-Term Combustion Rig Test Runs

Rig Run #	Objectives	Nominal Temp. (°C)	Run Time (h)	Si Injection ?	Outcome
1	Measure CMC recession rate; Evaluate CMC mechanical property degradation; Compare prepreg and slurry cast CMC durability; Evaluate effect of EBC in protecting CMC	1200	500	No	Samples w/o EBC generally showed decreased mechanical properties; EBC coated slurry cast CMCs showed internal oxidation and embrittlement; EBC coatings on prepreg CMCs were protective and maintained mechanical properties
2	Measure CMC recession rate; Evaluate CMC mechanical property degradation; Compare prepreg and slurry cast CMC durability; Evaluate effect of EBC in protecting CMC	1200	500	No	Samples w/o EBC generally showed decreased mechanical properties; EBC coated slurry cast CMCs showed internal oxidation and embrittlement; EBC coatings on prepreg CMCs were protective and maintained mechanical properties.
3a	Evaluate protective effect of Si gas doping on material durability and mechanical properties	1200	106	Yes, 5ppm	Extensive SiO_2 deposition on samples and in exhaust; Established need to identify optimum Si doping level
4	Measure CMC recession rate at a lower temperature; Evaluate CMC property degradation; Evaluate effect of EBC in protecting CMC	815	0	No	Poor control of temperature distribution in rig; Target run conditions were not achieved; Run stopped.
5	Determine optimum Si gas doping level*	1200	283	Yes, 0.7ppm	Visual evaluation of exposed samples showed that gas was over-saturated
6	Determine optimum Si gas doping level*	1200	206	Yes, 0.2ppm	Visual evaluation of exposed samples showed that gas was under-saturated
7	Determine optimum Si gas doping level*	1200	250	Yes, 0.23ppm	Visual evaluation of exposed samples showed that gas was under-saturated
3 cont	Evaluate protective effect of Si gas doping on material durability and mechanical properties	1200	734	Yes, 0.5ppm	Minimal SiO_2 deposition on samples - gas was slightly over-saturated; Mechanical properties degradation requires microstructural information for interpretation
8-1	Measure CMC recession rate; Evaluate CMC mechanical properties degradation; Evaluate effect of EBC in protecting CMC	1200	932	No	Segment stopped prematurely due to exhaust elbow failure. Less degradation noted on uncoated samples than in previous runs. No discernible degradation of EBC-coated specimens.
8-2	Same	1200	1148	No	Segment interrupted by Microturbine program: stopped due to cracked retaining rings
8-3	Same	1200	1417	No	Segment stopped due to fractured retaining ring
8-4	Same	1200	425	No	Segment stopped due to icing of area surrounding the exhaust stack

The test was interrupted only once by hardware issues, at about 327 hours of exposure, in order to replace a blocked cooling water filter. After the test all of the rig hardware, including the MI-CMC combustor-liner/transition piece, the main combustion gas tube, and the sample spacer tubes, were found to be in good condition.

The sample retaining rings did not fare as well. All of the rings cracked, many into several pieces, during the test. However, note that the rings were made with a hybrid structure, containing both reinforced and unreinforced (monolithic) regions. A typical ring following the rig test is shown in Figure 3-285. Fortunately the cracking was limited to the outer, unreinforced parts of the rings, and the inner parts of the rings, which were fiber reinforced, remained intact. Despite this cracking, the reinforced parts of the rings and the alumina cement maintained sufficient integrity through the test to keep the test samples well supported.

Figure 3-285. Photograph of one of the sample retaining rings following the first 500 hour test in the long-term combustion rig. The inner portion of the ring, which was fiber reinforced, maintained integrity whereas the outer monolithic SiC-Si portion broke in several locations.

Eighteen of the 28 samples exposed in rig run #1 were retained for a further 500h exposure under the same conditions in rig run #2. Nine mechanical properties test

samples and one sample for evaluation of SiC recession were added to replace the samples which had been removed from testing after rig run #1. A new set of sample retaining rings was fabricated, and the 28 samples were cemented into the retaining rings to form cartridges similar to those used in rig run #1. Two type K thermocouples were embedded in a SiC recession sample in the first (lowest) sample rank, and another two type K thermocouples were embedded in a similar sample in the fourth (highest) sample rank. The sample cartridges were loaded into the CMC combustor tube, and the rig was reassembled without making any changes in the operating conditions. The rig was restarted for rig run #2 on February 14, 2001, and the run was completed on March 9. The following rig operational parameters and sample exposure conditions were observed during the run: mean temperature = 1205 ± 4°C (first rank of samples ~1120°C); total pressure = 895 ± 20kPa (8.8 ± 0.2 atm); combustion equivalence ratio (ratio of fuel to air relative to stoichiometric combustion conditions) = 0.52; water vapor partial pressure = 91kPa (0.90 atm); and linear velocity of combustion gases in the sample exposure section = 203m/s (0.28 mach). These parameters were similar to those obtained in rig run #1.

The entire 500 hour exposure during rig run #2 was completed with only 5 automatic shut-downs of the rig; 3 times because of a spurious fluctuation in the cooling water pressure across the exhaust elbow, once because of an over-temperature condition caused by a momentary dip in air flow, and once because of a lock-up of the control computer. The only shutdown that caused concern for the samples and rig hardware was the one from the over-temperature condition. Borescope inspection of the rig following this shutdown showed no signs of damage, so the rig was restarted within 24 hours.

Inspection of the rig following completion of the test showed no signs of damage. Both the thermocouples and the sample retaining rings survived this entire rig run intact. A plot of the calculated and measured rig gas temperature during the rig run is shown in Figure 3-286, which indicates a very constant temperature history and very good agreement between the calculated and measured temperature.

Rig run #3 was originally intended to evaluate the viability of using fuel doping as a method of mitigating the silica volatility problem. Pre-saturating the combustion gases with Si(OH)x, by doping the fuel with a Si-containing compound, would remove the thermodynamic driving force for the volatilization reaction $SiO_2 + 2H_2O(g) = Si(OH)_4(g)$.

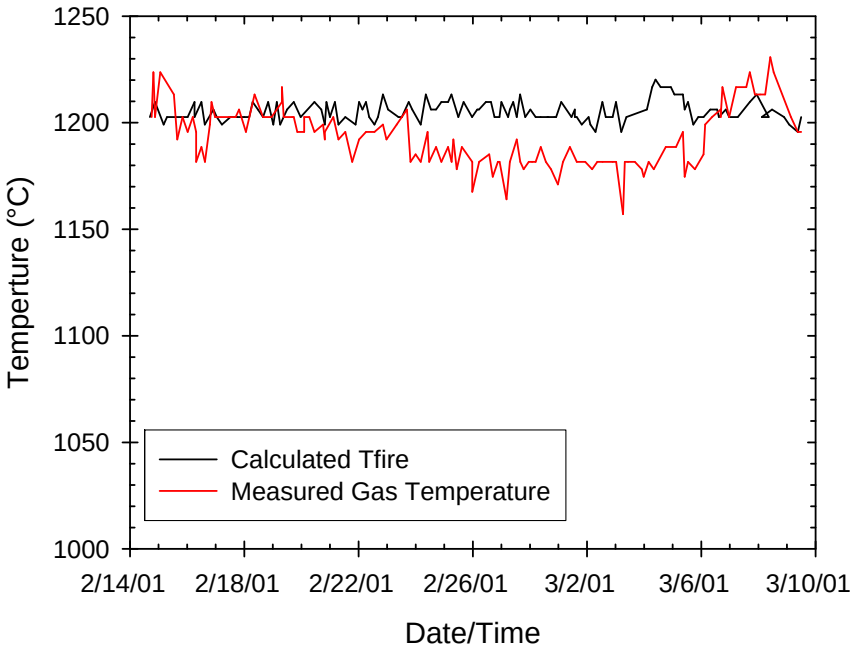

Figure 3-286. Temperature history during long-term rig run #2 comparing the calculated gas temperature (T_{fire}) to the actual gas temperature measured with a Type B thermocouple in the gas stream.

Apparatus for introducing a controlled amount of silicon to the fuel was developed and installed in the test rig fuel line. The run was then started on April 27, 2001. The initial fuel dopant level chosen for this experiment was selected to give a Si concentration in the combustion gases slightly in excess of saturation. The rig was otherwise run under conditions similar to those in rig runs #1 and #2, i.e. T = 1200°C, P = 830kPa (8.1 atm.), equivalence ratio $\phi \approx 0.5$, and gas velocity = 210m/s. The test contained 21 samples, of which 16 are uncoated mechanical properties test bars, 4 were EBC coated bars, and one was CVD SiC coated CMC bar for detailed evaluation of recession/oxidation phenomena.

Rig run #3 was stopped after 106h of exposure because the Si doping level was found to cause rapid accumulation of SiO_2 deposits on the retaining rings, thereby reducing the gas flow and changing the effective exposure temperature. This situation made it necessary to do a series of separate rig runs (#5-#7) where the silicon doping level was varied in order to determine a doping level beyond saturation, but not so oversaturated that significant deposition of SiO_2 would occur during the run.

While the Si doping experiments were on hold pending the identification of the optimum doping level, rig run #4 was initiated with the intent of measuring exposure effects at a reduced temperature of 815°C. Early in the run the operation of the rig at a sample temperature of 815°C without flameout was shown to be feasible; however, incomplete combustion was observed over a wide range of operating conditions. The fuel nozzle/combustor was subsequently removed from the rig and tested again in the open

flame test facility. The nozzle was subsequently modified in order to burn the fuel more completely at a firing temperature of 815°C by placing a perforated plate and a metal screen over the burner inlet to block swirling and operating in premixed mode only. Unfortunately, thermocouple traverses across the combustor exit showed a pronounced parabolic temperature profile, with cold temperatures near the walls. Changes in the swirler blockage configuration, as well as running with no swirler blockage, did not significantly change the undesirable profile.

Running the rig with the highly peaked temperature profile was not a viable option. Under these conditions the samples would be running too cold and probably with too low a water vapor concentration, owing to poor mixing of colder air with hotter combustion gases, to perform a viable exposure test at 815°C. Further development, testing and modification of a fuel nozzle system that would allow for complete combustion at 815°C with a flat temperature profile was judged to be relatively high in risk, and thus could potentially utilize a large amount of the program's testing resources. Rather than delay the rest of testing until a suitable fuel nozzle solution could be developed, run #4 was abandoned and testing was resumed with the fuel doping experiments at 1200°C.

Rig run #5 was started on August 21, 2001, with 14 samples in 2 tiers (level 2 and level 4). For the next 5 weeks the run was plagued with unpredictable blowouts. Combustion would stop abruptly with no prior warning in any of the measured rig operational parameters. These blowouts were eventually traced to water build-up in the compressed air line that then passed through the combustor. Water catch points in the compressed air line were found to contain an abundance of water. Numerous modifications were made to insert bleed points into the compressed air line to try to eliminate water build-up. These modifications helped increase the time between blowouts, but in reality the coming of Fall, with cooler, drier intake air, probably had as much effect on preventing blowouts as any modification to the air lines.

Two additional anomalies were noted in the operation of the rig during run #5 compared to rig runs #1 and #2:

- The split between air passing through the combustor and air bleeding around the combustor had changed compared to rig runs #1 and #2. This was believed to have been caused by a problem during the rig re-build following the aborted run #3 combustor testing. This situation was addressed with a partial rig re-build following run #5.
- The actual Si uptake from the fuel doping apparatus was about 0.7-0.8 grams/hour versus the 0.48 grams/hour predicted from the mass flow meter calibration. Combined with the lower combustion gas flow mentioned above, this consumption rate resulted in an actual Si level of roughly 0.7ppm rather than the desired 0.3ppm. The run was completed at this doping level with the intent to investigate lower levels in subsequent rig runs.

Due to the rig blow-out problems rig run #5 was not completed until October, 2001. Examination of the rig-exposed samples showed that this doping level (0.7ppm) corresponded to slow deposition of SiO_2 on the sample surfaces. The combustion gas

was thus oversaturated in Si, in agreement with the thermodynamic calculations. Rig run #6, the second short run for optimization of the Si doping level, was set up with a target Si doping level of 0.1ppm, or under-saturated with respect to the thermodynamic predictions.

Rig run #6 was started in November and completed in early December, 2001. The actual Si injection level measured during this run was approximately 0.2ppm, compared to a target Si injection level of 0.1ppm. The run was stopped after 206 elapsed hours owing to fracture of one of the sample retaining rings. Examination of exposed samples from this run shows that this doping level corresponded to a slow volatilization of SiO_2 from the sample surfaces. The combustion gas was thus undersaturated in Si, in agreement with the thermodynamic modeling calculations, which predict saturation at a Si injection level of approximately 0.3ppm.

A photograph of typical samples from rig runs #5 and #6 is given in Figure 3-287, and shows that the Si injection conditions from these two runs bracket the Si saturation level in the combustion gas at 1200°C. The sample in the center, exposed in rig run #5 with over-saturated conditions, shows SiO_2 deposition. The sample on the right, exposed in rig run #6 with under-saturated condition, shows volatilization of the surface matrix layer (compare the surface appearance of this sample to that of the as-fabricated sample on the left). In addition, the sample exposed in rig run #5 gained mass whereas the sample exposed in rig run #6 lost mass.

Rig run #7, the third short run for optimization of the fuel Si doping level for suppression of CMC volatilization, was also completed in December, 2001. The intended Si injection level for this run was 0.4ppm; however, the measured weight loss rate of dopant from the fuel doping apparatus corresponded to an injection level of approximately 0.23ppm. Visual examination and before-and-after weights of exposed samples from this run shows that this doping level corresponded to a slow volatilization of SiO_2 from the sample surfaces. The overall sample mass and thickness losses were similar to those from rig run #6, which confirmed that the actual Si injection level was roughly the same in both runs.

The next rig run to be performed was the continuation of rig run #3, initially intended to be a 500h exposure run at the optimum Si injection level inferred from rig runs #5, #6, and #7. Based on the above results, this run was performed at a Si injection level of about 0.5 ppm, corresponding to saturation or a slight over-saturation of the gas phase. The goal was to protect the samples from SiO_2 volatilization while simultaneously avoiding a large buildup of SiO_2 in the rig, which would alter the gas flows and change the total pressure and gas flow rate during the run.

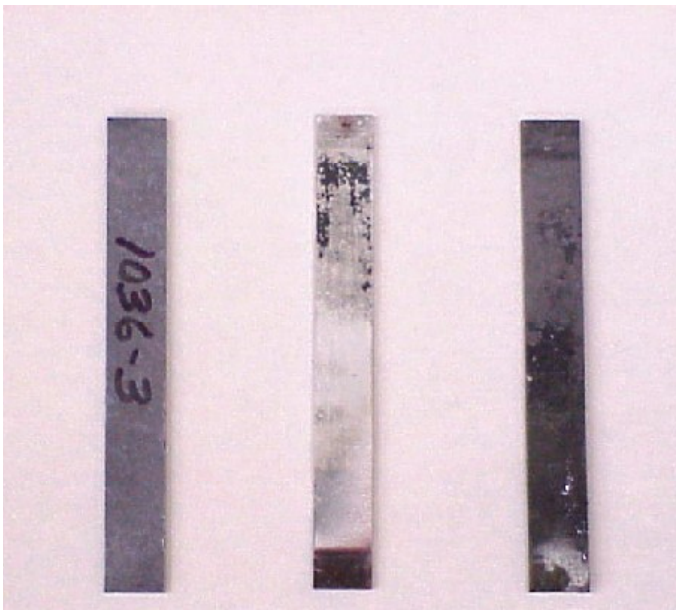

Figure 3-287. Photograph comparing prepreg MI CMC samples exposed in long-term rig runs #5 and #6 with a similar sample in the as-fabricated (unexposed) condition. Build-up of SiO_2 (whitish coating) was observed on the samples during run #5 whereas very slight surface recession was noted during run #6.

Visual examination of the 21 samples previously run for 106 hours in the first part of rig run #3 showed thick, chalky SiO_2 deposits on most of the samples. These deposits were ground away using an Al_2O_3 grinding wheel, which readily removed the SiO_2 deposits while avoiding significant damage to the samples. The four samples with environmental barrier coatings (EBC's) exhibited erosive damage of the EBC's caused by the high level of SiO_2 particulates in the gas stream. These four samples, as well as five uncoated samples, were replaced by similar samples that had not been previously exposed. The remaining 12 samples were retained from the first part of this rig run.

The continuation of rig run #3 was started in January 2002. Borescope examination of the exposed samples after approximately 500h exposure showed that they had thin surface layers of deposited SiO_2, thus the combustion gas was slightly over-saturated in Si in accord with thermodynamic predictions. The continuation of rig run #3 was completed on March 11, 2002. Twelve of the 21 samples that had been run for 106h in the original portion of rig run #3 accumulated a total of 840h or rig exposure whereas the nine samples that had been added for the continuation portion of this run were exposed for a total of 734h.

Rig run #8 was initiated on March 29, 2002, with the intention to run 4000 total hours in three segments of 1000, 1000 and 2000 hours. Samples were to be pulled from testing at 1000 and 2000 hours for characterization while a subset of the specimens was to be exposed for the full 4000 hours through all of the segments.

A rig anomaly was noted on May 31, 932 hours into the run, which necessitated a rig shutdown and inspection. The cause of the anomaly was a hole that formed in the inner shell of the water-cooled exhaust elbow, leading to water leaking into the rig. This elbow was a custom-made part and required 6-8 weeks to be remanufactured. Although the plan had been to remove a subset of the samples in run #8 following 1000 hours of exposure, the achieved exposure of 932 hours was considered close enough to the target to allow characterization of these samples to continue while awaiting repairs of the exhaust elbow. Ten prepreg MI composite samples were removed from the rig test and were characterized mechanically and microstructurally.

Rig run #8, segment 2, planned for 1068 h, was started on August 27, 2002. The samples in segment 2 had accumulated 408h exposure time as of October 10, 2002, when the run segment was stopped owing to cracking in several of the sample retaining rings. While new retaining rings were being fabricated use of the rig was given to the Microturbine Program so that combustion rig tests could be run on several monolithic Si_3N_4 candidate materials. This Microturbine Program run was completed on March 10, 2003. Rig run #8, segment 2, was then resumed on May 2, 2003.

By June 16, 2003, the samples in run #8 segment 2 had accumulated an additional 1148h exposure at 1200°C. Eleven of the 28 samples were withdrawn for mechanical properties testing and metallographic examination, and were replaced with 11 new samples.

Rig run #8 segment 3, planned for 2000h, was started on June 26, 2003. The segment was stopped after 1417 exposure hours on October 3, 2003, owing to fracture of a retaining ring and liberation of one of the samples. The test coupons were removed and it was determined that the retaining rings were too badly damaged for the segment to continue. At this time, eight samples, consisting of all of the remaining uncoated CMC samples and several EBC coated CMC samples that showed significant EBC damage, were withdrawn and were replaced by samples for evaluation in other programs. A new set of retaining rings was fabricated and the final segment of rig run #8, segment 4, was started on December 24, 2003. Twenty-one samples, of which 20 were EBC coated, were exposed in this final segment. Prior to this segment, the longest-running EBC coated CMC samples had accumulated 3497h of exposure time in run #8, hence segment 4 was planned for 503h to obtain the desired 4000 hours.

Segment 4 was concluded on January 25, 2004, after 425 h exposure owing to a safety problem related to ice originating from the rig exhaust. It was determined that the safety problem could not be remedied immediately to allow resumption of the rig run. Consequently the overall rig run #8 was concluded with a maximum sample exposure time of 3922h. The samples were removed for post-test measurement of mechanical properties and microstructural evaluation.

3.9.4 Long-Term Rig Coupon Exposure Results

All of the test samples exposed in the long-term combustion rig were in the form of 102mm x 12.7mm x ~2.4mm straight-sided rectangular bars. Samples were exposed in various conditions, including as-fabricated, with additional CVD SiC seal coatings, after pre-cracking to 0.2% strain, or with EBC coating.

3.9.4.1 Rig Run #1 Results

Photographs of typical samples removed from the first rig run after 500 hours exposure are shown in Figures 3-288 through 3-291. Figure 3-288 shows a typical exposed CMC sample. The fringe pattern at the left hand side of the sample indicates where eddy flow over the retaining ring gave way to turbulent flow along the sample. The CVD SiC seal coat on this sample was not completely removed by volatilization during the rig run. Figure 3-289 shows one of the samples that experienced partial spalling of the CVD SiC seal coat during the run. The seal coat spalls correspond to the lighter regions on the right hand side of the sample.

Figure 3-290 shows an EBC coated CMC sample that had been in the fourth (farthest downstream nearest the rig exit) rank. The EBC is intact except for a small chip in the center of the sample at the top. There is a small deposit of a brownish glassy material in the area just above where the retaining ring had been (left side of sample as pictured). SEM/EDS analysis of similar deposits from the preliminary rig runs showed this glassy material to be a calcium iron aluminosilicate. There is no evidence of reddish Fe oxide deposition on this sample. Figure 3-291 shows a similar EBC coated sample from the first (most upstream) rank. The portion of the sample that was shielded by the retaining ring (left hand side of photograph) is in pristine condition, but the rest of the sample exhibits a red deposit, presumably containing Fe_2O_3.

Figure 3-288. Photograph of a slurry cast MI CMC sample coated with a 10.25mm CVD SiC seal coat and exposed for 500h in long-term rig run #1. The gas flow direction is left to right.

Figure 3-289. Photograph of a slurry cast MI CMC sample on which approximately 50% of the CVD SiC seal coat has spalled during long-term rig run #1. The gas flow direction is left to right.

Figure 3-290. Photograph of a prepreg MI CMC sample with an environmental barrier coating (EBC) that was exposed in the fourth rank of the long-term rig during run #1. The gas flow direction is left to right.

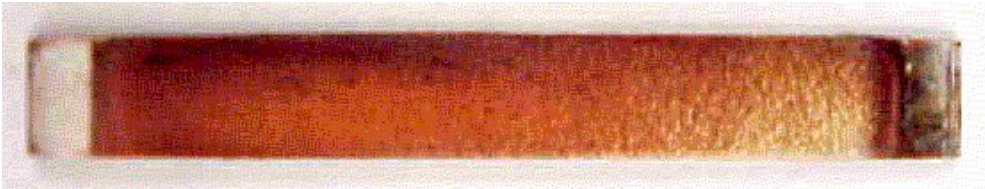

Figure 3-291. Photograph of a prepreg MI CMC sample with an environmental barrier coating (EBC) that was exposed in the first rank of the long-term rig during run #1. The gas flow direction is left to right.

Nine of the 28 total samples included in this rig run #1 were tensile tested at room temperature to compare the post-exposure retained strengths to those for unexposed bars taken from the same panels. The other 19 bars were included solely for recession rate measurements or were exposed in rig run #2 in order to accumulate 1000 hours of exposure. Strength measurement results for the nine samples tested after rig run #1 are shown in Table 3-65. The samples that were tested included CCP slurry cast MI composites with BN and Si-doped BN fiber coatings, and prepreg MI composites with configuration C fiber coatings. Some of the samples had external EBC coatings applied, and some were precracked to 0.2% strain prior to exposure testing in the rig. The properties of the exposed test samples (Y under the Exposed column) are compared to those of similar bars cut from the same panels and broken in the as-fabricated condition (N under the Exposed column). The numbers in parenthesis next to each property value gives the % difference measured between the exposed bar and the unexposed standard bar from the same panel (a negative number means the property was less after rig

exposure). Values of the initial modulus and matrix cracking stress for "precracked" samples are not meaningful, and thus are not listed in the table.

Table 3-65. Room Temperature Tensile Strength Data for Samples from the First Long Term Rig Test.

Sample Type / Fiber Coating	Exposed?	EBC?	Precracked?	Initial Modulus (GPa)	Proportional Limit Stress (MPa)	Ultimate Strength (MPa)	Strain to Failure (%)
Slurry Cast / BN, panel 1	N	N	N	1976	138	363	0.78
	Y	Y	N	246 (+25)	186 (+35)	363 (0)	0.54 (-31)
Slurry Cast / BN, panel 2	N	N	N	190	132	383	0.80
	Y	N	Y	-	-	237 (-38)	0.35 (-56)
	Y	Y	Y	-	-	250 (-35)	0.34 (-58)
Slurry Cast / Si-BN	N	N	N	185	138	343	0.67
	Y	N	N	234 (+26)	80 (-42)	337 (-2)	0.70 (+5)
	Y	N	Y	-	-	250 (-27)	0.59 (-12)
Prepreg / config C panel 1	N	N	N	249	144	276	0.84
	Y	N	N	307 (+23)	158 (+10)	194 (-30)	0.31 (-63)
	Y	N	Y	-	-	202 (-27)	0.66 (-21)
Prepreg / config C panel 2	N	N	N	264	181	335	0.84
	Y	Y	N	234 (-11)	161 (-11)	323 (-4)	0.82 (-2)
	Y	Y	Y	-	-	212 (-25)	0.77 (-6)

Values in parenthesis represent the % change in the listed property following exposure in the long-term rig for 500 hours compared to witness bars from the same composite panels that were tested without exposure.

Overall, most of the samples exposed in the rig during the initial 500 hour test showed degradation of strength and/or strain capability. The uncracked slurry cast sample with BN fiber coatings showed an anomalous increase in modulus and cracking stress, no change in ultimate strength, but a 30% reduction in strain to failure. When precracked this material showed a large ultimate strength decrease (35-40%), and a much larger reduction in the strain to failure (roughly 60%). Mechanical properties were degraded for samples in which the CVD SiC seal coat was not completely removed by volatilization in the combustion gas stream, as well as in samples in where the seal coat was volatilized or had partially spalled. Microstructural examination indicated that panel 1 had large matrix voids throughout the structure that were internally oxidized following rig exposure, but such voids were not present in panel #2, which showed even greater levels of degradation.

The slurry cast samples with the Si-doped BN fiber coating showed better property retention, but some degradation was still noted. The specimen exposed in the uncracked condition showed little degradation of the ultimate strength and strain values, but surprisingly showed a very substantial reduction in matrix cracking stress. The reasons for this behavior are not known. The precracked specimen showed some loss of ultimate strength and strain to failure, as would be expected. Both samples with Si-doped BN fiber coatings showed better ultimate strength and strain retention than the similar slurry

cast samples with BN fiber coatings. Surprisingly, the test bar with EBC coating showed slightly greater degradation than did the bar without EBC.

Degradation of the prepreg MI samples was larger than anticipated based on earlier results of steam furnace and shroud rig exposure of samples with configuration C fiber coatings. The samples from the first panel showed a roughly 30% decrease in ultimate strength and 20% to 60% reductions in strain to failure following rig exposure. Surprisingly the loss of strain capability was worse for the uncracked specimen than for the precracked specimen. Such a large loss in strength and strain capability is unusual in prepreg MI composites, and is probably related to the fact that the surface recession of these samples had penetrated into the first layer of fiber, thereby compromising one of only four tensile plies in the test bars.

Samples from the second panel, which had EBC coatings applied, showed essentially no loss of strength or strain to failure when exposed uncracked, and only a 25% loss of ultimate strength but no loss of strain to failure when exposed with matrix cracks. These results suggested that the EBC coating was indeed effective at protecting the samples.

3.9.4.2 Rig Run #2 Results

The samples from rig run #2 were removed from the rig following the run and visually inspected. Overall the samples appeared very similar to those exposed in the first rig run. Post-exposure strength tensile data from rig test #2 was combined with that measured following rig test #1 in order to compare the effects of 500 hour and 1000 hour exposure. The combined testing results for the samples without EBC coatings are given in Table 3-66, and data for samples with EBC coatings is given in Table 3-67.

Overall, the results in Tables 3-68 and 3-69 show some rather inconsistent trends. First, the prepreg MI samples without EBC coatings showed very substantial degradation, particularly in the strain to failure values. Moreover the degradation was more severe in uncracked samples than it was in precracked samples (specimens stressed to 0.2% strain prior to rig exposure). This result contrasted rather sharply with previous results from steam furnace tests and from coupon exposures in the shroud rig, where the prepreg MI materials with configuration B or C coatings showed no appreciable degradation.

Table 3-66. Summary of Residual Strength Properties of Non-EBC Coated Samples Exposed in Long-Term Rig Runs 1 and 2.

Exposure Time and Sample Condition	GE Prepreg MI* Config. C Fiber Coating			CCP Slurry Cast MI† BN Fiber Coating			CCP Slurry Cast MI‡ Si-BN Fiber Coating		
	σ_{PL} (MPa)	σ_f (MPa)	ε_f (%)	σ_{PL} (MPa)	σ_f (MPa)	ε_f (%)	σ_{PL} (MPa)	σ_f (MPa)	ε_f (%)
As-fabricated not exposed	144±10	276±4	0.84±0.08	132	383	0.80	138	342	0.67
500h uncracked	181±11 (+25%)	230±23 (-15%)	0.44±0.19 (-45%)	129 (-0%)	338 (-10%)	0.54 (-30%)	94 (-30%)	335 (-0%)	0.70 (+5%)
1000h uncracked	159 (+10%)	162 (-40%)	0.098 (-90%)	121 (-10%)	356 (-5%)	0.84 (+5%)	93 (-30%)	215 (-35%)	0.43 (-35%)
500h precracked	-	199±4 (-30%)	0.51±0.20 (-40%)	-	258±39 (-30%)	0.49±0.19 (-40%)	-	273±30 (-20%)	0.59±0.02 (-10%)
1000h precracked	-	24.2 (-40%)	0.34 (-60%)	-	49.6±3.9 (-10%)	0.64±0.02 (-20%)	-	35.4±8.1 (-30%)	0.44±0.16 (-35%)

σ_{PL} = proportional limit stress; σ_f = ultimate strength (failure stress); ε_f = strain to failure

Percentages in parenthesis are the relative change in the property from the as-fabricated values. Values listed with ± limits represent the range of values measured on two samples.

* Samples had 0.1 to 0.15mm unreinforced matrix layers on exposed faces; edges had exposed fibers.

† Samples had 0.25mm CVD SiC seal coats on exposed surfaces and edges; the precracked, 500-h samples had damaged or no seal coat.

‡ Samples had 0.25mm CVD SiC seal coats on exposed surfaces and edges; one precracked, 500h sample had no seal coat.

Table 3-67. Summary of Residual Strength Properties of EBC* Coated Samples Exposed in Long-Term Rig Runs 1 and 2

Exposure Time and Sample Condition	GE Prepreg MI, Configuration C Fiber Coatings			CCP Slurry-Cast MI BN Fiber Coatings		
	σ_{PL} (MPa)	σ_f (MPa)	ε_f (%)	σ_{PL} (MPa)	σ_f (MPa)	ε_f (%)
As-fabricated unexposed	181 ± 34	335 ± 35	0.84 ± .08	132	383	0.80
500h uncracked	149 ± 8 (-20%)	330 ± 16 (-0%)	0.95 ± 0.18 (+15%)	173 ± 33 (+30%)	316±89 (-20%)	0.48 ± 0.09 (-40%)
1000h uncracked	159 ± 10 (-10%)	341 ± 8 (+0%)	1.00 ± 0.09 (+20%)	139 ± 17 (+5%)	298 ± 58 (-20%)	0.46 ± 0.03 (-40%)
500h, precracked	-	321 ± 3 (-5%)	0.86 ± 0.12 (+0%)	-	272 ± 26 (-30%)	0.35 ± 0.01 (-60%)
1000h, precracked	-	252 ± 14 (-25%)	0.57 ± 0.03 (-30%)	-	284 ± 18 (-25%)	0.48 ± 0.21 (-40%)

σ_{PL}= proportional limit stress; σ_f = ultimate strength (failure stress); ε_f =strain to failure

* 3-layer Si/(BSAS+mullite)/BSAS EBC, ~0.4mm thick.

Figure 3-292 shows the progression of surface volatilization of GEGR prepreg CMC under rig conditions. The as-fabricated samples (Figure 3-292a) had a layer of

unreinforced matrix on the broad surfaces which was typically 0.13mm thick. Prepreg samples that had been tested in rig rank 1 (the lowest or farthest upstream level, closest to the combustor and running at ~1120°C) for 500 hours exhibited 0.048 to 0.074mm of recession on the inner surfaces that had been exposed to the combustion gas flow. A micrograph of the sample edge of such a sample is shown in Figure 3-292b. Prepreg samples that had been exposed in sample rank 3 (~1200°C sample temperature) exhibited complete volatilization loss of the unreinforced layer and initiation of attack on the first fiber ply after 500 hours exposure, as shown in Figure 3-292c. Prepreg samples exposed in level 4 for 1000h (Figure 3-292d) exhibited volatilization of the unreinforced layer and approximately 2/3 of the first fiber ply. Since the rate of volatilization exceeded the rate of oxidation, virtually no oxide appeared on the surface exposed to rapid gas flow. In general, prepreg samples exposed in the rig showed no signs of internal oxidation or other internal microstructural changes.

Since cut edges of the samples were exposed to the rig atmosphere, some environmental attack was expected starting at these cut edges and proceeding inward. Figure 3-293 shows that environmental attack of cut edges of prepreg samples was confined to the first layer of fibers near the cut surface. No evidence of internal oxidation proceeding from the cut edges was observed in non-EBC coated prepreg samples. While volatilization damage to the surface plies during exposure undoubtedly contributed to the loss in strength and strain capability observed in the prepreg MI samples, the extent of property degradation was more severe than could be explained by the microstructural analyses alone.

The rig testing results were also somewhat inconsistent for the slurry cast materials without EBC coatings. At 500h exposure the samples with pure BN fiber coatings showed somewhat larger degradation than did the samples with Si-doped BN fiber coatings; however, at 1000h this trend was reversed. This result suggests that the low Si content in the low-temperature fiber coatings of the slurry cast material may not be effective in preventing fiber coating oxidation/volatilization, which would be in contradiction with fatigue results obtained under the EPM program with Sylramic-reinforced slurry cast composites.

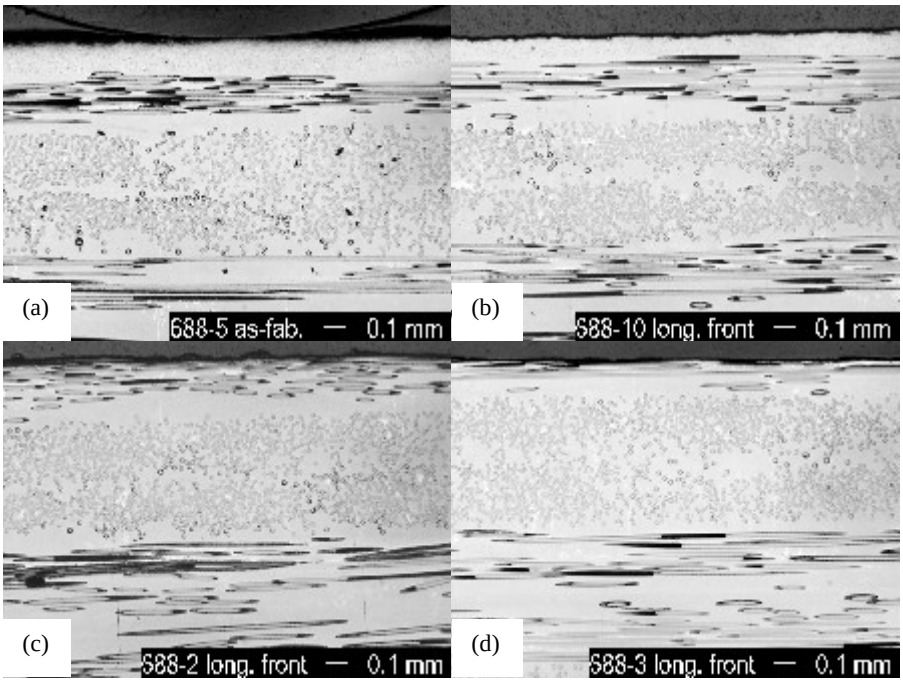

Figure 3-292. Optical micrographs of longitudinal cross-sections of GEGR prepreg MI CMC samples: (a) as-fabricated; (b) exposed in the long-term rig, level 1, for 500h; (c) exposed in the rig, level 3, for 500h; (d) exposed in the rig, level 4, for 1000h.

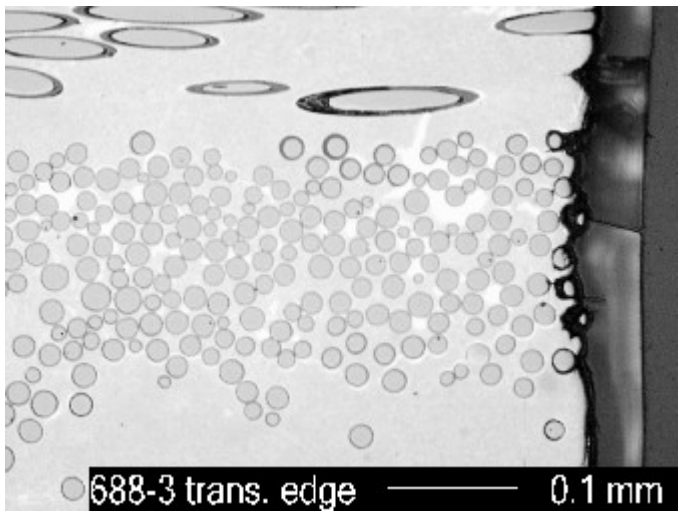

Figure 3-293. Optical micrograph of the cut edge a GEGR prepreg MI CMC, exposed in the long-term rig, level 4, for 1000h during rig runs #1 and #2. Environmental attack is confined to the first layer of fibers next to the surface and no evidence of internal oxidation was found.

Most of the CCP slurry-cast samples not coated with EBC and exposed in rig runs 1 and/or 2 had been coated on all sides with approximately 0.25mm of chemical vapor

deposited (CVD) SiC. Optical micrographs of typical rig-exposed slurry-cast CMC samples exposed in rig runs 1 and 2 are shown in Figure 3-294. Volatilization of the CVD SiC seal coat after 500h exposure ranged from 0.1mm to 0.2mm. A slurry-cast sample exposed for 1000h in level 1 showed only 0.1mm of volatilization loss of the SiC coating, whereas samples from levels 2 through 4 had 0.21 to 0.24mm of seal coat volatilization. These results were similar to those observed with the prepreg samples, and was further confirmation that the temperature in level 1 was lower than that in levels 2-4. The SiC seal coats on sample edges were generally intact and protective throughout the rig runs, as shown in Figure 3-294e. Seal coated slurry-cast CMC samples showed no evidence of edge or internal oxidation, indicating that the seal coats were effective in preventing such attack.

Two CCP slurry-cast samples were exposed for 500h in the rig without seal coats. A typical micrograph of one such sample, given in Figure 3-294f, shows volatilization of the front surface and oxidation of reinforcing fibers to a depth of 3-5 fiber diameters, as well as extensive internal oxidation within pores and fiber bundles. Mechanical properties of this sample were severely degraded, unlike those of the seal coated samples.

The third surprising result from rig tests #1 and #2 was that the EBC coatings appear to have protected the prepreg MI composite more effectively than the slurry cast composites. At 500 hours exposure the prepreg material with EBC showed essentially no degradation regardless of whether there were matrix cracks or not. Only at 1000h and with a cracked matrix did the EBC coated prepreg material begin to show degradation. Conversely, the EBC coated slurry cast samples showed substantial degradation at both 500 and 1000 hours, both cracked and uncracked. Again, it should be noted that the slurry cast samples without EBC had CVD SiC seal coatings applied to all surfaces whereas the EBC-coated samples had cut edges with exposed fibers (the EBC did not extend over the edges of the bars). Consequently oxidative attack from the exposed edges of the EBC-coated bars could explain some of the observed degradation.

A typical micrograph of an EBC coated GEGR prepreg MI sample after 1000h exposure in rig runs 1 and 2 is shown in Figure 3-295. This micrograph appears identical to micrographs of as-coated prepreg samples. Careful examination at higher magnification of the interface between the coating (dark layer at the top of Figure 3-295) and the Si bond coat (bright layer in the center of Figure 3-295) shows an oxide layer on the Si bond coat. This layer was difficult to image optically, and detailed evaluation of its morphology and thickness required scanning electron microscopy (SEM).

Surprisingly the prepreg CMC panels used for fabrication of EBC-coated rig samples exhibited regions that were poorly infiltrated. Such regions were preferentially attacked by the combustion atmosphere when cut edges of these samples were exposed in the rig. Under-infiltrated regions appear granular in the micrographs of Figure 3-296. These regions are invaded by oxide, which is uniformly gray in appearance. The depth of oxidation ranged from approximately 0.2 to several millimeters. Despite the appearance of several zones of oxidation of poorly infiltrated region in each sample exposed for

1000h, environmental damage was confined to regions within 0.2-2mm of the cut edges and mechanical properties were not appreciably compromised.

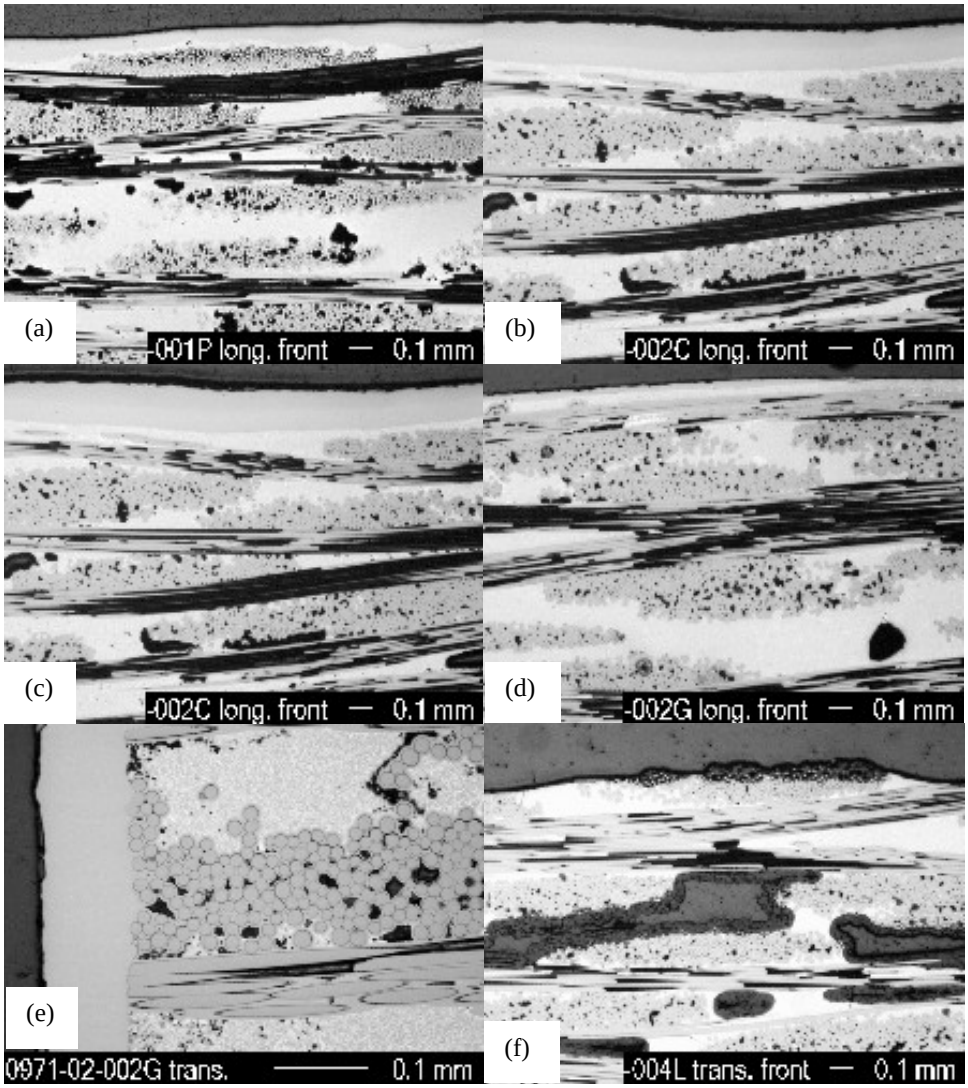

Figure 3-294. Optical micrographs of cross-sections of CCP slurry-cast CMC samples: (a) exposed in the rig, level 4, for 500 h; (b) exposed in the rig, level 2, for 500 h; (c) exposed in the rig, level 1, for 1000 h; (d) exposed in the rig, level 2, for 1000 h; (e) edge of sample exposed in the rig, level 2, for 1000 h; (f) exposed in the rig, level 3, for 500 h (without CVD SiC seal coat).

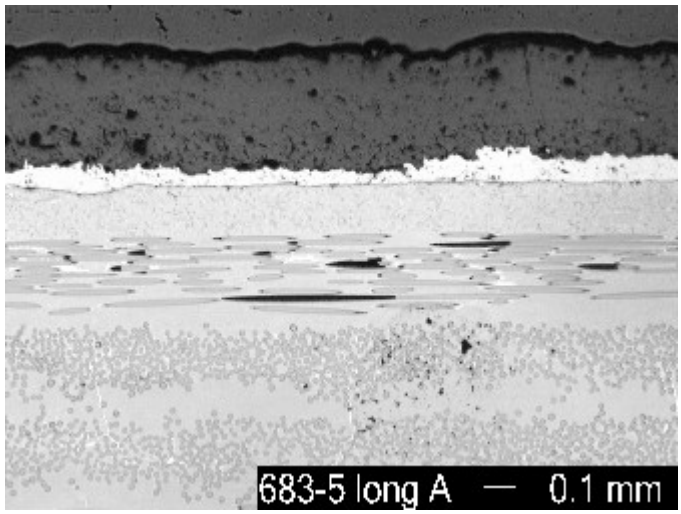

Figure 3-295. Optical micrograph of the cross-section of a typical EBC-coated GEGR prepreg MI CMC exposed in the long-term rig for 1000h during rig runs 1 and 2.

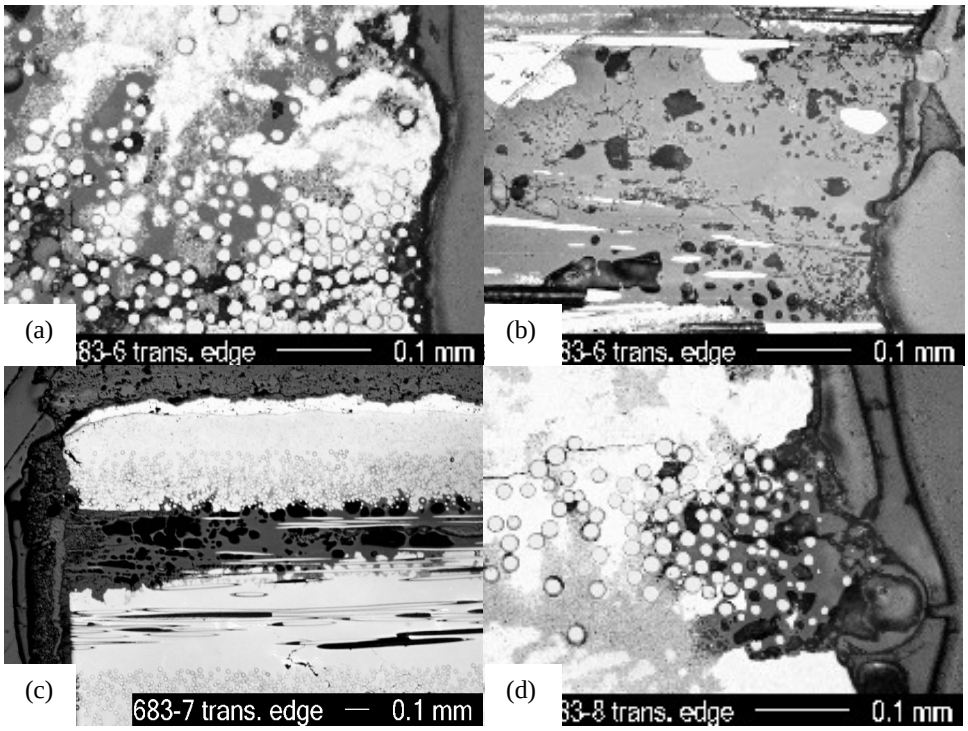

Figure 3-296. Optical micrographs of cut edges of EBC-coated GEGR prepreg CMC's exposed in the long-term rig for 1000h during rig runs 1 and 2. Samples were not typical in that they had substantial processing defects prior to rig exposure.

EBC coatings on CCP slurry-cast samples exhibited no observable microstructural changes when exposed for 500 or 1000h in rig runs 1 and/or 2, as shown in Figure 3-297a. However, the EBC-coated samples were not seal coated, and subsequently many

of them showed moderate to extensive internal oxidation caused by water vapor penetration from cut edges (see Figure 2-314, images b through d). The samples are internally oxidized within small pores (Figure 3-297b), large pores (Figure 3-297c), and within fiber bundles (Figure 3-297d). The degradation of mechanical properties of EBC-coated slurry-cast samples reported in Table 3-67 can generally be attributed to this internal oxidation, which began at cut edges and spread inward into the centers of the samples.

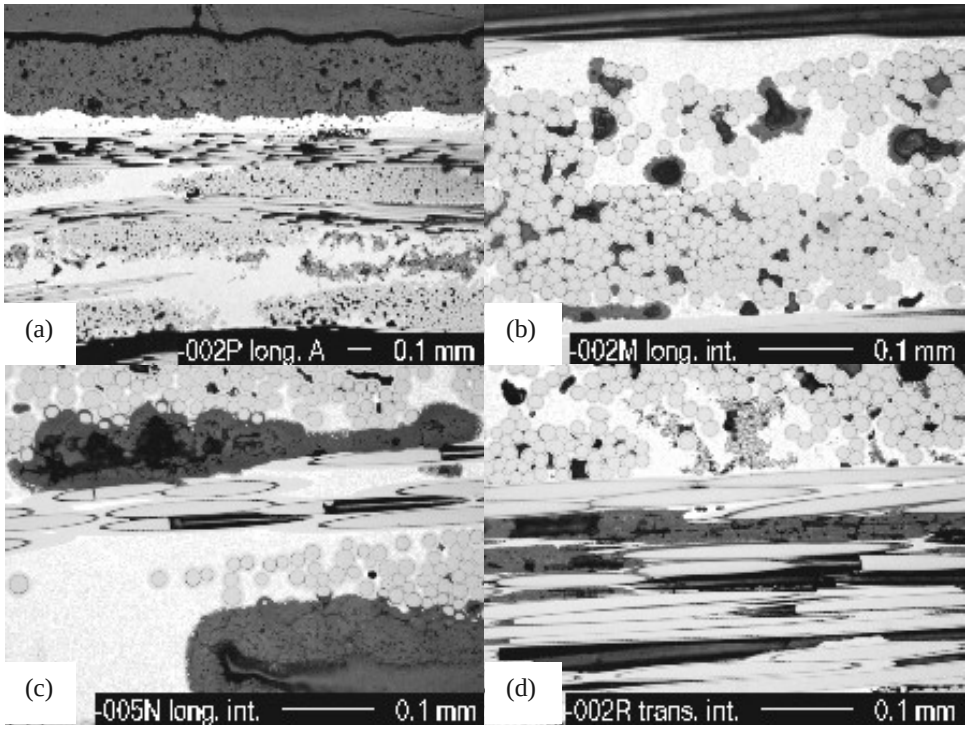

Figure 3-297. Optical micrographs of cross-sections of EBC-coated CCP slurry-cast MI CMC samples: (a) general microstructure of the EBC, showing lack a of microstructural change during the rig run; (b)-(d), samples showing oxidation of internal porosity: (b) exposed in the rig, level 1, for 500h; (c) exposed in the rig, level 4, for 1000h; (d) exposed in the rig, level 1, for 1000h.

3.9.4.3 Rig Runs #5-#7 Results

Long term rig runs 5-7 were relatively short runs aimed primarily at identifying the optimum fuel doping level to inhibit silica volatilization. Nevertheless, sample exposed in the rig during these runs were still characterized for retained mechanical properties using room temperature tensile tests. Mechanical properties of prepreg MI CMC samples exposed in rig runs 5, 6, and 7 are plotted as a function of total run time in Figures 3-298. All of the samples were taken from the same prepreg panel. Samples run for a total of 750h were exposed in rig runs 5, 6, and 7; one sample run for a total of 500h was exposed in rig runs 6 and 7; and the samples run for a total of 250h were exposed in run 7 only. The trend lines of proportional limit and fracture stress show virtually no degradation for

rig exposure times up to 750h. The trend line for strain to failure shows a modest (20%) reduction in 750h. These results indicate that suppression of volatilization from the sample surfaces by saturating the combustion gas with silicon was largely effective in preventing mechanical properties degradation of exposed CMC samples.

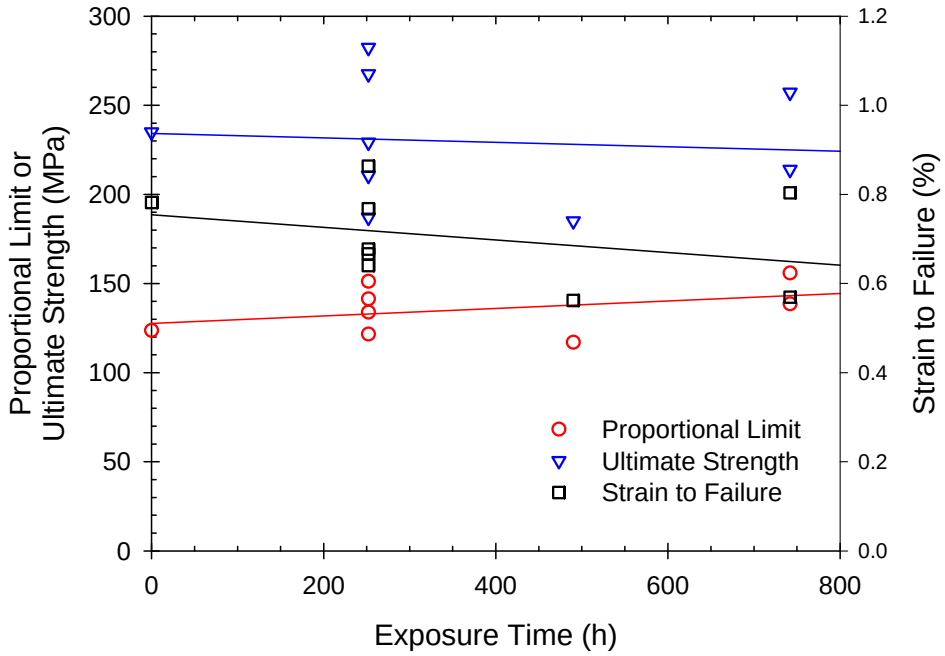

Figure 3-298. Residual strength properties of GEGR prepreg MI CMC samples exposed in rig runs 5, 6, and 7 as a function of total exposure time.

3.9.4.4 Rig Run #3 Results

In rig run #3, 21 CMC samples were exposed to a Si-saturated combustion gas atmosphere containing ~0.5 ppm Si. Twelve samples that had been run in the original portion of rig run #3 were exposed at 1200 °C for a total of 840h, and nine samples which had been added for the continuation of this run were exposed at the same temperature for a total of 734h. The samples consisted of Hi-Nicalon reinforced prepreg material fabricated at GEGR, Hi-Nicalon reinforced slurry-cast material fabricated at CCP, and Hi-Nicalon reinforced slurry-cast material fabricated at Goodrich Aerospace.

The typical appearance of the CMC samples not coated with EBC and exposed in rig run #3 is shown in Figure 3-299A. The combustion gas was slightly oversaturated in Si, leading to deposition of a thin, uniform chalky white layer of crystalline SiO_2. Buildup of a thick SiO_2 layer on the samples or in the exhaust piping of the rig was avoided by proper selection of the Si injection level.

The typical appearance of EBC-coated CMC samples exposed in rig run #3 is shown in Figure 3-299B. The SiO_2 deposit has reacted with the barium strontium aluminosilicate

top layer of the EBC to form a thin coating of a clear glass. The glass has relatively low viscosity and has thus overflowed the edges of the sample and has been swept by the gas flow towards the ends of the sample. Formation of a glassy product could be beneficial if it seals cracks and other defects in the EBC and prevents transport of oxidizing gases to the EBC/CMC interface.

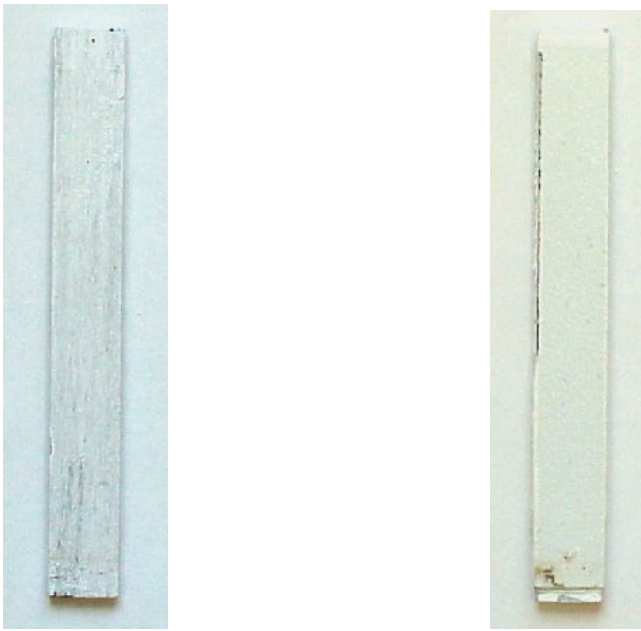

A B

Figure 3-299. Typical post-test appearance of CMC samples without EBC coating (A) and with EBC coating (B) following exposure in a Si-saturated combustion atmosphere during long-term combustion rig run #3 for 840h at 1200°C.

The residual ambient temperature mechanical properties of the samples that had been exposed in rig run #3 are summarized in Table 3-68. This table also includes tensile data measured on bars that were cut from the same panels as were used in the rig test but not exposed in the rig (0 time in the rig) to serve as a baseline to judge any property degradation.

GEGR prepreg MI samples without EBC coating and without outer layers of unreinforced matrix (panel 925) exhibited a significant (30-40%) decreases in proportional limit stress and fracture strength, and moderate to significant (15-30%) decreases in strain to failure after rig exposure in the Si-doped combustion gas stream. These results suggest that although CMC volatilization was prevented by Si doping of the gas stream, oxidation of the outer 0° orientation fiber plies caused a loss of load bearing capability in these layers, and hence a decrease in the proportional limit and ultimate fracture stresses.

Prepreg samples that had surface matrix layers or EBC coatings exhibited decreases in mechanical properties similar to or more severe than those of samples without surface matrix layers. These property losses were not well understood, especially since samples with surface matrix layers exposed to Si-doped combustion atmospheres in rig runs 5, 6, and 7 for up to 750 h showed only minor decreases in proportional limit and fracture stresses.

Table 3-68. Residual RT Tensile Strength Results for Samples Exposed in the Long-Term Rig During Run #3.

Sample No.	Material Type	Fiber Coating	EBC?	Precrack?	Total Time in Rig (h)	Proportional Limit (MPa)	Ultimate Strength (MPa)	Strain to Failure (%)
925H	Prepreg	Config C	No	No	0	153	328	1.16
925E	"	"	No	No	840	117	199	0.70
925B	"	"	No	No	734	103	202	0.90
925C	"	"	No	Yes	840	-	225	1.04
925F	"	"	No	Yes	734	-	199	0.90
923G	"	Config C	No	No	0	127	310	0.94
923B	"	"	Yes	No	734	93	230	1.22
923C	"	"	Yes	Yes	734	-	221	0.91
924I	"	"	No	No	0	152	330	0.96
924D	"	"	No	No	840	92	201	0.77
002V	CCP slurry	BN	No	No	0	216	417	0.77
002K	"	"	No	No	840	127	281	0.39
002H	"	"	No	Yes	734	-	288	0.60
002L	"	"	No	Yes	840	-	203	0.35
002O	"	"	Yes	No	734	112	185	0.34
002N	"	"	Yes	Yes	734	-	141	0.19
001-1	"	B(Si)N	No	No	0	138	343	0.67
001T	"	"	No	No	734	123	205	0.27
001S	"	"	No	No	840	121	252	0.38
001C	"	"	No	Yes	734	-	230	0.37
001O	"	"	No	Yes	840	-	279	0.61
98-59G	Goodrich slurry	BN	No	No	0	140	200	0.50
98-59H		"	No	No	0	140	203	0.55
98-59P	"	"	No	No	840	32	32	0.01
98-59R	"	"	No	No	840	59	59	0.03
98-59Q	"	"	No	Yes	840	-	125	0.04
98-59S	"	"	No	Yes	840	-	36	0.02

Residual ambient temperature mechanical properties of CCP slurry-cast MI samples that had been exposed in rig run #3 are also shown in Table 3-68. Samples without EBC and having BN-based fiber coatings (panel 0971-02-002) exhibited negligible to moderate (0-20%) decreases in elastic modulus, negligible decreases in proportional limit stress, and significant (40-50%) decreases in fracture stress and strain to failure after combustor rig exposure in the Si-doped gas stream. These results suggest that both external and

internal oxidation of the samples may have contributed to decreases in mechanical properties during rig exposure. Samples without EBC coatings and having silicon-doped BN fiber coatings (panel 0971-02-001) exhibited minor to moderate (10-25%) decreases in proportional limit stress, moderate to significant (25-35%) decreases in fracture stress, and significant (25-40%) decreases in strain to failure after exposure to Si-doped combustion gases. The two EBC coated slurry-cast samples exhibited severe losses in fracture stress and strain to failure.

The Goodrich samples (panel 01-98-59) exposed in rig run #3 exhibited complete embrittlement, with fracture stresses of 50-100MPa and failure strains of <0.05% following exposure. The observed degradation in mechanical properties was similar to, although more severe than, properties degradation measured after furnace exposure of samples from the same panel at 1200°C for 500-2000h in 90% H_2O + 10% O_2 atmospheres earlier in this program. The source of this embrittlement was not well understood.

3.9.4.5 Rig Run #8 Results

Long-term rig run #8 was divided into 4 individual segments of 932, 1148, 1417 and 425 hours. A complete listing of the samples exposed in this run is given in Table 3-69. As before, tensile data from witness bars that were not rig tested are included in the table as baselines for comparison with the rig exposed sample results. This rig test included only GEGR prepreg MI samples, both with and without EBC. A small number of the samples were also pre-cracked to 0.2% strain prior to exposure, as had been done in previous steam furnace tests. An additional sample pre-stress condition, whereby the samples were loaded to 96.5MPa tensile stress prior to rig exposure, was added in this test. There was a need to verify that stress at this level, even though it is well below the measured proportional limit stress of the prepreg MI system, was not introducing any damage that might lead to additional environmental degradation. It was also not known whether the EBC coatings would remain hermetic (i.e. uncracked) at strain levels corresponding to this level of stress in the CMC. Thus the pre-stressing treatment on coated composite samples was meant to evaluate whether the EBC remained an effective environment barrier at this level of applied stress (or strain). The strength and modulus values listed in Table 3-69 for the EBC coated samples were based on the uncoated sample thickness, which effectively assumes that the EBC coating supports no load during the tensile fracture process.

Samples exposed at ~1120°C, in the first (lowest) rank of rig, showed practically no effects of exposure regardless of the lack or presence of EBC or whether the samples were prestressed or precracked. The samples exposed at ~1204°C, in ranks 2-4 of the rig, also showed very little effect of exposure on the initial modulus and proportional limit stress. However, ultimate strength and strain to failure values varied widely; fracture stresses of exposed samples were up to 30% lower than those of as-fabricated material, and strain to failure values of exposed samples were up to 80% lower. Regardless of exposure time or extent of sample section loss by volatilization, all samples exhibited significant retention of strength and retention of tough composite behavior, i.e. full embrittlement of the CMC was never observed.

After 932 hours of exposure the one sample without EBC coating that was tested (sample 884-4) showed approximately 0.25mm of surface recession. When this loss of section thickness was allowed for, the elastic modulus, microcrack yield stress, and probably the fracture stress did not decrease from the 932 h exposure. The strain to failure was reduced by approximately 50%. The cause of this degradation was unknown, particularly since the EBC coated samples (discussed below) showed no degradation in strain to failure.

Uncoated samples exposed for longer times did exhibit some degradation of mechanical properties relative to the witness bars, particularly of ultimate strength and strain to failure, but there was no distinct trend of degradation with exposure time. On average for all of the exposures at 1204°C, including the precracked samples, there was an ~17% decrease in ultimate strength and an ~48% decrease in strain to failure. Some of these losses in properties were undoubtedly caused by loss of the outer tensile plies in the test samples from oxidation/volatilization.

The samples coated with EBC showed no appreciable properties degradation after 932h exposure in the rig for uncracked samples with either the 0.25mm or 0.76mm EBC top coat thicknesses, or for precracked samples with the 0.25mm EBC top coat. These results for the 0.25mm uncracked EBC were similar to those obtained for similar samples exposed in rig runs 1 and 2. The results for the 0.25mm precracked EBC were better than those for samples exposed in rig runs 1 and 2, perhaps reflecting improvements in EBC quality in the intervening time frame. In the previous runs, 1000h exposure of samples with precracked EBC's resulted in a 25% reduction in fracture stress and 30% reduction in strain to failure.

Most of the EBC coated samples that had not been preloaded or precracked exhibited essentially no loss of properties for exposure times between 932 and 3922h at either 1120° or 1204°C (positioned in the first rank or in ranks 2-4, respectively). However, there were anomalies in the data. For instance, of the 10 unstressed samples with 0.25mm EBC exposed between 932 and 3922 hours seven showed practically no degradation whereas three samples (1284-6, 1284-9 and 1092-2) exhibited very substantial degradation in both ultimate strength and strain to failure.

Precracked EBC coated samples exhibited approximately 30% decrease in fracture stress and approximately 45% decrease in fracture strain after 3922 hours of rig exposure. Preloaded EBC coated samples exhibited approximately 20% decrease in fracture stress and (with one possible outlier) 30% decrease in fracture strain after rig exposure, but again the degradation did not show a clear trend with exposure time. In general, the EBC was effective in preventing large decreases in CMC mechanical properties even after 3922h exposure and even in samples that had been precracked to compromise the protective qualities of the EBC.

Table 3-69. Summary of the Room Temperature Tensile Fracture Properties Measure on Samples Exposed in During the Long-Term Rig Run #8.

Sample Condition				Exposure Conditions		Tensile Test Results			
Sample No.	EBC Topcoat Thickness (mm)	Precracked to 0.2% strain?	Preloaded to 96.5MPa?	Total Exposure Time (h)	Exposure Temperature (°C)	Initial Modulus (GPa)	Proportional Limit Stress (MPa)	Ultimate Strength (MPa)	Strain to Failure (%)
883-1	-	-	-	0	-	201	150	298	0.832
884-1	-	-	-	0	-	241	175	284	1.010
883-4	-	No	Yes	1148	1120	240	191	276	0.824
884-4	-	No	No	932	1204	225	198	246	0.459
883-3	-	No	No	1148	1204	278	178	220	0.299
883-5	-	No	No	1417	1204	228	203	234	0.352
884-5	-	No	No	2080	1204	221	134	241	0.815
883-2	-	No	No	3497	1204	313	228	268	0.593
884-7	-	No	Yes	1148	1204	223	183	203	0.197
884-6	-	No	Yes	3497	1204	254	236	303	0.643
1089-5	-	-	-	0	-	272	179	298	0.855
1092-4	-	-	-	0	-	273	139	305	0.968
1094-8	-	-	-	0	-	263	144	323	1.050
1283-6	-	-	-	0	-	257	173	291	1.120
1284-7	-	-	-	0	-	275	165	290	1.090
1094-11	0.25	No	No	932	1120	291	170	314	0.925
1094-7	0.25	No	No	1148	1120	283	164	309	1.050
1283-7	0.25	No	No	1842	1120	289	196	300	1.440
1094-1-	0.25	No	No	3497	1120	281	183	329	1.120
1284-8	0.25	No	Yes	1148	1120	303	229	264	0.748
1284-2	0.25	No	Yes	2990	1120	268	193	268	0.930
1089-2	0.25	Yes	No	932	1120	-	-	303	0.941
1283-9	0.25	Yes	No	1842	1120	-	-	251	0.731
1094-4	0.25	Yes	No	3922	1120	-	-	321	1.060
1089-7	0.76	No	No	932	1120	275	192	309	0.948
1283-3	0.76	No	No	1842	1120	290	194	290	1.100
1094-6	0.30	No	No	3497	1120	252	170	305	1.120

Table 3-69 - Continued. Summary of the Room Temperature Tensile Fracture Properties Measure on Samples Exposed in During the Long-Term Rig Run #8.

Sample Condition				Exposure Conditions		Tensile Test Results			
Sample No.	EBC Topcoat Thickness (mm)	Precracked to 0.2% strain?	Preloaded to 96.5MPa?	Total Exposure Time (h)	Exposure Temperature (°C)	Initial Modulus (GPa)	Proportional Limit Stress (MPa)	Ultimate Strength (MPa)	Strain to Failure (%)
1089-3	0.25	No	No	932	1204	299	173	274	0.850
1092-7	0.25	No	No	932	1204	288	152	289	1.070
1094-1	0.25	No	No	932	1204	285	144	315	0.990
1094-12	0.25	NO	No	1148	1204	286	188	312	1.090
1284-6	0.25	No	No	1842	1204	350	170	191	0.136
1284-9	0.25	No	No	1842	1204	275	155	155	0.055
1092-2	0.25	No	No	3922	1204	325	159	174	0.045
1094-9	0.25	No	No	3922	1204	280	159	283	0.997
1089-9	0.25	No	No	3922	1204	281	150	288	1.090
1094-5	0.25	No	No	3922	1204	236	139	272	0.757
1284-3	0.25	No	Yes	1148	1204	289	201	273	0.966
1284-10	0.25	No	Yes	1148	1204	307	195	225	0.276
1283-5	0.25	No	Yes	1842	1204	236	176	209	0.502
1283-1	0.25	No	Yes	2565	1204	252	163	237	0.836
1092-1	0.25	Yes	No	932	1204	-	-	281	0.924
1089-4	0.25	Yes	No	1148	1204	-	-	230	0.693
1283-11	0.25	Yes	No	1842	1204	-	-	245	0.911
1283-4	0.25	Yes	No	1842	1204	-	-	282	0.938
1089-1	0.25	Yes	No	3497	1204	-	-	218	0.782
1092-5	0.25	Yes	No	3922	1204	-	-	237	0.664
1094-14	0.25	Yes	No	3922	1204	-	-	200	0.462
1092-8	0.76	No	No	932	1204	309	177	276	0.888
1094-3	0.76	No	No	932	1204	308	121	319	0.998
1092-3	0.76	No	No	1148	1204	284	161	272	0.922
12884-4	0.76	No	No	1842	1204	274	159	252	0.767
1283-8	0.76	No	No	1842	1204	256	142	200	0.337
1284-5	0.76	No	No	2990	1204	292	168	224	0.570

3.9.4.6 Recession Rate Measurement Summary

The CMC recession data obtained from the uncoated samples in rig run 8 was combined with the data obtained in rig runs 1 and 2 in order to determine the overall average measured recession rate during long-term rig exposure. Only samples with uniform SiC-Si or SiC surfaces were included in the analysis since the recession rates for such materials should be roughly equivalent. This requirement limited the samples to GEGR prepreg MI samples with unreinforced matrix surface layers or slurry cast MI composites with CVD SIC seal coatings. All of the appropriate long-term rig recession data are shown in Table 3-70 and plotted in Figure 3-300. The variation of recession with time is linear with a regression R^2 coefficient of 0.93. The mean recession rate of coupons in long-term combustion rig levels 2-4, which were exposed to combustion gas at approximately 1204°C, was 0.23mm per 1000h. The calculated recession rate under these conditions using the GEGR recession model is ~0.42mm per 1000 hr, in reasonable agreement with the observed rate given the uncertainties of gas velocity .

The combustion environment conditions for the samples exposed at ~1120°C, i.e. the first level of samples in the test rig, was somewhat ambiguous. The local gas chemistry in this region of the rig was not well defined because the combustion and dome plate cooling gases were not yet well mixed. Consequently, it is not possible to estimate the recession rate in this region from the GEGR model. The mean measured recession rate of coupons in combustor rig level 1, where the exposure temperature was approximately 1120°C, and under somewhat different flow conditions from the coupons in levels 2-4, was 0.084mm per 1000h.

Table 3-70. Summary of the Long-Term Combustion Rig CMC Measurements

Sample type*	Sample ID	Rig run #	Sample level	Exposure time (h)	Nominal Sample Temperature (°C)	Recession (mm)
Prepreg	688-10	1	1	500	1120	0.029
Prepreg	688-4	2	1	500	1120	0.075
SC-SiC	0971-02-001R	1 + 2	1	1000	1120	0.130
Prepreg	883-4	8	1	1148	1120	0.047
Prepreg	688-2	1	3	500	1204	0.151
Prepreg	688-8	2	3	500	1204	0.173
SC-SiC	0971-02-002C	2	2	500	1204	0.111
SC-SiC	0971-02-002E	1	3	500	1204	0.176
SC-SiC	0971-02-001D	1	2	500	1204	0.133
SC-SiC	0971-02-001P	1	4	500	1204	0.207
Prepreg	884-4	8	2	932	1204	0.142
Prepreg	688-3	1 + 2	4	1000	1204	0.261
Prepreg	688-9	1 + 2	2	1000	1204	0.230
SC-SiC	0971-02-002G	1 + 2	2	1000	1204	0.276
SC-SiC	0971-02-002D	1 + 2	4	1000	1204	0.233
SC-SiC	0971-02-002I	1 + 2	2	1000	1204	0.256
SC-SiC	0971-02-001I	1 + 2	2	1000	1204	0.315
SC-SiC	0971-02-001F	1 + 2	3	1000	1204	0.246
Prepreg	883-3	8	4	1148	1204	0.210
Prepreg	884-7	8	2	1148	1204	0.200
Prepreg	883-5	8	4	1417	1204	0.370
Prepreg	884-5	8	4	2080	1204	0.552
Prepreg	883-2	8	2	3497	1204	0.703
Prepreg	884-6	8	3	3497	1204	0.848

* SC-SiC refers to slurry cast MI composites with CVD SiC seal coatings on the surfaces.

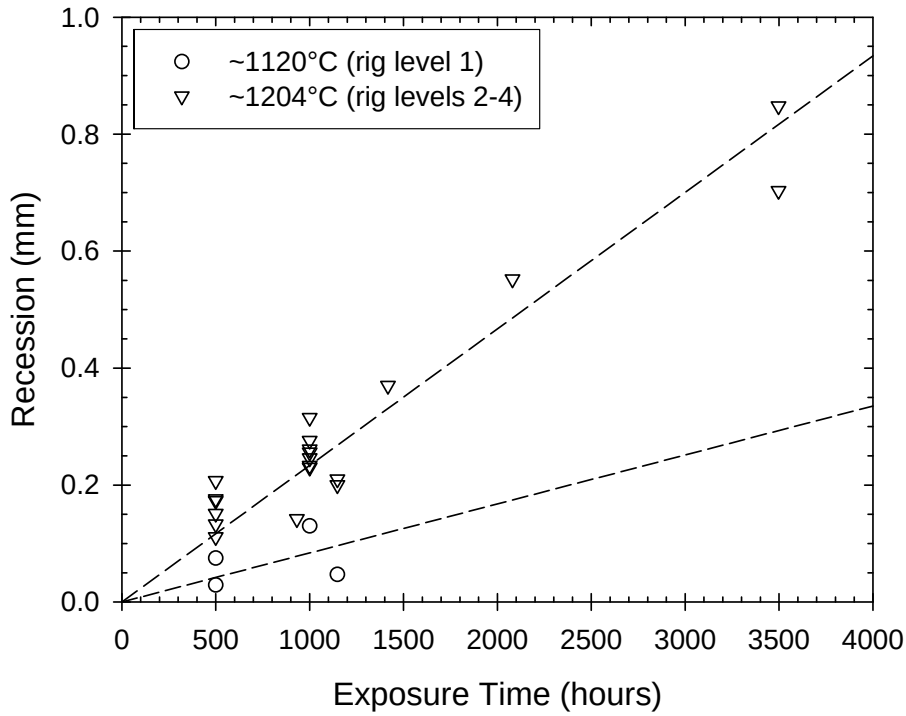

Figure 3-300. CMC recession as a function of exposure time in the long-term combustion rig.

4 SUMMARY AND CONCLUSIONS

Overall this program was considered to be a great success by GE. Considerable progress was made in the optimization of the MI composites based on CVD SiC monofilament reinforcing fibers. Unfortunately the carbon surface layers on the fibers that were needed to maintain high fiber strength also proved to be a fundamental flaw with that composite system. Nevertheless, should a new, oxidation resistant monofilament fiber be invented the technology developed on the monofilament fiber composites could be resurrected.

The development and optimization of the MI composite, based on fine diameter SiC fibers in tow form, was also highly successful. The GE prepreg MI approach has yielded CMC materials with the highest strain to failure, interlaminar strengths and thermal conductivities of any continuous fiber CMC material known, and all at a relatively modest fiber volume fraction of ~25%. This material system was repeatedly shown to be superior to other available CMC systems through detailed mechanical and oxidative stability tests, through the rig testing of shroud components, and by the exposure testing under turbine-like conditions in the long-term combustion rig.

The success of the material development efforts enabled GE to pursue rig testing of shroud and combustor liner components made from CMC material. These tests represented the first ever combustion rig testing of CMC components for a GE industrial turbine application. The success of these tests then lead to GE first ever industrial gas turbine engine test of CMC shroud components in a GE-2 engine.

While highlights of the program are mentioned above, numerous important milestones were successfully completed during the performance of this program. Several of the more important accomplishments are listed below. Important developments in the material system or fabrication process, or in the understanding of how to characterize and utilize these materials, that continue to have impact on GE's CMC development efforts are highlighted in bold text.

- Successful fiber coating systems for Textron SCS-0 and SCS-Ultra first pass fibers were demonstrated.
- A continuous coating process for Si_3N_4 on monofilament fibers was developed in cooperation with Textron.
- A new matrix composition was demonstrated for use with monofilament fiber reinforced MI composites.
- The effects of boron additions on the reaction between C and Si were investigated.
- Detailed interface oxidation studies of monofilament-reinforced MI CMCs clearly demonstrated the negative consequences that carbon surface layers on the fibers have on composite oxidation life.
- **The design and fabrication of tough composite joints in both monofilament-reinforced and fiber tow-reinforced MI CMCs was demonstrated.**
- The developed new matrix composition and composite joining technology allowed for the successful fabrication of the Phase 1 "ashtray" shroud design using the monofilament-reinforced composite system.

- **The CVD coating of fine diameter, tow-based fibers, such as Hi-Nicalon™, was investigated with four separate coating vendors: Advanced Ceramics Corp., 3M, Synterials, Inc., and General Atomics. Fiber coatings from Synterials, 3M and Advanced Ceramics Corp. were all shown to be capable of producing strong, tough MI composites. The performance of coatings from ACC were the most consistent, and consequently were developed and optimized to a greater degree than fiber coatings from the other vendors.**
- **A continuous tow coating process was developed at GEGR to handle multiple tows in a compact reactor. This CVD reactor was used to further optimize the fiber coating configuration and composition.**
- The silicon-doped boron nitride fiber coatings were developed, first with ACC and later optimized using the GEGR reactor, that were demonstrated to yield composites with improved oxidation resistance.
- A larger scale tow coater was subsequently designed and built at GEGR, having 5X the capacity of the small coater and 2X the capacity of ACC's production reactor. The fiber coating process in this reactor was developed to the point where it was giving comparable quality composites as the smaller tow coater.
- **A composite fabrication process, based on the prepregging of coated fiber tow, was developed and optimized. This composite system provides the highest mechanical properties for a given level of reinforcing fiber, as well as the highest overall thermal conductivity and interlaminar strength properties, of any CMC system we are aware of.**
- Three matrix composition variations were developed for the prepreg MI system with fiber tow and the effects of these variations on the composite mechanical properties was evaluated.
- The mechanical and thermal properties of the prepreg MI composite system with the "standard" matrix system were extensively characterized, including measurements of the fast fracture properties, thermal stability, fatigue, creep, thermal cycling resistance, thermal conductivity and thermal expansion. This effort provided a valuable material property database for component designers to work from.
- Detailed mechanical characterization of Goodrich Aerospace slurry cast MI composites was performed.
- **Methodology for testing CMC materials under high water vapor (i.e. steam) atmospheres was developed. Such cyclic steam furnace exposure testing proved to be highly valuable in screening CMC material candidates for use in gas turbine environments, for validating SiO_2 volatilization rate models, and for identifying CMC degradation mechanisms related to steam exposure.**
- **A methodology for evaluating the "foreign object damage" susceptibility of the CMC materials, based on ballistic impact testing, was developed and utilized to evaluate the damage initiation and damage propagation properties of CMC materials.**
- **The effects of 2-D fiber architectures on the elastic and mechanical properties of the prepreg MI composites were determined.**

- **Deposition of an Environmental Barrier Coating (EBC) system, utilizing a Celsian Barium-Strontium AlminoSilicate (BSAS) top coat, was demonstrated on GE's prepreg MI composite system.**
- Bond coat oxidation and impact damage studies of the EBC system were conducted for prepreg MI and slurry cast MI composite systems.
- The process economics of using the GE prepreg MI and the slurry cast MI processes were evaluated for the production of CMC shroud components.
- A preliminary shroud design was developed that had reduced stresses and improved manufacturability over the conceptual design developed in Phase 1.
- CMC inner shroud components were fabricated to the preliminary design using two GE prepreg MI composite variations. Shrouds of the slurry cast MI variety were also purchased from DuPont-Lanxide Composites (now GE Energy Ceramic Composite Products) and from Goodrich Aerospace. CVI SiC-SiC and DIMOX shrouds were also produced by DuPont-Lanxide Composites under their CFCC contract and turned over to GEGR for rig testing. Overall 33 CMC inner shroud components were fabricated for this program.
- All of the CMC shroud components underwent pre-test nondestructive evaluations and characterization of witness coupons.
- A combustion test rig, capable of operating at similar pressures and higher temperatures than those seen in a GE 7FA class engine, was designed and fabricated at GEGR. The rig was capable of testing four CMC shrouds, a CMC combustor liner, and up to 24 CMC test coupons to high temperature, high pressure and high gas velocity conditions simultaneously.
- The shroud test rig was operated for over 300 hours of hot component testing, with 27 CMC and 2 metal shrouds being exposure tested.
- Post rig test nondestructive and destructive characterization was done on most of the rig-tested shrouds, and the changes in shroud mechanical properties and microstructures were evaluated.
- **Shroud exposure data accumulated through the rig testing indicated that the GE prepreg MI composite system performed the best in this application, showing little to no degradation in material properties as a result of the rig tests.**
- Seven different NDE techniques were evaluated as to their applicability to the CMC shroud components and sensitivity to a shroud defect.
- The design process for a third generation CMC shroud was started under the CFCC program, but was then transitioned to the DOE-sponsored Advanced Materials for Advanced Industrial Gas Turbines program.
- A conceptual design for a CMC combustor system for a GE Frame 5 (35 MW) engine was developed.
- A rig test combustor liner configuration was developed, based on the combustor conceptual design, that was capable of testing two sections of CMC liner simultaneously.
- An innovative method of attaching and sealing the combustor liner to the metallic support structure, utilizing a set of nested metallic rings, was developed.

- A prepreg MI combustor liner was fabricated at GEGR, and a slurry cast MI liner was fabricated by GE CCP (then known as Allied Signal Composites).
- **The CMC combustor liners were successfully rig tested for 150 hours of hot exposure, both under cooled and uncooled conditions.**
- Designs for both stage 2 and stage 1 shroud rings for a GE Oil and Gas GE-2 engine (then known as Nuovo Pignone PGT-2) were designed and analyzed.
- First and second stage shroud rings were fabricated at GEGR using the GE prepreg MI composite system.
- Preliminary engine testing of each shroud ring was carried out for >100 hours of engine running time.
- Both shrouds experienced blade tip rub events during the preliminary testing without any damage being caused to the CMC shroud rings. The survival of the shroud rings through such an event dramatically demonstrated the durability and damage resistance of the CMC material.
- **During these preliminary tests the attachment and location features of the stage 2 shroud were modified, and the improved performance of the modified attachment was verified with additional instrumented engine tests.**
- **Both the second and first stage shroud rings were subsequently engine exposure tested for an additional 900 hours, giving total engine exposure times of over 1000 hours.**
- **Post-test characterization of the second stage shroud ring showed that material properties, even in regions where the blade tip rubs had occurred, were largely unaffected by the engine exposure.**
- **A unique, long-term test facility for exposing coupon samples to a high pressure, high velocity, combustion gas environment was designed and constructed at GEGR. This facility is highly automated and capable of safe, extended operation without operator intervention. The durability of the rig was maximized through the utilization of an all-CMC hot section.**
- Eight sets of combustion rig tests were performed, totaling roughly 6500 hours of test rig fired hours. Several individual test samples were exposed for up to 3922 hours.
- Post-exposure characterization of the coupons from the long-term exposure rig provided valuable information about the thermal and oxidative stability of bare and EBC-coated CMC samples.
- GEGR's SiO_2 volatilization model was further verified by the measurements of surface recession of CMC samples from this test rig.

At the outset of the CFCC program there was considerable skepticism within GE Energy regarding the fitness and utility of CMC turbine components. Much of this skepticism was based on a poor perception of the toughness of ceramics in general, and was partly justified based on the state of CMC material development at the time the program was initiated. However, with DOE's support, GE was able to develop and optimize the melt infiltrated CMC material, and to demonstrate conclusively that it was capable of surviving for up to several thousand hours in turbine-like conditions. The successes of the shroud and combustor component rig tests, and the shroud engine tests, dispelled much of the

skepticism within the turbine design community at GE. Toward the end of the program the success of the CMC materials had been demonstrated to such an extent that the design of the long-term combustion rig utilized CMC components extensively in order to ensure rig durability. The acceptance of CMC technology at GE Energy was demonstrated by the willingness of that organization to participate in the AMAIGT program and eventually push the CMC shroud to a field engine test in an F-class (160MW) engine, which was the first ever test of a ceramic component in a GE industrial turbine. GE's commitment to the technology has been further demonstrated by the acquisition of Honeywell Advanced Ceramics, Inc. and the incorporation of this business within GE Energy as GE Ceramic Composite Products, LLC.

Undoubtedly much work remains to be done to bring the CMC turbine components to final commercial introduction. Nevertheless, the support of DOE through the CFCC program has been instrumental in bringing GE this far in the development of this technology, and is partly responsible for the commercial availability of HiPerComp® composites.

The program has also been highly successful in disseminating information about the fabrication and use of CMC materials. Patents, presentations and publications related to the work performed on this CFCC program are listed in the Appendix. These publications are in addition to the numerous workshops and contractor meetings sponsored by DOE where program updates were discussed with the broader CMC development community.

5 ACKNOWLEDGEMENTS

This work was performed under Phase II of the U.S. Department of Energy Continuous Fiber Ceramic Composite (CFCC) program, contract number DE-FC26-92CE41000 (a revision of contract DE-FC02-92CE41000). The support of DOE and the contributions of the Contract Monitors, J. Mavec, P. Bakke, and D. Geiling, and of Program Mangers Debbie Haught, Merrill Smith and Scott Richlen are greatly appreciated.

The contractor team consisted of GE Global Research Center (formerly known as GE Corporate Research and Development), GE Energy (formerly known as GE Industrial and Power Systems–Power Generation Systems Division), Textron Specialty Materials, Inc., and Carborundum Co. Other organizations that contributed significantly to the program include Advanced Ceramics Corp. (now part of GE Specialty Materials), GE Ceramic Composite Products (formerly known as Allied Signal Composites, Inc. and as Honeywell Advanced Composites, Inc.), and Goodrich Corporation – SuperTemp Division. The authors would like to acknowledge the contributions of the following individuals: P. Meschter, M. Brun, M. Wotton, K. McEvoy, W. Minnear, W. Morrison, C. Montanaro, H. McGuigan, G. Buczkowski, L. Szala, D. VanUithuizen, A. Barbuto, R. Schnoor, E. Whitemore, A. Dean, K. McManus, K. Ryan, S. Brabetz, J. Hibshman, M. Roos, S. Brzozowski, P. Breslin, M. Hedrick-Villa and G. Battista of GE Global Research, P. Dimascio, R. Orenstein, M. Schroder, S. Shirzad, M. Mirdamadi, C. Grace, K. Bruce and H. Roberts of GE Energy, B. Thomson and R. Krutenat of Textron Specialty Materials, A. Moore of Advanced Ceramics Corporation, P. Craig, D. Landini and H. Wang of GE Ceramic Composite Products, R. Hines and S.K. Lau of Goodrich Corporation, R. Engdahl of Synterials, Inc., K. More, E. Lara-Curzio and P. Tortorelli of Oak Ridge National Laboratory, and W. Ellingson and J.G. Sun of Argonne National Laboratory.

6 LIST OF FIGURES

7 LIST OF TABLES

8 LIST OF ACRONYMS

ACC	Advanced Ceramics Corp., now a part of GE Advanced Materials
AES	Auger electron spectroscopy
AMAIGT	Advanced Materials for Advanced Industrial Gas Turbines
ANL	Argonne National Laboratory
ANSYS	Name for a particular finite element modeling code and for the company that produces that code
APS	Air plasma spray
ASME	American Society of Mechanical Engineers
BSAS	Barium strontium aluminosilicate
B(Si)N	Silicon-doped boron nitride
CCP	Ceramic Composite Products; a division of GE Energy
CFCC	Continuous Fiber Ceramic Composite (refers to the DOE-sponsored program)
CFD	Computational fluid dynamics
CMC	Ceramic matrix composite
CMM	Coordinate measuring machine
CT	Computed tomography; a methodology of x-ray imaging
CTA	Composite Testing and Analysis
CTE	Coefficient of thermal expansion
CTL	Cincinnati Testing Labs
CVD	Chemical vapor deposition
CVI	Chemical vapor infiltration
DIMOX™	Directed metal oxidation; refers to a process for making oxide ceramics or composites or to the materials produced by this process
DLN	Dry low NOx
DOE	U.S. Department of Energy
DoE	Design of experiments
EBC	Environmental barrier coating
EDS	Energy dispersive s-ray spectroscopy
EPM	Enabling Propulsion Materials; a part of the HSCT program
FEM	Finite element modeling
FOD	Foreign object damage
FPI	Fluorescent penetrant inspection
GA	General Atomics
GE	General Electric Company

GEAE	GE Aircraft Engines; now known as GE Aviation
GEE	GE Energy
GEGR	GE Global Research; previously known as GE Corporate Research and Development
GEL	GE Lighting
GEPS	GE Power Systems; a division of GE Energy
GE-2	2MW gas turbine engine fabricated by GE Oil&Gas
HCF	High cycle fatigue; a specific type of fatigue testing
HGS	High green strength; refers to a particular formulation of the GE prepreg MI composite matrix
HSCT	High Speed Civil Transport
HS-188	A cobalt-based superalloy invented by Haynes International
HTF	Hold time fatigue; a specific type of fatigue testing
ID	Inner diameter
IHPTET	Integrated High Performance Turbine Engine Technology
ILS	Interlaminar shear
ILT	Interlaminar tension
IR	Infrared
JETS	Jet engine thermal shock; a type of thermal fatigue testing
LCF	Low cycle fatigue; a particular type of fatigue testing
LHE	Lean head end; a type of combustor liner design
LVDT	Linear variable differential transformer
MCL	Materials Characterization Lab
MI	Melt infiltration or melt infiltrated (refers to the process or to the class of materials)
NASA	National Aeronautics and Space Administration
NDE	Nondestructive evaluation
NOx	Oxides of Nitrogen
NP	Nuovo Pignone; currently known as GE Oil and Gas
OD	Outer diameter
ORNL	Oak Ridge National Laboratory
O&G	Oil and Gas; a division of GE Energy based in Florence, Italy; previously known as Nuovo Pignone
RT	Room temperature; ~23°C
SCS	Trade name for SiC monofilament fibers from Textron Specialty Materials
SEM	Scanning electron microscope
TBC	Thermal Barrier Coating
TEM	Transmission electron microscope

TSM	Textron Specialty Materials
UDRI	University of Dayton Research Institute
UFP	“Ultra First Pass”; designation for a specific type of SCS fiber
UHC	Unburned Hydrocarbons
UT	Ultrasound transmission
XPS	X-ray Photoelectron Spectroscopy

9 REFERENCES

1.. "Continuous Fiber Ceramic Composite Benefit Analysis," DOE OIT report, 1993.

2. D.E. Brandt, **Mechanical Engineering**, 28 (July, 1987).

3. G.S. Corman, K.L. Luthra, M.K. Brun and P.J. Meschter, "Toughened Silcomp Composites for Gas Turbine Engine Applications," DOE report DOE/CE/41000-2, July 1994.

4. R. Eldrid, E. Brambani, R. Goetze and J. Palko, "Continuous Fiber Ceramic Composite (CFCC) Program Phase I; Task 1: Applications Assessment," DOE report DOE/CE/41000-01, August 1993.

5. Opila, E.J. and Hann, R.E., "Paralinear Oxidation of CVD SIC in Water Vapor," *J. Am. Ceram. Soc*., Vol 80 (1), pp. 197-205, 1997.

6. Opila, E.J., Fox, D.S. and Jacobson, N.S., "Mass Spectrometric Identification of Si-O-H(g) Species from the Reaction of Silica with Water Vapor at Atmospheric Pressure," *J. Am. Ceram. Soc*., Vol 80 (4), pp. 1009-1012, 1997.

7. R.E. Tressler and J.A. DiCarlo, "High Temperature Properties of Advanced Ceramic Fibers", in **High Temperature Ceramic Matrix Composites, Proceedings of the 6th European Conferenc on Composite Materials**, Woodhead Publishing, 1994.

8. M.Sutcu, "A Recursive Concentric Cylinder Model For Composites Containing Coated Fibers," *Int. J. Solids Structures*, Vol.29, No.2, pp.197-213, 1992.

9. A.W. Moore, "Facility for Continuous CVD Coating of Ceramic Fibers," Mater. Res. Symp. Proc. Vol. 250, 269-274 (1992).

10. T. Matsuda, "Stability to Moisture for Chemically Vapour-Deposited Boron Nitride," *J. Mater. Sci.*, **24**, 2353-57 (1989).

11. C.G. Cofer and J. Economy, "Oxidative and Hydrolytic Stability of Boron Nitride – A New Approach to Improving the Oxidation Resistance of Carbonaceous Structures," *Carbon*, **33** [4] 389-95 (1995).

12. N.S. Jacobson, G.N. Morscher, D.R. Bryant and R.E. Tressler, "High-Temperature Oxidation of Boron Nitride: II, Boron Nitride Layers in Composites," *J. Am. Ceram. Soc.*, Vol 82 (6), pp. 1473-1482 (1999).

13. A.W. Moore, M.B. Dowell, E.R. Stover and L.D. Bentsen, “Oxidation Protection of Carbon-Carbon Composites by (B+Si)N Coatings,” *Ceram. Eng. Sci. Proc*., Vol 16 (4), pp. 263-270 (1995).

14. A.W. Moore, H. Sayir, S.C. Farmer and G.N. Morscher, “Improved Interface Coatings for SiC Fibers in Ceramic Composites,” *Ceram. Eng. Sci. Proc*., Vol 16 (4), pp. 409-416 (1995).

15. A.W. Moore and M.B. Dowell, “Interface Coating for Ceramic Fibers,” US Patent 5,593,728, Jan. 14, 1997.

16. N. Patibandla and K.L. Luthra, "Chemical Vapor Deposition of Boron Nitride," ***J. Electrochem. Soc.***, 139 (1992) pp. 3558-65.

17. M. K. Brun, “Formation of Tough Composite Joints,” *J. Am. Ceram. Soc*., 81 (12) 3307-3312 (1998).

18. N. Bansal, “SiC Fiber-Reinforced Celsian Composites,” in **Handbook of Ceramic Composites**, N.P. Bansal ed., Kluwer Academic, Boston, 2005, pp. 227-249.

19. B. E. Deal and A. S. Grove, “General Relationship for the Thermal Oxidation of Silicon,” *J. Appl. Phys.*, vol. 36, pp. 3770-3778, 1965.

20. H.E. Eaton, G.D. Linsey, E.Y. Sun, K.L. More, J.B. Kimmel, J.R. Price, and N. Miriyala, “EBC Protection of SiC/SiC Composites in the Gas Turbine Combustion Environment - Continuing Evaluation and Refurbishment Considerations,” paper #2001-GT-0513 presented at the ASME Turbo Expo, June 4-7, 2001, New Orleans, La.

21. D. Singh, et al., *J. Am. Ceram. Soc*., 79(3) 591-96 (1996).

10 APPENDIX. PUBLIC DOCUMENTATION

10.1 Patents Granted or Applied For

1. U.S. Patent 5,952,100, “Silicon-Doped Boron Nitride Coated Fibers in Silicon Melt Infiltrated Composites,” G.S. Corman and K.L. Luthra, Sep. 14, 1999.
2. U.S. Patent 6,113,349, “Turbine Assembly Containing an Inner Shroud,” B.S. Bagepalli, G.S. Corman, A.J. Dean, P.S. DiMascio, M. Mirdamadi, Sep. 5, 2000.
3. U.S. Patent 6,168,827, “Fiber Coating Method,” G.S. Corman, Jan. 2, 2001.
4. U.S. Patent 6,315,519, “Turbine Inner Shroud and Turbine Assembly Containing Such Inner Shroud,” B.S. Bagepalli, G.S. Corman, A.J. Dean, P.S. DiMascio, M. Mirdamadi, Nov. 13, 2001.
5. U.S. Patent 6,365,233, “Silicon-Doped Boron Nitrid Coated Fibers In Silicon Melt Infiltrated Composites,” G.S. Corman and K.L. Luthra, April 2, 2002.
6. U.S. Patent 6,403,158, “Porous Body Infiltration Method,” G.S. Corman, June 11, 2002.
7. U.S. Patent 6,503,441, “Method for Producing Melt-Infiltrated Ceramic Composites Using Formed Supports,” G.S. Corman, M.K. Brun and H.C. McGuigan, Jan. 7, 2003.
8. U.S. Patent 6,517,341, “Method To Prevent Recession Loss Of Silica And Silicon-Containing Materials In Combustion Gas Environments,” M.K. Brun and K.L. Luthra, Feb. 11, 2003.
9. U.S. Patent 6,548,130, “Fiber Coating Method,” G.S. Corman, April 15, 2003.
10. U.S. Patent 6,910,853 B2, “Structures For Attaching Or Sealing A Space Between Components Having Different Coefficients Or Rates Of Thermal Expansion,” G.S. Corman, A.J. Dean, L. Tognarelli and M. Pecchioli, June 28, 2005.
11. U.S. Patent Application 11/263175, “Processing Of Ceramic Matrix Composites Using Fiber Ribbons,” M.K. Brun, K.L. Luthra, H.C. McGuigan, G.S. Corman, filed Nov. 11, 2005.
12. U.S. Patent Application, “Use and Application of Protective Surface Plies On Melt Infiltrated Ceramic Matrix Composites,” G.S. Corman, M.K. Brun and H.C. McGuigan, filed Nov. 25, 2005.
13. U.S. Patent Application, “Improved lay-Up Method for Prepreg Ceramic Matrix Composites,” G.S. Corman and H.C. McGuigan, filed Nov. 27, 2005.

10.2 Publications

1. “Toughened Silcomp Composites," M.K. Brun, G.S. Corman, P.J. Meschter, and K.L. Luthra, Proceedings 18th Annual Conference on Composites, Materials and Structures, Cocoa Beach, Florida, January 13, 1994.
2. "Toughened Silcomp for Gas Turbine Engine Applications," G.S. Corman, M.K. Brun, P.J. Meschter, K.L. Luthra, and R. Eldrid, **Proceedings of the 39th International SAMPE Symposium and Exhibition**, April 11-14, 1994, Anaheim California.

3. "Improved Properties of Gas Turbine Engine Components Utilizing CFCC and Melt Infiltration," G. Corman and K. Luthra, **Industrial Heating**, 39-40, December 1996.
4. "Ceramic Composites for Industrial Gas Turbine Engine Applications: DOE CFCC Phase 1 Evaluations," G.S. Corman, J.T. Heinen and R.H. Goetze, ASME conference proceedings paper 95-GT-387, presented at the International Gas Turbine and Aeroengine Congress and Exposition, Houston, Texas, June 5-8, 1995.
5. "SiC Fiber Reinforced SiC-Si matrix composites prepared by melt infiltration (MI) for Gas Turbine Engine Applications," G.S. Corman, M.K. Brun and KL. Luthra, ASME conference proceedings paper no. 99-GT-234 presented at the International Gas Turbine & Aeroengine Congress & Exhibition, Indianapolis, Indiana, June 7 - 10, 1999
6. "Design and Testing of CFCC Shroud and Combustor Components," A.J. Dean, G.S. Corman, B. Bagepalli, K.L. Luthra, P.S. DiMascio and R.M. Orenstein, ASME conference proceedings paper no. 99-GT-235 presented at the International Gas Turbine & Aeroengine Congress & Exhibition, Indianapolis, Indiana, June 7 - 10, 1999
7. "Rig and Engine Testing of Melt Infiltrated Ceramic Composites for Combustor and Shroud Applications," G.S. Corman, A.J.Dean, S. Brabetz, M.K. Brun, K.L. Luthra, L. Tognarelli and M. Pecchioli, ASME conferenc proceeding paper no. 2000-GT-0638, presented at the 45th ASME Gas Turbine and Aeroengine Technical Congress, Munich, Germany, May 8-11, 2000.
8. "Silicon Melt-Infiltrated Ceramic Composite for Gas Turbine Engine Applications," R.M. Orenstein, M.S. Schroder, G.S. Corman, and K.L. Luthra, in **Proceedings of PowerGen International 2000**, Orlando, Florida, November 14-16, 2000.
9. "Rig and Gas Turbine ENGINE Testing of MI-CMC Combustor and Shroud Components, " G.S. Corman, A.J. Dean, S. Brabetz, K. McManus, M.K. Brun, P.J. Meschter, K.L. Luthra, H. Wang, R. Orenstein, M. Schroder, D. Martin, R. De Stefano and L. Tognarelli, paper no. 2001-GT-593 presented at the 46th ASME Gas Turbine and Aeroengine Technical Congress (ASME Turbo Expo, Land, Sea & Air) New Orleans, LA, June 4-7, 2001.
10. "Melt Infiltrated (MI) SiC/SiC Composites for Gas Turbine Applications," K.L. Luthra and G.S. Corman, in **High Temperature Ceramic Matrix Composites**, W. Krenkel, R. Naslain and H. Schneider, eds., Wiley/VCH, Weinheim, FRG, 2001, pp. 744-53.
11. "Rig and Engine Testing of Melt Infiltrated Cermic Composites for Combustor and Shroud Applications," G.S. Corman, A.J. Dean, S. Brabetz, M.K. Brun, K.L. Luthra, L. Tognarelli and M. Pecchioli, **Transactions of the ASME - Journ. Eng. for Gas Turbines and Power**, vol. 124, Issue 3, July 2002.
12. "Ceramic Gas Turbine Programs at GE Power Systems," P.S. DiMascio, R.M. Orenstein, M.S. Schroder, L. Tognarelli, G.S. Corman and A.J. Dean, in **Ceramic Gas Turbine Design and Test Experience: Progress in Ceramic Gas Turbine Development, Vol. 1,** edited by Mark van Roode, Mattison K. Ferber, and David W. Richerson, ASME Press, New York, USA, 2002.
13. "Silicon Melt Infiltrated Ceramic Composites – Processes and Properties," G.S. Corman, K.L. Luthra, and M.K. Brun, in **Progress in Ceramic Gas Turbines Volume II: Ceramic Gas Turbine Component Development and Evolution: Fabrication, NDE, Testing, and Life Prediction**, M. van Roode, M. Ferber and D. Richerson, Editors, ASME PRESS, New York, USA, 2003.

14. “Silicon Melt Infiltrated Ceramic Composites (HiPerComp®)” G.S. Corman and K.L. Luthra, in **Handbook of Ceramic Composites,** edited by N.P. Bansal, Kluwer Academic Publishers, Boston, MA, 2005, pp99-116.

10.3 Technical Presentations

1. “Toughened Silcomp Composites," M.K. Brun, G.S. Corman, P.J. Meschter, and K.L. Luthra, Presented at the 18th Annual Conference on Composites, Materials and Structures, Cocoa Beach, Florida, January 13, 1994.
2. "Development of Toughened Silcomp Ceramic Composites for Gas Turbined Engine Applications," G.S. Corman, K.L.Luthra, M.K. Brun, and P.J. Meschter, presented at the 97th Annual Meeting of the American Ceramic Society, Cincinnati, Ohio, April 30 - May 3, 1995.
3. "Ceramic Composites for Industrial Gas Turbine Engine Applications: DOE CFCC Phase 1 Evaluations," G.S. Corman, J.T. Heinen and R.H. Goetze, presented at the International Gas Turbine and Aeroengine Congress and Exposition, Houston, Texas, June 5-8, 1995.
4. “SiC Fiber Reinforced SiC-Si Matrix Composites,” G.S. Corman, M.K. Brun, K.L. Luthra, J. Steibel and T. Dunyak, presented at the 2nd International Conference on High Temperature Ceramic Composites, Santa Barbara, CA, Aug. 22, 1995.
5. “Toughened Silcomp (SiC-Si) Composites from a Pre-Preg and Lamination Approach," G.S. Corman, K.L. Luthra, J.D. Steibel and T.J. Dunyak, presented at the 1996 Conference & Exposition on Composites, Advanced Ceramics, Materials and Structures, Cocoa Beach, FL, January 7-11, 1996.
6. "Toughened Silcomp (SiC-Si) Composites for Gas Turbine Engine Applications: CFCC Phase 2 Status," G.S. Corman, K.L. Luthra and M.K. Brun, presented at the 20th Annual Conference on Composites, Materials and Structures, Cocoa Beach, FL, January 23-25, 1996.
7. "Environmental Stability of Fiber Coatings in SiC Monofilament Reinforced Toughened Silcomp Composites," G.S. Corman and K.L. Luthra, presented at the 21st Annual Conference on Composites, Materials and Structures, Cocoa Beach, FL, January 26-31, 1997.
8. "Joining of Toughened Silcomp Composites," M.K. Brun, W.A. Morrison and G.S. Corman, presented at the 21st Annual Conference on Composites, Materials and Structures, Cocoa Beach, FL, January 26-31, 1997.
9. "Oxidation-Resistant Fiber Coatings for Non-Oxide Ceramics Composites," K.L. Luthra, J. Am. Ceram. Soc., 80 (1997), pp. 3253-57.
10. “Toughened Silcomp: Material Development Status,” G.S. Corman, K.L. Luthra and M.K. Brun, presented at the 22nd Annual Conference on Composites, Materials and Structures, Cocoa Beach, FL, January 20-24, 1998.
11. “Combustion Rig Testing of CFCC Shrouds and Combustor Liners”, P.S. DiMascio, M. Mirdamadi, A.J. Dean, G.S. Corman, K.L Luthra, P.A. Craig and P.A. Stopera, presented at the 22nd Annual Conference on Composites, Materials and Structures, Cocoa Beach, FL, January 20-24, 1998

12. “Prepreg Melt Infiltration (MI) Composites – A Status Report,” G.S. Corman and K. Luthra, presented at the 23rd annual Conference on Composites, Materials and Structures, Cocoa Beach, FL, January 25-28, 1999.
13. “High Pressure Rig Testing of CFCC Combustor and Shroud Components,” A.J. Dean, G.S. Corman, K.L. Luthra, R. Orenstein and P. DiMascio, presented at the 23rd annual Conference on Composites, Materials and Structures, Cocoa Beach, FL, January 25-28, 1999.
14. “Oxidation of SiC-Based CMC’s in Water Vapor Containing Environments,” M.K. Brun, G.S. Corman and K.L. Luthra, presented at the 23rd annual Conference on Composites, Materials and Structures, Cocoa Beach, FL, January 25-28, 1999.
15. “SiC Fiber Reinforced SiC-Si matrix composites prepared by melt infiltration (MI) for Gas Turbine Engine Applications,” G.S. Corman, M.K. Brun and KL. Luthra, paper no. 99-GT-234 presented at the International Gas Turbine & Aeroengine Congress & Exhibition, Indianapolis, Indiana, June 7 - 10, 1999
16. “Design and Testing of CFCC Shroud and Combustor Components,” A.J. Dean, G.S. Corman, B. Bagepalli, K.L. Luthra, P.S. DiMascio and R.M. Orenstein, paper no. 99-GT-235 presented at the International Gas Turbine & Aeroengine Congress & Exhibition, Indianapolis, Indiana, June 7 - 10, 1999
17. “Silicon-Doped Boron Nitride Fiber Coatings for Melt Infiltrated Composites,” G.S. Corman and K.L. Luthra, presented at the 24th annual Conference on Composites, Materials and Structures, Cocoa Beach, FL, January 24-28, 2000.
18. “Processing and High Pressure Combustion Rig Testing of Melt Infiltrated SiC/Si Composites,” G.S. Corman, K.L. Luthra, A.J. Dean, S. Brabetz, A. Kebbede, P.S. DiMascio and R.M. Orenstein, presented at the 24th annual Conference on Composites, Materials and Structures, Cocoa Beach, FL, January 24-28, 2000.
19. “Degradation of Mechanical Properties of SiC/SiC Composites by High-Temperature Environmental Exposures,” P.J. Meschter, M. Brun, G.S. Corman and K. L. Luthra, presented at the 24th annual Conference on Composites, Materials and Structures, Cocoa Beach, FL, January 24-28, 2000.
20. “Reduced NOx Diffusion Flame Combustors for Industrial Gas Turbines,” A.S. Feitelberg, V.E. Tangirala, R.A. Elliott, R.E. Pavri and R.B. Schiefer, paper No. 2000-GT-0085, presented at the 45th ASME Gas Turbine and Aeroengine Technical Congress (ASME Turbo Expo), Munich, Germany, May 8-11, 2000.
21. “Rig and Engine Testing of Melt Infiltrated Ceramic Composites for Combustor and Shroud Applications,” G.S. Corman, A.J.Dean, S. Brabetz, M.K. Brun, K.L. Luthra, L. Tognarelli and M. Pecchioli, paper no. 2000-GT-0638, presented at the 45th ASME Gas Turbine and Aeroengine Technical Congress (ASME Turbo Expo), Munich, Germany, May 8-11, 2000.
22. “Silicon Melt-Infiltrated Ceramic Composite for Gas Trubine Engine Applications,” R.M. Orenstein, M.S. Schroder, G.S. Corman and K.L. Luthra, Paper 00157 presented at Power Gen International, Orlando, FL, Nov. 14-16, 2000.
23. "Engine and High Pressure Combustion Rig Testing of of MI SiC/SiC-Si Composites," G.S. Corman, K.L. Luthra, A.J. Dean, S. Brabetz, P. Meschter, R. De Stefano and L. Tognarelli, presented at the 25th Annual Conferenc on Composites, Materials and Structures, Cocoa Beach FL, Jan. 22-25, 2001.

24. “Life Prediction for SiC/Sic Composites, Issues and Approaches”, K. L. Luthra, 24th Annual Conference on Composites, Materials, and Structures, Cocoa Beach, Florida, January 22-25, 2001
25. "Rig and Gas Turbine ENGINE Testing of MI-CMC Combustor and Shroud Components, " G.S. Corman, A.J. Dean, S. Brabetz, K. McManus, M.K. Brun, P.J. Meschter, K.L. Luthra, H. Wang, R. Orenstein, M. Schroder, D. Martin, R. De Stefano and L. Tognarelli, paper no. 2001-GT-593 presented at the 46th ASME Gas Turbine and Aeroengine Technical Congress (ASME Turbo Expo, Land, Sea & Air) New Orleans, LA, June 4-7, 2001.
26. “Melt Infiltrated CMCs for Gas Turbine Engine Applications,” G.S. Corman, K.L. Luthra, K.R. McManus, P.J. Meschter, M.K. Brun, D. Mitchell, M.S. Schroder, and H. Wang, presented at the 26th Annual Conference on Composites, Materials and Structures, Cocoa Beach, FL, Jan. 28 – Feb 1, 2002.Annual Conference on Composites, Materials and Structures, Cape Canaveral, FL, Jan. 27-30, 2003. “Melt Infiltrated CMC Gas Turbine Shroud Development and Testing,” G. Corman, K. Luthra, D. Mitchell, P. Meschter, R. Nimmer, K. Bruce, D. Landini,